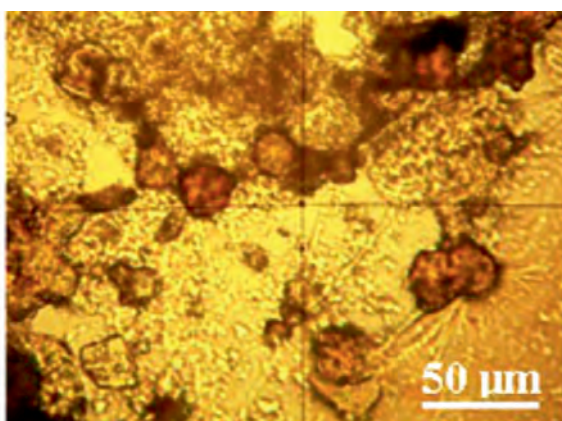
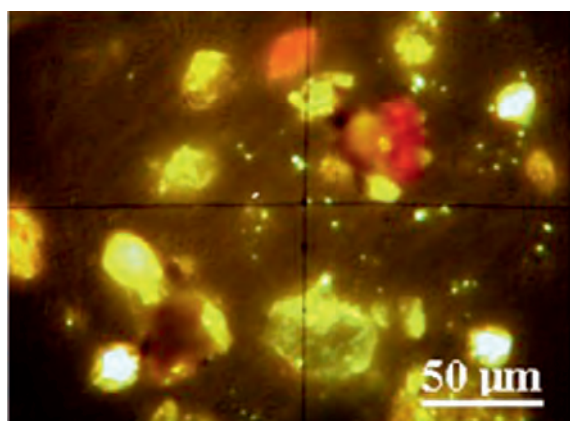
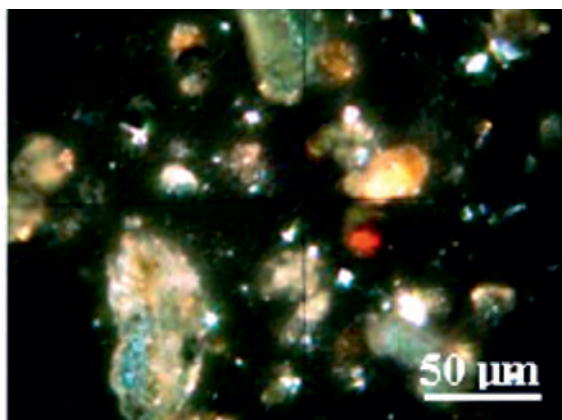
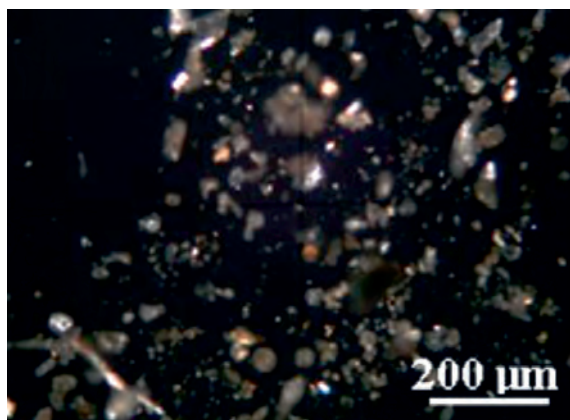




STUDIA UNIVERSITATIS
BABEŞ-BOLYAI



CHEMIA

4/2017
Tom I

**STUDIA
UNIVERSITATIS BABEȘ-BOLYAI
CHEMIA**

**4/2017
Tom I**

EDITORIAL BOARD OF STUDIA UNIVERSITATIS BABEȘ-BOLYAI CHEMIA

ONORARY EDITOR:

IONEL HAIDUC - Member of the Romanian Academy

EDITOR-IN-CHIEF:

LUMINIȚA SILAGHI-DUMITRESCU

EXECUTIVE EDITORS:

CASTELIA CRISTEA

AURORA MOCANU

MARIA TOMOAI COTIȘEL

EDITORIAL BOARD:

PAUL ȘERBAN AGACHI, Babeș-Bolyai University, Cluj-Napoca, Romania

LIVAIN BREAU, UQAM University of Quebec, Montreal, Canada

HANS JOACHIM BREUNIG, Institute of Inorganic and Physical Chemistry,
University of Bremen, Bremen, Germany

MIRCEA DIUDEA, Babeș-Bolyai University, Cluj-Napoca, Romania

JEAN ESCUDIE, HFA, Paul Sabatier University, Toulouse, France

ION GROSU, Babeș-Bolyai University, Cluj-Napoca, Romania

EVAMARIE HEY-HAWKINS, University of Leipzig, Leipzig, Germany

FLORIN DAN IRIMIE, Babeș-Bolyai University, Cluj-Napoca, Romania

FERENC KILAR, University of Pecs, Pecs, Hungary

BRUCE KING, University of Georgia, Athens, Georgia, USA

ANTONIO LAGUNA, Department of Inorganic Chemistry, ICMA, University
of Zaragoza, Zaragoza, Spain

JURGEN LIEBSCHER, Humboldt University, Berlin, Germany

KIERAN MOLLOY, University of Bath, Bath, UK

IONEL CĂTĂLIN POPESCU, Babeș-Bolyai University, Cluj-Napoca, Romania

CRISTIAN SILVESTRU, Babeș-Bolyai University, Cluj-Napoca, Romania

<http://chem.ubbcluj.ro/~studiachemia/>; studiachemia@chem.ubbcluj.ro

http://www.studia.ubbcluj.ro/serii/chemia/index_en.html

YEAR
MONTH
ISSUE
TOM

Volume 62 (LXII) 2017
DECEMBER
4
I

S T U D I A

UNIVERSITATIS BABEȘ-BOLYAI

CHEMIA

4

ISSUE DOI:10.24193/subbchem.2017.4

Tom I

Dedicated to the Memory of Prof. Emil Chifu

STUDIA UBB EDITORIAL OFFICE: B.P. Hasdeu no. 51, 400371 Cluj-Napoca, Romania,
Phone + 40 264 405352, www.studia.ubbcluj.ro

CUPRINS – CONTENT – SOMMAIRE – INHALT

ALEXANDRA CHIFU, AURORA MOCANU, MARIA TOMOAI-A-COTISEL, In Memoriam Prof. Emil Chifu (1925-1997)	7
ANCA-RUXANDRA LEONTIEȘ, ADINA RĂDUCAN, IOANA CATALINA GÎFU, DAN FLORIN ANGHEL, Catechin Oxidation Products: Mechanistic Aspects And Kinetics	11
THOMAS DIPPONG, FIRUTA GOGA, ALEXANDRA AVRAM, The Effect of Positional Isomerism of Propanediol on the Formation of Cobalt Oxides	21

IOAN PETEAN, AURORA MOCANU, GERTRUD-ALEXANDRA PĂLTINEAN, RALUCA ȚĂRCAN, DANA FLORINA MUNTEAN, LIANA MUREȘAN, GEORGE ARGHIR, MARIA TOMOAI A COTIȘEL, Physico-Chemical Study Concerning Atmospheric Particulate Matter Hazard	33
GEORGE ALEXANDRU POPA, GHEORGHE NECHIFOR, DANIELA FLORENTINA ENACHE (POPA), SZIDONIA-KATALIN TANCZOS, ADRIAN CIOCANEA, Polimeric Membranes Prepared with Surfactants Used for Ultrafiltration of Aqueous Solutions of Food Dye.....	47
FLORINA SCURTU, ANAMARIA POPA, RADU SILAGHI-DUMITRESCU, Periodate-Oxidized Alginate as Polycondensation Reagent for Hemoglobin	59
OANA CADAR, PETRE T. FRANGOPOL, GHEORGHE TOMOAI A, DANIEL OLTEAN, GERTRUD A. PALTINEAN, AURORA MOCANU, OSS I HOROVITZ, MARIA TOMOAI A-COTISEL, Silicon Release from Hydroxyapatites in Water and Simulated Body Fluid.....	67
ALEXANDRA AVRAM, MARIA GOREA, REKA BALINT, LUCIA TIMIS, STEFAN JITARU, AURORA MOCANU, MARIA TOMOAI A-COTISEL, Portland Cement Enriched with Hydroxyapatite for Endodontic Applications	81
ALEXANDRA AVRAM, TIBERIU FRENTIU, OSS I HOROVITZ, AURORA MOCANU, FIRUTA GOGA, MARIA TOMOAI A-COTISEL, Hydroxyapatite for Removal of Heavy Metals from Wastewater	93
MIHAI MEDELEANU, RALUCA POP, MIHAIELA ANDONI, MIRCEA V. DIUDEA, The Influence of Aza-Substitution on the Aromaticity of Sumanene	105
ANA-MARIA SĂCARĂ, CASTELIA CRISTEA, TAMAS LOVASZ, DAN PORUMB, EVA MOLNAR, LIANA MARIA MURESAN, Electrochemical Oxidation of 10 <i>H</i> -Phenothiazine-1-Carboxylic Acid	121
VIRGINIA COMAN, SIMION BELDEAN-GALEA, FLORINA COPACIU, MIHAELA VLASSA, MIUȚA FILIP, Chromatographic Analysis of some Antibiotics in Water and Sediment Samples Collected from the Romanian Tisza River Watershed.....	129
IOANA HODISAN, CRISTINA PREJMEREAN, IOAN PETEAN, DOINA PRODAN, TINCA BURUIANA, LOREDANA COLCERIU, LUCIAN BARBU-TUDORAN, MARIA TOMOAI A-COTISEL, Synthesis and Characterization of Novel Giomers for Dental Applications ..	143

ENIKŐ BITAY, BERNADETH KISS-PATAKI, GYÖRGY SZAKMÁNY, EMIL INDREA, IRÉN KACSÓ, IOAN BRATU, ERZSÉBET VERESS, Provenance Study on a Small Selection of Roman Potshards (Tășnad-Sere Site, Satu Mare County, Romania). 1.....	155
EDIT FORIZS, FIRUTA GOGA, ALEXANDRA AVRAM, AURORA MOCANU, IOAN PETEAN, OSSI HOROVITZ, MARIA TOMOAI- COTISEL, Thermal Analysis of Pure and Multisubstituted Hydroxyapatite Pastes.....	173
CARMEN SACALIS, FIRUTA GOGA, LEONTIN DAVID, Synthesis, Thermal Behavior and Spectroscopic Investigations of Metal Complexes with <i>N</i> -Modified Glycine as Ligand	181
ALEXANDRA POP, ROXANA A. POPA, CRISTIAN SILVESTRU, ANCA SILVESTRU, Hypercoordinated Organoselenium Compounds with O→Se Intramolecular Interactions	193
MIHAELA PĂSTRAV, ANDREA MARIA CHISNOIU, OVIDIU PĂSTRAV, LAURA SILAGHI DUMITRESCU, CODRUTA SAROSI, VIORICA TARMURE, Comparative <i>In Vitro</i> Study of the Different Orthodontic Brackets Using two Etching Techniques	201
ATTILA-ZSOLT KUN, BETTINA CSURKA, FIRUTA GOGA, EDIT FORIZS, ADRIAN PATRUT, Synthesis, Characterization and Molecular Modeling of Transition Metal Complexes with Theophylline	211

Studia Universitatis Babes-Bolyai Chemia has been selected for coverage in Thomson Reuters products and custom information services. Beginning with V. 53 (1) 2008, this publication is indexed and abstracted in the following:

- Science Citation Index Expanded (also known as SciSearch®)
- Chemistry Citation Index®
- Journal Citation Reports/Science Edition

IN MEMORIAM

EMIL CHIFU (1925-1997)

This year **2017** marks the **20th year** from the death of Professor **Emil Chifu**. This year also signifies **40 years** from the first scientific research project proposed by Professor **Chifu** and accepted for exploring in cosmos by **NASA** (National Aeronautics and Space Administration) of the United States of America.

The prominent Romanian scientist, Professor Emil Chifu was an outstanding physical chemist, recognized by the international scientific community. He was one of the founders of the modern science of colloids, surfaces and membrane phenomena, thermodynamics and hydrodynamics of thin layers formed by surface active substances self-assembled into supramolecular structures at liquid interfaces [1].

Professor Emil Chifu has created a modern research school in thermodynamics and physical chemistry of colloids and surfaces, at the Faculty of Chemistry and Chemical Engineering, “Babes-Bolyai” University of Cluj-Napoca (UBB) [1-7]. Currently, this school is known as the Center of Research in Physical Chemistry and it is accredited in the UBB.

Professor Emil Chifu was the *first Romanian scientist* whose original research proposal “Surface Flow of Liquids in the Absence of Gravity”, based on the highest rank scientific results [8], was selected in 1977 by NASA, of the USA, and after being rigorously valued by NASA, it was approved on the 28th of March, 1978, to be experimented on Space Laboratory (SpaceLab) in 1981. This research project proposed by Professor Emil Chifu represents the *first Romanian cosmic experiment* approved by the NASA of USA in 1978, and it refers to *two types* of space investigations: ♦surface flow between two liquid surfaces joined by surface channels and ♦surface flow on a liquid drop in the absence of gravity; both were planned by NASA to be realized on the *first flight* of the *Drop Dynamics Module* (DDM) known as “*Chifu’s experiment*”. The DDM experiment was scheduled by NASA to be explored on the SpaceLab-3.

On the basis of this research project, a *Framework Agreement (FA)* was settled between the Romanian Commission for Space Activities (CRAS) and the NASA of USA, as reported by Ioan Ursu, the president of the National Council for Science and Technology (CNŞT) in Romania, in the address no. 2460/16th December 1978 to the Ministry of National Education and Instruction.

The preparatory experiments in the laboratory phases were performed within the framework of a contract between UBB, Professor Emil Chifu being the project responsible and simultaneously the chair of the physical chemistry department and the CNŞT for the period of 1977-1980.

The setup model of *Chifu's experiment* was performed in the Jet Propulsion Laboratory (JPL) of the California Institute of Technology, Pasadena, USA in 1981, and it was implemented on the DDM in the NASA mission of the SpaceLab-3.

Professor Chifu and his research team studied the dynamics of a "free" liquid drop immersed in another liquid with equal density, in simulated microgravity laboratory conditions in UBB, Romania. Valuable theoretical and experimental results have been advanced by professor Chifu and his co-workers aiming at exploring the drop dynamics in cosmos, on SpaceLab-3, in which the microgravity conditions were rigorously satisfied.

The investigation of the professor Chifu's proposal in space conditions is a *premiere* in the study of the drop dynamics in imponderability, because the implied physical and chemical phenomena are of a major interest, both for the science and technology of liquids in the cosmic space and for industrial process as well as for examination of cell movements and biological membrane mobility.

The space experiment of professor Chifu has started the Romanian multi-disciplinary frontier research in the physical chemistry of thin films; over 60 published papers of which we recorded some [9-25] have been awarded with the "Gh. Spacu" Prize by the Romanian Academy in 1983. Professor Chifu became Emeritus Professor in 1990 at Babes-Bolyai University of Cluj-Napoca.

He published over 160 research articles and 14 books; 4 books were revised and completed posthumously by his collaborators [26-29].

The results of the scientific investigations in domains such as: thermodynamics of irreversible phenomena, liquid/liquid extraction, studies on nickel carbonyl powders, on sulphurous ores, on the foaming power of detergents have been implemented in the economic sphere on the basis of the research contracts concluded with important mining centres in Deva and Baia Mare, with chemical industries in Victoria, Ploiesti, Fagaras, as well as with the Central for drugs and cosmetics, in Bucharest.

REFERENCES

1. M. Tomoaia-Cotisel and D.A. Cadenhead, *Journal of Colloid and Interface Science*, **1997**, 195, 271.
2. M. Tomoaia-Cotisel and J. Zsako, *Studia Universitatis Babes-Bolyai, Chemia*, **1998**, 43 (1-2), 3.

3. P.T. Frangopol, *Revista de Chimie (București)*, **2002**, 53 (6), 495.
4. M. Tomoaia-Cotisel, A. Chifu, *Studia Universitatis Babeș-Bolyai, Chemia*, **2007**, 52 (3), 3.
5. P.T. Frangopol, *Emil Chifu în Personalități ale Istoriei Chimiei Românești, Mediocritate și Excelență, O radiografie a științei și învățământului din România*, Chapter III, vol. 3, Casa Cărții de Știință, Cluj-Napoca, **2008**, pp. 175-180.
6. P.T. Frangopol, *The first Romanian cosmic experiment approved by NASA- proposed by Emil Chifu*, în *Revista de Politică Științei și Scientometrie - Serie nouă*, **2015**, 4 (2), 155.
7. P.T. Frangopol, *Emil Chifu, în Mediocritate și Excelență, O radiografie a științei și învățământului din România*, Chapter VIII, vol. 6, Casa Cărții de Știință, Cluj-Napoca, **2016**, pp. 272-275.
8. E. Chifu, "Surface flow of liquids in the absence of gravity", **Proposal** selected by NASA's Office of Aeronautics and Space Technology, **1977**.
9. E. Chifu, I. Stan, Z. Finta and E. Gavrilă, Marangoni type surface flow on an undeformable free drop, *Journal of Colloid and Interface Science*, **1983**, 93 (1), 140.
10. E. Chifu, I. Stan, Z. Finta and E. Gavrilă, The Marangoni effect and translation of free non-deformable drops, *Revista de Chimie (București)*, **1980**, 31 (8), 765.
11. E. Chifu, I. Albu, C. I. Gheorghiu, E. Gavrilă, M. Sălăjan and M. Tomoaia-Cotișel, Marangoni flow-induced by temperature gradients-against gravity forces, *Revue Roumaine de Chimie*, **1986**, 31 (1), 105.
12. E. Chifu and I. Albu, Interfacial tension variation in the course of liquid-liquid extraction. II. Molecular associations on extracting some monocarboxylic aliphatic acids, *Annali di Chimica (Rome)*, **1975**, 65 (9-10), 519.
13. E. Chifu, M. Tomoaia, and A. Ioanette, Behaviour of canthaxanthin at the benzene/water and air/water interfaces, *Gazzetta Chimica Italiana*, **1975**, 105 (11-12), 1225.
14. M. Tomoaia-Cotisel, E. Chifu, V. Tămaș and V. Mărculețiu, Behaviour of some apocarotenoid derivatives at the air/water interface, *Revue Roumaine de Chimie*, **1980**, 25 (2), 175.
15. E. Chifu, J. Zsakó, and M. Tomoaia-Cotișel, Xanthophyll films. I. Single-component monolayers at the air/water interface, *Journal of Colloid and Interface Science*, **1983**, 95 (2), 346.
16. M. Tomoaia-Cotișel, J. Zsakó, E. Chifu and P. J. Quinn, Influence of electrolytes on the monolayers properties of saturated galactolipids at the air/water interface, *Chemistry and Physics of Lipids*, **1983**, 34 (1), 55.
17. J. Zsakó, M. Tomoaia-Cotisel and E. Chifu, Insoluble mixed monolayers. I. Phase equilibria at the collapse of binary monolayers at gas/liquid interfaces, *J. Colloid Interface Sci.*, **1984**, 102 (1), 186.
18. E. Chifu, J. Zsakó, M. Tomoaia-Cotișel, M. Sălăjan and I. Albu, Xanthophyll films. **IV**. Interaction of zeaxanthin and astaxanthin with electrolytes at the air/water interface, *Journal of Colloid and Interface Science*, **1986**, 112 (1), 241.
19. M. Tomoaia-Cotisel, J. Zsakó, E. Chifu and P.J. Quinn, Intermolecular interactions in lipid-carotenoid monolayers, *Biochemical Journal*, **1987**, 248, 877.

20. M. Tomoaia-Cotisel, J. Zsakó, A. Mocanu, E. Chifu, P.J. Quinn, Monolayer properties of membranes lipids of the extreme *Halophile Halobacterium Cutirubrum* at the air / water interface, *Biochimica et Biophysica Acta*, **1988**, 942, 295.
21. M. Tomoaia-Cotisel, J. Zsakó, E. Chifu and D.A. Cadenhead, Relaxation phenomena in apocarotenoid monolayers, *Langmuir*, **1990**, 6 (1), 191.
22. J. Zsakó, M. Tomoaia-Cotisel, E. Chifu, A. Mocanu and P.T. Frangopol, Influence of stearic acid monolayers upon the procaine adsorption from underlying alkaline aqueous solutions, *Biochimica et Biophysica Acta*, **1990**, 1024, 227.
23. M. Tomoaia-Cotisel, E. Chifu, J. Zsakó, A. Mocanu, P.J. Quinn and M. Kates, Monolayer properties of archaeol and caldarchaeol polar lipids of a methanogenic archaeobacterium, *Methanospirillum hungatei*, at the air/water interface, *Chemistry and Physics of Lipids*, **1992**, 63, 131.
24. J. Zsakó, M. Tomoaia-Cotisel, E. Chifu, A. Mocanu and P.T. Frangopol, Procaine interactions with phospholipid monolayers at the air/water interface, *Gazzetta Chimica Italiana*, **1994**, 124, 5.
25. M. Tomoaia-Cotisel, L.C. Stewart, M. Kates, J. Zsakó, E. Chifu, A. Mocanu, P.T. Frangopol, L.J. Noe and P.J. Quinn, Acid dissociation constants of diphytanyl glycerol phosphorylglycerol-methylphosphate, and diphytanyl glycerol phosphoryl glycerophosphate and its deoxy analog, *Chemistry and Physics of Lipids*, **1999**, 100, 41.
26. E. Chifu, "Chemistry of Colloids and Interfaces", Editors: M. Tomoaia-Cotisel, I. Albu, A. Mocanu, M. Salajan, E. Gavrilă and Cs. Racz, University Press, Cluj-Napoca, **2000**.
27. E. Chifu, M. Tomoaia-Cotisel, I. Albu, A. Mocanu, M.-I. Salajan, Cs. Racz and V.D. Pop, "Experimental Methods in Chemistry and Biophysics of Colloids and Interfaces", University Press, Cluj-Napoca, **2004**.
28. M. Tomoaia-Cotisel, I. Albu and E. Chifu, "Chemical Thermodynamics", The 2nd Edition, University Press, Cluj-Napoca, **2009**.
29. M. Tomoaia-Cotisel, I. Albu and E. Chifu, "Chemical Thermodynamics", The First Edition, University Press, Cluj-Napoca, **2009**.

**Alexandra Chifu, Aurora Mocanu,
Maria Tomoaia-Cotisel**

CATECHIN OXIDATION PRODUCTS: MECHANISTIC ASPECTS AND KINETICS

ANCA - RUXANDRA LEONTIEȘ^{a*}, ADINA RĂDUCAN^b, IOANA CATALINA GÎFU^a, DAN FLORIN ANGHEL^a

ABSTRACT. The oxidation of catechin in the presence of atmospheric oxygen in a methanol/buffer model solution was studied by investigating generated products using LC/MS and spectrophotometry. It was proved that catechin was slowly converted to dimeric species with similar structures and properties. The catechin autoxidation was investigated spectrophotometrically at different pH ranging between 5 and 10. Using the initial linear dependence of the kinetic curves $[\text{Dimers}] = f(t)$ the initial reaction rates were estimated for the autoxidation of catechin in methanol/buffered solutions. It was found that the dimer formation is favored at pH 8.

Keywords: catechin, autoxidation, dehydrocatechin

INTRODUCTION

Polyphenols are widely distributed in plants and in plant-derived products, mostly in wines and teas, where they contribute to food organoleptic properties and oxidative stability [1]. Polyphenols have several health benefits, acting as antioxidant, anticarcinogen, antimicrobial, anti-inflammatory and UV protection agents [2].

One of the most common natural polyphenols from the class of flavanols is catechin (Scheme 1). As polyphenol, catechin is susceptible to enzymatic and non-enzymatic oxidation. The oxidation products are the oxidation dimers. The dimers are linked either by C6 → C8 or C 6→ C6 interflavan linkages

^a Ilie Murgulescu Institute of Physical Chemistry, Spl. Independentei 202, Bucharest, 060021, Romania

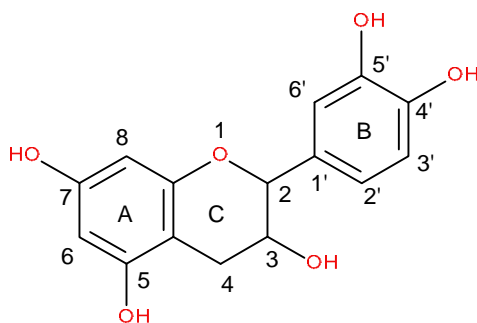
^b University of Bucharest, Faculty of Chemistry, Bulevardul Regina Elisabeta 4-12, Bucharest, 030018, Romania

* Corresponding author: ancaleonties@gmail.com

and are classified as B-type dehydrodicatechins, resulting from the repeated condensation reactions between the A-ring of the lower unit and the B-ring of the upper unit through a mechanism of so-called 'head to tail' polymerization [3] or they contain additional C–O–C ether-type interflavan linkages and are classified as A-type dehydrodicatechins [4].

During the past decades many studies focused on the protective effects on flavanols against lipid peroxidation and low-density lipoproteins, oxidation as well as on their antiproliferative and anticarcinogenic actions [5,6]. On the other hand, polyphenols are susceptible to autoxidation. In this process are generated large amounts of free radicals and active oxygen species, such as hydrogen peroxide, which are able to induce DNA damage and diseases [7, 8]. Therefore, much discussion and contradiction exist regarding the structure and activity of oxidation products resulting from the autoxidation process.

In the present paper, we describe the autoxidation of catechin in aqueous/methanol model solution under pH ranging between 5 and 10. On the basis of the LC-MS and HPLC we identified a series of B-type and A-type dimeric autoxidation products and proposed their structures and dissociation mechanisms. Furthermore, using a simple spectrophotometrical method we analyzed the kinetics of catechin autoxidation.



Scheme 1. Catechin structure

RESULTS AND DISCUSSION

The autoxidation of catechin was carried out in aqueous/ methanol solution under mildly basic conditions (pH 8.0). By using a LC-MS system the autoxidation products were identified (**Figure 1**).

CATECHIN OXIDATION PRODUCTS: MECHANISTIC ASPECTS AND KINETICS

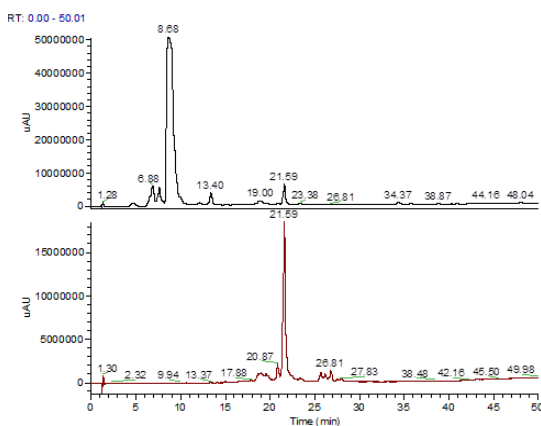


Figure 1. LC-MS chromatogram for the catechin autooxidation products

The peaks of the compounds eluted at retention times of 6.88 and 7.60 minutes were assigned to a dimer product resulted from autoxidation. These compounds have the same UV-Vis absorption spectrum with double maxima at 240 and 280 nm and similar ion fragments (**Figure 2. A and B**).

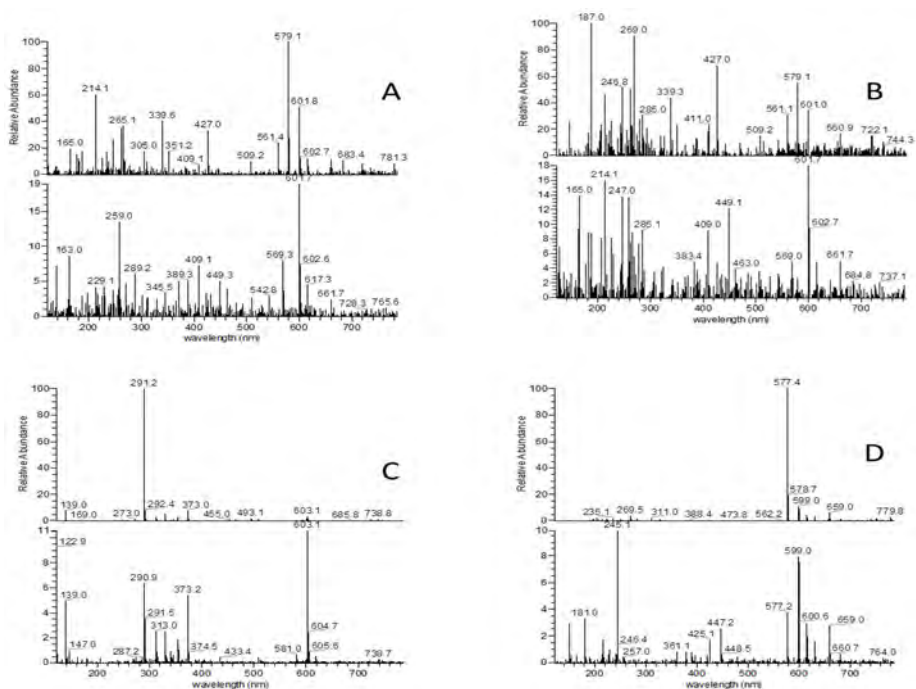
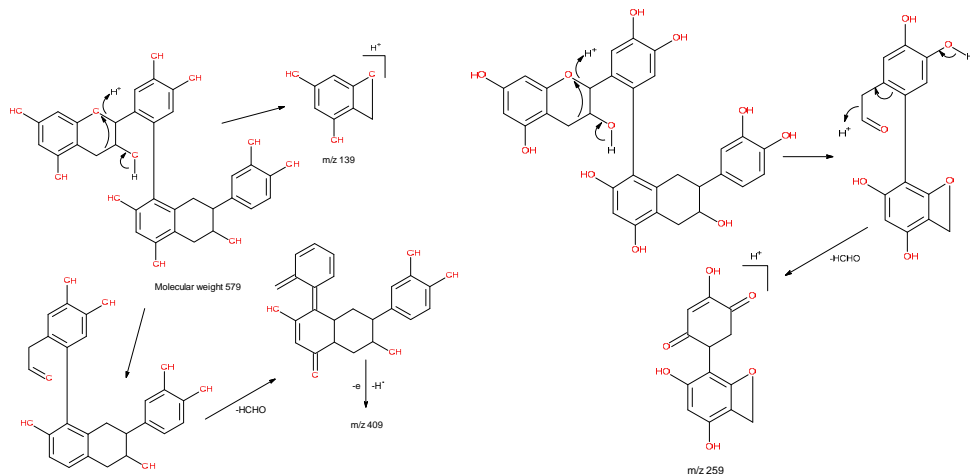


Figure 2. Mass spectra of identified catechin autooxidation products (retention time 6.88 minute - A, retention time 7.60 minutes - B, retention time 8.68 - C, retention time 21.59 D)

At retention time 8.68 minutes the peak of the eluted compound was assigned to the remaining non-reactive catechin. **Figure 2.B** shows the majority ion with mass m/z 291.2 typical for catechin. The compound eluted at retention time 13.40 minutes corresponds to catechin which lost a hydrogen atom, this fact being confirmed by the presence in the mass spectrum of the fragment ion with m/z 290 (**Figure 2.C**). The compound with the peak at the retention time of 21.59 minutes (**Figure 2.D**) was established as another type of dimer product due to the presence in the mass spectrum of the fragment m/z 577.4. It has also been observed that the products with peaks at retention times 18.64, 19.57 and 26.81 minutes have the same UV-Vis spectrum. Three maxima at 240, 256 and 376 nm in absorption spectrum were identified and similar ionic fragments to the compound found at retention time of 21.59 minutes. These compounds were supposed to be fragments of dimers resulting from MS fragmentation. During the autoxidation process, the B-type dehydrocatechin results from repeated condensation reactions between the A-ring of the lower unit and the B-ring of the upper unit in a 'head to tail' polymerization. At 6.88 and 7.60 minutes the elution peak was attributed to this type of dimer. The mechanistic formation of m/z 579 = M+1 and m/z 601 = M+23(M_{Na+}) sustains this idea. The supposed fragmentation path of B-type dehydrocatechin is presented in **Scheme 2**.



Scheme 2. Fragmentation of B-type dehydrocatechin dimer

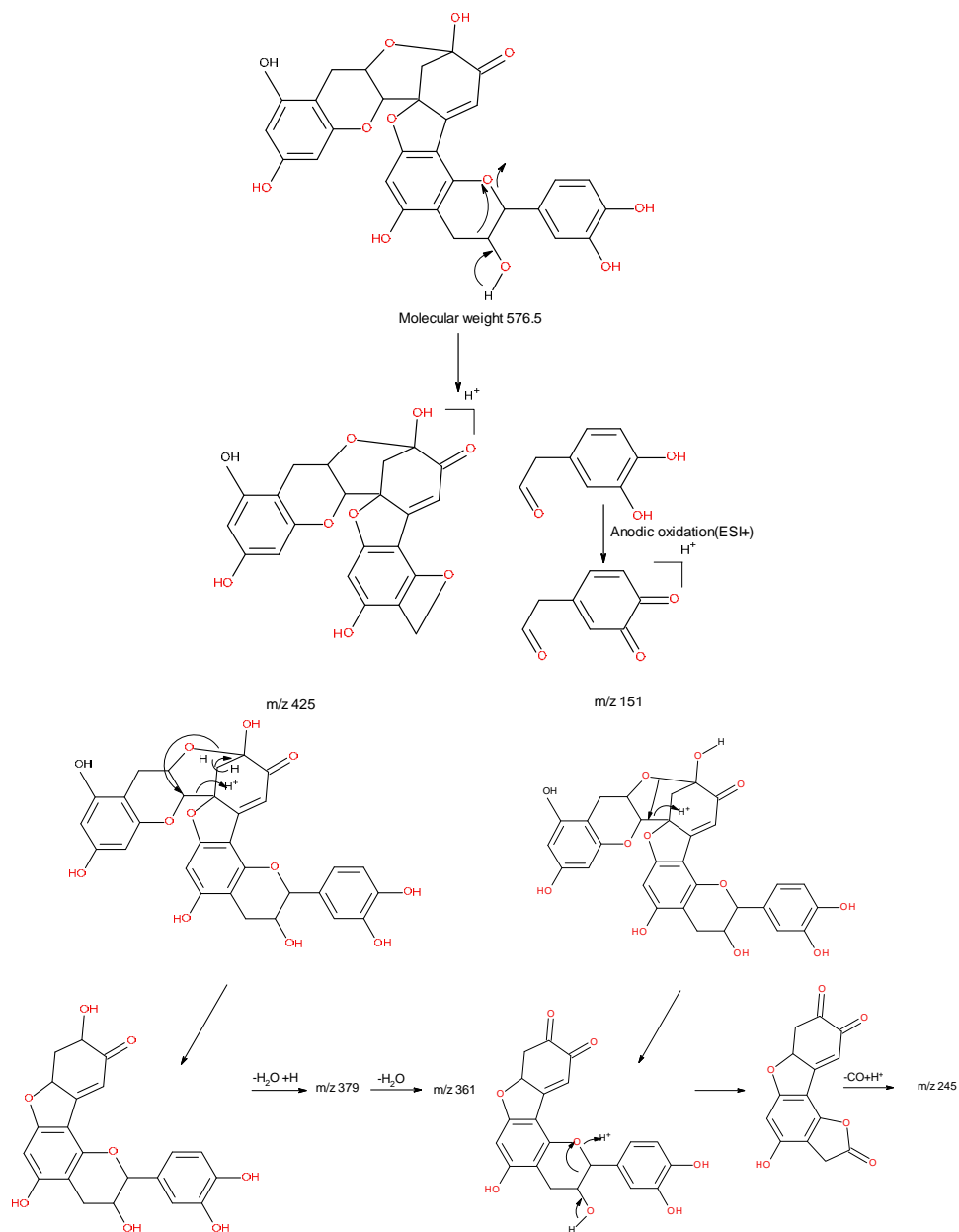
Another type of dimer formed during autoxidation is the A-type dehydrodicatechin. These compounds have C–O–C ether-type interflavan linkage. For retention time of 21.59 minutes the m/z 577 = $M + 1$ and m/z 599 = $M + 23$ (M_{Na^+}) were assumed. Fragmentation mechanisms for obtaining the daughter fragments m/z 425, m/z 151, m/z 245 from m/z 577, m/z 360 were proposed. **Scheme 3.** shows the proposed fragmentation path for a A-type dehydrodicatechin. It was also explained the formation of m/z 561 as $M - H_2O + H^+$ and m/z 463 as m/z 449 + $CH_3OH - H_2O$. Fragments with a mass greater than m/z 599 may be adducts of the dimer with solvents and other molecules. Other fragments were obtained as follows: m/z 447 = $424 + 23$ (M_{Na^+}), m/z 217 = m/z 245 - M_{CO} .

In order to analyze the kinetics of catechin autoxidation by atmospheric oxygen, the accumulation of oxidation products at different pH values was recorded in time. During the autoxidation of catechin the effect of pH cannot be ruled out, as the basic pH should increase the proportion of phenolate anions leading to a larger quantity of reaction dimers than the protonated phenol. **Figure 3 A** shows absorption spectra for dimers at different pHs. The characteristic absorbance of catechin reaction products indicated a bathochromic shift with the pH increase. The maxima present at 280 and 430 are characteristic for the autoxidation products obtained at neutral and basic pH and at 280 and 390nm for pH 5.5 reaction products.

The characteristic bands of the dimers were used for further kinetic analysis by monitoring and recording consecutive spectra for 90 minutes.

The UV-Vis spectra of catechin solution mixed with acidic buffer presents a minimal variation where dehydrocatechin dimers have characteristic wavelengths of 280 and 390 nm. For neutral and basic pHs the reaction takes place with a decrease in absorbance at 280 and an increase at 430 nm.

The dimers concentrations were calculated from their absorbance. The kinetic curves of dimer concentration ($[Dimer]$) as function of time are shown in **Figure 3 B**. Using the initial linear dependence of the kinetic curves $[Dimers] = f(t)$, the initial reaction rates for the autoxidation of catechin, in methanolic solutions with buffers of various pH were estimated. The results are presented in **Table 1**. In mild alkaline media (pH=8) the conversion of catechin in dimers is maximum.



Scheme 3. Fragmentation of A type dehydrocatechin dimer

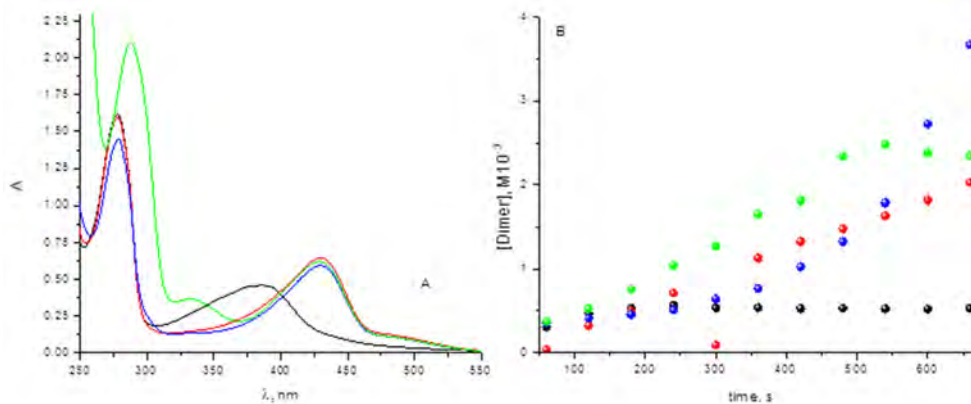


Figure 3. (A) Dimers spectra at different pHs and (B) Kinetic curve for dimer formation in catechin autoxidation process at different pHs: 5.5 (black), 7 (red), 8 (blue), 10 (green)

Table 1. The variation of the initial reaction rate with the pH for the autoxidation reaction of catechin solution

pH	$v_R^0 \cdot 10^8 / (Ms^{-1})$
5.5	(0.241±0.072)
7.2	(3.05±0.07)
8.0	(5.31±0.12)
9.9	(0.299±0.042)

CONCLUSIONS

The autoxidation of catechin was investigated in buffered methanolic solutions. The analysis of the reaction mixture indicates the presence of catechin dimers (dehydrocatechin A and B) with similar structures and properties. From the analysis of the UV-VIS absorption spectra, the dimers characteristic bands were identified and further used for the kinetic analysis. It was found that in catechin autoxidation the dimer formation is favored at pH 8. The results are in agreement with other literature data confirming an oxidation mechanism implying dimers as products, with intermediate formation of semiquinons.

EXPERIMENTAL SECTION

Materials

Methanol and glacial acetic acid were HPLC grade. Deionized water (<18 M resistance) was obtained from a Milli-Q Element water purification system (Millipore, Bedford, MA). Catechin and all the other chemicals were purchased from Sigma Aldrich.

Preparation of autoxidation products of catechin

In order to analyse the products resulting from the catechin autoxidation process, catechin was solubilized in methanol and a 0.1 mM solution was obtained. The catechin solution was diluted with phosphate buffer (0.1 M, pH 8) to a final concentration of 0.03 mM in catechin. The final mixture (100 mL) was incubated in dark at room temperature, in the presence of atmospheric oxygen. After 24 hours, the mixture was washed with ethyl acetate. The upper layer was collected and dried using a rotary evaporator with a water bath at 40° C for 40 minutes, during which complete evaporation of the ethyl acetate was carried out. The 0.02 mg of yellow powder obtained in the flask was solubilized in 2.5 mL of methanol.

Liquid chromatography–mass spectrometry

A Finnigan MAT Spectra System P4000 pump was used coupled with a UV6000LP diode array detector and a Finnigan AQA mass spectrometer. Analyses were carried out on a Superspher 100-RP18, 125 • 2 mm, 4 μm, column (Macherey-Nagel, Germany), protected by a guard column packed with the same material, and maintained at 40° C. Analyses were carried out employing electrospray ionization (ESI) at the positive ion mode, with acquisition set at 12 and 80 eV, capillary voltage 3.5 kV, source voltage 4.9 kV, detector voltage 650 V and probe temperature 400 C. Eluent (A) and eluent (B) were 2.5% aqueous acetic acid solution and methanol, respectively. The flow rate was 0.300 mL • min⁻¹, and the elution program used was as follows: 0–15 min, 80% A. 20%B; 15–25 min, 100% B. The injection volume was 2μL.

UV-Vis spectrophotometry

A stock solution of catechin in methanol 10⁻³ M was prepared. The dilution was made with buffer at pH 5.5, 7, 8 and 9.9 to a final concentration of 1.5 • 10⁻⁴ M. Catechin autoxidation process was recorded using a JASCO V-350 spectrophotometer. Kinetic studies in the presence of isolated strawberry peroxidases [9] have shown that the product formed at 5.5 pH has

a molar absorption coefficient $\epsilon = 4600 \text{ M}^{-1}\text{cm}^{-1}$. This value was used to determine the concentration of dimers at this pH and then extrapolated to the rest of pH, under conditions where Lambert-Beer law was tested for the range of concentrations considered. From the absorbance characteristic of the dimer wavelengths, the concentration was calculated. For catechin autoxidation process, the characteristic absorbance of the dimers at 430 nm was measured in time to obtain extended kinetic curves and estimate the initial reaction rates.

REFERENCES

1. J.M. Landete, *Critical Review in Food Science and Nutrition*, **2012**, 52, 936.
2. M. Friedman, *Journal of Agricultural and Food Chemistry*, **2014**, 62, 6025.
3. T. Tanaka, Y. Matsuo, I Kouno, *Internationa Journal of Molecular Science*, **2010**, 11, 14.
4. S. Guyot, V.B. Chewier, J.M. Souquet, M.Moutounet, *Journal of Agricultural and Food Chemistry*, **1995**, 43, 2458.
5. E.L. da Silva, D.S.P. Abdalla, J. Terao, *IUBMB Life*, **2000**, 49, 289.
6. M.K. Chahar, N.Sharma, M.P. Dobhal, Y.C. Joshi, *Pharmacognosy Reviews*, **2011**, 5, 1.
7. S.C. Forester, J.D. Lambert, *Molecular Nutrition & Food Research*, **2011**, 55, 844.
8. L. Pourcel, J.M. Routaboul, V.Cheynie, L.Lepiniec, I. Debeaujon, *Trends in Plant Science*, **2006**, 12, 29.
9. Reaction, M. Lopez-Serrano, A. Ros Barcelo, *Journal of Agricultural and Food Chemistry*, **2002**, 50, 1218.

THE EFFECT OF POSITIONAL ISOMERISM OF PROPANEDIOL ON THE FORMATION OF COBALT OXIDES

THOMAS DIPPONG^a, FIRUTA GOGA^b, ALEXANDRA AVRAM^b

ABSTRACT. This paper focuses on a comparative analysis between the carboxylate precursors obtained through the redox reaction between cobalt nitrate and 1,2-propanediol, and cobalt nitrate with 1,3-propanediol, respectively. The formation of the lactate and malonate precursors was followed with thermal analysis, FTIR spectrometry and acido-basic analysis (conductometric/potentiometric titrimetry). The decomposition of the carboxylate precursors and the formation rate of cobalt oxides were observed by X-ray diffractometry and FTIR spectrometry, following advanced thermal treatments at 500°C, 800°C and 1000°C, with a pretreatment at 300°C. The differences between the two positional diol isomers are comparatively discussed.

Keywords: lactate, malonate, Co₃O₄, electrometric titrimetry, thermal treatment

INTRODUCTION

Transitional metal oxides include a large spectrum of inorganic materials with distinctive compositions and morphologies, leading to a wide variety of characteristics [1,2].

Cobalt oxides have drawn increasing attention due to their unique size, shape dependent properties [3] and diverse spectrum of applications such as, ethylene oxidation [1], energy storage and conversion, glucose detection, water spitting [4], catalytic oxidation [5], lithium ion batteries [6], as a contrasting agent for magnetic resonance, in biomedical sensors [3] and targeted drug delivery [3,4,7].

^a *Technical University of Cluj-Napoca, Faculty of Sciences North University Center at Baia Mare, Department of Chemistry and Biology, 76 Victoriei Street, 430122 Baia Mare, Romania*

^b *Babeş-Bolyai University, Faculty of Chemistry and Chemical Engineering, 11 Arany Janos Street., RO-400028, Cluj-Napoca, Romania,*

**Corresponding author: fgoga@chem.ubbcluj.ro*

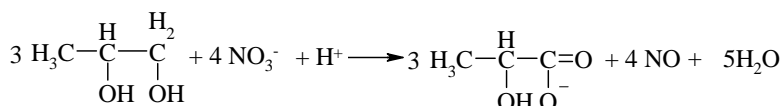
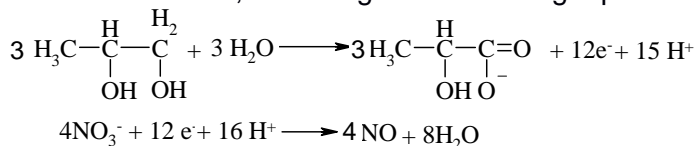
When falling in the nanosized range, cobalt oxides have been proven to exhibit even more attractive applications [8-9]. Up until now, cobalt oxide in the form of nanoparticles has been obtained through a number of methods, namely, thermal decomposition [4,10], sol-gel [2], hydrothermal [11], solvothermal [11], co-precipitation [12], photochemical synthesis, reversed micelles [13], microwave heating [9] etc. All these systems, comprising cobalt oxides of various compositions and stoichiometry, rely on the thermodynamic stability of $\text{Co}^{2+}/\text{Co}^{3+}$ oxidation states.

In solution-phase synthesis, the main cobalt oxide crystal phase is Co_3O_4 , followed by the less common CoO [1], both states being the most stable [8]. The greater thermodynamic stability of Co_2O_3 followed by the instant reducibility of CoO to Co , makes the synthesis of CoO in pure phase difficult. Relevant literature [14-15] studies the synthesis of single cobalt oxides and compound oxide nanoparticles through the redox reaction of metal salts with various diols, in different molar ratios.

This paper presents the synthesis of cobalt oxide precursors by the redox reaction between cobalt nitrate and 1,2-propanediol respectively 1,3-propanediol and the characterization of the precursors by Thermal analysis, FTIR and study of acido-basic properties, using conductometric and pH-metric titrations. Titration techniques have the advantage of ease of implementation, cost-effectiveness and accuracy. Electrometric titrations also have the advantage of automation, increasing the analysis throughput and securing the consistent quality of the results.

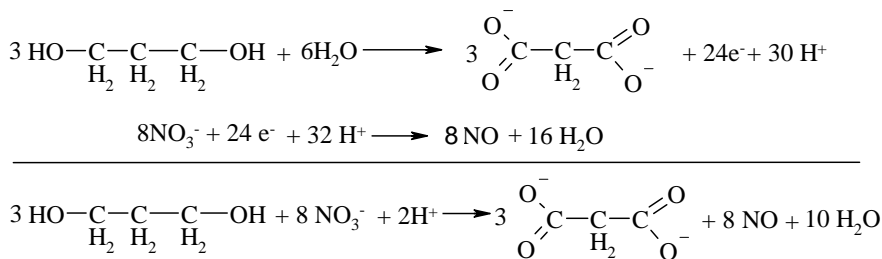
RESULTS AND DISCUSSION

Previous studies have shown the redox reactions between cobalt nitrate and diols (ethylene glycol, 1,2 propanediol, 1,3 propanediol) leads to the formation of coordination compounds of Co(II) with the carboxylate anions, diols' oxidation product, where only the primary C – OH groups participate. The secondary C –OH groups are not involved in the redox reactions. Thus, the oxidation of 1,2 propanediol leads, in particular working conditions, to the formation of lactate anions, according to the following equations (Scheme 1)



Scheme 1. The redox reaction leading to the formation of the lactate precursor

Similarly, the redox reaction between nitrate and 1,3-propanediol leads to the formation of malonate anions (Scheme 2).



Scheme 2. The redox reaction leading to the formation of the malonate precursor

The reaction is promoted by the formation of the coordination compounds between the resulted carboxylate ions and the Co(II) cations (the diol does not only interact with HNO₃).

The redox reaction between Co(NO₃)₂ și 1,2-PG, and Co(NO₃)₂ and 1,3-PG, respectively, was studied by thermal analysis. This entails the thin layer deposition of cobalt nitrate-diol solutions onto Pt pans, followed by an air heating up to 500°C. Figure 1 presents the thermal curves for the 1,2 propanediol, and 1,3 propanediol containing mixtures.

The presented DTA thermal curves show two exothermic processes. The first exothermic process, around 170°C, is attributed to the development of the Co(NO₃)₂-1,2PG redox reaction. The reaction unfolds integrally with the formation of a single oxidation product, respectively, of Co (II) combinations (visually confirmed by the evolving of the brown gas-nitrogen oxides). The second effect, around 280°C, corresponds to the oxidative decomposition of cobalt lactate into cobalt oxide.

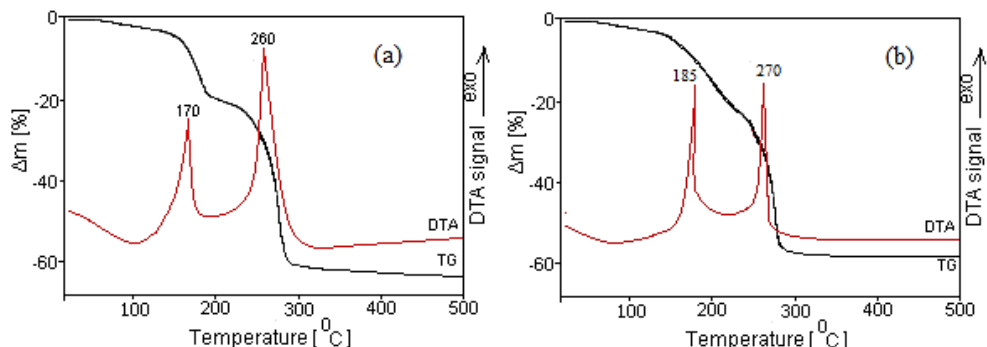


Figure 1. Thermal curves for the Co (NO₃)₂-1,2PG (a) and Co (NO₃)₂-1,3PG (b) solutions

In the case of 1,3 propanediol, the exothermic effects are slightly carried towards higher temperatures, the formation of cobalt malonate occurring at 185°C, and its decomposition at 270°C. Given the usage of 1,3 propanediol, the mass loss presented on the TG curve amounts to 21% for the first process, and 17% for the second one, a half reduced loss being observed in the case of utilizing a primary diol as opposed to a primary-secondary one.

In the case of 1,2 propanediol, the mass loss seen on the TG curve is 20% for the first process, and 41% for the second one.

Following the thermal analysis, the optimal carboxylate precursors synthesis temperature was established at 140°C. The products obtained at this temperature were characterized by FTIR analysis (fig 2). FTIR spectra of the lactate precursor obtained from 1,2 propanediol and malonate, and 1,3 propanediol, respectively, present all the characteristic bands of the carboxylate anions coordinated at metallic ions: $\nu_{as}(\text{COO}^-)$ la 1646 cm^{-1} , $\nu_s(\text{OCO})$ la 1360 cm^{-1} , and $\nu_s(\text{CO}) + \delta(\text{OCO})$ la ~ 1310 cm^{-1} , confirming the formation of this type of compound [18]. In the case of the lactate precursor's spectra, an intense band can be observed from 1070 cm^{-1} , characteristic to the secondary C-OH group (1,2-propanediol) that does not take part in the redox reaction, thus confirming the formation of the lactate precursor. The absence of bands characteristic to O-H groups suggests the formation of the carboxylate dianion (malonate) [17]. The bands at 2974 cm^{-1} , 2940 cm^{-1} and 2870 cm^{-1} are characteristic to the stretching vibrations of the C-H bonds from- CH_3 [16-17].

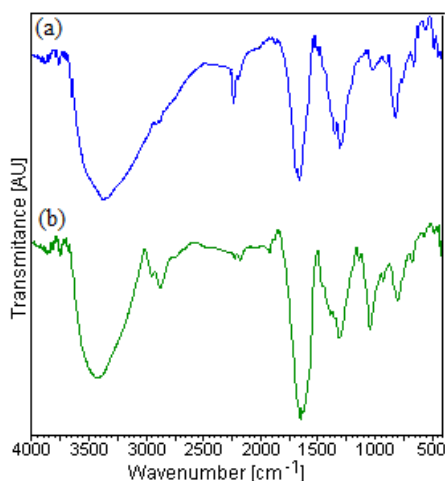


Figure 2. FTIR spectrum of the lactate (a), malonate (b) precursors synthesized at 140°C

Figure 3 presents the comparative thermal curves (TG, DTA) for the decomposition of lactate and malonate precursors, up to 1000°C. The 20% mass loss up to ~210°C can be attributed to the elimination of water from the complex combination. The one from the 220-300°C temperature range (42% for 1,2 propanediol and 21% for 1,3 propanediol), accompanied by an acute exothermic effect (at 280°C for 1,2-propanediol and 240°C for 1,3 propanediol, corresponds to the oxidative decomposition of formed complex combinations (lactate, malonate). This decomposition takes place with an *in-situ* generation of a reductive atmosphere, causing the reduction of Co(II) to metallic Co, followed by its reoxidation to a weakly crystallized oxide with an increased reactivity [21]. Between 950-1000°C, a final mass loss (4%) can be observed, corresponding to the transformations in the oxidic system, the reduction of Co_3O_4 to CoO , an endothermic effect on the DTA curve (950-960°C).

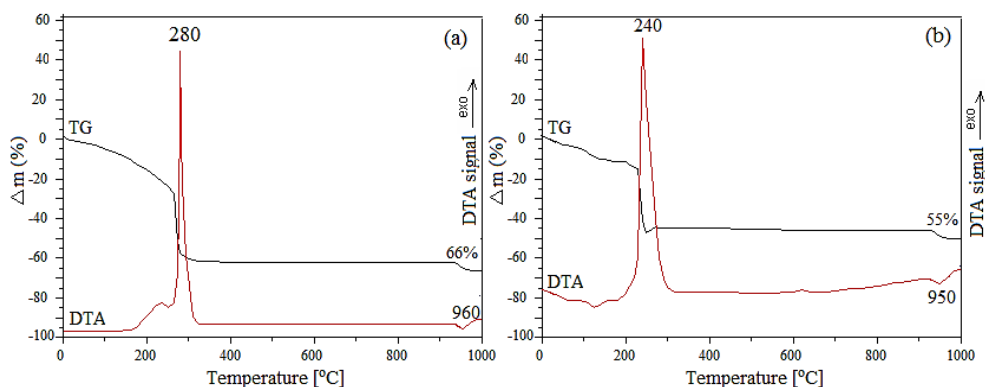
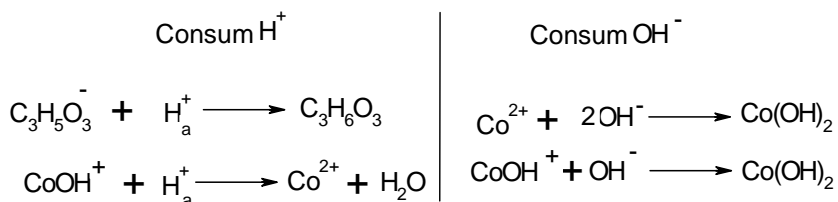


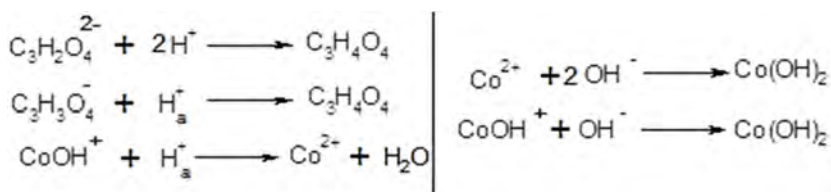
Figure 3. Thermal behaviour of the lactate (a) and malonate (b) precursors synthesized at 140°C

In order to establish if the precursor is a Co(II) lactate or a Co(II) hydroxylactate, and malonate or hydroxymalonate we have studied the acidobasic properties, by using conductometric and pH-metric titrations.

The processes that can take place in the precursor treated with a HCl solution, and NaOH respectively, are presented in schemes 3 and 4.



Scheme 3. The processes that can take place in the precursor (lactate) treated with HCl (left) and with NaOH (right)



Scheme 4. The processes that can take place in the precursor (malonate) treated with HCl (left) and with NaOH (right)

The consumed acid amount is calculated from the difference between the initial and the unreacted HCl volume (corresponding to the first point of equivalence). The utilized amount of NaOH is evaluated through the difference between the NaOH volume corresponding to the second point of equivalence and the volume of initial HCl. When the consumed HCl quantity (for the protonation of the lactate ion) is equal to the quantity of consumed NaOH (for the precipitation of Co(II) to Co(OH)₂) (H⁺/OH⁻=1), it can be considered that cobalt (II) lactate (Co(C₃H₅O₃)₂) is the precursor. Cobalt (II) hydroxylactate precursor (Co(OH)C₃H₅O₃) is formed when the volume of consumed HCl (for the precipitation of lactate and hydroxide ions) is double (H⁺/OH⁻ =2) when compared to the consumed NaOH (for the precipitation of Co(OH) to Co(OH)₂). The precursor of cobalt malonate (CoC₃H₂O₄), has a similar formation, when the quantity of consumed HCl is equal with the quantity of consumed NaOH (for the precipitation of Co(II) as Co(OH)₂). To confirm the formation of the hydroxycarboxylate anion (lactate), and dicarboxylate (malonate), neutral, basic or hydroxyde, studies on the acido-basic properties were carried out (conductometric and pH-metric titrations) Figure 4 presents the conductometric titration (Figure 4a), and pH-metric titration (Figure 4b) curves of the acid solutions of the sample with 1,2 propanediol and HCl solution (volume used to dissolve the precursor and process the experimental results).

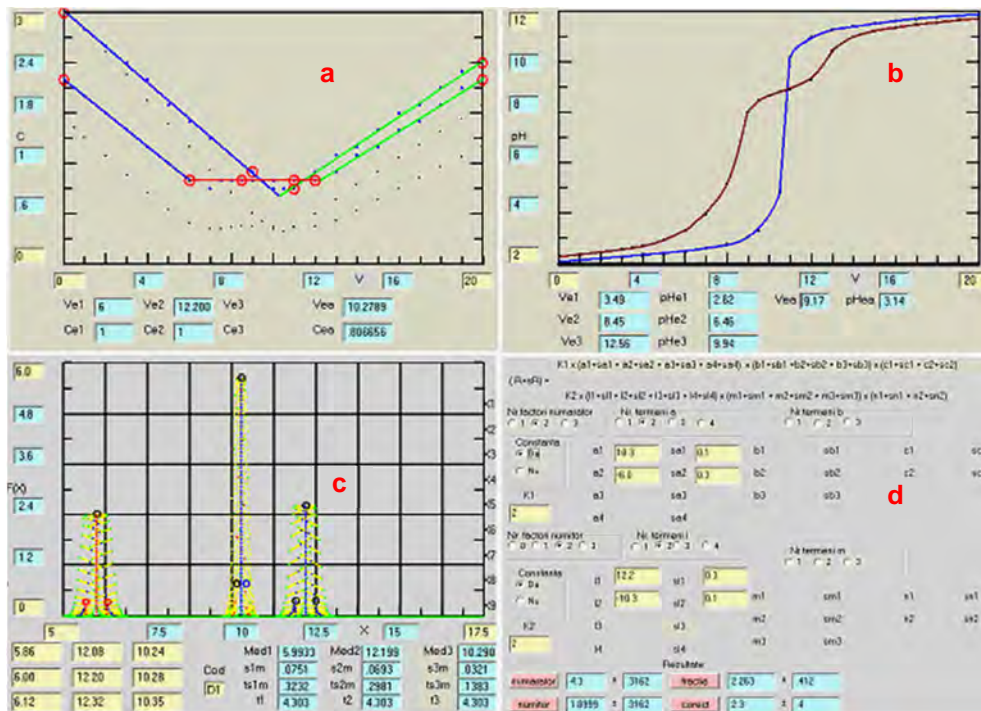


Figure 4. Conductometric titration curve (a), pH-metric titration curve (b), calculation of the medium equivalence volume (c), calculation of the reaction ratio (d) for the 1,2 propanediol sample

Figure 4c shows the statistical calculus method for the equivalence volumes, while figure 4d, presents the statistic calculus method for the consumed acid/ consumed base ratios from the equivalence volumes. In the case of using 1,2 propanediol, a mixture of neutral and basic salts is obtained, whereas in the case of 1,3 propanediol isomer, only hydroxymalonate is obtained. Similarly, the acido-basic curves in the case of 1,3-propanediol are presented (Figure 5a and 5b), followed by the statistical calculation of the acid/ base ratio (Figure 5c and 5d).

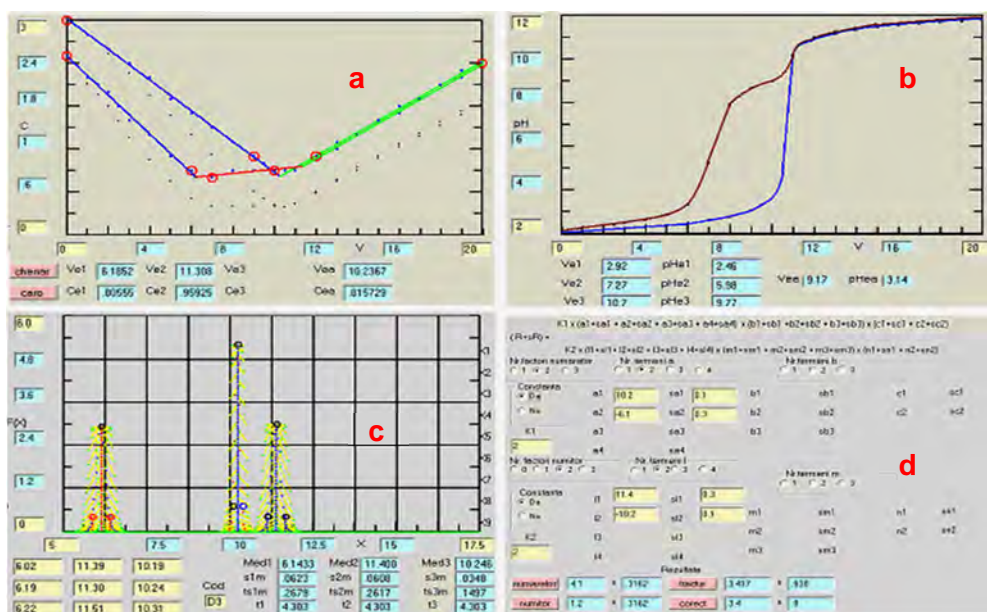


Figure 5. Conductometric titration curve (a), pH-metric titration curve (b), calculation of the medium equivalence volume (c), calculation of the reaction ratio (d) for the 1,3 propanediol sample

The results obtained following the conductometric and pH-metric titrations are presented in table 1.

Table 1. H^+/OH^- molar ratios and the compounds formed following the acido-basic titrations

Experimental molar ratio H^+/OH^-			Corresponding compound
Sample obtained from	Conductometric	pH-metric	
1.2 propanediol	$2.3 \pm 0,4$	1.5 ± 0.3	$Co(C_3H_5O_3)_2$ $(CoOH)C_3H_5O_3$
1.3 propanediol	4.0 ± 0.2	$4,2 \pm 0.3$	$n(CoOH)_2 \cdot CoC_3H_2O_4$

The acido-basic properties of the synthesized compounds confirm the results of thermal analysis and FTIR, advocating that the redox reaction forms carboxylate or hydroxycarboxylate compounds, that coordinate $Co(II)$ ions in the form of a compound with either a basic or a neutral character.

The precursor was thermally decomposed at $300^\circ C$ for 6 hours and then annealed for 3 hours at $500^\circ C$, at $800^\circ C$ and at $1000^\circ C$. Following the thermal analysis, it was observed that the thermal decomposition of the carboxylate precursors occurred up until $300^\circ C$ with the formation of cobalt

oxides through the in situ generation of a reductive atmosphere (C,CO) depending on the nature of the presumed complex combination. The reductive atmosphere can be influenced by the nature of the diol and the manner in which the decomposition (thermal treatment) takes place. The annealing products were studied by XRD analysis (fig. 6). Following the 500°C decomposition of cobalt lactate, a mixture of cobalt oxides (CoO and Co₃O₄) is formed. At 800°C Co₃O₄ is obtained as a single phase, while at 1000°C, CoO forms as a single phase (JCPDS 75-0393 chart [18]). In the case of cobalt malonate decomposition, Co₃O₄ is obtained as a single, crystalline phase (JCPDS 42-1467 chart [18]), both at 500 and 800°C, while at 1000°C, CoO becomes the unique crystalline phase. The reduction of Co₃O₄ to CoO takes place following the reaction:

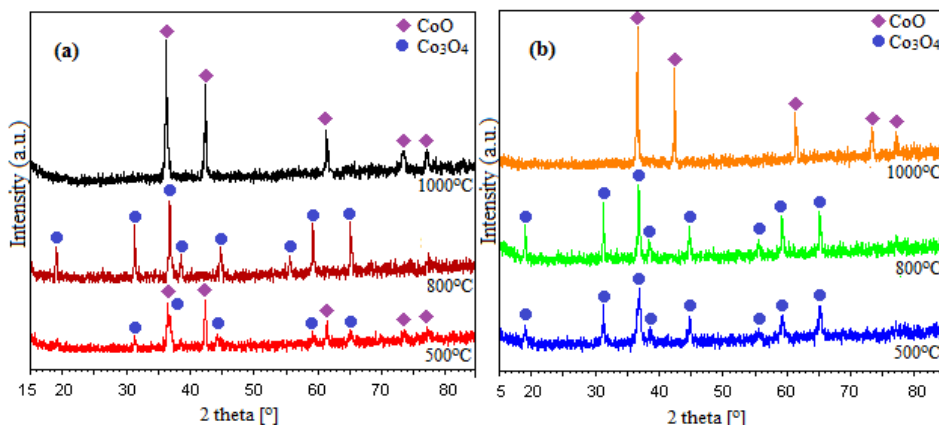


Figure 6. XRD diffractogram of samples obtained from 1-2-propanediol (a), 1,3-propanediol (b) at 500°C, 800°C and 1000°C

The average crystallite size (*D*) of CoO and Co₃O₄ was calculated from the XRD data using Debye-Scherrer formula ($D = C \cdot \lambda / \beta_{1/2} \cdot \cos \theta$) [19] and is presented in table 2.

Table 2. Average diameters of nanoparticles calculated with Scherrer equation

Temperature / °C	Average diameter / nm			
	din 1.2 propandiol		din 1.3 propandiol	
	CoO	Co ₃ O ₄	CoO	Co ₃ O ₄
500	20	23	-	26
800	-	28		30
1000	32	-	35	-

According to the data in table 2, the dimension of the nanoparticles increases with the increase in temperature and with that of the crystallization degree. In addition, purer oxides with larger nanoparticles are obtained from 1,3 propanediol when compared to those synthesized from 1,2 propanediol.

CONCLUSIONS

The redox reaction $\text{Co}(\text{NO}_3)_2$ -1,2-propanediol and $\text{Co}(\text{NO}_3)_2$ -1,3-propanediol, as evidenced by thermal analysis, takes place in the range of 160-190°C. The cobalt lactate and cobalt malonate formation of the redox reaction was confirmed by means of FT-IR spectrometry, thermal analysis and acido-basic analysis (conductometric and pH-metric). All techniques have evidenced the formation of coordination compounds of Co(II) with the lactate anions, resulted through 1,2-propanediol oxidation. According to the study of acido-basic properties of the product obtained from 1,2-propanediol, a mixture of Co(II) lactate and Co(II) hydroxylactate was obtained, while from 1,3-propanediol only cobalt malonate was synthesized. By thermal treatment of this product at 500°C, through the decomposition of cobalt lactate, a mixture of CoO and Co_3O_4 is obtained, while at 800°C only the Co_3O_4 crystalline phase results, phase that at 950°C reduces to the well crystallized CoO. In the case of cobalt malonate decomposition, Co_3O_4 results as a single phase, while at 1000°C the unique phase is CoO, the crystallization degree increasing with the increase in temperature. The size of nanoparticles increases with temperature, where Co_3O_4 obtained from 1,2 propanediol at 800°C has 28 nm, and from 1,3 propanediol, 30 nm. In a similar manner, the dimensions of CoO obtained through the decomposition of cobalt lactate, following the 1000°C thermal treatment, increases from 32 to 35 nm from the decomposition of malonate. In conclusion, it can be stated that the position of the second OH group can influence the conditions related to the formation of the carboxylic precursor, as well as the nature of oxides formed by advanced treatments.

EXPERIMENTAL SECTION

The reagents used in synthesis were: $\text{Co}(\text{NO}_3)_2 \cdot 6\text{H}_2\text{O}$ and 1,2 propanediol respectively 1,3-propanediol of purity p.a. (Merk). The synthesis method consists in dissolving cobalt nitrate in the corresponding 1,2PG respectively 1,3-propanediol in stoichiometric ratio, amount followed by controlled heating at 140°C. At these temperatures, the redox reaction

begins accompanied by nitrogen oxide emission (brown-reddish gas). The isolated reaction products were maintained at 140°C until the emission of brown gas stops (reaction end). The powder obtained at 140°C was washed with acetone for removing of the reactant excess. The obtained products were characterized by thermal analysis, FT-IR spectrometry and conductometric/pH-metric acido-basic titrations

For the conductometric and potentiometric titrations 0.2 mmoli Co(II) were used, adding volumes of 10,0 cm³ HCl 0.1M and subjected to titrations with NaOH 0.1M. The acido-basic properties of the precursors were studied through conductometric and pH-metric titrations using a Crison MM41 multimeter. The formation process of cobalt oxides was followed with thermogravimetry (TG), derivative thermogravimetry (DTG) and differential thermal analysis (DTA) using a SDT Q600 type instrument, in air up to 1000°C at 10 °C min⁻¹ and alumina standards. The FTIR spectra were recorded on 1% KBr pellets using a Spectrum BX II spectrometer. The XRD patterns were recorded using a high resolution Bruker D8 Advance diffractometer with Cu ($\lambda_{\text{CuK}\alpha 1}=1,54056 \text{ \AA}$) radiation.

REFERENCES

1. L. Qiao, M.T. Swihart, *Advances in Colloids and Interface Science*, **2017**, 244, 199.
2. H.M. Khaled, *Polymer Composites*, **2016**, 37, 1881.
3. E. Papis, F. Rossi, M. Raspanti, I. Dalle-Donne, G. Colombo, A. Milzani, G. Bernardini, R. Cornati, *Toxicology Letters*, **2009**, 189, 253.
4. H. Heli, J., Pishahang, *Electrochimica Acta*, **2014**, 123, 518.
5. M. Allen, D. Willits, M. Young, T. Douglas, *Inorganic Chemistry*, **2003**, 42, 6300.
6. S. Kundu, M. Jayachandran, *Journal of Nanoparticle Research*, **2013**, 15, 1.
7. Q.A. Pankhurst, J. Connolly, S.K. Jones, J. Dobson, *Journal of Physics D: Applied Physics*, **2003**, 36, 167.
8. R. Manigandan, K. Giribabu, R. Suresh, L. Vija Yalakshmi, V. Narayanan, *Chemical Science Transactions*, **2013**, 2, 47.
9. A. Ashok, A. Kumar, R.R. Bhosale, M.A.H. Saleh, U.K. Ghosh, M. Al-Marri, F.A. Almomani, M.M. Khader, *Ceramic International*, **2016**, 42, 12771.
10. S. Chattopadhyay, S.P. Chakraborty, D. Laha, R. Baral, P. Pramanik, S. Roy, *Cancer Nanotechnology*, **2012**, 3, 13.
11. K. Slinko, G. Szabo, M. Zrinyi, *Journal of Nanoscience and Nanotechnology*, **2011**, 11, 1.
12. K.F. Wadekar, K.R. Nemade, S.A. Waghuley, *Research Journal of Chemical Sciences*, **2017**, 7, 53.

13. M. Yarestani, A.D. Khalaji, A. Rohani, D. Das, *Journal of Sciences, Islamic Republic of Iran*, **2014**, 25, 339.
14. Q. Liu, X. Guo, J. Chen, J. Li, W. Song, W. Shen, *Nanotechnology*, **2008**, 19, 365608.
15. C. Luna, M. del Puerto Morales, C.J. Serna, M. Vazquez, *Nanotechnology*, **2003**, 14, 268.
16. R. Prasad, Sulaxna and A. Kumar, *Journal of Thermal Analysis and Calorimetry*, **2005**, 81, 441.
17. Vencat Narayan R., Kanniah V., Dhathathreyan A., *Journal of Chemical Sciences*, **2006**, 118, 179.
18. Joint Committee on Powder Diffraction Standards. International Center for Diffraction Data, **1999**.
19. Klug HP, Alexander LE. *X-Ray Diffraction Procedures*. 2nd ed. John Wiley & Sons Inc, **1974**.

PHYSICO-CHEMICAL STUDY CONCERNING ATMOSPHERIC PARTICULATE MATTER HAZARD

IOAN PETEAN^a, AURORA MOCANU^a,
GERTRUD-ALEXANDRA PĂLTINEAN^a, RALUCA ȚĂRCAN^a,
DANA FLORINA MUNTEAN^b, LIANA MUREȘAN^b, GEORGE ARGHIR^{c*},
MARIA TOMOAI A COTIȘEL^{a,d}

ABSTRACT. The particulate matter (PM) from the atmosphere is able to penetrate in the respiratory system presenting several health risks such as acute respiratory items, allergic issues, and chronic risks such as silicosis and asthma. PM from atmosphere is classified by diameter as PM10 – particles with aerodynamic diameter up to 10 μm , PM2.5 – particles with aerodynamic diameter up to 2.5 μm , and PM1 - particles with aerodynamic diameter up to 1 μm . The first major PM source is the street dust (SD) which induces mineral fraction into the atmosphere such as: quartz, kaolinite, calcite, muscovite, and goethite. The second PM source is the pollen from several species like *Tilia Cordata*, *Sambucus Nigra*, *Jasminus Communis*, *Rosaceae* Family, *Lilium Candidum*, and *Brassica Rapa*, during later spring and early summer. Elements from both sources were found in PM samples collected from atmosphere: sedimentary particles, PM10 and PM2.5. In vivo experiments show that PM10 affects upper respiratory pathways such as nasal cavity and pharynges meanwhile PM2.5 was found in the expectoration matter from tracheal area. These studies reveal that 5 minutes of exposure at a concentration of 125 $\mu\text{g}/\text{m}^3$ conducts to formation of severe deposits on respiratory mucosa.

Keywords: PM 10, PM 2.5, hazard

^a Babeș-Bolyai University, Faculty of Chemistry and Chemical Engineering, Arany Janos Str., No. 11, RO-400084 Cluj-Napoca, Romania.

^b Environmental Protection Agency Cluj, Calea Dorobanților Str., No. 99, RO-400609, Cluj – Napoca, Romania.

^c Technical University of Cluj - Napoca, Faculty of Materials and Environment Engineering, Muncii Ave., No. 103 -105, RO-400641 Cluj – Napoca, Romania.

^d Academy of Romanian Scientists, 54 Splaiul Independentei, 050094, Bucharest, Romania

*Correspondent author: georgearghir@hotmail.com

INTRODUCTION

Particulate matters (PM) dispersed in the atmosphere represent a great concern for the human health due to their ability to be inhaled [1 - 4]. Such particles are trapped by the respiratory system mucosa to prevent their penetration in the lungs. Thus, the hazard is a matter of particle size related to the penetration depth in the respiratory system. PM₁₀ is usually trapped into the nose cavity and nasal passages; meanwhile PM_{2.5} is able to be inhaled down to trachea and primary bronchi [5, 6]. The effect of inhaled particles leads to specific affections such as: acute pathologies including allergies, inflammations and respiratory insufficiency [7, 8]. Longer exposure to inhaled PM leads to the chronic affections such as: silicosis, lung cancer and autoimmune responses due to the disturbed neuronal activity of receptors sensing the presence of the particles [9 -12].

Recent developed studies related to the atmospheric PM evidence the silicate particles occurrence due to the environmental condition in the urban area [13 - 15]. Such particles could be very harmful if inhaled. The aim of this paper is to establish PM₁₀ and PM_{2.5} ability to be inhaled and to identify which kind of particles are able to penetrate in the respiratory system. Therefore, we consider some in vivo tests for the identification of those particles.

RESULTS AND DISCUSSION

The data in literature state that street dust (SD) is the most important source of atmospheric PM [13]. Therefore, we select a complex area situated in Dâmboviței Street, Cluj – Napoca, Romania, for present study. It features a street with average car traffic, around 15 cars per minute, bordered with complex environment containing decayed soils and green areas (e.g. Dâmboviței Park and Expo Transilvania Park) containing various plant species. The representative SD sample for this environment was physico – chemical investigated.

The minerals were identified by XRD analysis, Figure 1. Resulted XRD pattern has very well-developed peaks proving the cristalinity of SD sample.

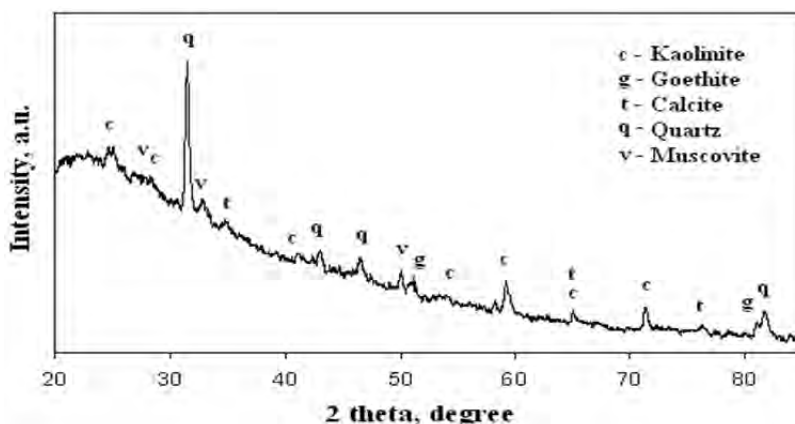


Figure 1. The X-ray spectrum for SD sample collected from Dâmboviței Street.

The dominant mineral is quartz followed by clay mixture (e.g. kaolinite and muscovite), calcite and goethite are the last minerals. XRD data were correlated with mineralogical microscopy performed in cross polarized light, Figures 2.

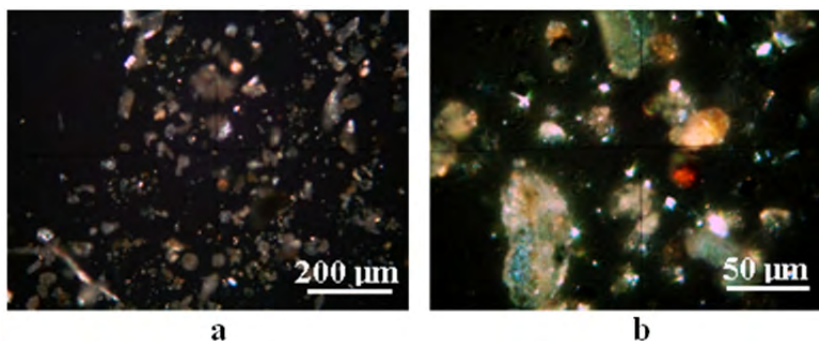


Figure 2. SD sample collected from Dâmboviței Street observed in cross polarized light: a) low magnification and b) high magnification.

A wide mixture of particles is observed at low magnification, Figure 2a, their size ranges from small microscopic level to grosser particles having over 100 µm diameter. At high magnification, Figure 2b, particles are seen better, each mineral species having its own specific color. The XRD and mineralogical microscopy data resulted for the SD sample are summarized in Table 1.

Table 1. Components properties of SD sample

Component	Quartz	Kaolinite	Muscovite	Calcite	Goethite
Formula	SiO ₂	Al ₂ Si ₂ O ₅ (OH) ₄	KAl ₂ (AlSi ₃ O ₁₀)(F,OH) ₂	CaCO ₃	αFeO(OH)
Particle size range, μm	2 - 100	1 – 20	1 - 25	10 - 40	5 - 50
Color in cross polarized light	Green - gray	White-Blue	Pink	Yellow-brown	Reddish - brown

The SD sample has mineral components derived from local decayed soils, representing a fingerprint of the investigated area. All SD particles could be suspended in the atmosphere due to various environmental factors such as natural air currents (affected by regional climate) and anthropogenic factors such as car traffic and industrial activities [16, 17]. Their ascension into the atmosphere depends on the particles physical properties, mainly their diameter. All SD minerals have small micro particles which are able to be lifted in the air.

Minerals are not only one source of particulate matters, pollen from various vegetal species is often found in the atmosphere during April and May. Such organic particles could be hazardous for human health due to the allergenic issues. Therefore, the pollen was extracted from fresh flowers collected during April and May 2017 from the adjacent area of Dâmboviței Street. These samples were investigated in transmitted light, Figure 3.

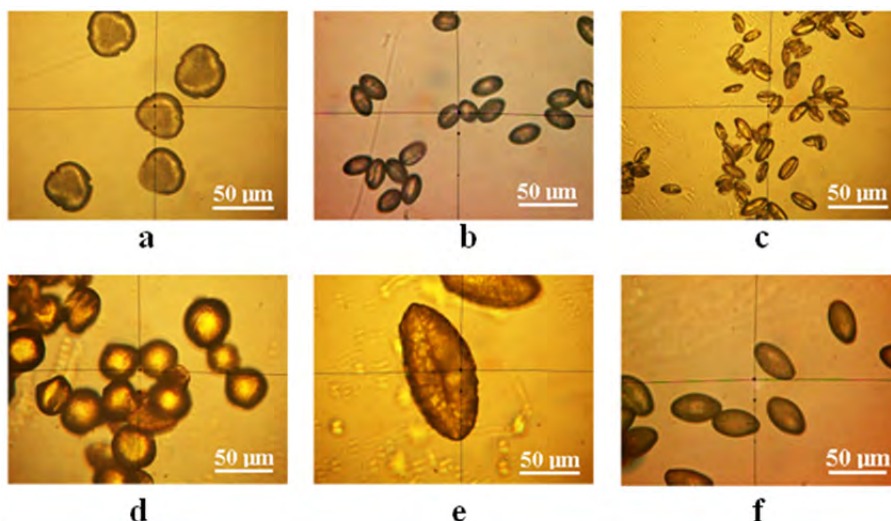


Figure 3. Pollen samples collected from Dâmboviței Street area observed in transmitted light: a) *Tilia Cordata*, b) *Sambucus Nigra*, c) *Jasminus Communis*, d) *Rosaceae* Family, e) *Lilium Candidum*, and f) *Brassica Rapa*.

The quantitative measurements performed on images in Figure 3 are centralized and systematized in Table 2. The obtained values related to pollen shape are in good agreement with pollinological databases.

Table 2. Pollen particles characteristics

Plant	<i>Tilia</i>	<i>Sambucus</i>	<i>Jasminus</i>	<i>Rosa</i>	<i>Lilium</i>	<i>Brassica</i>
Shape	sub-triangular	elongated	elongated	round	elongated	elongated
Length, μm		25	20		125	35
Diameter, Mm	35	10	5	25 - 30	50	15

Pollen particles from *Sambucus Nigra* and *Jasminus Communis* presents characteristic dimensions for PM10 being the most susceptible to be inhaled from all investigated range. The most inoffensive is the *Lilium Candidum* pollen due to its larger size and sticky surface.

Floating particles (FP) from atmosphere represents the most heterogenic particulate matter sample containing all kind of solids suspended in air due to various conditions, that's why some authors refer to total sedimentary particles [18, 19]. The maximum accepted level of FP emission is 17 $\text{g}/\text{m}^2/\text{h}$ according to Romanian and UE laws. The representative FP sample collected with the Automatic Station of Air Quality Monitoring was subjected to the XRD analysis, Figure 4a.

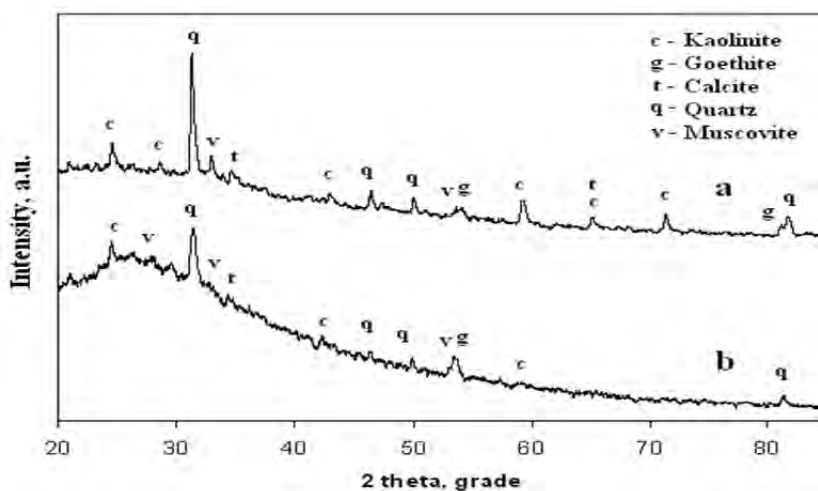


Figure 4. The X-ray spectra for FP (a) and PM10 (b) collected from Dâmboviței Street with Automatic Station for Air Quality Monitoring.

It features well developed peaks proving the high level of cristallinity of FP sample, Figure 4a. A great similitude with SD sample is observed, Figure 4b. Minerals found in FP sample are the same as in SD: quartz, kaolinite and muscovite, calcite and goethite. Optical microscopy performed on FP reveals two areas of interest, Figure 5.

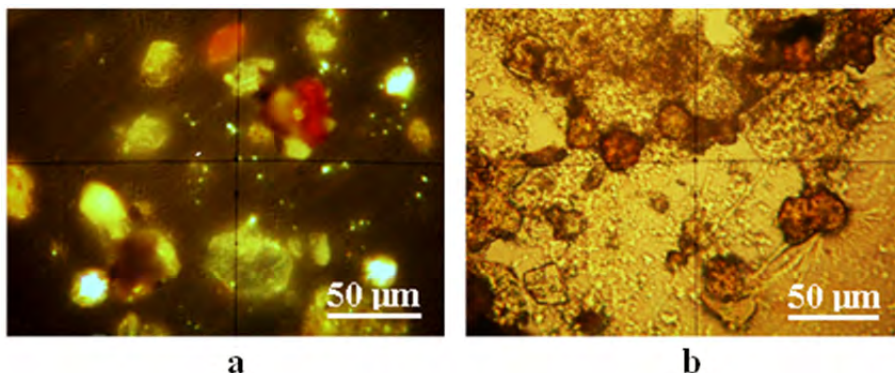


Figure 5. FP sample collected from Dâmboviței Street: a) reach mineral area observed in cross polarized light and b) organic reach area observed in transmitted light.

The first is the reach mineral area, Figure 5a, where appear fine particles with tabular aspect like kaolinite and muscovite [20, 21] mixed up with a various mixture of quartz calcite and goethite. A dimensional hierarchy is observed: clay particles are present mostly in PM2.5 area meanwhile quartz and calcite are rather found in PM10 category, Table 3.

Table 3. Components properties of FP sample

Component	Quartz	Kaolinite	Muscovite	Calcite	Goethite
Formula	SiO ₂	Al ₂ Si ₂ O ₅ (OH) ₄	KAl ₂ (AlSi ₃ O ₁₀)(F,OH) ₂	CaCO ₃	αFeO(OH)
Particle size range, μm	2 - 50	1 - 20	1 – 25	10 - 40	5 - 60
Color in cross polarized light	Green - gray	White-blue	Pink	Yellow-brown	Reddish - brown
Particle shape	round	tabular	tabular	round	elongated

The second is organic reach area, Figure 5b. A lot of organic matter is situated in micro-scaled conglomerates, but there are a few distinct pollen grains evidenced. Their shape and size is altered by the FP collecting method which uses sedimentation in bi-distilled water, most likely they are *Tillia Cordata* or *Sambucus Nigra* grains. This proves the importance of pollen as PM source during spring and early summer. It results that FP sample is SD lifted in the atmosphere combined with pollen from the in-blossom flowers in April and May 2017.

PM10 fraction contains also similar minerals like in SD and FP, fact evidenced by the pattern in Figure 4b. The diffraction peaks are no longer so well developed due to the smaller size of the diffractant particles. Quartz is the dominant mineral, proving that PM is mostly silica, followed by the clay mixture. The mineral arrangement in PM10 is observed by SEM imaging in Figure 6a: where several quartz particles having the range of 2.5 – 10 μm diameter surrounded by smaller particles which are supposed to be clay. Certain evidences were obtained by EDX analysis, Table 4. The major elements in the PM10 composition are Si and O, fact in good agreement with XRD information. Presence of significant amount of Al, K, and Mg certify the presence of clay particles into the PM 10 sample. Lower amount of C found in PM10 could be related by the traces of calcite found in XRD pattern and possibly to belong to some organic features.

PM2.5 shape is revealed in the SEM image, Figure 6b. There is a complex conglomerate based on lamellar – tabular particles having sizes below 2.5 μm . There are also found some rounded particles having typical aspect for grinded quartz. Particles shape and distribution in PM2.5 proves their origin in SD.

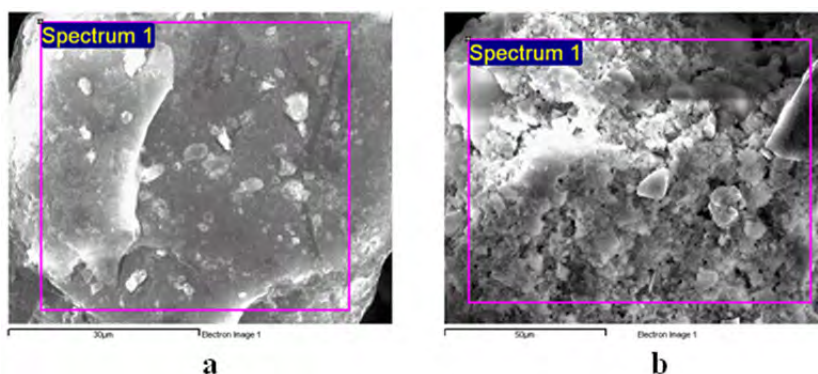


Figure 6. SEM images for particulate matters: a) PM10 and b) PM2.5.

PM2.5 was subjected also to the EDX analysis, results being displayed in Table 4. A significant amount of Al and K was observed proving the predominance of clay particles instead quartz ones. The amount of C is increased than in PM10 sample, fact sustained by traces of calcite (around of 1.38 wt. % Ca) and organic amorphous carbon.

Table 4. Elemental composition for PM10 and PM2.5 resulted from EDX

Element	PM10		PM2.5	
	weight %	atomic %	weight %	atomic %
C	2.86	4.62	13.04	19.99
O	56.27	68.27	55.77	64.18
Mg	1.54	1.23	0.61	0.46
Al	14.52	10.45	12.08	7.04
Si	17.31	11.96	5.09	3.34
S	-	-	0.25	0.14
K	5.65	2.80	10.39	4.06
Ti	0.52	0.21	-	-
Ca	-	-	1.39	0.33
Fe	1.33	0.46	1.38	0.46
Total	100.00	100.00	100.00	100.00

EDX analysis confirms the reach mineral composition of PM formed in Dâmboviței street area containing minerals with hazardous features which if are inhaled could lead to acute respiratory affections and to silicosis at longer term of exposure. The positive aspect revealed by EDX is the lack of heavy metals and or radioactive isotopes in PM10 and PM2.5 samples. This situation decreases the hazard because lack of carcinogenic elements.

Another aspect connected to the respiratory health is the emission level of each PM pollutant category. The data measured from the atmosphere with the Automatic Air Quality Monitoring Station are displayed in Table 5.

Table 5. PM emission level in Dâmboviței Street for April and May 2017

Emission type		April 2017	May 2017
PM2.5, μg/m ³	minim	5.43	12.32
	maxim	24.65	23.75
	average	11.45	18.05
PM10, μg/m ³	minim	2.35	7.61
	maxim	42.01	42.24
	average	18.18	21.44
FP, g/m ² /month	average	9.03	6.67

FP emission level is situated in the safe range, far below maximum limit of $17 \text{ g/m}^2/\text{month}$. The average values recorded for April and May 2017 for PM_{2.5} and PM₁₀ are far below the maximum accepted value. This is due to the relatively humid weather related with a good environmental management applied in the street.

The most humid days with the lowest car traffic lead to the lower values recorded, while the driest days with high car traffic lead to the higher values recorded. Only two limits overtake at PM₁₀ were recorded: $42.01 \text{ } \mu\text{g/m}^3$ on 27 April 2017 and $42.24 \text{ } \mu\text{g/m}^3$ on 12 May 2017. These overtakes do not generate hazard because of their low excess of PM₁₀ situated around $2 \text{ } \mu\text{g/m}^3$, and happened only once per month.

Nanoparticles from aqueous dispersion were transferred onto solid substrate (e.g. glass slide) by vertical adsorption [22 – 26]. The deposited film was investigated by AFM resulting the image in Figure 7. The film topography is observed in Figure 7a, the deposited layer is uniform and nanoparticles are well individualized. Cross section in Figure 7b allows calculating the average diameter of nanoparticles which is situated around 30 nm.

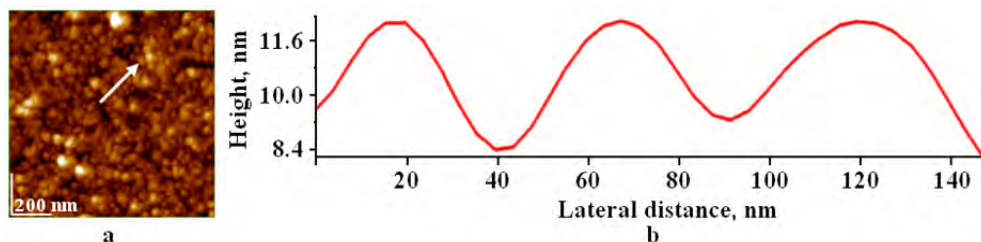


Figure 7. AFM images for nanoparticles derived from PM_{2.5}.

Nanoparticles presence in the PM_{2.5} sample is a risk factor due to their ability to penetrate tissues such as pulmonary alveoli. Fortunately, nanoparticles have low ability to travel alone into the atmosphere because of their high coalescence tendency. Such coalescence is proved by the formation of nanoparticles clusters observed in AFM images, Figure 7. They are also very sticky and are expected to be trapped into mucus immediately after they are inhaled.

In vivo exposure to the normal atmosphere (e.g. PM level below $40 \text{ } \mu\text{g/m}^3$) does not affect the nasal mucosa, or the mucus from trachea. It is clearly observed in cross polarized light Figures 8a and 8d: only organic compounds of the mucus are observed with no trace of mineral particles.

At an exposure of 5 minutes to a polluted air with PM10 level around of $125 \mu\text{g}/\text{m}^3$ leads to mineral deposits of PM10 in nose mucus consisting mainly in quartz and fewer clay particles, Figure 8b. The expectoration product contains some PM2.5 particles consisting in kaolinite and muscovite as seen in Figure 8e. The exposure to a polluted air with PM10 level around of $200 \mu\text{g}/\text{m}^3$ for 5 minutes leads to massive deposits of PM10 into the nose mucus containing mainly quartz particles followed by calcite and goethite, Figure 8c.

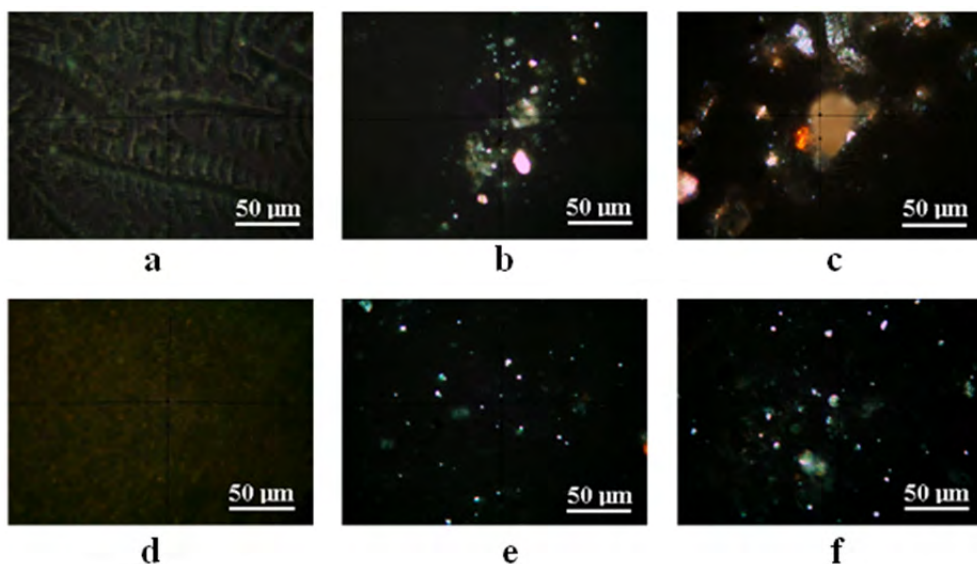


Figure 8. Cross polarized light images for in vivo experiment: Nose mucus: a) normal atmosphere, b) polluted atmosphere up to $125 \mu\text{g}/\text{m}^3$ PM10, and c) polluted atmosphere up to $200 \mu\text{g}/\text{m}^3$; Expectoration product: d) normal atmosphere, e) polluted atmosphere up to $125 \mu\text{g}/\text{m}^3$ PM10, and f) polluted atmosphere up to $200 \mu\text{g}/\text{m}^3$.

Significant mineral deposits are found in the expectoration product where PM2.5 consisting in clay particles is found predominantly, Figure 8f. There are found also some PM10 particles with quartz aspect, which means a severe penetration of PM into the respiratory system.

CONCLUSIONS

The analysis performed in present article proves that SD is the major source of PM in the atmosphere in environmental conditions from Dâmboviței Street, Cluj – Napoca. The minerals from SD are found in FP sample: quartz as dominant mineral followed by clay mixture with kaolinite and muscovite, calcite and goethite. Pollen was found in FP sample, proving that pollen could be considered as PM which could affect respiratory system especially in allergic affections. PM10 contains mainly quartz particles meanwhile PM2.5 contains kaolinite and muscovite predominantly. Such composition depends on the investigated specific area; some other sites could report other compositions. AFM imaging reveals some nanoparticles in PM2.5.

The minerals in PM10 and PM2.5 could be very hazardous for the respiratory system, if the standard limit is exceeded and the exposure time is long enough in vivo experiments. A short exposure at an intense dose of PM leads to an acute respiratory affection, and chronic affections could appear if exposure is extended for long time.

The air monitoring data shows that the PM emissions in the Dâmboviței Street area are below standard limit and no hazard risk appears if the environmental condition is maintained.

EXPERIMENTAL SECTION

The experimental area is situated in Dâmboviței Street, Cluj – Napoca. The SD samples were collected weekly during April and March 2017. Each week was taken 10 grams of SD and mixed together to obtain an average representative sample of SD. Dâmboviței Street has a lot of vegetal species which flowers during April and May. Therefore, the resulted pollen could emerge in the atmosphere like PM. Pollen from *Tilia Cordata*, *Sambucus Nigra*, *Jasminus Communis*, *Rosaceae* Family, *Lilium Candidum*, and *Brassica Rapa* was collected and investigated.

PM samples: FP, PM10, and PM2.5 were collected using Automatic Air monitoring Station from Environmental Protection Agency of Cluj-Napoca, and their level of emission in the atmosphere was monitored during April and May 2017 and the results were centralized.

In vivo experiment consists in a human subject (volunteer agreement) exposed for 5 minutes to normal atmosphere, average polluted atmosphere (aprox. $125 \mu\text{g}/\text{m}^3$ of PM10), and high polluted atmosphere (up to $200 \mu\text{g}/\text{m}^3$ of PM10). The polluted atmosphere was produced by street dust agitation with an air blower in the Dâmboviței Street area. Nose mucus and expectoration product was collected after each exposure. The exposures were effectuated in different days to avoid the cumulative effect on the subject.

The X-ray diffraction analysis was performed on a DRON 3 diffractometer equipped with data acquisition module and MATMEC VI.0 soft. A monochrome Co_{Kα} radiation was used for all X ray spectra. The mineral identification was effectuated using MATCH 1.0 X – ray standard data base from Crystal Impact co.

Optical microscopy was performed on a Laboval 2 microscope produced by Karl Zeiss Jena equipped with digital capture Kodak 10 Mpx camera. Quantitative analysis on the optical microphotographs was done using the Image J professional soft as freeware resource from National Institutes of Health USA.

SEM microscopy associated with EDX analysis was performed on a Jeol JSM 5600 LV microscope in secondary electrons imaging mode coupled with Everhart Thornley detector for EDX analysis

Samples for AFM investigation were prepared according to the data in literature [27 - 34]. The AFM investigation was performed on a Jeol JSPM 4210 microscope in tapping mode using NSC 15 cantilever. Topography, phase, and amplitude images were acquired simultaneously and were processed into the standard manner using Win SPM 2.0 processing soft.

REFERENCES

1. L.A. Jimoda, *Facta Universitatis, Series: Working and Living Environmental Protection*, **2012**, 9(1), 27.
2. J.S. Le Blond, S. Woskie, C.J. Horwell, B.J. Williamson, *Atmospheric Environment*, **2017**, 149, 34.
3. W.C. Lo, R.H. Shie, C.C. Chan, H.H. Lin, *Journal of the Formosan Medical Association*, **2017**, 116, 32.
4. M.R. Perrone, S. Becagli, J.A. Garcia Orza, R. Vecchi, A. Dinoi, R. Udisti, M. Cabello, *Atmospheric Environment*, **2013**, 71, 176.
5. K.H. Kim, E. Kabir, S. Kabir, *Environment International*, **2015**, 74, 136.
6. J. Londhal, J. Pagels, E. Swietlicki, J. Zhou, M. Ketznel, A. Massling, M. Boghard, *Aerosol Science*, **2006**, 37, 1152.
7. Q. Xu, S. Wang, Y. Guo, C. Wang, F. Huang, X. Li, Q. Gao, L. Wu, L. Tao, J. Guo, W. Wang, X. Guo, *Environmental Pollution*, **2017**, 220, 317.
8. M. Watanabe, H. Noma, J. Kurai, H. Sano, D. Hantan, M. Ueki, H. Kitano, E. Shimizu, *Allergology International*, **2017**, 66, 52.
9. A.C. Gungen, Y. Aydemir, H. Çoban, H. Düzenli, C. Tasdemir, *Respiratory Medicine Case Reports*, **2016**, 18, 93.
10. A.G. Cohen, F. Romero Ruperto, F.J. G. Sendra, M.J. Sánchez García-Altres, M.L. Parra Gordoc, *Medicina General y de Familia*, **2016**, 5(4), 169.
11. M. Tsugita, N. Morimoto, M. Tashiro, K. Kinoshita, M. Nakayama, *Cell Reports*, **2017**, 18, 1298.

12. P. Solaimani, A. Saffari, C. Sioutas, S.C. Bondy, *Neuro Toxicology*, **2017**, 58, 50.
13. G.A. Păltinean, I. Petean, G. Arghir, D.F. Muntean, L.-D. Boboș, M. Tomoaia-Cotișel, *Particulate Science and Technology*, **2016**, 34 (5), 580.
14. G.A. Păltinean, I. Petean, G. Arghir, D.F. Muntean, M. Tomoaia-Cotișel, *Revista de chimie*, **2016**, 67 (6), 1118.
15. D.F. Muntean, D. Ristoiu, G. Arghir, R.F. Campean, I. Petean, *Carpathian Journal of Earth and Environmental Sciences*, **2012**, 7 (3), 175.
16. S.S. Ram, R.V. Kumar, P. Chaudhuri, S. Chanda, S.C. Santra, M. Sudarshan, A. Chakraborty, *Ecological Indicators*, **2014**, 36, 334.
17. L. Makra, I. Ionel, Z. Csépe, I. Matyasovszky, N. Lontis, F. Popescu, Z. Sümegehy, *Science of the Total Environment*, **2013**, 458-460, 36.
18. J. Novak, K. Hilscherová, L. Landlová, P. Čupr, L. Kohút, J.P. Giesy, J. Klánová, *Environment International*, **2014**, 63, 64.
19. F. Mirante, P. Salvador, C. Pio, C. Alves, B. Artinano, A. Caseiro, M.A. Revuelta, *Atmospheric Research*, **2014**, 138, 278.
20. W. De Poel, S. Pinteá, J. Drnec, F. Carla, R. Felici, P. Mulder, J. Elemans, W. Van Enckevort, A.E. Rowan, E. Vlieg, *Surface Science*, **2014**, 619, 19.
21. M. S. Žbik, N.A. Raftery, R.S.C. Smart, R.L. Frost, *Applied Clay Science*, **2010**, 50, 299.
22. O. Horovitz, Gh. Tomoaia, A. Mocanu, T. Yupsanis, M. Tomoaia-Cotișel, *Gold Bulletin*, **2007**, 40 (4), 295.
23. M. Tomoaia-Cotișel, A. Tomoaia-Cotișel, T. Yupsanis, Gh. Tomoaia, I. Balea, A. Mocanu, Cs. Racz, *Revue Roumaine de Chimie*, **2006**, 51 (12), 1181.
24. M.A. Naghiu, M. Gorea, E. Mutch, F. Kristaly, M. Tomoaia-Cotișel, *Journal of Material Science and Technology*, **2013**, 29 (7), 628.
25. G. Tomoaia, O. Soritau, M. Tomoaia-Cotișel, L.-B. Pop, A. Pop, A. Mocanu, O. Horovitz, L.-D. Bobos, *Powder Technology*, **2013**, 238, 99.
26. Gh. Tomoaia, O. Horovitz, A. Mocanu, A. Nita, A. Avram, C.P. Racz, O. Soritau, M. Cenariu, M. Tomoaia-Cotișel, *Colloids and Surfaces B: Biointerfaces*, **2015**, 135, 726.
27. P.T. Frangopol, D.A. Cadenhead, Gh. Tomoaia, A. Mocanu, M. Tomoaia-Cotișel, *Revue Roumaine de Chimie*, **2015**, 60 (2-3), 265.
28. R.D. Pasca, G. Tomoaia, A. Mocanu, I. Petean, G.A. Paltinean, O. Soritau, M. Tomoaia-Cotișel, *Studia Univ. Babeș-Bolyai, Chimia*, **2015**, 60 (3), 257.
29. G. Tomoaia, A. Mocanu, L.D. Bobos, L.B. Pop, O. Horovitz, M. Tomoaia-Cotișel, *Studia Univ. Babeș-Bolyai, Chimia*, **2015**, 60 (3), 265.
30. G. Tomoaia, M. Tomoaia-Cotișel, L.B. Pop, A. Pop, O. Horovitz, A. Mocanu, N. Jumate, L.-D. Bobos, *Revue Roumaine de Chimie*, **2011**, 56, 1039.
31. M. Tomoaia-Cotișel, A. Mocanu, *Revista de Chimie (Bucharest)*, **2008**, 59 (11), 1230.
32. G. Furtos, M.A. Naghiu, H. Declercq, M. Gorea, C. Prejmerean, O. Pana, M. Tomoaia-Cotișel, *Journal of Biomedical Materials Research Part B. Applied Biomaterials*, **2015**, 104 (7), 1290.

I. PETEAN, A. MOCANU, G. PĂLTINEAN, R. ȚĂRCAN, D. MUNTEAN, L. MUREȘAN, G. ARGHIR, M. COTIȘEL

33. F. Goga, E. Forizs, A. Avram, A. Rotaru, A. Lucian, I. Petean, A. Mocanu, M. Tomoaia-Cotisel, *Revista de Chimie (Bucuresti)*, **2017**, 68 (6), 1193.
34. I. Cojocar, A. Tomoaia-Cotisel, A. Mocanu, T. Yupsanis, M. Tomoaia-Cotisel, *Revista de Chimie (Bucuresti)*, **2017**, 68 (7), 1470.

POLIMERIC MEMBRANES PREPARED WITH SURFACTANTS USED FOR ULTRAFILTRATION OF AQUEOUS SOLUTIONS OF FOOD DYE

GEORGE ALEXANDRU POPA^a, GHEORGHE NECHIFOR^{a,*},
DANIELA FLORENTINA ENACHE (POPA)^a,
SZIDONIA-KATALIN TANCZOS^b, ADRIAN CIOCANEA^c

ABSTRACT. The experiments carried out in this paper tested the effectiveness of the polysulfone-dimethyldioctodecylammonium bromide (PSU-DMOA) and polysulfone-Tween 80 in dead-end facilities. The efficiency of these membranes has been proved by determining the permeate flow and the retention coefficient. Analyzing the experimental data, it was found that for the polysulfone-dimethyldioctodecylammonium bromide composite membrane the retention rate is higher than for the polysulfone-Tween 80 composite membrane, the t values being obtained for the highest pressure used in the system.

Keywords: *composite membranes, ultrafiltration, surfactants, food dye*

INTRODUCTION

Polymeric membranes can be used in many simple and complex systems [1-3]. Obtaining membranes can be influenced by the addition of small amounts of surfactants [4,5]. The membrane process can be controlled by using surfactants [6,7].

^a *University Politehnica of Bucharest, Department of Analytical Chemistry and Environmental Engineering, 1-3 Gh. Polizu Str., 011061, Bucharest, Romania*

^b *Sapientia University, Liberty St., 500104, Miercurea Ciuc, Romania*

^c *Politehnica University of Bucharest, Power Engineering Faculty-Hydraulics, Hydraulic Machinery and Environmental Engineering Department, 313 Splaiul Independentei, 060042, Bucharest, Romania*

* *Corresponding author: gheorghe.nechifor@upb.ro*

Surfactants are chemicals which, in solutions, concentrate on the surface and solubilize materials that have little affinity with each other [8]. Accumulating on the separation surfaces, the surfactants are able to alter strongly, even in very low concentrations, the superficial properties of the liquids in which they dissolve [9-11].

The composite polymeric membranes are currently one of the most viable solutions for increasing process membrane performance in terms of permeability as well as selectivity [12-15]. Currently, the improvement of the membrane techniques culminated in their transition to the industrial area of applicability [16,17].

This paper presents the experimental results obtained from the use of polysulfone-dimethyldioctodecylammonium bromide (PMU-DMOA) and polysulfone-Tween 80 composite.

RESULTS AND DISCUSSION

Experiments were carried out to test the effectiveness of polysulfone-dimethyldioctodecylammonium bromide (PMU-DMOA) and polysulfone-Tween 80 membranes. The efficiency of these membranes has been proved by the calculation of permeate flow and retention coefficient [18-22].

The results obtained for the polysulfone-dimethyldioctodecyl ammonium bromide (PMU-DMOA) membranes:

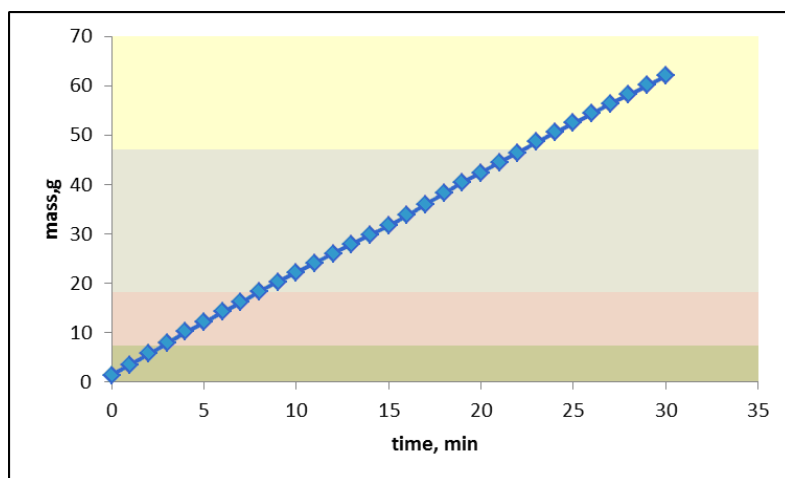


Figure 1. Time variation of the permeate mass at 0.1 MPa pressure for polysulfone - dimethyldioctodecylammonium bromide

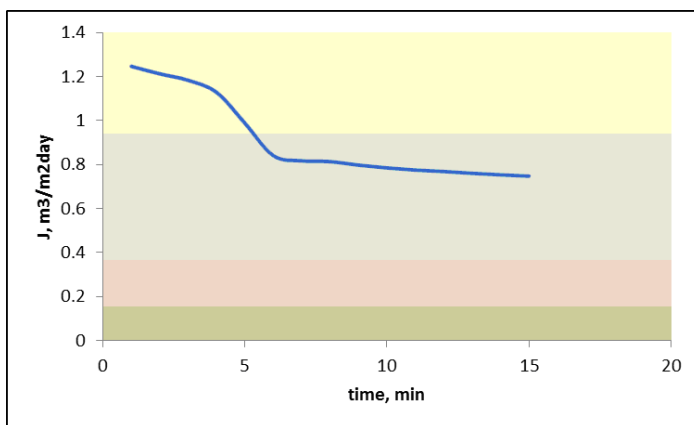


Figure 2. Flow variation at 0.1 MPa for polysulfone - dimethyldioctodecylammonium bromide

Working conditions: Initial solution: $C_{18}H_{13}NO_{5/8/11}S_{1/2/3}Na_{1/2/3}$, 10% (equivalent to 100 g / m^3) - E104; Process duration: 30 minutes; Spectrophotometric measurements at the wavelength of 575nm; Initial temperature: $21,1^\circ\text{C}$; Final temperature: $23,8^\circ\text{C}$; Pressure: 0.1MPa; Operation of the installation: dead-end.

Compared to classical polysulfone membranes, the membrane incorporating surfactant has a better flow for the same operating pressure, ranging from 0,7471 to 1,2463 $\text{m}^3/\text{m}^2\text{day}$.

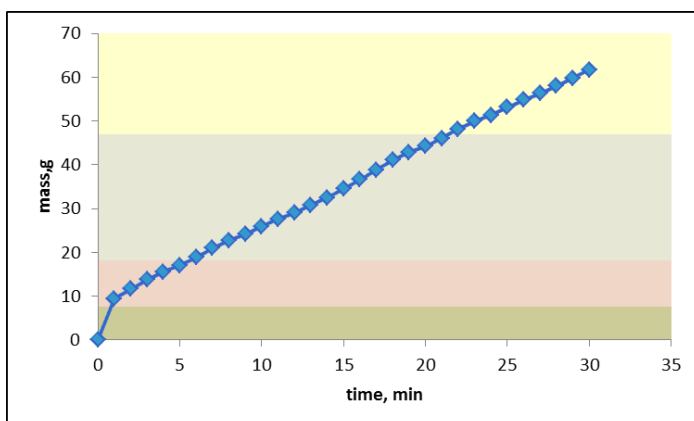


Figure 3. Time variation of the permeate mass at 0.2 MPa pressure for polysulfone - dimethyldioctodecylammonium bromide

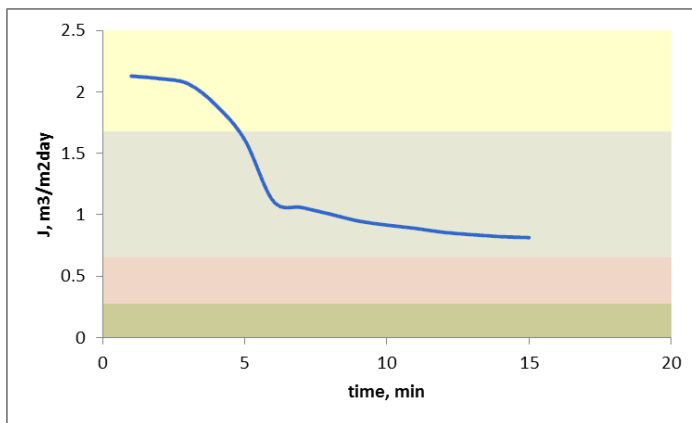


Figure 4. Flow variation at 0.2 MPa for polysulfone - dimethyldioctodecylammonium bromide

Working conditions: Initial solution: $C_{18}H_{33}NO_{5/8/11}S_{1/2/3}Na_{1/2/3}$, 10% (equivalent to $100 \text{ g} / \text{m}^3$) - E104; Process duration: 30 minutes; Spectrophotometric measurements at the wavelength of 575nm; Initial temperature: $21,3^\circ\text{C}$; Final temperature: $23,1^\circ\text{C}$; Pressure: 0.2MPa; Operation of the installation: dead-end.

For the same solution analyzed, at a pressure of 0.2MPa, the flow value ranged between $0,8145$ and $2,129 \text{ m}^3/\text{m}^2\text{day}$, considerably higher than those obtained under the same conditions at 0.1MPa.

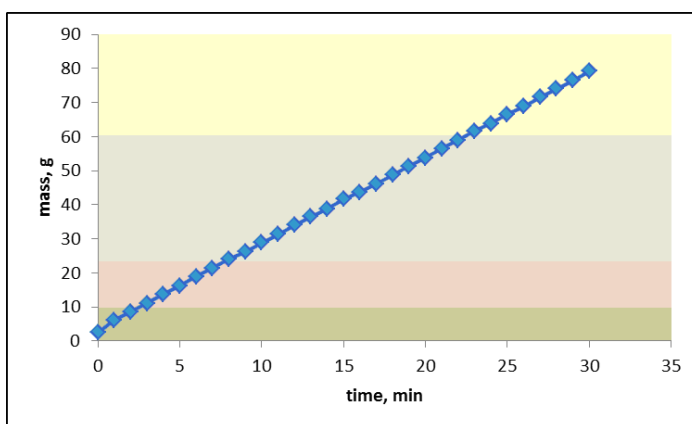


Figure 5. Time variation of the permeate mass at 0.3 MPa pressure for polysulfone - dimethyldioctodecylammonium bromide

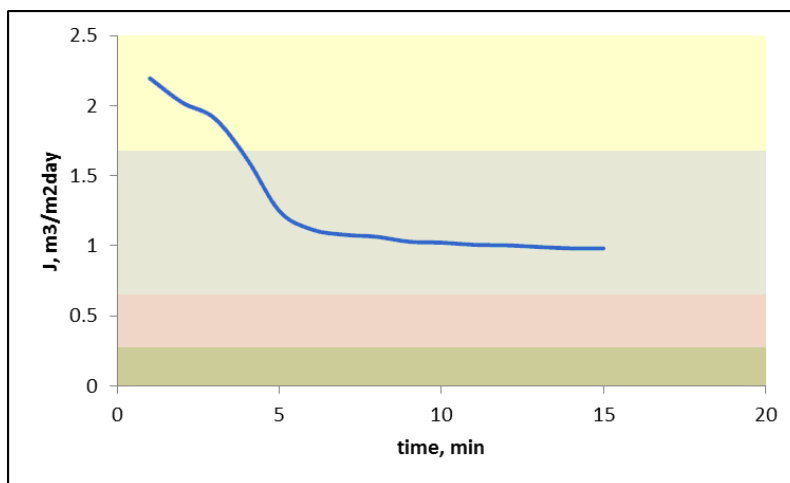


Figure 6. Flow variation at 0.3 MPa for polysulfone - dimethyldioctodecylammonium bromide

Working conditions: Initial solution: $C_{18}H_{33}NO_{5/8/11}S_{1/2/3}Na_{1/2/3}$, 10% (equivalent to 100 g / m^3) - E104; Process duration: 30 minutes; Spectrophotometric measurements at the wavelength of 575nm; Initial temperature: $20,2^\circ\text{C}$; Final temperature: $24,5^\circ\text{C}$; Pressure: 0.3MPa; Operation of the installation: dead-end;

The flow value ranges from 0,9818 to 2,1577 $\text{m}^3/\text{m}^2\text{day}$, also maintaining a downward trend. The flow values for the highest pressure are also high. It can be seen that the polysulfone-dimethyldioctodecyl ammonium bromide composite membrane presents a better flux compared to the polysulfone membrane and polysulfone-polyaniline membrane.

Also, the degree of retention for this type of membrane was higher, given that the presence of the surfactant in the membrane structure caused the formation of micelles and the retention of a considerable amount of dye. The retention determined for the composite polysulfone-dimethyldioctodecylammonium bromide membrane is shown graphically below.

The retention coefficient for solution containing dye E 104 ranged from 34,3 to 43,8% for composite membranes made of polysulfone-dimethyldioctodecylammonium bromide using dead-end filtration. To determine the retention coefficient, we measured the concentration of permeate and retentate solutions using spectrophotometric measurements of absorbance at the wavelength of 575 nm.

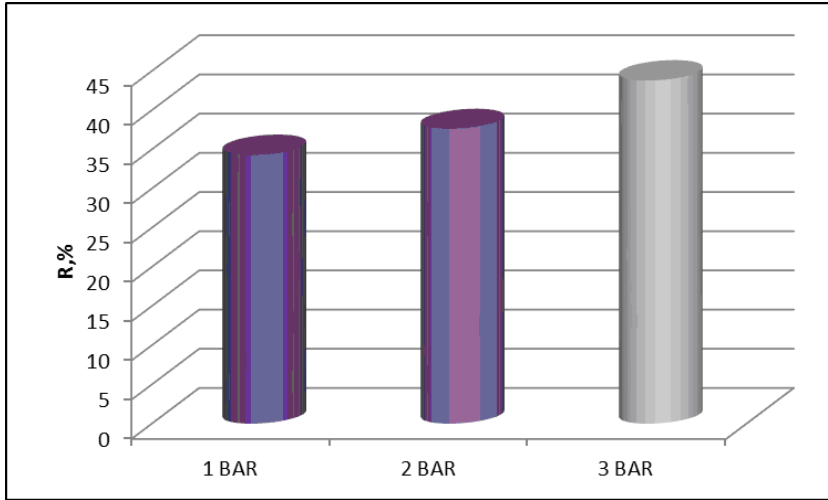


Figure 7. The retention ratio of the dye (R) for the polysulfone-dimethyldioctodecylammonium bromide

The results obtained for polysulfone - Tween 80 composite membrane:

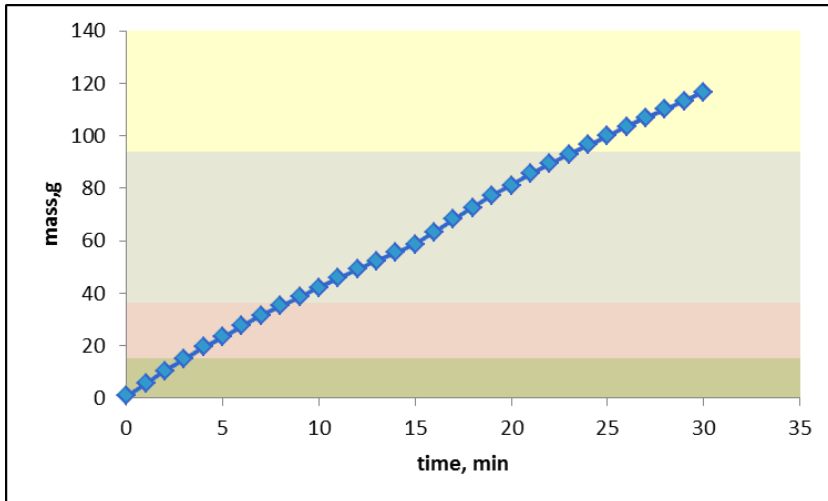


Figure 8. Time variation of the permeate mass at 0.1 MPa pressure for polysulfone - Tween 80

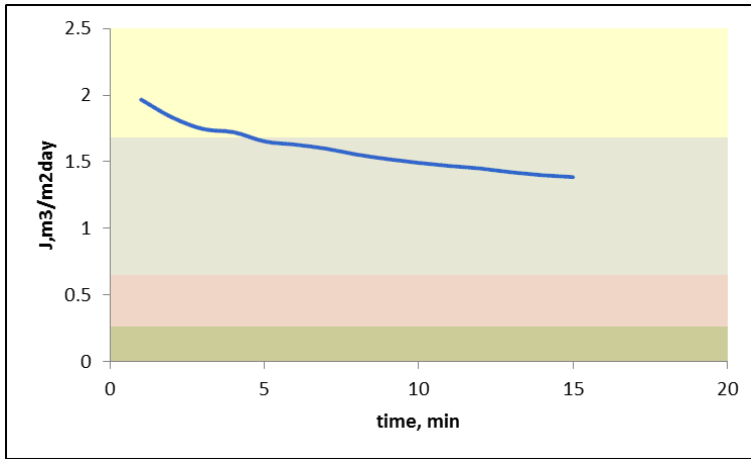


Figure 9. Flow variation at 0.1 MPa for polysulfone – Tween 80

Working conditions: Initial solution: $C_{18}H_{13}NO_{5/8/11}S_{1/2/3}Na_{1/2/3}$, 10% (equivalent to 100 g / m³) - E104; Process duration: 30 minutes; Spectrophotometric measurements at the wavelength of 575nm; Initial temperature: 19,8°C; Final temperature: 21,4°C; Pressure: 0.1MPa; Operation of the installation: dead-end.

For this membrane, flows were obtained which varied at an operating pressure of 0.1MPa, from 1,3862 to 1,9671 m³/m²day.

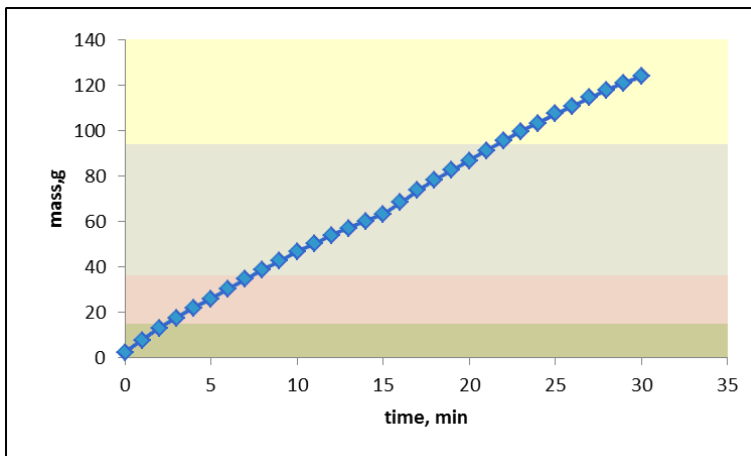


Figure 10. Time variation of the permeate mass at 0.2 MPa pressure for polysulfone – Tween 80

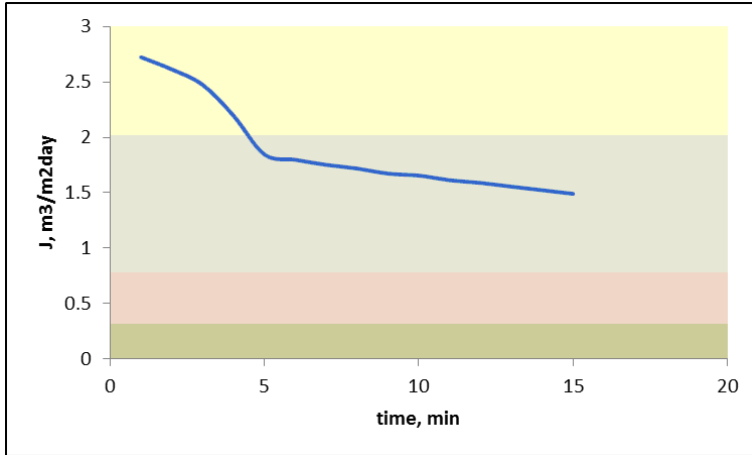


Figure 11. Flow variation at 0.2 MPa for polysulfone – Tween 80

Working conditions: Initial solution: $C_{18}H_{13}NO_{5/8/11}S_{1/2/3}Na_{1/2/3}$, 10% (equivalent to 100 g / m^3) - E104; Process duration: 30 minutes; Spectrophotometric measurements at the wavelength of 575nm; Initial temperature: 20°C ; Final temperature: $22,2^\circ\text{C}$; Pressure: 0.2MPa; Operation of the installation: dead-end.

For the 0.2MPa, the flow value is between 1,491 and 2,7226 $\text{m}^3/\text{m}^2\text{day}$, considerably higher than those obtained under the same conditions at 0.1MPa.

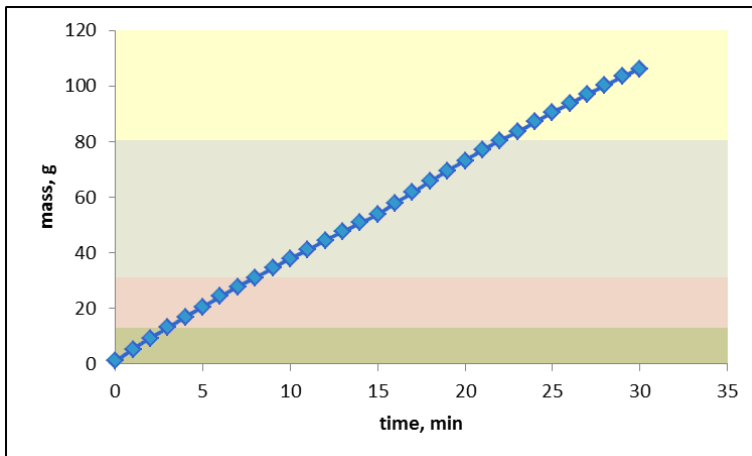


Figure 12. Time variation of the permeate mass at 0.3 MPa pressure for polysulfone – Tween 80

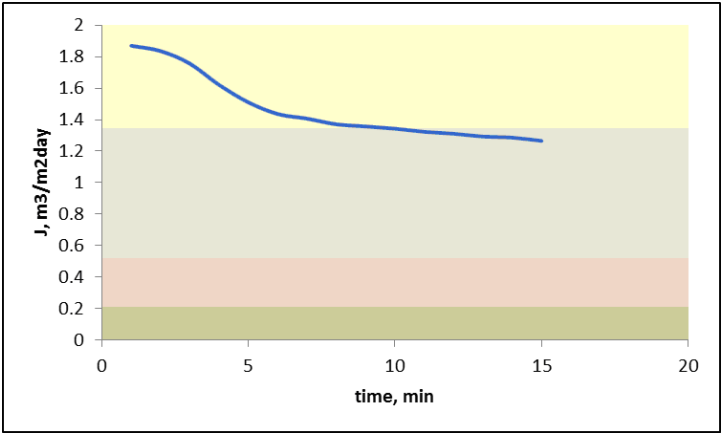


Figure 14. Flow variation at 0.3 MPa for polysulfone – Tween 80

Working conditions: Initial solution: $C_{18}H_{13}NO_{5/8/11}S_{1/2/3}Na_{1/2/3}$, 10% (equivalent to 100 g / m³) - E104; Process duration: 30 minutes; Spectrophotometric measurements at the wavelength of 575nm; Initial temperature: 20,3°C; Final temperature: 24,2°C; Pressure: 0.3MPa; Operation of the installation: dead-end;

The flow rate at 0.3MPa is between 1,2657 and 1,8695 m³/m²day. For this type of membrane, the best fluxes were obtained for the pressure of 0.2MPa, and for the other pressure values the data obtained is similar. The retention degree for this type of membrane can be compared to that obtained for the other membrane types, the results being represented graphically.

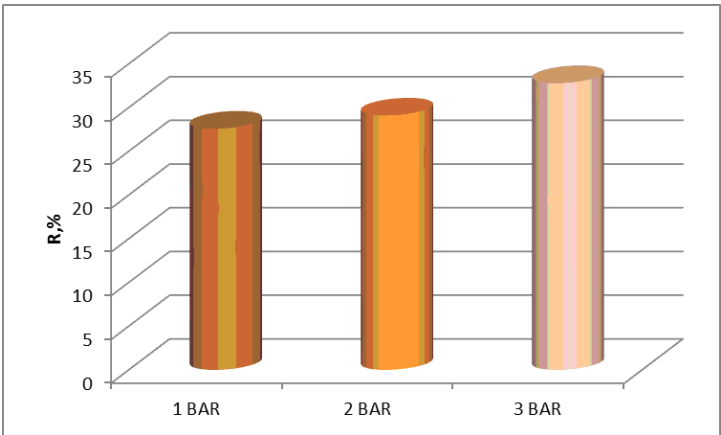


Figure 15. The retention ratio of the dye (R) for the polysulfone - Tween 80

The retention coefficient for solution containing dye E 104 ranged from 27,6 to 32,8% for Tween 80 polysulfone - based composite membranes using dead - end filtration. The results are similar to those obtained for polysulfone - polyaniline and polysulfone membranes.

To determine the retention coefficient, we measured the concentration of permeate and retentate solutions using spectrophotometric measurements of absorbance at the wavelength of 575 nm.

CONCLUSIONS

Membranes undergoing this experimental study showed good mechanical and chemical resistance. Flows presented comparative values with literature data.

The best fluxes were obtained for the polysulfone – dimethyl dioctadecylammonium bromide membrane at 0.2 MPa and at the highest pressure used in the instalation, 0.3 MPa for the polysulfone - Tween 80 membrane.

Regarding the retention, it was observed that the best results were recorded for the dimethyldioctodecylammonium polysulfone - bromide membrane compared to the polysulfone - Tween 80 membrane.

EXPERIMENTAL SECTION

This study used non-commercial membranes [13-16]. The ultrafiltration membranes developed were polysulfone-dimethyldioctodecylammonium bromide (PMU-DMOA) and polysulfone-Tween 80.

The properties of the ultrafiltration membranes regarding transport and separation were determined on solutions containing E104 quinoline yellow synthetic dye. The molecular formula of E 104 is: $C_{18}H_{13}NO_{5/8/11}S_{1/2/3}Na_{1/2/3}$ and the molecular weight amounts to 477.38g/mol. It is used as a synthetic colouring agent in food and drink products, as well as in cosmetics.

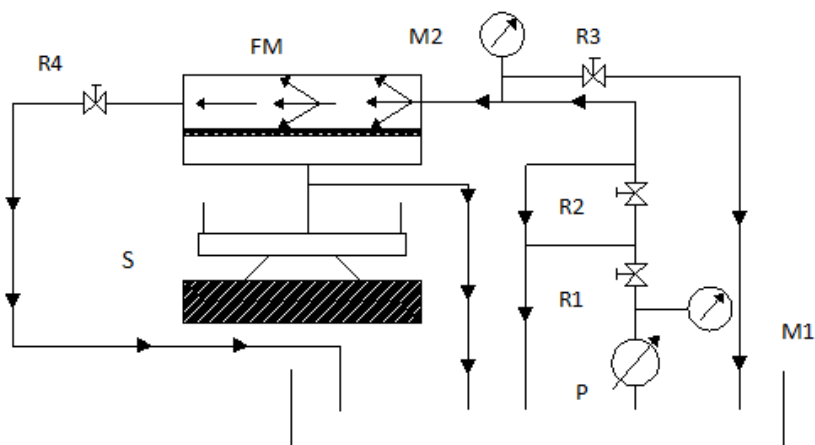
The ultrafiltration process in the presence of surfactants was investigated in a pilot laboratory set – up [14]. The membrane being tested had a diameter of 36mm. The pressures used in the ultrafiltration process were 0.1, 0.2 and 0.3 MPa. Permeate volume fluxes and retention coefficients were determined on steady flow conditions. Permeate volume flow was calculated

as shown below: $J = \frac{V}{t \cdot A} (m^3 / m^2 day)$, where V is the permeate volume (m^3),

t stands for the time (day), and A represents the effective membrane surface area (m^2).

Dye retention coefficient (R) was determined as:
$$R = \frac{C_k - C_p}{C_k} \cdot 100(\%)$$

where C_k and C_p denote the dye concentration (g/m^3) in retentate and permeate, respectively [16].



Scheme 1. Pilot set-up: P –centrifugal pump, FM – filtration module, S –digital scale, R – valve, M – manometer

To obtain a wider range of flow a centrifugal pump was used ($Q=40 \text{ l}/\text{min}$), driven by a variable speed ($n = 287\text{rpm}$). A digital laboratory balance, Mettler Toledo model, was used for weighing. The substrate surfaces used for the membranes will be molecular sieves, made of stainless steel. For this, AISI304MESH94 mesh sieve 110μ ($0,11\text{mm}$) mesh opening 150μ ($0,15\text{mm}$) was used. This is mainly used in the pharmaceutical industry. To track the flow parameters through the membrane, equipment has been developed to highlight these aspects.

ACKNOWLEDGMENTS

The work has been funded by UEFISCDI PN-II-PT-PCCA-2013-4-0742 Project for PhD students support and the Sectoral Operational Programme Human Resources Development 2007-2013 of the Ministry of European Funds through the Financial Agreement POSDRU/159/1.5/S/134398.

REFERENCES

1. G. Nechifor, N. Luca, G. Popescu, M. Nechifor, *Revue Roumaine de Chimie*, **1989**, *34*, 2047.
2. G. Batrinescu, M.A. Constantin, A. Cuciureanu, G. Nechifor, *Polymer Engineering and Science*, **2014**, *54*, 1640.
3. K. Scott, „Handbook of industrial membranes”, First edition, Elsevier Science Publishers Ltd, **1995**.
4. G., Nechifor, B. Albu, D. Rata, G. Popescu, *Revista de Chimie*, **1996**, *47*, 260.
5. K. Lintner, S. Bragulla, *Internationale Zeitschrift fur Lebensmittel*, **1987**, *38*, 120.
6. K. Majewska-Nowak, *Environment Protection Engineering*, **2009**, *4*, 111.
7. G. Nechifor, S.I. Voicu, A.C. Nechifor, S. Garea, *Desalination*, **2009**, *241*, 342.
8. E. Chifu, „Chimie coloidala” Editura Didactică și Pedagogică, Bucuresti, **1969**.
9. N. Rubingh, P. M. Holland (ed.), „Cationic Surfactants – Physical Chemistry”, Marcel Dekker, New York, **1991**.
10. M.J. Schick (ed.), „Nonionic Surfactants”, Marcel Dekker, New York, **1966**.
11. K.L. Mittal, D.O. Shoh, „Surfactants in solution”, Vol. 11, Springer Science & Business Media, New York, **1991**.
12. B. Van der Bruggen, B. Daems, D. Wilms, C. Vandecasteele, *Separation and Purification Technology*, **2001**, *22-23*, 519.
13. Ștefan Ioan Voicu, Florin Aldea, Marin Răduț, Gheorghe Nechifor, Nanostructured polysulfone composite membranes, *U.P.B. Sci. Bull., Series B*, **2008**, *70*, 3.
14. G.A. Popa, D.F. Popa (Enache), D.D. Slave (Clej), I.S. Din, C.M. Mirea, A., Ciocanea, *Revista de Chimie*, **2017**, *68*, 6.
15. A. Cuciureanu, G. Batrinescu, N.N. Badea, D.A. Radu, G. Nechifor, *Materiale Plastice*, **2010**, *47*, 416.
16. A.A.K.K. Rikabi, A. Cuciureanu, M. Chelu, A.R. Miron, C. Orbeci, A.G. Popa, M.E. Craciun, *Revista de Chimie*, **2015**, *66*, 1093.
17. C.K. Kima, S.S. Kimb, J.C. Limc, J.J. Kimd, *Journal of Membrane Science*, **1998**, *147*, 13.
18. K. Majewska-Nowak, I. Kowalska, M. Kabsch-Korbutowicz, *Desalination*, **2006**, *198*, 157.
19. K. Majewska-Nowak, I. Kowalska, M. Kabsch-Korbutowicz, *Desalination*, **2006**, *200*, 283.
20. C.K. Kima, S.S. Kimb, J.C. Limc, J.J. Kimd, *Journal of Membrane Science*, **1998**, *147*, 13.
21. A.C. Archer, A.M. Mendes, R.A.R. Boaventura, *Environmental Science and Technology*, **1999**, *33*, 2758.
22. K. Majewska-Nowak, *Environment Protection Engineering*, **2005**, *31*, 229.
23. J. Huang, L. Peng, G. Zeng, X. Li, Y. Zhao, L. Liu, F. Li, Q. Chai, *Separation and Purification Technology*, **2014**, *125*, 83.

PERIODATE-OXIDIZED ALGINATE AS POLYCONDENSATION REAGENT FOR HEMOGLOBIN

FLORINA SCURTU^a, ANAMARIA POPA^a,
RADU SILAGHI-DUMITRESCU^{a*}

ABSTRACT. We have previously demonstrated that derivatization of hemoglobin with periodate-modified sugar derivatives incurs increases in the pro-oxidant reactivity and, also, that serum bovine serum albumin can resolve this problem entirely. Here, we described a new polymer based on hemoglobin and another oxygen-containing compound, alginate. The rate of autooxidation increases after derivatization, but serum albumin alleviates this problem. The peroxide reactivity and oxygen affinity were also tested but no significant differences were observed between derivatized and native hemoglobin.

Keywords: *blood substitute, hemoglobin, alginate, oxidative stress*

INTRODUCTION

It was demonstrated that acellular hemoglobin, even when carefully purified, does not represent by itself a solution for hemoglobin-based oxygen carriers (HBOC) because of negative side-effects:[1-3] the first key problem with free hemoglobin is its slow molecular volume, leading to extravasation and indirectly other to problems (high oxygen affinity, vasoactive properties, renal toxicity).[4,5] The challenge in creating a reasonable blood substitute is to increase their molecular weight by chemical and/or genetic modification.[6-8] On the other hand, modification of the protein structure can affect other properties, including autooxidation rates, oxygen affinity, cooperativity, affinity for nitrosative and/or oxidative stress agents, and other functions of hemoglobin such as NO and CO₂ transport.[9]

^a Babes-Bolyai University, Faculty of Chemistry and Chemical Engineering, 11 Arany Janos str. RO-400028, Cluj-Napoca, Romania

*Corresponding author; email: rsilaghi@chem.ubbcluj.ro

Intermolecularly-crosslinked hemoglobins produced using polyaldehydes have been used extensively to modify the negative properties of native Hb. The most common reagents in this respect are glutaraldehyde, formaldehyde, acetaldehyde;[10,11] however, a variety of dialdehydes can also be obtained via oxidation by sodium periodate of diverse water-soluble sugar derivatives (dextran, ATP, starch), or even compounds like polyethylene glycol.[12,13] Here, for the first time, we report that sodium alginate can also be used for crosslinking hemoglobin. Parameters like molecular size, autooxidation rate and oxygen affinity appears to be affected after the polymerization process. The process may in principle be applicable to crosslinking of other materials as well.

RESULTS AND DISCUSSION

Oxidation of alginate with sodium periodate was performed in order to ring-open the 1,2-diols to yield dialdehydes (Figure 1) which can then be employed for polycondensation of proteins, namely hemoglobin and albumin. Figure 2 shows an SDS-PAGE gel and gel-filtration chromatograms illustrating that oxidized alginate indeed induces an increase in molecular weight. Introduction of BSA in the reaction mixture leads to lower molecular weights for copolymers comparative to the polymers as illustrated in Table 1.

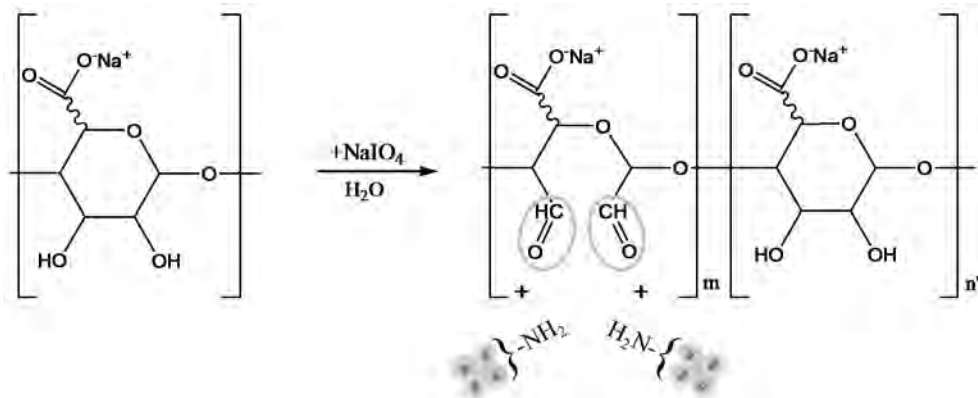


Figure 1. Oxidation of sodium alginate by periodate

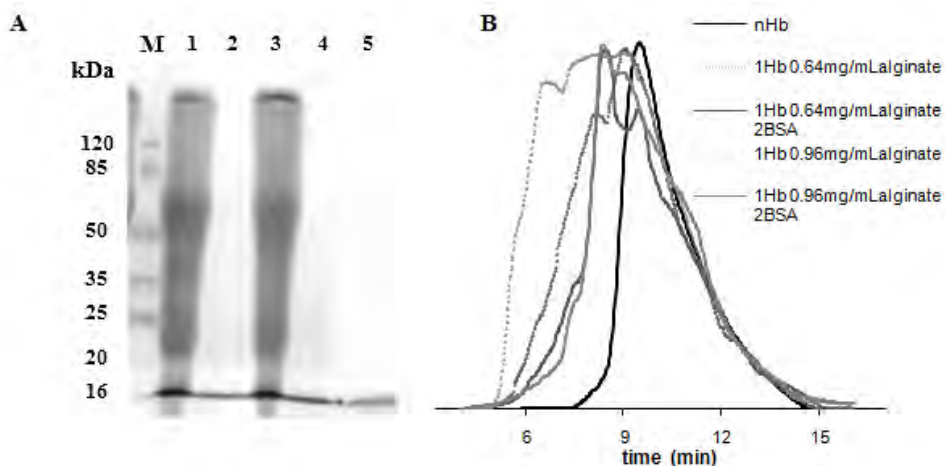


Figure 2. **A)** SDS-PAGE illustrating the influence of alginate concentration upon polymerization degree. **1-** 1 mM Hb + 0.96 mg/mL alginate + 2 mM BSA, **2-** 1mM Hb + 0.96 mg/mL alginate, **3-** 1 mM Hb + 0.64 mg/mL alginate + 2 mM BSA, **4-** 1 mM Hb + 0.64 mg/mL alginate, **5-** native Hb. **B)** Size-exclusion chromatograms for Hb derivatized with different concentration of alginate. Conditions: 20mM Tris pH 7.4, 150 mM NaCl, room temperature

Table 1 also shows the autooxidation rate values. While oxidized alginate induces drastic autooxidation, bovine serum albumin can alleviate this problem. Thus, the amount of metHb formed is ~two times lower if in the reaction mixture is added BSA.

Table 1. Molecular weight and autooxidation rates (express in percentage of metHb formed) values.

	Molecular weight [kDa]	Autooxidation rate(%)
native Hb	64	14.29
1Hb + 0.64 mg/mL alginate	210 – 77	30.81
1Hb + 0.64 mg/mL alginate + 2BSA	230 – 64	18.22
1Hb + 0.96 mg/mL alginate	>500(850) – 80	44.82
1Hb + 0.96 mg/mL alginate + 2BSA	170 – 64	22.03

Figure 3 illustrates the time course at 425 nm during the reaction of hydrogen peroxide with poly- and copolymerized Hb. This wavelength is characteristic of ferryl form (FeIV – so called Compound II). [7,14,15] There is no significant difference between the derivatized Hb and the native: both the yield of ferryl form and its stability is similar with to that of native Hb.

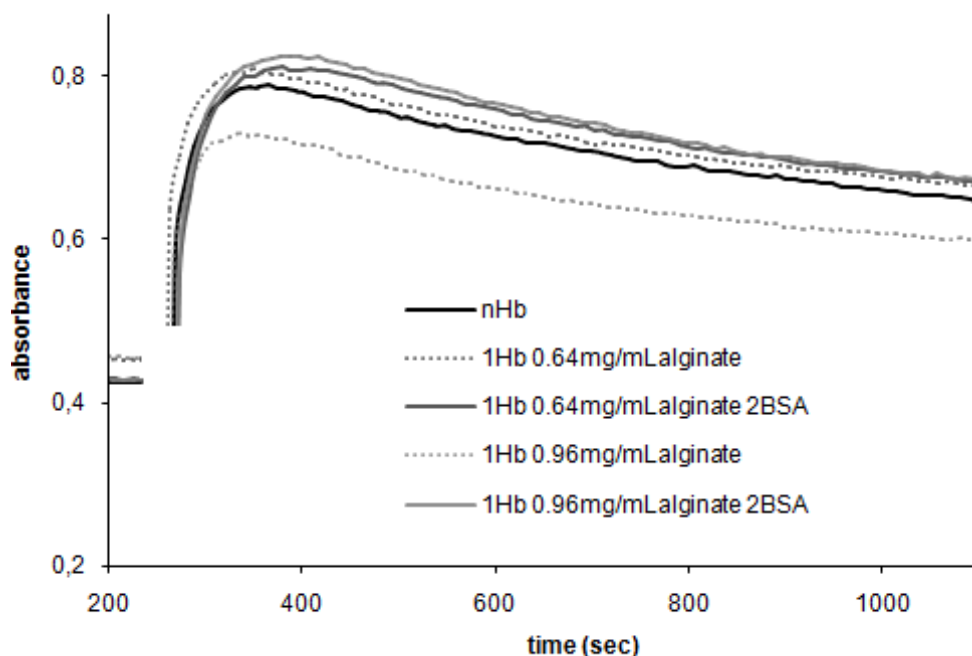


Figure 3. Time course for the reaction of ferric native Hb, poly- and copolymerized Hb with hydrogen peroxide. Conditions: 10 μ M protein, 80 μ M peroxide, PBS, room temperature

Figure 4 illustrates oxygen binding curves for copolymerized and native hemoglobin. It may be seen that the cooperativity effect disappears in derivatized Hb while affinity towards oxygen increases compared with native hemoglobin, in line with observations previously noted for most other polycondensates based on hemoglobin or other related proteins.[10,16-22]

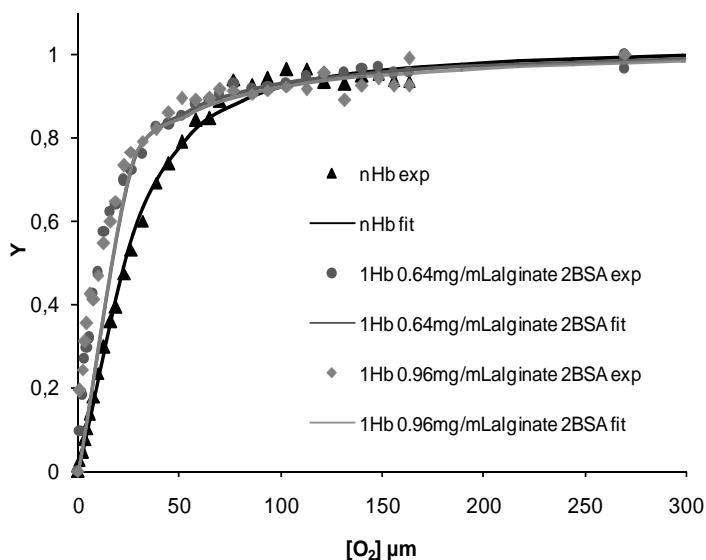


Figure 4. Oxygen saturation curves of native Hb and polymerized Hb. Conditions: PBS, room temperature

Table 2. K_d values and Hill coefficients (n) for poly- and copolymers.

	K_d	n
native Hb	22.99	1.55
1Hb + 0.64 mg/mL alginate + 2BSA	10.46	1.04
1Hb + 0.96 mg/mL alginate + 2BSA	9.11	0.92

CONCLUSIONS

The derivatization procedure described here show that polymerization of hemoglobin with oxidized alginate lead to an increase in autooxidation rate, but addition of bovine serum albumin alleviates this problem. Also, molecular size and oxygen affinity was higher in polyHb than in nativeHb. By analogy with other periodate-derived hemoglobin polymers,[13] one should expect this lack of reactivity to be paralleled by improved performance on cellular cultures if using such polycondensates as (semi)-artificial carriers for molecular oxygen. On the other hand, the protocol described here can be viewed as generally applicable for protein derivatization/conjugation.

EXPERIMENTAL SECTION

Bovine hemoglobin was purified from bovine blood following a general protocol of Antonini and Brunori.[23] The blood, freshly drawn on citrate, was centrifuged 15 minutes at 5000 rpm to separate the red blood cells, which were then washed three times with 5 mM phosphate pH 7.4 + 150 mM NaCl. Hemoglobin was manipulated in phosphate buffer saline (PBS) unless otherwise mentioned and concentration in text are given per heme rather than per tetramer. The met form of the hemoglobin were prepared by ferricyanide treatment as previously described.[24-26] Bovine serum albumin (BSA, fraction V, from Sigma-Aldrich, Germany) was used as provided without further purification.

For alginate oxidation 0.01 g/mL solution were prepared in 18.1 MΩ deionized water. The solution was oxidized with sodium periodate (NaIO₄, Merck) (0.1 g/mL) for 1 hour at room temperature in order to ring-open the 1,2-diols to yield dialdehydes (Figure 1). For polymerization of Hb with alginate, 1 mM Hb was reacted with 0.64 mg/mL or 0.96 mg/mL alginate oxidized. The reaction was performed under stirring at 4°C. The reaction was stopped by addition of NaBH₄, which reduces imine bonds to stable amines and also quenches excess carbonyl groups. The product was dialyzed in 50 mM Tris buffer with 150 mM NaCl, 7.4 to remove excess NaBH₄ and side-products. The resulting protein solutions were subsequently analyzed by 15% SDS-PAGE and by analytical size exclusion chromatography on a Superdex 200 5/150 GL column (GE Healthcare, Sweden), 0.25 mL/min flow rate with a mobile phase of 20 mM Tris pH 7.4 buffer with 150 mM NaCl. The absorbance was monitored at 280 nm. Molecular weights were determined based on a calibration curve employing a molecular weight standard kit (Sigma-Aldrich) containing carbonic anhydrase (29 kDa), bovine serum albumin (BSA, 66 kDa), alcohol dehydrogenase (150 kDa), amylase (200 kDa), apoferritin (443 kDa), thyroglobulin (669 kDa) and blue dextran (void volume marker).

Autooxidation experiments were performed by incubation of oxy-Hb (native or polymerized) at 37°C in an incubator and measuring UV-vis spectra of the Hb before and after incubation times of up to 4 hours. The change in absorbance at 630 nm was used to determine the rate of autooxidation. UV-vis spectra were recorded on Agilent 8453 (Agilent, Inc.) and Cary 50 (Varian, Inc) instruments Cary 50 (Varian, Inc) instruments.

Dioxygen affinity and autooxidation measurements were in PBS 7.4 at room temperature.

REFERENCES

1. H. Bunn, J.H. Jandl, *Journal of Experimental Medicine*, **1969**, 129, 925
2. X. Liu, M. J.S. Miller, M.S. Joshi, H. Sadowska-Krowicka, D.A. Clark, J.R. Lancaster, *Journal of Biological Chemistry*, **1998**, 273, 18709
3. J.R. Hess, R.F. Reiss, *Translational Medicine Reviews*, **1996**, 10, 276
4. A.I. Alayash, *Nature Reviews in Drug Discovery*, **2004**, 3, 152
5. D.H. Doherty, M.P. Doyle, S.R. Curry, R.J. Vali, T.J. Fattor, J.S. Olson, D.D. Lemon, *Nature Biotechnology*, **1998**, 16, 672
6. R.M. Winslow, *Artificial Organs*, **2004**, 28, 800
7. B.J. Reeder, M. Grey, R.L. Silaghi-Dumitrescu, D.A. Svistunenko, L. Bulow, C.E. Cooper, M.T. Wilson, *Journal of Biological Chemistry*, **2008**, 283, 30780
8. I. Portoro, L. Kocsis, P. Herman, D. Caccia, M. Perrella, L. Ronda, S. Bruno, S. Bettati, C. Micalella, A. Mozzarelli, A. Varga, M. Vas, K.C. Lowe, A. Eke, *Biochimica Biophysica Acta*, **2008**, 1784, 1402
9. J.G. Riess, *Chemical Reviews*, **2001**, 101, 2797
10. F. Deac, A. Todea, R. Silaghi-Dumitrescu *Glutaraldehyde derivatization of hemoglobin: a potential blood substitute*; Silaghi-Dumitrescu, R. and Garban, G., Ed.; Cluj University Press: Cluj-Napoca, Romania, 2009, pp 165
11. S.G.R.C., H.H.D., *Journal of Biological Chemistry*, **1986**, 261, 6811
12. J.H. Eike, A.F. Palmer, *Biotechnology Progress*, **2004**, 20, 953
13. F. Deac, B. Iacob, E. Fischer-Fodor, G. Damian, R. Silaghi-Dumitrescu, *Journal of Biochemistry*, **2011**, 149, 75
14. B.J. Reeder, D.A. Svistunenko, C.E. Cooper, M.T. Wilson, *Antioxidants & Redox Signaling*, **2004**, 6, 954
15. R. Silaghi-Dumitrescu, B.J. Reeder, P. Nicholls, C.E. Cooper, M.T. Wilson, *Biochemical Journal*, **2007**, 403, 391
16. A.C. Mot, A. Roman, I. Lupan, D.M. Kurtz, R. Silaghi-Dumitrescu, *Protein Journal*, **2010**, 29, 387
17. M. Arkosi, F. Scurtu, A. Vulpoi, R. Silaghi-Dumitrescu, D.M. Kurtz, Jr., *Artificial Cells and Blood Substitutes*, **2016**, 45, 218
18. D. Hathazi, A.C. Mot, A. Vaida, F. Scurtu, I. Lupan, E. Fischer-Fodor, G. Damian, D.M. Kurtz, Jr., R. Silaghi-Dumitrescu, *Biomacromolecules*, **2014**, 15, 1920
19. F. Scurtu, O. Zolog, B. Iacob, R. Silaghi-Dumitrescu, *Artificial Cells, Nanomedicine and Biotechnology*, **2014**, 42, 13
20. V.F. Scurtu, A.C. Mot, R. Silaghi-Dumitrescu, *Pharmaceuticals*, **2013**, 6, 867
21. F. Deac, B. Iacob, E. Fischer-Fodor, G. Damian, R. Silaghi-Dumitrescu, *Journal of Biochemistry*, **2011**, 149, 75
22. O. Zolog, A. Mot, F. Deac, A. Roman, E. Fischer-Fodor, R. Silaghi-Dumitrescu, *Protein Journal*, **2011**, 30, 27
23. E. Antonini, M. Brunori, *Hemoglobin and Myoglobin in their Reaction with Ligands*; North-Holland: Amsterdam, 1971

24. B.J. Reeder, D.A. Svistunenko, M.A. Sharpe, M.T. Wilson, *Biochemistry*, **2002**, *41*, 367
25. J. Dunne, D.A. Svistunenko, A.I. Alayash, M.T. Wilson, C.E. Cooper, *Advances in Experimental Medicine and Biology*, **1999**, *471*, 9
26. J. Dunne, A. Caron, P. Menu, A.I. Alayash, P.W. Buehler, M.T. Wilson, R. Silaghi-Dumitrescu, B. Faivre, C.E. Cooper, *Biochemical Journal*, **2006**, *399*, 513

SILICON RELEASE FROM HYDROXYAPATITES IN WATER AND SIMULATED BODY FLUID

OANA CADAR^a, PETRE T. FRANGOPOL^b, GHEORGHE TOMOAIA^{c,d},
DANIEL OLTEAN^c, GERTRUD A. PALTINEAN^b, AURORA MOCANU^b,
OSSI HOROVITZ^b, MARIA TOMOAIA-COTISEL^{b,d,*}

ABSTRACT. Nanostructured hydroxyapatite (HAP) and silicon substituted hydroxyapatites (HAP-Si), with 0.47 and 2.34 wt% Si, were prepared by wet precipitation method. Their structure was investigated by X rays diffraction (XRD), FTIR spectroscopy, energy dispersive X ray (EDX) spectroscopy and their images were obtained by TEM, SEM and AFM. Their behavior in water and SBF was investigated by inductively coupled plasma optical emission spectrometry (ICP-OES) for an immersion time from 1 to 90 days. While Ca and P release from HAP is very low, the presence of Si enhances greatly their release in water, along with a continuous and long lasting Si release. In simulated body fluid, SBF, Ca, P and Mg are removed from the solution, by the formation of a new HAP enriched in Mg, while silicon is released as in water. Thus, Si doped HAP might have advantageous applications as bone and tooth materials.

Keywords: *hydroxyapatite, silicon doped HAP, elements release, simulated body fluid*

^a INCDO INOE 2000, Research Institute for Analytical Instrumentation, 67 Donath str., RO-400293, Cluj-Napoca, Romania

^b Babeş-Bolyai University, Faculty of Chemistry and Chemical Engineering, 11 Arany Janos str., RO-400028, Cluj-Napoca, Romania

^c Iuliu Hatieganu University of Medicine and Pharmacy, Orthopedics and Traumatology Department, 47 Traian Mosoiu Str., RO-400132 Cluj-Napoca, Romania

^d Academy of Romanian Scientists, 54 Splaiul Independentei, RO-050094 Bucharest, Romania

* Corresponding author: mcotisel@chem.ubbcluj.ro

INTRODUCTION

Silicon is shown to be an essential element in biological bone growth and development [1]. Therefore, silicon substituted hydroxyapatites (HAP-Si) are a promising biomaterial for bone grafting [2, 3], and different methods were proposed in order to synthesize and characterize them from chemical, physical and biological point of view [3-7]. The role of HAP-Si based biomaterials in bone formation, mineralization and remodeling, by stimulation of human osteoblasts bioactivity and promotion of bone regeneration is approached by numerous investigations, both *in vitro* and *in vivo* [3, 7-13].

Silicon may enter in the hydroxyapatite, $\text{Ca}_{10}(\text{PO}_4)_6(\text{OH})_2$ (HAP) lattice as silicate ions, SiO_4^{4-} , substituting phosphate ions, PO_4^{3-} , but for the conservation of electroneutrality, some of the OH^- ions should be eliminated, leading to the formula $\text{Ca}_{10}(\text{PO}_4)_{6-x}(\text{SiO}_4)_x(\text{OH})_{2-x}$. Obviously, x should remain less than 2; for $x = 2$ the maximum theoretically possible Si content in HAP-Si would be 5.8 wt%. But because of lattice distortions, the real limit should be lower, e.g. 5 wt% ($x = 1.7$) [14, 15], 4.35 wt% ($x = 1.5$) [16], 4 wt% ($x = 1.4$) [17, 18], 3.1 wt% ($x = 1.1$) [19]. But silicon can also be present as SiO_2 , crystallized as quartz or as amorphous silica. There are authors suggesting the optimal bioactivity of HAP-Si to be attained for 0.8 wt% Si ($x = 0.28$) [13, 20, 21], but also for 0.47% and 2.34% Si an enhanced adhesion and proliferation of osteoblasts was observed [3].

In order to achieve its biological effect, HAP-Si has to release the necessary elements in the biological medium. For osteoblast activity and new bone tissue formation and development a continuous supply of elements is essential [22]. This is why in the present article we investigate the behavior of HAP-Si samples as compared with HAP in presence of water and simulated body fluid for a long time (90 days).

RESULTS AND DISCUSSION

Two silicon containing hydroxyapatites (HAP-Si) were prepared and compared with pure hydroxyapatite (HAP). Their composition is given in Table 1. The theoretical formulas were calculated assuming the entire amount of Si to be included in SiO_4^{4-} , which partially substitutes PO_4^{3-} ions.

Table 1. Composition of HAP and HAP-Si

Name	Composition (wt%)			Theoretical formula
	Ca	P	Si	
HAP	39.89	18.50	0	$\text{Ca}_{10}(\text{PO}_4)_6(\text{OH})_2$
HAP-Si0.47	40.03	18.04	0.47	$\text{Ca}_{10}\text{PO}_4)_{5.83}(\text{SiO}_4)_{0.17}(\text{OH})_{1.83}$
HAP-Si2.34	40.56	16.22	2.34	$\text{Ca}_{10}\text{PO}_4)_{5.18}(\text{SiO}_4)_{0.82}(\text{OH})_{1.18}$

In order to identify the crystalline phosphate species present, the XRD spectra of the three samples were compared with Powder Diffraction Files (PDF) for pure hydroxyapatite (HAP) and pure β -calcium phosphate (TCP). As an example, the spectrum of the sample containing 0.47% Si is compared with the PDF no. 09-0432 for stoichiometric HAP in Fig. 1a. HAP was the only phase identified in the pure hydroxyapatite sample and in HAP-Si0.47, while in HAP-Si2.34 a content of 83.6% HAP and 16.4% β -TCP was estimated. Thus, the increasing Si content favours the conversion of HAP to β -TCP, as observed also in literature [4, 23-25]. No quartz phase was identified in the XRD patterns, but this fact does not exclude the presence of amorphous silica (SiO_2).

From the breadth of the peaks as compared to the XRD pattern of crystalline HAP taken as etalon, it is evident that all samples present a nanocrystalline structure. The average size of crystallites was calculated from the Debye-Scherrer relation. The estimated size of the crystallites in the samples is about 47 nm for HAP, 23 nm for HAP-Si0.47 and 25 nm for HAP-Si2.34. The crystallinity degree of the samples, also estimated from the XRD patterns, was about 40-50% for all the samples.

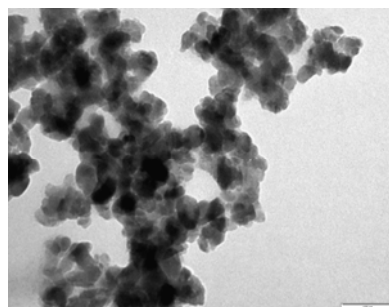
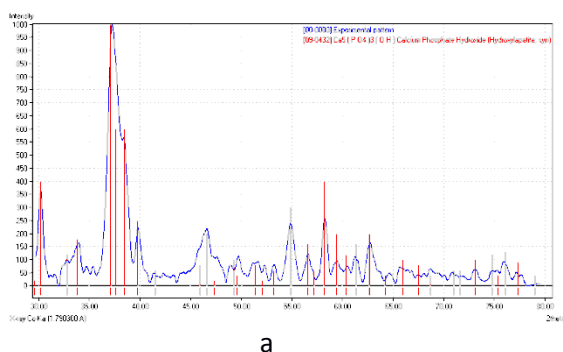


Figure 1. XRD patterns (a) for HAP-Si0.47 and the PDF no. 09-0432 file for stoichiometric HAP. (b) TEM image of a HAP-Si2.34 sample; bar length is 100 nm.

As an example, a TEM image for HAP-Si 2.34 is given in Fig. 1b. From TEM images the sizes of several hundreds of particles were measured, and the mean particle diameter was found to be about 26.5 ± 5.2 nm, with sizes between 16 and 42 nm. The mean value is in substantial agreement with the particle diameter estimated from X-ray diffraction.

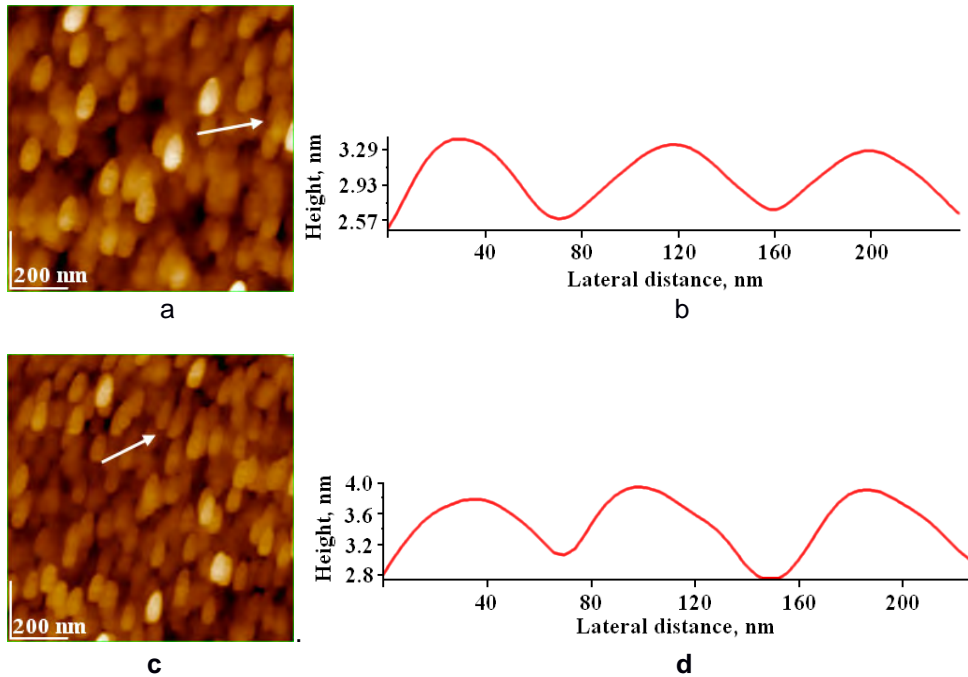


Figure 2. AFM images 2D-topography (ac) and cross section profile (b, d) along the arrows in pannel (a) and (c) respectively, for HAP-Si 0.47 (a, b) and HAP--Si2.34; scanned areas: $1 \mu\text{m} \times 1 \mu\text{m}$; surface roughness, RMS, on area 1.00 nm^2 (a) and 0.90 nm^2 (c); RMS profile 0.34 nm (b), 0.24 nm (d).

AFM images (Figure 2) also confirmed for HAP-Si powders the average size of particles in the nanoscale range, as following 42 ± 3 nm for HAP-Si 0.47, and 45 ± 4 nm for HAP-Si2.34. Thus, AFM images indicated that the nano suspensions of HAP-Si powders are formed of particles of almost identical size in good agreement with TEM values.

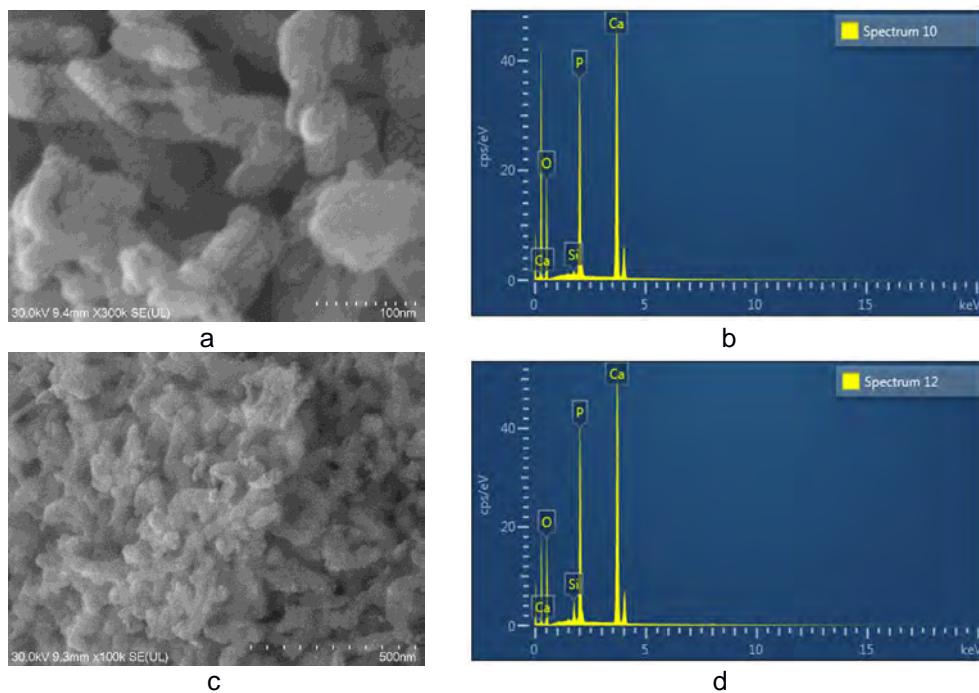


Figure 3. SEM image (a) and EDX spectrum (b) of HAP-Si_{0.47}; SEM image (c) and EDX spectrum (d) of HAP-Si_{2.34}. Bar length: 100 nm (a), and 500 nm (c). Examples of SEM images are given in Fig.3 for the HAP-Si_{0.47} and HAP-Si_{2.34}, along with EDX spectra, which confirm the presence of Si, together with Ca and P in both samples.

The FTIR spectrum of the HAP-Si_{0.47} sample is presented in Fig. 4a. The IR spectra of the HAP-Si samples are very similar to each other. Like the HAP sample, they present the characteristic peaks of the PO₄ group: stretching vibrations: ν_3 at 1032-1033 and 1089-1091 cm⁻¹; ν_1 at 962 cm⁻¹; bending vibrations: ν_4 at 565 and 602-603 cm⁻¹; ν_2 at 473 cm⁻¹ and of the structural OH (stretching at 3571-3572 cm⁻¹ and libration at 633 cm⁻¹). The last reduced to a shoulder in HAP-Si_{2.34} (Fig. 4b) as a consequence of the diminution of the OH groups in HAP by the substitution of phosphate by silicate ions. Peaks for absorbed water are visible at 3420 - 3440 and 1637 cm⁻¹. Peaks for the SiO₄ group have their frequencies very near to those of PO₄, and are therefore not observable. Nor can be detected vibrations characteristic for Si-O-Si bridges from silica [27, 28], and this could be an argument against the presence of free SiO₂ in the HAP-Si samples.

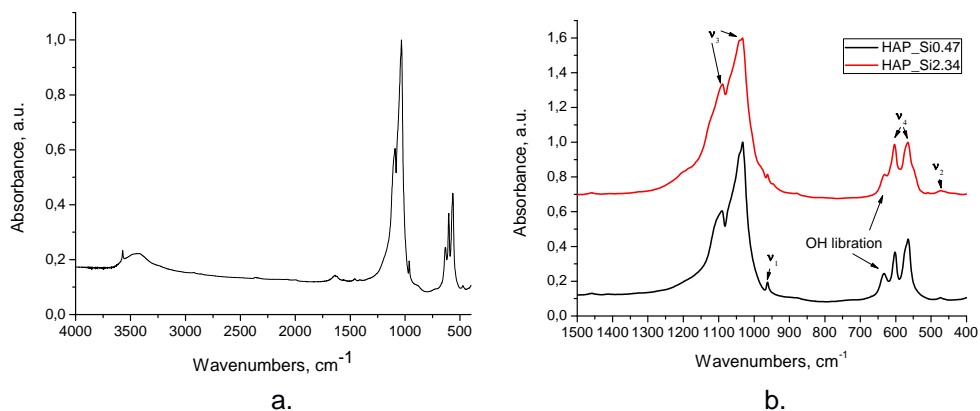


Figure 4. FTIR spectrum for HAP-Si0.47 (a) and comparison between FTIR spectra for HAP-_{Si} samples (detail) (b).

The Ca, P, and Si contents in the solution resulted after contact of the samples with ultrapure water, for 1, 3, 7, 14, 21, 30, 60, and 90 days are presented graphically in Fig. 5 a, b and c respectively.

Pure HAP has a very low solubility in water; its solubility product

$$K_{sp} = [\text{Ca}^{2+}]^{10}[\text{PO}_4^{3-}]^6[\text{OH}]^2$$

is very difficult to assess, and values in literature vary between 10^{-114} and 10^{-120} [29]; an international standard [30] recommends the value $(4.12 \pm 0.16) \cdot 10^{-118}$. Therefore, the Ca and P content in the aqueous solution in contact with the HAP sample is very low and nearly constant in time (Fig 5a, b). The Ca/P ratio in the solution is different from that in the solid because of the incongruent (nonstoichiometrical) solubility of HAP in water [29, 31, 32]. There is not a simple dissolution process, but a series of complex chemical reactions, with the formation of different calcium phosphate phases as surface coats [33, 34]. In the solution, P appears mainly as HPO_4^{2-} ions, the predominant form at nearly neutral pH.

SILICON RELEASE FROM HYDROXYAPATITES IN WATER AND SIMULATED BODY FLUID

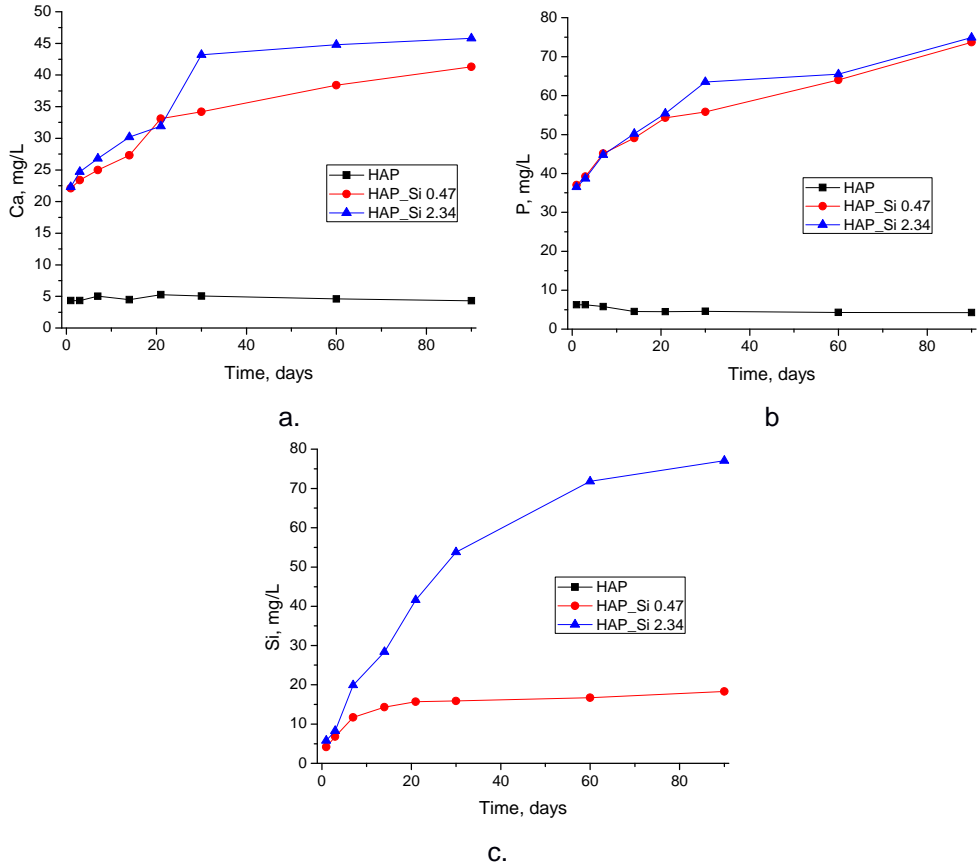


Figure 5. Ca (a), P (b) and Si (c) release from HAP and HAP-Si samples in water

The presence of Si dramatically enhances both the Ca and P release, therefore it increases the solubility of the calcium phosphate, and the amount released increases continuously in time. Such an augmentation of the HAP solubility due to the presence of Si was observed both *in vivo* [12], and *in vitro* [9, 22, 25, 26]. This ion release over a long period of time is important for the biomedical applications of substituted apatites, since this continuous supply of elements is essential for osteoblast activity and new bone tissue formation and development [22]. Based on HR-TEM results, it was suggested that an increased number of defects in the HAP-Si lattice causes the increase of calcium, phosphate and silicate ions release in the solution [12]. The Si release also is increasing in time, especially for the HAP-Si2.34 sample. The values

of Si/Ca and Si/P ratios in the solution are much higher than in the solid, thus there is much more Si in the solution than expected from a congruent dissolution of HAP-Si. Probably not only the silicate ions in the crystals are released, but also Si from amorphous silica in the sample.

The elements contents (Ca, P, Mg) in pure SBF are compared with those in SBF in presence of the samples for immersion times from 1 to 90 days in Fig. 6 a-c, while the variation in time of the Si content in the solution in contact with HAP-Si samples is shown in Fig. 6 d.

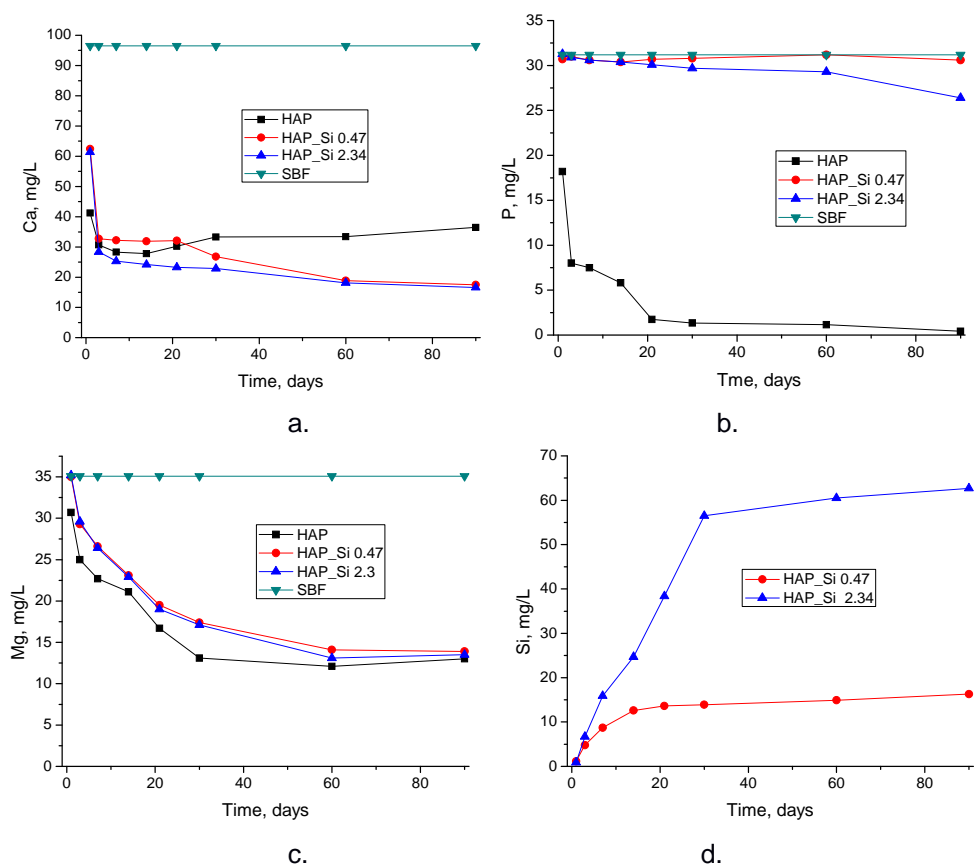


Figure.6. Ca (a), P (b), Mg (c) and Si (d) content in SBF in absence and in presence of the HAP and HAP-Si samples.

In SBF the Ca^{2+} concentration in presence of HAP is decreasing in time from its initial value in SBF (96.5 ± 0.5 mg/L) as seen in Fig. 6a. The diminution is rapid in the first 30 days, then it is much slower, and even a slight increase is observed. It can be explained by uptake of Ca^{2+} along with PO_4^{3-} ions from SBF for the building of new solid HAP and/or the sorption of Ca^{2+} in the HAP lattice, which are partially counterbalanced by the release of Ca^{2+} ions from the HAP lattice and/or the ion exchange with Mg^{2+} ions from the SBF solution, leading to new HAP enriched in Mg.

The decrease of the P content in the SBF, from the initial value (31.2 ± 1.3 mg/L) is more pronounced, and continues down to its near consumption from the solution (Fig. 6b). In the HAP-Si samples, this P uptake is compensated by the increased release of P due to the enhanced dissolution of the HAP-Si.

There is also a decrease in the Mg^{2+} content (Fig. 6c) of the SBF, from its initial value (35.1 ± 3.6 mg/L), probably due to the ion exchange with Ca^{2+} from HAP and formation of Mg substituted HAP.

The Si release in SBF shows the same trends as in water, but the released amount is somewhat diminished. It was signalled in literature that the simultaneous presence of Mg and Si diminishes the elements release [22]. This could suggest the formation of complexes containing these two ions, more strongly bound to the HA crystal structure or to its amorphous part [22]. The excess of Ca^{2+} ions in SBF could also downgrade the dissolution equilibrium of HAP-Si. The Si content in the solution was larger for higher Si content in the HAP-Si.

In histological studies, an increase in the rate of bone apposition to HAPs implants by the substitution of silicate ions into HAP has been observed [12]. This higher bioactivity of HAP-Si was assigned to the effect of the accelerated dissolution caused by the silicate ions.

CONCLUSIONS

HAP and silicon substituted HAPs (0.47 and 2.34 wt% Si) were prepared by wet precipitation method. XRD investigations showed the presence of the HAP lattice as single phase present in HAP and HAP-Si0.47, and as majoritary phase in HAP-Si2.34. They possess nanostructure and a medium crystallinity degree. The HAP structure was confirmed by FTIR spectroscopy and the particles were visualized by TEM, AFM and SEM imaging. The elements release in water was much higher in HAP-Si than in pure HAP and continued till the end of the experiments. This long lasting elements release is an important premise for biomedical use of HAP-Si based biomaterials.

The behavior of the samples in SBF could be explained in terms of Ca, P and Mg uptake in the new HAP lattice and/or ion exchange, with a precipitation of HAP enriched in magnesium. The Si release showed a similar responsive behavior of HAP-Si, both in water and in SBF. Also, the increased Si concentration in HAP-Si significantly influenced the Si release in both media. Therefore, silicate ions have an important role in the structure of HAP-Si and might simultaneously bring physiological effects as a result of Si release.

EXPERIMENTAL SECTION

The nanostructured phosphates were prepared by the precipitation method previously developed by us for the synthesis of HAP and substituted HAPs [3, 35-38]. Briefly, HAP was obtained by rapidly mixing, at room temperature, equal volumes of 0.15 M calcium nitrate solution [$\text{Ca}(\text{NO}_3)_2 \cdot 4\text{H}_2\text{O}$ from Merck] and 0.09 M diammonium phosphate solution [$(\text{NH}_4)_2\text{HPO}_4$ from Sigma-Aldrich] at pH 11.5 (settled by adding a 25% ammonia solution). The maturation of the obtained suspension was achieved by maintaining it for 24 h at 22 °C, and for another 24h at 70°C, in a reactor, under intermittent stirring. The so obtained precipitate was filtered and washed repeatedly with ultrapure water until nitrate free. It was dried by lyophilization, then calcined at 300°C for one hour and disintegrated in a ball mill.

For the preparation of HAP-Si samples [3], in each solution nonylphenol was added (this surfactant helping to control nucleation and growth of nuclei). Sodium silicate ($\text{Na}_2\text{O}:\text{SiO}_2 = 1:3.2$) was introduced in the phosphate solution in amounts calculated for the respective Si content in the final product. The pH of both solutions was adjusted to 11, using ammonia solution. The solutions were fast mixed at 60°, and the maturation was achieved at 80 °C for 48 h. After filtration, washing and lyophilisation the samples were calcined at 650 °C for 6-8 h.

The *X-rays diffraction* (XRD) patterns were investigated with a DRON-3 diffractometer, in Bragg-Brentano geometry, using a X-ray tube with cobalt target (K_α line, wavelength 1.79030 Å).

FTIR spectra were measured on KBr pellets, containing the samples powders with a spectrometer JASCO 6100 in the 4000-400 cm^{-1} range of wave numbers, with a 2 cm^{-1} resolution.

Transmission electron microscope: TEM JEOL –JEM 1010 was used to determine the shape and the size of the phosphates nanoparticles. The samples were dispersed in deionized water, and the resulted colloidal dispersion was adsorbed on the TEM grids.

For the examination with the *scanning electron microscope* SEM JEOL 5600 LV (backscattered-electron imaging technique, BSE), the samples were deposited as an uniform layer an adhesive graphitized tape. For local elemental analysis of different samples the energy-dispersive X-ray (EDX) spectroscopy was used coupled with SEM imaging.

Atomic force microscopy (AFM) images were obtained using the AFM JEOL 4210 equipment, operated in tapping mode [39-48], using standard cantilevers with silicon nitride tips (resonant frequency in the range of 200-300 kHz, and spring constant 17.5 N/m). The particles were adsorbed from their aqueous dispersion for 20 s on optically polished glass support.

Elements release tests: The Ca, P, Si and Mg amounts were measured in the solutions after immersion of 0.15 g of each sample in 15 mL ultrapure water, respectively Kokubo simulated body fluid (SBF) and incubation 37°C in separated closed flasks for each sample/day. SBF solutions were prepared according to *Kokubo's SBF* solution [49], containing the following ions (mmol/dm³): Na⁺ (142.0); K⁺ (5.0); Mg²⁺ (1.5); Ca²⁺ (2.5); Cl⁻ (147.8); HCO₃⁻ (4.2); HPO₄²⁻ (1.0); SO₄²⁻ (0.5), and buffered at the physiologic pH 7.40 at 37 °C, with tris(hydroxymethyl)amino methane and hydrochloric acid.

After 1, 3, 7, 14, 21, 30, 60, and 90 days, the supernatant (after centrifugation) was filtered through 0.45 µm paper filter Ca, Mg, P and Si contents were determined using an inductively coupled plasma optical emission spectrometer (ICP-OES) OPTIMA 3500 DV (Perkin-Elmer, USA) . For calibration, multi-element standard solutions were prepared by the dilution of stock multi-element 1000 mg/L solutions Merck IV (0, 0.1, 0.5, 1, 2, 4, 6, 8 and 10 mg/L).

All the experiments were performed in triplicate and the results were calculated as average values. The elements content in SBF solution without samples was also measured in the same days, and the average value was calculated.

ACKNOWLEDGMENTS

The authors gratefully acknowledge the financial support from the Executive Agency for Higher Education, Research, Development and Innovation Funding (UEFISCDI) through grants no. 241 and no. no. 83.

REFERENCES

1. E.M. Carlisle, *Calcified Tissue International*, **1981**, 33, 27.
2. W. Waked, J. Grauer, *Orthopaedics*, **2008**, 31, 591.
3. Gh. Tomoiaia, A. Mocanu, I. Vida-Simiti, N. Jumate, L.-D. Bobos, O. Soritau, M. Tomoiaia-Cotisel, *Materials Science and Engineering C*, **2014**, 37, 37.
4. I.R. Gibson, S.M. Best, W. Bonfield, *Journal of Biomedical Materials Research*, **1999**, 44, 422.
5. T. Leventouri, C.E. Bunaciu, V. Perdikatsis, *Biomaterials*, **2003**, 24, 4205.
6. C.M. Botelho, M.A. Lopes, I.R. Gibson, S.M. Best, J.D. Santos, *Journal of Material Science: Materials in Medicine*, **2002**, 13, 1123.
7. Z.Y. Qiu, I.S. Noh, S.M. Zhang, *Frontiers of Materials Science*, **2013**, 7, 40.
8. A.F. Khan, M. Saleem, A. Afzal, A. Ali, A. Khan, A.R. Khan, *Materials Science and Engineering C*, **2014**, 35, 245.
9. F. Balas, J. Pérez-Pariente, M. Vallet-Regí, *Journal of Biomedical Materials Research*, **2003**, 66, 364.
10. A.E. Porter, N. Patel, J.N. Skepper, S.M. Best, W. Bonfield, *Biomaterials*, **2003**, 24, 4609.
11. A.E. Porter, N. Patel, J.N. Skepper, S.M. Best, W. Bonfield, *Biomaterials*, **2004**, 25, 3303.
12. A.E. Porter, C.M. Botelho, M.A. Lopes, J.D. Santos, S.M. Best, W. Bonfield, *Journal of Biomedical Materials Research*, **2004**, 69A, 670.
13. K.A. Hing, P.A. Revell, N. Smith, T. Buckland, *Biomaterials*, **2006**, 27, 5014.
14. E.S. Thian, J. Huang, M.E. Vickers, S.M. Best, Z.H. Barber, W. Bonfield, *Journal of Materials Science*, **2006**; 41, 709.
15. M. Vallet-Regí, D. Arcos, *Journal of Materials Chemistry*, **2005**, 15, 1523.
16. D. Marchat, M. Zymelka, C. Coelho, L. Gremillard, L. Joly-Pottuz, F. Babonneau, C. Esnouf, J. Chevalier, D. Bernache-Assollant, *Acta Materialia*, **2013**, 9, 6992.
17. G. Gasquères, C. Bonhomme, J. Maquet, F. Babonneau, S. Hayakawa, T. Kanaya, A. Osaka, *Magnetic Resonance in Chemistry*, **2008**, 46, 342.
18. X.L. Tang, X.F. Xiao, R.F. Liu, *Materials Letters*, **2005**, 59, 3841.
19. S. Gomes, J.M. Nedelec, E. Jallot, D. Sheptyakov, G. Renaudin, *Crystal Growth and Design*, **2011**, 11, 4017.
20. S.M. Best, S. Zou, R.A. Brooks, J. Huang, N. Rushton, W. Bonfield, *Key Engineering Materials*, **2008**, 361-363, 985.
21. C.M. Bothelo, R.A. Brooks, S.M. Best, M.A. Lopes, J.D. Santos, N. Rushton, W. Bonfield, *Journal of Biomedical Materials Research*, **2006**, 79A, 723.
22. S. Sprio, A. Tampieri, E. Landi, M. Sandri, S. Martorana, G. Celotti, G. Logroscino, *Materials Science and Engineering C*, **2008**, 28, 179.
23. J.L. Xu, K.A. Khor, *Journal of Inorganic Biochemistry*, **2007**, 101, 187.

24. A.J. Ruys, *Journal of the Australian Ceramic Society*, **1993**, 29, 71.
25. S.L. Seet, *Science Asia*, **2009**, 35, 255.
26. D.M. Ibrahim, A.A. Mostafa, S. Ibrahim Korowash, *Chemistry Central Journal*, **2011**, 5:74, 11 pp
27. M.A. Karakassides, D. Gournis, D. Petridis, *Clay Minerals*, **1999**, 34, 429.
28. E.R. Lippincott, A. Van Valkenburg, C.E. Weir, E.N. Bunting, *Journal of Research of the National Bureau of Standards*, **1958**, 61, 61.
29. H.W. Kaufman, I. Kleinberg, *Calcified Tissue International*, **1979**, 27, 143.
30. *** International Standard ISO 13779-6 *Implants for Surgery – Hydroxyapatite, Part 6: Powders*, **2015**.
31. A.N. Smith, A.M. Posner, J.P. Quirk, *Journal of Colloid and Interface Science*, **1974**, 48, 442.
32. S.V. Dorozhkin, *Journal of Colloid and Interface Science*, **1997**, 191, 489.
33. R.P. Shellis, F.K. Wahab, B.R. Heywood, *Caries Research*, **1993**, 27, 365.
34. R.P. Shellis, B.R. Heywood, F.K. Wahab, *Caries Research*, **1997**, 31, 71.
35. Gh. Tomoaia, M. Tomoaia-Cotisel, L.B. Pop, A. Pop, O. Horovitz, A. Mocanu, N. Jumate, L.-D. Bobos, *Revue Roumaine de Chimie*, **2011**, 56, 1039.
36. Gh. Tomoaia, O. Soritau, M. Tomoaia-Cotisel, L.-B. Pop, A. Pop, A. Mocanu, O. Horovitz, L.D. Bobos, *Powder Technology*, **2013**, 238, 99.
37. C. Garbo, M. Sindilaru, A. Carlea, G. Tomoaia, V. Almasan, I. Petean, A. Mocanu, O. Horovitz, M. Tomoaia-Cotisel, *Particulate Science and Technology*, **2017**, 35, 29.
38. A. Mocanu, R. Balint, C. Garbo, L. Timis, I. Petean, O. Horovitz, M. Tomoaia-Cotisel, *Studia Universitatis Babeş-Bolyai, Chemia*, **2017**, 62(2), Tom I, 95.
39. M.A. Naghiu, M. Gorea, E. Mutch, F. Kristaly, M. Tomoaia-Cotisel, *Journal of Material Science and Technology*, **2013**, 29(7), 628.
40. O. Horovitz, Gh. Tomoaia, A. Mocanu, T. Yupsanis, M. Tomoaia-Cotisel, *Gold Bulletin*, **2007**, 40 (4), 295.
41. M. Tomoaia-Cotisel, A. Tomoaia-Cotisel, T. Yupsanis, G. Tomoaia, I. Balea, A. Mocanu, Cs. Racz, *Revue Roumaine de Chimie*, **2006**, 51 (12), 1181.
42. A. Danistean, M. Gorea, A. Avram, S. Rapuntean, Gh. Tomoaia, A. Mocanu, C. Garbo, O. Horovitz, M. Tomoaia-Cotisel, *Studia Universitatis Babeş-Bolyai, Chemia*, **2016**, 61 (3), 275.
43. Gh. Tomoaia, O. Horovitz, A. Mocanu, A. Nita, A. Avram, C.P. Racz, O. Soritau, M. Cenariu, M. Tomoaia-Cotisel, *Colloids and Surfaces B: Biointerfaces*, **2015**, 135, 726.
44. P.T. Frangopol. D.A. Cadenhead, Gh. Tomoaia, A. Mocanu, M. Tomoaia-Cotisel, *Revue Roumaine de Chimie*, **2015**, 60(2-3), 265.
45. G. Furtos, M.A. Naghiu, H. Declercq, M. Gorea, C. Prejmerean, O. Pana, M. Tomoaia-Cotisel, *Journal of Biomedical Materials Research Part B. Applied Biomaterials*, **2016**, 104, 1290.
46. M. Tomoaia-Cotisel, A. Mocanu, *Revista de Chimie (Bucharest)*, **2008**, 59, 1230.

O. CADAR, P.T. FRANGOPOLO, G. TOMOAI, D. OLTEAN, G.A. PALTINEAN,
AURORA MOCANU, O. HOROVITZ, M. TOMOAI-COTISEL

47. R.D. Pasca, G. Tomoiaia, A. Mocanu, I. Petean, G.A. Paltinean, O. Soritau, M. Tomoiaia-Cotisel, *Studia Universitatis Babes-Bolyai, Chemia*, **2015**, 60(3), 257.
48. G. Tomoiaia, A. Mocanu, L.D. Bobos, L.B. Pop, O. Horovitz, M. Tomoiaia-Cotisel, *Studia Universitatis. Babes-Bolyai, Chemia*, **2015**, 60 (3), 265.
49. T. Kokubo, H. Kushitani, S. Sakka, T. Kitsugi, T. Yamamuro, *Journal of Biomedical Materials Research*, **1990**, 24, 721.

PORTLAND CEMENT ENRICHED WITH HYDROXYAPATITE FOR ENDODONTIC APPLICATIONS

ALEXANDRA AVRAM^a, MARIA GOREA^{a,*}, REKA BALINT^a,
LUCIA TIMIS^{a,b}, STEFAN JITARU^{a,b}, AURORA MOCANU^a,
MARIA TOMOAI-COTISEL^{a,c}

ABSTRACT Endodontic cement based on calcium silicate has been the focus of many studies. However, the quality of resulted endodontic cement needs improvement. This paper focuses on endodontic cement obtained from Portland cement enriched with two types of hydroxyapatite, simple and doped with 5% Zn. Hydroxyapatites were synthesized using a wet precipitation method and investigated by X-ray diffraction, FTIR, TEM and AFM. From a structural point of view, both hydroxyapatites were obtained in a single crystalline phase, containing particles in the nanometric range, as judged by XRD, TEM and AFM. FTIR analysis presents O-H and P-O bands specific to those in pure hydroxyapatite, confirming a hydroxyapatite lattice in both materials. Several experimental compositions of commercial Portland cement mixed with hydroxyapatite were prepared. The influence of stoichiometric and Zn doped hydroxyapatite on the resulted endodontic cement was observed in the setting time. The setting time for both cements decreased exponentially at both temperatures (22 °C and 37 °C). The normal consistency water remains constant for all experimented slurries.

Keywords: *Endodontic cement, hydroxyapatite, Zn doped hydroxyapatite, Portland cement*

^a Babeş-Bolyai University, Faculty of Chemistry and Chemical Engineering, 11 Arany J. Str., 400028, Cluj-Napoca, Romania

^b Iuliu Hațieganu University of Medicine and Pharmacy, Faculty of Dentistry, 8 Babeş V. Str., 400012, Cluj-Napoca, Romania

^c Academy of Romanian Scientists, 54 Splaiul Independentei, 050094, Bucharest, Romania

*Corresponding author: mgorea@chem.ubbcluj.ro

INTRODUCTION

Cement and ceramic-based biomaterials have been the subject of a wide number of studies regarding root repair cements, due to their properties: nontoxicity, biocompatibility, non-shrinkage, and chemical stability in biological conditions [1,2]. Their ability to chemically bond to the tooth, forming an hermetic seal, promote osseointegration, as well as having a good radiopacity have led to these material being widespread in the area of endodontics [3,4]. Endodontic bioceramics have the advantage of not being moisture or blood sensitive, therefore not being technique sensitive. When unset, they present antibacterial properties and when set, bioactive capabilities [2].

While the field of material science has produced no ideal material, synthetic hydroxyapatite (HAP, $\text{Ca}_{10}(\text{PO}_4)_6(\text{OH})_2$) has become one of the most interesting bioceramics, being similar to inorganic components from the human body [4-8]. Its ability to generate hard tissue, thus increasing the bioactivity of dental cements is of particular significance. The bioactivity of hydroxyapatite is closely related to both the type and size of the amorphous and crystalline phases present in its structure as well as in its ion release capability [9]. Due to the promising endodontic applications of hydroxyapatite, several studies have analyzed its addition to dental fillers [10].

Water-based cements have been introduced to dentistry through the use of MTA or mineral trioxide aggregate [11,12]. Broadly defined as a fine inorganic powder that has the ability to set and harden independently [13], cement is another material clinically used in dentistry. Used as filling materials, endodontic cements come in direct contact with the alveolar bone having many applications, namely: root canal fillings and sealers, apical replacement of dentine, pulp capping and root perforation repair [9,14]. Bone defects can be easily filled by the cement paste without leaving any gap between the two interfaces.

Due to its self-setting property at physiological temperatures, ample availability and lower cost, Portland cement has a long history in the reconstruction of bone defects. These materials could be an alternative to MTA, and are currently the main focus of studies in the dental fields [4,13,15,16]. This hydraulic material is mainly composed of dicalcium silicate ($2\text{CaO}\cdot\text{SiO}_2$), and tricalcium silicate ($3\text{CaO}\cdot\text{SiO}_2$), tricalcium aluminate ($3\text{CaO}\cdot\text{Al}_2\text{O}_3$) and tetracalcium aluminoferrite ($4\text{CaO}\cdot\text{Al}_2\text{O}_3\cdot\text{Fe}_2\text{O}_3$) [17].

Portland cement has been proven to be biocompatible through previous studies that showed cements are not genotoxins [17-20]. The main component in cement, namely tricalcium silicate (C3S), has been shown to induce cell proliferation and HAP deposition on its surface [21]. Endodontic materials using a mixture of tricalcium silicate and calcium phosphates have been reported to present a modified hydration process [22].

Endodontic cements present many disadvantages, the main one being a delayed setting time, limiting its uses [23-25]. The advertised setting time of commercial endodontic cements ranges from 2 to 3 minutes (EndoChe Zr) to 4 hours (Trioxident) [15] and even 72 hours [25,26]. Given this discrepancy that can be confusing to clinicians, the influence of different additives, such as synthetic hydroxyapatite, on cement characteristics, especially setting time, is very important to know.

There are few studies on endodontic sealers with Ca and P ions release abilities and antibacterial properties [14].

Thus, our main purpose was to study the characteristics and influence of two types of synthetic hydroxyapatite, namely stoichiometric and Zn doped, on the setting time of endodontic cement.

RESULTS AND DISCUSIONS

Nanomaterials

The hydroxyapatite compositions, with and without Zn as dopant for Ca ions, are presented in Table 1.

Table 1. Composition of hydroxyapatites, stoichiometric and doped with Zn

Nanomaterial	Zn [wt%]	Ca substituted with Zn [mol%]	Theoretical formula
Stoichiometric hydroxyapatite	0	0	$\text{Ca}_{10}(\text{PO}_4)_6(\text{OH})_2$
Zn doped hydroxyapatite	5.0	7.83	$\text{Ca}_{9,217}\text{Zn}_{0,783}(\text{PO}_4)_6(\text{OH})_2$

In the experiments, the stoichiometric, uncalcined hydroxyapatite and Zn doped hydroxyapatite were mixed together with Portland cement. The compositions of endodontic cement samples are presented in Table 2.

Table 2. The studied compositions of endodontic cements

Sample/material [%]	Stoichiometric HAP	Zn doped HAP	Portland Cement
S0	-	-	100
S1	1	-	99
S2	2	-	98
S3	3	-	97
S4	5	-	95
S5	-	1	99
S6	-	2	98
S7	-	3	97

The S0 sample is composed only of Portland cement and is the standard sample. The S1, S2, S3 and S4 cements contain the various amounts of stoichiometric hydroxyapatite, while the S5, S6 and S7 cements comprise different quantities of Zn doped hydroxyapatite.

X-ray diffraction of hydroxyapatite

The X-ray diffraction (XRD) patterns of synthesized hydroxyapatite presented in Figure 1 (up) for uncalcined hydroxyapatite and in Figure 1 (down) for Zn doped hydroxyapatite, calcined at 300 °C, reveal the presence of crystalline hydroxyapatite in both samples.

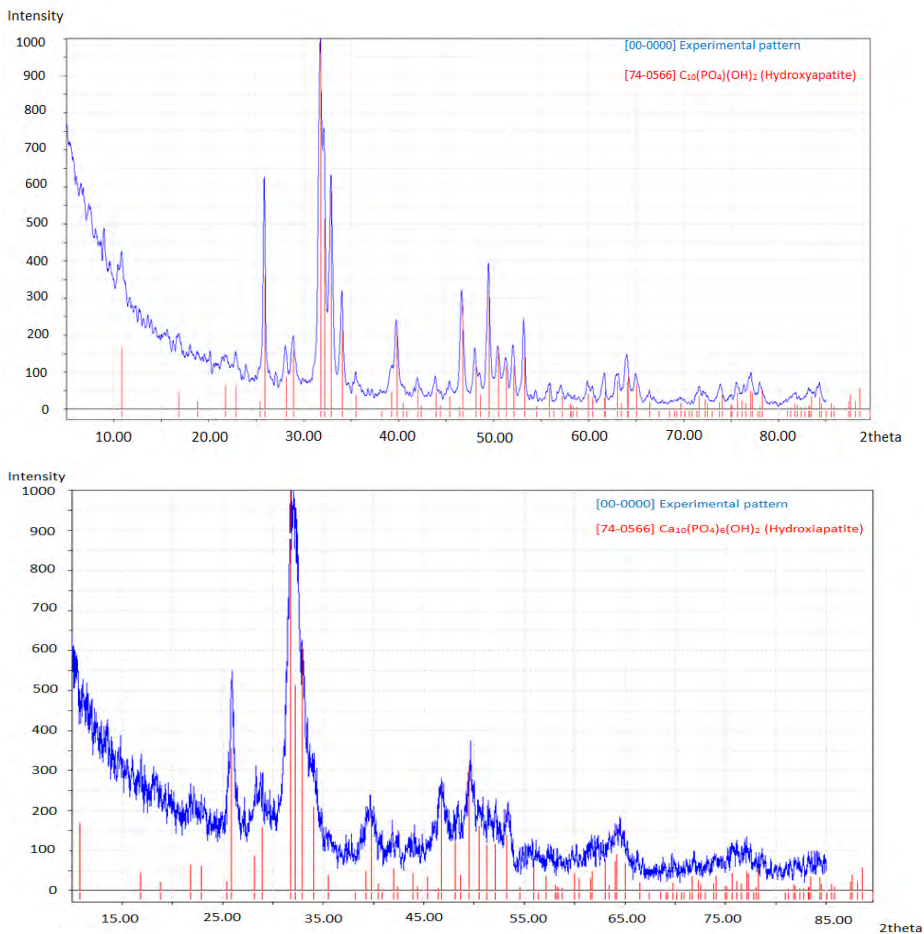


Figure 1. XRD pattern for pure, uncalcined hydroxyapatite (up) and Zn doped hydroxyapatite (down) compared with PDF 74-0566 for stoichiometric hydroxyapatite, $\text{Ca}_{10}(\text{PO}_4)_6(\text{OH})_2$.

A decrease in crystallite size and crystallinity index for Zn doped hydroxyapatite can be observed. These effects are supposedly determined by the presence of Zn ions and the sample calcination at 300 °C (Table 3).

Table 3. Crystallite sizes and crystallinity index of hydroxyapatites

Nanomaterial	Average crystallite size [nm]	Crystallinity index [%]
Stoichiometric hydroxyapatite	35.6	50.4
Zn doped hydroxyapatite	24.7	38.6

FTIR analysis for studied HAP

The FTIR spectra for both hydroxyapatite samples are presented in Figure 2. The specific vibration bands of P-O bonds from PO₄ groups can be evidenced. The peak from 962-963 cm⁻¹ appears in the apatite spectra because of the low symmetry of elemental tetrahedral cells of doped hydroxyapatite compared to free PO₄ ions from phosphates.

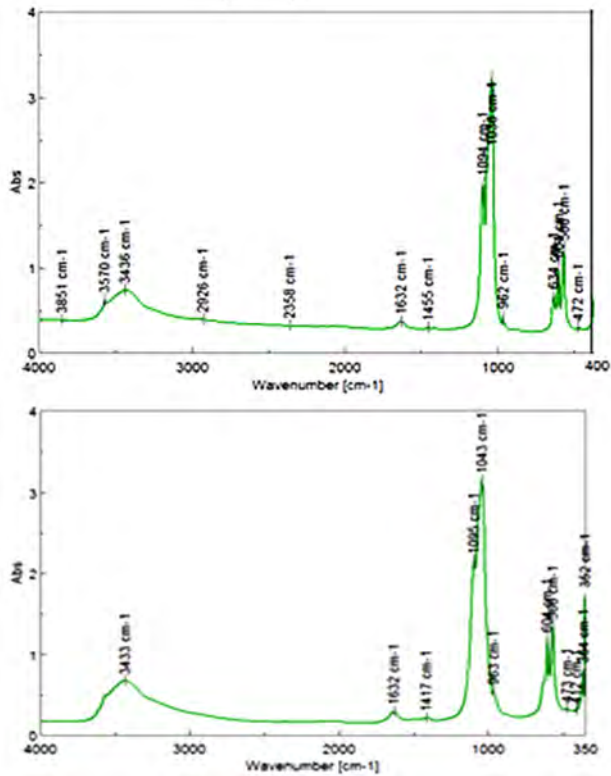


Figure 2. FTIR analysis for stoichiometric, uncalcined hydroxyapatite (up) and Zn doped hydroxyapatite calcined at 300 °C for 1h (down)

The most intense absorption band of apatite is formed from two peaks, at $1035\text{-}1044\text{ cm}^{-1}$ and $1093\text{-}1096\text{ cm}^{-1}$. The P-O asymmetric distortion is cleaved in two peaks, at 566 and $603\text{-}604\text{ cm}^{-1}$. The wide band at $3600\text{-}3300\text{ cm}^{-1}$ (with a maximum at $3420\text{-}3440\text{ cm}^{-1}$) is attributed to the O-H vibrations in the adsorbed water molecules. The narrow band at $3579\text{-}3571\text{ cm}^{-1}$, overlaid on the wide band attributed to water, is due to OH structural groups of hydroxyapatite. This observation is in accordance to the increase of water quantities in the hydroxyapatite network at a higher Zn content.

TEM images for HAP biomaterials

Transmission electron microscopy was used for investigating the morphology and size of particles in the hydroxyapatite powder (Figure 3). The image illustrates that polycrystalline hydroxyapatite with rather uniform sized particles is formed by this process. The crystallite size of hydroxyapatite measured from TEM is in the nanometric range, with a length of $40\text{-}50\text{ nm}$ and a diameter of $20\text{-}30\text{ nm}$, in accordance to XRD patterns.

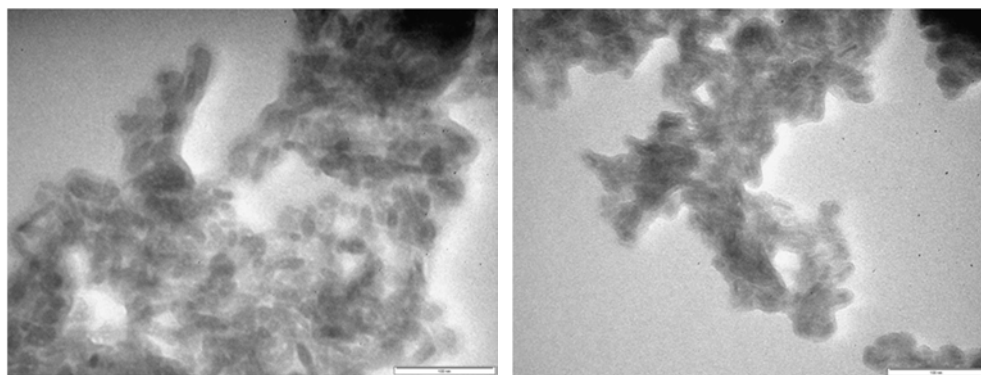


Figure 3. TEM images for stoichiometric, uncalcined hydroxyapatite (left) and Zn doped hydroxyapatite calcined at $300\text{ }^{\circ}\text{C}$ for 1h (right); 100 nm scale.

Atomic force microscopy (AFM)

AFM images and cross section profiles are given in Figure 4, for uncalcined hydroxyapatite and in Figure 5 for Zn doped hydroxyapatite, calcined at $300\text{ }^{\circ}\text{C}$ for 1h.

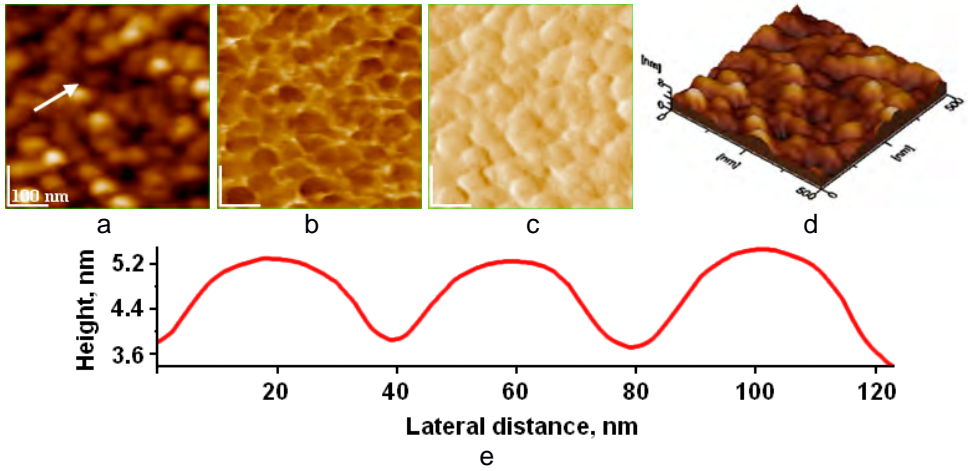


Figure 4. AFM images of HAP particles adsorbed on glass for 10 sec from aqueous dispersion: 2D topography (a), phase (b), amplitude (c), 3D- topography (d) and cross section profile (e) along the arrow in image (a); scanned area of $0.5 \mu\text{m} \times 0.5 \mu\text{m}$; average nanoparticle size of 32 nm.

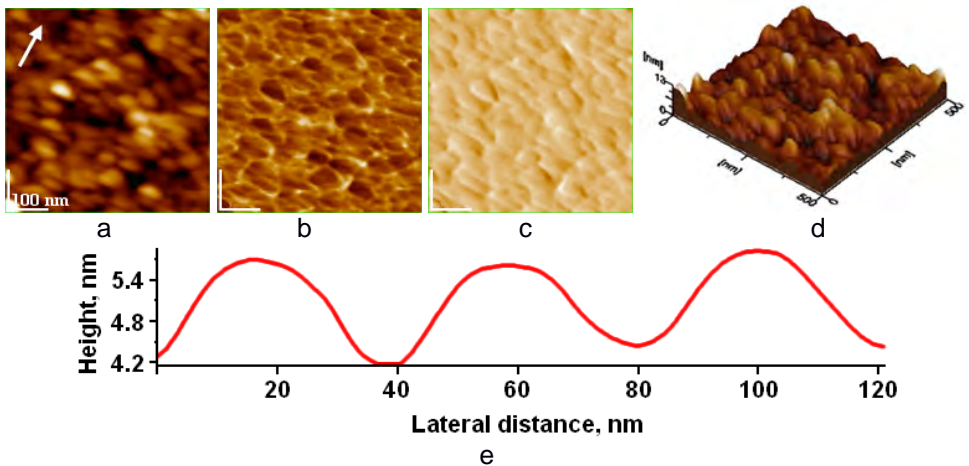


Figure 5. AFM images of HAP-5%Zn particles adsorbed on glass for 10 sec from aqueous dispersion: 2D topography (a), phase (b), amplitude (c), 3D- topography (d) and cross section profile (e) along the arrow in image (a); scanned area of $0.5 \mu\text{m} \times 0.5 \mu\text{m}$; average nanoparticle size of 27 nm.

There are mostly oblong particles, with a length of about 50 nm and diameters of 30 nm for stoichiometric hydroxyapatite and 40/20 nm for Zn doped hydroxyapatite. The size of particles is found to be in the range of 27-32 nm. These values are comparable with those determined by X-ray diffraction and SEM analysis.

Consistency water for investigated endodontic cements

Determining the normal consistency water of cement (the water quantity needed for cement slurry consistency) is an important first step towards proceeding with setting time experiments. After several trials, the normal consistency water of 87 ml for Carpat Cement Portland cement slurry was found. The predetermined consistency water for Portland cement slurry remained constant for all hydroxyapatite/cement ratios of the endodontic cements. It can be said that hydroxyapatite does not have any influence on this parameter. So, the porosity of the endodontic cement is maintained constant and, consequently, the mechanical strength.

Setting time for studied endodontic cements

The experimental data of setting time obtained from studied endodontic cements containing a consistency water of 87 ml, at temperatures of 22 °C and at 37°C, are presented in Table 4.

Table 4. Setting time of Portland cement and studied endodontic cements

Sample	Consistency water [ml]	Setting time [min]	
		at 22°C	at 37°C
S0	87	85	70
S1		70	60
S2		70	60
S3		55	45
S4		45	35
S5		70	65
S6		65	60
S7		55	45

The setting times for all experimental samples, including the standard, S0, decreases with the increasing in temperature from 22°C to 37°C, the normal body temperature. No difference can be seen through the addition of 1 and 2 wt% uncalcined hydroxyapatite (samples S1 and S2). Sample S3, containing 3 wt% hydroxyapatite, shows a more pronounced decreasing of the setting

time at both working temperatures. By increasing the hydroxyapatite content to 5 wt%, as seen in sample S4, a halving of the endodontic cement setting time can be observed. A progressive decrease of setting time in all samples containing Zn doped hydroxyapatite, namely S5, S6 and S7, can also be evidenced. Sample S7, containing 3 wt% Zn doped hydroxyapatite, shows similar behavior to that of sample S3, containing 3 wt% stoichiometric hydroxyapatite. The two types of hydroxyapatite present comparable results in the decrease of endodontic cement setting time.

CONCLUSIONS

Endodontic cements containing Portland cement and stoichiometric hydroxyapatite as well as Portland cement and Zn doped hydroxyapatite in different ratios were realized. Commercial Portland cement, having as main mineralogical components calcium silicates, was used as binder. Nanometric uncalcinated stoichiometric hydroxyapatite and Zn doped hydroxyapatite were successfully synthesized.

Quantities of 1, 2, 3 and 5 wt% of both types of hydroxyapatite were mixed with Portland cement and processed in accordance to cement standards. The workability of the cement mixtures was not influenced by adding small amounts of hydroxyapatite. The normal consistency water remains constant for all experimental slurries. The setting time for both sets of samples, with added stoichiometric, uncalcined hydroxyapatite (S1-S4) and Zn doped hydroxyapatite (S5-S7) has decreased exponentially at both working temperatures.

In conclusion, the properties, especially the setting time of studied endodontic cements obtained by adding nanometric stoichiometric and Zn doped hydroxyapatites in Portland cement mixtures can be improved. The research will continue with the testing of biological compatibility and antimicrobial activity of endodontic cements enriched with Zn doped hydroxyapatite.

EXPERIMENTAL SECTION

Materials and methods

The nanometric hydroxyapatite was prepared by the direct reaction of calcium nitrate and diammonium hydrogen phosphate at basic pH. A solution of calcium nitrate (0.25 M) was prepared by dissolving $\text{Ca}(\text{NO}_3)_2 \cdot 4\text{H}_2\text{O}$ (pure p.a., Poch S.A., Merck) in ultrapure water. Then, a 25 wt% ammonia solution was added to reach a pH of 8.5. The final solution was mixed at room temperature

with an equal volume of 0.15 M $(\text{NH}_4)_2\text{HPO}_4$ (pure p.a., Sigma-Aldrich), with pH 11 (fixed with ammonia solution). A peristaltic pump and an impact reactor type Y were used for a rapid and good homogenization. The obtained dispersion was maintained for maturation at room temperature (22 °C) for 24 h. After subsequent filtration and washing with ultrapure water (until no nitrate ions were detected), the wet precipitate was dried by lyophilization (freeze drying).

For Zn doped hydroxyapatite, a 0.25 M ($\text{Ca}^{2+} + \text{Zn}^{2+}$) solution, was prepared by dissolving the calculated amounts of $\text{Ca}(\text{NO}_3)_2 \cdot 4\text{H}_2\text{O}$ and $\text{Zn}(\text{NO}_3)_2 \cdot 6\text{H}_2\text{O}$ (from Sigma-Aldrich) in ultrapure water. The second solution was a 0.15 M PO_4^{3-} solution with L-asparagine monohydrate (purity $\geq 99.0\%$, from Merck, Germany) as surfactant. The identical processing steps were followed. The dried solid was calcined at 300 °C for one hour.

X-ray diffraction analysis was carried out using a Bruker D8 Advance diffractometer in Bragg Brentano geometry, equipped with an X-ray tube with copper K_α line and a wavelength of 1.541874 Å.

The size and morphology of hydroxyapatite crystallites were investigated by transmission electron microscopy (TEM) on a JEOL-type JEM 1010 equipment.

Atomic force microscopy analysis was carried out on a JEOL 4210 AFM apparatus, operated in tapping mode [27-35], using standard cantilevers with silicon nitride tips (resonant frequency in the range of 200–300 kHz).

Commercial Portland cement (Carpat Cement brand) as the matrix for endodontic cement mixtures was used.

Normal consistency water for investigated endodontic cements was determined following standard laboratory procedures. A quantity of 300 g cement were mixed with water ranging from 85 to 90 ml (standard for the type of Portland cement used) until a slurry was formed in the mixing bowl. The slurry was quickly poured in the mold of the Vicat apparatus and smoothed out. A 10 mm plunger was lowered to the surface of the sample and then let to fall freely. The depth was then read on the Vicat ruler. For a normal consistency, this depth should be in the 5-7 mm range.

The endodontic cement samples were prepared in a standard laboratory cement mixer. The cement and hydroxyapatite, in ratios according to Table 3, were added and homogenized for approximately 30 seconds. After this time, the water was added, the mixing continued for 1 minute on slow speed and 2 minutes on high speed, respectively. The final mixture was poured into a hard rubber truncated cone mold.

To measure the setting time of cement slurry with normal consistency water, a standard VICAT Apparatus was employed.

ACKNOWLEDGMENTS

Authors acknowledge the financial support from the Executive Agency for Higher Education, Research, Development and Innovation Funding (UEFISCDI) through grant no. 241.

REFERENCES

1. L.H. Silva Almeida, R.R. Moraes, R.D. Morgental, F.G. Pappen, *Journal of Endodontics*, **2017**, *43*, 527.
2. G. Debelian, M. Trope, *Giornale Italiano di Endodonzia*, **2016**, *30*, 70.
3. P. Bali, A.K. Shivekshith, C.R. Allamaprabhu, H.P. Vivek, *International Journal of Contemporary Dental and Medical Reviews*, **2014**, doi: 10.15713/ins.ijcdmr.17
4. F. Panahi, S.M. Rabiee, R. Shidpour, *Materials Science and Engineering C*, **2017**, *80*, 631.
5. I.R. Oliveira, T.L. Andrade, K.C.M.L. Araujo, A.P. Luz, V.C. Pandolfelli, *Ceramics International*, **2016**, *42*, 2542.
6. F. Goga, E. Forisz, A. Avram, A. Rotaru, A. Lucian, I. Petean, A. Mocanu, M. Tomoaia-Cotisel, *Revista de Chimie*, **2017**, *68*, 1193.
7. J.A. Lett, M. Sundareswari, K. Ravichandran, *Materials Today: Proceedings*, **2016**, *3*, 1672.
8. S.M. Rabiee, F. Moztaizadeh, M. Solati-Hashjin, *Journal of Molecular Structure*, **2010**, 969, 172.
9. M. Hosseinzade, R.K. Soflou, A. Valian, H. Nojehdehian, *Biomedical Research*, **2016**, *27*, 442.
10. Y.A. Moreno-Vargas. J.P. Luna-Arias, J.O. Flores-Flores, E. Orozco, L. Bucio, *Ceramics International*, **2017**, *43*, 13290.
11. J. Camilleri, F.E. Montesin, R.V. Curtis, T.R. Pitt Ford, *Dental Materials*, **2006**, *22*, 569.
12. V. Bortolotti, P. Fantazzini, R. Mongiorgi, S. Sauro, S. Zanna, *Cement and Concrete Research*, **2012**, *42*, 577.
13. K. Ishikawa, *Bioactive Ceramics: Cements*, Comprehensive Materials II, Elsevier, **2017**, 369.
14. S. Jitaru, I. Hodisan, L. Timis, A. Lucian, M. Bud, *Clujul Medical*, **2016**, *89*, 470.
15. W.N. Ha, D.P. Bentz, B. Kabler, L.J. Walsh, *Journal of Endodontics*, **2015**, *41*, 1146.
16. A.M. Negm, E.E. Hassanien, A.M. Abu-Seida, M.M. Nagy, *Experimental and Toxicologic Pathology*, **2017**, *69*, 115.
17. M.G. Gandolfi, P. Taddei, A. Tinti, E. De Stefano Dorigo, C. Prati, *Materials Science and Engineering C*, **2011**, *31*, 1412.
18. N.J. Coleman, J.W. Nicholson, K. Awosanya, *Cement and Concrete Research*, **2007**, *37*, 1518.

19. D. Araki Ribeiro, M.A. Hungaro Duarte, M. Akemi Matsumoto, M.E. Alencar Marques, D.M. Favero Salvadori, *Journal of Endodontics*, **2005**, 31, 605.
20. A. Chaipanich, P. Torkittikul, *Applied Surface Science*, **2011**, 257, 8385.
21. J. Camilleri, *Dental Materials*, **2011**, 27, 836.
22. P. Scembri-Wismayer, J. Camilleri, *Journal of Endodontics*, **2017**, 43, 751.
23. N. Wongkornchaowalit, V. Lertchirakarn, *Journal of Endodontics*, **2011**, 37, 387.
24. P. Torkittikul, A. Chaipanich, *Materials Science and Engineering C*, **2012**, 32, 282.
25. K.B. Wiltbank, S.A. Schwartz, W.G. Schindler, *Journal of Endodontics*, **2007**, 33, 1235.
26. L. Wang, X. Xie, C. Li, H. Liu, K. Zhang, Y. Zhou, X. Chang, H.H.K. Xu., *Journal of Dentistry*, **2017**, 60, 25.
27. G. Tomoaia, O. Soritau, M. Tomoaia-Cotisel, L.-B. Pop, A. Pop, A. Mocanu, O. Horovitz, L.-D. Bobos, *Powder Technology*, **2013**, 238, 99.
28. G. Tomoaia, M. Tomoaia-Cotisel, L.B. Pop, A. Pop, O. Horovitz, A. Mocanu, N. Jumate, L.-D. Bobos, *Revue Roumaine de Chimie*, **2011**, 56, 1039.
29. A. Mocanu, R. Balint, C. Garbo, L. Timis, I. Petean, O. Horovitz, M. Tomoaia-Cotisel, *Studia Universitatis Babes-Bolyai, Chemia*, **2017**, 62(2), Tom I, 95.
30. R.D. Pasca, G. Tomoaia, A. Mocanu, I. Petean, G.A. Paltinean, O. Soritau, M. Tomoaia-Cotisel, *Studia Universitatis Babes-Bolyai, Chemia*, **2015**, 60(3), 257.
31. M.A. Naghiu, M. Gorea, E. Mutch, F. Kristaly, M. Tomoaia-Cotisel, *Journal of Material Science and Technology*, **2013**, 29(7), 628.
32. G. Tomoaia, O. Horovitz, A. Mocanu, A. Nita, A. Avram, C.P. Racz, O. Soritau, M. Cenariu, M. Tomoaia-Cotisel, *Colloids and Surfaces B: Biointerfaces*, **2015**, 135, 726.
33. O. Horovitz, G. Tomoaia, A. Mocanu, T. Yupsanis, M. Tomoaia-Cotisel, *Gold Bulletin*, **2007**, 40 (4), 295.
34. M. Tomoaia-Cotisel, A. Tomoaia-Cotisel, T. Yupsanis, G. Tomoaia, I. Balea, A. Mocanu, Cs. Racz, *Revue Roumaine de Chimie*, **2006**, 51 (12), 11832.
35. P.T. Frangopol. D.A. Cadenhead, G. Tomoaia, A. Mocanu, M. Tomoaia-Cotisel, *Revue Roumaine de Chimie*, **2015**, 60(2-3), 265.

HYDROXYAPATITE FOR REMOVAL OF HEAVY METALS FROM WASTEWATER

ALEXANDRA AVRAM^a, TIBERIU FRENTIU^a, OSSII HOROVITZ^{a,*},
AURORA MOCANU^a, FIRUTA GOGA^a, MARIA TOMOAI-COTISEL^{a,b}

ABSTRACT. HAP powder of a low crystallinity and rather large specific surface area was synthesized by an environmentally friendly, cost effective precipitation method, and characterized by XRD, FTIR, and BET isotherms. TEM and AFM are used to envisage the surface of HAP nano particles, showing a high porosity of this ceramic powder. It was used for the removal of metals (Al, Cd, Co, Cr, Cu, Fe, Mn, Ni, Pb, and Zn) from mine wastewater. Metal contents in the initial and treated samples were quantified by inductively coupled plasma atomic emission spectrometry and high-resolution continuum source atomic absorption spectrometry. By the use of HAP, an efficient removal of all metals was ensured. The increase of Ca²⁺ ions content in the treated water suggests an ion exchange mechanism.

Keywords: *hydroxyapatite, heavy metal removal, mine wastewater, sorption kinetics*

INTRODUCTION

The presence of heavy metals in wastewater [1-6], resulting from mining operations, various manufacturing industries, leather tanning, paper production, fertilizers, photographic materials, explosives, is a major environmental concern. These elements can enter the human body both in a direct manner and following the food chain [7, 8]. Easily accumulated by organisms and non-biodegradable [1] heavy metals can lead to a large number of potentially deadly health issues [8-10] Some metals can be toxic even in small concentrations [11]. The admissible levels of heavy metals are regulated in most countries [12, 13], during the wastewater treatment.

^a Babeş-Bolyai University, Faculty of Chemistry and Chemical Engineering, 11 Arany Janos str., RO-400028, Cluj-Napoca, Romania

^b Academy of Romanian Scientists, Splaiul Independenței 54, 050094 Bucharest, Romania

*Corresponding author: ossihor@yahoo.com

With water playing a crucial role in a sustainable development, the removal of heavy metals from contaminated waters has been the subject of many studies. Some examples are: strontium [14], iron [2, 15-18], lead [1-4, 6, 15, 18-28], cadmium [2, 3, 7, 18, 25, 29-33], zinc [2, 5, 15, 16, 18, 22, 23, 29, 32], nickel [2, 8, 10, 17, 18, 31], chromium [18, 32, 35], arsenic [9], copper [17-20, 22, 24, 25, 32, 33], manganese [15, 16, 23], mercury [36], cobalt [18, 37]).

Some of the methods employed in the removal of these elements involve physical (e.g., membrane filtration, coagulation, adsorption on both stable and floating beds, reverse osmosis), chemical (such as, neutralization with various materials, including lime, ion exchange, adsorption, chemical oxidation or reduction) and biological processes [2-4, 9, 14, 15, 23, 34, 35]. The latter category presents certain models that are not easily implemented in industrial conditions as they require high manufacturing costs and are too complex [2].

The published data revealed that adsorption onto solids has been a preferred method, due to being simple, highly-selective, relatively low cost and showing very few to no problems [11, 14]. Among organic and inorganic materials used are: both natural [7, 10, 32, 35] and synthetic hydroxyapatite (HAP) [1, 2, 19, 21, 24], and various composites containing it [3, 4, 6, 25, 37], zeolites [23] polymers, organic resins [8], silicate sand, bentonite [6, 23], carbon nanotubes [4], coals [8, 9], bone charcoals [17], and natural waste materials (spent coffee grounds, fruit waste, nut and eggshells, rice husks, bamboo, saw dust, tea waste, grape stalks, algae, wood) [1, 9, 26, 32, 34, 37].

Hydroxyapatite (HAP, $\text{Ca}_{10}(\text{PO}_4)_6(\text{OH})_2$), a naturally available form of calcium phosphate and a component of hard tissues [15, 26, 27]), has been reported to act as an efficient ion removal material for various heavy metals from aqueous solutions due to its excellent reactivity and low water solubility [8, 14, 35]. The high structure stability of HAP, along with its flexibility permit a large variety of substitutions (especially Ca with divalent heavy metal ions, such as Pb, Cu, Sb, Zn, Cd, Co, Ni, U, Hg, As [6, 8, 18, 27, 28, 33, 34, 38-40], of great importance in the field of environmental science [34].

HAP can be synthesized through various methods, including sol-gel [24], wet precipitation [6, 31, 41-44], combustion and ultrasonic [32]. Its slightly-alkaline pH and high biocompatibility will not likely cause any form of secondary environmental damage [19]. The efficiency of HAP in removing heavy metal ions heavily depends on ion nature, charge, diameter and concentration, as well as the properties of the treated water (pH, temperature) [8, 25]. In addition, the removal of HAP from the purified aqueous solution is not without problems [38], as is the isolation of some important heavy metals from it [3, 36].

Some studies have tried to enhance the properties of hydroxyapatite (improved porosity, specific surface area, mechanical properties, etc. [6, 27]) through the addition of non-toxic polymers, abundantly found in nature – dextran [27], chitosan [4, 38], carboxymethyl cellulose [26, 36], alginate, gelatin [21]. However, these additions do tend to increase the manufacturing cost, thus making it difficult to translate from a laboratory level to an industrial one. Other studies have tried to combine the reactivity of hydroxyapatite as an adsorbent with a magnetic separation process for an increased adsorption of heavy metal ions, synthesizing magnetic HAP particles [22] or magnetic core-shell nanocomposites [5]. Ca deficient HAP has also been reported to exhibit different ion substitution ability to stoichiometric HAP [18], due to its large number of Ca-deficient sites. While the main focus of some research groups is to enhance the properties of HAP by using its composites with various polymers, such as chitosan, others choose to focus on cost effectiveness, by synthesizing hydroxyapatite, using environmental friendly methods.

The aim of this study was to develop a rapid and low cost method to remove metal ions from mine wastewaters, using a low crystalline HAP prepared by a precipitation method [41]. This study meant to correlate the ion adsorption behaviour of a low crystallinity HAP, and its efficiency in removal of a large range of various metals (Al, Cd, Co, Cr, Cu, Fe, Mn, Ni, Pb, and Zn) from a multi-component Roşia Montana mine wastewater.

RESULTS AND DISCUSSION

Hydroxyapatite characterization

X-ray diffraction pattern (Fig. 1) shows, by comparison with PDF 74-0566 (characteristic for stoichiometric HAP) that synthesized HAP sample contains only pure hydroxyapatite. Average crystallite size was evaluated, using Scherrer formula, to be 23.3 nm, and the degree of crystallinity was obtained, using Reflex computer program, as 32.3%. This nanoHAP with rather low crystallinity is expected to present good adsorptive properties.

The *FTIR spectrum* (Fig. 2) presents the absorption bands of hydroxyapatite, corresponding to vibrations of PO₄ and OH groups characteristic for HAP, and of OH groups from adsorbed water

An example of *TEM image* (Fig.3) for the HAP sample in aqueous dispersion reveals acicular assemblies of particles, with a diameter of 15-20 nm. These dimensions are confirmed by the *atomic force microscopy (AFM)* images (an example is given in Fig. 4).

Brunauer-Emmett-Teller (BET) analysis on HAP powder gave a specific surface area of 106.5 m²/g and a specific volume of the pores of 0.358 cm³/g.

The large specific surface area recommends HAP as a good adsorbent. From the surface area, a rough estimation of the particles size is possible, using the formula

$$d = \frac{6}{S\rho} \quad (1)$$

where d is the average diameter of particles, S is the specific surface area and ρ is the density of the material; using the theoretical density of HAP: 3.14 g/cm^3 [45], a value of 17.9 nm is found for the average diameter of a HAP particle.

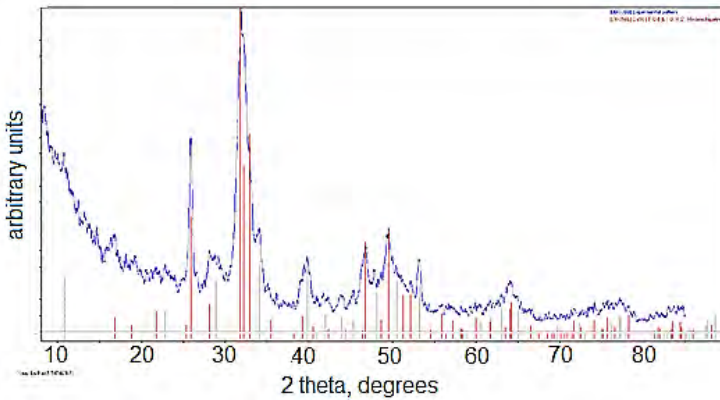


Figure 1. XRD pattern for HAP sample, compared with PDF 74-0566 for stoichiometric hydroxyapatite

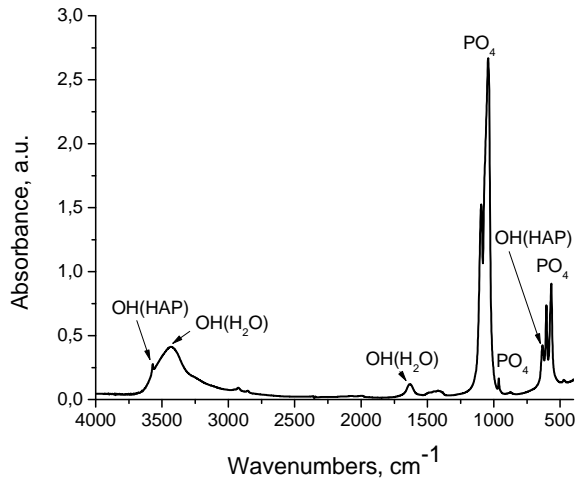


Figure 2. FTIR spectrum of HAP

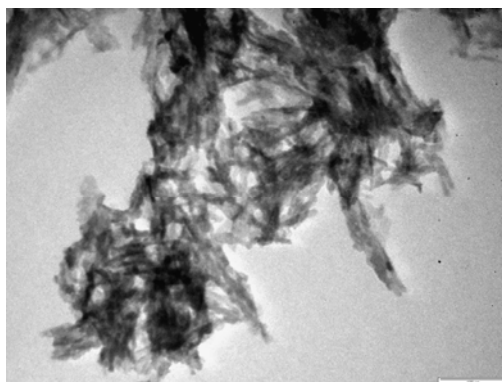


Figure 3. TEM image of HAP; the bar is 100 nm

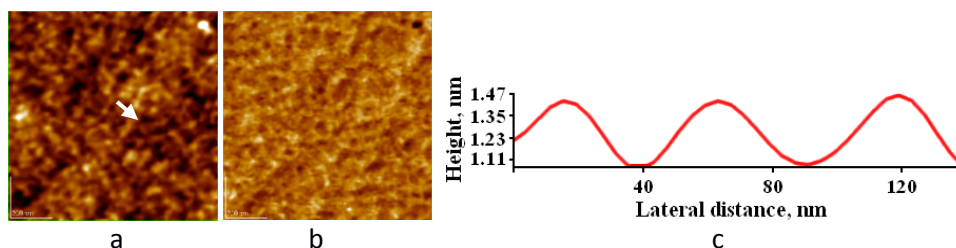


Figure 4. AFM images for HAP, adsorbed on glass support: 2D topography (a), phase image (b), cross section profile (c) along the arrow in panel (a); scanned area of $1\mu\text{m} \times 1\mu\text{m}$

Metal ions removal from mine wastewater samples

The removal degree, R (%), was calculated as

$$R (\%) = 100 \frac{c_0 - c_e}{c_0} \quad (2)$$

where c_0 is the element' content (mg/L) in the initial mine wastewater sample, while c_e is its final content at equilibrium, after adsorption for 120 min on HAP. The initial and final content, and the calculated removal degree for each metal are given in Table 1, along with the standard errors from determinations on 3 parallel samples. In the same table the limit values for the metal content admissible in wastewater discharged in natural waters [12] are indicated.

All metal ions are removed to final values below the values admitted in standards for wastewaters. The removal degree is near to 100% for metals existent in higher amounts in the wastewater, and lower (60-80%) for those present initially only in very low concentration (even under the admitted limit value – Table 1). Probably, their sorption on the surface of HAP nanoparticles

is limited by the simultaneous sorption of ions existent in high excess in the wastewater. The confidence intervals are wide due to the existence of some metals (Cu, Cr, Pb, Ni) near the quantification limit of analytical methods. However, an efficient removal of these metals below the values of admitted levels in wastewater in the presence of those in high concentrations can also be observed.

Table 1. Metal removal from mine wastewaters using nano HAP powder (results are given as mean \pm confidence interval for $n = 3$ and 95% confidence level)

Metal	Initial content c_0 , mg/L	Final content c_e , mg/L	Removal degree, % ^a	Limit value for wastewater, mg/L [12]
Al	313 \pm 37	1.9 \pm 0.6	99 \pm 12	5
Cd	0.21 \pm 0.07	0.068 \pm 0.043	68 \pm 58	0.2
Co	1.1 \pm 0.6	0.15 \pm 0.07	86 \pm 63	1
Cr	0.046 \pm 0.024	0.009 \pm 0.006	80 \pm 66	1
Cu	1.0 \pm 0.7	0.014 \pm 0.011	99 \pm 71	0.1
Fe	92 \pm 9	0.9 \pm 0.6	99 \pm 10	5
Mn	190 \pm 5	0.81 \pm 0.48	100 \pm 3	1
Ni	0.47 \pm 0.22	0.16 \pm 0.09	66 \pm 77	0.5
Pb	0.16 \pm 0.07	0.066 \pm 0.045	59 \pm 88	0.2
Zn	14.4 \pm 0.9	0.18 \pm 0.08	99 \pm 6	0.5

^a the removal degree and its confidence interval were calculated by a concentration difference and pooled standard deviation

Adsorption kinetics of Mn^{2+} ions on HAP

The concentration of Mn^{2+} ions in mine wastewater was measured at different time points. The Mn uptake, x , from the contaminated solution on the HAP, was calculated in mg Mn/g HAP for each moment by the formula:

$$x = \frac{(c_0 - c_t)V}{m} \quad (3)$$

where c_0 is the initial Mn^{2+} content, c_t is the content at time t (mg/L), V is the volume of solution (0.1 L), and m is the mass of HAP (10 g).

In order to assess the kinetics of Mn removal from the solution, three kinetic models were used [3], assuming a pseudo-first-order kinetic [46], a pseudo-second order kinetic [47], and an intraparticle diffusion model [48].

The first order kinetic (Lagergren kinetic) would be described by the equation:

$$\frac{dx}{dt} = k_1(x_e - x) \quad (4)$$

where x_e is the sorbed amount at equilibrium, assumed to be the value at 960 min, and k_1 is the first order adsorption rate constant. The representation of the linearized form of the integrated equation:

$$\ln(x_e - x) = \ln x_e - k_1 t \quad (4a)$$

as $\ln(x_e - x) = f(t)$ should give a straight line if the equation would apply. The poor linearity observed in Fig. 5a ($r^2 = 0.62$) shows this model to be inadequate here.

The 2nd order kinetic equation:

$$\frac{dx}{dt} = k_2(x_e - x)^2 \quad (5)$$

with k_2 as second order sorption rate constant, linearized after integration as:

$$\frac{t}{x} = \frac{1}{k_2 x_e^2} + \frac{t}{x_e} \quad (5a)$$

gives in the representation: $t/x = f(t)$ a perfect straight line (Fig. 5b), with $r^2 = 0.9999$; thus this model best describes the kinetics of Mn sorption on HAP.

The third model assumes the diffusion to be the rate-limiting step in the sorption, using an equation for intraparticles diffusion rate:

$$x = k_d t^{1/2} + const. \quad (6)$$

where k_d is the diffusion rate constant and *const.* an integration constant. The representation of $x = f(t^{1/2})$ in Fig. 5c shows no linear correlation ($r^2 = 0.32$), so this model is not applicable in our case. Nevertheless, for the first 15 minutes of sample contact with HAP, a quite good correlation is found ($r^2 = 0.985$, Fig. 5d) with $k_d = 0.480 \pm 0.034$ and *const.* = 0.02 ± 0.07 .

From the parameters of the linear plot of equation (5a) for the pseudo second order kinetics: intercept, $a = 0.57502$, and slope, $b = 0.52808$, we can calculate the x_e value: $x_e = 1/b = 1.894$ mg/g, very close to the assumed value 1.891, and the pseudo second order rate constant $k_2 = 1/(ax_e^2) = 0.485$ g·mg⁻¹·min⁻¹ = 29.1 g·mg⁻¹·h⁻¹. A second order reaction kinetic was observed also for the sorption on hydroxyapatite of other metal ions, such as Cd²⁺ [3], Cu²⁺ [19], Ni²⁺ [10], Zn²⁺ [34], Cr(VI) [35], or Pb²⁺ [3, 19, 21]. For the adsorption of Co²⁺ on a HAP/zeolite composite [34], Pb²⁺ on a HAP/bentonite composite [6], Cr(VI), Zn²⁺, and Cd²⁺ on HAP/chitosan composite [38], of Mn²⁺, Fe²⁺, Ni²⁺, and Cu²⁺ on charcoal [17], the same pseudo-second order kinetic was found.

We could assume that for the initial stage (about 15 min), diffusion is important; subsequently, the second order chemical process is rate determining.

Hydroxyapatite immobilizes heavy metal ions from aqueous solutions in various ways. Some of these mechanisms include: surface complexation, ion exchange, dissolution followed by the precipitation of metal phosphates, and the substitution of Ca²⁺ present in the HAP structure by other divalent heavy metals during co-precipitation [16, 18, 28, 34]. Literature presents very little information on the specific contribution of these processes, leading researchers to believe that they are all employed at the same time [16, 34] (in aqueous solutions containing multiple competing heavy metal ions [33]).

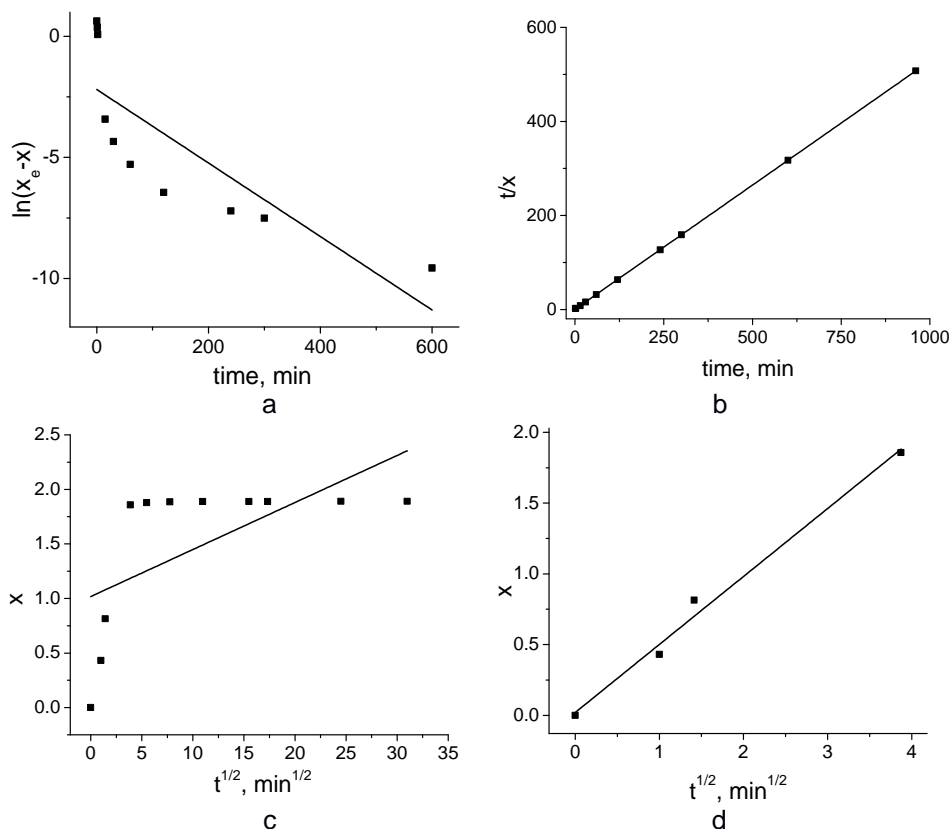


Figure 5. Plots of linearized kinetic equations for pseudo first order (a), pseudo second order (b) and intramolecular diffusion (c, d) kinetics of Mn sorption on HAP

The sorption process of metal ions involves complex adsorption on the adsorption sites on the HAP surface [19]. For the mechanism of ions retention, ion exchange was considered, for instance for Pb^{2+} [1, 15], where the incorporation of Pb in the HAP lattice was evidenced, or for Cd^{2+} [33]. For Zn^{2+} , Fe^{2+} and Mn^{2+} the formation of metal phosphates was considered [15], by dissolution of HAP and precipitation of phosphate ions with the heavy metal ions.

During the metals removal process, an increase of the Ca^{2+} content in the solution was observed, from initially 115.5 mg/L to 287.3 mg/L (after 120 min), which corresponds to the release of 4.29 mmol/L. The total amount of heavy metal ions removed from the solution (Table 1) in the same time is 5.35 mmol/L. So, most of the heavy metal ions were exchanged with Ca^{2+} ions during sorption, while other were simply adsorbed on the surface of HAP.

CONCLUSIONS

Our study has evidenced that low crystallinity HAP can be successfully used in heavy metal removal from mine wastewater. For all the 10 metals analyzed (Al, Cd, Co, Cr, Cu, Fe, Mn, Ni, Pb, and Zn), their content was rapidly reduced by contact with HAP under the legal admissible limits for wastewater discharge in natural environment. The importance of ion exchange in sorption processes was revealed and the pseudo-2nd order kinetics of manganese ions sorption on HAP was assessed.

EXPERIMENTAL SECTION

The nano-hydroxyapatite was prepared by the direct reaction of calcium nitrate and diammonium hydrogen phosphate at basic pH. The calcium nitrate solution (0.25 M), prepared from $\text{Ca}(\text{NO}_3)_2 \cdot 4\text{H}_2\text{O}$ (pure p.a., Merck) in ultrapure water, with addition of 25% ammonia solution to pH 8.5 was mixed at room temperature with an equal volume of 0.15 M $(\text{NH}_4)_2\text{HPO}_4$ (pure p.a., Sigma-Aldrich), with pH 11 (fixed with ammonia solution). The mixing was achieved rapidly, using a peristaltic pump (Masterflex L/S Digital Drive, 600 RPM, 115/230 VAC, EW-07523-80) and an impact reactor type Y To assist the formation of the HAP lattice, the so obtained dispersion was maintained for a maturation stage at room temperature (22°C) for 24 h. After subsequent filtration and washing with ultrapure water (until no nitrate ions were detected), the wet precipitate was dried by lyophilization (freeze drying process). The dried material was dispersed by grinding in an agate mortar.

X-Ray Diffraction (XRD) investigations: a DRON-3 diffractometer was used, in Bragg-Brentano geometry, equipped with a X-ray tube with Co K_α radiation (wavelength 1.79026 Å), 25 kV/20 mA. *FTIR spectra* were determined on the HP powder in KBr pellets, using a FTIR spectrometer JASCO 6100 in the 4000-400 cm^{-1} range of wave numbers, with a 4 cm^{-1} resolution.

TEM images were obtained with a transmission electron microscope (TEM, JEOL – JEM 1010); the aqueous dispersion of the HAP sample was adsorbed on the specimen grids. The same HAP dispersion was used for the preparation of samples for atomic force microscopy, AFM JEOL 4210 used in tapping mode, [49-53], after HAP adsorption for 10 s on glass. The images were processed by the standard AFM-JEOL procedures.

For BET analysis an automated Sorptomatic 1990 instrument was used, with nitrogen adsorption at 77 K. The calculation of surface area was made in the P/P_0 range between 0.03 and 0.3, and the total pore volume was determined at $P/P_0 = 0.95$. Before the analysis the samples were outgassed for 6 h at 70 °C.

The ion adsorption capacity of synthetic hydroxyapatite was studied using raw, non-treated wastewater collected from Roşia Montană, Alba County, Romania. Adsorption experiments were carried out in controlled conditions using a predetermined wastewater/HAP ratio, namely 100 ml wastewater to 10 g HAP. All experiments were performed by submitting the HAP/wastewater mixture to magnetic stirring for 100 minutes, followed by a 20 minutes sedimentation period. For manganese, samples were collected in a time span ranging from one minute to 960 minutes, for kinetics determination purposes. All samples were filtered using Millipore syringe filters (0.22 µm).

Treated water samples were analyzed by Inductively Coupled Plasma Atomic Emission Spectrometry using a Spectro Ciros CCD spectrometer (Spectro Ciros, Germany) and High-Resolution Continuum Source Atomic Absorption Spectrometry using a ContrAA 300 flame spectrometer (Analytik Jena, Germany). The results are calculated as the mean values of 3 independent measurements.

ACKNOWLEDGMENTS

This work was supported by the Romanian Executive Agency for Higher Education, Research, Development and Innovation Funding (UEFISCDI) through grant 241/2014 and 83/2017.

REFERENCES

1. V.N. Narwade, M.P. Mahabole, K.A., Bogle, R.S. Khaimar, *International Journal of Engineering Science and Innovative Technology*, **2014**, 3, 324.
2. N. Moayyeri, K. Saeb, E. Biazar, *International Journal of Material Science and Engineering*, **2013**, 3, 13.
3. S. Park, A. Gomez-Flores, Y.S. Chung, H. Kim, *Journal of Chemistry*, **2015**, Article ID 396290, 12 pp.
4. Y. Lei, J.-J. Guan, W. Chen, Q.-F. Ke, C.-Q. Zhang, Y.-P. Guo, *RCS Advances*, **2015**, 5, 25462.
5. F. Foroughi, S.A. Hassanzadeh-Tabrizi, J. Amighian, A. Saffar-Teluri, *Ceramics International*, **2015**, 41, 6844.
6. T.M. Hieu Do, P.T.T. Tran, A.K. Ton, M.V. Le, *Journal of Environmental Science and Technology B*, **2016**, 5, 371.
7. O.K. Ince, M. Ince, N.M. Karaaslan, V. Yonten, *Analytical Letters*, **2016**, 49, 2513.
8. S. Sharma, S. Garg, *Research Cell: An International Journal of Engineering Sciences*, **2014**, 3, 201.
9. M. Mirhosseini, E. Biazar, K. Saeb, *Current World Environment*, **2014**, 9, 331.

10. S. Zamani, E. Salahi, I. Mobasherpour, *Canadian Chemical Transactions*, **2013**, 1, 173.
11. L.V. Constantin, S. Iconaru, C.S. Ciobanu, *Romanian Reports in Physics*, **2012**, 64, 788.
12. *** HOTĂRÂRE nr. 352 din 21 aprilie 2005 privind modificarea si completarea Hotărârii Guvernului nr. 188/2002 pentru aprobarea unor norme privind condițiile de descărcare in mediul acvatic a apelor uzate, *Monitorul Oficial* Nr 398, 11 mai **2005**, Art. I, 35.
13. *Guidelines for drinking-water quality: fourth edition incorporating the first addendum*, Geneva, World Health Organization, **2017**, Licence: CC BY-NC-SA 3.0 IGO.
14. Y. Nishiyama, T. Hanafusa, J. Yamashita, Y. Yamamoto, T. Ono, *Journal of Analytical and Nuclear Chemistry*, **2016**, 64, 1279.
15. J. Oliva, J. De Pablo, J.-L. Cortina, J. Cama, C. Ayora, *Journal of Hazardous Materials*, **2010**, 184, 364.
16. S. Varvara, M. Popa, R. Bostan, A. Lancranjan, M. Moldovan, C. Rosu, *Studia UBB Ambientum*, **2015**, 60, 145.
17. J.C. Moreno, R. Gomez, L. Giraldo, *Materials*, **2010**, 3, 452.
18. T. Miriguchi, S. Nakagawa, F. Kaji, *Phosphorus Research Bulletin*, **2008**, 22, 54.
19. Y. Song, J. Gao, Y. Zhang, S. Song, *Nanomaterials and Nanotechnology*, **2016**, 6, 1.
20. J.R. Parga, J.L. Valenzuela, V. Vazquez, M. Rodriguez, H. Moreno, *Materials Sciences and Applications*, **2013**, 4, 231.
21. K. Sangeetha, G. Vasugi, E.J. Girija, *Journal of Chemtech Research*, **2015**, 8, 117.
22. C. Stotzel, F.A. Muller, F. Reinert, F. Niederdraenk, J.E. Barralet, U. Gbureck, *Colloids and Surfaces B: Biointerfaces*, **2009**, 74, 91.
23. S. M. Abdallah, *Journal of Novel Applied Sciences*, **2014**, 3, 5
24. A. Deptula, J. Chwastowska, W. Lada, T. Olczak, D. Wawszczak, E. Sterlinska, B. Sartowska, M. Brykala, K.C. Goretta, *Advances in Science and Technology*, **2006**, 45, 2198.
25. M. Vila, S. Sanchez-Salcedo, M. Cicuendez, I. Izquierdo-Barba, M. Vallet-Regi, *Journal of Hazardous Materials*, **2011**, 192, 71.
26. D.C. Manatunga, R.M. De Silva, K.M.N. De Silva, R. Ratnaweera, *RSC Advances*, **2016**, 6, 105618.
27. A. Costescu, E. Andronescu, B.S. Vasile, R. Trusca, P. Le Coustumer, E.S. Barna, S.L. Iconaru, M. Motelica-Heino, C.S. Ciobanu, *U.P.B. Scientific Bulletin, Series B*, **2014**, 76, 71.
28. Q.Y. Ma, S.J. Traina, T.J. Logan, *Environmental Science and Technology*, **1993**, 27, 1803.
29. Y. Feng, J.-L. Gong, G.-M. Zeng, Q.-Y. Niu, H.-Y. Zhang, C.-G. Niu, J.-H. Deng, M. Yan, *Chemical Engineering Journal*, **2010**, 162, 487.
30. K.A. Matis, A.I. Zoubulis, S. Mandjiny, D. Zamboulis, *Separation Science and Technology*, **1997**, 32, 2127.
31. M. Nehru, S. Sumathi, *International Journal of Applied Engineering Research*, **2013**, 8, 2179.

32. K. Chojnacka, I. Michalak, *Global Nest Journal*, **2009**, 11, 205.
33. A. Corami, S. Mignardi, V. Ferrini, *Journal of Colloid and Interface Science*, **2008**, 317, 402.
34. R. Bazargan-Lari, M.E. Bahrololoom, A. Nemati, *International Journal of Chemical, Molecular, Nuclear, Materials and Metallurgical Engineering*, **2012**, 6, 105.
35. T. Faezeh, M. Omid, H. Ebrahimzadeh, *Indian Journal of Science and Technology*, **2015**, 8, 1.
36. Z. Abbasi, M. Aghababaei, *Universal Journal of Engineering Science*, **2014**, 2, 124.
37. N. Gupta, A.K. Kushwaha, M.C. Chattopadhyaya, *Advanced Materials Letters*, **2011**, 2, 309
38. E. Kusriani, N. Sofyan, D.M. Nurjaya, S. Santoso, D. Trisnantini, *Advanced Materials Research*, **2013**, 789, 176.
39. F. Fernane, S. Boudia, H. Saouli, *Matec Web of Conferences*, **2013**, 5, 1.
40. H. Sawa, A. Takenaka, M. Hasegawa, K. Aoki, *Phosphorus Research Bulletin*, **1998**, 8, 55.
41. A. Mocanu, R. Balint, C. Garbo, L. Timis, I. Petean, O. Horovitz, M. Tomoaia-Cotisel, *Studia UBB Chemia*, **2017**, 62, 95.
42. C. Garbo, M. Sindilaru, A. Carlea, G. Tomoaia, V. Almasan, I. Petean, A. Mocanu, O. Horovitz, M. Tomoaia-Cotisel, *Particulate Science and Technology*, **2017**, 35, 29.
43. Gh. Tomoaia, A. Mocanu, I. Vida-Simiti, N. Jumate, L.D. Bobos, O. Soritau, M. Tomoaia-Cotisel, *Materials Science and Engineering C*, **2014**, 37, 37.
44. G. Tomoaia, O. Soritau, M. Tomoaia-Cotisel, L.-B. Pop, A. Pop, A. Mocanu, O. Horovitz, L.-D. Bobos, *Powder Technology*, **2013**, 238, 99.
45. D. Loca, M. Sokolova, J. Locs, A. Smirnova, Z. Irbe, *Materials Science and Engineering C*, **2015**, 49, 106.
46. S. Lagergren, *Kungliga Svenska Vetenskapsakademiens Handlingar*, **1898**, 24, 1.
47. Y.S. Ho, G. McKay, *Process Biochemistry*, **1999**, 34, 451.
48. W.J. Weber, J. C. Morris, *Journal of the Sanitary Engineering Division—American Society of Civil Engineers*, **1963**, 89, 31.
49. Gh. Tomoaia, O. Horovitz, A. Mocanu, A. Nita, A. Avram, C.P. Racz, O. Soritau, M. Cenariu, M. Tomoaia-Cotisel, *Colloids and Surfaces B: Biointerfaces*, **2015**, 135, 726
50. R.D. Pasca, G. Tomoaia, A. Mocanu, I. Petean, G.A. Paltinean, O. Soritau, M. Tomoaia-Cotisel, *Studia Univ. Babeş-Bolyai, Chemia*, **2015**, 60(3), 257.
51. G. Tomoaia, A. Mocanu, L.D. Bobos, L.B. Pop, O. Horovitz, M. Tomoaia-Cotisel, *Studia Univ. Babeş-Bolyai, Chemia*, **2015**, 60 (3), 265.
52. O. Horovitz, Gh. Tomoaia, A. Mocanu, T. Yupsanis, M. Tomoaia-Cotisel, *Gold Bulletin*, **2007**, 40 (4), 295.
53. M. Tomoaia-Cotisel, A. Tomoaia-Cotisel, T. Yupsanis, Gh. Tomoaia, I. Balea, A. Mocanu, Cs. Racz, *Revue Roumaine de Chimie*, **2006**, 51 (12), 1181.

THE INFLUENCE OF AZA-SUBSTITUTION ON THE AROMATICITY OF SUMANENE

MIHAI MEDELEANU^a, RALUCA POP^{b*}, MIHAIELA ANDONI^b,
MIRCEA V. DIUDEA^{c*}

ABSTRACT. The influence of aza-substitution on sumanene and C₅₂ fullerene was investigated. Various substitution patterns, derived for the structures of pyrrole, indolizine and pyridine have been proposed and aromaticity indices like HOMA, NICS, delocalization indices PDI and FLU were considered, at B3LYP/6-311+G(d) level of theory. The results outlined an enhanced aromatic character for the sumanene derivatives where similar aza-substitution patterns as encountered in pyrrole and indolizine have been considered.

Keywords: *sumanene, fullerene, aromaticity, aza-substitution*

INTRODUCTION

During the last decades, specific properties of fullerenes – mainly due to their extended π electron system – attracted a continuous interest of scientists, as well as for their possible precursors. The presence of one (or more) isovalent atoms like nitrogen may modify the extended π electron system. Literature survey outlines a number of studies regarding the effects of heteroatoms doping the carbon-based nanomaterials. This way, researches regarding the curvature evolution and cross-linkage in carbon nitride have demonstrated that incorporation of N atom determines an increased reactivity of the C atoms in the vicinity of heteroatom, the most stable isomer being the one containing one N atom per pentagon [1]. Investigations of the structure

^a University POLITEHNICA Timisoara, Faculty of Industrial Chemistry and Environmental Engineering, 300006 Timisoara, Romania

^b University of Medicine and Pharmacy “Victor Babeş” Timisoara, Faculty of Pharmacy, Eftimie Murgu Square 2, 300041 Timișoara, Romania

^c Department of Chemistry, Faculty of Chemistry and Chemical Engineering, Babes-Bolyai University, 400028 Cluj, Romania

*Corresponding authors: pop.raluca@umft.ro; diudea@gmail.com

and stability of heteroannulated [8-10] circulenes with N, P and As atoms have proved the influence of steric factors and heteroatom electronegativity on the π electron delocalization [2]. Also, a study, regarding the effects of N doping on the electronic properties of a small carbon chain with distinct sp^2 termination, showed that incorporation of a nitrogen atom influences the conformation, charge distribution and the spin states of structures consisting in corannulene/ coronene-like pieces connected by atomic chains [3]. Another theoretical investigation of nitrogen disubstituted corannulenes suggested an increased stability for the isomer containing two N atoms within the benzene ring, in para position [4].

Concerning the properties of doped fullerenes, their electronic behavior was reported in [5]; then properties of $C_{59}X$ -type fullerenes (where $X = B, N, Al, Si, P, Ga, Ge$ and As) [6], applications of N-doped carbon nanotubes [7], electron delocalization and dimerization in solid $C_{59}N$ doped C_{60} fullerene [8], structure and electronic properties of heterofullerene $C_{30}B_{15}N_{15}$ [9], stability of boron nitride fullerenes [10], also small fullerenes doped with boron and nitrogen [11] have been reported. Possible isomers of heterofullerenes of the type X_nC_{20-n} ($X = B, N, P$ and $n = 2, 4, 5, 6, 10$) were also studied [12]. The stability of compounds is directly related to the number and type of heteroatoms, as well as to the substitution pattern, the N- and P- doped fullerenes being thermodynamically favoured in comparison to their boron analogues [16]. In another study [13], various isomers of N-doped fullerenes of the type $C_{42}N_{18}$ and $C_{40}N_{20}$ have been investigated, including structures with separated N atoms and nitrogen belts. The results outlined a reasonable stability for the compounds with a belt of N atoms, with possible applications in molecular electronics [13].

Researches regarding the influence of hetero-substitution of carbon-based nanomaterials have also been extended to graphenes and nanotubes; properties like magnetism and mobility [14], sensing applications [15], electronic and optical properties [16] have been studied.

Our previous studies dealt with the investigation of aromaticity of fullerenes and their precursors [17-18], as well as of their N- and P-substituted analogues [19-22]. A comparison between the calculated properties of both fullerenes and circulene-type precursors was made.

DATA SET

The present paper is focused on the influence of aza-substitution on both sumanene and C_{52} derivatives, containing a sumanene patch. Three substitution patterns, derived from the structures of pyrrole, indolizine and pyridine, are proposed.

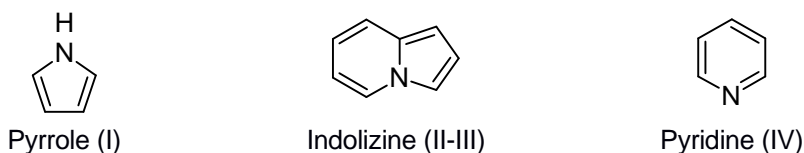


Figure 1. Substitution patterns: I – pyrrole type; II and III – indolizine type; IV – pyridine type

The structures of investigated sumanene and its aza-derivatives are depicted in Figure 2; the same pattern has been employed for the design of aza-fullerenes $C_{49}N_3$:

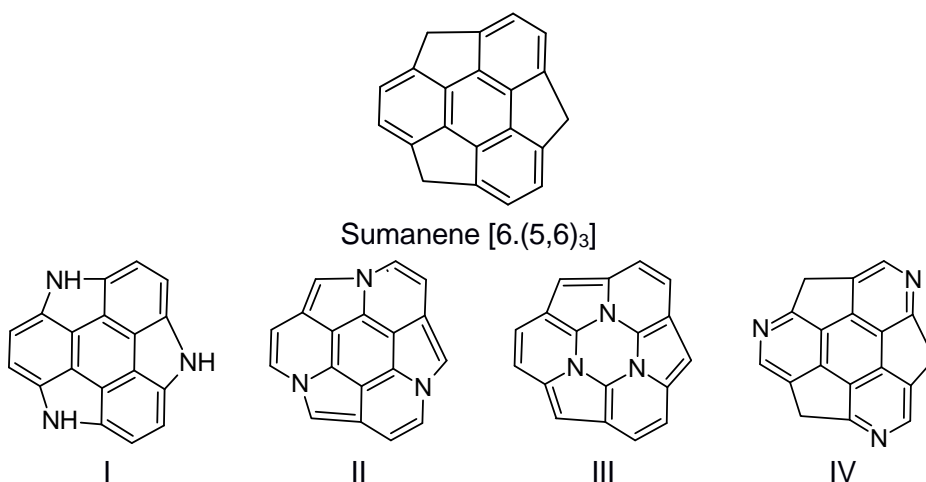


Figure 2. Aza-substitution patterns used throughout the study

Observe the two different indolizine-type patterns: II – with the N atom placed “outer” of the pentagon-hexagon pair, and III - with the N atom in “inner” position. While the all-Carbon structure II is bowl-shaped, the presence of N atoms leads to a planar geometry. Geometry optimization and vibrational analysis showed that structures I, III and IV are true minima, but the compound II is a transition state (with an imaginary frequency).

RESULTS AND DISCUSSION

Various local aromaticity descriptors, like the geometric index HOMA, magnetic index NICS, reactivity descriptors (condensed Fukui functions), and cohesion energy have been computed.

1. Geometric index

The optimized structures of the investigated aza-sumanene derivatives are shown in Figure 3. Values of the convex angle for the sumanene and its four aza-derivatives are listed in Table 1.

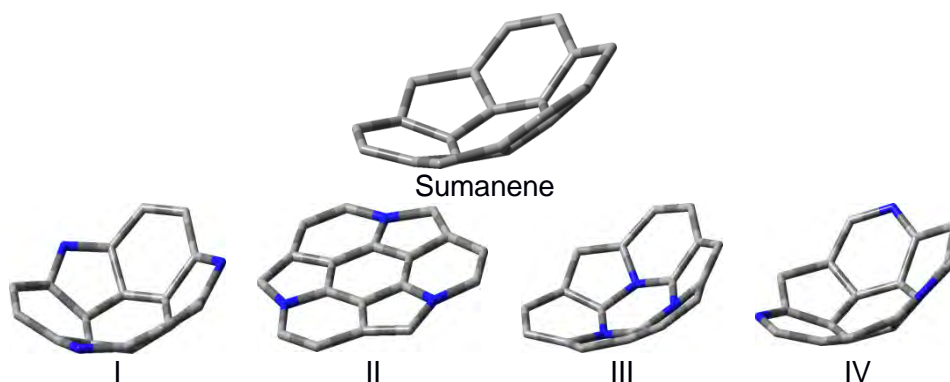


Figure 3. Optimized geometries (B3LYP/6-311+G(d)) of sumanene and its aza-derivatives

Table 1. Values of the convex angle in the bowl-shaped sumanene derivatives

Structure	Convex angle
All C	152.8
I	146.7
II	0.0
III	151.3
IV	145.1

Table 2. HOMA index computed for the core and 5- and 6-membered rings

HOMA	Sumanene	I-aza	II-aza	III-aza	IV-aza
core	0.703	0.853	0.728	0.953	0.738
6- ring	0.862	0.898	0.068	0.364	0.784
5- ring	0.472	0.800	0.354	0.588	0.624

The following observations can be made:

- I-type aza-substitution leads to an improvement of the HOMA index value (compared to the bare sumanene); the most significant difference appears for the 5-membered ring, when the substitution of sp^3 C atom with N leads to a bond shortening from 1.562 Å to 1.420 Å;

- II-type aza substitution is characterized by lower values of the HOMA index for the outer rings, due to the planar conformation;
- III-type substitution: the alternation carbon-nitrogen in the core ring results in the highest value of the HOMA index;
- IV-type substitution shows the smallest differences compared to the reference sumanene molecule.
- The main stabilization seems to appear at the ring bearing N atom and it is higher at the core hexagonal ring (in I-aza and III-aza substitution).

2. Magnetic index

Data on nucleus independent carbon shift NICS are listed in Table 3.

Table 3. NICS(0) values computed for the core and petals of sumanene and aza-sumanenes (B3LYP/6-311+G(d))

Position	Sumanene	I-aza	II-aza	III-aza	IV-aza
core	-3.01	1.05	-8.10	15.39	-3.64
6-ring	-9.03	-11.96	-3.34	0.81	-8.15
	-9.11	-11.96	-3.55	0.90	-8.10
	-9.18	-12.29	-3.34	0.84	-8.08
5- rings	2.47	-8.60	-15.99	-10.74	1.88
	2.41	-8.87	-15.87	-11.00	1.84
	2.47	-8.78	-15.89	-10.87	1.84

The results are in good agreement with the predictions of the geometric index HOMA; this way, similar values have been obtained for the bare sumanene and for the IV-aza substitution (that proves the small influence of replacing by nitrogen one C atom from outer 6-membered rings). The presence of N atom in the 5-membered rings (similar to pyrrole) leads to their "aromatization" (see the negative NICS values). The negative values of NICS index obtained for all the rings of II-type aza-sumanene can be attributed to the stronger electron delocalization, favoured by the planar structure. Again, there are small differences between sumanene and IV-type aza-substitution.

3. Delocalization indices

Smallest values of the FLU index (highest aromaticity) have been obtained for the petal 6-ring of sumanene and IV-type aza-sumanene, proving again the similarity of these two molecules. The presence of N atom within the 5-membered ring of I-, II- and III-aza-sumanenes promotes an increase in their aromaticity.

A lower local aromaticity has been obtained for the 6-membered rings of III-aza-sumanene, result that is in good agreement with NICS(0) values. Concerning the calculated PDI values for the 6-membered rings, closer results to the standard PDI for benzene, 0.105, have been obtained for the 6-outer cycles of sumanene and IV-aza-sumanene. Lowest PDI values are attributed to the 6-core of I- and III-aza-sumanenes and correlate well with FLU and NICS(0) results.

Graphical representation of the Electron Localization Function is shown in Appendix (Figure A1); it outlines the similarity between the structures of sumanene and the aza-derivative IV, as well as the differences among the planar structure of aza-sumanene II and the other bowl-shaped compounds.

Table 4. FLU and PDI results for sumanene and its aza-derivatives

Compound	Cycles	FLU	PDI
Sumanene	core	0.034	0.030
	6-ring	0.008	0.082
	5-ring	0.054	-
I-aza-sumanene	core	0.032	0.029
	6-ring	0.012	0.068
	5-ring	0.039	-
II-aza-sumanene	core	0.021	0.046
	6-ring	0.034	0.041
	5-ring	0.033	-
III-aza-sumanene	core	0.059	0.015
	6-ring	0.039	0.041
	5-ring	0.030	-
IV-aza-sumanene	core	0.034	0.030
	6-ring	0.009	0.082
	5-ring	0.057	-

4. Reactivity indices

In order to investigate the effect of N incorporation on the reactivity of carbon atoms, the condensed Fukui functions (for an electrophilic attack) have been computed (numbering of atoms in the aza-patches is shown in Figure 4).

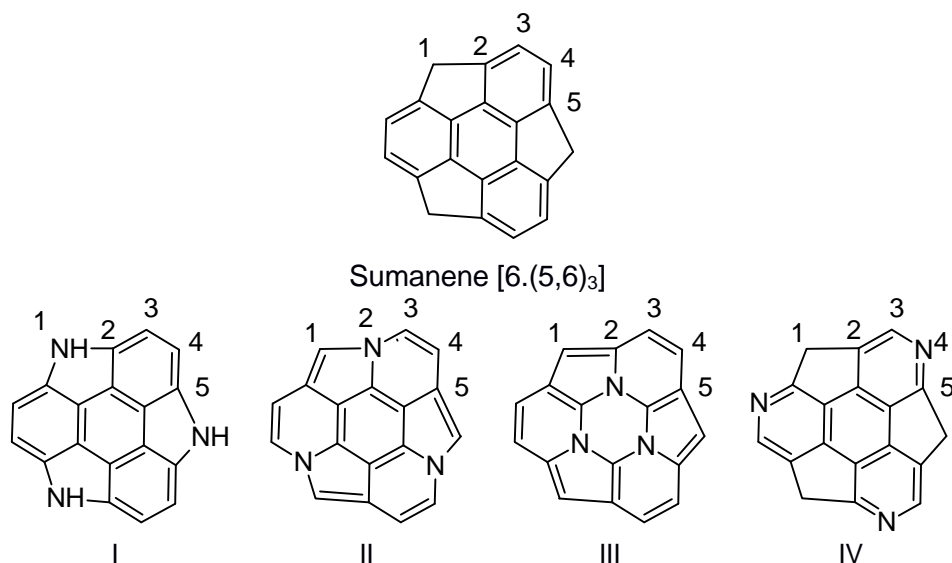


Figure 4. Atom numbering of sumanene and aza-sumanene moieties

The results, listed in Table 5, show an increased reactivity only for the C atoms from structure III, less significant results being obtained for the compounds where the N atom is placed in “outer” rings.

Table 5. Condensed Fukui functions computed for an electrophilic attack

f^- (HOMO)	Sumanene	I-aza	II-aza	III-aza	IV-aza
1	0.370	-	0.078	0.272	0.066
2	0.174	0.078	0.003	0.227	0.094
3	0.182	0.106	0.010	0.055	0.060
4	0.054	0.127	0.002	0.215	-
5	0.149	0.184	-	0.431	0.053

5. Global parameters of the investigated fullerenes: HOMO-LUMO gap, singlet-triplet gap and cohesive energy.

Keeping in mind the above-mentioned aza-patches, the structures including these patches in the molecule of C_{52} fullerene (isomer with four joint sumanene patches, D2 symmetry), namely aza-fullerenes $C_{49}N_3$ have been designed.

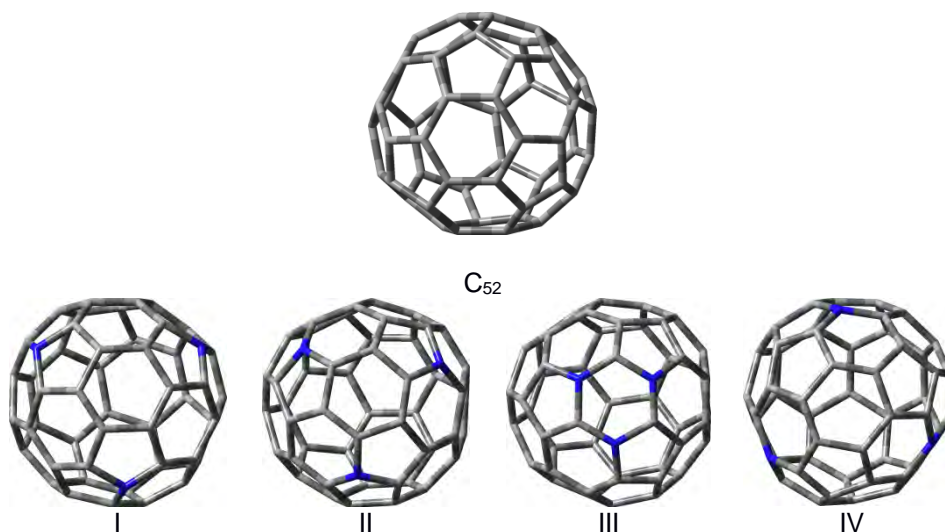


Figure 5. Optimized geometry (B3LYP/6-311G) of C_{52} and $C_{49}N_3$ fullerenes

Computation of global parameter HOMO-LUMO gap for both sumanene and C_{52} derivatives has shown that, the III-aza substitution leads to the less stable compounds (Table 6). The trend within the sumanene series follows the results of magnetic and geometric indices, which outlined the similarities between the all-carbon compound and the IV-aza substitution.

Table 6. HOMO-LUMO gap of sumanene and C_{52} , and of their aza-derivatives

HL gap (eV)	Sumanene	C_{52}
All carbon	4.63	1.09
I	3.94	0.89
II	3.62	0.89
III	3.47	0.62
IV	4.63	0.91

Regarding the C_{52} derivatives, smaller difference appear among C_{52} and $C_{49}N_3$ characterized by I-, II- and IV-aza-substitution.

Computation of the singlet-triplet ST gap, another important parameter for characterizing nanomaterials, shown a significant decrease for the N-substituted fullerenes and especially for the III $C_{49}N_3$ (Table 7).

Table 7. ST gap of C₅₂ and C₄₉N₃ compounds (B3LYP/6-311+G(d))

Compound	ST gap (eV)
C ₅₂	0.257
C ₄₉ N ₃ (I)	0.049
C ₄₉ N ₃ (II)	0.060
C ₄₉ N ₃ (III)	0.008
C ₄₉ N ₃ (IV)	0.061

Another parameter that is widely used for characterizing the stability of nanomaterials, like fullerenes, is the cohesive energy, calculated according to the equation:

$$E_{\text{coh (at)}} = -(E_{\text{total}} - n_{\text{C}}E_{\text{C}} - n_{\text{N}}E_{\text{N}})/(n_{\text{C}} + n_{\text{N}})$$

The results listed in Table 8 suggest no differences among the four types of aza-substitution herein proposed; however, with respect to the homo-sumanene, the aza-substitution seems to decrease the cohesive energy.

Table 8. Cohesive energy computed for C₅₂ and C₄₉N₃ fullerenes

Compound	E _{coh} (a.u.)
C ₅₂	0.307
C ₄₉ N ₃ (I)	0.282
C ₄₉ N ₃ (II)	0.282
C ₄₉ N ₃ (III)	0.280
C ₄₉ N ₃ (IV)	0.280

6. Properties of aza-fullerenes C₄₉N₃: polarizability, hyperpolarizability, magnetizability and dipole moment

Properties like polarizability and hyperpolarizability, magnetizability and the dipole moment, playing an important role in the behaviour of nanomaterials, are significantly influenced by the four types of aza-substitution (Table 9).

Table 9. Polarizability, hyperpolarizability magnetizability and dipole moment of the aza-fullerenes (BLYP/TZ2P)

Compound	Polarizability (a.u.)	Hyperpolarizability (a.u.)	Magnetizability (a.u.)	Dipole moment
C ₄₉ N ₃ (I)	459.19	563.39	-191.26	0.579
C ₄₉ N ₃ (II)	465.18	546.07	-211.26	1.307
C ₄₉ N ₃ (III)	472.25	674.61	-250.99	2.112
C ₄₉ N ₃ (IV)	469.64	521.93	-209.82	1.465

Also, two types of atomic charges, namely CM5 and the Voronoi Density Deformation (VDD) charges, have been computed. The atomic charges CM5 [33] (Charge Model 5) show an increased accuracy in predicting the dipole moment and are based on the Hirshfeld analysis combined with a parametrization method. The VDD method [34, 35] relies on the dividing of space into non-overlapping atomic areas and the consequent calculation of the deformation density of these cells. Figure A2 (see Appendix) depicts only the charge values of the nitrogen atoms.

CONCLUSIONS

The influence of aza-substitution in sumanene and C_{52} fullerene on their stability/aromaticity was investigated; a bowl-shaped polycyclic aromatic hydrocarbon, four aza-substitution types derived from the structures of pyrrole, indolizine and pyridine have been considered. Structures of aza-fullerenes $C_{49}N_3$, where the aza-substitution follows the same pattern as in case of sumanene, have been optimized and a series of global parameters were computed for their characterization. Calculation of the local aromaticity indices like NICS and HOMA, as well as delocalization indices PDI and FLU outlined the enhanced aromatic character of sumanene derivatives where the 5-membered ring was replaced by a pyrrole moiety (I-aza-substitution type). Also, an increase of the aromaticity has been obtained for the II-aza-sumanene, where the outer 5- and 6-membered rings have a common nitrogen atom at the outer junction (similar to the indolizine ring). No significant variations of aromaticity (compared to the values obtained for the all-carbon sumanene) have been obtained for the structure IV (where the aza-substitution occurs as in the pyridine moiety).

The proposed structures of fullerenes $C_{49}N_3$ were characterized by smaller HL gap and singlet-triplet gap for the III- $C_{49}N_3$ structure, while the computations of cohesive energy lead to similar values for all the four investigated fullerenes. As an overall conclusion, the III-aza patch seems to induce the most reactivity among all the studied aza-containing structures.

COMPUTATIONAL DETAILS

All the computations regarding the sumanene and its derivatives have been carried out at B3LYP/6-311+G(d) level of theory. Geometry optimization and vibrational analysis of the fullerene C_{52} and the corresponding aza-derivatives have been performed by using the basis set 6-311G. The obtained

structures were refined by performing a single point computation at B3LYP/6-311+G(d) level of theory. The calculations of the magnetic index, reactivity descriptors, and delocalization indices were performed by means of the same combination B3LYP/6-311+G(d). The delocalization indices were computed with Multiwfn_3.3.4 software [23], while Gaussian 09W [24] has been employed for the computations of sumanene and its aza-derivatives, as well as for the geometry optimizations of the C₅₂ and C₄₉N₃. ADF2014 software [25-27] has been employed for the calculation of polarizability [28,29], hyperpolarizability [30,31], magnetizability [32] and dipole moment. Also, the atomic charges CM5 [33] and VDD [34,35] have been computed by means of ADF2014. For the computations performed with the ADF2014 software, the combination of BLYP with basis set TZ2P [36] has been used.

REFERENCES

1. G.K. Gueorguiev, J. Neidhardt, S. Stafstrom, L. Hultman, *Chemical Physics Letters.*, **2005**, *410*, 228.
2. T. N. Gribanova, N.S. Zefirov, V. I. Minkin, *Pure and Applied Chemistry.*, **2010**, *82(4)*, 1011.
3. R.B. dos Santos, R. Rivelino, F. de Brito Mota, G.K. Gueorguiev, *Physical Review B*, **2011**, *84*, 075417.
4. P.A. Denis, *Journal of Molecular Structure: THEOCHEM*, **2008**, *865*, 8.
5. L. Forro, L. Mihaly, *Reports on Progress in Physics*, **2001**, *64*, 649.
6. H. Bai, W. Ji, X. Liu, L. Wang, N. Yuan, Y. Ji, *Journal of Chemistry*, **2013**, 571709.
7. P. Ayala, R. Arenal, M. Rummeli, A. Rubio, T. Pichler, *Carbon*, **2010**, *48*, 575.
8. A. Rockenbauer, G. Csany, F. Fulop, S. Garaj, L. Korecz, R. Lukacs, F. Simon, L. Forro, S. Pekker, A. Janossy, *Physical Review Letters*, **2005**, *94*, 066603.
9. S. Erkoc, *Journal of Molecular Structure: THEOCHEM*, **2004**, *684*, 117.
10. R.J.C. Batista, M.S.C. Mazzoni, H. Chacham, *Chemical Physics Letters*, **2006**, *421*, 246.
11. L. Viani, M. C. dos Santos, *Solid State Communications*. **2006**, *138*, 498.
12. M.Z. Kassae, F. Buazar, M. Koochi, *Journal of Molecular Structure: THEOCHEM*, **2010**, *940*, 19.
13. A.-R. Nekoei, S. Haghgoo, *Computational and Theoretical Chemistry*, **2015**, *1067*, 148.
14. Y. Ma, A.S. Foster, A.V. Krashennnikov, R.M. Nieminen, *Physical Review B*, **2005**, *72*, 205416.
15. K.P. Prathish, M.M. Barsan, D. Geng, X. Sun, C.M.A. Brett, *Electrochimica Acta*, **2013**, *114*, 533.
16. P. Nath, S. Chowdhury, D. Sanyal, D. Jana, *Carbon*, **2014**, *73*, 275.
17. R. Pop, M. Medeleanu, M.V. Diudea, B. Szeffler, J. Cioslowski, *Central European Journal of Chemistry*, **2014**, *12(1)*, 90.
18. R. Pop, M. Medeleanu, M.V. Diudea, B. Szeffler, J. Cioslowski, *Central European Journal of Chemistry*, **2013**, *11(4)*, 527.

19. R. Pop, M. Andoni, Iulia Pausescu, Mihai Medeleanu, *Revista de Chimie*, **2013**, 64(9), 942.
20. R. Pop, J. Van Staden, M. Diudea, *Z. Naturforschung A*, **2015**, 70(3), 171.
21. R. Pop, M. Diudea, M. Medeleanu, M. Andoni, *Studia Universitatis Babeş-Bolyai Chemia*, **2015**, 60(1), 195.
22. R. Pop, M. Andoni, J. Van Staden, I. Păușescu, M. Medeleanu, *Digest Journal of Nanomaterials and Biostructures*, **2013**, 8(4), 1739.
23. T. Lu, F.J. Chen, *Journal of Computational Chemistry*, **2012**, 33, 580.
24. Gaussian 09, Revision B.01, M.J. Frisch, G.W. Trucks, H.B. Schlegel, G.E. Scuseria, M.A. Robb, J.R. Cheeseman, G. Scalmani, V. Barone, B. Mennucci, G.A. Petersson, H. Nakatsuji, M. Caricato, X. Li, H.P. Hratchian, A.F. Izmaylov, J. Bloino, G. Zheng, J.L. Sonnenberg, M. Hada, M. Ehara, K. Toyota, R. Fukuda, J. Hasegawa, M. Ishida, T. Nakajima, Y. Honda, O. Kitao, H. Nakai, T. Vreven, J.A. Montgomery, Jr., J.E. Peralta, F. Ogliaro, M. Bearpark, J.J. Heyd, E. Brothers, K.N. Kudin, V.N. Staroverov, T. Keith, R. Kobayashi, J. Normand, K. Raghavachari, A. Rendell, J.C. Burant, S.S. Iyengar, J. Tomasi, M. Cossi, N. Rega, J.M. Millam, M. Klene, J.E. Knox, J.B. Cross, V. Bakken, C. Adamo, J. Jaramillo, R. Gomperts, R.E. Stratmann, O. Yazyev, A.J. Austin, R. Cammi, C. Pomelli, J.W. Ochterski, R.L. Martin, K. Morokuma, V.G. Zakrzewski, G.A. Voth, P. Salvador, J.J. Dannenberg, S. Dapprich, A.D. Daniels, O. Farkas, J.B. Foresman, J.V. Ortiz, J. Cioslowski, and D.J. Fox, Gaussian, Inc., Wallingford CT, 2010.
25. G. Te Velde, F.M. Bickelhaupt, E.J. Baerends, C. Fonseca Guerra, S.J.A. van Gisbergen, J.G. Snijders and T. Ziegler, *Journal of Computational Chemistry*, **2001**, 22, 931.
26. C. Fonseca Guerra, J.G. Snijders, G. Te Velde, E.J. Baerends, *Theoretical Chemistry Accounts*, **1998**, 99, 391.
27. ADF2014, SCM, Theoretical Chemistry, Vrije Universiteit, Amsterdam, The Netherlands, <http://www.scm.com>.
28. S.J.A. van Gisbergen, J.G. Snijders, E.J. Baerends, *Journal of Chemical Physics*, **1995**, 103, 9347.
29. S.J.A. van Gisbergen, J.G. Snijders, E.J. Baerends, *Computer Physics Communications*, **1999**, 118, 119.
30. S.J.A. van Gisbergen, J.G. Snijders, E.J. Baerends, *Journal of Chemical Physics*, **1998**, 109, 10644.
31. S.J.A. van Gisbergen, J.G. Snijders, E.J. Baerends, *Physical Review Letters*, **1997**, 78, 3097.
32. M. Krykunov, J. Autschbach, *Journal of Chemical Physics*, **2007**, 126, 24101.
33. A.V. Marenich, S.V. Jerome, C.J. Cramer, D.G. Truhlar, *Journal of Chemical Theory and Computation*, **2012**, 8, 527.
34. G. Te Velde, Numerical integration and other methodological aspects of band structure calculations, in Chemistry. 1990, Vrije Universiteit: Amsterdam.
35. C. Fonseca Guerra, J.-W. Handgraaf, E. J. Baerends, F. M. Bickelhaupt, *Journal of Computational Chemistry*, **2004**, 25, 189.
36. E. van Lenthe, E.J. Baerends, *Journal of Computational Chemistry*, **2003**, 24, 1142.

APPENDIX

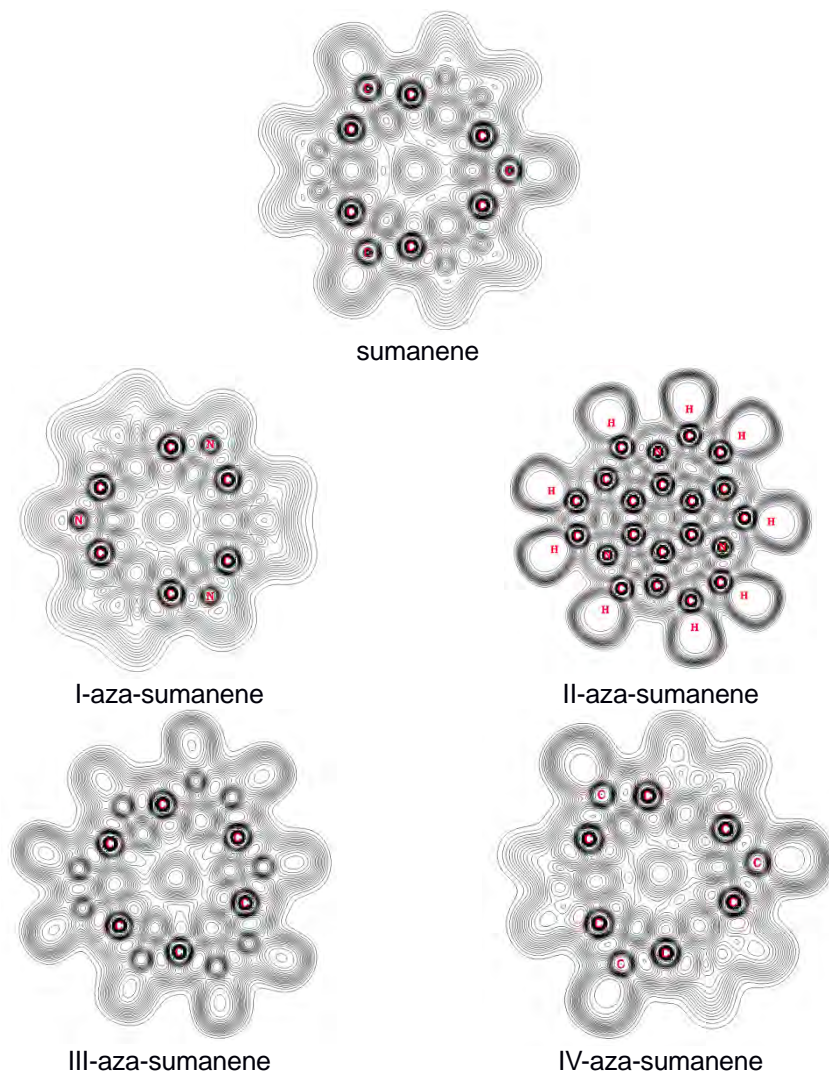
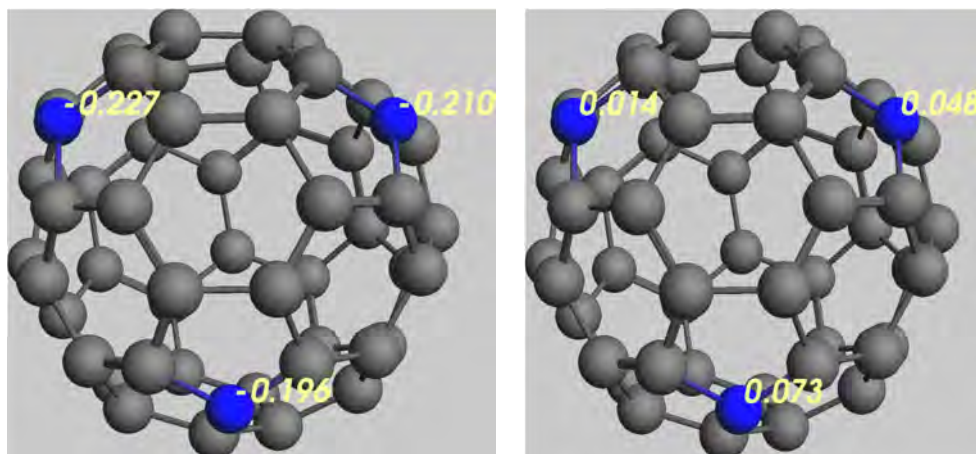
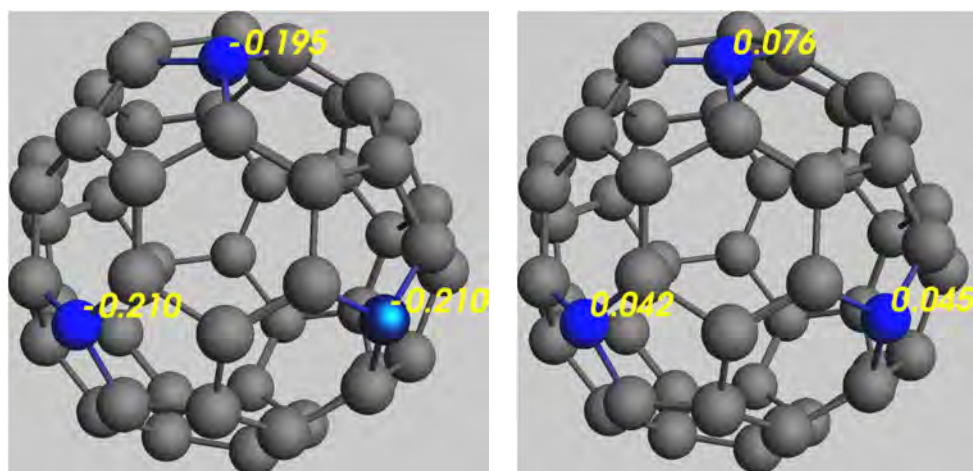


Figure A1. ELF (Electron Localization Function) computed for sumanene and the four aza-derivatives



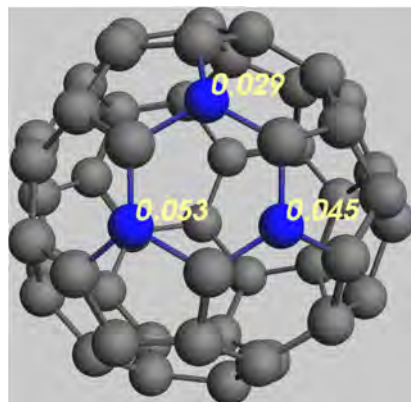
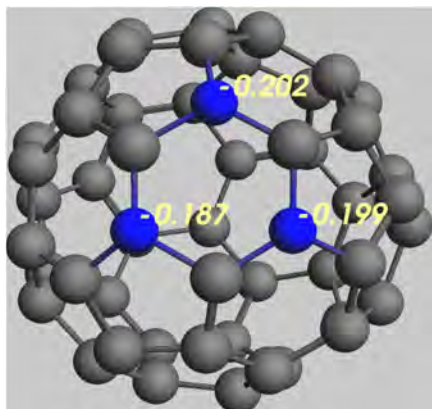
Atomic charges CM5 (left) and VDD (right) computed for C₄₉N₃ (I)



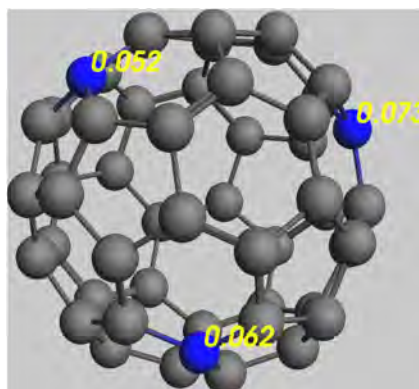
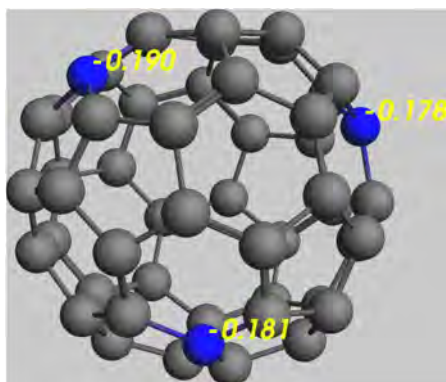
Atomic charges CM5 (left) and VDD (right) computed for C₄₉N₃ (II)

Figure A2. CM5 atomic charges of the aza-fullerenes

THE INFLUENCE OF AZA-SUBSTITUTION ON THE AROMATICITY OF SUMANENE



Atomic charges CM5 (left) and VDD (right) computed for C₄₉N₃ (III)



Atomic charges CM5 (left) and VDD (right) computed for C₄₉N₃ (IV)

Figure A2 (continued). CM5 atomic charges of the aza-fullerenes

ELECTROCHEMICAL OXIDATION OF 10H-PHENOTHIAZINE-1-CARBOXYLIC ACID

ANA-MARIA SĂCARĂ^a, CASTELIA CRISTEA^a, TAMAS LOVASZ^a,
DAN PORUMB^a, EVA MOLNAR^a and LIANA MARIA MURESAN^{a*}

ABSTRACT. The electrochemical behavior of 10H-phenothiazine-1-carboxylic acid was investigated by square wave anodic stripping voltammetry (SWASV) at a glassy carbon electrode, which evidenced the first monoelectronic oxidation step at low potentials (around 0.25 V), slightly modulated by the nature of the solvent. The effect of three different solvents (acetonitrile, dimethyl sulfoxide and chloroform) on the strength of intramolecular hydrogen bonding associations was evidenced by DFT calculations. The computed electron density at the heterocyclic nitrogen atom appeared well correlated to the recorded oxidation potential. The possibility to use of 10H-phenothiazine-1-carboxylic acid as potential mediator for electrochemical detection of Malachite Green was explored, but the phenothiazine derivative appeared not suitable for the detection of the dye.

Keywords: 10H-phenothiazine-1-carboxylic acid, SWASV, intramolecular hydrogen bonds

INTRODUCTION

A significant characteristic of phenothiazine derivatives appeared to be their ability to readily generate various oxidation products under chemical, photochemical, enzymatic, or electrochemical conditions. The redox properties of several phenothiazine derivatives with important medicinal applications were largely exploited in analytical procedures tailored for the advanced detection of phenothiazine based neuroleptic drugs [1,2]. The electrochemical oxidation of phenothiazine and its derivatives proceeds on conventional

^a Babeş-Bolyai University, Faculty of Chemistry and Chemical Engineering, 11 Arany Janos str., RO-400028, Cluj-Napoca, Romania

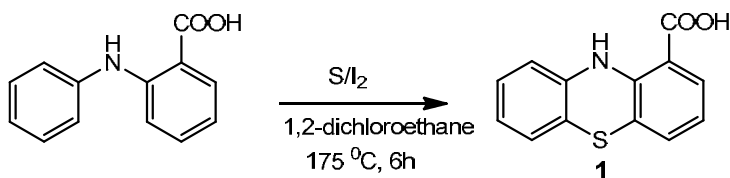
* Corresponding author: limur@chem.ubbcluj.ro

electrodes (Pt, glassy carbon electrode and Au) either in organic or in aqueous acidic medium. The oxidation of the phenothiazine core takes place by the intermediate stage of radical cation with a stability influenced by the nature and position of the substituents on the heterocyclic core, the acidity and the presence of various salts in the reaction medium. Further oxidation steps imply the formation of the phenothiazinium cation which usually generates a colorless phenothiazine sulfoxide, colored hydroxy-substituted or polymeric derivatives [3]. Based on the reversibility of its first monoelectronic redox process, phenothiazine was described to be an efficient mediator in various electrochemical oxidation processes. For instance, it displayed excellent electrochemical catalytic activities for oxidase enzymes (glucose, lactate and cholesterol oxidase) even when immobilised on the surface of the electrode [4,5] and enzyme glucose dehydrogenase [6]. Several phenothiazine derivatives, were studied as electron transfer mediators in different electrochemical systems [7,8]. On the other hand, a series of 1-carboxyphenothiazine derivatives was synthesized and characterized [9], but there are no reported evidences for their utility as mediators for electrochemical systems.

Considering our previous interest in the electrochemical detection of Malachite Green (MG) [10], the aim of this work was to explore the electrochemical reactivity of 10*H*-phenothiazine-1-carboxylic acid and its potential as mediator for the electrochemical detection of the dye. Based on the electrostatic attraction between a carboxy functionality attached to the phenothiazine core and the positively charged MG cationic dye, it was expected that the diffusion/adsorption of the dye to a carboxyphenothiazine modified electrode surface would be facilitated.

RESULTS AND DISCUSSION

10*H*-Phenothiazine-1-carboxylic acid **1** was synthesized by optimizing a previously reported synthetic protocol [9] based on the thiation of *N*-phenyl-antranilic acid (scheme 1).



Scheme 1

The structure of **1** was confirmed by spectroscopic methods. ¹H-NMR spectrum of **1** displayed a deshielded signal characteristic to the acidic proton situated at 10.15 ppm, accompanied by the signals of aromatic protons situated in the region 6.7-7.6 ppm.

The position of the carboxyl group in the neighborhood of the heterocyclic NH group favors the formation of intramolecular hydrogen bonds. Density functional theory (DFT) calculations were applied to emphasize the possible intramolecular hydrogen bond formation. Thus, the structure of **1** was initially optimized using Spartan 06 with DFT B3LYP 6-31 G* method in gas phase. Free rotation of the carboxyl substituent generated two conformers of **1** with computed minimal energy which are presented in Figure 1. Conformer **1a** is characterized by hydrogen bond interaction between heterocyclic NH and carboxyl substituent, while conformer **1b** does not contain a hydrogen bond.

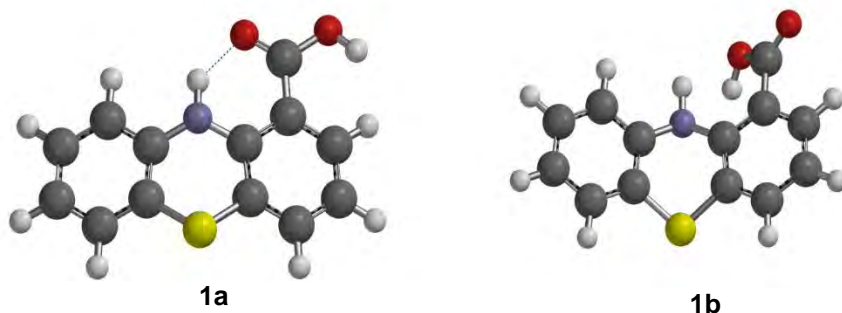


Figure 1. Conformers of 10*H*-phenothiazine-1-carboxylic acid **1** with optimized geometry

Due to the fact that solvents may influence the hydrogen bonding [11], conformer **1a** has been optimized by B3LYP/6-31++G(d,p) Gaussian method using three data sets for the following solvents: acetonitrile, chloroform and DMSO. The results are illustrated in Table 1.

As it may be seen from table 1, **1a** appears to be more stable than **1b** (molecular energy difference 5.25 kcal/mole in gas phase) and the interactions with the aprotic dipolar solvents suggested further stabilization effects upon **1a**.

Square wave anodic stripping voltammetry experiments were performed in order to explore the electrochemical reactivity of 10*H*-phenothiazine-1-carboxylic acid dissolved in three different solvents and deposited on the surface of a glassy carbon electrode. The voltammograms presented in Figure 2 are showing well defined oxidation peaks corresponding to phenothiazine radical cationic species.

Table 1. Gaussian B3LYP/6-31++G(d,p) computational results for 10*H*-phenothiazine-1-carboxylic acid: optimized geometry, molecular energy (E) and electrostatic charge on heterocyclic nitrogen atom in gas phase and different solvents

Conformer	Environment	E (kcal/mol)	Electrostatic charge on N atom
1b	Vacuum	-692898.748	-0.709
1a	Vacuum	-692904.000	-0.630
	Acetonitrile	-693049.921	0.126
	Chloroform	-693047.637	0.132
	DMSO	-693050.015	0.125

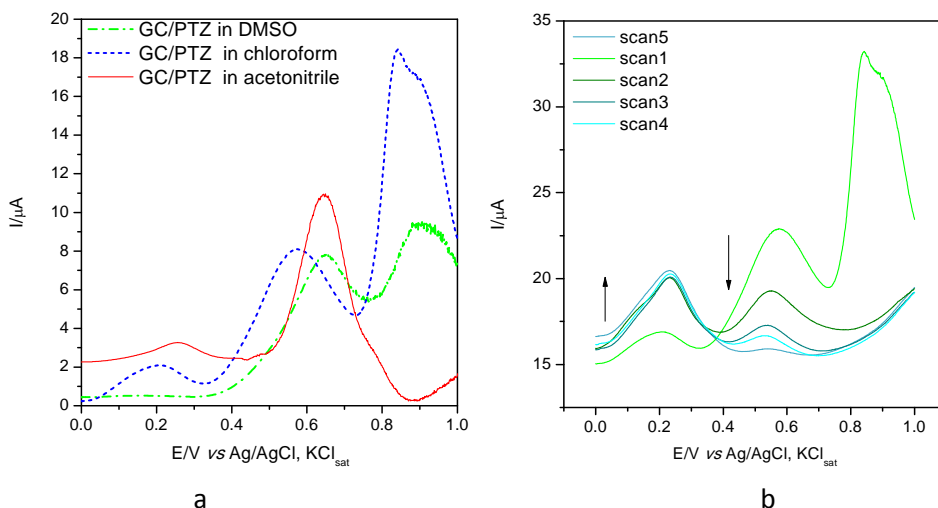
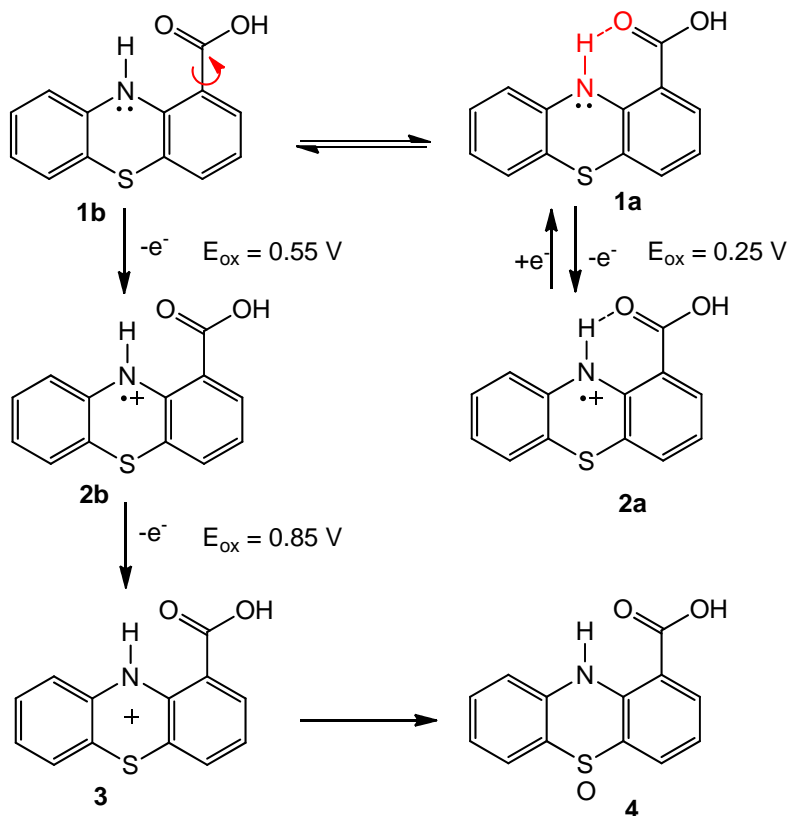


Figure 2. SWASV at glassy carbon (GC) electrodes modified with 10*H*-phenothiazine-1-carboxylic acid (PTZ) a) in different solvents; b) several scans in acetonitrile. Experimental conditions: pH=3, accumulation time 300 s; frequency 25 Hz; potential oxidation processes interval 0-1 V.

In scheme 2 are described the oxidation steps proposed in order to assign the SWASV peaks observed in figure 2. The first monoelectronic oxidation step generates the radical cation **2** and the values of the typical potentials may be correlated to the computational results related to electron density at the heterocyclic nitrogen atom presented in table 1. The lowest oxidation potential (0.25 V) may be assigned to **1a** characterized by higher electron density as compared to **1b**, which in turn may be responsible for the oxidation peak situated at 0.55 V. Further step requires a higher oxidation potential and generates the cation **3** which may end up as a colourless sulfoxide **4**. As it may be seen in figure

2b, after several scans the intensity of the first oxidation peak increases (maybe due to the reversibility of the oxidation processes of **1a**), while the oxidation of **1b** proceeding towards the chemical reaction may explain the consumption of the radical cationic species **2b** and consequently the decrease in intensity of the second oxidation peak.



Scheme 2

A characteristic signal of the sulfoxide was recorded by $^1\text{H-NMR}$ (in deuterated acetonitrile solution) at chemical shift 11.65 ppm.

The SWASV experiments performed in the presence of MG indicated a decrease in intensity of the first oxidation peak (figure 3a), which may be correlated to steric interactions between **1** and the bulky cationic dye in control for weakening the intramolecular hydrogen bond associations. Calibration curves presented in figure 3b indicate a feeble correlation with the MG concentration and do not sustain the possibility of elaborating an analytical procedure for MG detection.

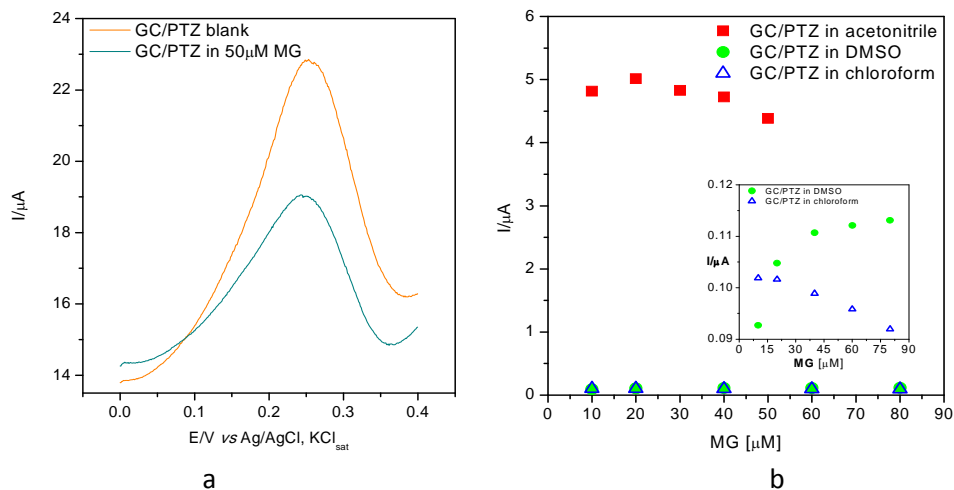


Figure 3. SWASV at GC/10H-phenothiazine-1-carboxylic acid (PTZ) electrodes: a) in the presence of malachite green (MG). b) Calibration curves obtained for increasing amounts of MG. Experimental conditions: accumulation time 300 s; frequency 25 Hz; potential interval 0-0.4 V; electrolyte phosphate buffer (pH 3).

CONCLUSIONS

The oxidation potential of 10H-phenothiazine-carboxylic acid appeared to be lowered by intramolecular hydrogen bond associations. The first mono-electronic oxidation step generating the radical cation occurred around 0.25 V, this value being slightly modulated by the nature of the solvent.

No favourable interactions between MG and 10H-phenothiazine-carboxylic acid occurred and, consequently the tested electrochemical system based on GC/10H-phenothiazine-carboxylic acid is not suitable for the detection of MG.

EXPERIMENTAL SECTION

Chemicals

All the chemicals used for the experiments in this study were of analytical grade quality and were used as received, without further purification or alteration.

Malachite Green oxalate salt was purchased from Penta, Czech Republic and all solutions were made in pH 3 phosphate buffer (PB). Phosphate buffer solution was made starting from $\text{NaH}_2\text{PO}_4 \cdot \text{H}_2\text{O}$ and Na_2HPO_4 salts and pH adjusted with $\text{o}-\text{H}_3\text{PO}_4$ acid, all from Merck, Germany.

10H-Phenothiazine-1-carboxylic acid 1 preparation

N-phenylanthranilic acid 6.4 g (0.03 mole), sulfur powder 1.92 g (0.06 mole) and iodine 0.8 g (0.006 mole) were dissolved in 60 ml 1,2-dichlorobenzene. The reaction mixture was heated at 175 °C for 6 h under constant stirring. After cooling at room temperature, 10 ml solution of sodium thiosulphate 40% was added to the reaction mixture. The organic layer was separated and the organic solvent was removed by vacuum distillation. The product was purified by column chromatography on silica gel using eluent toluene to give orange coloured 10H-phenothiazine-1-carboxylic acid (1.4 g, yield 19%). M.p. 248 °C (lit. [9])

¹H NMR(DMSO-d₆, 400 MHz, ppm): 6,88-7,04 (m, 5H, Ar-H), 7,18 (d, 1H, Ar-H), 7,65 (d, 1H, Ar-H), 9,63(s, 1H, -N-H), 10,15 (s, 1H, -COOH)

Electrode preparation

Before conducting any measurements, the glassy carbon (GC) working electrode was thoroughly cleaned on a piece of felt with γ-alumina slurry until mirror-like shine aspect was obtained. In order to remove any traces of impurities, further cleaning was applied by sonication in acetone and distilled water respectively.

For modifying the electrode, saturated 10H-phenothiazine-1-carboxylic acid solutions were prepared, in three different solvents: chloroform, acetonitrile and dimethyl-sulfoxide. Each solution was applied by drop-casting on the electrode's active surface and allowed to dry freely. In the case of DMSO solutions, a warm air current was applied to accelerate the evaporation process. Constant 5 μL volumes of solutions were employed for all electrode modification purposes. No other protective coatings were applied on the modified electrode as the evaporated phenothiazine carboxylic acid layer had a good stability during measurements in aqueous solutions.

Electrochemical measurements

All electrochemical experiments were performed on a Metrohm Autolab PGSTAT 302N, electrochemical workstation (Eco Chemie, Netherlands). A three-electrode system composed of a Ag/AgCl, KCl_{sat} reference electrode, a platinum counter-electrode and a bare or modified glassy carbon (GC) working electrode was used. The electrolyte solution contained 0.1 M phosphate buffer adjusted with o-H₃PO₄ at pH 3. All experiments were performed at a room temperature of 25 °C.

REFERENCES

1. K. Madej, P. Koscielniak, *Critical Reviews in Analytical Chemistry*, **2008**, 38 50.
2. K. Nesměrác V. Červený, J. Hraníček, P. Rychlovský, *Microchemical Journal*, **2013**, 106, 226.
3. H. Puzanowska-Tarasiewicz, L. Kuzmicka, J. Karpinska, K. Mielech-Lucasiewicz, *Analytical Sciences*, **2005**, 21, 1149.
4. A.N. Sekretaryova, M.Yu. Vagin, V. Beni, A.P.F. Turner, A.A. Karyakin, *Biosensors and Bioelectronics*, **2014**, 53, 275;
5. J. Kulysa, T. Buch-Rasmussenb, K. Bechgaard, V. Razumasa, *Journal of Molecular Catalysts*, **1994**, 91, 407.
6. T Hoshino, S. Sekiguchi, H. Muguruma, *Bioelectrochemistry*, **2012**, 84, 1.
7. B. Brunetti, P. Ugo, L.M. Moretto, C.R. Martin, *Journal of Electroanalytical Chemistry*, **2000**, 491, 166.
8. H. Dai, H. Xu, X. Wu, Y. Lin, M. Wei, G. Chen, *Talanta*, 2010, 81, 1461.
9. V.B. Kataria, M.J. Solanki, A.R. Trivedi, V.H. Shah, *Letters in Drug Design & Discovery*, **2013**, 10(10), 951.
10. A. Sacara, C. Cristea, L.M. Muresan, *Journal of Electroanalytical Chemistry*, **2017**, 792, 23.
11. J.L. Cook, C.A. Hunter, C.M.R. Low, A. Perez-Velasco, J.G. Vinter. *Angewandte Chemie International Ed.*, **2007**, 46, 3706.

CHROMATOGRAPHIC ANALYSIS OF SOME ANTIBIOTICS IN WATER AND SEDIMENT SAMPLES COLLECTED FROM THE ROMANIAN TISZA RIVER WATERSHED

VIRGINIA COMAN^{a*}, SIMION BELDEAN-GALEA^b, FLORINA COPACIU^a,
MIHAELA VLASSA^a, MIUȚA FILIP^a

ABSTRACT. Antibiotics are natural or semi-synthetic compounds used for many decades in human, veterinary and plant medicine to prevent and/or to treat bacterial infections and also to promote productivity in animal farming. Traces of antibiotics are found in waste, surface and ground waters, the main source of water pollution being considered waste waters from the industrial production, hospitals, livestock farms, households and incompletely metabolized drugs. The uncontrolled input of antibiotics in surface waters can lead to some unexpected health effects and to an increased resistance to these drugs.

The aim of this work consists in the monitoring of six antibiotics (Ampicillin, Amoxicillin, Penicillin G, Ceftazidime, Tetracycline and Doxycycline) in river waters and sediment samples from the Romanian Tisza River Watershed.

Solid-phase extraction (SPE) on Oasis HLB Waters cartridges was used for the isolation of antibiotics from water matrices and ultrasound-assisted extraction (USAE) followed by SPE for the sediment samples. Then, the antibiotics were analysed by high-performance liquid chromatography coupled with diode array detector or mass spectrometer (HPLC-DAD/MS). The developed SPE/USAE-HPLC-DAD/MS procedures were applied to monitor these antibiotics in river waters during thirteen months and to analyse them in some sediment samples. The obtained results showed the presence of Tetracycline, Doxycycline and Ceftazidime in the investigated samples.

Keywords: *antibiotics, high-performance liquid chromatography, mass spectrometry, solid-phase extraction, ultrasound-assisted extraction, river waters, sediments*

^a Babeş-Bolyai University, Raluca Ripan Institute for Research in Chemistry, 30 Fântânele str., Cluj-Napoca, Romania

^b Babeş-Bolyai University, Faculty of Environmental Science and Engineering, 30 Fântânele str., RO-400294, Cluj-Napoca, Romania

* Corresponding author: virginia.coman@ubbcluj.ro

INTRODUCTION

Antibiotics are natural or semi-synthetic compounds with antibacterial, antifungal or antiparasitical activity [1] used for preventing and treating human and animal diseases, different plant infections and also for advancing growth in livestock farms [2]. The amount of antibiotics released in the European Union environment might be approximately 15,000 tons/year. The main sources of antibiotic pollution come from the industrial production, hospitals, domestic use and their incomplete metabolism [3].

Due to the fact that antibiotics are not completely removed by the sewage treatment plants, they are released into the natural water courses [1] causing potential environmental risks and the extension of antibacterial resistance among the microorganisms [4].

Different studies showed that antibiotics are persistent and pseudo-persistent contaminants [5, 6] causing toxicological impacts on the fauna of natural water bodies [1] including synergistic and antagonistic combination effects [7].

In the aquatic matrices, the concentrations of antibiotics have values of micrograms per liter in hospital effluents and municipal waste waters, nanograms per liter in surface waters, ground water and sea water [8, 9], tens nanograms per grams in estuary and marine sediments [10, 11] and hundreds nanograms per grams in surface water sediments respectively [12, 13]. Consequently, to prevent the risks of environmental exposure, the monitoring of antibiotics that reach the environmental factors is recommended [14, 15].

Taking into consideration the low level of the antibiotic residues in the environmental matrices, the development of sensitive analytical methods for the extraction and the analysis of these compounds represents a major challenge. The most used methods for the extraction of antibiotics from water samples involve solid-phase extraction [6, 8, 9, 12, 13] and miniaturized liquid-phase or solid-phase extraction [16–18] and from sediment samples, ultrasound-assisted extraction [11, 13, 19].

For the analysis of antibiotics, liquid chromatography (LC) techniques coupled with ultraviolet/diode-array (UV/DAD) detector [9, 18], mass spectrometry (MS) detector [9, 20] or tandem MS/MS ones [5, 10–12, 20] were used. Good results have been also obtained by high-performance thin-layer chromatography [6] or capillary electrophoresis [16, 17] techniques.

The aim of this work consists in the monitoring of some classes of antibiotics (penicillins, tetracyclines, cephalosporins) widely used for the human and veterinary treatments in different river water and sediment samples collected from the Romanian Tisza River Watershed using solid-phase extraction (SPE) and ultrasound-assisted extraction (USAE) followed by liquid chromatography coupled with diode-array or mass spectrometry detector.

RESULTS AND DISCUSSION

Two analytical procedures, based on solid-phase extraction followed by high-performance liquid chromatography with diode array detector, respectively mass spectrometer (SPE-HPLC-DAD and SPE-LC-MS), have been developed for the analysis of six antibiotics (Amoxicillin – AMOX, Ceftazidime – CFZ, Ampicillin – AMP, Tetracycline – TET, Doxycycline – DOXY and Penicillin G – PEN G) in river water samples collected from the three established monitoring points in the Romanian Tisza River Watershed. For the sediment samples, the ultrasound-assisted extraction was used for the isolation of the target compounds from the matrix followed by the SPE-HPLC-DAD procedure.

The HPLC separation tooks place in less then 12 minutes with very good resolution. For the DAD detection was necessary two wavelengths, 197 nm for penicillins (AMOX, AMP, PEN G) and 272 nm for tetracyclines (TET, DOXY) and ceftazidime (CFZ) (Figure 1).

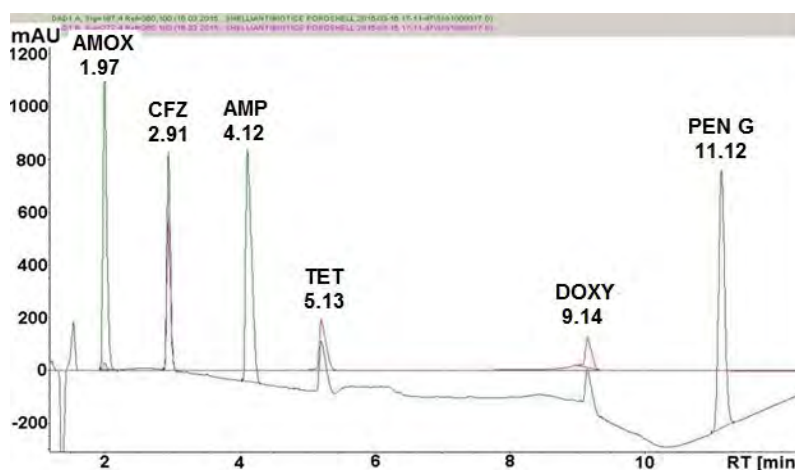


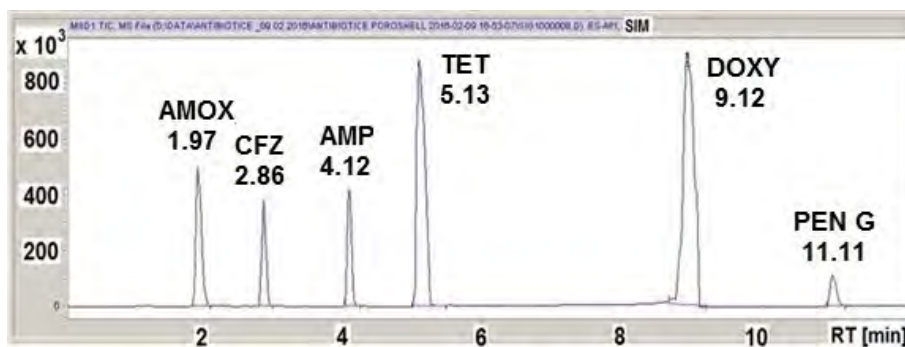
Figure 1. HPLC-DAD chromatogram of studied antibiotics

The developed HPLC-DAD method shows good linearity in the range of 5.21–166.7 $\mu\text{g/mL}$, correlation coefficients (r) exceeding 0.999 for all selected antibiotics, good repeatability (three replicates) measured for the 0.85 $\mu\text{g/mL}$ concentration, low limit of detection (LOD) and limit of quantification (LOQ) in the range of $\mu\text{g/mL}$ (Table 1). The LOD and LOQ were calculated taking into account the slope of each calibration curve and the corresponding standard deviation.

Table 1. Performances of the developed HPLC-DAD method

Antibiotic	Calibration curve equation	r	LOD [$\mu\text{g/mL}$]	LOQ [$\mu\text{g/mL}$]	Repeatability RSD [%]
Amoxicillin	$Y = 50.42292X$	0.99968	0.61	1.86	5.43
Ceftazidime	$Y = 25.64547X$	0.99999	0.18	0.57	11.39
Ampicillin	$Y = 63.61580X$	0.99996	0.25	0.75	9.31
Tetracycline	$Y = 15.78180X$	0.99970	0.70	2.14	4.55
Doxycycline	$Y = 8.71137X$	0.99735	0.75	2.29	8.48
Penicillin G	$Y = 71.33844X$	0.99971	0.25	0.79	9.74

For LC-MS analysis, the selected ion monitoring (SIM) mode was chosen in order to obtain a better sensitivity. In Figure 2, the chromatogram acquired in SIM mode is presented.

**Figure 2.** LC-ESI(+)-MS SIM chromatogram of studied antibiotics

The characteristic ion for each studied antibiotic was obtained by electrospray ionisation in positive mode (ESI(+)). In Figure 3 are presented the mass spectra (scan mode ranging from 100 to 1000 uam) and the m/z ions for the studied antibiotics.

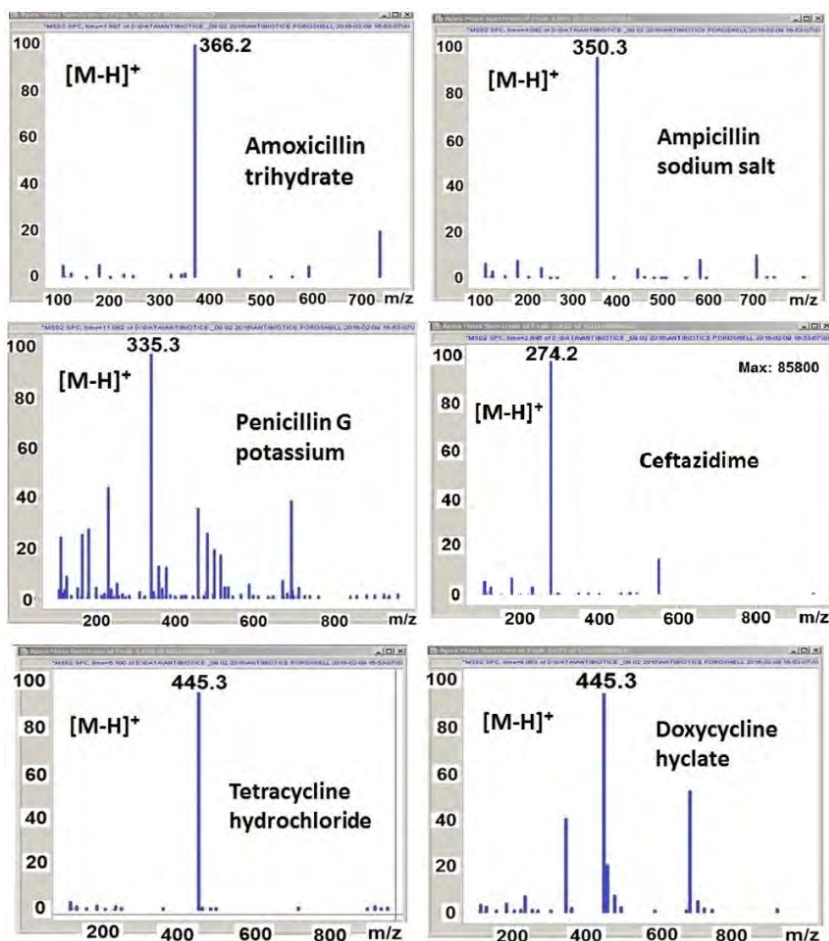


Figure 3. LC-ESI(+)-MS spectra of the studied antibiotics

The developed LC-ESI(+)-MS method shows good linearity in the range of 0.65–166.7 $\mu\text{g/mL}$, correlation coefficients (r) exceeding 0.99 for all selected antibiotics, good repeatability (three replicates) measured for the 0.85 $\mu\text{g/mL}$ concentration, lower LOD and LOQ in the range of ng/mL (Table 2).

Comparing the two developed LC methods, differing only by detectors, one can observe that these methods have the same linearity ($r > 0.99$), but the LC-ESI(+)-MS method is ten to hundred times more sensitive than the HPLC-DAD method (Table 3).

Table 2. Performances of the LC-ESI(+)-MS method

Antibiotic	Calibration curve equation	r	LOD [µg/mL]	LOQ [µg/mL]	Repeatability RSD [%]
Amoxicillin	$y = 17773.39271x + 115572.17582$	0.99383	0.0210	0.0636	4.79
Ceftazidime	$y = 11192.38273x + 59245.64014$	0.99548	0.0196	0.0595	5.12
Ampicillin	$y = 11725.36209x + 39962.45772$	0.99654	0.0157	0.0475	3.70
Tetracycline	$y = 45458.20719x + 38326.00614$	0.99629	0.0178	0.0539	6.74
Doxycycline	$y = 67695.85510x - 350854.03308$	0.99608	0.0205	0.0622	6.00
Penicillin G	$y = 3007.03091x + 36758.78717$	0.99084	0.0315	0.0955	3.11

Table 3. Comparison of the performances of the developed methods: HPLC-DAD *versus* LC-ESI(+)-MS

Antibiotic	RT [min]		Correlation coefficient (r)		LOD [µg/mL]		LOQ [µg/mL]	
	DAD	MS	DAD	MS	DAD	MS	DAD	MS
Amoxicillin	1.97	1.97	0.99968	0.99383	0.61	0.021	1.86	0.064
Ceftazidime	2.91	2.86	0.99999	0.99548	0.18	0.019	0.57	0.059
Ampicillin	4.12	4.12	0.99996	0.99654	0.25	0.016	0.75	0.048
Tetracycline	5.13	5.13	0.99970	0.99629	0.70	0.018	2.14	0.054
Doxycycline	9.14	9.12	0.99735	0.99608	0.75	0.021	2.29	0.062
Penicillin G	11.12	11.11	0.99971	0.99084	0.25	0.032	0.79	0.096

However, LC-ESI(+)-MS method can be applied only for the analysis of samples of low complexity (water samples). In the case of complex (sediments) samples, HPLC-DAD method is recommended.

The accuracy has been tested only for Tetracycline and Doxycycline, considering that these antibiotics are the most prevalent in environmental samples. For this purpose, real river water samples were spiked with different amounts of Tetracycline and Doxycycline, and then extracted and analysed by SPE-LC-ESI(+)-MS procedure. The obtained results show good accuracy for both antibiotics, the recovery ranging between 95–100% (Table 4).

Table 4. Accuracy of the SPE-LC-ESI(+)-MS procedure

Antibiotic	Amount [$\mu\text{g/mL}$]			Recovery [%]	Mean recovery \pm SD [%]
	Initial	Added	Found		
Tetracycline	0.58	0.46	1.08	103.84	100.31 \pm 3.09
			1.02	98.07	
			1.03	99.04	
	0.58	0.58	1.11	95.68	99.41 \pm 3.89
			1.20	103.44	
			1.15	99.13	
	0.58	0.69	1.30	102.36	99.20 \pm 4.17
			1.20	94.48	
			1.28	100.78	
Doxycycline	0.98	0.78	1.70	96.66	98.50 \pm 2.34
			1.78	101.13	
			1.72	97.72	
	0.98	0.98	1.94	98.98	97.26 \pm 1.57
			1.90	96.90	
			1.88	95.91	
	0.98	1.18	2.06	95.37	95.21 \pm 2.09
			2.10	97.22	
			2.01	93.05	

The developed SPE-LC-ESI(+)-MS procedure was applied for monitoring of selected antibiotics in the Romanian Tisza River Watershed during 13 months from July 2014 to September 2015, thus covering all four seasons. Our results show the presence of some antibiotics in the river water samples. The most common antibiotics found are in concentrations of $\mu\text{g/L}$ as follows: Tetracycline in the range of 0.10–5.24, Doxycycline in the range of 0.11–2.46 and Ceftazidime in the range of 0.01–4.20 $\mu\text{g/L}$ (Table 5). One can also observe that their concentrations are depending by the time and point of sampling.

Table 5. Antibiotics found in Tisza River Watershed analysed by SPE-LC-ESI(+)-MS procedure

Sampling date	Sampling point	Antibiotics found and their amounts [$\mu\text{g/L}$]
July 2014	Vișeu (1)	Doxycycline (0.68), Ceftazidime (2.56)
	Iza (2)	Tetracycline (1.24), Ceftazidime (3.43)
	Tisza (3)	Doxycycline (2.40)
August 2014	Vișeu (1)	Not detected
	Iza (2)	Not detected
	Tisza (3)	Ceftazidime (4.20)
November 2014	Vișeu (1)	Doxycycline (0.11), Tetracycline (0.10)
	Iza (2)	Tetracycline (2.56), Ceftazidime (0.01)
	Tisza (3)	Tetracycline (0.82)
December 2014	Vișeu (1)	Tetracycline (0.11)
	Iza (2)	Tetracycline (0.56)
	Tisza (3)	Tetracycline (0.13)
January 2015	Vișeu (1)	Tetracycline (3.96)
	Iza (2)	Tetracycline (1.24), Doxycycline (0.23)
	Tisza (3)	Tetracycline (2.07)
February 2015	Vișeu (1)	Tetracycline (2.65)
	Iza (2)	Tetracycline (1.42), Doxycycline (0.19)
	Tisza (3)	Tetracycline (2.32)
March 2015	Vișeu (1)	Not detected
	Iza (2)	Not detected
	Tisza (3)	Tetracycline (3.07), Doxycycline (2.16), Ceftazidime (4.15)
April 2015	Vișeu (1)	Ceftazidime (4.19), Penicillin G (3.41)
	Iza (2)	Not detected
	Tisza (3)	Not detected
May 2015	Vișeu (1)	Not detected
	Iza (2)	Tetracycline (5.24)
	Tisza (3)	Penicillin G (4.67)
June 2015	Vișeu (1)	Tetracycline (1.47), Doxycycline (0.78)
	Iza (2)	Tetracycline (3.32), Ceftazidime (0.06)
	Tisza (3)	Tetracycline (1.83), Doxycycline (0.26), Ceftazidime (0.17)
July 2015	Vișeu (1)	Tetracycline (1.01), Doxycycline (0.94)
	Iza (2)	Tetracycline (0.03)
	Tisza (3)	Tetracycline (0.69), Doxycycline (0.19)
August 2015	Vișeu (1)	Tetracycline (0.49)
	Iza (2)	Tetracycline (0.60)
	Tisza (3)	Tetracycline (0.52)
September 2015	Vișeu (1)	Tetracycline (0.78), Doxycycline (0.36)
	Iza (2)	Tetracycline (0.47), Doxycycline (2.46)
	Tisza (3)	Tetracycline (1.88), Doxycycline (0.26), Ceftazidime (0.15)

A SIM chromatogram of an extract of a real river water sample is presented in Figure 4 where one can be observed the presence of Tetracycline and Doxycycline.

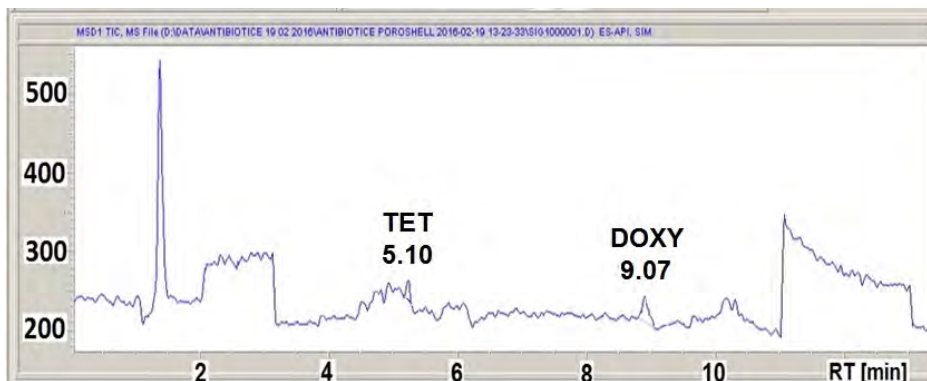


Figure 4. SIM chromatogram of a river water extract from Vişeu River, Sampling point (1), July 2015

Regarding the sediment samples, the results showed the presence of Tetracycline in the range of 143.9 and 248.8 $\mu\text{g}/\text{kg}$ and of Doxycycline in the range of 14.6 and 27.9 $\mu\text{g}/\text{kg}$ (Table 6). These results are quite logical taking into account that these two antibiotics are the most prevalent in river water samples.

Table 6. Antibiotics found in sediment extracts from Tisza River Watershed by USAE-SPE-HPLC-DAD procedure

Sampling date	Sampling point	Antibiotics found and their amounts [$\mu\text{g}/\text{Kg}$]
July 2015	Vişeu (1)	Tetracycline (143.9)
	Iza (2)	Tetracycline (156.8), Doxycycline (27.9)
	Tisza (3)	Tetracycline (248.8), Doxycycline (14.6)

CONCLUSIONS

Two analytical procedures, SPE-HPLC-DAD and SPE-LC-ESI(+)-MS, have been developed in order to determine some antibiotics in river water samples collected from the Romanian Tisza River Watershed (Vişeu, Iza and Tisza Rivers).

The developed procedures show good linearity and limits of detection and quantification, being applicable to the analysis of the selected antibiotics in real river water samples. SPE-LC-ESI(+)-MS is more suitable for the analysis of antibiotics in surface waters being more sensitive than HPLC-DAD.

The SPE-LC-ESI(+)-MS procedure has been applied to monitor the target antibiotics in river water samples collected during 13 months. The most found antibiotics were Tetracycline (0.10–5.24 $\mu\text{g/L}$), Doxycycline (0.11–2.46 $\mu\text{g/L}$) and Ceftazidime (0.01–4.20 $\mu\text{g/L}$). Also, Penicillin G was found two times (3.41 and 4.67 $\mu\text{g/L}$).

For the sediment samples, the USAE-SPE-HPLC-DAD procedure has been developed, based on the previous SPE-HPLC-DAD procedure.

In the analysed sediments, Tetracycline and Doxycycline in concentration of hundred, respectively tens $\mu\text{g/kg}$ were found.

The presence of antibiotics in river waters is a growing environmental problem, therefore the periodical monitoring is recommended.

EXPERIMENTAL SECTION

Chemicals and materials

For the optimization of the extraction protocols and of the qualitative and quantitative analysis, a standard mixture containing the six selected antibiotics (Figure 5) was prepared. The considered antibiotic standards were commercial powders used for oral treatment (Amoxicillin trihydrate 500 mg per capsule with talcum and magnesium stearate as excipients, Tetracycline chlorhydrate 250 mg per capsule with lactose and magnesium stearate as excipients, and Doxycycline 100 mg per capsule as hyclate 119 mg with corn starch, magnesium stearate and talcum as excipients) or for injection (Ampicillin sodium salt 1 g per vial, Penicillin G potassium salt 1.000.000 U.I. per vial, and Ceftazidime 1 g per vial). The antibiotics were purchased from “Antibiotice” Romania (Amoxicillin, Ampicillin, Penicillin G, Tetracycline), “GlaxoSmithKline” Romania (Ceftazidime) and “Sandoz” Romania (Doxycycline).

Standard solutions in the concentration range of 0.65 to 166.7 ng/mL prepared by the dilution of standard mixture in Milli-Q water were used for calibration. Methanol and acetonitrile of HPLC grade purity and formic acid of 99.9% purity were purchased from Merck (Germany). The Milli-Q water was prepared using a Milli-Q Plus water system from Millipore (USA). Before injection, the samples were passed through Teknokroma syringe filters, PTFE 0.45 μm .

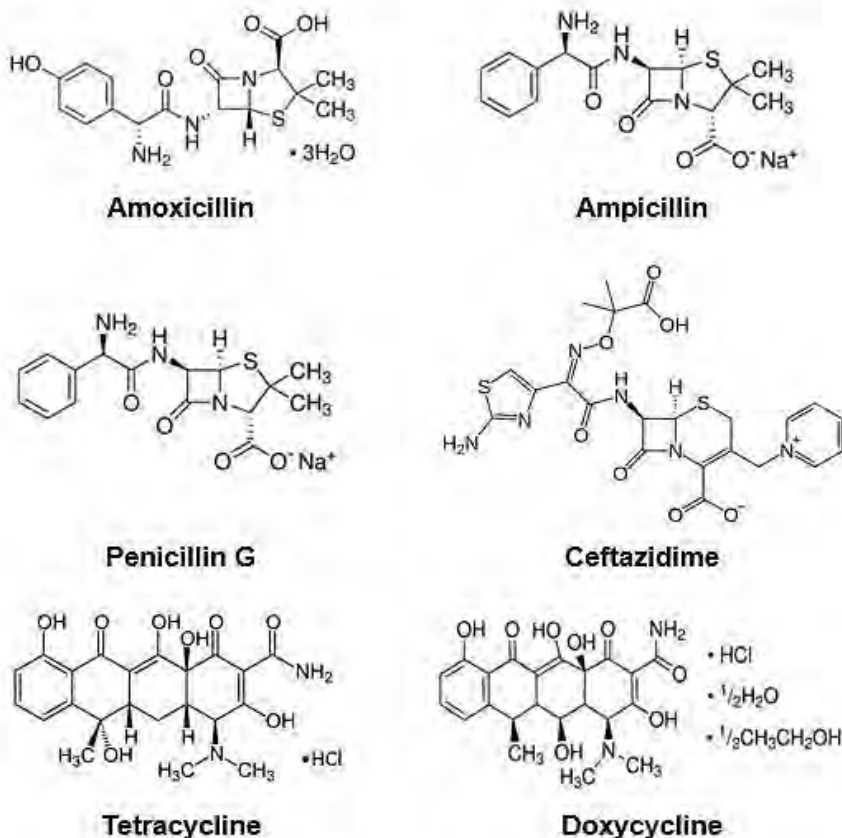


Figure 5. Structure formula of the studied antibiotics

Instrumentation and chromatographic separation

For the chromatographic analyses, an HPLC Agilent 1200 Series system, equipped with G1322A degasser, G1311A quaternary pump, G1329A autosampler, G1315D DAD detector, and G1316B TCC SL column thermostat and a LC-MS system model Agilent 1200 Series coupled with 6110 Quadrupole LC/MS detector with AP-ESI ionization were used. The chromatographic data were collected and processed by means of the ChemStation software.

The separation was carried out on Agilent Poroshell 120 EC-C18 column (4.6 × 150 mm, 2.7 μm) at a flow rate of 1.1 mL/min using a mobile phase consisting in a mixture of (A) acetonitrile and (B) 0.1% formic acid in water (v/v) operated under the following gradient (Table 7):

Table 7. Gradient elution used for the separation of target antibiotics

Time [min]	Mobile phase composition [%]	
	A: (Acetonitrile)	B: (0.1% formic acid in water)
0	10	90
3	20	80
6	20	80
8	40	60
10	10	90
13	STOP elution	

The column temperature was fixed at 35°C. A volume of 20 μL sample was injected for the DAD detection and one of 1.0 μL for the MS detection respectively.

For the DAD detection, two wavelengths were used, one of 197 nm for penicillins and another one of 272 nm for tetracyclines and cephalosporins. MS was operated in SIM mode using positive electrospray ionization (ESI (+)).

Samples collection and extraction conditions

The present study was performed in the Romanian Tisza River Watershed. Two monitoring points were selected on the main tributaries (Vișeu and Iza Rivers) and one on the Tisza River. The first sampling point was located at Vișeu Valley village, near the confluence of Vișeu River with Tisza River, the second one at Sighetu Marmației town where Iza River flows into Tisza River and the third one at Teceu Mic village where Tisza River leaves the Romanian territory (Figure 6).

Monitoring in Tisza River Watershed was conducted over the course of 13 months, from July 2014 to September 2015. During this period, water river samples were collected using a manual water sample device and kept in a brown glass bottle at 5°C before analyses.

Sediment samples were collected in July 2015 using a stainless steel grab sampler and were kept in glass jars at 5°C before analysis.

Isolation of the target antibiotics from the water samples was done by solid-phase extraction while from the sediment samples by ultrasound-assisted extraction followed by solid-phase extraction (USAE-SPE).

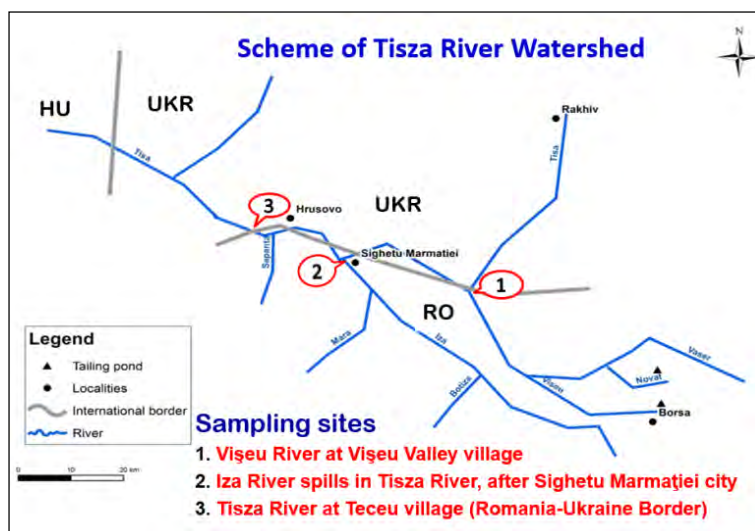


Figure 6. The three monitoring points selected for study

OASIS HLB cartridges (500 mg/6 mL) were used for the extraction of antibiotics from water samples. Before extraction, the cartridges were conditioned by washing with 5 mL methanol and then with 5 mL Milli-Q water. The sorbent was equilibrated by washing with 5 mL solution of 5% methanol in Milli-Q water.

For SPE, a volume of 400 mL river water sample was passed through cartridges at a flow rate of 5 mL/min, subsequent by the elution of retained antibiotics with 5 mL methanol+acetonitrile (1:1, v/v) mixture. After evaporation to dryness under nitrogen, the residue was dissolved in 1 mL acetonitrile and subjected to the HPLC analysis.

For the extraction of antibiotics from sediment samples, 3 g of dried sediment (room temperature) was extracted with 20 mL methanol in an ultrasonic bath for 30 minutes. After centrifugation at 4000 rpm for 15 minutes, the supernatant was collected and evaporated to dryness under nitrogen. The residue was reconstituted in 100 mL distilled water and subjected to the SPE extraction under the procedure used for the river water samples.

ACKNOWLEDGMENTS

This work was conducted within the NATO Science for Peace 984440/2014–2017 Project.

REFERENCES

1. K. Kümmerer, *Chemosphere*, **2009**, *75*, 417.
2. J.L. Martinez, *Environmental Pollution*, **2009**, *157*, 2893.
3. S. Manzetti, R. Ghisi, *Marine Pollution Bulletin*, **2014**, *79*, 7.
4. X. Chang, M.T. Meyer, X. Liu, Q. Zhao, H. Chen, J. Chen, Z. Qiu, L. Yang, J. Cao, W. Shu, *Environmental Pollution*, **2010**, *158*, 1444.
5. B. Li, T. Zhang, Z. Xu, H.P. Fang, *Analytica Chimica Acta*, **2009**, *645*, 64.
6. O. Opreș, V. Coman, F. Copaciu, M. Vlassa, *Journal of Planar Chromatography*, **2012**, *25*(6), 516.
7. C. Marx, V. Mühlbauer, P. Krebs, V. Kuehn, *Science of the Total Environment*, **2015**, *524–525*, 269.
8. W.H. Xu, G. Zhang, S.C. Zou, X.D. Li, Y.C. Liu, *Environmental Pollution*, **2007**, *145*, 672.
9. O. Opreș, M.L. Soran, V. Coman, F. Copaciu, D. Ristoiu, *Central European Journal of Chemistry*, **2013**, *11*(8) 1343.
10. X. Liang, B. Chen, X. Nie, Z. Shi, X. Huang, X. Li, *Chemosphere*, **2013**, *92*(11), 1410.
11. H. Shi, Y. Yang, M. Liu, C. Yan, H. Yue, J. Zhou, *Marine Pollution Bulletin*, **2014**, *83*, 317.
12. D. Cheng, X. Liu, L. Wang, W. Gong, G. Liu, W. Fu, M. Cheng, *Science of the Total Environment*, **2014**, *476–477*, 266.
13. J. Xu, Y. Zhang, C. Zhou, C. Guo, D. Wang, P. Du, Y. Luo, J. Wan, W. Meng, *Science of the Total Environment*, **2014**, *497–498*, 267.
14. S. Zhao, X. Liu, D. Cheng, G. Liu, B. Liang, B. Cui, J. Bai, *Science of the Total Environment*, **2016**, *569–570*, 1350.
15. L. Yao, Y. Wang, L. Tong, Y. Deng, Y. Li, Y. Gan, W. Guo, C. Donga, Y. Duana, K. Zhaoa, *Ecotoxicology and Environmental Safety*, **2017**, *135*, 236.
16. B. Suárez, B. Santos, B.M. Simonet, S. Cárdenas, M. Valcárcel, *Journal of Chromatography A*, **2007**, *1175*(1) 127.
17. M.I. Bailón-Pérez, A.M. García-Campaña, C. Cruces-Blanco, M. del Olmo Iruela, *Journal of Chromatography A*, **2008**, *1185*(2), 273.
18. A.V. Herrera-Herrera, J. Hernández-Borges, T.M. Borges-Miquel, M.Á. Rodríguez-Delgado, *Journal of Pharmaceutical and Biomedical Analysis*, **2013**, *75*, 130.
19. Y. Li, Q. Li, K. Zhou, X.-L. Sun, L.-R. Zhao, Y.-B. Zhang, *Chemosphere*, **2016**, *147*, 25.
20. P. Bottoni, S. Caroli, *Journal of Pharmaceutical and Biomedical Analysis*, **2015**, *106*, 3.

SYNTHESIS AND CHARACTERIZATION OF NOVEL GIOMERS FOR DENTAL APPLICATIONS

IOANA HODISAN^{a,d}, CRISTINA PREJMEREAN^{b*}, IOAN PETEAN^a,
DOINA PRODAN^b, TINCA BURUIANA^c, LOREDANA COLCERIU^d,
LUCIAN BARBU-TUDORAN^e, MARIA TOMOAI-A-COTISEL^{a,f}

ABSTRACT. The aim of the present work was to prepare and characterize a series of dental giomers and their corresponding dental adhesive and to evaluate the adhesion of the new materials at the restoration/tooth interface. The experimental giomers were prepared as monopastes by blending the resin matrices, a new pre-reacted glass, a radiopaque glass and fluorhydroxyapatite. The novelty of the work is represented by the using of a polyalkenoic acid based on acrylic acid, itaconic acid and N-acryloyl -L-leucine as the main component of the pre-reacted glass and of the primer in the adhesive system. In addition, the using of an original synthesized urethane tetra-methacrylate Bis-GMA analogue (Bis-GMAexp) as base monomer in the resin represents another element of novelty. The morphology of giomer samples was investigated by scanning electron microscopy. The sealing ability was tested by dye penetration method completed with atomic force microscopy investigation. The microleakage was evaluated using the score method. The results pointed out a remarkable dentin sealing for the new adhesive system and a strong adhesion at Bis-GMAexp-based giomer/adhesive system/tooth interfaces in substantial agreement with very low value of microleakage.

Keywords: dental giomers, adhesive system, microleakage, SEM, AFM

^a Babeş-Bolyai University, Faculty of Chemistry and Chemical Engineering, 11 Arany J. str., RO-400028, Cluj-Napoca, Romania

^b Babeş-Bolyai University, Raluca Ripan Institute of Research in Chemistry, 30 Fantanele str., RO-400294, Cluj-Napoca, Romania

^c Petru Poni Institute of Macromolecular Chemistry, Iasi, Romania

^d Iuliu Hațieganu University of Medicine and Pharmacy, Faculty of Dental Medicine of Cluj-Napoca, 8 Babeş V. str., RO-400012, Cluj-Napoca, Romania

^e National Institute for Research and Development of Isotopic and Molecular Technologies, 65-103 Donath str., RO-400293 Cluj-Napoca, Romania

^f Academy of Romanian Scientists, 54 Splaiul Independentei, 050094 Bucharest, Romania

* Corresponding author: cristina.prejmerean@gmail.com

INTRODUCTION

Longevity, fluoride release and fluoride recharge abilities are crucial for the clinical performances of aesthetic dental restorative materials. Considering these requirements, during the last decade, a new class of hybrid materials which combine the chemistry of diacrylic resin composites (DRCs) with the one of the glass ionomer cements (GICs) were introduced on the market by Shofu (Kyoto, Japan). These hybrid materials were named giomers. They present long-term aesthetics and durability (which are characteristics of DRCs) as well as controllable ion release and recharge properties (which represent features of GICs).

Giomers are new restorative materials used in adhesive dentistry based on pre-reacted filler technology, where pre-reacted glass ionomer (PRG) was ground and used as fillers in a polymer matrix. PRG fillers are fabricated by acid–base reactions between fluoride containing glass and poly acrylic acid in the presence of water forming wet siliceous hydrogel.[1] Giomers are fluoride release dental materials [2] having the advantage of inhibiting dental tissues demineralization process [3]. This new class of restorative materials combines the bioactivity and biocompatibility of glass ionomer with the physical and optical properties of composites offering the practitioners an excellent alternative for amalgam restoration. The giomers bond chemically to tooth structure by an intermediate adhesive system [4].

Restorative materials used in dentistry should provide a good sealing at the tooth/restorative material interface in order to prevent microleakage and postoperative complication. Adhesive systems used in restorative dentistry provide the sealing between tooth and restorative composites and should create a strong adhesive bond associated with minimal shrinkage of the resin during curing [5].

The adhesive dentistry is known to be confronted with the limitation of the dentin adhesion. That's why it is important to investigate the tooth/adhesive system/restoration interface for the new materials in order to improve the quality of the sealing of restoration giving the opportunity of obtaining a hermetic restoration without any microleakage [6]. Microleakage was reported as the main reason for replacement of composite resin restoration [7-9]. Microleakage is usually associated with the bacterial penetration through the restoration-tooth interface, causing short-term or/and long-term clinical problems such as postoperative sensitivity, marginal staining, secondary caries, and/or pulpal inflammation and failure of endodontic treatment [10-12]. *In vitro* studies of microleakage are done using methods like: dye penetration method [13], measurement by scanning electron microscope [14], bacterial activity, electrochemical test, fluid filtration [15].

The aim of this work was to prepare and characterize a series of new giomers and their corresponding adhesive system, including the primer and the bonding. The sealing ability was tested by dye penetration method completed with AFM investigation at the interface in order to demonstrate their potential for clinical use.

RESULTS AND DISCUSSION

1. Giomers components

1.1. Resins

The experimental resins were formulated using monomer mixtures of Bis-GMAcom or an original synthesized urethane tetra-methacrylate Bis-GMA analogue (Bis-GMAexp) as base monomer and TEGDMA as diluting monomer.

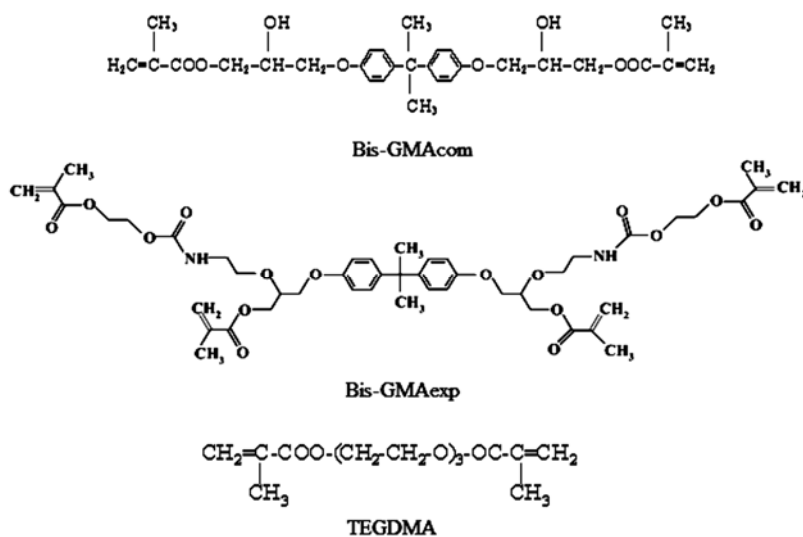


Fig.1. Chemical structures of the monomers used in this study.

The synthesis and characterization of Bis-GMAexp was presented elsewhere [16]. The ratio between the base monomer and diluting monomer was 70/30. In the composition of the resins, besides the methacrylic oligomers and monomers, a photosensitizer, camphorquinone (CQ) in an amount of 0.5% (by weight), and an accelerator N,N-dimethylaminoethyl methacrylate (DMAEMA), in an amount of 1% (by weight), were added.

1.2. Pre-reacted glass ionomer filler

The experimental pre-reacted glass ionomer filler was prepared using the conventionally method employed in the preparation of traditional glass ionomer cements. PRG was prepared by hand-mixing of 50% aqueous solution of PAlk-Leu polyalkenoic acid (ternary copolymer resulted from acrylic acid, itaconic acid and N-acryloyl-L-leucine, average molecular weight 23500) with the superficially active glass powder G having the composition: SiO₂ (49%), Al₂O₃ (22%), CaF₂ (29%), in a weight ratio of 1/2.4. After 24 hours, the PRG was dried in an oven at 95°C for 24 hours. Finally, it was grounded in a ball mill and sifted to fine powder.

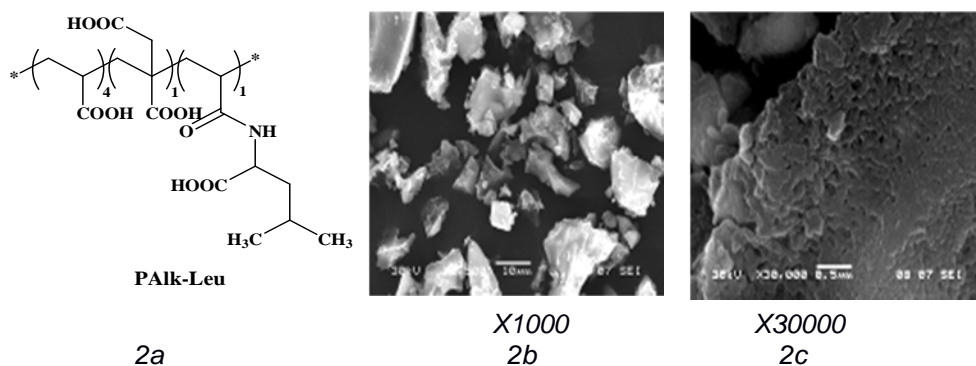


Figure 2. Structure of PAlk-Leu (2a; *structural unit*) and SEM micrographs of the corresponding PRG (2b, 2c)

SEM images presented in Fig.2 show the morphology of the experimental PRG powder. One can observe the irregular shape of the particles with a sharp particle edges (Fig. 2b). The particle sizes showed an average diameter about 20 μm . The higher magnification details presented in Fig.2c reveal a porous structure of the pre-reacted glass.

2. Giomers

The experimental light-curing giomers were prepared as monopastes by mixing the resin matrices (20%) with the hybrid fillers (80%). For the obtaining of hybrid fillers, the pre-reacted glass ionomer filler (28%) fluorohydroxyapatite (12%), the silanized radiopaque glass powder (40%) were mixed and then sifted together. Silanation of radiopaque glass was carried out with 3-methacryloyloxypropyl-1-trimethoxy-silane (A-174 silane). The method of obtaining and the characterization of radiopaque glass and FHAP was shown elsewhere [16, 17].

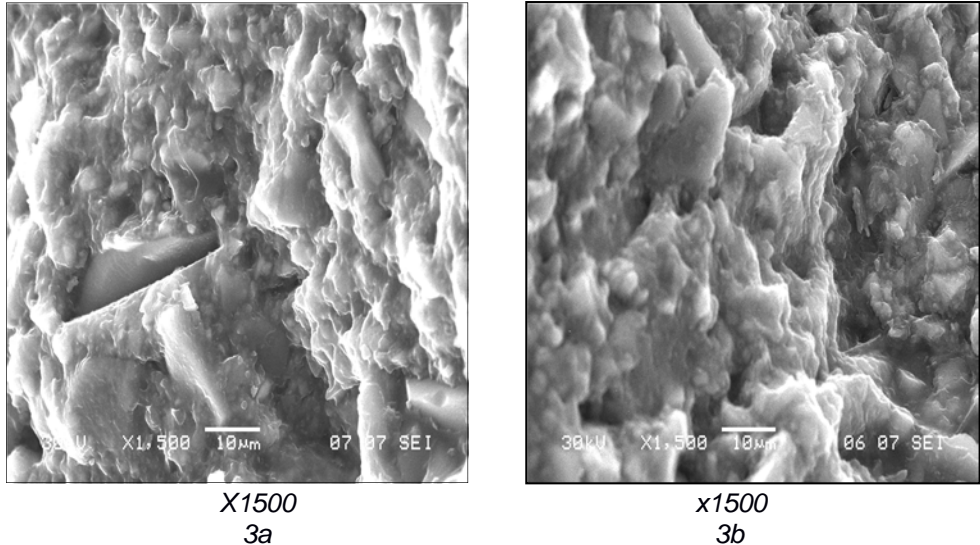


Figure 3. SEM micrographs of the Giomer G1 (3a) and Giomer G2 (3b)

Fig. 3 shows the fracture images of Giomer G1 based on Bis-GMAcom (3a) and Giomer G2 based on Bis-GMAexp (3b). G1 and G2 giomers present a similar surface organization. The morphology of giomer samples is complex consisting of a high amount of fine particles well embedded in a compact polymer matrix structure. A large amount of particles measuring less than 10 microns with sharp or rounded edges (shapes) as well as a few particles having a diameter of about 20 microns can be visualized. Base on the particle size analysis, the first can be attributed to the radiopaque filler particles or small sizes PRG particles and the second ones can be attributed to the large sizes PRG filler particles [16].

3. Obtaining of adhesive system

The adhesive system comprising 3 components: etchant, primer and bonding (known as three-step adhesives systems) were prepared. The primer and bonding were prepared according to the method described elsewhere [26]. The composition of the adhesive system and of the G1 and G2 giomers is shown in Table 1.

Table 1. Composition of adhesive system and of G1 and G2 giomers

Product		Main components	Diluting monomers	Initiating system	Solvents	Filler(s)
Adhesive system	Primer	PAlk-Leu (30%)	HEMA (32%) TEGDMA (10.7%)	CQ (0.18%) CDFI (1.12%)	Water (20%) Acetone (6%)	-
	Bonding	Bis-GMAexp (60%)	HEMA (10%) TEGDMA (28.53%)	CQ (0.49%) DMAEMA (0.98%)	-	-
Giomers	Giomers G1	Bis-GMAcom (14%)	TEGDMA (5.72%)	CQ (0.09%) DMAEMA (0.19%)		SPRG (28%) HAF (12%) Radiopaque glass (40%)
	Giomers G2	Bis-GMAexp (14%)	TEGDMA (5.72%)	CQ (0.09%) DMAEMA (0.19%)		SPRG (28%) HAF (12%) Radiopaque glass (40%)

4. Determination of microleakage

Thirty box-type Class V standardized cavities were prepared on premolar teeth on the facial (the face oriented in the mouth towards the cheek) and oral surfaces (the face oriented towards the tongue) of each tooth. The preparations had one margin in enamel and one margin in dentin. The preparations were divided randomly into two equal groups (n=15) and restored with: group I: giomer G1 and adhesive system; group II: giomer G2 and the same adhesive system. The teeth were thermocycled, then immersed in 2% methyl blue solution for 24 h. The specimens were sectioned longitudinal, buccolingually into slices of 1 mm and the resulted sections were examined for microleakage using a stereomicroscope. The extend of microleakage at the restoration/tooth interface was evaluated assessing scores: 0, 1, 2, 3 for each restoration at the enamel/restoration and dentin /restoration interface.

The microleakage behavior examined using the scoring method is presented in Table 2.

Table 2. Microleakage scores

Groups	Microleakage score in dentin				Microleakage score in enamel			
	0	1	2	3	0	1	2	3
I	3	0	4	8	13	2	0	0
II	5	2	4	4	14	1	0	0

The results, given in table 2, show that almost all the samples presented a minimal microleakage at the enamel margins proving that both groups of giomer restorations were sealed with the experimental adhesive system at this level and the values are comparable with the ones found in the literature for the commercial giomer materials and their adhesive systems [18-20].

The microleakage values in dentin were significantly higher than enamel values. The problem of microleakage has been largely demonstrated mainly below the cement-enamel junction in several studies [21, 22] because the bonding to dentin is far more difficult and less predictable than bonding to enamel. This behavior could be explained by the morphological differences of the tooth structures: dentin and enamel because dentin is less mineralized, about 75% as opposed to enamel which is 98%. Moreover, dentin has a more complex histologic pattern, such as tubular structure and intrinsic wetness [23].

Dentin is more hydrophilic with canalicular structure with 48% vol. Hap, 29% vol. organic materials and 23% vol. water. The dentinal tubules traverse entire dentin, oriented from the dentin-enamel junction towards the pulp. This structure of dentin allows the substance to infiltrate at interface dentin/composite and to travel by water in dentinal fluid along the canalicular system towards the pulp resulting in a higher percentage of dentin microleakage than the enamel.

Between the two groups there were no significant differences concerning the microleakage value. However, it can be noticed that there were only three scores 0 for group I, while there were 5 scores 0 for group II. In addition, there were registered 8 scores 3 for group I, while were obtained only 4 scores 3 for group II.

AFM investigations were made to examine the sealing at the dentin/adhesive system interface, which is a condition for a good restoration. The dentin surface observed by AFM microscopy is presented in Fig. 4. The topographic image, Fig. 4a, reveals the dentin tubule. Peritubular dentin is observed around the tubule in good agreement with literature data [24 – 26].

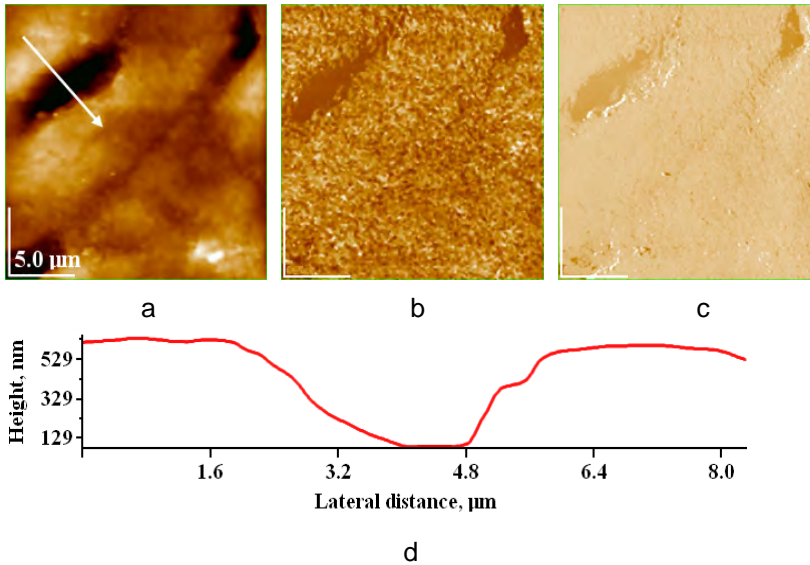


Figure 4. AFM images of dentin at the interface with the G2 giomer restoration: a) topographic image, b) phase image, c) amplitude image, d) cross section on white arrow in figure (a). Scanned area 20 μm x 20 μm.

Fig. 4c also reveals the peritubular dentin as a compact matrix having light color and the tubules appear in dark due to their depth. Cross section in Fig. 4d gives the opportunity to measure precisely the size of tubule of about 3 μm [27]. The darker zone in the middle of the scanned area is the adhesive sealing the dentin surface and the tubules and thus, offering a binding with the giomer G2.

CONCLUSIONS

A series of dental gomiers (G1 and G2) were prepared by dispersing a novel pre-reacted glass ionomer, a radiopaque glass and fluorhydroxyapatite in the resin matrices. An original synthesized urethane tetra-methacrylate Bis-GMA analogue (Bis-GMAexp) was used as base monomer in giomer G2 while commercial Bis-GMA was contained in G1 giomer. PAlk-Leu (ternary copolymer resulted from acrylic acid, itaconic acid and N-acryloyl-L-leucine) was used as polyalkenoic acid for the obtaining of PRG and as main component of the primer in the adhesive.

The combination of adhesive system and giomer G2 performed better in terms of adhesion to the tooth structures than the same adhesive system in combination with giomer G1.

We can conclude that the giomer G2 containing Bis-GMA_{exp} could be used successfully with the experimental adhesive system based on PAIk-Leu in clinical application.

EXPERIMENTAL SECTION

1. Materials

Reagent grade chemicals of 2,2-bis[4-(2-hydroxy-3-methacryloxypropoxy)phenyl]propane (Bis-GMA), triethyleneglycol dimethacrylate (TEGDMA), 2-hydroxyethyl methacrylate (HEMA) were purchased from Aldrich Chemical, Milwaukee, WI, USA and used without further purification. Camphorquinone (CQ), N,N-dimethylaminoethyl methacrylate (DMAEMA), diphenyliodonium chloride (CDFI) were supplied by Sigma Chemical, St. Louis, MO, USA. PAIk-Leu was synthesized by our group as reported elsewhere [28]. 3-methacryloyloxypropyl-1-trimethoxy-silane (A-174 silane) were purchased from Sigma Aldrich Chemical Co. (Taufkirchen, Germany) and used without additional purification. The oxides and fluorides SiO₂, Al₂O₃, ZnO, CaO, Na₂O, B₂O₃, CaF₂, BaF₂ were purchased from Merk (Darmstadt, Germany).

2. Preparation of the adhesive system

2.1. The experimental primer. In a round-bottomed flask equipped with a stirrer, reflux condenser and a dropping funnel 30g of PAIk-Leu were introduced, and then 32g of HEMA were added. The mixture was stirred at 40°C for 30 min. Then 20g water was dosed from the dropping funnel, and the mixture was stirred further until the complete dissolution. After about 1 h, 10.7g of TEGDMA, in which the components of the initiating system (CQ (0.18g) and CDFI (1.12g)) were previously added, was dosed under continuous stirring for another hour, and finally, 6 g of acetone was added. All operations were done in rooms protected from visible light.

2.2. The experimental bonding. 28.53 g TEGDMA in which the initiator system was dissolved (CQ (0.49g) and DMAEMA (0.98g)) and 10 g HEMA were dosed in the round-bottomed flask in which 60 g bis-GMA had been previously introduced. The mixture was stirred for 2 h at 40°C. All operations were done in rooms protected from visible light.

3. Preparation of the giomers

3.1. The resin. 60g of Bis-GMA type monomer (Bis-GMA_{com} or Bis-GMA_{exp}) were introduced in a round-bottomed flask equipped with a stirrer, reflux condenser and a dropping funnel. The initiator system, (CQ (0.49g) and respectively DMAEMA (0.98g), was dissolved in 29.47g TEGDMA in another

flask. After complete dissolution, the mixture was dosed under continuous stirring for two hours over the Bis-GMA monomer. All operations were done in rooms protected from visible light.

3.2. *The hybrid filler.* 35g pre-reacted glass ionomer filler, 15g fluorohydroxy-apatite and 50g silanized radiopaque glass powder were mixed and then sifted together.

3.3. *The giomers.* The experimental light-curing giomers G1 and G2 were prepared as monopastes by mixing the resin matrices with the hybrid fillers.

4. Sample preparation

Fifteen freshly extracted premolars for orthodontic reason were kept in distilled water at 4°C for 24 hours. Standardized class V cavities measuring 4 mm length 3 mm width and 1.5 mm depth were prepared on facial and oral face of each tooth. The preparation was positioned with the gingival margin in cement (dentin) and the occlusal margin in enamel. The bur used for cavities preparation was a bur no. 4 for a high speed hand piece with water cooling system purchased from Shofu (Kyoto, Japan). The cavities were then divided randomly into 2 groups: group I cavities were restored using adhesive system and giomer G1 and group II was restored with the same adhesive system and giomer G2. The clinical protocol for the restoration included etching the cavities 30 sec with orthophosphoric acid 37% then rinse it off and gently dry the dental tissue. Next step was applying the primer on the dentin area using a microbrush, dry it using the air spray for 3 sec and then applying the bonding on the entire surface of the cavity. Once in place, the bonding was light-cured for 20 sec using light-curing device Spectrum 800 470 nm wavelength (Dentsply Germany). The giomer was placed in the cavity using the incremental oblique layers technique, each layer of maximum 2 mm. The layers were light-cured 20 sec each before applying the next one. Finishing and polishing of the restorations was done using Super Buffs disks from Shofu (Kyoto, Japan). The teeth were thermocycled 500 times in a 5°C-55°C water baths. Each cycle lasted 60 sec. This is an artificial aging method according to the ISO /TS11405:2003 [29]. After that the teeth were bloated dried with paper towels and the roots were sealed with composite resin. The exterior surface of the teeth was isolated using two layers of nail varnish on all their surface except 1 mm around the restoration. All samples were then immersed in 2% methylene blue solution for 24 hours. After rinsing the dye under running water the teeth were dried and embedded in methyl methacrylate and sectioned longitudinally in slices of 1 mm through both restorations using a diamond saw (Isomet 1000, Buehler, USA) under water cooling system [30]. Each slice was examined at optical microscope and scores were assessed for the dye penetration along the restoration /tooth interface according to the ISO standards: 0-no dye penetration; 1-dye penetration till ½ of the wall examined; 2-dye penetration to the full depth of the wall; 3-dye penetration reaches the axial wall.

5. Scanning electron microscopy (SEM). The morphology of the pre-reacted glass particles and of the fracture morphology of giomers was determined by SEM (JEOL, JSM 5510 LV) operated at 30 kV. The samples were prepared by dispersing a thin layer of the glass powders on a carbon tape and coated with 8 nm gold evaporated in an argon atmosphere (Sputter Coater Agar) prior to analysis

6. Atomic force microscopy. The AFM investigation of the surfaces of the tooth slice was done using the scanning probe microscope, AFM, JEOL 4210 equipment operating in the intermittent contact, also known as tapping mode [31-34]. The cantilever used was triangular, with a tip made from silicon nitride (NSC11, Micromasch Co. Estonia). The probe (tip) was on the cantilever, oscillating with a resonant frequency in the range of 260-330 kHz and having a spring constant of 48 N/m. Both a low scanning rate, 1 Hz, and a higher rate, in the range 2-6 Hz, were used, in order to detect possible scanning artifacts or those resulting from the sample preparation. The AFM images consist of multiple scans displaced laterally from each other in Y direction, the resolution being 512 x 512 pixels. An adequate low pass filtering was performed to remove the statistical noise without loss in the structural features of the material. All AFM experiments were carried out under ambient laboratory temperature conditions (about 20°C). All the images were processed according to standard AFM proceeding.

ACKNOWLEDGEMENTS

This work was supported by two grants of the Romanian National Authority for Scientific Research and Innovation, UEFISCDI, project PN-III-P2-2.1-PED-2016-1936 and project PNIII-P2-2.1-PED-2016-1907.

REFERENCES

1. M.C. Sunico, K. Shinkai, Y. Katoh, *Operative Dentistry*, **2005**, 30, 282.
2. T. Itota, T.E. Carrick, M. Yoshiyama, J.F. McCabe, *Dental Materials*, **2004**, 20, 789.
3. H. Ede Gonzalez, A.U. Yap, S.C. Hsu, *Operative Dentistry*, **2004**, 29, 578.
4. K. Ikemura, F.R. Tay, T. Endo, D.H. Pashley, *Dental Materials*, **2008**, 27, 315.
5. J.F. McCabe, A. Walls, "Applied Dental Materials", ninth edition, Blackwell Publishing Ltd., Singapore, **2008**.
6. R.M. Carvalho, J.C. Pereira, M. Yoshiyama, D.H. Pashley, *Operative Dentistry*, **1996**, 21, 17.
7. I.A. Mjör, *Acta Odontologica Scandinavica*, **1997**, 55, 58.
8. I.A. Mjör, *Operative Dentistry*, **1985**, 10, 88.
9. V. Qvist, J. Qvist, I.A. Mjör, *Acta Odontologica Scandinavica*, **1990**, 48, 305.

10. A.H. Tjan, D.E. Tan, *Quintessence International*, **1991**, 22, 565.
11. M.J. Taylor, E. Lynch, *Journal of Dentistry*, **1992**, 20, 3.
12. I. Yavuz, H. Aydin, *Biotechnology and Biotechnological Equipment*, **2005**, 19, 181.
13. J.B. De Almeida, J.A. Platt, Y. Oshida, B.K. Moore, M.A. Cochran, G.J. Eckert, *Operative Dentistry*, **2003**, 28, 453.
14. F.M de Goes, M.A. Montes, *Journal of Dentistry*, **2004**, 32, 391.
15. B. Karagenç, N. Gençoglu, M. Ersoy, G. Cansever, G. Külekçi, *Oral Surgery, Oral Medicine, Oral Pathology, Oral Radiology, and Endodontology*, **2006**, 102, 110.
16. C. Prejmerean, D. Prodan, M. Vlassa, M. Streza, T. Buruiana, L. Colceriu, V. Prejmerean, S. Cuc, M. Moldovan, *Measurement Science and Technology*, **2016**, 27, 124008.
17. C. Prejmerean, M. Moldovan, C.M. Petrea, D. Prodan, L. Silaghi-Dumitrescu, E. Vasile, G. Furtos, S. Boboia, R. Silaghi-Dumitrescu, *Materiale Plastice*, **2011**, 48, 279.
18. A. Abo El Naga, *Journal of American Science*, **2012**, 8, 27.
19. B.M. Owens, W.W. Johnson, E.F. Harris, *Operative Dentistry*, **2006**, 31, 60.
20. C.E. Dörfer, H.J. Stachle, M.W. Wurst, H. Duschner, T. Pioch, *European Journal of Oral Science*, **2000**, 108, 346.
21. C. Prati, L. Tao, M. Simpson, D.H. Pashley, *Journal of Dentistry*, **1994**, 22, 49.
22. K. Derhami, P. Coli, M. Brännström, *Operative Dentistry*, **1995**, 20, 100.
23. A. Thylstrup, S.A. Leach, V. Quist, "Dentine and Dentine Reactions in the Oral Cavity", Eds., Inform. Print. Ltd., Oxford, **1987**, p. 17.
24. S. Habelitz, M. Balooch, S.J. Marshall, G. Balooch, G.W. Marshall, *Journal of Structural Biology*, **2002**, 138, 227.
25. L.E. Bertassoni, G.W. Marshall, M.V. Swain, *Micron*, **2012**, 43, 1364.
26. X. Zheng, H. Pan, Z. Wang, H. Chen, *Journal of Microscopy*, **2011**, 241, 162.
27. M.B. Lopes, M.A. Sinhoretii, A. Gonini Jr., S. Consani, J.F. McCabe, *Brazilian Dental Journal*, **2009**, 20, 279.
28. T. Buruiana, M. Nechifor, V. Melinte, V. Podasca, E.C. Buruiana, *Journal of Biomaterials Science Polymer Edition*, **2014**, 25, 749.
29. International Organization for Standardization (ISO). "Dental materials—testing of adhesion to tooth structure", ISO/TS 11405: **2003** (Edition).
30. S. Deliperi, D.N. Bardwell, C. Wegley, M.D. Congiu, *Operative Dentistry*, **2006**, 31, 227.
31. C. Prejmerean, M. Tomoiaia-Cotisel, E. Vasile, G. Furtos, L. Pop, M. Moldovan, I. Petean, *International Journal of Nano and Biomaterials*, **2011**, 3, 344.
32. G. Tomoiaia, O. Soritau, M. Tomoiaia-Cotisel, L.-B. Pop, A. Pop, A. Mocanu, O. Horovitz, L.-D. Bobos, *Powder Technology*, **2013**, 238, 99.
33. M. Tomoiaia-Cotisel, A. Tomoiaia-Cotisel, T. Yupsanis, G. Tomoiaia, I. Balea, A. Mocanu, Cs. Racz, *Revue Roumaine de Chimie*, **2006**, 51, 1181.
34. O. Horovitz, G. Tomoiaia, A. Mocanu, T. Yupsanis, M. Tomoiaia-Cotisel, *Gold Bulletin*, **2007**, 40, 295.

PROVENANCE STUDY ON A SMALL SELECTION OF ROMAN POTSHARDS (TĂȘNAD-SERE SITE, SATU MARE COUNTY, ROMANIA). 1.

ENIKŐ BITAY^a, BERNADETH KISS-PATAKI^b, GYÖRGY SZAKMÁNY^c,
EMIL INDREA^d, IRÉN KACSÓ^d, IOAN BRATU^d, ERZSÉBET VERESS^e

ABSTRACT. Five representative potshards collected from the Tășnad-Sere C 52 archaeological site were investigated in order to evaluate the occurring differences of the raw materials used and the technology applied. The structural and compositional differences shown by petrographic analysis (optical microscopy /OM/ and XRD) and FTIR spectroscopy data indicate that according to both the raw materials composition (clay sediments and temper) and the pottery technique the samples studied form two distinct groups.

Keywords: *ancient ceramics, provenance, optical microscopy, PXRD, FTIR spectroscopy*

INTRODUCTION

Correct archaeological conclusions require, besides the typological characterization of the archaeological findings unearthed at a certain site, their complex archaeometric (structural, compositional and technological) characterization. The possible source of the raw materials used and the

^a *Sapientia Hungarian University of Transylvania, Faculty of Technical and Human Sciences, OP 9 CP 4, RO-540485 Targu-Mures, Romania, ebitay@ms.sapientia.ro*

^b *Bosch Group in Hungary, Postbox 331, H-1475 Budapest Hungary, bernadethpataki@gmail.com*

^c *Eötvös Loránd University, Institute of Geography and Earth Sciences, Pázmány Péter allée 1/C, H-1117 Budapest, Hungary*

^d *National Institute for Research and Development of Isotopic and Molecular Technologies, Donath Str. 65-103, RO-400293 Cluj, Romania.*

^e *Transylvanian Museum Society, Napoca Str. 2-4, RO-400750 Cluj, Romania, veresserzsebet@gmail.com*

technical peculiarities together could confirm some of the archaeologist's technology-related suppositions and answer some of the questions related to the dynamics of local or regional trade. [1]

Archaeometric characterization of ceramic vestiges usually is carried out on large sample populations, concluding in the end on the basis of statistical analysis of the experimental data obtained. However, the quantity of the available samples sometimes is strongly limited. This study tries to evaluate the efficiency and reliability of the most frequently applied analytical methods in case of a few-numbered selection of ancient ceramic samples. Five potshard samples collected from the same archaeological site (Tășnad-Sere, one of the Complex 52 dwellings) were investigated in order to establish their differences by the most traditional mineralogical analyses (polarized optical microscopy (OM), powder X-ray diffraction (PXRD) analysis and Fourier transformed (FTIR) spectroscopy).

ARCHAEOLOGICAL CONTEXT

Tășnad is located in Satu-Mare County, NW Romania, on one of the main geothermal areas of the country. The settlement and its surroundings are provenly continuously inhabited at least since the Neolithic Age, their Starčevo-Criș and Coțofeni type finds being among the most important ones from the area. The stratigraphy of the location shows generally an approx. 0.30 m thick vegetal soil layer followed in-depth by a 0.30-0.80 m grayish-black culture layer containing an impressive quantity of ceramic remains, mostly Starčevo-Criș IIIB-IVA dated shards [2-5]

The *Tășnad-Sere* location was necessarily opened to rescue archaeology by reason of the developments effectuated on the neighbouring thermal baths, *Tășnad-Strand* (Figure 1).



Figure 1. Location of the Tășnad Sere archaeological site.

On the site excavated during eight salvage campaigns between 1989 and 2006 more than 100 archaeological complexes were discovered: (dwellings, huts, pits, graves, ditches), each holding varied materials (fine pottery, stone pieces, terracotta figurines, animal bones). The complexes unearthed were mostly Neolithic, however, ten Roman sites dating from the 2nd and 3rd centuries AD (three of them without any material remains) were also found. Although the Roman ceramic material is significantly less, they are of great relevancy, being the first such discovery in the area in archaeological context [5-7].

The five Roman-period potshards selected as representative samples for the present study turned up in each others' close vicinity from one dwelling of Complex 52 (C52), the richest of the sites, and cover the main Roman-period pottery types found at the site.

RESULTS AND DISCUSSION

Macroscopic and microscopic characterization

The specimens selected for this study are representative pot fragments covering the main pottery types found at the site (Figure 2).

Their first grouping was provided by their **macroscopic features** (Table1): color and homogeneity of the ceramic body, the visible porosity and inclusions (type, shape, dimension, relative distribution, orientation) and the occurrent technological failures or deviations (signs of incomplete firing or over-firing, cracks).
















Sample	5-2-1	5-2-2	5-2-3	5-2-4	5-2-5
Outer surface					
Inner surface					
Core					

Figure 2. Macroscopic aspect of the shards selected for characterization.

Sample 5-2-1, a hand-made coarse ceramic tempered with rock fragments and grog (ceramic debris) represents statistically approximately 23 % of the total of findings. It is dark grey, on the outside being covered with a "rusty" crust while on the inner side appears a white, carbonated deposit; most probably both of depositional origin. The homogeneous sample body is moderately porous. Sample 5-2-2 (16 %) is potter's wheel worked from a coarse ceramic paste containing many inclusions of quartzitic sand (naturally tempered?). This shard is sandwich structured with grayish core grading into light reddish-brown zones towards the margins. The wheel-modelled fine ware type sample 5-2-3 (13 %) has homogeneous, uniformly light grey body with approximately plan parallel smooth surfaces.

Shards coded 5-2-4 and 5-2-5 are unique as type. The most porous, slightly cracked, brownish-grey sample 5-2-4 is worked on the potter's wheel from fine ceramic paste and holds a stamped sign on the outside. Sample 5-2-5 is part of a wheel thrown, black painted fine ware with homogeneous grey body; its blackish interior presents stress cracks.

Table 1. Macroscopic features of the samples.

Sample		Macroscopic features		
Code	No.	Color	Paste appearance	Inclusions, pores
5-2-1	49345	dark grey	coarse	moderately porous
5-2-2	49333	sandwich, greyish core, reddish-brown margins	coarse	many inclusions
5-2-3	49301	light grey	fine	-
5-2-4	49275	greyish-brown, stamped	fine	porous
5-2-5	49278	light grey, ornamented	fine	stress cracks inside

Shards coded 5-2-4 and 5-2-5 are unique as type. The most porous, slightly cracked, brownish-grey sample 5-2-4 is worked on the potter's wheel from fine ceramic paste and holds a stamped sign on the outside. Sample 5-2-5 is part of a wheel thrown, black painted fine ware with homogeneous grey body; its blackish interior presents stress cracks.

Microscopic characteristics of the samples are presented by Figure 3 and Table 2.

The 5-2-1 sample has hiatal fabric with anisotropic matrix and many non plastic constituents: mostly monocrystalline quartz associated with some polycrystalline quartz presenting sutured contacts of the individual grains, chert, even a little amount of glass. The argillaceous rock fragments (ARF) in the clayish matrix indicate the use of a clay mixture for the ceramic paste. The sample show limonitic concretions and a grog inclusion with concentric appearance due to the occurred natural transformations and inhomogeneous mixing. This and the anisotropic matrix lead to the conclusion that the possible firing temperature was quite low.

Sample 5-2-2 also has hiatal fabric and presents the same anisotropy characteristics. The identified coarse grain fragments allow a temper grouping. The first group is formed by monocrystalline quartz with strong wavy extinction, moreover strongly oriented quartzite and micaceous quartzite, probably of crystalline metamorphic schist origin. Granitoid fragments and individual K-feldspars are also present. The second group contains vulcanite fragments with plagioclase phenocrysts. Individually broken, zoned plagioclases and weakly altered green amphibole clasts may also originate from the vulcanite. In the vulcanite fragments (and only there) occur a few weakly altered individual biotite grains; epidote-zoisite grains and rutile are also present as accessories. Fine grained sericite-muscovite minerals are present in the groundmass. Opaque minerals with an isometric appearance (possibly magnetite) occur perhaps as a result of the firing process; isotropic clasts, most probably glass fragments can be observed too. The presence of ARFs with some altered rock fragments and limonitic-hematitic nodules lead to the consideration that the raw material used was a *clay mixture*.

The last three samples are very similar from the point of view of their production technology which employed a higher firing temperature. They are not presenting downright coarse grain sizes except of 5-2-4.

In case of sample 5-2-3 the largest amount of the non plastic inclusions is constituted by monocrystalline quartz with wavy extinction. Polycrystalline quartz grains are also present, suggesting a metamorphic origin. K-feldspars and plagioclases are present only in a few amounts. Occasionally normal extinction monocrystalline quartz of volcanic origin also occurs, as well as a few amounts of parallel oriented sericite-muscovite.

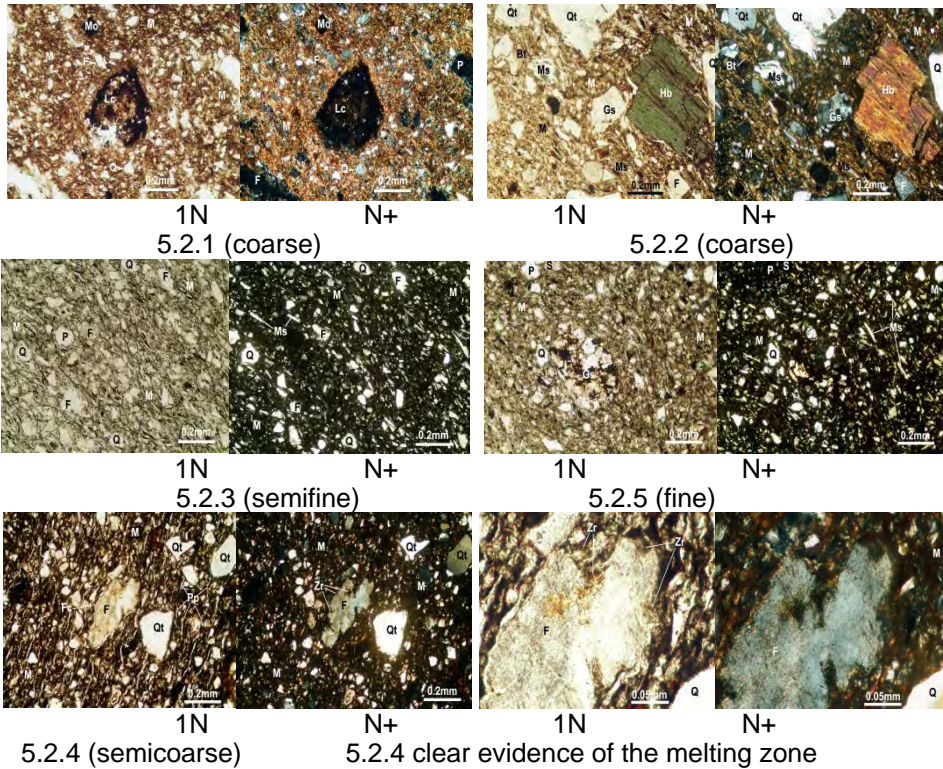


Figure 3. OM petrographic characteristics of the ceramic samples. Microphotographs of thin sections with single nicol (1N) and crossed nicols (N+) M: matrix, Q: quartz, Qt: quartzite, Hb: hornblende, F: feldspar, Ms: muscovite, Bt: biotite, Gs: gneiss, P: pore, Pp: primary pore, Zr: reaction zone

The large amount of finely grained isometric opaque mineral occurring is probably magnetite formed during firing. The possible raw material in this case too was a *mixture of levigated clays*.

Characterization of sample 5-2-5 roughly follows that of sample 5-2-3, evidencing a series of common features.

Sample 5-2-5, as compared to 5-2-3 is finer and more oriented. It contains a large amount of monocrystalline quartz with both wavy and normal extinction; occasionally K-feldspars occur. The very rare occurrence of zoned plagioclases might indicate a volcanic origin. The sample contains a little more of fine flakes of micas in forms of sericites-muscovites with parallel orientation. Large amount of isometric opaque minerals (magnetite) are also present due to the firing process. The ARFs are dark brown. All these features lead to the consideration that it was made by another clay type or the raw material was better mixed.

PROVENANCE STUDY ON A SMALL SELECTION OF ROMAN POTSHARDS

Table 2. Mineralogic-petrographic characterization of the ceramics.

Property	Sample				
	5.2.1	5.2.2	5.2.3	5.2.4	5.2.5
Paste	coarse	coarse	semifine	semicoarse	fine
Grain size distrib.*	18% R 36% A 46% L:	24% R 35% A 41% L	8% R 35% A 57% L:	12% R 35% A 53% L:	4% R 36% A 60% L:
Matrix	surface layer: microcryst.- amorphous; core: amorphous- microcryst.	-sandwich structure; -core:black, amorphous; -ext. layers: brownish- red, cryst.; -intermed.: microcryst.- amorphous.	amorphous	amorphous	amorphous
Texture	mostly oriented; homogeneous, elongated primary pores	oriented	oriented; primary and secondary pores	oriented; many elongated pores and contraction cracks	weakly oriented; secondary pores, contraction cracks
Clasts	ceramoclasts, lithoclasts, crystalloclasts	lithoclasts, crystalloclasts			
OM identified main minerals	quartz, quartzite feldspar muscovite biotite hornblende zircon hematite montmorillonite	quartz, quartzite feldspar hornblende muscovite biotite pyroxene titanite gneiss hematite zircon rutile	quartz, quartzite feldspar muscovite biotite hematite zircon rutile	quartz, quartzite feldspar muscovite biotite hornblende rutile staurolite	quartz, quartzite feldspar muscovite biotite gneiss
Grain size distrib.*	18% R 36% A 46% L:	24% R 35% A 41% L	8% R 35% A 57% L:	12% R 35% A 53% L:	4% R 36% A 60% L:
Firing temp.	800-850°C	≈ 850°C	≈ 1000°C	950-100 °C	>950°C

* R: rudite /pebble/ (mean diameter $d_R > 1$ mm); A: arenite /sand/ ($1 \text{ mm} > d_A > 0.0625$ mm); L: lutite /silt, mud/ ($d_L < 0.0625$ mm) [8]

The presence of well classified, fine grained non plastic inclusions in samples 5-2-3 and 5-2-5 suggests that in this case the raw material should be naturally tempered and the clay was levigated, whilst in case of samples 5-2-1 and 5-2-2 a deliberate tempered raw material was used, allowing to classify the investigated samples into *two groups*.

The 5-2-4 sample stands for a *transition group* between the two previously mentioned being closer to the second one concerning the production technique, the composition and its hiatal fabrics. The production technique seems to imply a higher firing temperature. The raw material was tempered with coarser grained clasts of vulcanite and crystalline schist origin, similarly to sample 5-2-2, containing, in comparison, a larger amount of polycrystalline quartz and micaceous quartzite and less of vulcanites. Additionally, there are a few plagioclases, K-feldspars, green amphiboles; which one's limonitic concretions and textural features allow the supposition of their clayish origin. Clinozoisite also appears as accessory mineral. The sample contains opaque minerals as 5-2-3 and 5-2-5 (though lesser) supposed to be mostly magnetite resulted from the firing process conducted at higher temperature, or longer time, or both, as indicated by the argillaceous rock fragments (ARF) better fired than those present in samples 5-2-1 and 5-2-2.

PXRD analysis

PXRD analysis was used as complementary petrographic method for OM. [9] Through the OM investigation the phenocrysts present in the ceramic samples could be identified, but the information hid in the groundmass have to be explored by PXRD, with the limitation that PXRD is characterized by a 5% threshold.

The results of the PXRD analysis performed on the ceramic selection investigated are presented on Figure 4 and Tables 3 and 4.

The PXRD patterns of the ceramic samples are in concordance with the optical microscopy data (Table 2).

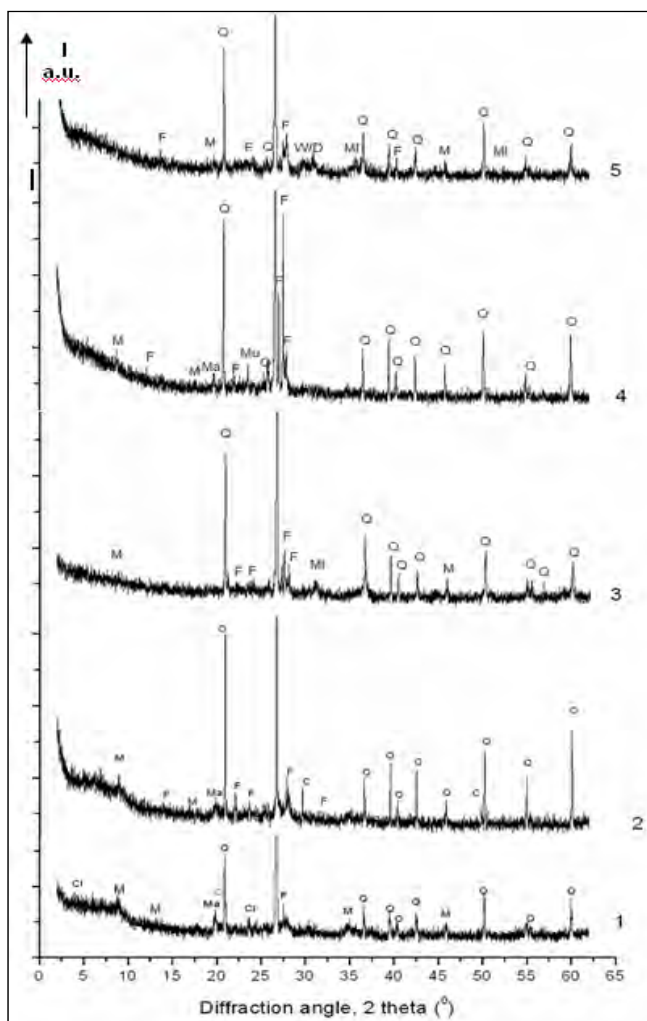


Figure 4. PXRD patterns of the investigated ceramic samples.

Q: quartz, quartzites - SiO_2 ; M: micas (biotite) - $\text{Mg}_{2.001}\text{Al}_{1.999}\text{KSi}_3\text{O}_{12}\text{H}_2$;
 Mu: muscovites - $\text{Al}_{1.94}\text{Si}_{3.86}\text{K}_{0.86}(\text{O}_{12}\text{H}_2)$; $\text{Al}_{1.96}\text{Si}_{3.8}\text{K}_{0.94}(\text{O}_{12}\text{H}_2)$; F: feldspars (mostly
 K- feldspars: orthoclase, microcline - KAlSi_3O_8 , possible some albite - $\text{NaAlSi}_3\text{O}_8$);
 Cl: chlorite - $(\text{Mg,Fe})_3(\text{Si,Al})_4\text{O}_{10}(\text{OH})_2 \cdot (\text{Mg,Fe})_3(\text{OH})_6$.

The high and noisy baselines of the diffractograms indicate that the samples contain a large amount of weakly crystallized material, otherwise on the diffractograms appear the same mineral phases over and over again.

Quartzitic minerals (Q) constitute the dominant mineral phase in each case. The rest of the significant diffraction lines correspond to micas, mostly biotite (Bt): $Mg_{2.001}Al_{1.999}KSi_3O_{12}H_2$; K-feldspars (F) like microcline or orthoclase (Orth): $KAlSi_3O_8$, plagioclases like albite: $NaAlSi_3O_8$; muscovites (Mu) of slightly different compositions like Mu2: $Al_{1.94}Si_{3.86}K_{0.86}O_{12}H_2$ and Mu3: $Al_{1.96}Si_{3.8}K_{0.94}O_{12}H_2$; finally, in case of sample 5-2-3 and 5-2-5, an reduced amount of mullite (M): $Al_6Si_2O_{13}$ (Table 4).

Table 3. Relative intensities I_R of the main mineral components

Sample	I_R (%)					
	Bt	Mu2	Mu3	Orth	M	Q
5-2-1	11.2	30.0	-	16.6	-	42.2
5-2-2	9.5	41.8	-	8.9	-	39.8
5-2-3	8.3	25.3	7.7	-	1.3	57.4
5-2-4	2.5	4.0	62.4	-	-	31.1
5-2-5	6.2	36.5	4.8	-	3.8	48.7

The results of the semi-quantitative mineralogical phase analysis permitted by the diffraction data obtained on the five ceramic samples are presented in Table 4.

Table 4. Semiquantitative results of the XRD analysis.

Sample	Mineral*						
	Q	F	Plg	Phy	Mi	Gh	G
5-2-1	xxxx	x	xx	x	x	X	
5-2-2	xxxx	x	xx	x			
5-2-3	xxxx	x	xx			X	x
5-2-4	xxxx	xx	xxx	x	tr		
5-2-5	xxxx	x	xx		x		

Q: quartz; F: K-feldspars; Plg: plagioclases; Phy: "10 Å phases"; Mi: micas; Gh: gehlenite; G: goethite.

*Number of (x) characterize the mineral phase abundance; tr: only traces.

The relative PXRD peak intensities of the main mineral constituents in case of the different samples (Table 3) as well as the variant heavy mineral contents observed in the OM study indicate that the ceramics investigated, although from the very same archaeological site, are made from raw

materials obtained from at least three different sources. The differences of the firing mineral phases indicate different pottery technologies (different firing conditions) also.

As might be seen above, characteristically all investigated samples presented dominantly high quartz content and contained larger amounts of plagioclases than K-feldspars. Sample 5-2-4 contains some traces of mica, showing comparatively larger K-feldspar and plagioclase content, while both "10 Å phases" and micas are totally absent in case of 5-2-3 ("10 Å phases" are dehydroxylated illite-like phases formed from phyllosilicates which remain in the ceramic material after being fired at relatively low temperatures [10]).

The mineral composition of the supposed raw materials generally corresponds to that of samples 5-2-2, 5-2-3 and 5-2-4, indicating a possible local origin, however, the presence of micas in 5-2-1 and 5-2-5 denote that in these cases the green paste might be prepared using different clay(s).

Due to the very reduced quantity of the 10 Å phases, the ceramics had to be fired above 700-750°C. In samples 5-2-1 and 5-2-3 even gehlenite ($\text{Ca}_2\text{Al}[\text{AlSiO}_7]$) could be observed, which is peculiar to the fired pots (gehlenite appears at 800°C). [9]

The moderate presence of 10 Å phases in items 5-2-1, 5-2-2 and 5-2-4 could be attributed to their incipient re-hydration during the burial.

PXRD data in conjunction with the optical microscopy data allowed the identification of several thermal processes, mainly affecting the clayish matrix. The most important such processes are sintering (samples 5-2-1 and 5-2-2); formation of isotropic, amorphous and/or glassy areas in the matrix (5-2-3, 5-2-4, 5-2-5); developing of secondary pores and of stress cracks (5-2-3, 5-2-4, 5-2-5); partial decomposition of micas (5-2-3, 5-2-4, 5-2-5); appearance of reaction zones between the quartz clasts and matrix (especially in 5-2-4); melting of quartz rims and formation of a scalloped texture (5-2-4); finally, the almost totally lack of the small 2θ value kaolinite lines in the XRD of all ceramic samples.

On basis of these observations, the firing temperature estimated even in case of samples 5-2-1 and 5-2-2 was at least of 800°C, while in case of samples 5-2-3, 5-2-4 and 5-2-5 a firing temperature of approximately 1000°C can be assumed.

FTIR spectroscopy

FTIR spectra and the resultant data are presented in the Figure 5 and 6, and respectively in Table 5. Absorption frequencies were assigned considering the available literature data referring to the most common clay mineral components and previous investigations carried on (mainly ancient) ceramic samples [9-19].

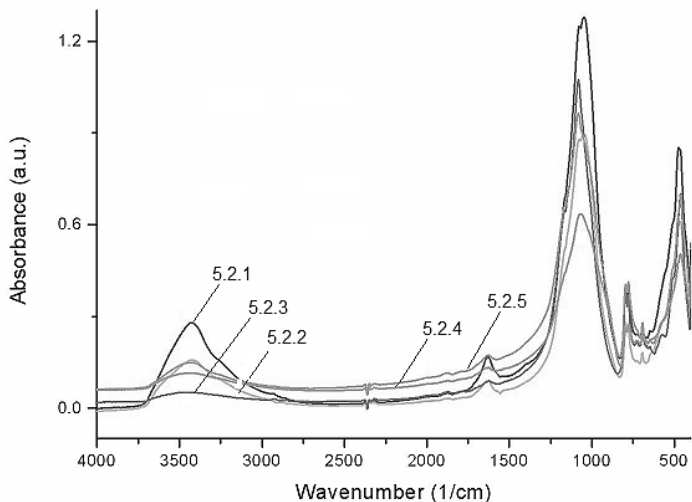


Figure 5. FTIR spectra of the ceramic samples (4000-400 cm^{-1}).

Figure 6 shows in more details the absorption bands of the 1600-400 cm^{-1} spectral domain (the SiO / AlO / MeO region).

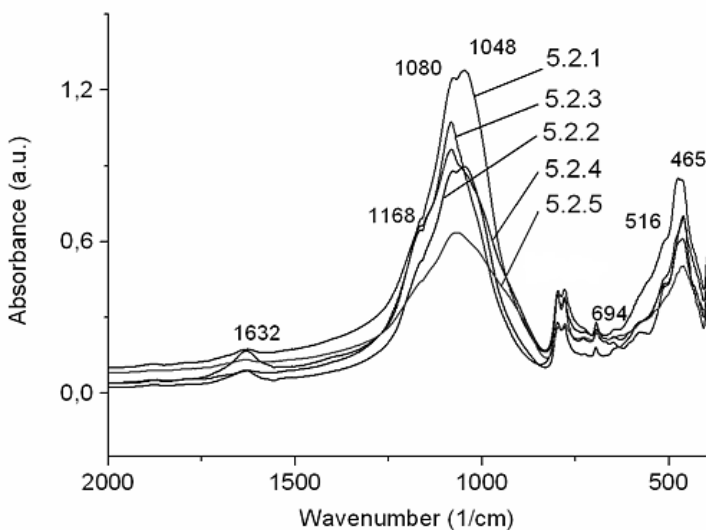


Figure 6. Extended FTIR spectra in the SiO / AlO / MeO domain.

Table 5. Experimental absorption frequencies and their assignments. [7-12]

Absorption frequencies (cm ⁻¹)					Assignment
5-2-1	5-2-2	5-2-3	5-2-4	5-2-5	
3429	3425	3455	3429	3439	Al-O-H (Mo)
			3333 sh		H-O-H, free O-H stretch of ads. water (Mo, Mu)
3285 sh	3285 sh				
2927		2927	2929		
2856		2857			
1631 m	1629 m	1625 v.w	1629 v.w	1631 v.w	H-O-H (Mo)
1162 sh	1162 sh	1164	1166 sh	1164 sh	H-O-H (Mo) Si-O (Mu)
1078	1078	1084	1082	1080	Si-O (Q)
1048	1046		1046 sh	1050	Si-O (Mo) Si-O-Si (Mu)
797	798	797	797	799	Si-O Si-O ⊥ opt. axis (Q) (Al,Mg)-OH (Mo) Si-O-Al (Mu)
780	778	780	778	780	Si-O opt. axis (Q)
722	725	729	724 sh	723	Si-O-Al (Mu)
693	695	695	693	693	Si-O-Al (Mo, Mu) Si-O (Q)
	572 sh	577	577 sh	575 sh	Al-O-H (Mo)
553 sh					Si-O (Q, Mu)
512 sh	510 sh	512	510 sh	510 sh	Si-O (Q)
476	472 sh		478 sh	474 sh	Si-O(Q, Mo, Mu)
465	461	461	461	463	Si-O (Q, Mu) Si-O-Mg (Mo)
433 sh	431				Si-O (Q, Mo, Mu)

Abbreviations: sh: shoulder, s: sharp, m: medium intensity, w: weak, v, w: very weak; Q: quartz, Mo: montmorillonite, Mu: muscovite.

Infrared spectroscopy is a sensitive monitor of thermal processes (dehydration, dehydroxylation, redox transformations) occurred during the firing of clay minerals. Between 300-500°C the dehydroxylation of octahedral layers of most clay minerals occur, as reflected by the marked attenuation of the bands due to Al-OH in-plane vibration at 920 cm⁻¹ and respectively to translational vibrations involving OH at 522 cm⁻¹. By attaining 600°C the intensity of hydroxyl bands in the 3700-3200 cm⁻¹ region, respectively at 1100 and 920 cm⁻¹ strongly decrease or disappear. The silicate structure collapses; a broad, nearly symmetrical band is formed at 1030 cm⁻¹.

Simultaneously, the iron oxides attributed 540 and 580 cm^{-1} bands appear. Between 700-900°C crystallized hematite is formed, under reducing conditions magnetite also may form. The peak appearing at 572 cm^{-1} is due to Fe-O vibration of iron oxides, but the exact nature of oxide can not be determined from the IR spectrum. Quartz and feldspar are usually present in pottery clays. Bands occurring at 462 and 514 cm^{-1} are assigned to mixed Si-O-Si and O-Si-O bending mode; the band at 470 cm^{-1} is due to Si-O stretching. Sharp bands around 790 along with 695 cm^{-1} in all samples means the presence of quartz (Si-O).

Concerning the discussed samples, the relative weakness or the absence of characteristic OH bands around 3400 cm^{-1} and at 1600 cm^{-1} and the presence of a broad symmetry band centered around 1050 cm^{-1} in all cases means that all items were made of disordered clays and had to be fired above 600°C. The presence and the intensity of the 3400 cm^{-1} and 1600 cm^{-1} peaks in this case depends on the rehydration processes taking place during the burial, in function of the environmental conditions and the ceramic composition and structure. Consequently, the most porous sample 5-2-1 shows the most intense hydroxyl peaks while they are almost totally missing from the spectrum of the most compact 5-2-3 probe.

Well resolved distinct peaks at 540 and 580 cm^{-1} reveal the presence of iron oxides, confirm that firing temperature was above 600°C, and indicate that the sample was fired in oxidizing conditions, or at least that air has to be present from the beginning of cooling, which did enable (at least partly) the oxidation of the Fe content to Fe_2O_3 causing the red color of the pottery (air admission during cooling is still a common practice for coloration of the baked clays). The band around 540 cm^{-1} with a weak shoulder at 580 cm^{-1} in the sandwich structured items indicate that the sample is fired under reducing atmosphere, and air (oxygen) is admitted only at lower temperature (sandwich structure: inner black layer with outer red surface – sample 5-2-2).

The FTIR data and their possible interpretation, in concordance with the conclusions resulting from the OM and XRD analysis, confirm the presence of rehydrated amorphous glassy phases and the (re)apparition of $\text{Fe}(\text{OH})_2$ and/or $\text{FeO}(\text{OH})$. The presence of rehydrated clayish minerals is not excluded either, but their presence is of minimal importance.

CONCLUSIONS

The Tășnad-Sere Roman potshard selection subjected to investigation is formed by five samples, chosen as the most representative ones regarding the studied archaeological context.

Optical microscopy (OM), PXRD and FTIR spectral analysis are all in agreement when allowing the classification of the samples into two distinct groups and a transitional item.

The first group (samples 5-2-1 and 5-2-2) is formed by deliberate tempered ceramics fired at lower temperatures (850-950°C). The temper in these cases seems to be partly rock fragments as vulcanites and crystalline rocks (granitoides and crystalline schists). These ceramics could not be used as cooking wares due to their hiatal fabric resulted from the production technology: the thermal dilatation differences appearing in the fine and coarse grain connection zones eventually would cause the break of the ceramic body.

The specimens of the second group (5-2-3 and 5-2-5) were produced from naturally tempered levigated clay paste fired at higher temperatures, resulting suitable cooking wares.

Sample 5-2-4 is transitional between the first and the second group, its mineralogical characteristics approaching it to the first group while technologically (modelling, firing temperature and conditions) matching with the second one.

The concordance of the results obtained by the OM, PXRD and FTIR spectroscopy analysis proves that the pursued archaeometric study is fairly efficient and reliable to categorize and roughly estimate the provenance of the artifacts even in case of a few-numbered selection.

However, for correct conclusions regarding the provenance of the raw materials used it is compulsive the completion of the investigation with element analysis (especially trace element characterization) of the investigated items as well as of the corresponding clayish soils in the neighbourhood of the site (in ancient pottery proximity of the outcrops could assure considerable economic savings). In order to correctly characterize the technical parameters (especially the firing conditions) applied to the production process it is necessary to proceed to supplementary determinations. (like thermoanalytical measurements). [23]

EXPERIMENTAL

In order to estimate the variability of the raw material sources and of the technology used, after a macroscopic characterization, the samples were investigated by petrographic-mineralogic thin layer microscopy (OM), PXRD analysis and FTIR spectroscopy.

Polarized light microscopy was carried out in transmission mode on polished thin sections of $d=30\ \mu\text{m}$, with a Leitz Wetzlar Laborlux 11 Pol microscope provided with Nikon Coolpix 995 camera.

PXRD analysis was performed using a BRUKER D8 Advance diffractometer (working parameters: 45 kV, 45mA, Ni filtered Cu K_{α} radiation collimated with Soller slits, step-scanning mode with $\Delta 2\theta$ of 0.01° steps, spectral pure Al_2O_3 internal standard). The sample support was uniformly coated with the finely pulverized ceramic sample (agate ball mill, mean particle diameter $< 63\ \mu\text{m}$, PVC-based adhesive). The *crystalline phase composition* was determined using the MATCH! phase identification software and the IUCr/COD/AMCSD reference database [20-22].

FTIR absorption spectra were recorded on KBr-pelletized samples (1 mg finely pulverized sample to 300 mg KBr) in the $4000\text{-}400\ \text{cm}^{-1}$ region with a JASCO FTIR-6100 spectrometer ($1.0\ \text{cm}^{-1}$ resolution).

ACKNOWLEDGEMENTS

The presented work is partly supported by the research project entitled "Transylvanian technical and cultural legacy. Industrial archaeology, archaeometallurgy and archaeometry" started by the Science and Engineering Department of the Research Institute of the Transylvanian Museum Society.

Our special thanks to Dr. Viorel Ciubotă and Róbert Gindele from the Satu Mare County Historical Museum for entrusting the samples.

REFERENCES

1. R. Martineau, A.V. Walter-Simonnet, B. Grobéty, M. Buatier, *Archaeometry*, **2007**, 49, 23.
2. N. Iercoşan, , *Studii și Comunicări Satu Mare*, **1994-1995**, 11-12, 9.
3. C. Astalos, U. Sommer, C. Virag, *Archaeology International*, **2012-2013**, 16, 47.
4. C. Virag, "Some aspects about the Neolithic settlement from Tasnad (Satu Mare County, Romania)", C. Virag, Ed., Proceedings of the Int. Conf. on Neolithic Cultural Phenomena in the Upper Tisa Basin, Satu Mare 2014, Editura Muzeului Sătmărean, **2015**, 97.
5. *** "Cronica cercetărilor arheologice din România – campania 2004". XXXIX. Sesiune Națională de Rapoarte Arheologice, Jupiter-Mangalia 2005, M.V. Angelescu, I. Oberlander-Târnoveanu, F. Vasilescu, Eds.: cIMeC – Institutul de Memorie Culturală, Bucuresti, ISBN 973-7930-03-7, **2005**, 375.

6. *** "Cronica cercetărilor arheologice din România – campania 2005", XL. Sesiune Națională de Rapoarte Arheologice, Constanța 2006, M.V. Angelescu, F. Vasilescu, Eds.; cImeC – Institutul de Memorie Culturală, Bucuresti, ISBN 973-7930-07-X, **2006**, 359 and 479.
7. *** "Cronica cercetărilor arheologice din România – campania 2006", XLI. Sesiune Națională de Rapoarte Arheologice, Tulcea 2006, M.V. Angelescu, F. Vasilescu, Eds.; cImeC – Institutul de Memorie Culturală, Bucuresti, ISBN 978-973-87004-9-9, **2007**, 365 and 477.
8. R.L. Folk, P.B. Andrews, D.W. Lewis, *New Zealand Journal of Geology and Geophysics*, **1970**, 13, 937.
9. J. Kiuberis, A. Merkevičius, R. Juškėnas, A. Kareiva, *Materials Science*, **2004**, 10, 334.
10. G. Cultrone, C. Rodriguez-Navarro, E. Sebastian, O. Cazalla, M.J. de la Torre, *European Journal of Mineralogy*, **2001**, 13, 621.
11. De Benedetto, G.E., Laviano, R., Sabbatini, L., Zambonin, P.G., *Journal of Cultural Heritage*, **2002**, 3, 177.
12. S. Shoval, *Optical Materials*, **2003**, 24, 117.
13. R. Venkatachalapathy, E. Manoharan, S. Dhanapandian, T. Sundareswaran, K. Deenadayalan, "Concepts of Biophysics", Kumar, A., Ed., APH (New Delhi). **2005**, 71.
14. R. Palanivel, G. Velraj, *Indian Journal of Pure and Applied Physics*, **2007**, 45, 501.
15. C. Manoharan, K. Veeramuthu, R. Venkatachalapathy, T. Radhakrishna, R. Ilango, *Lithuanian Journal of Physics and Technical Sciences*, **2008**, 48, 195.
16. R. Ravisankar, S. Kiruba, P. Eswaran, G. Senthilkumar, A. Chandrasekaran, *E-Journal of Chemistry*, **2010**, 7, S185.
17. R. Palanivel, U.R. Kumar, *Romanian Journal of Physics*, **2011**, 56, 195.
18. S. Kramar, J. Lux, *Materials and technology*, **2015**, 49, 503.
19. S. Kiruba, S. Ganesan, *Spectrochimica Acta Part A: Molecular and Biomolecular Spectroscopy*, **2015**, 145, 594.
20. <http://www.crystalimpact.com/match/>
21. <http://sdpd.univ-lemans.fr/cod>
22. R.T. Downs, M. Hall-Wallace, *American Mineralogist*, **2003**, 88, 247.
23. P. Comodi, S. Nazzareni, D. Perugini, M. Bergamini, *Periodico di Mineralogia*, 2006, 75, 95.

THERMAL ANALYSIS OF PURE AND MULTISUBSTITUTED HYDROXYAPATITE PASTES

**EDIT FORIZS^a, FIRUTA GOGA^a, ALEXANDRA AVRAM^a,
AURORA MOCANU^{a,*}, IOAN PETEAN^a, OSSY HOROVITZ^a,
MARIA TOMOAIA-COTISEL^{a,b}**

ABSTRACT. The thermal stability over time of the pure and multisubstituted hydroxyapatite (HAP) pastes, doped with magnesium, silicon, strontium and zinc, synthesized using aqueous precipitation method were investigated by thermal analyses (TG-DTA). Results show high thermal stability of pure and multidoped hydroxyapatite pastes, up to 1000 °C and even after ageing for 1 year, making these pastes promising nano materials for medical applications.

Keywords: *hydroxyapatite, doped hydroxyapatites, paste, thermal analysis*

INTRODUCTION

The hydroxyapatite, $\text{Ca}_{10}(\text{PO}_4)_6(\text{OH})_2$ (HAP), composition is similar to bone, has good biocompatibility and bioactivity therefore is increasingly used in medicine, especially in repairing bone defects as bone grafts, coating material for metallic implants, dental implants, and drug delivery systems [1-3]. Nanocrystalline HAP paste is suitable bone substitute in dental and orthopedic surgery for filling bone defects in minimally invasive surgery. HAP pastes have various applications: as tooth pastes for remineralising and repairing of teeth enamel, for the fabrication of 3D printed bioactive ceramic scaffolds [2, 4].

The biological properties of HAP based materials can be improved by the incorporation of divalent essential metal ions. The effect of silicon [5, 6], magnesium [7, 8], strontium [9, 10], manganese [11] and zinc [11-13] as doping elements on characteristics of hydroxyapatite with potential biomedical applications has been studied extensively [1, 2, 11].

^a Babeş-Bolyai University, Faculty of Chemistry and Chemical Engineering, 11 Arany János str., RO-400028, Cluj-Napoca, Romania

^b Academy of Romanian Scientists, 54 Splaiul Independentei, RO-050094 Bucharest, Romania

* Corresponding author amocanu@chem.ubbcluj.ro

Multidoped hydroxyapatites with improved properties are more suitable for biomedical application, thus many recent studies have focused on simultaneous doping of hydroxyapatite with copper, zinc and carbonate ions [14]; manganese and strontium [15], strontium and copper [16] and magnesium, zinc and silicon [17, 18]. Hydroxyapatite co-doped with strontium and magnesium, strontium and zinc, magnesium and zinc [19] and simultaneously doped with three essential elements Sr, Mg and Mn [20] and Sr, Mg and Zn [21] were also reported.

Continuing our interest in the field of bioactive materials [22-26] we present here some results concerning thermal stability of three HAP pastes simultaneously doped with essential elements magnesium, strontium, silicon and zinc, with previously described compositions [27]. Water content of pastes was determined by thermal analysis. The thermal stability of the pastes was monitored for one year, namely thermal analyses were performed after 4 months and one year from their preparation.

RESULTS AND DISCUSSION

Thermal stability over time, of four hydroxyapatite pastes, with previously reported composition [27] were investigated, namely pure hydroxyapatite (HAP, 1) and doped HAP pastes, containing Mg 1.5 wt%, Zn 0.2 wt% and Si 0.2 wt% (2); Mg 1.5 wt%, Zn 0.2 wt%, Si 0.2 wt% and Sr 5 wt% (3) and Mg 1.5 wt%, Zn 0.2 wt%, Si 0.2 wt% and Sr 10 wt% (4). The pure and doped pastes kept under storage conditions for 4 months, respectively 1 year, at room temperature in well-closed conditions, were heated in air with the rate of 10 °C/min from the room temperature up to 1000 °C. Thermogravimetric data are presented in Table 1 and in Figures 1 and 2.

Table 1. Thermogravimetric data of pure and doped HAP pastes, after 4 months

Paste	Temperature (°C)	Weight loss (%)
1. HAP	30-160	65.96
	160-1000	1.19
	30-1000	67.15
2. HAP 1.5%Mg, 0.2%Si, 0.2%Zn	30-162	71.08
	162-1000	1.68
	30-1000	72.76
3. HAP 1.5%Mg, 0.2%Si, 0.2%Zn, 5%Sr	30-163	64.11
	163-1000	1.67
	30-1000	65.78
4. HAP 1.5%Mg, 0.2%Si, 0.2%Zn, 10%Sr	30-150	53.22
	150-1000	1.93
	30-1000	55.15

THERMAL ANALYSIS OF PURE AND MULTISUBSTITUTED HYDROXYAPATITE PASTES

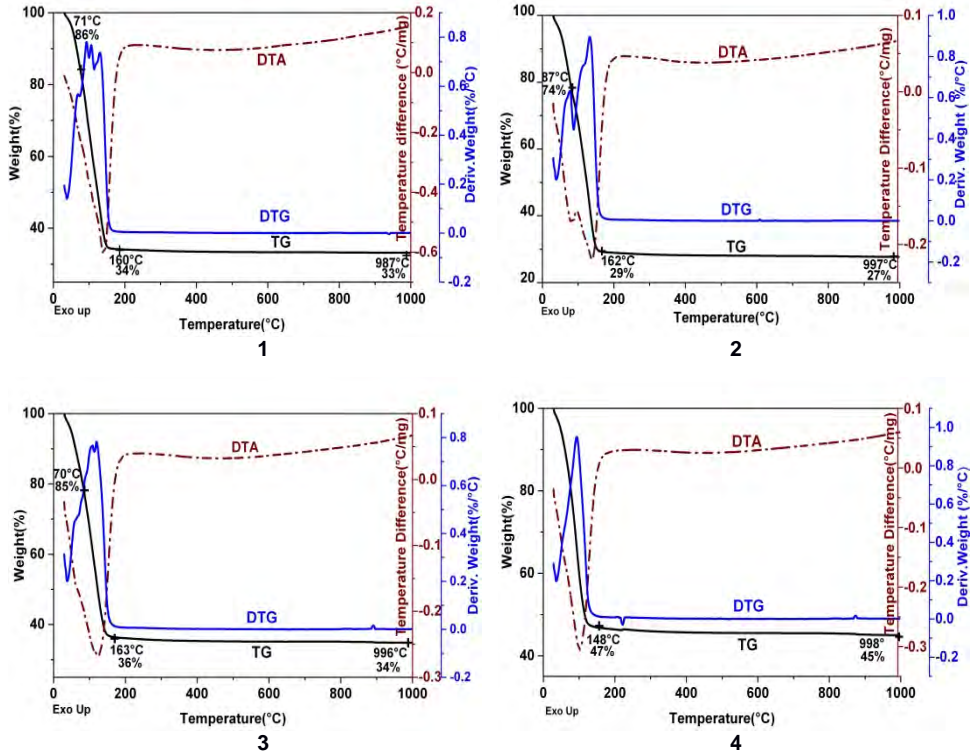


Figure 1. Thermal curves of the four pastes: 1) pure HAP (sample 1); 2) HAP 1.5%Mg, 0.2%Si, 0.2%Zn (sample 2); 3) HAP 1.5%Mg, 0.2%Si, 0.2%Zn, 5%Sr (sample 3); 4) HAP 1.5%Mg, 0.2%Si, 0.2%Zn, 10%Sr (sample 4), after 4 months.

Thermal analysis shows that the thermal curves (TG, DTA) of the pure and the doped HAP pastes have the same shape in the range of 30-1000 °C. After 4 months no significant differences were observed in thermal behavior. The only differences refer to the moisture content of the sample. Thermogravimetric monitoring of weight loss shows that weight of all samples decreases continuously with increasing temperature. The highest weight loss occurs in the range 30-200 °C and can be attributed to very high water content of pastes, since the water molecules surround the hydroxyapatite particles. The corresponding DTA data indicate an endothermic transformation for all samples at around 160 °C (Fig. 1 and 3).

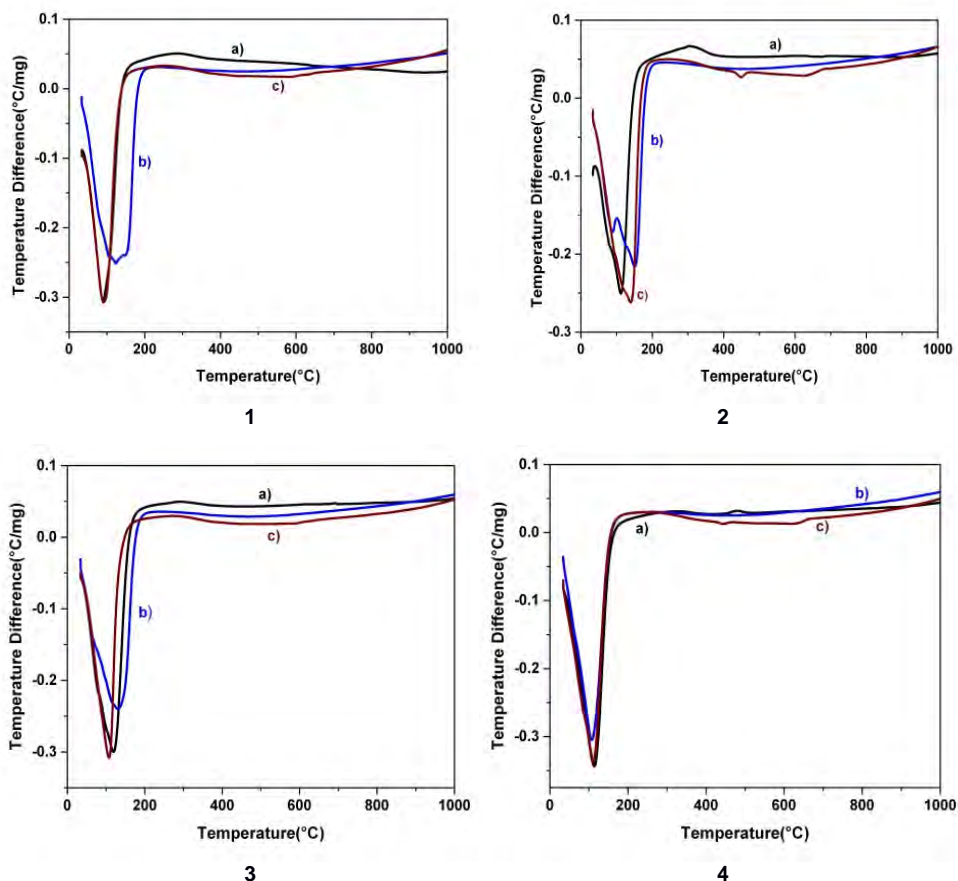


Figure 2. Comparative DTA curves for fresh (a), 4 months (b) and 1 year (c) old samples: 1) pure HAP (sample 1); 2) HAP 1.5%Mg, 0.2%Si, 0.2%Zn (sample 2); 3) HAP 1.5 % Mg, 0.2%Si, 0.2%Zn, 5%Sr (sample 3); 4) HAP 1.5% Mg, 0.2%Si, 0.2%Zn, 10%Sr (sample 4).

The weight loss in the range 30-200 °C was 53.5-71.3%; it indicates the removal of moisture and physically adsorbed water, followed in the temperature range of 200-1000 °C by small gradual weight loss, 1-2%, which can be associated with the removal of chemically adsorbed water on the surface of HAPs particles, in agreement with the literature data [27, 28].

Above 200 °C the thermogravimetric curves became parallel to each other and up to 1000 °C (Figure 1 and 3) with x-axis. Pure and doped HAP pastes are very stable up to 1000 °C, as found for at least one year aged samples.

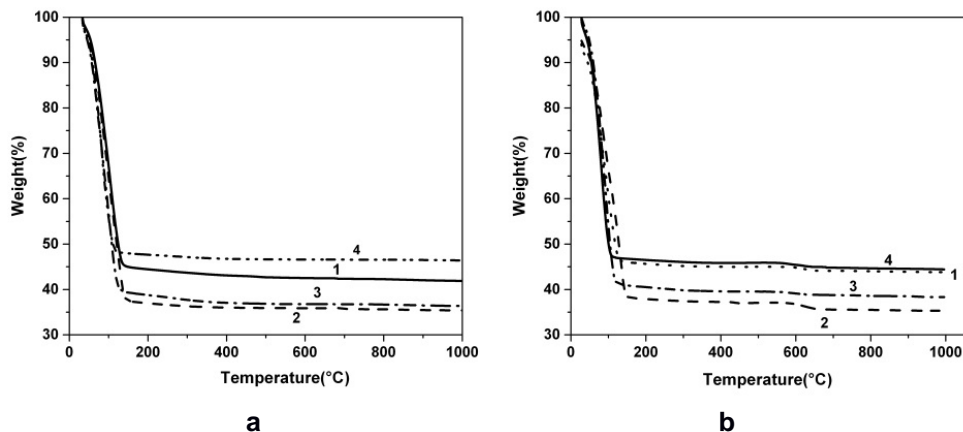


Figure 3. TG curves for fresh pastes (a) and 1 year aged (b) pastes: 1) pure HAP (sample 1); 2) HAP 1.5% Mg, 0.2%Si, 0.2%Zn (sample 2); 3) HAP 1.5%Mg, 0.2%Si, 0.2%Zn, 5%Sr (sample 3); 4) HAP 1.5%Mg, 0.2%Si, 0.2%Zn, 10%Sr (sample 4).

The pure and doped hydroxyapatite pastes may contain small content of carbonate, whose decomposition cause insignificant mass loss. The moisture content of these pastes is high but comparable with those found for commercial available pure HAP paste [27].

CONCLUSIONS

The results of thermal analysis confirm high thermal stability of pure and multidoped hydroxyapatite pastes, up to 1000 °C, even after ageing for 1 year from their preparation. The thermal behavior of pure and doped hydroxyapatite pastes in time shows that this depends mainly on the loss of physically adsorbed and chemically bounded water. The high stability of these ceramic pastes without significant modifications in the structure of pastes makes them appropriately for further use in biomedical applications, as drug delivery systems of antimicrobials and for coating of metallic implants.

EXPERIMENTAL SECTION

Materials and methods

The following compounds were used as starting materials: $\text{Ca}(\text{NO}_3)_2 \cdot 4\text{H}_2\text{O}$, $(\text{NH}_4)_2\text{HPO}_4$, $\text{Mg}(\text{NO}_3)_2 \cdot 6\text{H}_2\text{O}$, $\text{Zn}(\text{NO}_3)_2 \cdot 6\text{H}_2\text{O}$, $\text{Sr}(\text{NO}_3)_2$ and tetraethyl orthosilicate $(\text{C}_2\text{H}_5\text{O})_4\text{Si}$, (TEOS). Pure HAP and three doped

hydroxyapatites with the same content of Mg, Zn, Si and different contents in Sr were obtained by a wet precipitation method, previously reported [6, 10, 13, 26]. All chemicals were reagent grade procured from Merck and Sigma-Aldrich, solutions were prepared with double distilled water, deionized in Elgastat purification system.

Synthesis of pure HAP and doped HAP

A pure HAP paste was prepared by wet precipitation method, previously described [6, 10, 13, 26]; using equal volumes of aqueous 0.25 M Ca^{2+} solutions and 0.15 M PO_4^{3-} solutions. The pH of the reaction mixture was fixed at 11.5 using 25% ammonia solution (Ca/P atomic ratio 1.67). The reaction mixture was stirred 24 h at 22 °C, and 24 h at 70 °C. The precipitated solid phase was filtered, washed with distilled water until pH 7. The wet precipitate, considered paste was used as it is.

The doped hydroxyapatites were obtained similarly, with the following modification: the Ca^{2+} containing solution contains also the doping cations (0.25 M in $\text{Ca}^{2+}+\text{Mg}^{2+}+\text{Zn}^{2+}+\text{Sr}^{2+}$) in calculated amount for the proposed composition of the doped HAP. The anions containing solution (0.15 M in $\text{PO}_4^{3-}+\text{SiO}_4^{4-}$) was obtained from $(\text{NH}_4)_2\text{HPO}_4$, and tetraethyl orthosilicate, TEOS. The pH was fixed at 11.5 by adding a 25% ammonia solution. Equal volumes of the two solutions were mixed at 22 °C keeping the mole ratio (Ca+Mg+Zn+Sr)/(P+Si) at the value of 1.67. The obtained pastes were processed in the same way as the pure HAP.

Characterization methods

Thermal behavior of pure HAP and doped HAP pastes was determined by thermogravimetric analysis (TGA), for the temperature range from 30-1000 °C, using Universal SDTQ600 TA Instruments. Samples were heated in alumina crucibles at a constant heating rate of 10 °C/min, in flowing air, using simultaneous TG/DTG-DTA/DSC techniques.

ACKNOWLEDGMENTS

Authors acknowledge the financial support from the Executive Agency for Higher Education, Research, Development and Innovation Funding (UEFISCDI) through grant no. 83.

REFERENCES

1. M. Bayani, S. Torabi, A. Shahnaz, M. Pourali, *Biotechnology & Biotechnological Equipment*, **2017**, 31(2), 215.
2. N. Eliaz, N. Metoki, *Biomaterials*, **2017**, 10(4), 334.
3. V. Hruschka, S. Tangl, Y. Ryabenkova, P. Heimel, D. Barnewitz, G. Möbus, C. Keibl, J. Ferguson, P. Quadros, C. Miller, R. Goodchold, W. Austin, H. Redl, T. Nau, *Scientific Reports*, **2017**, 7:43425.
4. L. Witek, Y. Shi, J. Smay, *Journal of Advanced Ceramics*, **2017**, 6(2), 157.
5. Z.-Y. Qiu, I.-S. Noh, S.-M. Zhang, *Frontiers of Materials Science*, **2013**, 7(1), 40.
6. Gh. Tomoaia, A. Mocanu, I. Vida-Simiti, N. Jumate, L.-D. Bobos, O. Soritau, M. Tomoaia-Cotisel, *Materials Sciences and Engineering C*, **2014**, 37, 37.
7. D. Laurencin, N. Almora-Barrios, N.H. de Leeuw, C. Gervais, C. Bonhomme, F. Mauri, W. Chrzanowski, J.C. Knowles, R.J. Newport, A. Wong, Z. Gan, M.E. Smith, *Biomaterials*, **2011**, 32, 1826.
8. A. Farzadi, F. Bakhshi, M. Solati-Hashjin, M. Asadi-Eydivand, N.A.A. Osman, *Ceramics International*, **2014**, 40, 6021.
9. C.F. Marques, A. Lemos, S.I. Vieira, O.A.B. da Cruz e Silva, A. Bettencourt, J.M.F. Ferreira, *Ceramics International*, **2016**, 42, 2706.
10. P.T. Frangopol, A. Mocanu, V. Almasan, C. Garbo, R. Balint, G. Borodi, I. Bratu, O. Horovitz, M. Tomoaia-Cotisel, *Revue Roumaine de Chimie*, **2016**, 61(4-5), 337.
11. E. Boanini, M. Gazzano, A. Bigi, *Acta Biomaterialia*, **2010**, 6, 1882.
12. Z.-S. Tao, W.-S. Zhou, X.-W. He, W. Liu, B.-L. Bai, Q. Zhou, Z.-L. Huang, K.-K. Tu, H. Li, T. Sun, Y.-X. Lv, W. Cui, L. Yang, *Materials Science and Engineering C*, **2016**, 62, 226.
13. C. Garbo, M.Sindilaru, A. Carlea, Gh. Tomoaia, V. Almasan, I. Petean, A. Mocanu, O. Horovitz, M. Tomoaia-Cotisel, *Particulate Science and Technology*, **2017**, 35(1), 29.
14. O. Livitska, N. Strutynska, I. Zatoovsky, I. Nikolenko, N. Slobodyanik, Y. Prylutsky, M. Epple, O. Prymak, A. Byeda, *Mat.-wiss. u. Werkstofftech.*, **2016**, 47(2-3), 85.
15. Y. Huang, H. Qiao, X. Nian, X. Zhang, X. Zhang, G. Song, Z. Xu, H. Zhang, S. Han, *Surface and Coating Technology*, **2016**, 291, 205.
16. Y. Huang, M. Hao, X. Nian, H. Qiao, X. Zhang, X. Zhang, G. Song, J. Guo, X. Pang, H. Zhang, *Ceramics International*, **2016**, 42, 11876.
17. Gh. Tomoaia, M. Tomoaia-Cotisel, L.-B. Pop, A. Pop, O. Horovitz, A. Mocanu, N. Jumate, L.-D. Bobos, *Revue Roumaine de Chimie*, **2011**, 56 (10-11), 1039.
18. Gh. Tomoaia, O. Soritau, M. Tomoaia-Cotisel, L.-B. Pop, A. Pop, A. Mocanu, O. Horovitz, L.-D. Bobos, *Powder Technology*, **2013**, 238, 99.
19. O. Kaygili, S. Keser, *Materials Letters*, **2015**, 141, 161.

20. M.P. Moreira, G.D. de Almeida Soares, J. Dentzer, K. Anselme, L.A. de Sena, A. Kuznetsov, E.A. dos Santos, *Materials Science and Engineering C*, **2016**, *61*, 736.
21. D. Gopi, E. Shinyjoy, L. Kavitha, *Ceramics International*, **2015**, *41*, 5454.
22. E. Forizs, A. Debreczeni, A. Patrut, A.-Z. Kun, I.B. Cozar, L. David, I. Silaghi-Dumitrescu, *Revue Roumaine de Chimie*, **2010**, *55(10)*, 697.
23. P. Bombicz, J. Madarasz, E. Forizs, M. Czugler, G. Pokol, S. Gal, A. Kalman, *Zeitschrift fur Kristallographie*, **2000**, *215*, 317.
24. F. Goga, E. Forizs, A. Avram, A. Rotaru, A. Lucian, I. Petean, A. Mocanu, M. Tomoaia-Cotisel, *Revista de Chimie (Bucharest)*, **2017**, *68(6)*, 1193.
25. O. Horovitz, Gh. Tomoaia, A. Mocanu, T. Yupsanis, M. Tomoaia-Cotisel, *Gold Bulletin*, **2007**, *40(4)*, 295.
26. G. Furtos, M. Tomoaia-Cotisel, C. Garbo, M. Senila, N. Jumate, I. Vida-Simiti, C. Prejmerean, *Particulate Science and Technology*, **2013**, *31(4)*, 392.
27. F. Goga, E. Forizs, G. Borodi, Gh. Tomoaia, A. Avram, R. Balint, A. Mocanu, O. Horovitz, M. Tomoaia-Cotisel, *Revista de Chimie (Bucharest)*, **2017**, *68(12)*, in press.
28. Y.Y. Özbek, F.E. Bastan, F. Üstel, *Journal of Thermal Analysis and Calorimetry*, **2016**, *125*, 745.

SYNTHESIS, THERMAL BEHAVIOR AND SPECTROSCOPIC INVESTIGATIONS OF METAL COMPLEXES WITH *N*-MODIFIED GLYCINE AS LIGAND

CARMEN SACALIS^{a*}, FIRUTA GOGA^a, LEONTIN DAVID^b

ABSTRACT. The Cu(II), Co(II) and Ni(II) complexes with *N*-modified glycine derived from *p*-nitrophenylserinol were synthesized and characterized by their spectral and thermal properties. The thermal stability of the ligand and synthesized complexes was discussed in the 20-700°C temperature range. The results indicate that the organic compound acts as a bidentate ligand, its coordination involving the carboxylate oxygen and the nitrogen atom belonging to the amino group of the glycine fragment. All complexes correspond to the molar ratio M : L : H₂O = 1 : 2 : 2. The shape of the ESR spectra at room temperature and the principal values of the g tensor suggest a pseudotetrahedral local symmetry around the metal ions.

Keywords: *glycine, metal complexes, thermal behavior, spectroscopic studies*

INTRODUCTION

Amino acids play a crucial role in intra-cellular process of living organism. A lot of biochemical processes involve metal ions. The metal-amino acid interaction can be treated as a model of metal-protein system. The study of model species such as the simple amino acids can assist in the interpretation of more complex system. Complexes of transition metals with amino acids like glycine, very small biomolecules, have received much attention because they proved biological activity such as antibacterial, antimicrobial or antifungal activities [1-4].

^a Babeş-Bolyai University, Faculty of Chemistry and Chemical Engineering, 11 Arany Janos str., RO-400028, Cluj-Napoca, Romania

^b Babeş-Bolyai University, Faculty of Physics, 1 Mihail Kogalniceanu str., RO-400084, Cluj-Napoca, Romania

* Corresponding author: cbatiu@chem.ubbcluj.ro

In-vitro studies of coordination complexes of Mn(II), Co(II), Ni(II), Cu(II), Cd(II) with glycine and phenylalanine indicated antimicrobial activity for Gram-positive bacteria such as *Bacillus subtilis* and *Staphylococcus aureus*, and Gram-negative such as *E.coli*, *Pseudomonas aeruginosa*, *Proteus vulgaris* and *Candida albicans* [3].

Recently studies of copper (II) complex with glycine report that is a very good antifungal agent for *Phytophthora Capsici*, an important pathogenic species which causes serious disease on plants [5].

Other research indicates that *N*-substituted glycine and their transition metal complexes act as hydrogen buffers in biological reactions [6]. *N*-modified glycines have a lot of applications in biomedicine as analogue of anticonvulsant and antiepileptic agent Milacemide, as *building-units* for *N*-backbone cyclic peptides, even in the detergent industry [7-9].

The ligand **L**=2-[(1*S*,2*S*)-1,3-dihydroxy-1-(4-nitrophenyl)propan-2-yl-amino]acetic acid (Figure 1), was obtained by a literature procedure by treatment of *p*-nitrophenylserinol with the monochloroacetic acid/Na₂CO₃ system and investigated by spectroscopic methods [10].

Taking into account the important biochemical applications of *N*-modified glycine, we report the synthesis, the spectroscopic and thermogravimetric investigation of the ligand **L** and its transition metal complexes with Cu(II), Co(II) and Ni(II).

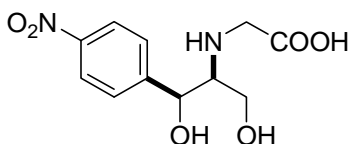


Figure 1. Structure formula of ligand **L** : 2-[(1*S*,2*S*)-1,3-dihydroxy-1-(4-nitrophenyl)propan-2-yl-amino]acetic acid

RESULTS AND DISCUSSION

The structure of the metal complexes

The complexation reaction of Cu(II), Co(II) and Ni(II) salts with the ligand solution in each case yields a solid product. All complexes are colored, microcrystalline and stable at room temperature. They are also insoluble in water, non-polar organic solvents (diethyl ether, CHCl₃, CCl₄, benzene and toluene) but soluble in methanol or DMSO. Higher melting points of these products as well their different colors when compared to that of the ligand **L**, indicate the formation of metal complexes.

The elemental analysis data (Table 1) and thermal analysis data (Table 2) indicate the molar ratio Metal : Ligand : H₂O = 1 : 2 : 2., for each complex.

The UV-VIS spectra in CH₃OH_{abs} for the complexes (**1-3**) indicate a slight bathochromic shift by 4-6 nm, but a considerable hyperchromic increase effect of absorbance comparative to the spectrum of the initial ligand (L), like the other similar complexes [4, 11, 12]. The shift of $n \rightarrow \pi^*$ characteristic band in the UV spectra attributed to the C=O bond (262.4 nm for the ligand; lit. for glycine 270 nm [4]) is due to the involving of the non-bonding electron pairs of the oxygen in the metal-ligand bond formation. The study shows that the absorption spectra of the obtained complexes are determined by the coordinated organic ligand provides from amino acids what is typical for transitional metal complexes [13-15].

Another proof for the complexation process is the HRMS spectrum for the ligand and its metal complexes (Figure 2a-c). The M+1 peak supports the complexation idea with the transition metal ions, for each of them.

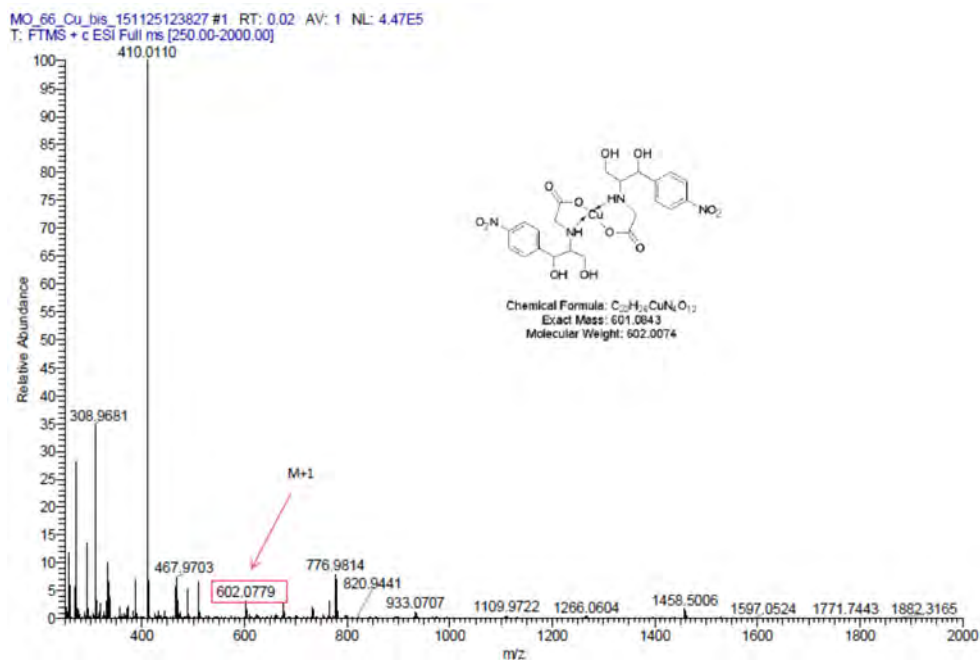


Figure 2a. HRMS spectrum (ESI) of copper complex

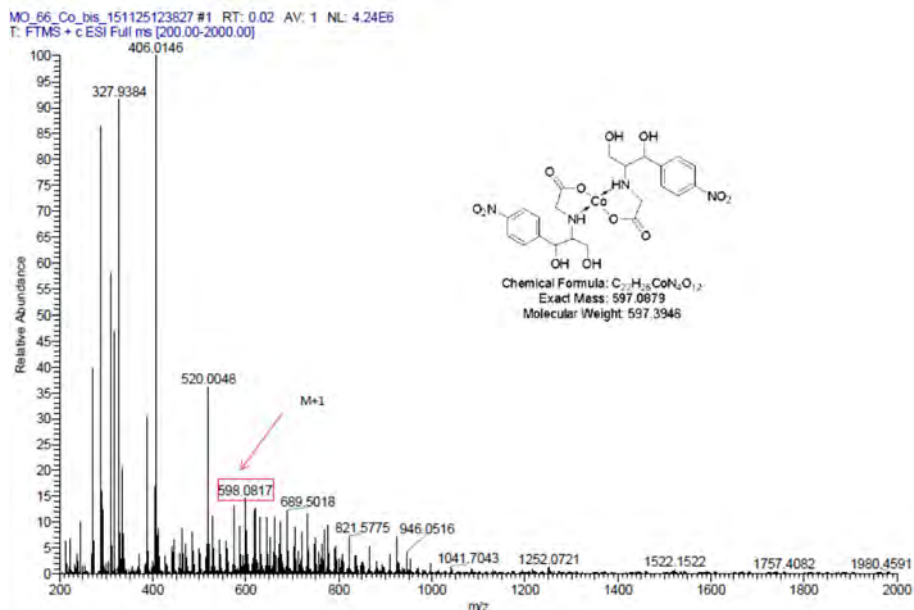


Figure 2b. HRMS spectrum (ESI) of cobalt complex

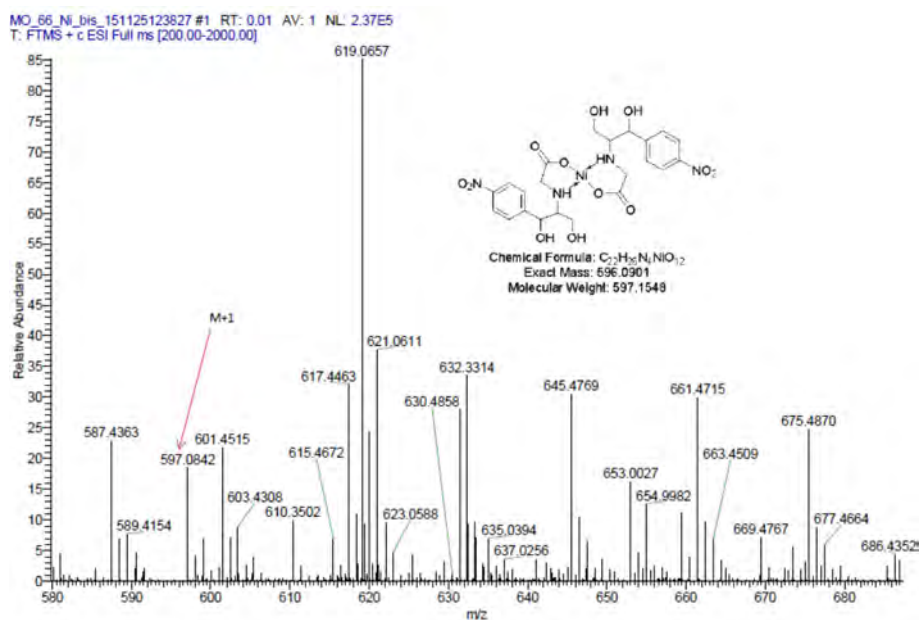


Figure 2c. HRMS spectrum (ESI) of nickel complex

Table 1. Physico-chemical and elemental analysis data of the ligand **L** and its metal complexes (**1-3**)

Compound	C ₁₁ H ₁₄ N ₂ O ₆ (L)	C ₂₂ H ₃₀ CuN ₄ O ₁₄ (1)	C ₂₂ H ₃₀ CoN ₄ O ₁₄ (2)	C ₂₂ H ₃₀ NiN ₄ O ₁₄ (3)	
Molec.Weight	270.2387	638.0380	633.4252	633.1854	
Yield [%]	58	94	79	40	
Colour	yellow-pale powder	green-turquoise powder	ecru powder	greenish-yellow powder	
[α] ₅₄₆ ²⁵ (c=0.5 CH ₃ OH)	+52.42	-53.13	-92.88	-126.51	
Melting point [°C]	213-4	233-4	285-6	254-5	
Visible absorption spectrum data, in CH ₃ OH _{abs}	λ_{max} (nm)	262.4	266.9	268.1	267.5
	ϵ	963	3854	3383	3420
	A	0.499155	1.429968	0.962325	1.088011
Elemental analysis data [%] found. (calcd.)	C	48.57 (48.89)	40.66 (41.41)	40.61 (41.72)	41.67 (41.73)
	H	4.90 (5.22)	4.37 (4.74)	4.32 (4.77)	4.39 (4.78)
	N	10.36 (10.37)	8.77 (8.78)	8.61 (8.85)	8.84 (8.85)

Thermal investigation

The thermal behaviors of the ligand (**L**) and its metal complexes (**1-3**) are summarized in Table 2 and Figure 3a-d.

The thermogravimetric analysis indicated that the ligand (**L**) is anhydrous and the decomposition involved three steps. In the temperature range 30-194°C a small endothermic peak at 56°C with a mass loss of 1.12% represented the loss of residual water present in the pores. This phenomenon could be explained by the general synthesis of the ligand from aqueous solution [10].

The first decomposition step occurred in the temperature range 194-240°C and it has been accompanied by an endo peak at 233°C. This process could be assigned to the NO₂ group cleavage from the aromatic ring accompanied by the melting, according to the literature data for other nitro-derivatives analogous [10, 16-18]. In the second stage of decomposition of ligand two exothermic peaks at 248°C, respectively at 347°C, indicated the cleavage of glycine rest accompanied by oxidation processes. The last step occurred in the temperature range 452-700°C and it has been accompanied by two strongly exothermic effects at 580°C and at 616°C which indicated the pyrolysis of organic rest. The theoretic weight loss (50.05%) and the experimental one (49.55%) agree with the loss of remaining organic rest. At 637°C the ligand was completely pyrolyzed.

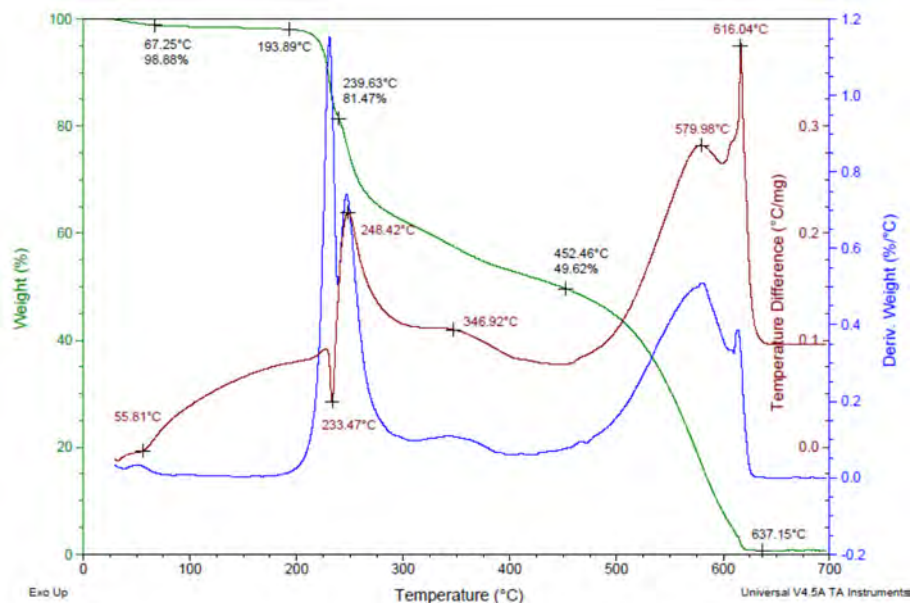


Figure 3a. TG-DTG-DTA diagram for the ligand **L**

The aim of the thermal analysis of the metal complexes is to obtain information concerning their thermal stability of these and to decide whether the water molecules are inside or outside the coordination sphere.

The decomposition of each metal complex occurs in two or three steps. First step corresponds to the loss of water molecules. After that, partial decomposition and then total decomposition of organic ligands takes place. The final products of the pyrolysis are metal oxides.

Thermal decomposition of the copper complex (**1**) was achieved in three stages. These mass losses occur in the temperature range of 30-192^oC, 192-250^oC and 250-700^oC. The first step with an estimated mass loss of 6.40% (calculated 5.64%) could be assigned to loss of 2 moles of hydration water. The second stage of decomposition was observed in the 192-250^oC with a mass loss of 40.93% (calculated 38.88%) and corresponds to a glycine rest and nitro-groups loss. The third-stage decomposition takes place at 250-700^oC with two exothermic peaks at 325^oC, respectively 352^oC and corresponds to the pyrolysis of organic rest. The final product is CuO residue.

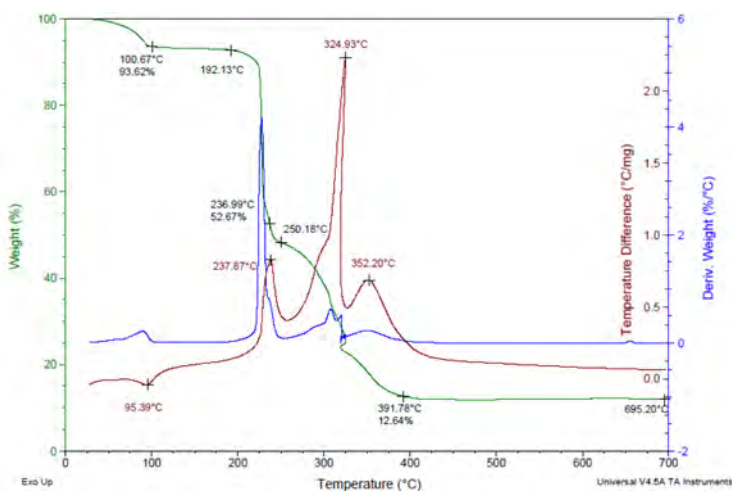


Figure 3b. TG-DTG-DTA diagram for copper complex (1)

For the cobalt complex (2), the first stage decomposition starts in the range 30-211°C, with an endothermic peak at 87°C and a mass loss of 6.26% which correspond to the loss of two moles of hydration water (calculated 5.69%). A strong exothermic effect (see Figure 3c), was assigned to the total pyrolysis of metal complex. The recorded mass loss of 81.34% is in good agreement to the calculated data (81.76%). Finally, the metal oxide remains in the crucible.

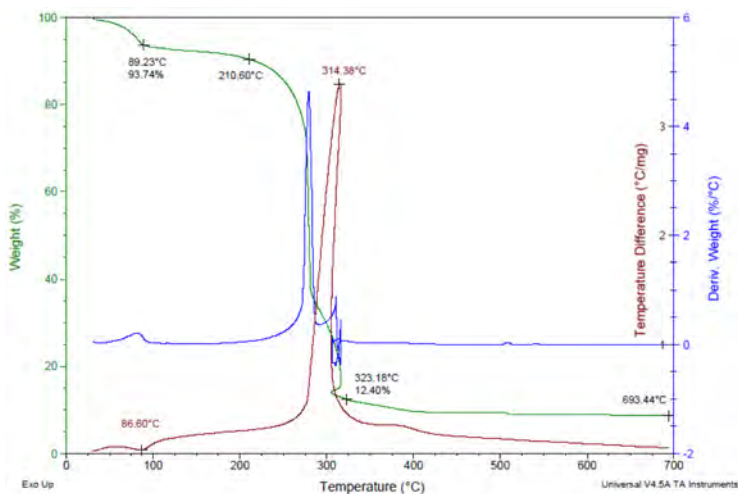


Figure 3c. TG-DTG-DTA diagram for cobalt complex (2)

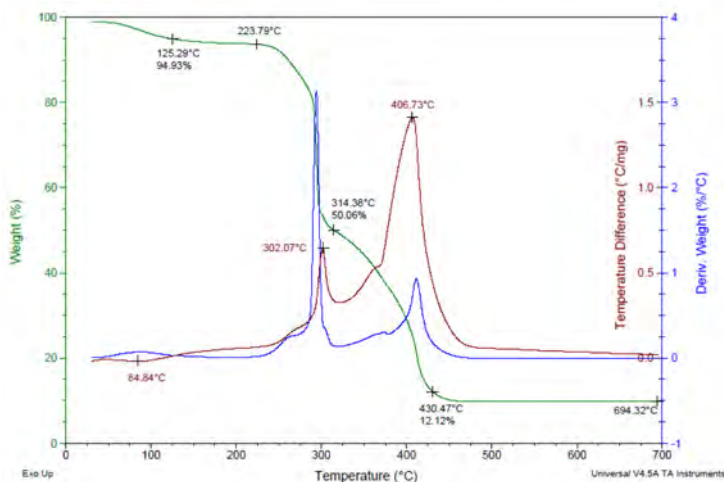


Figure 3d. TG-DTG-DTA diagram for nickel complex **(3)**

Table 2. Thermal analysis data of the ligand **L** and its metal complexes **(1-3)** in air atmosphere (10⁰C/min)

Compound	Heat effect on DTA	Temperature (°C)			Mass loss (%)		Assignment
		T _i	T _{max}	T _f	Calcd.	Exp.	
L	Endo	30	56	194	-	1.12	-residual water present inside pores
	Endo	194	233	240	17.02	17.41	-melting accompanied by NO ₂ cleavage group
	Exo	240	248	452	33.03	31.85	-glycine rest (C ₂ H ₄ O ₂ N) and oxidation process
	Exo	452	580	700	50.05	49.55	-pyrolysis of organic rest
	Exo		616				
Cu(L)•2H ₂ O (1)	Endo	30	95	192	5.64	6.40	-2 moles of hydrating water and probably residual water inside pores
	Exo	192	238	250	39.88	40.93	-2 moles of glycine rest and NO ₂ groups (2 C ₄ H ₈ O ₈ N ₄)
	Exo	250	325	700	41.27	40.49	-pyrolysis of organic rest
					13.21	12.64	CuO residue
Co(L)•2H ₂ O (2)	Endo	30	87	211	5.69	6.26	-2 moles of hydrating water
	Exo	211	314	323	81.76	81.34	-quickly cleavage and pyrolysis of organic rest
					12.54	12.40	CoO residue
Ni(L)•2H ₂ O (3)	Endo	30	85	224	5.69	5.07	-2 moles of hydrating water
	Exo	234	302	314	41.28	42.76	-2 moles of glycine rest and NO ₂ groups (2 C ₄ H ₈ O ₈ N ₄)
	Exo	314	407	430	40.39	38.89	-pyrolysis of organic rest
					12.54	12.12	NiO residue

T_i=initial temperature, T_{max}=maximum temperature, T_f=final temperature

The TG data showed that the nickel complex starts its decomposition at 85°C. The first decomposition step starts with dehydration and corresponds to loss of two moles of water. Organic ligand molecule is stable until 302°C. The second and third stages correspond to the organic ligand decomposition. The final product is NiO (12.12% exp., calcd. 12.54%).

ESR spectra

Powder ESR spectra of metallic complexes at room temperature (Figure 4) are typical for pseudotetrahedral monomeric species. The principal values of the g tensor $g_{\parallel}=2.560$ and $g_{\perp}=2.071$ for Cu complex, correspond to a CuN_2O_2 chromophore [19]. Similar value for Co complex ($g_{\parallel}=2.0719$, $g_{\perp}=2.019$) and for Ni complex ($g_{\parallel}=2.065$, $g_{\perp}=2.071$) suggest the same local symmetry around the metal ions.

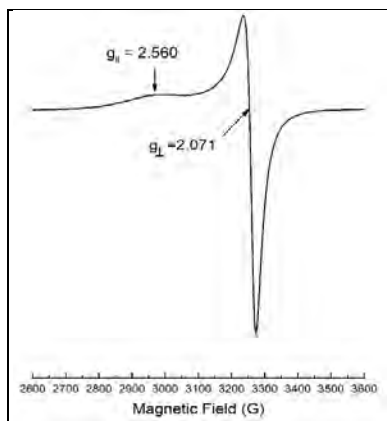


Figure 4. Powder ESR spectrum of copper complex at room temperature

CONCLUSIONS

Three new transition metal complexes (**1-3**) of an *N*-modified glycine (**L**) as ligand were synthesized and analyzed by elemental, thermogravimetric analysis and spectral studies. The results are in good agreement with the corresponding formulae: $\text{C}_{11}\text{H}_{14}\text{N}_2\text{O}_6$ (**L**), $[\text{Cu}(\text{C}_{11}\text{H}_{13}\text{N}_2\text{O}_6)_2] \cdot 2\text{H}_2\text{O}$ (**1**), $[\text{Co}(\text{C}_{11}\text{H}_{13}\text{N}_2\text{O}_6)_2] \cdot 2\text{H}_2\text{O}$ (**2**), respectively $[\text{Ni}(\text{C}_{11}\text{H}_{13}\text{N}_2\text{O}_6)_2] \cdot 2\text{H}_2\text{O}$ (**3**). The ligand coordinated the metal ions through N and O donor atoms. The ESR spectra at room temperature indicated pseudotetrahedral local symmetry around the metal ions.

During heating in air atmosphere, both the ligand and its metal complexes decompose in multistage. Some stages of pyrolysis are weakly separated one from another. Decomposition of investigated compounds begins with total loss of water, then with gradual destruction of ligand. The final products of pyrolysis are the metal oxides from each of transition metal complexes.

Mass spectra data indicated the M+1 peak corresponding for each of investigated compounds.

EXPERIMENTAL SECTION

Materials and instrumentation

All reagents and chemicals were purchased from commercial sources and used as received. Elemental analyses were determined on Thermo Scientific Flash EA 1112 Elemental Analyzer. Melting points were measured on an ELECTROTHERMAL[®] instrument and were not corrected. The electronic absorption spectra were performed on CECIL CE 9500 spectrophotometer. Specific rotations were estimated on a Polamat A Karl Zeis Jena photopolarimeter. GC-MS spectra were recorded on a Gas Chromatograph with Mass Spectrometer Shimadzu[®] QP 2010 PLUS. Mass spectra were carried out on a LTQ ORBITRAP[®] XL (Thermo Scientific) instrument which was externally calibrated using the manufacturer's APCI or ESI(+) calibration mix. The samples were introduced into the spectrometer by direct infusion. The EPR measurements were carried out on a Bruker Biospin EMX^{micro} spectrometer operating at X-band (9-10 GHz) with continuous wave at X-band (\approx 9 GHz). The spectra were recorded at room temperature with a microwave frequency of 9.4353 GHz, microwave power of 2 mW, modulation frequency of 100 kHz, modulation amplitude of 2 G. Thermogravimetry and differential thermal analysis (TG/DTA) curves were recorded with a Thermal Analyzer TA Instruments SDT Q600 V20.9 Build 20 on an interval 30-700^oC, at a heating rate of 10^oC/min, in alumina crucibles and a dynamic air atmosphere.

General synthesis of the metal complexes

Cu(II), Co(II) and Ni(II) complexes of the ligand L were prepared by following a general method. The metal salt [Cu(NO₃)₂•3H₂O, Co(NO₃)₂•6H₂O or Ni(NO₃)₂•6H₂O] (1.24mmol) was dissolved in 10 mL distilled water. To a solution of ligand (L) (2mmol) dissolved in NaOH 1M at pH=12, was added slowly, dropwise, a solution of the metal salt, at room temperature. The mixture was stirred for 2h. By adding a solution of metal ions to a solution of ligand,

immediate color change was observed depending on the metal ion. Also the pH was changed at 5.5-6.00 for the copper complex, 6.50-7.00 for the cobalt complex and 7.00-7.50 for the nickel complex. After standing overnight at room temperature, the resulted precipitates were vacuum filtrated and washed with distilled water and finally dried in air at room temperature.

REFERENCES

1. L. Lomozik, A. Wojciechowska, *Monatshefte für Chemie*, **1985**, 116, 719.
2. I. Sakiyan, E. Loğoğlu, S. Arslan, N. Sari, N. Sakiyan, *BioMetals*, **2004**, 17(2), 115.
3. A. Temitayo, O. Isaac, A. Olugbenga, *International Journal of Chemistry*, **2012**, 4(2), 49.
4. A. Marcu, A. Stanila, D. Rusu, M. Rusu, O. Cozar, L. David, *Journal of Optoelectronics and Advanced Materials*, **2007**, 9(3), 741.
5. G. Indira Devi, P. Smitha, *International Research Journal of Biological Sciences*, **2013**, 2(6), 16.
6. L. Menabue, M. Saladini, *Journal of Crystallographic and Spectroscopic Research*, **1992**, 22(6), 713.
7. K. Nishimura, X. Lu, R.B. Silverman, *Journal of Medicinal Chemistry*, **1993**, 36, 446.
8. G. Byk, C. Gilon, *Journal of Organic Chemistry*, **1992**, 57, 5687.
9. K. Yahagi, K. Tsujii, H. Hirota, Y. Matsumura, *Eur. Pat. 0248294 A2*, **1987**.
10. M. Darabantu, C. Maieranu, G. Plé, C. Berghian, E. Condamine, Y. Ramondenc, *Heterocyclic Communications*, **2001**, 7(6), 593.
11. L. Zapala, M. Kosińska, E. Woźnicka, L. Byczyński, W. Zapala, *Journal of Thermal Analysis and Calorimetry*, **2016**, 124, 363.
12. N.S. Al Radadi, S.M.A. Al Ashqar, M. M. Mostafa, *Synthesis and Reactivity in Inorganic, Metal-Organic and NanoMetal Chemistry*, **2011**, 41(2), 203.
13. E. Prenesti, S. Berto, P.G. Daniele, *Spectrochimica Acta Part A*, **2003**, 59, 201.
14. T. Stalin, N. Rajendiram, *Journal of Photochemistry and Photobiology A: Chemistry*, **2006**, 182, 137.
15. F. Dimiza, S. Fountoulaki, A.N. Papadopoulos, C.A. Kontogiorgis, V. Tangoulis, C.P. Raptopoulou, V. Psycharis, A. Terzis, D.P. Kessisoglou, G. Psomas, *Dalton Transactions*, **2011**, 40, 8555.
16. K. Raha, P.S. Makashir, E.W. Kusian, *Journal of Thermal Analysis and Calorimetry*, **1989**, 35, 1173.

17. L. Ghizdavu, C. Bălan, L. David, C. Bătiu, O. Cozar, D. Ristoiu, *Journal of Thermal Analysis and Calorimetry*, **2000**, 62, 729.
18. L. David, C. Craciun, C. Bălan, O. Cozar, L. Ghizdavu, C. Bătiu, *Acta Chimica Slovenica*, **2001**, 48, 407.
19. F. Mabbs, D. Collisson, "Electron Paramagnetic Resonance of *d* Transition Metal Compounds", Elsevier, Amsterdam, **1992**, p.102.

HYPERCOORDINATED ORGANOSELENIUM COMPOUNDS WITH O→Se INTRAMOLECULAR INTERACTIONS

ALEXANDRA POP^a, ROXANA A. POPA^a, CRISTIAN SILVESTRU^a,
ANCA SILVESTRU^{a*}

ABSTRACT. Single-crystal X-ray diffraction studies revealed a monomeric structure with O→Se intramolecular coordination in compounds [Me₂C(OH)CH₂][2-(Me₂NCH₂)C₆H₄]Se (**1**) and [2-(O=CH)C₆H₄]Se[S(S)P(OPrⁱ)₂] (**2**). These interactions result in distorted T-shaped coordination geometries around selenium in both compounds and prevent a C,N-chelating behavior of the 2-(Me₂NCH₂)C₆H₄ group in **1** and a bidentate behaviour of the dithiophosphorus ligand in **2**, respectively.

Keywords: organoselenium compounds; intramolecular coordination; solid state structure; dithiophosphato ligands.

INTRODUCTION

A continuously increased interest was observed during last years for main group organometallic compounds bearing organic groups with pendant arms capable for intramolecular E→M (E = O, N; M = main group metal or metalloid) interactions, mainly due to the specific properties induced by such an interaction, e.g. increased thermal and hydrolytic stability or adjustable conformation rigidity [1,2]. In most cases, the use of functionalized aromatic groups with potential for intramolecular coordination results in chelate species stabilized in a monomeric form. Such compounds proved to be valuable candidates in catalysis, medicine or materials science, as they display

^a Babeş-Bolyai University, Faculty of Chemistry and Chemical Engineering, Department of Chemistry, Supramolecular Organic and Organometallic Chemistry Centre (SOOMCC), 11 Arany Janos str., RO-400028, Cluj-Napoca, Romania,

* Corresponding author: ancas@chem.ubbcluj.ro

improved catalytic properties, biological activity or thermal behavior than the species without such intramolecular interactions [3,4]. In organoselenium compounds the N→Se intramolecular interaction was observed to reduce the Lewis acidity and to increase the electrophilic reactivity of the chalcogen atom, thus making it more suitable for additional Se→M coordination. In this way, organoselenium compounds bearing organic groups with potential for building hypercoordinated species become useful multidentate ligands using both hard (O, N) and soft (Se) donor atoms [5-10].

During the last years our research interest was focused on organoselenium compounds with organic groups of type 2-(R₂NCH₂)C₆H₄ (R = Me, Et, Prⁱ) [11-14], 2,6-(R₂NCH₂)C₆H₃ [15], (RN=CH)C₆H₄ (R = Bn, Mes, Ph) [16] or 2-(O=CH)C₆H₄ [17] groups, as well as several metal complexes, either metal organoselenolates [18-20], or compounds bearing the alkoxo functionalized ligands, [R₂C(OH)CH₂](2-Me₂NCH₂C₆H₄)Se [21]. As a continuation of our studies we discuss here the crystal and molecular structure of two organoselenium(II) compounds with potential for hypercoordination, namely [Me₂C(OH)CH₂](2-Me₂NCH₂C₆H₄)Se (**1**) and [2-(O=CH)C₆H₄]Se[S₂P(OPrⁱ)₂] (**2**), with emphasis on the intramolecular E→Se (E = N, O) possible interactions.

RESULTS AND DISCUSSION

We described previously the synthesis and the solution behavior of compounds [Me₂C(OH)CH₂](2-Me₂NCH₂C₆H₄)Se (**1**) [21] and [2-(O=CH)C₆H₄]Se[S₂P(OPrⁱ)₂] (**2**) [17], but at that time we didn't succeed to obtain single crystals suitable for X-ray diffraction studies.

Single-crystal X-ray diffraction studies

The molecular structures of compounds **1** and **2** were determined by single-crystal X-ray diffraction. The ORTEP-like diagrams with the atom numbering schemes for compounds **1** and **2** are displayed in Figures 1 and 2, respectively, while important interatomic distances and angles are given in Tables 1 and 2, respectively.

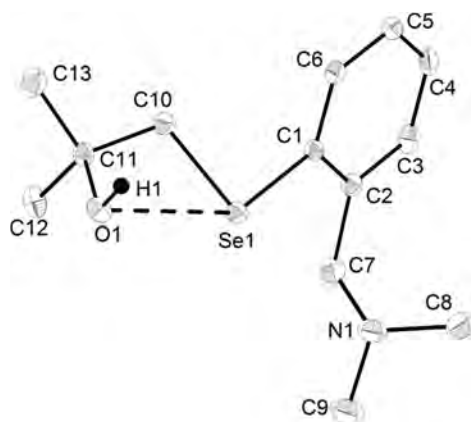


Figure 1. ORTEP-like diagram at 30% probability for compound **1**. Hydrogen atoms, except H1 were omitted for clarity.

Table 1. Selected interatomic distances [Å] and angles [°] in **1**.

Se1–C1	1.928(4)		C1–Se1–C10	98.20(18)
Se1–C10	1.967(4)		C1–Se1...O1	146.48(13)
Se1...O1	3.121(3)		C10–Se1...O1	50.71(13)

Both compounds have monomeric structures with a distorted T-shaped coordination geometry around selenium (O1...Se1–C1 146.48° in **1** and O1...Se1–S1 176.10° in **2**) and chelate rings, *i.e.* four-membered SeC₂O in **1** and five-membered SeC₃O in **2**, respectively. In compound **1** the nitrogen-selenium interatomic distance (3.44 Å) is just at the limit of the sum of the van der Waals radii of the two elements [Σr_{vdW} (N,Se) 3.54 Å] [22], while typically such interactions were observed in the range 2.358(2) - 3.135(3) Å in other related species, *i.e.* [2-(Me₂NCH₂)C₆H₄]₂Se₂, [2-(Me₂NCH₂)C₆H₄]₂Se [23] or [2,6-(Me₂NCH₂)C₆H₃]₂Se⁺ [15]. The OH hydrogen atom is not involved in any intra- or intermolecular interaction. This contrasts with the phenyl substituted analogue [Ph₂C(OH)CH₂][2-(Me₂NCH₂)C₆H₄]₂Se, where a strong N...H–O interaction of 2.03 Å [Σr_{vdW} (N,H) 2.74 Å] is established [21]. In compound **1** the N1...H1 interatomic distance is much greater (6.51 Å) than the sum of the van der Waals radii of these two elements. This behavior can be explained by the constraint determined by the intramolecular O→Se interaction (Se1...O1 3.12 Å) [*cf.* Σr_{vdW} (O,Se) 3.40 Å] [22], which prevents any further participation of the OH hydrogen to hydrogen bonding.

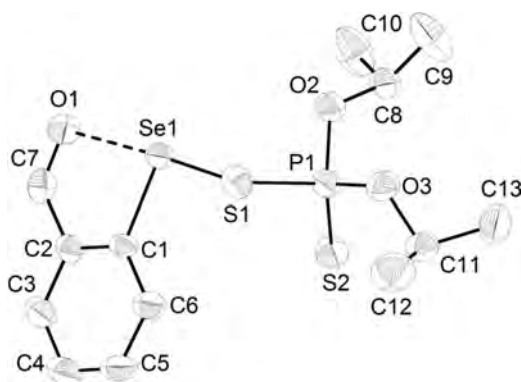


Figure 2. ORTEP-like diagram at 30% probability for compound **2**. Hydrogen atoms were omitted for clarity.

Table 2. Selected interatomic distances [Å] and angles [°] in **2**.

Se1–C1	1.934(4)		C1–Se1–S1	101.41(14)
Se1–S1	2.216(1)		C1–Se1...O1	76.50(15)
Se1...O1	2.575(4)		S1–Se1...O1	176.10(10)
P1–S1	2.0865(16)			
P1–S2	1.9087(19)			

In compound **2** the O→Se intramolecular interaction of 2.575 Å is similar with that one found in [2-(O=CH)C₆H₄]Se[S(S)PPh₂] (2.568 Å) and much stronger than the sum of the van der Waals radii of oxygen and selenium. The dithiophosphorus ligand is coordinated in a monodentate fashion to selenium, with single P–S [P1–S1 2.086(2) Å] and double P=S [P1–S2 1.908(2) Å] bonds [cf. P–S 2.077(1) and P=S 1.954(1) Å in Ph₂P(S)SH] [24]. These values are similar with those found in the related [2-(O=CH)C₆H₄]Se[S(S)PPh₂] [17] or the compounds of type [2-(ⁱPr₂NCH₂)C₆H₄]Se[S(S)PR'₂] (R' = Ph, OPrⁱ) [13].

CONCLUSIONS

The single-crystal X-ray diffraction studies revealed the presence of O→Se intramolecular interactions in the monomeric species [Me₂C(OH)CH₂](2-Me₂NCH₂C₆H₄)Se (**1**) and [2-(O=CH)C₆H₄]Se[S(S)P(OPrⁱ)₂] (**2**). In compound **1** the intramolecular O→Se coordination pushed the nitrogen atom in the pendant arm of the 2-(Me₂NCH₂)C₆H₄ group away from the coordination sphere of selenium, thus preventing any intramolecular N→Se interaction, while in compound **2** the intramolecular C=O→Se interaction determines a monodentate monoconnective behavior of the organophosphorus ligand.

EXPERIMENTAL SECTION

X-ray structure determination

The details of the crystal structure determination and refinement for compounds **1** and **2** are given in Table 3. Data were collected on a Bruker SMART APEX diffractometer by using graphite-monochromated Mo- K_{α} radiation ($\lambda = 0.71073 \text{ \AA}$). The crystals were attached with paratone/N oil on cryoloops. The structures were refined with anisotropic thermal parameters. The hydrogen atoms were refined with a riding model and a mutual isotropic thermal parameter. For structure solving and refinement the software package SHELX-97 was used [25]. The drawings were created with the Diamond program [26].

Table 3. Crystal data and structure refinement for $[\text{Me}_2\text{C}(\text{OH})\text{CH}_2][2-(\text{Me}_2\text{NCH}_2)\text{C}_6\text{H}_4]\text{Se}$ (**1**) and $[2-(\text{O}=\text{CH})\text{C}_6\text{H}_4]\text{Se}[\text{S}(\text{S})\text{P}(\text{OPr}^i)_2]$ (**2**)

	1	2
Empirical formula	$\text{C}_{13}\text{H}_{21}\text{NOSe}$	$\text{C}_{13}\text{H}_{19}\text{O}_3\text{PS}_2\text{Se}$
Formula weight	286.27	397.33
Temperature (K)	150(2)	293(2)
Wavelength (\AA)	0.71073	0.71073
Crystal system	Tetragonal	Monoclinic
Space group	I-4	C2/c
a (\AA)	19.9049(12)	28.106(5)
b (\AA)	19.9049(12)	8.0787(13)
c (\AA)	7.0189(8)	16.977(3)
α ($^\circ$)	90	90
β ($^\circ$)	90	114.002(3)
γ ($^\circ$)	90	90
Volume, (\AA^3)	2780.9(5)	3521.5(11)
Z	8	8
Density (calculated) (g/cm^3)	1.367	1.499
Absorption coefficient (mm^{-1})	2.682	2.463
$F(000)$	1184	1616
Crystal size, mm	0.30 x 0.25 x 0.19	0.20 x 0.22 x 0.38
θ range for data collections, $^\circ$	1.447 to 24.929	1.60 to 25.00
Reflections collected	13389	16308
Independent reflections	2445 [$R_{\text{int}} = 0.0484$]	3099 [$R_{\text{int}} = 0.049$]
Refinement method	Full-matrix least-squares on F^2	
Data / restraints / parameters	2445 / 0 / 150	3099 / 0 / 185
Goodness-of-fit on F^2	1.037	1.172
Final R indices [$ I > 2\sigma(I)$]	$R_1 = 0.0274$ $wR_2 = 0.0588$	$R_1 = 0.0536$ $wR_2 = 0.1144$
R indices (all data)	$R_1 = 0.0288$ $wR_2 = 0.0593$	$R_1 = 0.0649$ $wR_2 = 0.1192$
Largest diff. peak and hole, $\text{e}\text{\AA}^{-3}$	0.355 and -0.188	0.751 and -0.261

ACKNOWLEDGMENTS

Financial support from the Ministry of Education and Research of Romania (Research Project No. PN-II-ID-PCE-2011-3-0659) is greatly appreciated. Roxana Popa is grateful for financial support from the Babes-Bolyai University through a grant offered by the College for Advanced Performance Studies.

SUPPLEMENTARY DATA

CCDC 1587750 and 1571839 contain the supplementary crystallographic data for **1** and **2**, respectively. These data can be obtained free of charge via <http://www.ccdc.cam.ac.uk/conts/retrieving.html>, or from the Cambridge Crystallographic Data Centre, 12 Union Road, Cambridge CB2 1EZ, UK; fax: +44 1223 336 033; or e-mail: deposit@ccdc.cam.ac.uk.

REFERENCES

1. Kin-ya Akiba (Ed), "Chemistry of Hypervalent Compounds", Wiley-VCH, 1999, Weinheim.
2. C.I. Rat, C. Silvestru, H.J. Breunig, *Coordination Chemistry Reviews*, **2013**, 257 818, and references therein.
3. C. Coza, A. Stegarescu, R. Suteu, A. Silvestru, *Journal of Organometallic Chemistry*, **2015**, 777, 71.
4. C.A. Caputo, N.D. Jones, *Dalton Transactions*, **2007**, 41, 4727.
5. G. Mugesh, H.B. Singh, *Chemical Society Reviews*, **2000**, 29, 347.
6. T. Wirth (Ed.), "Organoselenium Chemistry: Modern Developments in Organic Synthesis", *Topics in Current Chemistry*, vol. 208, Springer, Berlin, **2000**.
7. G. Mugesh, W.-W. du Mont, H. Sies, *Chemistry Reviews*, **2001**, 101, 2125 (and references therein).
8. A.J. Mukherjee, S.S. Zade, H.B. Singh, R.B. Sunoj, *Chemistry Reviews*, **2010**, 110, 4357 (and references therein).
9. K. Kandasamy, H.B. Singh, G. Wolmershauser, *Inorganica Chimica Acta*, **2005**, 358, 207.
10. S. Panda, S.S. Zade, H.B. Singh, R.J. Butcher, *European Journal of Inorganic Chemistry*, **2006**, 172.
11. C. Deleanu, J.E. Drake, M.B. Hursthouse, M. Kulcsar, M.E. Leight and A. Silvestru, *Applied Organometallic Chemistry*, **2002**, 16, 727.
12. M. Kulcsar, A. Silvestru, C. Silvestru, J.E. Drake, C.L.B. Macdonald, M.B. Hursthouse, M.E. Light, *Journal of Organometallic Chemistry*, **2005**, 690, 3217.

13. E. Duhamel, A. Pöllnitz, A. Stegarescu, A. Silvestru, *Zeitschrift für Anorganische und Allgemeine Chemie*, **2011**, 637, 1355.
14. A. Pöllnitz, V. Lippolis, M. Arca, A. Silvestru, *Journal of Organometallic Chemistry*, **2011**, 696, 2837.
15. A. Pop, A. Silvestru, E.J. Juárez-Pérez, M. Arca, V. Lippolis, C. Silvestru, *Dalton Transactions*, **2014**, 43, 2221.
16. A. Pöllnitz, C. Silvestru, J.-F. Carpentier, A. Silvestru, *Dalton Transactions*, **2012**, 41, 5060.
17. R.A. Popa, A. Pop, C. Silvestru and A. Silvestru, *Revue Roumaine Chimie*, **2016**, 61, 495.
18. A. Pöllnitz, A. Rotar, A. Silvestru, C. Silvestru, M. Kulcsar, *Journal of Organometallic Chemistry*, **2010**, 695, 2486.
19. A. Pop, L. Wang, V. Dorcet, T. Roisnel, J.-F. Carpentier, A. Silvestru, Y. Sarazin, *Dalton Transactions*, **2014**, 43, 16459.
20. A. Pop, C. Bellini, R. Şuteu, V. Dorcet, T. Roisnel, J.-F. Carpentier, A. Silvestru, Y. Sarazin, *Dalton Transactions*, **2017**, 46, 3179.
21. A. Pop, R. Mitea, A. Silvestru, *Journal of Organometallic Chemistry*, **2014**, 768, 121.
22. J. Emsley, "Die Elemente", de Gruyter, Berlin, **1994**.
23. A. Panda, G. Mugesh, H.B. Singh, R.J. Butcher, *Organometallics*, **1999**, 18, 1986.
24. B. Krebs, G. Henkel, *Zeitschrift für Anorganische und Allgemeine Chemie*, **1981**, 475, 143.
25. G. M. Sheldrick, *Acta Crystallographica, Section A*, **2008**, 64, 112.
26. *DIAMOND*, Visual Crystal Structure Information System, Crystal Impact, Postfach 1251, 53002 Bonn, Germany, **2001**.

COMPARATIVE *IN VITRO* STUDY OF THE DIFFERENT ORTHODONTIC BRACKETS USING TWO ETCHING TECHNIQUES

MIHAELA PĂSTRAV^a, ANDREA MARIA CHISNOIU^b,
OVIDIU PĂSTRAV^{c*}, LAURA SILAGHI DUMITRESCU^d,
CODRUTA SAROSI^d AND VIORICA TARMURE^a

ABSTRACT. Direct bonding of the bracket to the enamel is the elective procedure for the orthodontic treatment. Among various factors influencing the adhesive force at the enamel level, the etching technique seems to be the most important one. The present study aims at evaluating the influence of the storage media and the etching technique used, on the bond strength between different bracket types and dental structures. The results of this study showed that, regardless of the brackets and the immersion solution used, by working with the classic etch and rinse technique the adhesion force is higher than by using a self etching adhesive.

Keywords: SEM, etching technique, *in vitro*, adhesion

^a Department of Orthodontics and Orofacial Orthopaedics, Faculty of Dental Medicine, University of Medicine and Pharmacy "Iuliu Hațieganu", 33 Motilor Street, 400001, Cluj-Napoca, Romania

^b Department of Prosthetic Dentistry, Faculty of Dental Medicine, University of Medicine and Pharmacy "Iuliu Hațieganu", 32 Clinicilor Street, 400006, Cluj-Napoca, Romania

^c *Department of Odontology and Oral Pathology, Faculty of Dental Medicine, University of Medicine and Pharmacy "Iuliu Hațieganu", 33 Motilor Street, 400001, Cluj-Napoca, Romania

^d "BabesBolyai" University - "RalucaRipan" Chemistry Research Institute, 30 Fântânele Street, 400294, Cluj-Napoca, Romania.

*Corresponding author: pastravovidiu@yahoo.com

INTRODUCTION

Direct bonding of the bracket to the enamel is the elective procedure for the orthodontic treatment. The process involves the enamel, the adhesive and the bracket surface, therefore, the analysis of the two interfaces: enamel- adhesive and adhesive-bracket is an important subject of research [1]. The different physical and chemical properties of these components could establish the adhesive conditions in orthodontics [2].

There are many factors influencing the adhesive force at the enamel level, such as etching technique, adhesive application, photopolymerisation time, or mechanical properties of resin based materials for bracket bonding [3, 4].

The differences between the bonding forces by using selfetching adhesives or the common etching technique, followed by the use of adhesive, still represents a subject of debate [5, 6].

Schnebel states that the adhesive force of the selfetching systems is not appropriate for bracket bonding and suggests that in order to gain enough bond strength orthodontists should use the classic etching technique [7]. The type of adhesive influences the bond strength, the risk of damaging the enamel and the presence of composite resin on the tooth surface [8].

The bracket type used, as well as the way the orthodontic forces are applied, influence the bond strength and the tensions that appear in the bonding layer and in the enamel [9, 10]. Also, the environmental factors such as soft drinks accelerate the damage of the enamel surface [11].

At the end of an orthodontic treatment the debonding of the brackets shouldn't influence the enamel surface. Though, during bracket debonding, some undesirable effects can be observed: cracks, scarring scratches, loss of enamel, adhesive scraps on the enamel surface. In addition to bracket debonding, the removal of adhesive residue with a dental bur may also lead to local enamel damage [12].

The purpose of this study was to evaluate the influence of the storage media and the etching technique used on the bond strength between bracket and dental structures.

RESULTS AND DISCUSSIONS

Table 1 shows the average values of the adhesion force for metallic, ceramic and sapphire brackets immersed in Coca Cola, tea and artificial saliva (controls).

Table 1. Mean values of strength bond forces.

Immersion solution	Artificial saliva (control) [MPa]		Coca Cola [MPa]		Tea [MPa]	
	Etch and rinse	Self-etch	Etch and rinse	Self-etch	Etch and rinse	Self-etch
Bracket type						
Ceramic	4.1 ± 0.02	4.4 ± 0.12	2.7 ± 0.12	5 ± 0.12	6.9 ± 0.15	6.6 ± 0.07
Metal	20 ± 0.02	11.6 ± 0.15	10.7 ± 0.11	9.1 ± 0.06	29.4 ± 0.02	26.5 ± 0.01
Sapphire	20.3 ± 0.12	10.9 ± 0.11	12.5 ± 0.12	8 ± 0.11	26.2 ± 0.12	15 ± 0.12

The highest strength bond forces were obtained for metallic brackets, using the etch and rinse technique, for the samples immersed in tea solution (29.4 ± 0.02 MPa) - Table 1.

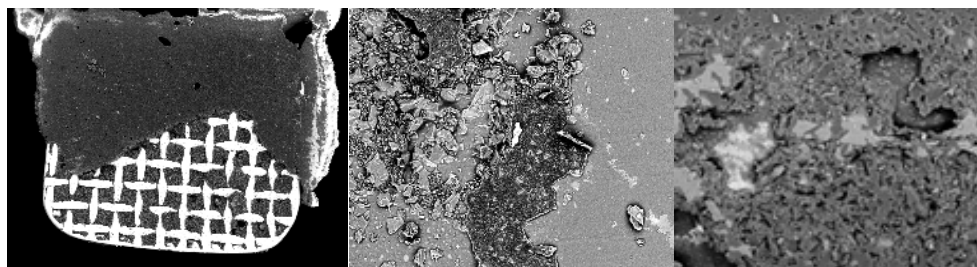
Significant differences were observed between the groups where brackets were bonded using etch and rinse technique compared to those where self-etch technique was used ($p < 0,005$) - Table 2.

Table 2. Test statistics- Wilcoxon test

	Self-etching technique	Ceramic	Metallic	Sapphire
Z	-3,393 ^b	-1,726 ^b	-2,981 ^c	-2,903 ^c
Asymp. Sig. (2-tailed)	,001	,084	,003	,004

Based on the negative value ranks we proved that by using the classic etch and rinse technique the adhesion force is higher than by using a self etching adhesive, regardless of the immersion solution.

SEM evaluation is essential for observing the enamel surface morphology after various bonding and debonding procedures, as well as for subsequently necessity of polishing the tooth surface. The results of our investigation are based on images of the bracket bases (**Figure 1**) and enamel surface after bracket debonding (**Figure 2, 3**). Different aspects of cement debris on the enamel surface, according to the type of etching technique, are visible after debonding for all three bracket types.



a. Metallic bracket

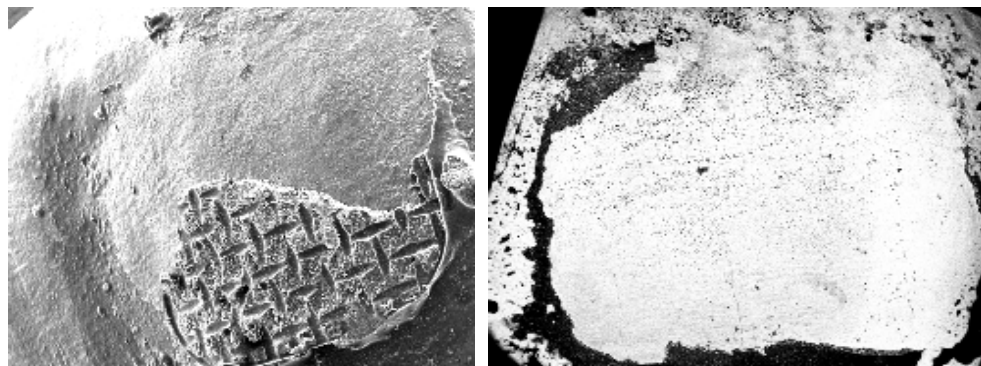
b. Sapphire bracket

c. Ceramic bracket

Figure 1. SEM images from bracket bases after debonding; 1000 magnification

The use of different materials and etching techniques can determine various degrees of wear that were observed on both the tooth surface and bracket level. The gaps and cracks of different sizes were initiated probably by the shear forces at the bracket-cement interface.

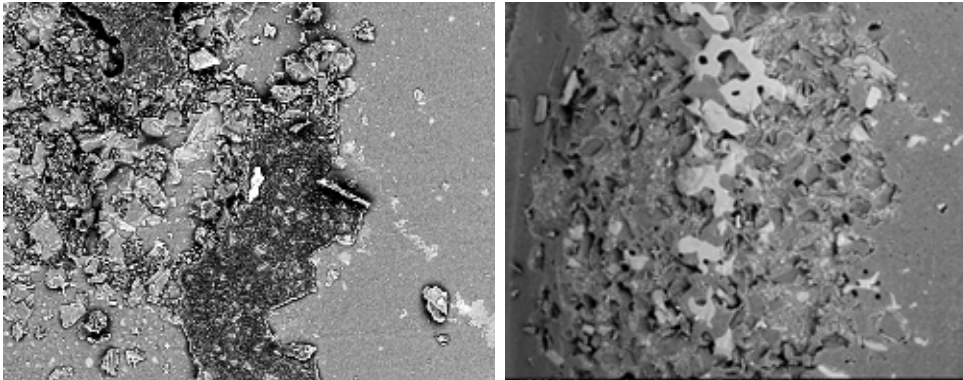
All acid etched enamel surfaces presented a porous, relatively rough aspect on SEM investigation (**Figure 2a, 3a**); in comparison, the self-etched enamel surfaces showed a smooth and almost clean aspect on SEM analysis (**Figure 2b, 3b**). Enamel fractures were frequently observed on tooth surfaces with brackets bonded through etch and rinse technique.



a. Metallic bracket -etch and rinse technique

b. Metallic bracket- self-etch technique

Figure 2. SEM images of the enamel surface after metallic bracket debonding; 5000 magnification



a. ceramic bracket using etch and rinse technique

b. Sapphire bracket using self-etch technique

Figure 3. SEM images of the enamel surface after sapphire bracket debonding; 5000 magnification

Various factors can influence the bonding strength force of the brackets to the enamel such as the type of adhesive, the thickness of the adhesive layer, humidity, geometry of the bracket base, oral habits, etc, but the main one seems to be the etching technique[5-9].

The white spots observed around the brackets are mostly due to bad hygiene or the use of acidic beverages that lower the pH of the oral cavity [13]. Soft drinks consumption can determine erosion of the enamel and corrosion of the materials [14,15]. For this reason we used in our study, the immersion in artificial saliva, but also in Coca Cola and tea.

In our study the highest strength forces were obtained when using the etch and rinse technique. By enlarging the adhesive surface and creating microretentions at enamel level, adequate conditions were created for adhesive penetration [1,2].

SEM images show us a significant difference between the debonding appearance of the metallic brackets when comparing to sapphire and ceramic brackets.

In case of etch and rinse technique, after metallic bracket debonding, we can observe a relatively uniform layer of cement, both on the bracket base and on enamel. For the sapphire and ceramic brackets, the largest amount of cement seems to remain on the enamel surface.

In the case of etch and rinse technique, an almost complete distribution of the adhesive layer on the enamel surface after sapphire bracket debonding is observed, when compared to metallic brackets, where the adhesive seems to be distributed on both bracket base and enamel

surface, in varying proportions. When self-etching adhesives are used, most cement layer remains on the enamel surface after debonding sapphire and ceramic brackets.

The concept of an ideal debonding consists of failure at the support/adhesive interface, and the remained adhesive on the enamel surface to be carefully removed using suitable tools, in order to allow a minimum or no loss of enamel [9, 10]. Cement debris at enamel level can favor plaque adherence, producing demineralized areas and cavities. The residual adhesive may be colored through bacteria action, or due to different alimentary pigments or cosmetics and discolorations can occur, affecting aesthetics [4]. Given the current procedures for debonding and teeth polishing, some layers of enamel could be accidentally removed causing tooth morphology changes and eventual developing of cracks [12]. Literature reports the loss of enamel ranging from 27.5 to 48 μm [12], or 26.1-41.2 μm to 55.6 μm [13], depending on the characteristics of the adhesive system used, the instruments or the final polishing technique. The loss of the enamel is not clinically significant compared to the average thickness of the enamel, which range from 1500 to 2000 μm [12]. Finishing is considered an indispensable process to minimize enamel damage during cement removal from enamel after debonding [5, 9,12].

In vitro, orthodontic bonding is carried out in ideal conditions. *In vivo*, the enamel surfaces can easily be contaminated and extra humidity is sometimes unavoidable. It should be noted that, in these cases, the strength of composite resins adhesion, respectively C = C covalent bonds, will decrease. Vallolah et al. [16] reported that the air at the back of the metal bracket mesh net can significantly affect complete polymerization of light-curing composite resin cements, due to the known inhibitor role of oxygen; it can alter the bond strength between metal and composite material support. But this type of failure was found only in the case of light-cured composite resin cements. Careful application of material on the support base and/or using liquid - paste systems, can avoid air entrapment. This type of failure identified at the resin - bracket interface, implies the possibility that after debonding all cement can remain on the enamel surface, which then should be cleaned. The bracket-cement interface carried out in our tests with remaining cement on both the bracket and the enamel, are partially different from the results obtained by Artun and Ozturk [17], Zarrin, Eid and Kehoe [18], which showed a higher amount of residual cement on the brackets after debonding by applying a force on the support base. The differences can be explained by the use of brackets, adhesive cements and techniques in different combinations.

Etching time before bonding is proportional with the quantity of residual adhesive on enamel surfaces [16-18]. Fjeld et al [19] described in their study fewer irreversible changes to the enamel surface after bonding with self-etching adhesives in comparison to conventional etching.

The aspect of enamel after bracket debonding and final polishing, should be comparable to adjacent surfaces. Clinical examination of both dry and wet enamel is important because of the reflection and refraction of light, which can mask some defects on wetted surfaces of enamel [20].

No universally approved protocol has been established for adhesive resin removal after orthodontic bracket debonding, and there is no instrument that can achieve complete composite removal without affecting the enamel surface.

CONCLUSIONS

Regardless of the brackets and the immersion solution used in this study, all results indicate that by using the classic etch and rinse technique the adhesion force is higher than by using a self etching adhesive.

Metallic brackets are preferable to brackets made of monocrystalline alumina in terms of base design for minimum possible superficial destructions of enamel after debonding. Also, for the same reasons, the bonding technique using the total etch and rinse protocol seems to be a more inspired choice than the self-etching adhesives.

Using conservative instruments and techniques becomes very important, due to multiple possibilities for bracket bonding and to surface treatments that may reduce the loss of the superficial layer of enamel.

EXPERIMENTAL SECTION

Three types of brackets (metallic, ceramic and sapphire) were used. All brackets were bonded to enamel using two etching techniques (self-etch and classic) followed by adhesive application.

All samples were altered rapidly by physical and chemical stress, using several immersive solutions at body temperature. The samples from each group (metal, ceramic or sapphire) were randomly distributed in three subgroups immersed and stored for 3 month, in artificial saliva (controls), Coca Cola or tea. The strength bond force on bracket enamel interface was evaluated.

The comparisons within the statistical part were done between the specimens with the same bracket type, immersed in the same solution, ones bonded with the self-etching technique, others using the etch and rinse technique.

By using one single bonding agent, but different etching techniques, the differences area was restricted to the bonding technique.

The bracket bondig procedure was done accordingly to the manufacturers indications and kept in artifical saliva for 24 hours.

The solutions were prepared and used as follows:

1. Black tea (The mélange angles, Breakfast Black tea)-was kept at 37°C for 20 minutes per day, in order to simmlate the necessary time for each person to drink a cup of tea, as well as the temperature.
2. Coca Cola- the probes were immeresed for 20 minutes per day, at 37°C.
3. Control group for this group the probes were immersed in artificial saliva at 37°C, in thermosthatic bath,without any other treatment.

The brackets were debonded three months after the initial moment of the experiment. Strenght bond force was evaluated out using Llyod Universal Testing machine. A sharp blade was used to apply an oclusogingival force at the bracket-adhesive interface, with a speed of 1mm/min.

The values of the strenght bond force were mesured in MPa, using NEXYGEN Plus Materials Testing Software. The statistical analisys was performed using we used the nonparametric two-pired Wilcoxon statistic test, paired type. The specimens were also examined by using scanning electron microscopy (SEM) and energy dispersive X-ray (EDAX) spectrometry.

ACKNOWLEDGEMENT

This work was funded by the Romanian Ministry of Education and Research, National projects: PNIII-P2-2.1-PED-2016-1907 and PNIII-P2-2.1-PED-2016-1415.

REFERENCES

1. M. Hashimoto, H. Ohno, E. Yoshida, M. Hori, H. Sano, M. Kaga, H. Oguchi, *European Journal of Oral Science*, **2003**, 111, 447.
2. C. Raposo, I.L. Santana, *Revista Odontologia Ciencia*,**2012**, 27,143.
3. B.C. Parrish, T.R. Katona, S.C. Isikbay, K.T. Stewart, K.S. Kula, *Angle Orthodontics*, **2012**, 82, 131.

4. M. Schroeder, A.C.S. Gama, A.G.V. Moares, L.C. Yamasaki, A.D. Loguercio, J. Bauer, *Dental Materials*, **2011**, 27, 20.
5. P.S. Fleming, *Evidence Based Dentistry*, **2014**, 15, 48.
6. A. Elkhadem, N. Orabi, *Evidence Based Dentistry*, **2013**, 14, 52.
7. A. Schnebel, S. Mateer, A.L. Maganzini, K. Freeman, *Journal of Orthodontics*, **2012**, 39, 256.
8. T. Lamper, N. Ilie, K. C. Huth, I. Rudzki, A. Wichelhaus, E. Paschos, *Clinical Oral Investigations*, **2014**, 18, 313.
9. S.E. Elsaka, S. M. Hammad, N. F. Ibrahim, *Progress in Orthodontics*, **2014**, 16, 33.
10. V. Bolaños-Carmona, B. Zein, M. Menéndez-Núñez, P. Sánchez-Sánchez, L. Ceballos-García, S. González-López, *Dental Materials Journal*, **2015**, 34, 449.
11. J.A. von Fraunhofer, M. M. Rogers, *General Dentistry*, **2004**, 52, 308.
12. C. Speera, D. Zimnyb, W. Hopfenmuellerc, E. Holtgrave, *Angle Orthodontist*, **2005**, 75, 5.
13. J.F. Tahmassebi, M.S.Duggal, G. Malik-Kotru, M.E. Curzon, *Journal of Dentistry*, **2006**, 34, 2.
14. H.H. Yip, R.W. Wong, U. Hägg, *World Journal of Orthodontics*, **2009**, 10, 33.
15. J.M. Steffen, *Angle Orthodontist*, **1996**, 66, 449.
16. A. Valiollah, N. Fatemeh, R. Mehdi, K. Ahmad, Mohammad S. Barati. *Electron physician*, **2017**, 9, 3584.
17. F. Öztürk, M. Ersöz, S.A. Öztürk, E. Hatunoğlu, S. Malkoç. *European Journal of Orthodontics*, **2016**, 38, 163.
18. K. Zarrinnia, N.M. Eid, M.J. Kehoe, *American Journal of Orthodontics and Dentofacial Orthopaedics*, **1995**, 108, 284.
19. M. Fjeld, B. Øgaard, *American Journal of Orthodontics and Dentofacial Orthopaedics*, **2006**, 130, 575.
20. E. İşman, E.S. Karaarslan, R. Okşayan, A.R. Tunçdemir, S. Üşümez, N. Adanir, M.A. Cebe, *Dental Materials Journal*, **2012**, 31, 947.

SYNTHESIS, CHARACTERIZATION AND MOLECULAR MODELING OF TRANSITION METAL COMPLEXES WITH THEOPHYLLINE

ATTILA-ZSOLT KUN^a, BETTINA CSURKA^a, FIRUTA GOGA^a,
EDIT FORIZS^{a,*}, ADRIAN PATRUT^a

ABSTRACT. Mixed-ligand complexes of Cu(II) and Ni(II) with deprotonated theophylline (th) and propane-1,2-diamine (pda) were synthesized and characterized by elemental analysis, IR spectroscopy, and thermal analysis. Calculations and geometry optimization were made applying Mopac 2012 program at the level of semi-empirical method PM6.

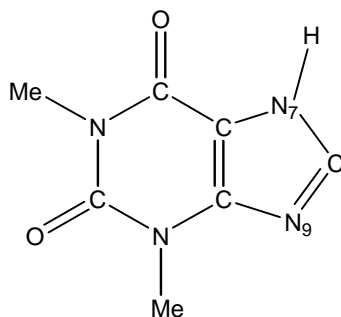
Keywords: propane-1,2-diamine, theophylline, mixed-ligand complexes, PM6

INTRODUCTION

Theophylline is a purine alkaloid, with important biological properties. Theophylline (Scheme 1) is used in medicine to treat diseases such as asthma and chronic obstructive pulmonary disease. Transition metal complexes of theophylline may serve as model compounds for studying the interaction between metal ions and the oxopurine bases of nucleic acids. According to the literature, in basic medium the theophyllinato anion coordinates *via* N(7) [1-3] as monodentate ligand. Typically, the neutral theophylline ligand exhibits a similar coordination [4]; however, N(9) coordination was also described [5]. In some cases it acts as bidentate N(7)/O(6) chelating ligand [6,7] or as bridging ligand, involving simultaneously N(7)/O(6) chelation and N(9) coordination [8].

^a Babeş-Bolyai University, Faculty of Chemistry and Chemical Engineering, 11 Arany János Str., RO-400028, Cluj-Napoca, Romania,

* Corresponding author: eforizs@chem.ubbcluj.ro

**Scheme 1.**

Continuing our interest in the field of bioactive materials [9-13] we started a systematic study on the coordination compounds of purine alkaloids. In the last years complexes containing theophylline and various N and N,N-donor ligands were prepared and characterized [14-16]. Here we report the synthesis of two new compounds, with the general formula $[M(\text{th})_2\text{L}]$, where M: Cu(II) (1), Ni(II) (2) and L: propane-1,2-diamine (pda) is a simple bidentate ligand [17-19]. The complexes were characterized by elemental analyses, FTIR spectroscopy and thermogravimetric analysis. Semiempirical calculations were made on the PM6 level to provide the possible structure of the complexes.

RESULTS AND DISCUSSION

FTIR spectra

The two strong bands in the IR spectrum of theophylline (1714s, 1667s), assigned to the stretching vibration of the carbonyl groups are shifted in the spectra of both complexes toward lower wavenumbers (1700 and 1660 cm^{-1} in **1**, and 1696, 1653 cm^{-1} in **2**) as a consequence of the deprotonation of theophylline at N(7) atom [9,14]. In complexes, the C=N ring vibrations (1566 cm^{-1}) of theophylline are shifted toward lower values, suggesting that the ligand coordinates *via* the imidazole N(7) atom.

There are significant changes in the bands assigned to N–H vibrations, as a consequence of the deprotonation of theophylline at N(7) atom and coordination of the diamine type ligands. The symmetric and antisymmetric stretching vibrations of the coordinated NH_2 groups of the diamine can be assigned at 3232 and 3133 cm^{-1} in complex **1**, and 3230 and 3199 cm^{-1} in complex **2**. The ν_{CH} vibrations of propane-1,2-diamine are recorded at 2956 – 2878 cm^{-1} for the aliphatic CH_2 and CH_3 groups.

The FTIR spectra of both complexes, **1** and **2**, suggest that theophylline acts as a monodentate ligand and coordinates the metal ion *via* the N(7) atom. The diamine behaves as a bidentate chelating ligand.

Thermal analysis

The thermogravimetric curve of complex **1** indicates a stepwise decomposition. First 1.69% of adsorbed water was removed. The complex is stable up to 287 °C. In the first well defined endothermic step, the chelating propane-1,2-diamine molecule and a theophylline moieties are eliminated in the temperature range of 287 – 347 °C (experimental weight loss 50,6%, calculated 51%), suggesting that both molecules are strongly bonded (Figure 1).

The next mass loss in the temperature range 380 – 425 °C, corresponds to the release and pyrolysis of second theophyllinato moiety. The last decomposition step is exothermic, showing maxima at 412 °C; the final decomposition product is CuO (exp. solid residue 15 %; calc. 16,04%).

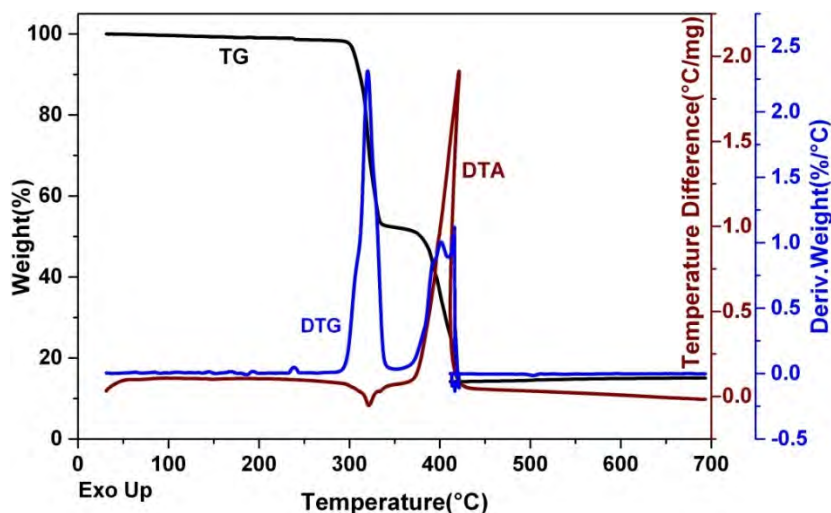


Figure 1. Thermal curves of complex **1**.

The complex **2** undergoes a single step decomposition. First the strongly adsorbed water was eliminated. The complex is stable up to 350 °C; above this value the two theophyllinato moieties and the propane-1,2-diamine molecule are evolved in the same step, in the range 390–440°C (exp. weight

loss 88.5%, calc. 88%). The oxidative decomposition in air is exothermic. The high decomposition temperature is a consequence of the bidentate binding mode of the diamine. The final decomposition product is NiO.

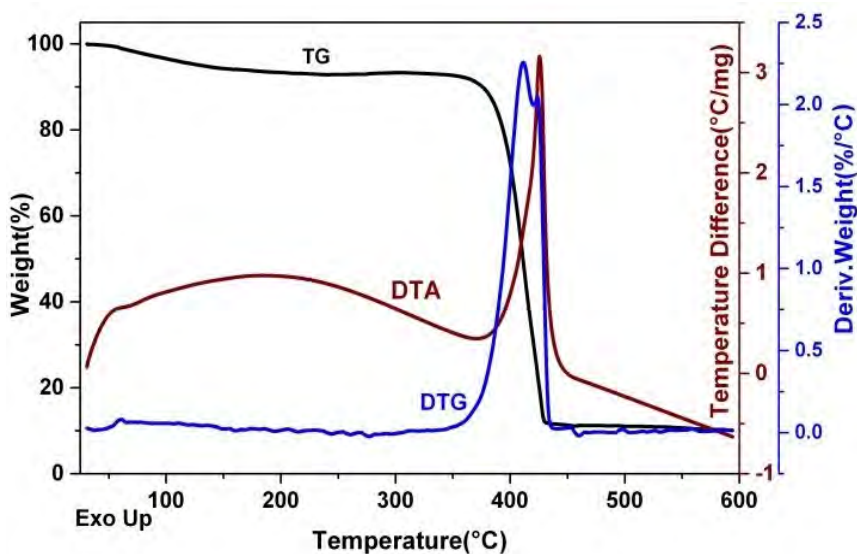


Figure 2. Thermal curves of complex 2.

Computational details

The assumed starting structures of the complexes were generated by Spartan'06 [20] program. Geometry optimization of the structures was performed using the PM6 [21] semi-empirical method with the Mopac 2012 [22] program. By performing the vibrational analysis of the optimized structures, it was verified that real minimum points were found on the potential energy surface of the molecule. The molecular structure of the complexes **1** and **2** was optimized in the gas phase.

Optimized geometries

The presumed starting structure for complexes containing one propane-1,2-diamine ligand was a distorted tetrahedron. In this case the M(pdca) chelate fragment provides only two basic structures assuming an axial or equatorial methyl group. As the two theophyllinate anions can rotate

freely around the M-N(7) bonds, a total of 36 rotamers (six-fold rotation around the bonds) were considered. For the Ni(II) complex high-spin (triplet) and low-spin (singlet) states were optimized. Tables 1 to 3 display data of the most stable optimized [M(th)₂(pda)] structure types.

Table 1. Data of [Cu(th)₂(pda)] complex conformers

Structure	E (kJ/mol)	Cu-N(7), Å	Cu-N(7)', Å	N(7)-Cu-N(7)', °
Cu-ax-1	-346.75	1.910	1.909	95.17
Cu-ax-2	-342.95	1.866	1.866	93.94
Cu-ax-3	-342.05	1.915	1.863	94.20
Cu-eq-1	-355.63	1.907	1.906	94.73
Cu-eq-2	-351.69	1.911	1.862	93.96
Cu-eq-3	-349.92	1.866	1.865	93.95

Table 2. Data of [Ni(th)₂(pda)] complex conformers – singlet state

Structure	E (kJ/mol)	Ni-N(7), Å	Ni-N(7)', Å	N(7)-Ni-N(7)', °
Ni-ax-1-s	-609.26	1.880	1.880	92.55
Ni-ax-2-s	-588.07	1.885	1.885	94.22
Ni-eq-1-s	-616.55	1.881	1.881	92.41
Ni-eq-2-s	-597.76	1.884	1.883	94.74

Table 3. Data of [Ni(th)₂(pda)] complex conformers – triplet state

Structure	E (kJ/mol)	Ni-N(7), Å	Ni-N(7)', Å	N(7)-Ni-N(7)', °
Ni-ax-1-t	-530.07	1.928	1.924	148.95
Ni-ax-2-t	-520.29	1.954	1.950	95.70
Ni-eq-1-t	-543.44	1.928	1.926	150.09
Ni-eq-2-t	-540.90	1.951	1.942	96.14

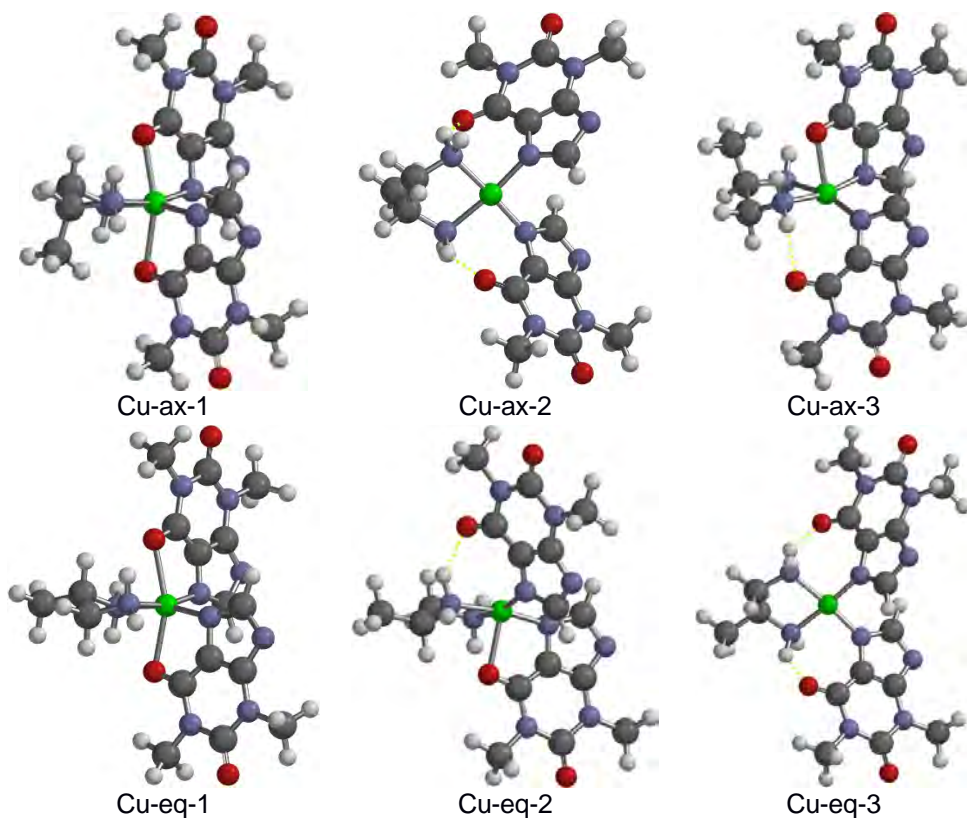


Figure 3. Optimized structures of the complex 1.

The equatorial orientation of the methyl group on the M(pda) chelate ring is favored energetically by ≈ 10 kJ/mol, on many occasions the conformation changed from axial to equatorial during the optimization.

Optimization of copper(II) complex rotamers led to 3 different structure types. The most stable structures (Cu-eq-1 and Cu-ax-1) are hexa-coordinated, both theophyllinato anions behaving as N,O chelating ligands, having 2.27 – 2.29 Å Cu-O bond distances and 160 – 165° O-Cu-O bond angles. In the case of Cu-eq-2 and Cu-ax-3, only one theophyllinato anion behaves as a chelating ligand (Cu-O distance 2.1 – 2.3 Å), the second is N(7)-coordinated, and forms an O...H hydrogen bond with the pda ligand. Structures Cu-eq-3 and Cu-ax-2 show a square planar coordination stabilized by two hydrogen bonds. The energy difference between the structure types is low – intermolecular interactions may lead to the stabilization of any of them.

Energy results for the optimization of the Ni(II) complex show the stabilization of low-spin (singlet) state by 60-70 kJ/mol.

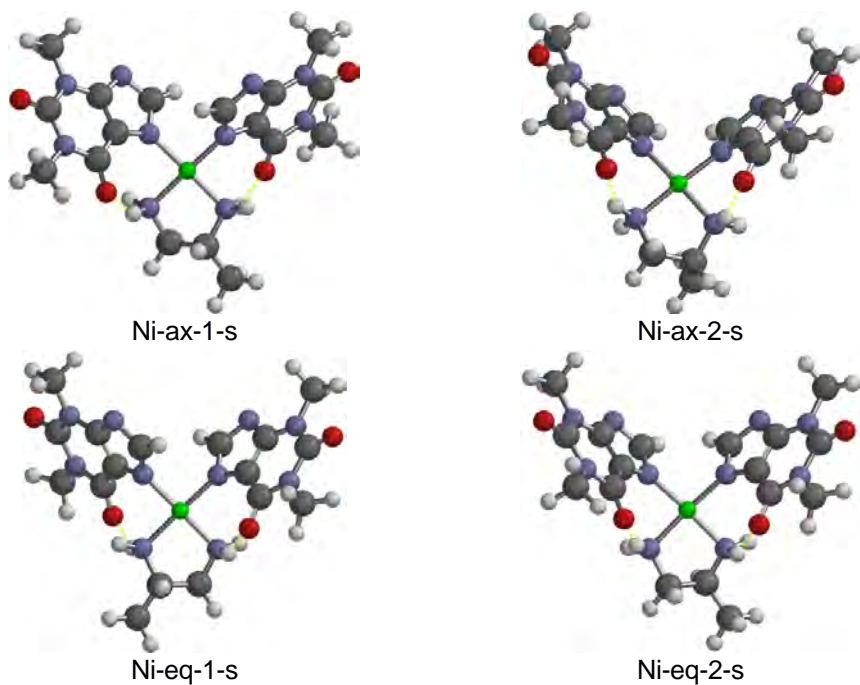


Figure 4. Optimized structures of the complex 2 – singlet state.

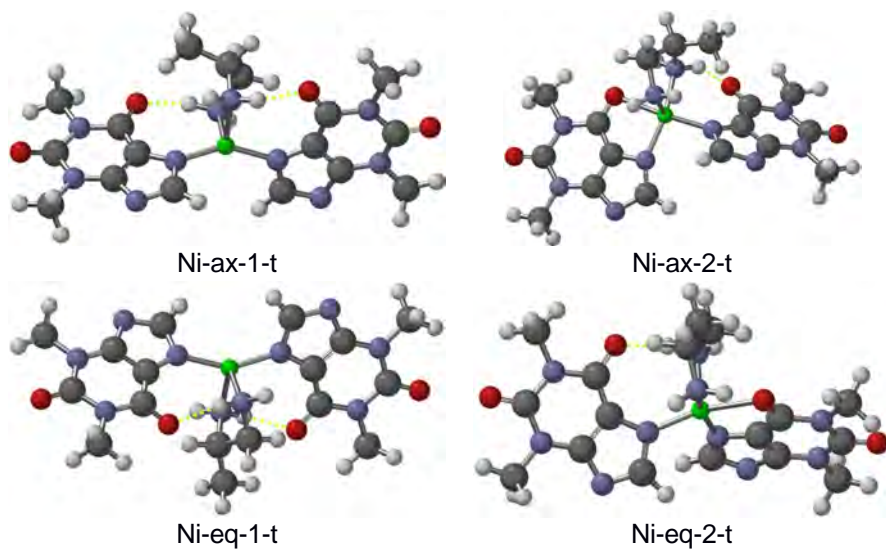


Figure 5. Optimized structures of the complex 2 – triplet state.

The low-spin Ni(II) complex structure shows a square-planar coordination and the stabilization of the complex by hydrogen bonds. The theophyllinato ligands adopt antiparallel orientation (Ni-eq-1-s, Ni-ax-1-s), the parallel orientation (Ni-eq-2-s, Ni-ax-2-s) is higher in energy by ≈ 30 kJ/mol.

CONCLUSIONS

FTIR spectra and thermal data of **2** indicate a tetra-coordinated structure, while a higher coordination of the metal ions with bidentate bonding of diamine and at least of one theophyllinato ligand is suggested for **1**. The theophylline coordinates *via* the N(7) nitrogen or as an N(7)-O(6) bidentate ligand. The obtained theoretical data are compatible with the experimental results.

EXPERIMENTAL SECTION

The complexes were prepared in aqueous solution as previously reported [2, 14]. FTIR spectra were recorded on a Jasco FTIR 600 spectrophotometer in the 4000–400 cm^{-1} range, using KBr pellets. Thermal decomposition was investigated with a Universal V2.3C TA Instruments, at a heating rate of 10°C min^{-1} . The composition of complexes was determined by elemental analysis (C, H, N).

Syntheses of [Cu(th)₂(pda)]·(1). To a suspension of theophylline (0.2 g, 1.1 mmol) in water (10 mL) was added propane-1,2-diamine (0.5 mL). The resulted clear solution was mixed with a second solution of Cu(CH₃COO)₂·H₂O (0.14 g, 0.7 mmol) in a propane-1,2-diamine–water mixture (1 mL of propane-1,2-diamine in 4 mL of water). The dark violet reaction mixture was stirred for 30 minutes at 40 °C. The resulted violet polycrystalline powder was filtered, washed with ethyl alcohol and dried. Analysis: found (calc. for CuC₁₇H₂₄N₁₀O₄ MW 495.74) C 41.08 (41.15), N 28.22 (28.25), H 5.00 (4.88). Yield: 32.7%, M.P.: > 300 °C.

IR (KBr pellet), cm^{-1} : $\nu(\text{NH}_2)$ 3232m, 3133m; $\nu(\text{CH}_2)$ 2953m, 2878m; $\nu(\text{C}=\text{O})$ 1700s, 1660s; $\nu(\text{C}=\text{N})$ 1531s.

[Ni(th)₂(pda)]·(2) was obtained hydrothermally. The theophylline (0.186 g, 1 mmol) was dissolved in 2 mL of distilled water and 0.082 mL of propane-1,2-diamine. Next, 0.117 g (0.5 mmol) of NiCl₂·6H₂O aqueous solution (8 mL) was added to this mixture dropwise under stirring. The orange solution was introduced in a 23 mL Teflon-lined stainless steel autoclave and heated at 160°C under

autogenous pressure in an oven for 4 days. The resulting solution was cooled at room temperature at a rate of 5°C/h 5°C h⁻¹. Red crystals were collected, filtered and washed with acetone. Analysis: found (calc. for NiC₁₇H₂₄N₁₀O₄ MW 490.89) C 41.28 (41.56), N 28.18 (28.53), H 4.88 (4.93), M.P.: >300 °C.

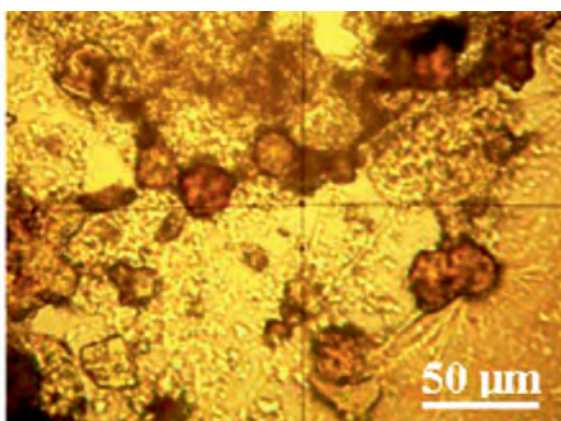
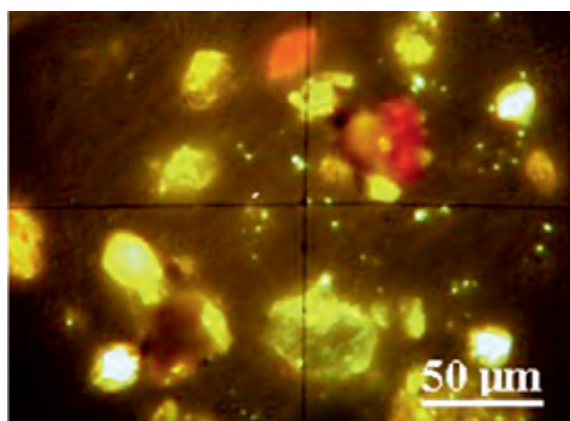
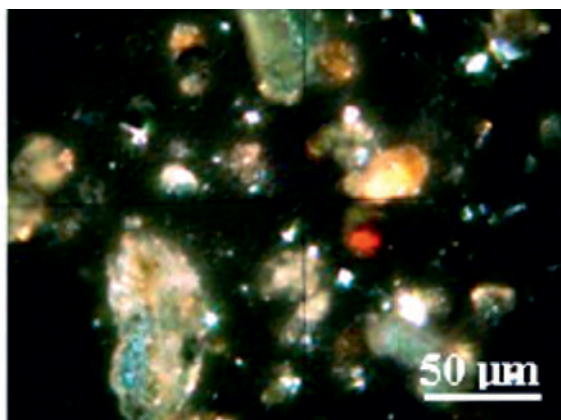
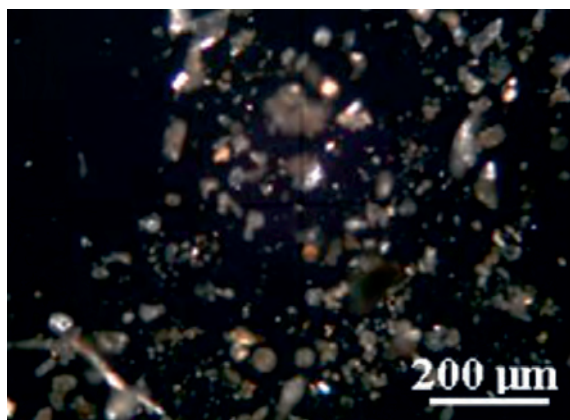
IR (KBr pellet), cm⁻¹: ν(NH₂) 3230m, 3199m; ν(CH₂) 2956m, 2879w; ν(C=O) 1696vs, 1653vs; ν(C=N) 1528m.

Abbreviations: m - medium, s – strong, vs – very strong, w – weak.

REFERENCES

1. T.J. Kistenmacher, D.J. Szalda, L.G. Marzilli, *Inorganic Chemistry*, **1975**, *14*, 1686.
2. W.J. Birdsall, M.S. Zitzman, *Journal of Inorganic & Nuclear Chemistry*, **1979**, *41*, 116.
3. N.S. Begum, H. Manohar, *Polyhedron*, **1994**, *13*, 307.
4. M.B. Cingi, A.M.M. Lanfredi, A. Tiripicchio, M. Tiripicchio-Camellini, *Transition Metal Chemistry*, **1979**, *4*, 221.
5. K. Aoki, H. Yamazaki, *Journal of the Chemical Society - Chemical Communications*, **1980**, 186.
6. D.J. Szalda, T.J. Kistenmacher, L.G. Marzilli, *Journal of the American Chemical Society*, **1976**, *98*, 8371.
7. D. Cozak, A. Mardhy, M.J. Olivier, A.L. Beauchamp, *Inorganic Chemistry*, **1986**, *25*, 2600.
8. J. Lorberth, W. Massa, M.E. Essawi, L. Labib, *Angewandte Chemie-International Edition in English*, **1988**, *27*, 1160.
9. E. Forizs, L. David, O. Cozar, V. Chis, G. Damian, J. Csibi, *Journal of Molecular Structure*, **1999**, *482*, 143.
10. E. Forizs, L. David, O. Cozar, C. Craciun, M. Venter, M. Kilyen, *Journal of Molecular Structure*, **1997**, *408*, 195.
11. F. Goga, E. Forizs, A. Avram, A. Rotaru, A. Lucian, I. Petean, A. Mocanu, M. Tomoaia-Cotisel, *Revista de Chimie (Bucharest)*, **2017**, *68(6)*, 1193.
12. O. Horovitz, Gh. Tomoaia, A. Mocanu, T. Yupsanis, M. Tomoaia-Cotisel, *Gold Bulletin*, **2007**, *40(4)*, 295.
13. G. Furtos, M. Tomoaia-Cotisel, C. Garbo, M. Senila, N. Jumate, I. Vida-Simiti, C. Prejmerean, *Particulate Science and Technology*, **2013**, *31(4)*, 392.
14. P. Bombicz, J. Madarász, E. Forizs, M. Czugler, G. Pokol, S. Gál, A. Kálmán, *Zeitschrift für Kristallographie*, **2000**, *215*, 317.
15. E. Forizs, A. Debreczeni, A. Patrut, A.-Z. Kun, I.B. Cozar, L. David, I. Silaghi-Dumitrescu, *Revue Roumaine de Chimie*, **2010**, *55(10)*, 697.
16. C. Nagy, C. Somesan, A.-Z. Kun, B. Mihaly, E. Forizs, L. David, *Studia UBB Chemia*, **2011**, *56(3)*, 265.

17. I. Potočník, M. Vavra, D. Steinborn, C. Wagner, *Acta Crystallographica Section E - Structure Reports Online*, **2008**, *64*, m235.
18. E. Colacio, R. Kivekas, F. Lloret, M. Sunberg, J. Suarez-Varela, M. Bardaji, A. Laguna, *Inorganic Chemistry*, **2002**, *41*, 5141.
19. X. Hu, X. Xu, D. Wang, X. Li, *Acta Crystallographica Section E- Structure Reports Online*, **2008**, *64*, m1636.
20. Spartan'06, Wavefunction, Inc., Irvine, CA **2006**.
21. J.J.P. Stewart, *Journal of Molecular Modeling*, **2007**, *13*, 1173.
22. MOPAC2012, J.J.P. Stewart, Stewart Computational Chemistry, Colorado Springs, CO, USA, [HTTP://OpenMOPAC.net](http://OpenMOPAC.net) (**2012**).



CHEMIA

4/2017
Tom II

**STUDIA
UNIVERSITATIS BABEȘ-BOLYAI
CHEMIA**

**4/2017
Tom II**

EDITORIAL BOARD OF STUDIA UNIVERSITATIS BABEȘ-BOLYAI CHEMIA

ONORARY EDITOR:

IONEL HAIDUC - Member of the Romanian Academy

EDITOR-IN-CHIEF:

LUMINIȚA SILAGHI-DUMITRESCU

EXECUTIVE EDITOR:

CASTELIA CRISTEA

EDITORIAL BOARD:

PAUL ȘERBAN AGACHI, Babeș-Bolyai University, Cluj-Napoca, Romania

LIVAIN BREAU, UQAM University of Quebec, Montreal, Canada

HANS JOACHIM BREUNIG, Institute of Inorganic and Physical Chemistry,
University of Bremen, Bremen, Germany

MIRCEA DIUDEA, Babeș-Bolyai University, Cluj-Napoca, Romania

JEAN ESCUDIE, HFA, Paul Sabatier University, Toulouse, France

ION GROSU, Babeș-Bolyai University, Cluj-Napoca, Romania

EVAMARIE HEY-HAWKINS, University of Leipzig, Leipzig, Germany

FLORIN DAN IRIMIE, Babeș-Bolyai University, Cluj-Napoca, Romania

FERENC KILAR, University of Pecs, Pecs, Hungary

BRUCE KING, University of Georgia, Athens, Georgia, USA

ANTONIO LAGUNA, Department of Inorganic Chemistry, ICMA, University of
Zaragoza, Zaragoza, Spain

JURGEN LIEBSCHER, Humboldt University, Berlin, Germany

KIERAN MOLLOY, University of Bath, Bath, UK

IONEL CĂȚĂLIN POPESCU, Babeș-Bolyai University, Cluj-Napoca, Romania

CRISTIAN SILVESTRU, Babeș-Bolyai University, Cluj-Napoca, Romania

<http://chem.ubbcluj.ro/~studiachemia/>; studiachemia@chem.ubbcluj.ro

http://www.studia.ubbcluj.ro/serii/chemia/index_en.html

**YEAR
MONTH
ISSUE
TOM**

**Volume 62 (LXII) 2017
DECEMBER
4
II**

S T U D I A UNIVERSITATIS BABEŞ-BOLYAI CHEMIA

4

ISSUE DOI:10.24193/subbchem.2017.4

Tom II

**On the occasion of the 45th anniversary of Chemical
Engineering studies at Babeş-Bolyai University**

STUDIA UBB EDITORIAL OFFICE: B.P. Hasdeu no. 51, 400371 Cluj-Napoca, Romania,
Phone + 40 264 405352

CUPRINS – CONTENT – SOMMAIRE – INHALT

- LIVIU LITERAT, 45 Years of Chemical Engineering in the University City of Cluj-Napoca 1971-2016. Landmarks on the Establishment, Development and Affirmation of Chemical Engineering Education in the University City of Cluj-Napoca vii
- VASILE-MIRCEA CRISTEA, Control Approaches of the Carbonation Column for Soda Manufacturing..... 221
- LETITIA PETRESCU, ARPAD IMRE-LUCACI, CRISTINA IZABELLA BERCI, Modelling and Simulation of Fuels Production from Syngas 231

DANIELA-MARIA LOHAN, CALIN-CRISTIAN CORMOS, Evaluation of Hydrogen Production from Catalytic Reforming of Liquefied Petroleum Gas with Carbon Capture and Storage	241
RÉKA BARABÁS, NORBERT MUNTEAN, GABRIELLA SZABÓ, KRISZTINA MAURER, LILIANA BIZO, Preparation and Characterizations of New Biomaterials by Anthocyanins Adsorption on Hydroxyapatite-Based Materials	253
OANA CADAR, REKA BALINT, GHEORGHE TOMOAI, DIANA FLOREA, IOAN PETEAN, AURORA MOCANU, OSSY HOROVITZ, MARIA TOMOAI-COTISEL, Behavior of Multisubstituted Hydroxyapatites in Water and Simulated Body Fluid.....	269
SIMION DRĂGAN, Experimental Study of Sulfur Dioxide Absorption into Carbonate Suspensions with Sulfites Addition.....	283
SILVIA BURCĂ, CERASELLA INDOLEAN, ANDRADA MĂICĂNEANU, Malachite Green Dye Adsorption from Model Aqueous Solutions using Corn Cob Activated Carbon (CCAC)	293
ADINA GHIRIȘAN, VASILE MICLEĂUȘ, Comparative Study of Spray-Drying and Freeze-Drying on the Soluble Coffee Properties.....	309
FLORIN DUMITRU BORA, DONICI ALINA, ANAMARIA CALUGAR, IOAN VALENTIN PETRESCU MAG, EMESE GÁL, CLAUDIU IOAN BUNEA, Determination of Heavy Metals and Lead-Strontium Isotope Characterization from Merlot Soil Samples, Dealu Bujorului Vineyard	317
DELIA PIRȘAN, ANAMARIA TOROK, CLAUDIU TĂNĂSELIA, PAULA PODEA, Mineralogical and Chemical Characterization of the Soil from Bârzava River Area.....	333
LILIANA HORNEA, MARIA GOREA, NICOLAE HAR, Study of (Pb, Ba) - CRT Glass Waste Behaviour as a Partial Aggregate Replacement in Cement Mortars	343
JULIETA DANIELA CHELARU, DOVRAN AYLAKOV, LIANA MARIA MUREȘAN, Corrosion Inhibition of Low Carbon Steel in Simulated Wastewater from Petroleum Industry.....	357
MISCA B.R.H., CHIRA G.C., The Study of Dissolving Urea Granules Based on the Generalised Dimensional Anaysis	369
RALUCA ANAMARIA SEPTLEAN, MYRAT VELNAZAROV, DOINA PRODAN, IOANA PERHAITA, OVIDIU NEMES, MARIOARA MOLDOVAN, New Functionalized Glass Fibers Employing Calixarenic Systems	381
SIMONA POPA, SORINA BORAN, Quantitative Measurement of the Leather Degree of Swelling.....	391

DOINA PRODAN, MIUȚA FILIP, IOANA PERHAIȚA, MIHAELA VLASSA, VIOLETA POPESCU, IOAN MARCUS, MARIOARA MOLDOVAN, The Influence of Minerals and Lactose Content on the Stability of Whey Protein Powders	397
NOÉMI DEAK, SONIA MALLET-LADEIRA, LUMINITA SILAGHI-DUMITRESCU, DAVID MADEC, GABRIELA NEMES, New Phosphorus Containing Bis-Sulfone Ligands	411
GULZIYA A. SEILKHANOVA, ANDREY P. KURBATOV, YENLIK ZH. USSIPBEKOVA, ANDREY V. BEREZOVSKIY, MICHAEL K. NAYRYZBAEV, Electrochemical Deposition and Dissolution of Thallium Oxide (III)	421
RUSUL KHALEEL IBRAHIM, MAAN HAYYAN, MOHAMMED ABDULHAKIM ALSAADI, SHALIZA IBRAHIM, ADEEB HAYYAN, MOHD ALI HASHIM, Diethylene Glycol Based Deep Eutectic Solvents and Their Physical Properties	433
RÉKA KOTHENCZ, ROLAND NAGY, LÁSZLÓ BARTHA, Determination of HLB Values of Some Nonionic Surfactants and their Mixtures	451
OSMAN ISMAIL, An Experimental and Modeling Investigation on Drying of Chicken Meat in Convective Dryer	459
O. I. MAILE, E. MUZENDA, Carbon Dioxide Removal using Ammonia in Biogas Upgrading and Purification	471
CSILLA NOÉMI TÓTH, SÁNDOR HARANGI, ANIKÓ KÁROLYI, ISTVÁN FÁBIÁN, EDINA BARANYAI, Method Development for the Elemental Analysis of Organic Rich Soil Samples by Microwave Plasma Atomic Emission Spectrometry	483
IZABELLA IRSAI, ALEXANDRU LUPAN, CORNELIA MAJDIK, RADU SILAGHI-DUMITRESCU, Computational Investigation of Spectroscopic Parameters in Putative Secondary Structure Elements for Polylactic Acid and Comparison with Experiment	495

Studia Universitatis Babes-Bolyai Chemia has been selected for coverage in Thomson Reuters products and custom information services. Beginning with V. 53 (1) 2008, this publication is indexed and abstracted in the following:

- Science Citation Index Expanded (also known as SciSearch®)
- Chemistry Citation Index®
- Journal Citation Reports/Science Edition

45 YEARS OF CHEMICAL ENGINEERING IN THE UNIVERSITY CITY OF CLUJ-NAPOCA 1971-2016 LANDMARKS ON THE ESTABLISHMENT, DEVELOPMENT AND AFFIRMATION OF CHEMICAL ENGINEERING EDUCATION IN THE UNIVERSITARY CITY OF CLUJ-NAPOCA

Prof. Univ. Emerit Dr. Ing. LIVIU LITERAT¹

²*Quorum pars magna fui*
Vergiliu, Eneida, II, 6

In Cluj, **chemistry engineering** education officially begins in **1971/72** with the **Polytechnic Institute (IPC)** setting up an **Industrial Chemistry faculty** [1] with engineering and sub-engineers, specializing in **Technology of Inorganic Substances (TIS)** and **Technology of Building Materials (TBM)**, forms of higher education with a **chemical engineering** profile, science, discipline and profession with a specific field, and its own and autonomous organization status. [2] Unfortunately only the last proposal [3] (sub-engineers) was approved at the **Faculty of Civil Engineering**, which was a necessary, but insufficient solution for a viable faculty with legal personality, structure and autonomy of organization that had the approval of the Ministry of Forest Economy and Building Materials (**MEFMC**), and not for the first one by the Ministry of Chemical Industry (**MICH**), with the observation: “lack of material basis, specialists and experience” in the field. Considering, however, the intensive priority development of the chemical industry in the Transylvanian area, requiring highly qualified specialists, it was agreed to reopen the proposal for the next five-year period (1976-1980), conditioned in some ways also by the evolution, respectively, the performance of the already approved TBM Section [4]. It was,

¹ Department of Chemical Engineering, Faculty of Chemistry and Chemical Engineering, Babeş-Bolyai University, Cluj-Napoca

² *Quorum pars magna fui* – At which I played a significant role.

nevertheless, a hope, an encouragement, a motivation to mobilize, at any cost, for success. **The process was completed** in **1977**, however, not in the **Polytechnic**, but in the **University** as a result of the transfer, in **1974**, of the TBM Section from the Faculty of **Civil Engineering** to **Chemistry** in 1974, by **Decree No.147/1974** [5], so that the decision came too late and not in favour of the demanded **Industrial Chemistry** faculty [1], which was never established, but merely changed one master for another. [6]

As a consequence, the “**chemical engineering**” phenomenon in Cluj, in the absence of a free and independent structure of organization, **as a faculty**, will continue an atypical course in the shadow of the two higher education institutions, both with too few areas of common interest and concerns in the field.

The solution, perseverance and the implementation of modern technology in the university tradition by the compatibility of the principles of Humboldt's academic education of “pure ideas” [7] with the “applied” ones of the American Taylor's [8], from the technical education, the basic idea which was anticipated in “**The Duty of Our Life**” [9] by the great historian, archaeologist, professor and academician **Vasile Pârvan** (1882-1927), rightly considered “gray eminence”, spiritual mentor, ideologist, architect, architect and strategist of the National University of Upper Dacia [9], which, on the basis of a thorough and rigorous study of the Western European and American universities of the times, made a visionary project of great scope and broad perspective, adapted to the conditions of the recently united Romania (1918), which became a corner stone and Charter of our University. [10]

It is very difficult to encompass in a few words the excitement of four decades and a half of the life of some institutions, without taking account of their specificity, tradition, their historical time and the paradigms of their evolution. That is why, in the analysis of the events, there is no place to tell, except with parsimony, the “epic of chemical engineering” in Cluj, not completely as in the story of Vergiliu of Oneidas, which I chose as a motto. [11]

THE ITINERARY OF THE CHEMICAL ENGINEERING EDUCATION IN CLUJ. LANDMARKS OVER TIME

In the evolution of the chemical engineering education in Cluj-Napoca, several moments, events and important stages were distinguished, marking its course and development. These are related to the administrative affiliation to the **Polytechnic Institute** of Cluj-Napoca (1971-1974) and the **Babeş-Bolyai University** (1974/75), respectively.

I. The first stage (1971-1974) belongs to the Polytechnic Institute

1971 The beginning of chemical engineering at the Polytechnic Institute of Cluj-Napoca.

The Polytechnic of Cluj represents for the chemical engineering education of the Cluj-Napoca University Center the chance to exist and the first steps in its development. [3]

1971 Establishment of the TBM Section, a chemical engineering course (day course) at the Department of Civil and Industrial Buildings of the Faculty of Civil Engineering (initiator: assistant professor Liviu Literat).

1971-1974 The organization and development of the TBM Section and of the chemical engineering education in the Politehnica of Cluj takes place.

1974 The transfer of the TBM Section to the Faculty of Chemistry in the Babeş-Bolyai University under Decree 147/1974 on the Restructuring of Higher Education [5].

II. The second stage (from 1974 - present) continues in the Babeş-Bolyai University, where several periods of administrative and organizational evolution are distinguished:

1974 By transferring the TBM Section to *the Faculty of Chemistry*, the University diversifies and extends its scope also for technical-engineering higher education (in chemistry).

II. a. 1974-1977 TBM Section at the Faculty of Chemistry. (Dean, Prof. Dr. Liviu Oniciu, Deputy Prof. Dr. Ionel Haiduc). The TBM Section is assigned to the *Department of Organic Chemistry and Technology* of the Faculty of Chemistry and managed (according to the transfer document) in teaching, instructional and administrative terms, jointly by the University (UBB) and the Polytechnic Institute (IPC) [6].

II. b. 1977 The Faculty of Chemical Technology (1977-1990) was founded with the same name, status and competencies as those in the Polytechnic Institutes (Bucharest, Iasi, Timisoara). The deans of the new faculty were professor Zeno Andrei (1976-1984), professor dr. Liviu Oniciu (1984-1988) and Prof. Dr. Ionel Haiduc (1988-1990).

1977 To the head of the *Department of Organic Chemistry and Technology* (DOCT) is appointed Prof. Dr. Eng. Liviu Literat (Rector's Decision No. 485/17 January 1977 and the Ministry of Education, No. 24513/6 January 1977). From his position, he acts for the **establishment of the Organic Substances Technology (TSO)** specialization section, engineers, and activates until 1985 (two legislatures) in the organization, development, material and documentary endowment, attracting and employing engineering staff, subordinate and faculty departments.

1977 Establishment of the **Organic Substances Technology (TSO)** and **Inorganic Substances Technology (TSA)** specialization sections, engineers, day courses, the last one requested initially (1971) in the Polytechnics [4].

1985 There is an administrative restructuring of the faculty under which the Departments of Organic Chemistry and Technology (**COT**) and Chemistry-Physics (**CF**) are united under the leadership of Prof. Dr. Emil Chifu (1985-1990) under the name of the Department of Physical Chemistry, Organics and Technology (CFOT) and the Inorganic and Analytical Chemistry under the leadership of Prof. Gh. Marcu.

II. c. 1990 **The Faculty of Chemistry and Industrial Chemistry** (1990-1992) was established as a result of the reorganization of chemistry and chemical engineering education from the former Faculty of Chemical Technology (Dean, Prof. Dr. Emil Cordos, Vice-Chancellor Sorin Mager).

1990 Professor dr. Ionel Haiduc is elected Rector of Babeş-Bolyai University.

1990 The **Department of Chemical Engineering** (Chief of the Department, Prof. dr.ing. Liviu Literat) was established and the **Department of Technological Chemistry** (Head of the Department, lecturer, Florin Jugrestan, Ph.D.) was re-established [5]. It is proposed (by Prof. Liviu Literat) to structure the faculty into two representative departments for the new faculty: the **Department of Chemistry** and the **Department of Chemical Engineering**. The former, comprised the classical departments of Analytical Chemistry, Inorganic, Organic and Chemistry-Physics, and the latter, the departments of Chemical Engineering and Chemistry of Technology. [4]

1990 The Specialization Section (Engineers) of **Oxidation Materials Science and Engineering (SIMO)** (initiator Prof. L. Literat) is established and a PhD degree in chemical engineering is granted to professor dr.ing. Liviu Literat in Cluj (first Ph.D. in Chemical Engineering from the Cluj-Napoca University Center). [6]

1991 20th Anniversary of **Chemical Engineering Education in Cluj-Napoca** (Jubilee Symposium, September 19-22, 1991).

II. d. 1992 **The Faculty of Chemistry and Chemical Engineering was established** (name change approved by Order No. 6540/1994 from the 1994/95 school year). Newly elected Dean, Prof. Dr. Sorin Mager (1992-1996 and 1996-2000). Rector, reelected, was acad. Prof. Dr. Ionel Haiduc.

1992 The **Department of Chemical Engineering also includes the Science and Engineering of Oxide Materials** profile and is named the **Department of Chemical Engineering and Oxide Materials Science** (Chief of the department: Prof. Eng. Liviu Literat).

1993 Dr. Dulămiță Nicu (1993-2003) is elected head of the **Department of Chemical Technology**.

1993 Continuing study was approved (evening classes, not mandatory attendance) for the **TBM** sub-engineers series is obtained under Government Decision no. 1156 of 30 Oct 1990, published in the Official Gazette no. 109 of May 27, 1992 (Prof. L. Literat).

1994 Certification of two new chemical engineering specialties: **Biochemical Engineering (BE)** (Prof. Eng. Florin Irimie, PhD.) and **Informatics of Chemical Systems (ISC)**, Prof. Eng. Șerban Agachi, which is approved in 1995 by the Provisional Operating Authorization (GD No. 568/16 08.1995). [8].

1994 The first postgraduate programs in chemical engineering are initiated through **in-depth and master studies**: [9]

- Border Process Engineering (1994 / 95-2000 / 2001)
- Oxide systems engineering with special properties and applications (1995 / 96-2000 / 2001)

- Heterogeneous Catalysis and Biocatalysis (1995)

- Advanced Process Engineering (2001 / 2002-2008 / 2009).

1995 Accreditation (GD No. 568/1995) of Specialization sections, engineers: TSA, TSO and SIMO [10].

1995 The first **SIMO** engineers graduated (1990-1995).

1995 The Department of Chemical Engineering and Oxide Material Science initiates and becomes a founding member of the **Chemical Engineering Society of Romania (SICHR)**, Branch President Prof. Eng. Liviu Literat and Vice-President of the National Leadership Council [11].

1995 Professor **Liviu Literat** retires and becomes a **consultant teacher** (Rector's Decision No. 10.504 / 20.11.1995). [6]

The new Chief of the Department is Professor Eng. Eugenia Gavrilă (1995-1997).

1996 The Department of Chemical Engineering and Oxide Material Science is completed by the team of **Informatics of Chemical Systems** led by prof. Dr. Ing. Șerban Agachi.

1997 Professor PhD. Eng. Paul Șerban Agachi, General Chancellor of UBB (1996-2000) is elected chairman of the department. At the same time, he is also granted the right to conduct a PhD in **Applied Informatics**.

1997 The former proposal of Professor Liviu Literat for the establishment of the **Chemical Engineering Department** is implemented. Selected department directors: Prof. Dr. Nicu Dulămiță (1997 - 2003) and Prof. Ph. Eng. Florin Irimie (2003 - 2012).

1997 Official participation in the **60th anniversary of chemical engineering at the "Gh. Asachi" Technical University, Jassi**, 23.10.1997.

2000 A new **Department of Chemical Engineering** is established: the **Department of Biochemistry and Biochemical Engineering** (Chief of Prof. Eng. Florin Irimie, PhD).

2001 *The National Symposium “30 Years of Chemical Engineering in Cluj-Napoca”*, organized by the Department of Chemical Engineering and Oxidation Science, takes place (6-9 September).

2003 New Nomenclature of Specializations (GD No. 693 / 12.06.2003, published in OG No. 436/30 June 2003), changes the name of the TSA, TSO and ISC Sections into Engineering and Chemistry of Inorganic Substances (**ICSA**), Engineering and Chemistry of Organic Substances (**ICSO**) and respectively Chemical Engineering (**IC**) [12]

2004 Professor Liviu Literat is elected *honorary member* of the **Academy of Technical Sciences of Romania (ASTR)**, Chemical Engineering Section.

2005 *International Symposium Computer Aided Chemical Engineering Forum* (CAPE Forum), Cluj-Napoca, organized by the Department.

2005 Professor Șerban Agachi is elected a *correspondent member* of the ASTR, Automatic Section.

2006 National Chemical Engineering Symposium dedicated to the **35th anniversary of the Chemical Engineering education in Cluj-Napoca**, (July 3, Cluj-Napoca).

2006 Two new chemical engineering specialization sections are established: **Food Chemistry** and **Biochemical Technologies** and **Engineering and Environmental Protection in the Chemical and Petrochemical Industries**.

2007 The **Economic Engineering Section of the Chemical and Materials Industry is established**. The section has a short life, only 3 promotions (Figure 4 and 5).

2007 *European Symposium on Computer Aided Process Engineering (ESCAPE 17th)* 27-30 May 2007, Bucharest (jointly organized with POLITEHNICA University, Bucharest)

2008 (May) As the chairman of the Department is elected Prof. Vasile Mircea Cristea, Ph.D. (2008-2012).

2008 The 3rd **National Conference of the Romanian Academy of Technical Sciences organized by the ASTR Cluj branch**. “*Romanian Engineering: Past, Present and Future*” Cluj-Napoca, November 12-13 (co-organizers, Prof.L.Literat and Ș. Agachi, members of the Academy).

2008 Official participation at the **60th anniversary of the Faculty of Industrial Chemistry of Timisoara** (1948-2008). Timisoara, Oct. 2008.

2008 Participation of the Department at the **60th Anniversary of the Department of Oxidation and Nanomaterials Science and Engineering (ȘIMONA)**, Polytechnic University of Bucharest, Faculty of Applied Chemistry and Materials Science, Bucharest 17.11.2008.

2009-2012 New PhD consultants in Chemical Engineering: Prof. Dr. Petre Ilea and Ioan Bătiu.

2012 New system of university administrative organization. The functional unit becomes a Department, which includes, by individual or group option, the members of the former structures in specialized colleges. On this occasion, the bioengineering team (the former chair) goes from the chemical engineering department to the chemistry department lead by Prof. Dr. ing. F. Irimie.

2012 *The Hungarian teaching language chemistry and chemical engineering department is established.* Department Director assoc. prof. dr. Majdik Cornelia (2012-2016) and assist. prof. dr. Szabó Gabriella (2016 - present) (Figure 3).

2012 Professor Mircea Vasile Cristea is elected director of the Department of Chemical Engineering (2012-2016).

2012 Professor L. Literat receives the honorary title of professor emeritus.

2014 Professor Ioan Batiu retires.

2016 Professor Șerban Agachi retires, but remains a member (chairman) of the Doctoral School of Chemical Engineering.

2016 Professor Ph. Eng. Cormos Călin-Cristian becomes a PhD consultant in chemical engineering and a member of the Doctoral School.

2016 Assoc.prof.dr.ing. Graziella Turdean is elected Chief of the Department of Chemical Engineering.

2017 Prof. dr. Ing. Mircea Vasile Cristea becomes a PhD consultant in chemical engineering and a member of the Doctoral School.

2017 A third chemistry engineer member of the university, elected an ASTR correspondent member, is Professor Alexandru Ozunu, Dean of the Faculty of Environmental Science and Engineering.

CONCLUSIONS

As a succinct synthesis of the brief presentation above, the chemical engineering in Cluj, despite the difficulties and impediments of all kinds, managed to exist, to develop and to assert itself. Founded late (1971), within the Polytechnics, with a great time gap (1937), compared to those in Bucharest (1938) and Timisoara (1948) and very late compared with the age of the University (1919), it is a product of the two brand-name institutions in Cluj. "The first one prepared and accomplished his establishment, guiding its first steps, the second watched its development and affirmation" [4]. To both institutions chemical engineering is grateful, and so is the signatory of these lines, in turn, as a disciple of the (pure) Chemistry School of Cluj and of the Chemical Engineering of the Polytechnics in Bucharest, a link and an interface between the two schools and Professions, an initiator and militant convinced of the "idea" of a "**chemical engineering faculty**" in Cluj, express their gratitude and respect

to the eminent professors and colleagues of the two Institutions, as well as to the other older sister-schools, (from Jassy and Timisoara) who unconditionally supported us.

With the same deference, we apologize to colleagues who have provided basic, theoretical and practical chemistry training for chemist engineers, for the space, time, and information that has overwhelmed us.

Also, as a picture speaks more than a thousand words, or tens of pages printed, below I have tried to encompass this history in some easy-to-understand schemes.

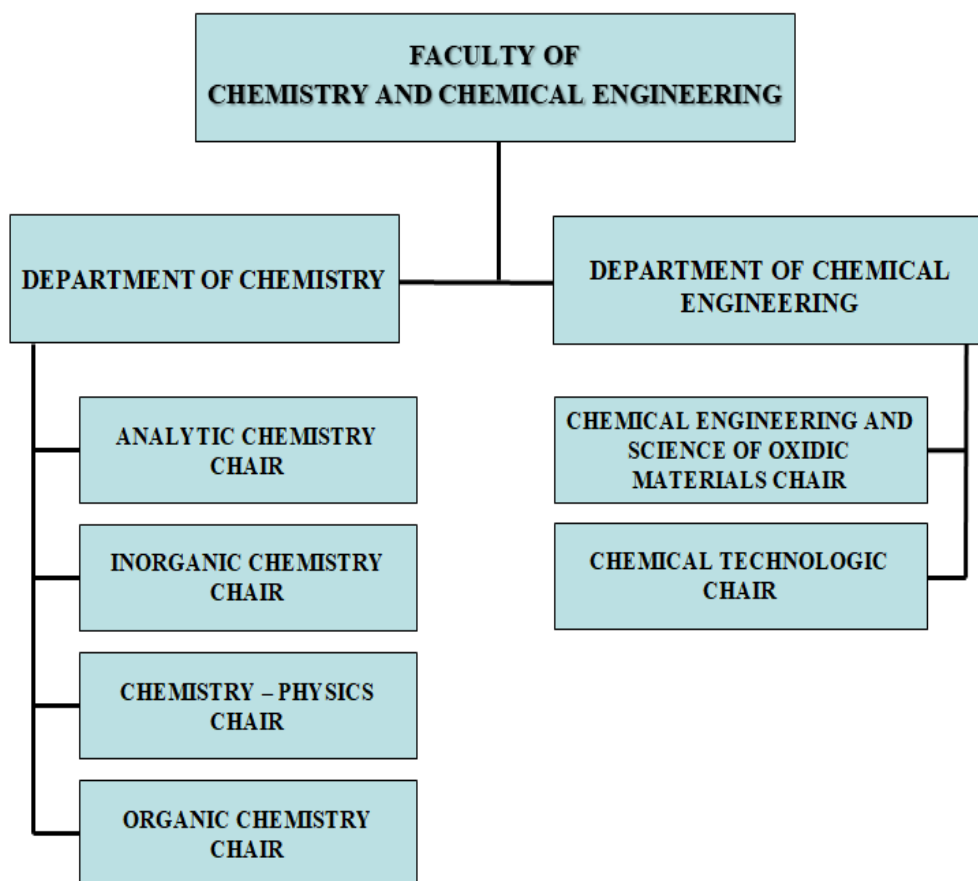


Figure 1. The structure of the Faculty of Chemistry and Chemical Engineering between 1995 – 2000

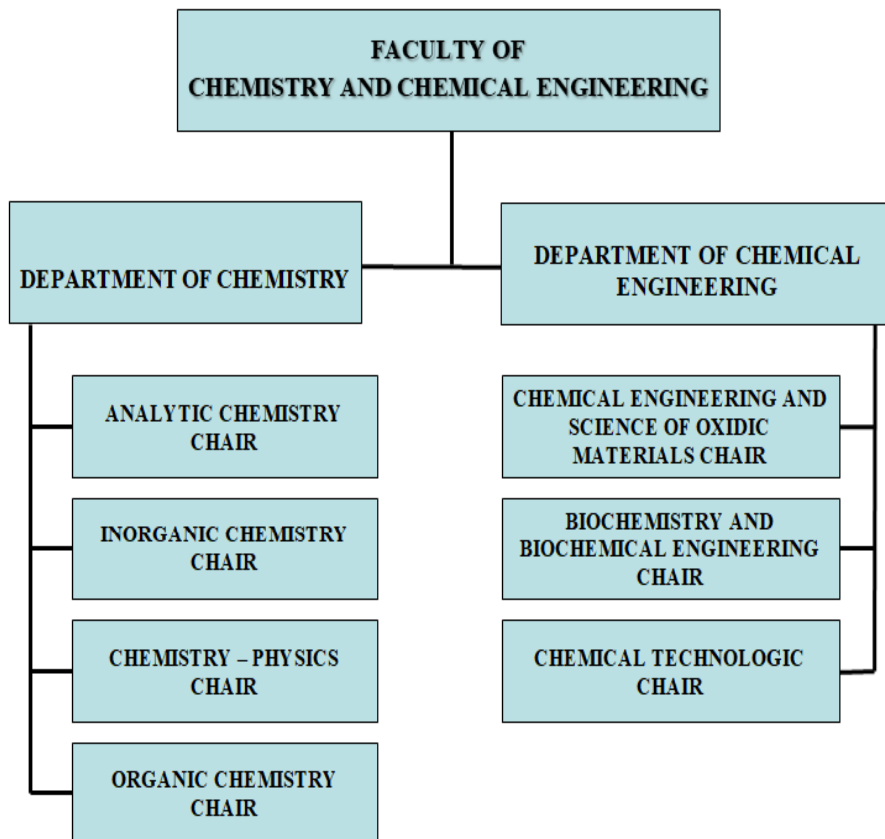


Figure 2. The structure of the Faculty of Chemistry and Chemical Engineering between 1999 – 2012

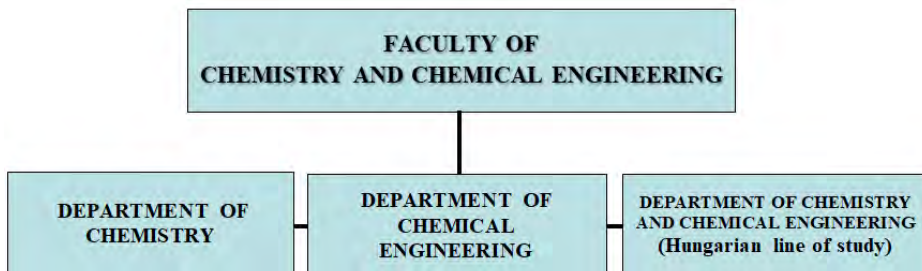


Figure 3. The structure of the Faculty of Chemistry and Chemical Engineering since 2012

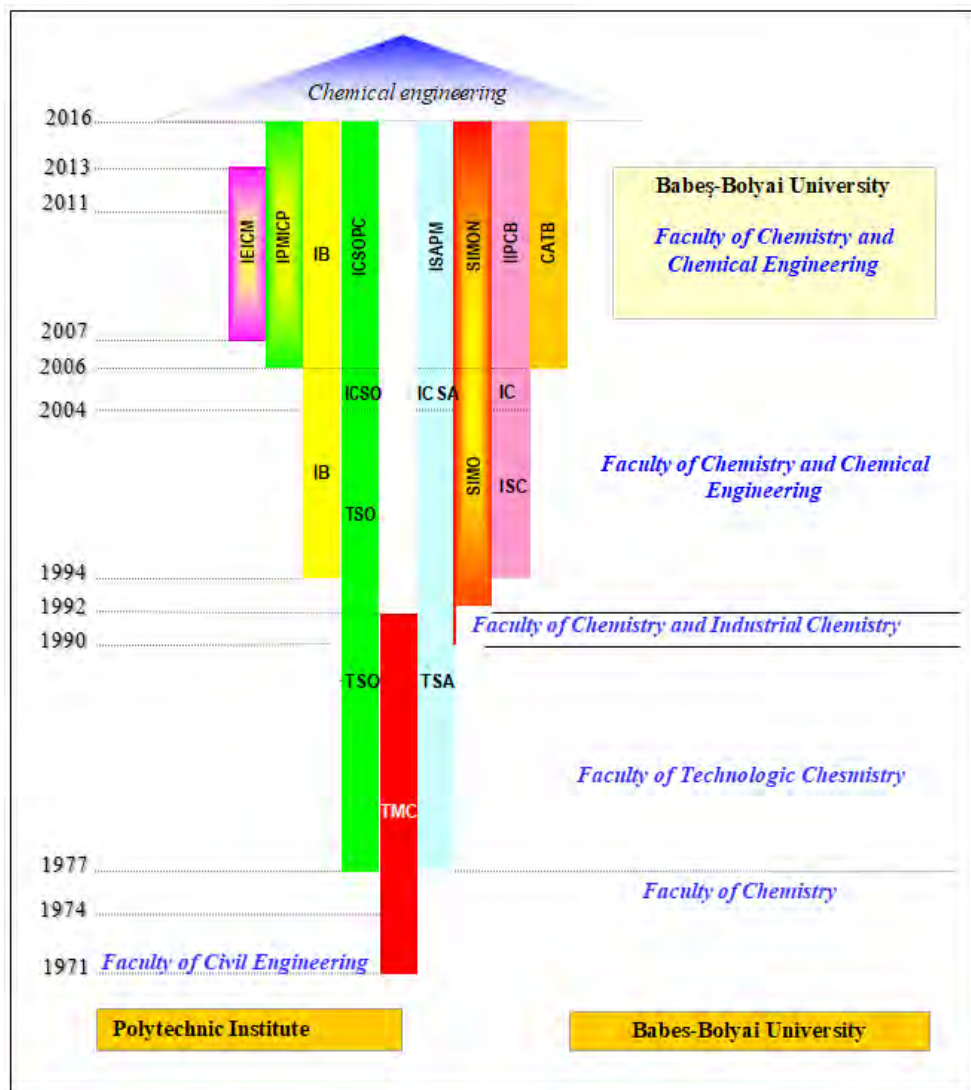


Figure 4. Structure of the chemical education in Cluj-Napoca

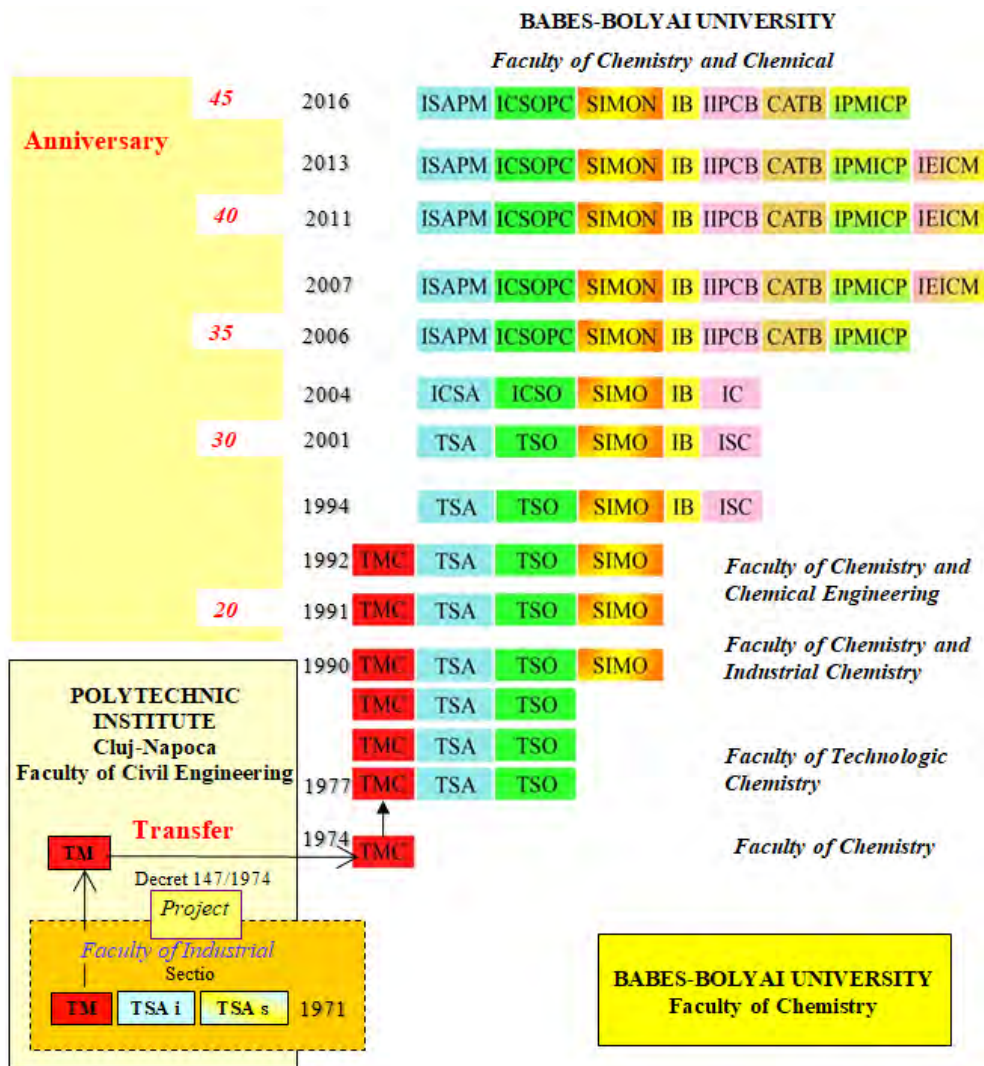


Figure 5. Structure of the chemical education in Cluj-Napoca

LEGEND: TMC Technology of Building Materials, TSAi Technology of Inorganic Substances, engineers, TSAs Technology of Inorganic Substances, subengineers, TSA Technology of Inorganic Substances, TSO Technology of Organic Substances, SIMO Science and Engineering of Oxide Materials, IB Biochemical Engineering, ISC Computer Systems Informatics, ICSA Engineering and Inorganic Substances Chemistry, ICSO Engineering and Chemistry of Organic Substances, IC Chemical Engineering, SIMON Science and Engineering of Oxide and Nanomaterials, ISAPM Inorganic Substances Engineering and Environmental Protection, ICSOPC Engineering and Chemistry of Organic and Petrochemicals, IIPCB Engineering and Informatics of Chemical and Biochemical Processes, CATB Food Chemistry and Biochemical Technology, IPMICP Engineering and Environmental Protection in Chemical and Petrochemical Industry, IEICM Economic Engineering in Chemical and Materials Industry.

REFERENCES

1. "Report on establishing a Faculty of Industrial Chemistry within the Polytechnic Institute Cluj", Archive of the Polytechnic Institute Cluj (Doc. No 872/C/8.XII.1970 and no.139/7 January 1971) (in Romanian language)
2. L. Literat, *From the history of chemical engineering education in Cluj-Napoca*, in Monographic breviary, 1971-1991, Anniversary Symposium „20 years of chemical engineering education in the university city of Cluj-Napoca, 19 – 22 September 1991, Babeş-Bolyai University, Faculty of Chemistry and Industrial Chemistry, Chair of Chemical Engineering, 1991, p.24-29. Editor L. Literat. (in Romanian language)
3. L. Literat, *Cluj chemical engineering education in data and archive documents*. In Anniversary Symposium „30 years of chemical engineering education in the university city of Cluj-Napoca, Babeş-Bolyai University, Faculty of Chemistry and Industrial Chemistry, 6 – 9 September 2001, CD, Accent Publishing House, ISBN 973-99821-8-2, September 2001, Cluj-Napoca. (in Romanian language)
4. L. Literat, *Cluj chemical engineering education at its 35th anniversary, 1971-2006*, p.1 and 6-14. Accent Publishing House, 2006, Cluj-Napoca, ISBN (10)973-8915-18-X,(13) 978-973-8915-18-3. Editor Liviu Literat. (in Romanian language)
5. Decree 147/1974, Official Gazette, Year X-Nr. 81, Part I, 14 June 1974. (in Romanian language)
6. L. Literat, *From the book of life*, Anniversary Symposium Liviu Literat, 85 years, Babeş-Bolyai University, Cluj-Napoca, 13 September 2013, CD, 2013. (in Romanian language)
7. V. Pârvan, *National University of Upper Dacia*, Institute of graphic Arts „Ardealul”, 1928. (in Romanian language)
8. L. Literat, *Technical education in the Upper Dacia University according to professor Vasile Pârvan*, in Academy of Technical Sciences in Romania, Cluj-Napoca Branch, *Romanian engineering past, present and future*, Works of the third National Conference of the Academy of Technical Sciences in Romania, Cluj-napoca, 12 – 13 November, 2008, p.171-176, Mediamira Publishing House Cluj-Napoca, 2008, ISBN 978-973-713-223-9 62(063). (in Romanian language)
9. S. Neagoie, *Cluj interbelic university life*, DACIA Publishing House, Cluj-Napoca, vol.1, 1980.p. 81-82. (in Romanian language)
10. O. Ghibu, *Cluj University and its education institutes*, Cluj, 1922. (in Romanian language)
11. B. Marian, *Dictionary of quotations and foreign phrases*, Enciclopedică Română Publishing House, 1973, p.122. (in Romanian language)
12. Order MEI no. 6540/1994, Name of the Faculty: *Chemistry and Chemical Engineering*. (in Romanian language)
13. GD. no. 693/12.06.2003, published in OG no. 436/30 June 2003), New names of the sections TSA, TSO and ISC. (in Romanian language)
14. GD 1156/30.10.1990 published in OG no.109/27 May 1992 continuing the studies TMC-ŞIMO. (in Romanian language)
15. GD 568/16.08.1995 Accreditation of the sections ŞIMO, IB and ISC. (in Romanian language)

CONTROL APPROACHES OF THE CARBONATION COLUMN FOR SODA MANUFACTURING

VASILE-MIRCEA CRISTEA^a

ABSTRACT. The paper presents the design of decentralized control systems for the carbonation column of the ammonia-soda production process. The proposed control structures are tested on the basis of an experimentally identified multiple-input-multiple-output dynamic model, capable of describing the behavior of the main carbonation column variables. Two new control structures are investigated. The first one proposes a new pairing of the manipulated to the controlled variables, based on the Relative Gain Array Matrix. The second one implements ratio control aimed to ensure the desired relationship between the inlet ammoniacal-brine and CO₂ flows. Behavior of the designed control structures are tested in the presence of setpoint changes and action of typical disturbances. Results are compared to the traditional decentralized control system configuration in order to reveal both the incentives and the limitations of the proposed control structures.

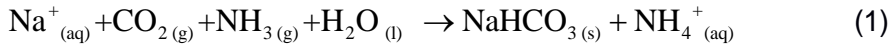
Keywords: *carbonation column, decentralized control, flowrate ratio control.*

INTRODUCTION

Sodium carbonate (Na₂CO₃), also denoted as soda ash, is a very important chemical compound as it is a main raw material for several other products obtained in different commodity manufacturing fields, such as glass, paper, steel, detergent and chemical industries or for water treatment and flue gases purification. Nowadays, about three quarters of the world sodium carbonate production (exceeding since 2005 the value of 6 kg per each Earth's inhabitant) is synthetically manufactured, while the rest is obtained from naturally formed sodium (bi)carbonate (such as trona minerals or nahcolite) [1]. The sodium hydrogen carbonate (NaHCO₃), from which soda

^a *Babeş-Bolyai University, Faculty of Chemistry and Chemical Engineering, 11 Arany Janos str., RO-400028, Cluj-Napoca, Romania, mcristea@chem.ubbcluj.ro*

ash is subsequently obtained by calcination, uses brine solution (NaCl), lime stone (for CO₂ and Ca(OH)₂), ammonia and water as raw materials. They are processed according to the ammonia-soda process, also called Solvay process due to the contribution Belgian chemist had to its development during the 1860s. In an overall, but very simplified form, the reactions of the Solvay process for bicarbonate production may be represented by:



Even today, the Solvay process may be considered as a very good lesson of chemical engineering process design, wisely integrating heat and mass flows.

The core of the synthetically manufactured sodium bicarbonate is the carbonation column. It is the unit where very complex physical and chemical three-phases heterogeneous processes are taking place in order to obtain sodium bicarbonate crystals. The operation of the carbonation tower for obtaining the quantitative and qualitative specifications of the product, associated to low energy costs and while satisfying the environment regulations, is a very challenging task. Therefore, it asks for an appropriate control system.

The present paper presents two decentralized control system configurations aimed to provide smooth and efficient functioning of the carbonation column. The first one emerges from an alternative to the traditional controlled-manipulated variables pairing, while the second one proposes a control structure which correlates the ammoniacal-brine and CO₂ flows. Performance of both control structures have been tested in the presence of disturbances and setpoint changes.

RESULTS AND DISCUSSION

The ammoniacal brine, entering at the top of the carbonation column, is contacted in countercurrent with two carbon dioxide flows. One is the low CO₂ concentration (38%) flow, which is issued by the limestone decomposition in the lime kiln and is introduced at the middle of the carbonation tower. The second one is the high CO₂ concentration (70%) flow, supplied by the recycled carbon dioxide from the sodium bicarbonate calcination, and is introduced at the bottom of the carbonation column. CO₂ is gradually absorbed by the ammoniacal brine and sodium bicarbonate is formed increasing its concentration as it descends the column, until it precipitates. Formation of the sodium bicarbonate crystals is assisted by the water based cooling section situated at the lower part of the of the carbonation tower.

The schematic representation of the carbonation column and its associated traditional decentralized control system structure is presented in Figure 1 [2]. The significance of the presented flows is: 1 – cooling water inlet flow, 2 – outlet flow of sodium bicarbonate, 3 – feed flow of ammoniacal-brine, 4 – feed of 38% CO₂ flow, 5 – feed of 70% CO₂ flow, 6 – gases (CO₂ and ammonia) leaving the column and 7 – cooling water outlet flow. The controlled variables considered in this work are: temperature of the sodium bicarbonate outlet flow (y1), column's sodium bicarbonate outlet flowrate (y2), level of the ammoniacal-brine at the top of the carbonation column (y3), flowrate of the 38% CO₂ entering the column (y4) and flowrate of the 70% CO₂ entering the carbonation tower (y5). The available manipulated variables are the valve openings of the control valves situated on the following flows: cooling water inlet flow (u1), ammoniacal-brine inlet flow (u2), sodium bicarbonate outlet flow (u3), 38% CO₂ inlet flow (u4) and 70% CO₂ inlet flow (u5) [2, 4].

The traditional decentralized control system structure consists in the following control loops: I – temperature control of the sodium bicarbonate leaving the column, II – flow control of sodium bicarbonate extracted from the column, III – level control at the top of the column, IV – flow control of the 38% CO₂ fed at the middle of the column and V – flow control of the 70% CO₂ entering at the bottom of the column [2, 5]. They are also shown in Figure 1.

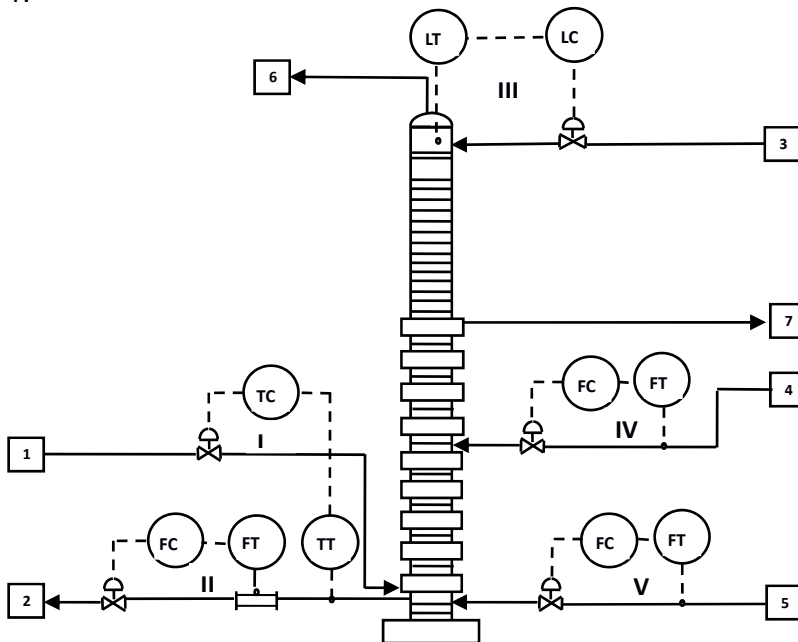


Figure 1. Layout of the carbonation tower, its associated flows and the traditional structure of the control loops [2, 4].

The carbonation column is a multivariable (MIMO) system and the pairing of the manipulated to the controlled variables, for the decentralized control system design, may be performed on the basis of the steady state Relative Gain Array (RGA) matrix [3]. As the experimentally identified model under the form of the MIMO transfer function matrix was available [4], the RGA was computed and presented in Table 1. The new manipulated to the controlled variables pairing was suggested by RGA matrix and it is carried out according to the diagonal elements of the matrix shown in Table 1. Their associated values show the suggested pairing importance for making the suitable tradeoff aimed to reduce control loops interactions.

Table 1. Relative Gain Array Matrix

	u1	u2	u3	u4	u5
y1	1.000	0	0	0	0
y2	0	0.4761	0.4891	0.0348	0
y3	0	0.4691	0.5303	0.0001	0.0004
y4	0	0.0545	-0.0195	0.9650	0
y5	0	0.0002	0.0001	0	0.9996

This RGA proposed decentralized control structure is shown in Figure 2.

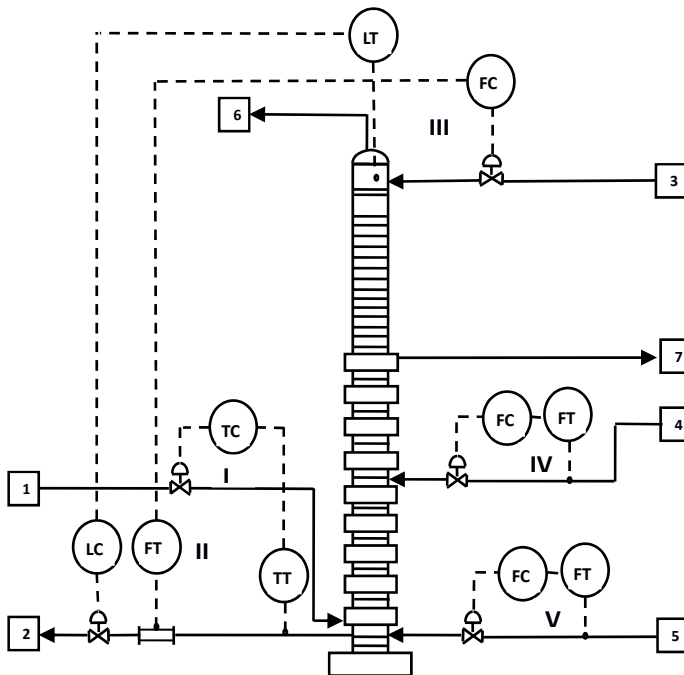


Figure 2. Layout of the RGA proposed structure of the control loops.

The new pairing of the manipulated-controlled variables, generating the proposed control loops structure, has been tested in order to assess its setpoint tracking and disturbance rejection capability. Simulation results of the control system for the step sodium bicarbonate outlet setpoint change from 26 to 32 m³/h, introduced at the time moment of 2000s, are presented in Figure 3. Figure 3 also presents the control performance of the traditional control pairing.

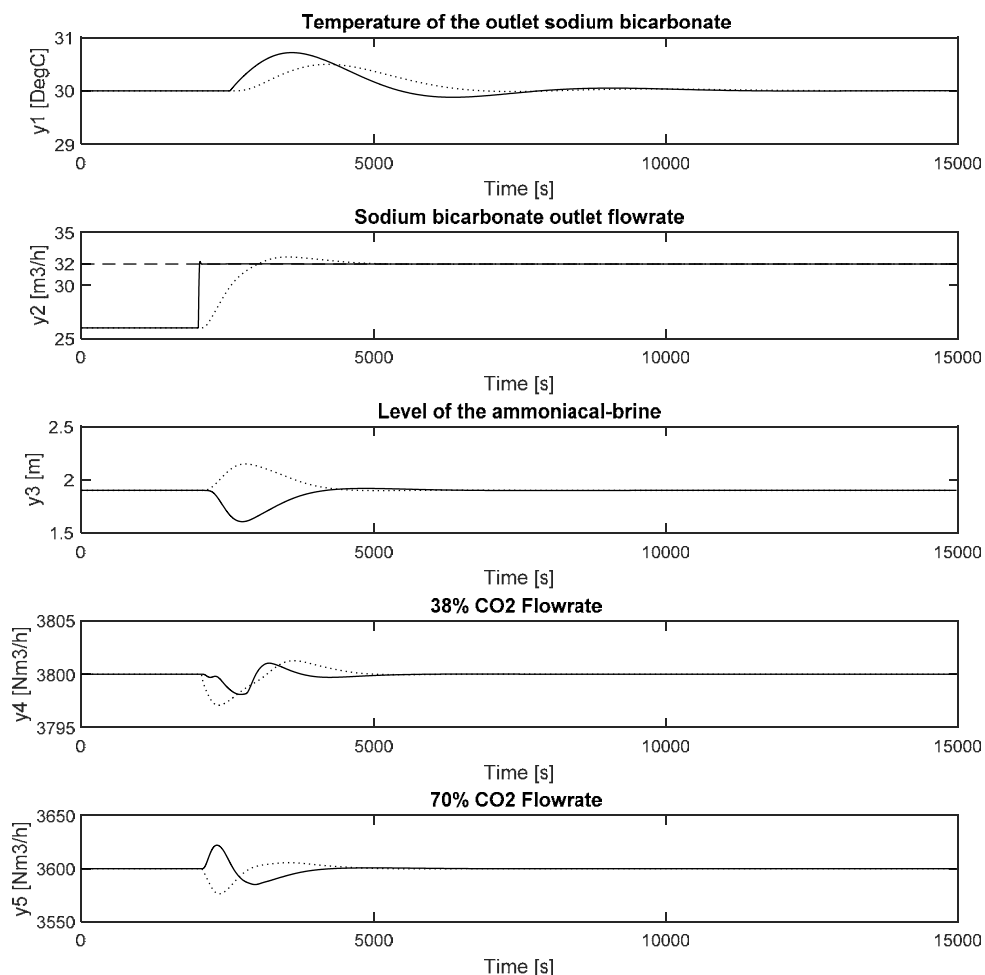


Figure 3. Comparative setpoint tracking performance of the traditional (plain line) and proposed (dotted line) control systems, for the case of the sodium bicarbonate step outlet setpoint change from 26 to 32 m³/h, introduced at the time of 2000s.

The steady state RGA analysis promises a slightly better pairing, compared to the traditional control approach. The dynamic simulation results partially confirm this expectation. For the proposed pairing control of the temperature (y1), level (y3) and 70% CO₂ flowrate (y5) show improved control performance, while sodium bicarbonate flowrate (y2) reveals an increased setpoint tracking time. Both control structures provide zero steady state offset and the proposed one enhances stability.

One of the most desired requirements for the carbonation column operation is to keep the ratio between the input ammoniacal-brine flowrate and the input CO₂ flowrates, as close as possible to desired values.

Achieving this goal ensures the optimal (off-line computed or experimentally obtained) reactants ratio entering the carbonation reactor, during both steady state and dynamic periods. Neither the traditional control structure, nor the previously proposed one is aimed to fulfill this objective. The second proposed control system structure proposed in this work is designed to accomplish this goal. The layout of this decentralized control system is presented in Figure 4.

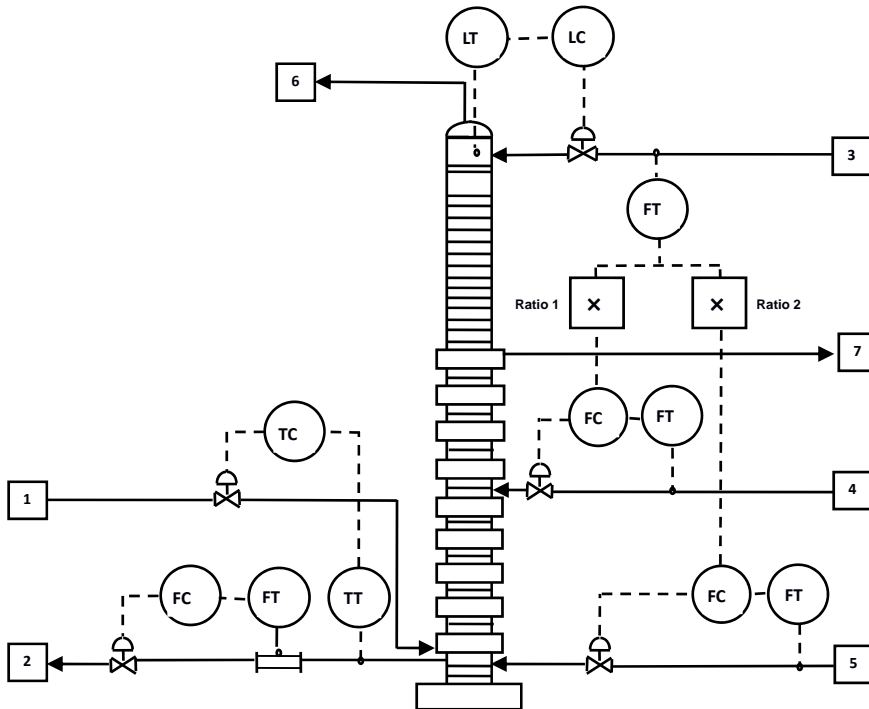


Figure 4. Layout of the flow proposed ratio control loops structure.

As implied by the ratio control system structure, the changes in the ammonia-brine input flow are automatically followed by the necessary changes of both input CO₂ flowrates. The desired ratios are: Ratio1=146.15 [Nm³/h 38% CO₂ / m³/h ammoniacal-brine] and Ratio2=128.46 [Nm³/h 70% CO₂ / m³/h ammoniacal-brine].

In order to demonstrate the capability of the ratio control system to keep the desired flowrates ratio, dynamic simulation results of two disturbance rejection tests are presented in Figure 5. The first test considers the typical ammoniacal-brine inlet flowrate disturbance, acting according to the scenario presented in the top graph of Figure 5. It consists of the ammoniacal-brine inlet flowrate step increase of 1.85 m³/h disturbance, introduced at moment t=1000s, followed by a flowrate ramp decrease of 2.5 [m³/h / h] starting at moment t=12000s, down to the flowrate initial value of 24 [m³/h]. The second test considers another typical disturbance consisting in a flowrate step decrease of the outlet flow of sodium bicarbonate of 11 m³/h, introduced at time t=30000s (not shown in Figure 5).

Results presented in Figure 5 show the ability of the ratio control system to tightly keep the CO₂ controlled flowrates at the desired ratios and the other controlled variables at their setpoint/nominal values when influent ammoniacal brine flowrate changes. The ratio-control scheme discloses the same favourable control performance as it efficiently rejects the sodium bicarbonate flowrate disturbance.

CONCLUSIONS

Efficient and smooth operation of the carbonation column is essential for soda production. As three phase complex chemical heterogeneous processes compete for achieving the desired throughput and product specifications, appropriate control system is asked to meet the operation challenges. Two decentralized control system structures are proposed and tested. The first one, based on RGA matrix, recommends a new 5×5 manipulated to controlled variables pairing. The dynamic simulation results reveal advantages of the new control structure, compared to the traditional one, for the majority of the controlled variables and with slower response for sodium bicarbonate flowrate, but increased stability. The second control structure is designed to maintain the desired ratios between the inlet ammoniacal-brine flowrate and the inlet CO₂ flowrates. Tested in the presence of typical inlet ammoniacal-brine and extracted sodium bicarbonate flowrate disturbances, the proposed control structure demonstrates its success in promptly rejecting their undesired effects, while preserving the required flowrate ratios. The obtained results propose the investigated control structures as potential control system solutions for the industrial implementation.

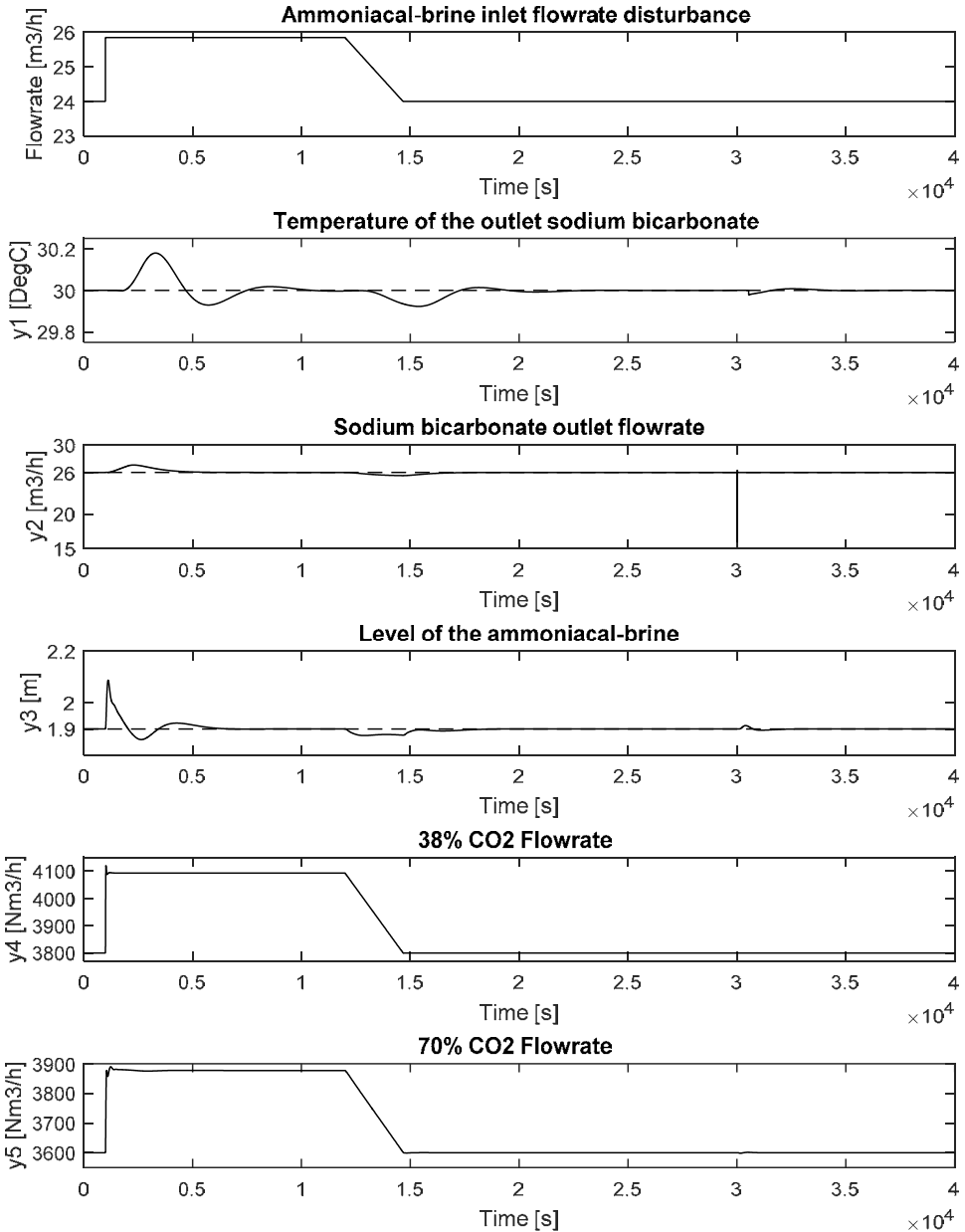


Figure 5. Disturbance rejection performance results of the ratio control system as response to the ammoniacal-brine flowrate increasing-step-decreasing-ramp disturbance and to the sodium bicarbonate flowrate step-decreasing disturbance (plain line); setpoint/nominal values of the control loops (dashed line).

EXPERIMENTAL SECTION

The carbonation column dynamic model used in the present work has the transfer matrix form and was identified experimentally in [2, 4]. The PID/PI controllers have a parallel form and have been tuned by making a good balance between performance and robustness. Dynamic simulations were carried out in Matlab and Simulink® software environment.

REFERENCES

1. IPPC BAT Reference Document, "Large Volume Solid Inorganic Chemicals Family, Process BREF for Soda Ash", **2004**, 3, 11.
2. V. Gheorghiu, *Revista de Chimie*, **1978**, 2, 155.
3. M.V. Cristea, S.P. Agachi, *Revista Română de Informatică și Automatică*, **1997**, 7(4), 45.
4. V. Gheorghiu, *Revista de Chimie*, **1978**, 3, 238.
5. X. Jin, Q. Zhang, H. Su, *Journal of Chemical Industry and Engineering*, **2008**, 59, 1761.

MODELLING AND SIMULATION OF FUELS PRODUCTION FROM SYNGAS

LETITIA PETRESCU^{a*}, ARPAD IMRE-LUCACI^a,
CRISTINA IZABELLA BERCI^a

ABSTRACT. Syngas is a very important product, with a variety of uses; it may even become a primary source of fuel, and replace natural gas. This is because, syngas has the building blocks to create all the products and chemicals currently generated in the petrochemical industry. Fuels manufactured from synthesis gas offer special opportunities based both on environmental and energy performance. The aim of the present work is to design and compare different chemical production processes for fuels generation using syngas as raw-material. ChemCAD process simulator software was used as the main tool for process modelling and simulation. The investigation was focused on the conversion of syngas to methanol, dimethyl ether and hydrogen at a large scale. For comparison reasons, the same amount of syngas (e.g. 10000 kmol/h) was used in all three cases under investigation. After comparison, syngas to hydrogen process seems to be the best option from thermal energy point of view and in terms of environmental impact.

Keywords: *syngas, process modelling and simulation, hydrogen, methanol, dimethyl ether (DME)*

INTRODUCTION

Synthetic gas called also syngas is a fundamental chemical intermediate which can be obtained from many sources (e.g. coal, natural gas, biomass, different solid waste, recycled plastics), using different technologies (e.g. gasification, reforming) and can be used in various applications. In its simplest form, syngas is composed of two diatomic molecules, CO and H₂ that provide the building blocks upon which an entire field of fuel science and technology is based. According to PR Newswire global syngas production accumulated to

^a Department of Chemical Engineering, Faculty of Chemistry and Chemical Engineering, Babeş-Bolyai University, 11 Arany Janos str., RO-400028, Cluj-Napoca, Romania

* Corresponding author: letitiapetrescu@chem.ubbcluj.ro

116 GWth in 2014 and is projected to reach 213 GWth by 2020 [1]. The important role of syngas in both chemical and petrochemical industries has been widely recognized since it is currently utilized as a main feedstock for producing environment-friendly synthetic fuels and methanol via respective Fischer-Tropsch synthesis [2]. Syngas is a crucial intermediate resource for production of hydrogen and ammonia [3] being also attractive as a fuel for internal combustion engines, gas turbines and high temperature fuel cells, and as a chemical feedstock for the production of methanol, synthetic hydrocarbon fuels [4, 5]. The most important syngas applications are briefly presented in Figure 1.

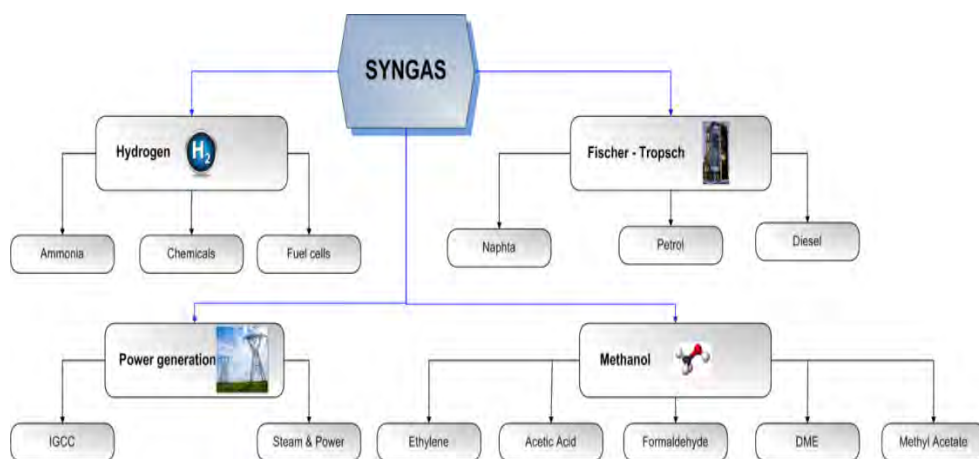


Figure 1. Syngas application in various industrial sectors

The goal of the present work was to investigate and compare the production of different fuels from syngas. The attention was focused on three fuels, more exactly: methanol, dimethyl ether (DME) and hydrogen. A brief overview of the importance, production methods, advantages and disadvantages of the three fuels is presented the next section.

The first fuel investigated was methanol. Methanol is an important chemical intermediate used to produce a number of chemicals, including: formaldehyde, dimethyl ether, methyl tert-butyl ether, acetic acid, olefins and others. Currently, for economic reasons, the majority of methanol is synthesized from syngas that is produced via steam reforming of natural gas. One of the distinct advantages of employing methanol as a sustainable source of fuel is the diverse array of feed stocks from which this simple alcohol can be produced. Besides industrial production from natural gas and coal, methanol can be made from anything that is, or ever was, a plant (e.g. timber waste, landfill gas, trash, pulp mill black liquor, agricultural waste [6]). Fuel methanol has similar properties to gasoline and can be stored and transported in a similar manner.

The second fuel which arouses our interest is dimethyl ether (DME). This fuel is obtained from methanol, its production process becoming one of the most important issues of the world industry in the recent years. There are different methods of DME production: an indirect synthetic method using the dehydration reaction of methanol, a direct synthetic method from natural gas, gasification of coal, biomass, or electrolysis using solar, wind, hydro or wave energy. DME is more like liquefied petroleum gas (LPG) in its physical properties. But by contrast, it is more suitable for use in a diesel engine due to its high cetanic value. Unlike methanol, it has a sufficient cetanic number without the use of additives or spark assistance. DME has low octane and is not used as a gasoline substitute, in contrast to methanol, which has excellent properties for this use. The calorific value is higher than methanol but lower than conventional fuels. Like methanol, DME can be used directly in gas turbines [7].

The third fuel investigated was hydrogen. Hydrogen can be produced using a number of different processes (e.g. reforming of natural gas, gasification of coal, oil and / or biomass, water electrolysis, fermentation of biomass). Hydrogen, as an important energy carrier in the future has a number of advantages. For example, a large volume of hydrogen can be easily stored in a number of different ways [8]. Hydrogen is also considered as a high efficiency, low polluting fuel that can be used for transportation, heating, and power generation in places where it is difficult to use electricity. The only emissions are water vapour. In some instances, it is cheaper to ship hydrogen by pipeline than sending electricity over long distances by wire [9].

A comparison between the three fuels investigated in the present work, underlining their advantages and disadvantages is presented in Table 1.

Table 1. Advantages and disadvantages of methanol, DME and hydrogen as fuels

Fuel	Facts	Advantages	Disadvantages
CH ₃ OH	Predominately from syngas made via SMR. Several automakers have developed prototypes using CH ₃ OH as fuel. Commodity chemical.	Mature technology. Many uses for CH ₃ OH	Poor solubility in gasoline and phase separation problems. More corrosive than gasoline.
DME	Many potential uses e.g. diesel, cooking fuel, refrigerant, chemical feedstock.	In situ dehydration of CH ₃ OH to DME increases CH ₃ OH yields.	DME is very reactive. Sensitive to traces of pollutants.
H ₂	Largest use of syngas. Predominately made via steam methane reforming (SMR).	H ₂ itself is a clean fuel. Mature technology. High yields.	Delivery price can be significantly higher than plant gate price. Have to compete with mega methanol plants.

RESULTS AND DISCUSSION

The following cases have been investigated in the present work:

Process 1: Methanol from syngas production process;

Process 2: DME from methanol production process;

Process 3: H₂ from syngas production process.

The main streams for *Process 1* are reported in Table 2. Starting from a quantity of 10000 kmol/h (stream 1, Table 2), a quantity of 3331.48 kmol/h of methanol with a purity of 99.9% was obtained, as shown in Table 2 (stream 7).

Table 2. Relevant flows for *Process 1*

Stream Name	Unit of measure	1	4	5	7	9
Temperature	°C	160	221.3	267	38	38
Pressure	bar	29	65	65	105	105
Component flow-rate	kmol/h					
H ₂		6667	10255	3591	2.71	3589
CO		3333	5125	1794	1.47	1792
CH ₃ OH		0	17	3348	3331.48	17
CO ₂		0	0	0	0	0
H ₂ O		0	0	0	0	0
DME		0	0	0	0	0
Total flow	kmol/h	10000	15397	8734	3335.66	5398
Total flow	kg/h	106805	164765	164765	106794	57971

The main streams for *Process 2* are reported in Table 3. In this case the flow-rate of the main product obtained (DME) has a value of 1665.66 kmol/h (see stream 10 from Table 3). The purity of the product obtained is about 99.56%.

The main streams for *Process 3* are reported in Table 4. The quantity of the desired product (H₂) obtained in this case 9670.65 kmol/h (see stream 10, Table 4). The quantity of syngas consumed to produce de desired product is 10000 kmol/h, correspondent to a mass flow-rate of 106805 kg/h (stream 1, Table 4).

Table 3. Relevant flows for *Process 2*

Stream Name	Unit of measure	1	5	6	10	23
Temperature	°C	38	256	364	25	25
Pressure	bar	105	14.7	13.9	11.4	1
Component flow-rate	kmol/h					
H ₂		2.71	2.71	0	0	0
CO		1.47	1.47	0.12	0.12	0
CH ₃ OH		3331.48	4144.03	829.14	7.29	8.77
CO ₂		0	0	0	0	0
H ₂ O		0	16.46	1674.73	0	1658.27
DME		0	18.31	1676.58	1658.26	0
Total flow	kmol/h	3335.66	4182.97	4180.57	1665.66	1667.05
Total flow	kg/h	106794	133987	133979	76631	30155

Table 4. Relevant flows for *Process 3*

Stream Name	Unit of measure	1	3	7	10	11
Temperature	°C	160	325	250	20	20
Pressure	bar	29	16.2	14.7	14.7	14.7
Component flow-rate	kmol/h					
H ₂		6667	0	9670.70	9670.65	0
CO		3333	0	329.30	329.29	0
CH ₃ OH		0	0	0	0	0
CO ₂		0	0	3004.03	2984.69	19.33
H ₂ O		0	3333	328.97	19.57	309.39
DME		0	0	0	0	
Total flow	kmol/h	10000	3333	13333	13004.21	328.78
Total flow	kg/h	106805	60044	166852	160427	6425

The processes presented in the present work use data from literature [11]. All the models have been validated using the initial literature source. After validation, the models have been scaled up to the same syngas flow-rate and composition.

In order to establish which process is the best option from thermal energy point of view, a comparison has been made between the three case studies. Table 5 shows the process values from thermal energy point of view.

Usually, when monitoring the thermal energy, the comparisons and conclusions are made based on the low heating value (LHV). The lower heating value (also known as net calorific value) of a fuel is defined as the amount of heat released by combusting a specified quantity (initially at 25°C) and returning the temperature of the combustion products to 150°C, which assumes the latent heat of vaporization of water in the reaction products is not recovered [12]. The thermal energy obtained using the flow-rates of fuels derived from process modelling and simulation and from the correspondent LHV values of the fuels considered are reported in Table 5.

Table 5. Thermal comparison for the simulated processes

Processes	Fuel flow-rate (kmol/h)	Fuel flow-rate (kg/h)	Fuel LHV (MJ/kg)	TE(L) (MW _{th})
<i>Process 1</i>	3331.48	106607	20.09	594.93
<i>Process 2</i>	1658.26	76280	28.88	611.94
<i>Process 3</i>	9670.65	19341	120.21	645.83

LHV - lower heating value, TE(L) - thermal energy based on the LHV

As shown in Table 5, from thermal energy point of view, *Process 3* is the best option, with a quantity of 645.83 MW_{th} generated compared to *Process 1* and *Process 2* where 594.93 MW_{th} respectively 611.94 MW_{th} are generated. Since for *Process 3*, there is no CO₂ involved in the reaction, in terms of environmental impact, this process is also the best option, compared to *Process 1* and *Process 2* which result in one, respectively two molecules of CO₂ / molecules of fuels emitted by burning CH₃OH and DME.

Further, using the best thermal energy obtained in the three cases back calculations were performed in order to determine the necessary amount of syngas requested to produce the fixed amount of thermal energy (e.g. 645.83 MW_{th}). The results are reported in Table 6.

Table 6. Syngas flow-rate values calculated using low heating thermal energy value

Process	Syngas (kmol/h)	Fuel (kg/h)	LHV (MJ/kg)	TE(L) (MJ/h)	TE (L) (MW _{th})
<i>Process 1</i>	10855.59	115728.62	20.09	2324988	645.83
<i>Process 2</i>	10553.89	80505.12	28.88	2324988	645.83
<i>Process 3</i>	10000	9670.53	120.21	2324988	645.83

LHV - lower heating value; TE(L) - thermal energy based on the LHV

The syngas flow-rate obtained after using 645.83 MW_{th} of thermal energy increased compared to the initial syngas flow-rates. For *Process 1*, the syngas flow-rates has increased with 8.55% (e.g. from 10000 kmol/h to 10855.59 kmol/h), while for *Process 2* the value increased with 5.54%. For the last process, *Process 3*, syngas flow-rates have the same value as the initial ones, because the highest thermal energy generated, which belongs to this process (syngas to hydrogen) has been used.

CONCLUSIONS

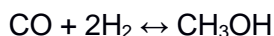
Three processes for fuels production starting from syngas as raw-material have been investigated in the present work. The processes under investigation are: *Process 1* is the equivalent of syngas conversion to methanol, *Process 2* represents syngas to DME route, and *Process 3* describes syngas conversion to hydrogen. For all cases under study the same amount of syngas (e.g. 10000 kmol/h) was used. The methanol flow-rate obtained for *Process 1* was 3335.66 kmol/h with a purity of 99.9%, 1665.66 kmol/h DME was obtained in *Process 2*, with a purity of 99.69% respectively 9670.65 kmol/h of hydrogen was obtained in *Process 3*. The three fuels have been also investigated from thermal energy point of view. *Process 3* represents the best option form energy point of view but also from environmental point of view because no CO₂ is released by burning this fuel. The second best option is *Process 1*, followed by *Process 2*.

EXPERIMENTAL SECTION

The three processes have been modelled using ChemCAD process simulator developed by Chemstations [13]. Details about the data used for modelling and simulation are presented in the next section.

The Process flow-diagram for syngas to methanol is presented in Figure 2.

The production capacity of this plant is 2563 tons/day of methanol with a purity of 99.9% at atmospheric pressure. The raw-material syngas is introduced into the process at T = 160°C and p = 29 bar. Syngas enters the heat exchanger E-201 and is cooled to T = 125°C. Further, in order to achieve a pressure p = 45 bar, syngas is compressed in compressor C-201 with an efficiency of 75%. Syngas enters the second compressor C-202, together with the recycled CO and H₂, and it will be compressed to a pressure of 65 bar, with the same efficiency of 75%. The mixture furthermore sent to an equilibrium reactor R-201, where the reaction taking place is:



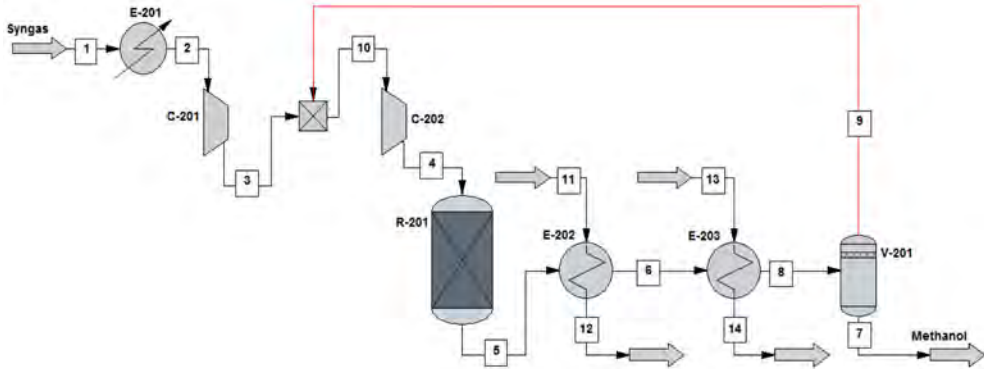


Figure 2. Syngas to methanol process flow diagram (Process 1)

The molar ratio of the reactants is 1:2. The conversion was assumed to be 65% [11]. The mixture exits the reactor at $T = 267^{\circ}\text{C}$ and is further cooled, using a cooling water agent, twice, in heat exchangers E-202 and E-203, until it reaches a temperature of 125°C . Furthermore, methanol is separated from the unreacted syngas through a flash vessel (V-201), and the syngas is recycled to the reactor. The methanol product exits as a liquid at 38°C and 105 bar.

Figure 3 shows the process flow diagram for the DME production using methanol as raw-material.

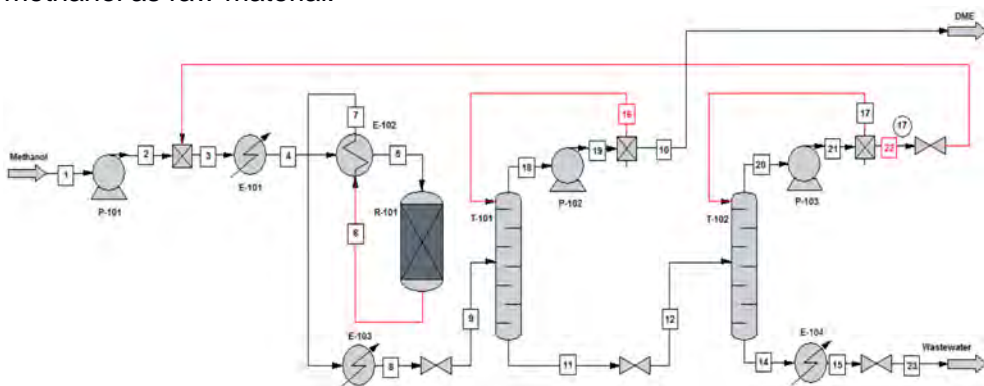
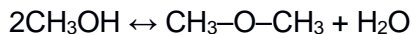


Figure 3. DME production process from methanol (Process 2)

The production capacity of this plant is 1839 tons/day of DME with a purity of 99.96 % at atmospheric pressure. The raw-material used is composed of fresh methanol and a small amount of water, which enters the process at $T = 25^{\circ}\text{C}$ and $p = 1$ bar. Further, this mixture is compressed to a pressure of 15.5 bar, in a compressor having an efficiency of 60%. Combined with the recycled reactant, the mixture is preheated by the first heat exchanger E-101 to a temperature

of $T = 154^{\circ}\text{C}$. Then, it is vaporized by the second heat exchanger E-102, prior to being sent to R-101 reactor, having a temperature of $T = 364^{\circ}\text{C}$ and a pressure $p = 13.9$ bar. The reaction taking place in the reactor is:



Methanol conversion is around 80% [11]. The stream leaving reactor, is then cooled in heat exchanger E-103 ($T = 100^{\circ}\text{C}$) prior to being sent to the first of the two distillation columns T-101 and T-102. DME product is taken overhead from the first column. Water and methanol enters the second distillation column (T-102) at $T = 140^{\circ}\text{C}$ and $p = 7.4$ bar, where water from the unused methanol will be separated. The water is sent to wastewater treatment to remove trace amounts of organic compounds while methanol is recycled back to the process.

Figure 4 shows the process flow diagram for the hydrogen production using syngas as raw-material.

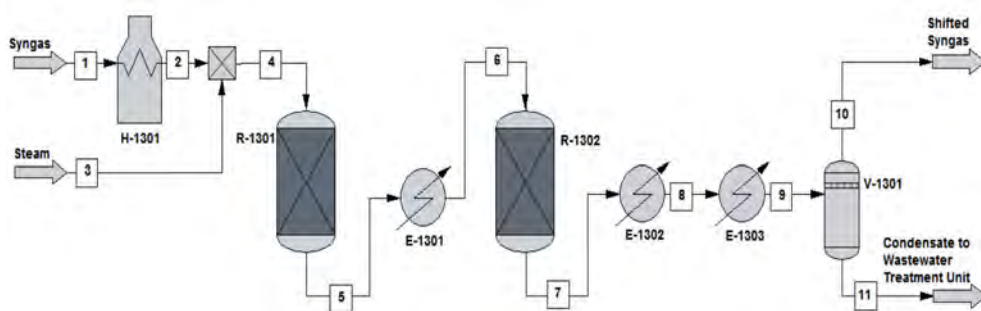
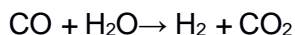


Figure 4. Hydrogen production from syngas (Process 3)

The production capacity of this plant is 464 tons/day of hydrogen with a purity of 98% at atmospheric pressure. The raw-material used is a mixture of carbon monoxide ($p = 16.7$ bar, $T = 115^{\circ}\text{C}$) and hydrogen ($p = 16.7$ bar, $T = 115^{\circ}\text{C}$) in a molar ratio of 1:1. The mixture is heated up to 320°C using a fired heater. The heated syngas is further mixed with steam (water at $T = 325^{\circ}\text{C}$ and $p = 16.2$ bar) and enters in the high temperature shift reactor. The reaction taking place in the reactor is:



The conversion considered is 63% [11]. The mixture leaves the reactor R-1301 at $T = 425^{\circ}\text{C}$ and enters a simple heat exchanger E-1301, where it will be cooled to a temperature of $T = 250^{\circ}\text{C}$. After the temperature is reached, the mixture is transferred to the second stage reactor (R-1302) which operates at $T = 250^{\circ}\text{C}$ and represents the low temperature shift reactor. The reactor effluent is further

cooled using cooling water in heat exchangers E-1302 and E-1303, before being sent to the flash separator V-1301. The effluent is first cooled from $T = 250^{\circ}\text{C}$ to 185°C in the first heat exchanger (E-1302), and finally it achieves a temperature of $T = 20^{\circ}\text{C}$ in the second heat exchanger (E-1303). The off-gas resulted in V-1301 flash separator is a mixture of CO , H_2 and CO_2 gases, that is usually sent to a hydrogen-recovery process or to a combustion system, while the bottom product, water, is sent to a wastewater treatment unit. A significant amount of CO_2 is obtained, which is further purified using a CO_2 capture plant. The CO_2 capture rate is about 90%, the CO_2 removal uses an amine-based process. This is a standard industrial process, but not a subject included in the present work. For our process, it is considered that CO_2 was already purified.

REFERENCES

1. <http://www.pnnewswire.com/news-releases/syngas-and-derivatives-market-worth-213100-mwthermal-by-2020-521372871.html> (Accessed on August), **2017**.
2. O. Omoregbe, H.T. Huong, T. Danh, C. Nguyen-Huy, H.D. Setiabudi, S.Z. Abidin, Q.D. Truong, N.V. Dai-Viet. *International Journal of Hydrogen Energy*, **2017**, 42, 283.
3. J. Rostrup-Nielsen, L.J. Christiansen. *Catalytic Science Series*, 10, chapter 1, **2011**.
4. J.D. Holladay, J. Hu, D.L. King, Y. Wang. *Catalys Today*, **2009**, 139, 244.
5. J. Van deLoosdrecht, J.W. Niemantsverdriet. *Chemical Energy Storage*, "Synthesis gas to hydrogen, methanol and synthetic fuels", R. Schloegl (Ed.), De Gruyter, Berlin, **2013**.
6. G.A. Olah, and G.K.S. Prakash. "Beyond oil and gas: the methanol economy", John Wiley & Sons, **2011**.
7. S. Lee. *Methanol Synthesis Technology*, **1990**.
8. G.A. Olah, A. Goeppert, G.K.S. Prakash. *Journal of Organic Chemistry*, **2009**, 74(2), 487.
9. L.F. Brown. *International Journal of Hydrogen Energy*, **2001**, 26(4), 381.
10. C.E. Thomas, B.D. James, F.D. Lomax Jr., I.F. Kuhn Jr. *International Journal of Hydrogen Energy*, **2000**, 25(6), 551.
11. R. Turton, R.C. Bailie, W.B. Whiting, J.A. Shaeiwitz. "Analysis, Synthesis, and Design of Chemical Processes", New Jersey: Prentice Hall International Series in the Physical and Chemical Engineering Sciences, **2003**.
12. <http://hydrogen.pnl.gov/tools/lower-and-higher-heating-values-fuels> (accessed on August), 2017.
13. ChemCAD Chemical Process Simulation - version 6.5. Chemstations, Huston, USA, www.chemstations.com (accessed on August), **2017**.

EVALUATION OF HYDROGEN PRODUCTION FROM CATALYTIC REFORMING OF LIQUEFIED PETROLEUM GAS WITH CARBON CAPTURE AND STORAGE

DANIELA-MARIA LOHAN^a, CALIN-CRISTIAN CORMOS^{a*}

ABSTRACT. The objective of this study was to describe the hydrogen production from catalytic reforming of liquefied petroleum gas (LPG) with carbon capture and storage (CCS). Nowadays, hydrogen requires a lot of attention as a clean fuel as well as a chemical used in industrial applications (e.g. hydrogenation processes especially in oil refinery sector). The size of evaluated plant was 100000 Nm³/h hydrogen with a purity of 99.95% (vol.) to be in line with industrial hydrogen production capacities used in the oil refinery sector. A pre-combustion CO₂ capture process based on Methyl-DiEthanol-Amine (MDEA) was also considered to reduce the greenhouse gas emissions (decarbonisation of fossil LPG used). The carbon capture rate was about 78%. The evaluation was made using process flow modeling (ChemCAD) and the simulation results were compared with experimental data reported in the literature. A similar hydrogen production process from LPG reforming without carbon capture was also considered to assess the energy penalty for CO₂ capture. This work is an important study for evaluation of reducing carbon footprint in oil refinery sector.

Keywords: *Liquefied petroleum gas (LPG); Hydrogen production; Carbon capture and storage (CCS).*

INTRODUCTION

Hydrogen and liquefied petroleum gas (LPG) are one of the most often used fuels in various industrial applications. For instance, LPG is utilized in hundreds of industrial, transport and domestic applications. This fuel is composed mostly of propane, butane and ethane and it is used as a fuel for

^a *Babeş-Bolyai University, Faculty of Chemistry and Chemical Engineering, 11 Arany Janos str., RO-400028, Cluj-Napoca, Romania,*

** Corresponding author: cormos@chem.ubbcluj.ro*

many residential, commercial and agricultural applications, including cooking, hot water systems and heating. LPG is also employed as a propellant, refrigerant, vehicle fuel and petrochemical feedstock [1]. Petroleum refining processes are the chemical engineering operations used in oil refineries in order to transform crude oil into useful products like liquefied petroleum gas (LPG), gasoline, diesel, kerosene, jet fuel, diesel oil and fuel oils [2].

Petroleum refineries are very developed industrial complexes that include a lot of various processing units and auxiliary facilities such as utility units and storage tanks. The primary end-products produced in petroleum refining can be grouped into four categories: light distillates, middle distillates, heavy distillates and others [3]. LPG is a light distillates product. Petroleum refinery represents one of the biggest parts of the chemical industry for the production of products from petroleum and crude oil; either by the technical method, distillation or by chemical reaction of the crude oil includes treating the raw products by a vast variety of finishing processes to yield marketable end-products. A petroleum refinery is a complex group of manufacturing plants [4].

LPG is the third most popular fuel for automotive in the world, with a number of approximate 16 million users of cars with this kind of fuel, which represent about 3% of the total market share. The countries that are shown more interest to used LPG in the transport sector are Turkey, South Korea, Poland, Italy and Australia and other countries as well, but with fewer consumers [1]. The price is the biggest motivation for using LPG in the transport sector, which is almost with 40% lower than other fuels. The second advantage is that, LPG-powered vehicles produce fewer pollutants (e.g. carbon dioxide, sulphur oxides etc.) from their exhausts in comparison with gasoline and diesel-fuelled vehicles. However, the use of this kind of fuel also has disadvantage like the installations of those cars which are become recently old and in bad condition, which can be dangerous [1]. The importance of LPG for this study is giving by the fact that it is the main raw material for the production of decarbonised hydrogen [5].

Hydrogen is the most common element in the Earth (combined as water) and also in the whole Universe with a lot of uses in very different areas. The primarily role of this chemical element is to create water which is almost the definition of life. Other industrial usage for hydrogen are in petrochemical industries, e.g. for hydrochloric acid production, methanol or ammonia production etc. It is often used as fuel because of its high calorific value and combustion generates plenty of energy [6].

The production of hydrogen can be made in several ways, for which the most common technique is hydrocarbons steam reforming. Other methods include bio-hydrogen production, thermolysis or electrolysis. Hydrogen and

steam reforming are also used by many industries. Steam reacts with methanol to generate carbon monoxide and hydrogen. The whole process is done at high temperatures. When the temperature is set down, carbon monoxide will be produced and it can produce carbon dioxide and hydrogen. The overall energy efficiency is about 65 - 75%.

Hydrogen is considered one of the cleanest fuels, because when burnt, it does not produce greenhouse gases (e.g. CO₂), only water vapor and because of that its production is very important in a lot of industries and maybe in the future would replace gasoline, oil and natural gas [7].

Hydrogen can also be obtained from the reforming of liquefied petroleum gas (LPG), which is the method that will be discussed in this article. Liquefied petroleum gas (LPG) is a mixture of hydrocarbon gases, predominantly of propane and butane. In winter, LPG contains more propane, while in summer, it contains more butane, but its average composition is about 35% propane and 65% butane [1]. LPG exists as a gas at normal atmospheric pressure and temperature, but to minimize its volume, it is liquefied at high pressure [9]. Specification of the composition of LPG is required as traces of hydrocarbon impurities which can negatively affect the fuel quality and processing [8].

According to the literature, the chemicals present in a reaction system for the steam reforming of LPG are: C₄H₁₀, C₃H₈, C₂H₆, C₂H₄, CH₄, CO, CO₂, H₂, H₂O and solid carbon (C). However, this reaction causes a side production of carbon dioxide and carbon monoxide, which are greenhouse gases and contribute to global warming [9]. The reactions which represent the system for the production of hydrogen are a set of 7 linearly independent reactions there are presented in Table 1 [10].

Table 1. Reactions of steam reforming of LPG

Reaction 1:	$C_4H_{10} + H_2O \leftrightarrow C_3H_8 + CO + 2H_2$
Reaction 2:	$C_3H_8 + H_2O \leftrightarrow C_2H_6 + CO + 2H_2$
Reaction 3:	$C_2H_6 + H_2O \leftrightarrow CH_4 + CO + 2H_2$
Reaction 4:	$C_2H_4 + H_2O \leftrightarrow CH_4 + CO + H_2$
Reaction 5:	$CH_4 + H_2O \leftrightarrow CO + 3H_2$
Reaction 6:	$CO + H_2O \leftrightarrow CO_2 + H_2$
Reaction 7:	$CO + H_2 \leftrightarrow C_{(s)} + H_2O$

The production of hydrogen from catalytic reforming of liquefied petroleum gas (LPG) is accompanied by production of carbon dioxide (CO₂) which is a greenhouse gas. The fossil CO₂ emissions need to be controlled in order to prevent or at least diminishes the global warming, melting glaciers and other environmental effects [11].

Carbon capture and storage (CCS) is the process of capturing waste carbon dioxide (CO₂) from various fossil fuels-intensive processes (e.g. power generation, metallurgy, cement, petro-chemicals etc.) [12]. Once captured CO₂ is then transport and stored to a storage site, where it will not return to the atmosphere, normally an underground geological formation. The purpose of this is to prevent the release of large quantities of carbon dioxide (CO₂) into the atmosphere, which unfortunately has the potential to induce severe climate changes.

Capturing carbon dioxide (CO₂) is most effective at emission point sources, especially in the case of chemical industries with major carbon dioxide (CO₂) emissions. Capturing CO₂ from air is also possible, but not very practical because the carbon dioxide (CO₂) is not concentrated. Impurities in this CO₂ stream, like sulphur's and water, could have a significant effect on their phase behaviour and could pose a significant threat of increased corrosion of pipeline and well materials. In instances where CO₂ impurities exist, especially with air capture, a scrubbing separation process would be needed to initially clean the flue gas and gasifying coal, it is possible to capture approximately 65% of carbon dioxide embedded in it and sequester it in a solid form [13].

The conceptual methods used for the carbon capture and storage (CCS) are the following:

- Post-combustion capture option in which the CO₂ is removed after the combustion of the fossil fuel, using for a broad range of methods e.g. gas-liquid absorption by methyl-diethanol-amine (MDEA). The post-combustion capture processes are the most popular because of existing fossil fuel power plants that can be easily retrofitted to include carbon capture and storage (CCS) technology;
- Oxy-fuel combustion option in which the fuel is burned in oxygen instead of air. This technique is promising in reducing the complexity of CO₂ separation from the flue gases (avoiding nitrogen contamination), but the initial air separation step (by cryogenic air distillation) demands a significant amount of energy and also the cost of air separation technology is significant;
- Pre-combustion CO₂ capture option which is more often applied in the fertilizer production (ammonia, urea), various chemical industries (e.g. hydrogen production) and power production. Gas-liquid absorption is the most straightforward method for pre-combustion CO₂ capture using either chemical (e.g. MEA, MDEA etc.) or physical (e.g. Selexol™, Rectisol® etc.) solvents

According to the literature, the carbon capture rate in all these three conceptual CO₂ capture processes is about 90 % to be commercially and economically viable.

PLANT CONFIGURATIONS AND MAIN DESIGN ASSUMPTIONS

Figure 1 presents the conceptual design of hydrogen production method from gas petroleum liquefied (LPG) with CCS using MDEA-based gas-liquid absorption (noted as Case 2). In this figure, the operational steps which are required in order to obtain hydrogen and in the same time also to reduce the greenhouse gas emissions, by CO₂ capture are illustrated. For CO₂ capture process, a pre-combustion configuration was used based on gas-liquid absorption process using methyl-diethanol-amine (MDEA). The hydrogen-rich gas resulted after syngas decarbonisation is purified by a Pressure Swing Adsorption (PSA) unit to the required quality specification (purity higher than 99.95 % vol.).

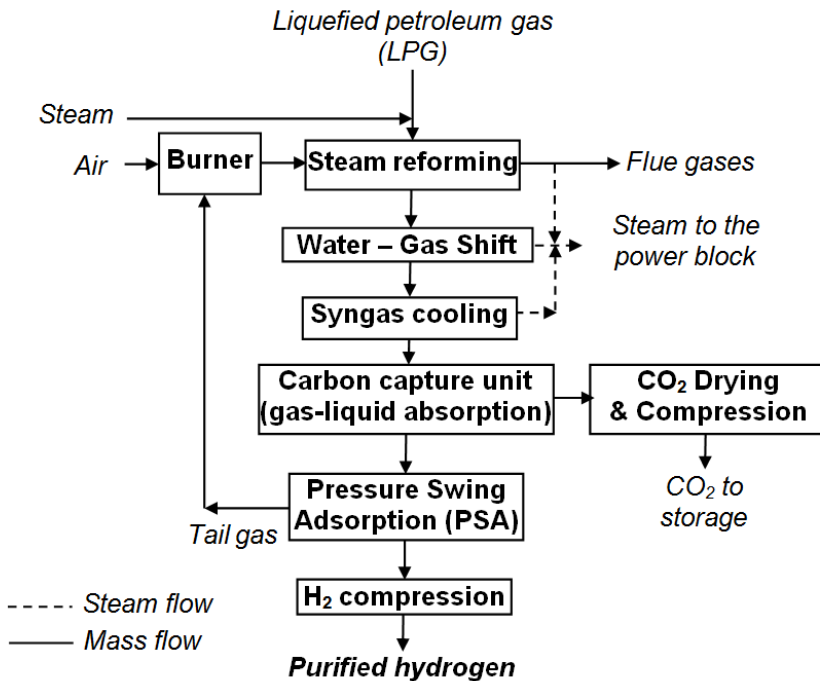


Figure 1. Hydrogen production from gas petroleum liquefied with carbon capture and storage using Methyl-Diethanol-Amine (MDEA)

Figure 2 illustrates the conceptual design of hydrogen production from gas petroleum liquefied (LPG) without carbon capture and storage (noted as Case 1). This scheme was also evaluated (as a benchmark case of

the carbon capture design) with the purpose of presented a comparison between the two hydrogen production methods by LPG catalytic reforming with and without capture and storage of carbon dioxide (CCS). This comparison has the main purpose to underline the advantages and the disadvantages of carbon capture technology. Nowadays, the implementation of CCS technologies to whole industrial sector has a remarkable importance considering the facts that the fossil fuels (oil, natural gas, coal etc.) are predicted to remain the backbone of many industrial processes as well the fact that the carbon dioxide is a greenhouse gas producing global warming.

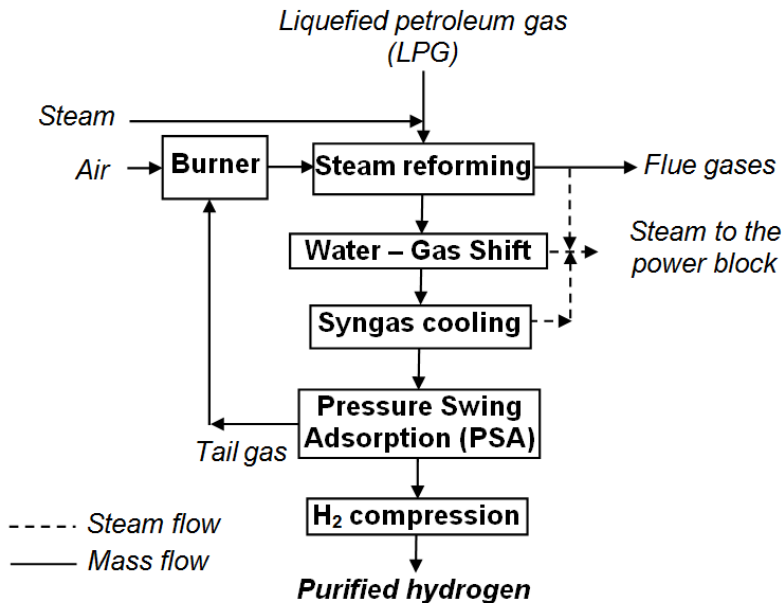


Figure 2. Hydrogen production from gas petroleum liquefied without carbon capture and storage

In order to evaluate the hydrogen production method from catalytic reforming of liquefied petroleum gas with and without carbon capture and storage, the both processes with and without CCS were assessed by a process flow modeling software (ChemCAD). Table 2 presents the main modeling assumptions used in the evaluation [14]. The developed models were validated by comparison to the literature data [11,15-16], no significant variations being noted. The simulation results were used to calculate the overall technical and environmental indicators.

Table 2. Main design assumptions of evaluated cases

Unit	Parameters
Hydrogen production capacity & purity	100000 Nm ³ /h Hydrogen purity: 99.95% (vol.)
Fuel used: liquefied petroleum gas (LPG)	Composition (% vol.): 65% butane, 35% propane Pressure: 30 bar Outlet temperature: 25°C
LPG catalytic reformer	Outlet temperature: 900°C Reactor type: Gibbs reactor Thermal mode: heat exchanger Pressure drop: 1 bar Heat duty (to be supplied by an external burner): 148 MW _{th} Overall heat of reaction: 88 MW _{th}
Water Gas Shift (WGS) conversion	Outlet temperature: 400°C Reactor type: Equilibrium reactor Thermal mode: adiabatic Steam to CO ratio: 2 (molar) Pressure drop: 1 bar
Hydrogen-rich gas (after shift conversion)	Temperature: 40°C Pressure: 28.75 bar Composition (% vol.): 73.48% hydrogen, 21.32 % carbon dioxide, 2.54 % methane, 2.38 % carbon monoxide, 0.28 % water
CO ₂ capture process	Solvent used for CO ₂ capture: methyl-diethanol-amine (MDEA) Concentration: 50 % wt.
Absorption column:	No. of stages: 30 Column pressure drop: 1 bar Top pressure: 28 bar
Desorption column:	No. of stages: 10 Column pressure drop: 1 bar Top pressure: 4 bar Reboiler duty: 18 MW _{th}
CO ₂ drying & compression	CO ₂ drying: Tri-Ethylene-Glycol (TEG) 3 compression steps with inter-cooling Final delivery pressure: 120 bar CO ₂ quality specification (vol. %) [14]: >95% CO ₂ ; <2000 ppm CO; <250 ppm H ₂ O; <100 ppm H ₂ S
Hydrogen compression unit	Delivery pressure: 60 bar Outlet temperature: 40°C
Heat recovery steam generation unit	Steam conditions: 470°C & 40 bar Steam turbine efficiency: 85 % Condensing pressure: 48 mbar
Pumps and compressors	Energy efficiency: 85 % Pressure ration: max. 3
Heat exchangers	$\Delta T_{\min.} = 10^\circ\text{C}$; Pressure drop: 3 - 5% of inlet pressure

RESULTS AND DISCUSSIONS

The evaluated concepts of hydrogen production from liquefied petroleum gas (LPG) catalytic reforming process with and without carbon capture were modeled and simulated using process flow modeling software (ChemCAD). The size of evaluated hydrogen production concepts was 100000 Nm³/h hydrogen with a purity of 99.95% (vol.) to be comparable with other industrial hydrogen production capacities used for instance in the oil refinery or various chemical sectors.

By comparing the two methods of obtaining hydrogen from catalytic reforming of LPG with and without capture and storage of carbon dioxide (CCS), one can evaluate the technical and environmental advantages and disadvantages of carbon capture method e.g. overall energy efficiency, energy penalty for CO₂ capture, specific CO₂ emissions etc. These technical and environmental indicators are very important in any CCS project [17].

All concepts were modeled and stimulated in a fully thermally integrated design [18]. Pinch analysis was used as main heat and power integration analysis tool with 10°C as minimum temperature difference. As an illustrative example of the thermal integration analysis, Figure 3 presents the Hot and Cold Composite Curves (HCC and CCC) for the LPG reforming case with carbon capture and storage.

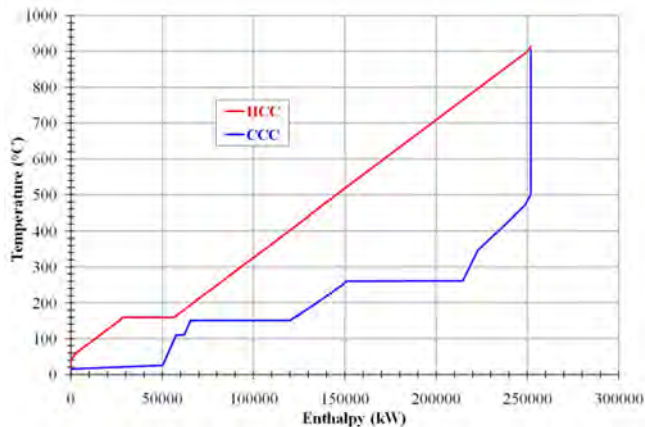


Figure 3. Hot and cold composite curves for LPG catalytic reforming with CCS

In order to assess the overall performance of the process of hydrogen production from catalytic LPG reforming, the modeling and simulation of both plant configurations yields the required process data like mass and molar flows, pressures, composition, temperatures, heat and power generated and consumed.

For the calculations of overall plant performance, the following technical and environmental indicators were used:

- *Cold gas efficiency* (CGE) represent the overall efficiency of reforming process and it is calculated with the following formula:

$$CGE = \frac{\text{Syngas thermal energy [MW}_{th}]}{\text{Feedstock thermal energy [MW}_{th}]} * 100 \quad (1)$$

- *Syngas treatment efficiency* (STE) shows the energy losses through the syngas conditioning line (shift conversion, CO₂ capture) and is calculated with the below formula:

$$STE = \frac{\text{Syngas thermal energy ex. AGR [MW}_{th}]}{\text{Syngas thermal energy ex. quench [MW}_{th}]} * 100 \quad (2)$$

- *Net electrical and hydrogen efficiencies* (η_{power} and $\eta_{Hydrogen}$) indicates conversion process. These indicators are calculated using the following formulas:

$$\eta_{power} = \frac{\text{Net power output [MW}_e]}{\text{Feedstock thermal energy [MW}_{th}]} * 100 \quad (3)$$

$$\eta_{hydrogen} = \frac{\text{Hydrogen thermal output [MW}_e]}{\text{Feedstock thermal energy [MW}_{th}]} * 100 \quad (4)$$

- *Carbon capture rate* (CCR) is obtained considering the molar flow of captured carbon dioxide divided with carbon molar flow from the feedstock (LPG):

$$CCR = \frac{\text{Captured CO}_2 \text{ molar flow [kmole / h]}}{\text{Feedstock carbon molar flow [kmole / h]}} * 100 \quad (5)$$

- *Specific CO₂ emissions* (SE_{CO_2}) are calculated considering emitted CO₂ mass flow for each MW power plus hydrogen generated within the process:

$$SE_{CO_2} = \frac{\text{Emitted CO}_2 \text{ mass flow [kg / h]}}{\text{Net power + Hydrogen output [MW]}} * 100 \quad (6)$$

- *Specific Primary Energy Consumption for CO₂ Avoided* (SPECCA) is considering the energy consumption for CO₂ capture and it was calculated with the formula:

$$SPECCA = \frac{\text{Heat rate}_{\text{Capture}} \left[\frac{\text{MJ}_{LHV}}{\text{MWh}} \right] - \text{Heat rate}_{\text{No capture}} \left[\frac{\text{MJ}_{LHV}}{\text{MWh}} \right]}{\text{Emissions}_{\text{No capture}} \left[\frac{\text{kg CO}_2}{\text{MWh}} \right] - \text{Emissions}_{\text{Capture}} \left[\frac{\text{kg CO}_2}{\text{MWh}} \right]} \quad (7)$$

One of the main purposes of the modeling and simulation work for the production of hydrogen through LPG catalytic reforming was to generate the mass and energy balances to calculate the overall plant performance indicators. The technical and environmental performance indicators for the evaluated hydrogen production processes from catalytic reforming of LPG without carbon capture (Case 1) and the similar process with carbon capture (Case 2) are presented in Table 3.

Table 3. Performance indicators of hydrogen production from LPG reforming

Main Plant Data	Units	Case 1	Case 2
LPG flowrate	t/h	35.82	35.82
LPG lower heating value (LHV)	MJ/kg	45.75	
Feedstock thermal energy (A)	MW _{th}	455.27	455.27
Steam turbine output	MW _e	8.69	8.55
Expander output	MW _e	2.60	1.54
Gross power output (B)	MW _e	11.29	10.09
Hydrogen output (C)	MW _{th}	300.00	300.00
CO ₂ capture & compression	MW _e	0.00	5.71
Hydrogen compression	MW _e	3.89	3.88
Power island	MW _e	0.18	0.19
Ancillary consumption (D)	MW _e	4.07	9.78
Net power output (E = B - D)	MW _e	7.22	0.31
Net power efficiency (E/A * 100)	%	1.58	0.06
Hydrogen efficiency (C/A * 100)	%	65.89	65.89
Cumulative energy efficiency	%	67.47	65.95
Carbon capture rate	%	0.00	78.87
CO ₂ specific emissions (H ₂ +power)	kg/MWh	351.77	75.97
SPECCA	MJ/kg CO ₂	-	0.44

As can be noticed from Table 3, the hydrogen production process without CCS (Case 1) is slightly more efficient than the concept with CCS (Case 2) by about 1.5 net energy (hydrogen + power) efficiency percentage points. Comparing this energy penalty for CO₂ capture with literature data [17,19] for other energy conversion systems with CCS (e.g. natural gas catalytic reforming, coal gasification etc.) one can notice that the LPG catalytic reforming

process is combining a high energy efficiency with low energy penalty for CO₂ capture. The carbon capture rate of Case 2 is about 79 % in line with other pre-combustion CO₂ capture concepts applied for hydrocarbon reforming processes (e.g. natural gas, naphtha etc.) [20-21]. The specific primary energy consumption for CO₂ avoided (SPECCA) is also promising in comparison to other CO₂ capture methods (e.g. post-combustion capture option has a SPECCA value of about 3 MJ/kg CO₂).

CONCLUSIONS

This paper evaluates the technical and environmental performances of hydrogen production (as a clean decarbonised fuel) from catalytic reforming of liquefied petroleum gas (LPG) with and without carbon capture and storage (CCS). A hydrogen production unit with 100000 Nm³/h (corresponding to 300 MW thermal output) was evaluated. The simulation results showed that the carbon capture concept (Case 2) has an overall energy efficiency with just about 1.5 net efficiency percentage points (as CO₂ capture energy penalty) lower compared to the case without carbon capture (Case 1). The carbon capture rate for Case 2 was about 79 % and the specific CO₂ emissions per MW of produced energy (hydrogen and power) are decreasing accordingly. The specific primary energy consumption for CO₂ avoided (SPECCA) is also very promising for the hydrogen production through LPG reforming with CCS.

In conclusion, the proposed LPG catalytic reforming process with carbon capture is a very promising option for reducing the CO₂ emissions from hydrogen production processes (as the case of oil refinery sector as well as other large scale chemical applications e.g. ammonia, fertilizers).

ACKNOWLEDGMENTS

This work was supported by a grant of Ministry of Research and Innovation, CNCS – UEFISCDI, project ID PN-III-P4-ID-PCE-2016-0031: “Developing innovative low carbon solutions for energy-intensive industrial applications by Carbon Capture, Utilization and Storage (CCUS) technologies, within PNCDI III”.

REFERENCES

1. D. Brzezinska, A.S. Markowski, *Process Safety and Environmental Protection*, **2016**, 116, 90.
2. E. Elnajjar, M.O. Hamdan, M.Y.E. Selim, *Renewable Energy*, **2013**, 56, 110.
3. R.F. Colwell, *Excellence in Applied Chemical Engineering*, **2009**.
4. D. James, H. Gary, G.E. Handwerk, M.J. Kaiser, "Petroleum Refining: Technology and Economics", Fifth Edition, **2007**.
5. C.Y. Li, J.Y. Wu, C.Y. Zheng, R.Z. Wang, *Applied Thermal Engineering*, **2017**, 115, 315.
6. J. Kim, C. Bae, G. Kim, *Fuel*, **2016**, 183, 304.
7. A. Boretti, *Fuel Processing Technology*, **2017**, 161, 41.
8. A. Ruissen, "The Analysis of Hydrocarbon Composition in LPG by Gas Chromatography using the DVLS Liquefied Gas Injector", PhD Thesis, *Da Vinci Laboratory Solutions B.V.*
9. Technical Data for Propane, Butane, and LPG Mixtures, Alternate Energy Systems, Inc.
10. J.A. Sousa, P.P. Silva, A.E.H. Machado, M.H.M. Reis, L.L. Romanielo, C.E. Hori, *Brazilian Journal of Chemical Engineering*, **2013**, 30, 83.
11. International Energy Agency - *Greenhouse gas R & D Programme* "Decarbonisation of fossil fuels", March **1996**.
12. G. Lozza, P. Chiesa, "Natural gas decarbonization to reduce CO₂ emission from combined cycles, Part B: Steam-methane reforming", *Proceedings of ASME TURBOEXPO* May 8-11, Munich Germany, **2000**.
13. E. Elnajjar, M.Y.E. Selim, M.O. Hamdan, *Energy Conversion and Management*, **2013**, 76, 32.
14. C.C. Cormos, K. Vatopoulos, E. Tzimas, *Energy*, **2013**, 51, 37.
15. M. Voldsund, K. Jordal, R. Anantharaman, *International Journal of Hydrogen Energy*, **2016**, 41, 4969.
16. P. Nikolaidis, A. Poullikkas, *Renewable and Sustainable Energy Reviews*, **2017**, 67, 597.
17. B. Metz, O. Davidson, H. de Coninck, M. Loos, L. Meyer, Carbon Dioxide Capture and Storage, Intergovernmental Panel on Climate Change (IPCC), Geneva, Switzerland, **2005**.
18. C.C. Cormos, *International Journal of Hydrogen Energy*, **2010**, 35, 7485.
19. O. de Queiroz F. Araújo, J.L. de Medeiros, *Current Opinion in Chemical Engineering*, **2017**, 17, 22.
20. N. Muradov, *International Journal of Hydrogen Energy*, **2017**, 42, 14058.
21. International Energy Agency - *Greenhouse gas R & D Programme* "The reduction of greenhouse gas emissions from the oil refinery and petrochemical industry", June **1999**.

PREPARATION AND CHARACTERIZATIONS OF NEW BIOMATERIALS BY ANTHOCYANINS ADSORPTION ON HYDROXYAPATITE-BASED MATERIALS

RÉKA BARABÁS^a, NORBERT MUNTEAN^a, GABRIELLA SZABÓ^a, KRISZTINA MAURER^a, LILIANA BIZO^{b*}

ABSTRACT. Anthocyanins (ACNs) are water-soluble plant pigments belonging to the group of flavonoids, with antioxidant, anti-inflammatory and antibacterial activity. The antioxidant activities of extracts from berries and hibiscus were tested with the Briggs–Rauscher method. Adsorption of anthocyanins on biomaterials is a method for their stabilization. Hydroxyapatite (HAP) doped with inorganic silica has an increased specific surface, porosity and chemical reactivity. Anthocyanins from extracts of different berries were adsorbed on hydroxyapatite-based materials. The adsorption and desorption capacity of hydroxyapatite-based materials were measured and the adsorption capacity of different anthocyanin extracts were compared. It was concluded that the highest adsorption capacity and efficiency were obtained in the case of blueberry. Based on the results of the desorption experiments, it has been proven that HAP-Si-blueberry is more adequate to obtain a retard effect, despite the fact that the antioxidant activities of blueberry and blackcurrant are similar.

Keywords: *anthocyanin, antioxidant activity, hydroxyapatite-based materials, berries extract, hibiscus extract.*

INTRODUCTION

Silica doped hydroxyapatite was mainly used for biomedical purposes. Besides biocompatibility, hydroxyapatite shows a very high reactivity with metal ions, which can lead to the use of this material in new application fields,

^a Babeş-Bolyai University, Faculty of Chemistry and Chemical Engineering, Department of Chemistry and Chemical Engineering of the Hungarian Line, 11 Arany Janos str., RO-400028, Cluj-Napoca, Romania

^b Babeş-Bolyai University, Faculty of Chemistry and Chemical Engineering, Department of Chemical Engineering, 11 Arany Janos str., RO-400028, Cluj-Napoca, Romania

* Corresponding author lbizo@chem.ubbcluj.ro

for example using water purification agents for heavy metal immobilization. Based on its ion exchange property (regarding calcium and other metal ions), HAP is widely used as a metal retainer material [1].

Due to the introduction of silica, the specific surface, porosity and in this way the chemical reactivity of the apatite material is enlarged; doping the hydroxyapatite with silica can be a better material for metal removal [2-4]. HAP doped with inorganic silica has an increased specific surface, porosity and chemical reactivity. Heat-treated materials have a very low specific surface area, which explains the weak metal sorption properties of these materials. Materials containing silica have better sorption efficiency than unmodified hydroxyapatite and 10%wt silica-containing hydroxyapatite with low particle size has the highest copper sorption efficiency. Increase of the initial copper concentration decreases saturation time and increase of temperature increases copper sorption. Silica-containing hydroxyapatite shows very good copper sorption capacity, which can lead to the enlargement of the application fields of apatites [5].

Definition of antioxidant effect (AOX)

Anthocyanins are water-soluble phytochemicals with a typical red to blue color. Anthocyanins belong to the group of flavonoids, they can be found in tea, honey, wine, fruits, vegetables, nuts, olive oil, cocoa and cereals. Anthocyanin extracts from plants are promising as a treatment for hypertension and hyperlipidemia [6]. Many authors have also reported about the antioxidant activity [7], anti-inflammatory activity [8, 9], cardioprotective activity [10], hepatoprotective activity [11] and antibacterial activity [12] of anthocyanins.

Antioxidant activity denotes the ability of a bioactive compound to maintain cell structure and function by effectively clearing free radicals, inhibiting lipid peroxidation reactions and preventing other oxidative damage [13]. It is also a foundation of many other biological functions, such as anti-cancers, anti-inflammation and anti-aging [14, 15]. On the other hand, the prevention of many chronic diseases, such as cancer, diabetes and cardiovascular disease, has been suggested to be associated with the antioxidant activity [16, 17].

Antioxidant activity measurements (AOX)

Therefore, a deep study of natural antioxidants, such as those from fruits and vegetables, is of great importance to human health. There are different antioxidant testing methods, for example ORAC (oxygen radical absorbance capacity), TRAP (total radical trapping antioxidant parameter), TEAC (Trolox equivalent antioxidant capacity), FRAP (ferric ion reducing antioxidant parameter), reaction with DPPH (2, 2-diphenyl-1-picrylhydrazyl), TOSC (total oxidant scavenging capacity), etc., which provide different ranking orders for antioxidant capacity due to different experimental conditions [18-20].

In this study the Briggs-Rauscher method (BR) was used, which is based on the inhibition of the oscillations due to the antioxidants reaction with the free radical intermediates. This method [21] was chosen because it works at pH 2 and partially mimics the physiological conditions similar to those of the fluids in the human stomach, and it is applicable for the investigation of hydrophilic as well as lipophilic compounds [22, 23]. The Briggs-Rauscher method was described by Cervellati et al. (2001) and it has been widely used since then [24-27]. Briefly, when antioxidants are added to an active BR mixture, there is an immediate quenching of the oscillations and the time elapsed between the cessation and the return of the oscillating regime, the so called inhibition time. The dependence of the inhibition time on the antioxidant concentration is suitable for determination of the antioxidant capacity. The slope of the curve representing inhibition time vs. antioxidant concentration (inhibition time versus concentration) can be used to calculate the relative antioxidant activity. The relative activity with respect to the slopes (RAS) of a compound is the ratio between the slope of the straight line of the respective compound and that of the chosen standard: $RAS = \text{slope (sample)} / \text{slope (standard)}$, so that a high RAS number means a better antioxidant effectiveness. The efficiency of the corresponding antioxidant is expressed as the length of time in minutes before oscillations restart. A prolonged inhibition time ($t_{\text{inhib.}}$) means a better antioxidant activity.

Adsorption of anthocyanins on biomaterials is a method for their stabilization. Hydroxyapatite (HAP) is an important biomaterial, although it does not possess all the necessary properties to be the perfect biomaterial (mechanical strength, chemical reactivity, etc.). Silica is also a component of the bone; therefore, several methods for the synthesis of silicon-substituted hydroxyapatites have been described.

The aim of this work was the extraction of anthocyanins with AOX effect and their adsorption and desorption on hydroxyapatite (HAP) and silica-substituted hydroxyapatite (HAP-Si). Anthocyanins stabilized by adsorption on HAP-based materials should be applied in stomatology as anti-inflammatory treatments to avoid the inflammation of the cardiac system. Consequently, our research was focused on:

1. Extracting antioxidants from hibiscus and different berries; separation of anthocyanins from hibiscus extract and comparison of their antioxidant activity (the antioxidant activity was measured using the BR analytical method based on the inhibition of the Briggs-Rauscher oscillating reaction),
2. Testing the adsorption capacity of anthocyanin extracts on HAP-Si,

3. Testing the antioxidant activity of extracts from hibiscus and anthocyanins from hibiscus extract,
4. Testing the antioxidant activity of extracts from berries (blueberry, hawthorn, blackcurrant, blackthorn).

RESULTS AND DISCUSSION

Antioxidant activity evaluation

Perturbation of the oscillatory BR system with a diluted extract causes the immediate cessation of the oscillations; the time elapsed between cessation and returns of oscillations (the so called inhibition time) are illustrated in Figure 1.

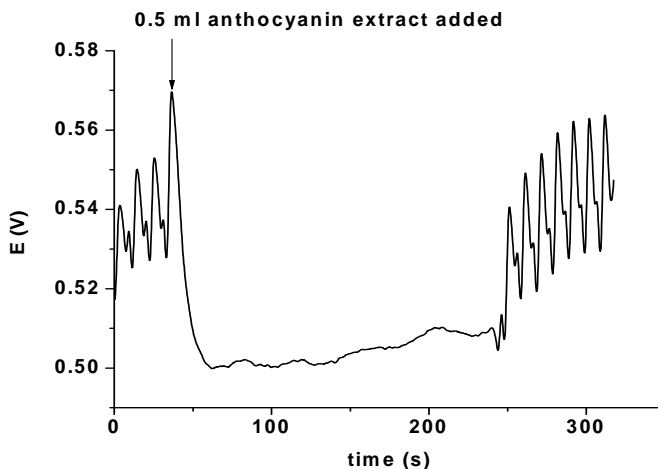


Figure 1. The effect of AEH extract on BR oscillating reaction.

Analysis of AOX activities of AEH and HE

Preliminary experiments regarding the AOX activity of anthocyanins were made in the case of AEH (anthocyanin from hibiscus extract) and HE (hibiscus extract). Stock solutions of HE and AEH were prepared by dissolving 0.001 g of extract in 10 ml of distilled water. The antioxidant activity was determined for several dilutions and the calibration curves were drawn for each of them. Variation of the inhibition time depending on the antioxidant concentration was found to be linear as can be seen in the figure below (Figure 2).

The relative antioxidant effect can be calculated from the slope of the calibration curves (see next paragraph). The relative activity with regard to slopes (RAS) is the ratio between the slope of the straight line of the sample and that of the standard; i.e. $RAS = \text{slope (sample)}/\text{slope (standard)}$. As listed in Table 1, the chosen standard was the pure anthocyanin with a slope of 656.8, the slope of the extract calibration curve was 1371.1, the RAS of the extract was 2.1, thus *the extract had more than double antioxidant capacity than the pure separated anthocyanin*. This superior behavior is probably caused by the synergistic effect of other compounds present in the extract.

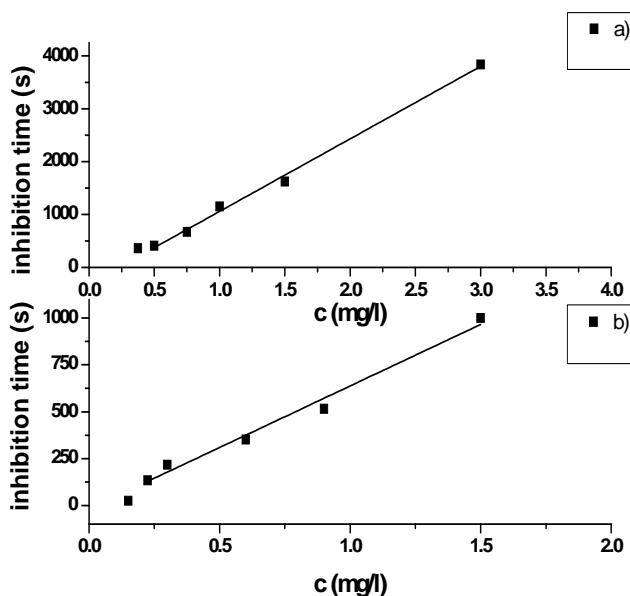


Figure 2. Concentration dependence of the inhibition time for: a) hibiscus extract; b) anthocyanin from hibiscus extract.

Table 1. Relative activity calculated for hibiscus extract (HE) and for anthocyanin from hibiscus extract (AEH).

Hibiscus	Slope of calibration curves	RAS
HE	1371.1	2.1
AEH	656.8	1

Testing the antioxidant activity of different types of berry extracts

The antioxidant activities of different AOX extracts were determined for several dilutions and the calibration curves were drawn for each of them. Variation of the inhibition time depending on the antioxidant concentration was found to be linear as can be seen in Figure 3.

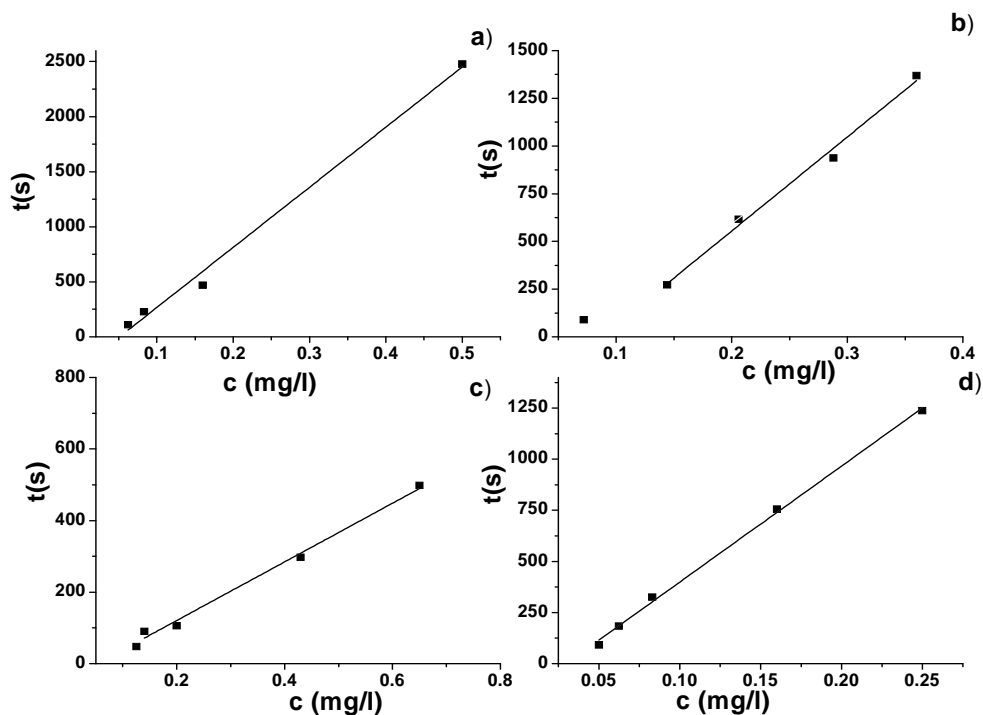


Figure 3. Concentration dependence of the inhibition time for: a) blueberry extract; b) hawthorn extract; c) blackthorn extract; d) blackcurrant extract.

Relative antioxidant activity was calculated using the slopes of the calibration curves of the berry extracts. The chosen standard was blackcurrant. The results are summarized in Table 2.

Table 2. Relative antioxidant activity calculated for different types of berry extracts.

Berry extracts	Slope of calibration curves	RAS
Blackcurrant	5673.9	8.6
Blueberry	5456.3	8.3
Hawthorn	4475.7	6.8
Blackthorn	856.98	1.3

Based on the RAS values calculated, the following ranking of antioxidant activity could be concluded:

Blackcurrant ≈ Blueberry > Hawthorn >> Blackthorn

There is no significant difference between blackcurrant and blueberry.

Adsorption results

Preliminary experiments carried out with hibiscus and regarded to the extraction of anthocyanins and measurements of AOX activity showed that the adsorption capacity of the hibiscus extract (anthocyanins and other compounds) was higher than that of the pure anthocyanins (without other accompanying components), see Figure 4.

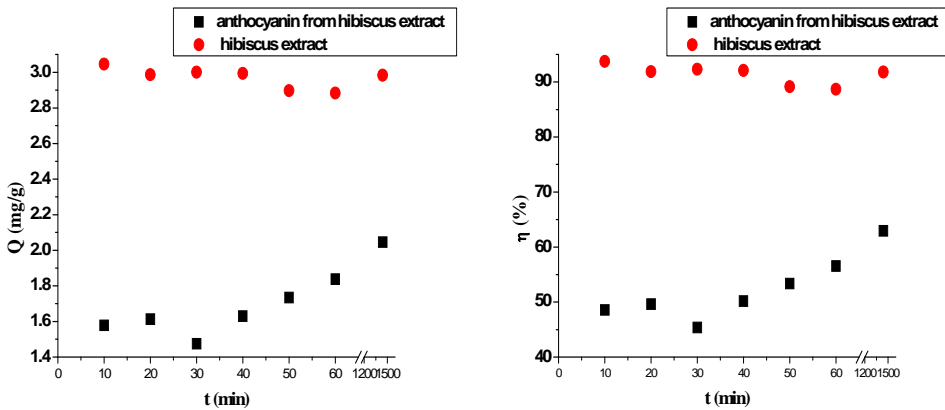


Figure 4. The adsorption capacity q_t (mg/g) and the adsorption efficiency η (%) of HAP-Si.

Based on these results, the adsorption experiments were carried out with berry extracts from: blueberry, hawthorn, blackthorn, and blackcurrant.

The following table (Table 3) contains the adsorption capacity and adsorption efficiency of HAP-Si measured for extracts of different types of berries, obtained after 24 hours - time necessary to achieve the equilibrium.

Table 3. Adsorption capacity q_t (mg/g) and adsorption efficiency η (%) of HAP-Si measured for extracts of different types of berries.

Anthocyanin mixture from:	Adsorption capacity q_t (mg/g) of HAP-Si	Adsorption efficiency η (%) of HAP-Si
Blueberry	50.29	41.91
Hawthorn	45.06	37.55
Blackcurrant	32.52	27.10
Blackthorn	13.09	10.91

It can be concluded (see Table 3), that the highest adsorption capacity and efficiency were obtained in the case of blueberry. Differences between adsorption capacities and efficiencies can be explained with the different types of anthocyanins found in the berries.

Desorption experiments

Preparation of HAP-Si-AOX tablets

For desorption experiments, HAP-Si powder with anthocyanins adsorbed from berries was used. Samples were prepared using a Specac hydraulic presser to obtain tablets on which surfaces anthocyanins were adsorbed. After the tablets were made, the adsorbed anthocyanin was calculated from the adsorption capacity defined in the previous experiments (see Table 4).

Table 4. Calculated adsorbed anthocyanin (mg and %) from HAP-Si-AOX tablets.

Berries	Tablet weight (g)	Adsorbed anthocyanin (mg)	Adsorbed anthocyanin %
Blueberry	0.1345	6.76	5.0
Hawthorn	0.1296	5.84	4.5
Blackcurrant	0.1413	4.59	3.2
Blackthorn	0.3383	4.43	1.3

Desorption of anthocyanins from HAP-Si-AOX tablets

Desorption experiments were carried out as follows: tablets were immersed in simulated body fluid [28, 29] and the process was monitored by using a UV-VIS spectrophotometer. The desorbed amount of anthocyanin was calculated from the calibration curves of each extract. Desorption of the active compound from tablets is presented in Figure 5.

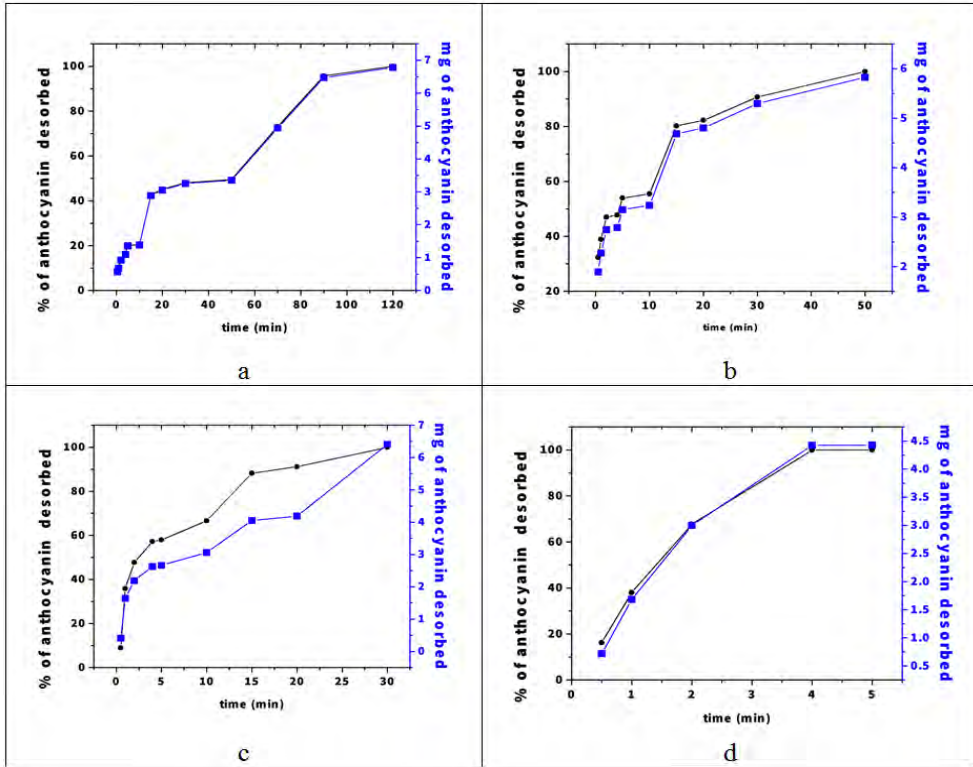


Figure 5. The amounts (blue line) and percentages (black line) of desorbed anthocyanins were plotted versus time in the case of: a) blueberry; b) hawthorn; c) blackcurrant; d) blackthorn.

Based on the desorption curves, the half-life values of the HAP-Si-anthocyanin samples could be predicted, as summarized in Table 5. The results of the desorption experiments were well correlated with the adsorption experiments: the HAP-Si-blueberry sample had the highest adsorption capacity and the longest retention time of the adsorbed material at the same time. The order of adsorption capacity and the order of half-life were the same.

Table 5. Predicted half-life values of the HAP-Si-anthocyanins.

HAP-Si-anthocyanins	Predicted half-life (min)
HAP-Si-blueberry	40
HAP-Si-hawthorn	15
HAP-Si-blackcurrant	10
HAP-Si-blackthorn	2

On the other hand, the antioxidant activities of blueberry and blackcurrant were similar (see Table 2), but the half-life values of the samples were different: HAP-Si-blueberry was more adequate to obtain a retard effect.

Transmission Electron Microscopy (TEM) measurements

Transmission electron microscopy was performed on HAP-Si and HAP-Si-AOX (HAP-Si powder with adsorbed anthocyanins from berries) samples. The resulted images are presented in Figure 6. As the TEM pictures show, there is a difference between HAP-Si and HAP-Si-AOX; the latter presents gelified materials (berry extract) containing polysaccharides and anthocyanins.

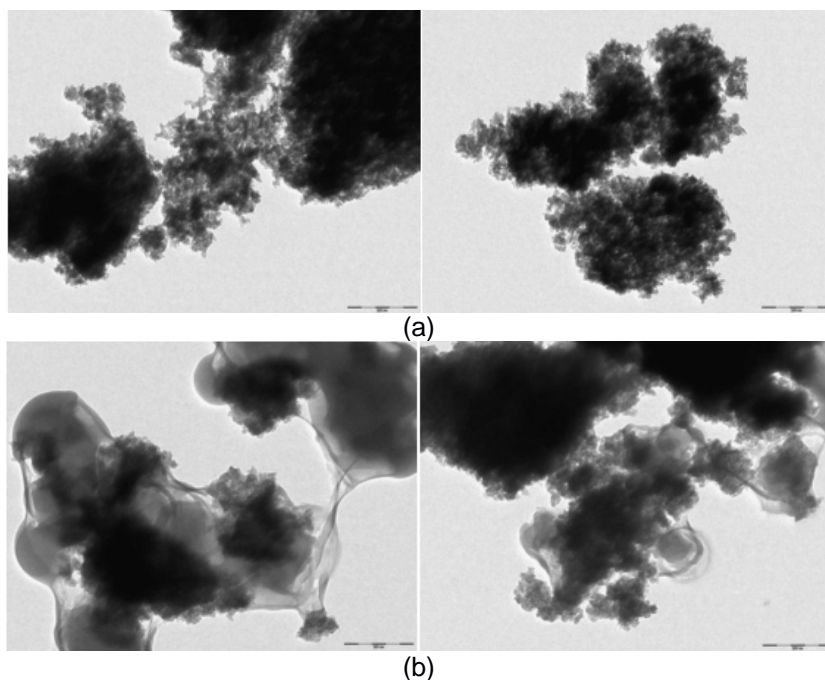


Figure 6. TEM images at 200nm resolution of (a) HAP-Si and (b) HAP-Si-AOX (HAP-Si powder with adsorbed anthocyanins from berries).

CONCLUSIONS

It can be concluded, that the adsorption capacity of hibiscus extract (anthocyanins and other compounds) was higher than that of the separated anthocyanins (without other accompanying components), due to the synergistic effect.

Based on the first results (with hibiscus), further experiments were carried out with various berries using berry extracts containing anthocyanins and other compounds (such as polysaccharides). These extracts were compared based on their antioxidant activity and the following ranking was made: *Blackcurrant* \approx *Blueberry* > *Hawthorn* \gg *Blackthorn*.

The resulted extracts were adsorbed on HAP-Si, and the adsorption capacity and efficiency of each were evaluated. Based on the results it can be concluded, that the HAP-Si of the blueberry extract had the highest adsorption capacity and efficiency.

The desorption experiments in SBF showed that the HAP-Si-blueberry composite had the highest half-life value. Due to these favorable properties, this composite can be used as supplement or dental filling/inlay with high antioxidant activity.

EXPERIMENTAL SECTION

Extraction and separation of anthocyanins from different plants

Preparation of hibiscus extract (HE) by ultrasound-assisted extraction method

The hibiscus (*Hibiscus sabdariffa* L.) petals used in this study is a bio-product obtained from a Hungarian company. The powder of dried and mild hibiscus petals was mixed with different solvents in a conical flask. The conical flask was immersed in an ultrasonic bath at room temperature for 30 minutes. To avoid the oxidation of anthocyanins, nitrogen gas was led in the flask to ensure an oxygen-free environment. Vacuum filtration was performed, and the filtered material was extracted from the filter and treated with solvent in the ultrasonic bath for 30 minutes. The filtrate was transferred into a single-neck flask and the solvent removed by a rotary evaporator using low temperature (40°C) and pressure to avoid the degeneration of the anthocyanin molecules. The filtrate was placed in the refrigerator to freeze overnight and then placed in the freeze drying apparatus to get rid of water. The hibiscus extract resulted from the above presented method will be denoted: HE.

Extraction of anthocyanin from hibiscus extract (AEH)

Separation by solid phase extraction was used to extract pure anthocyanin from hibiscus extract. Oszmianski and Lee [30] developed this method and the steps of the extraction used in our study are summarized in Figure 7.

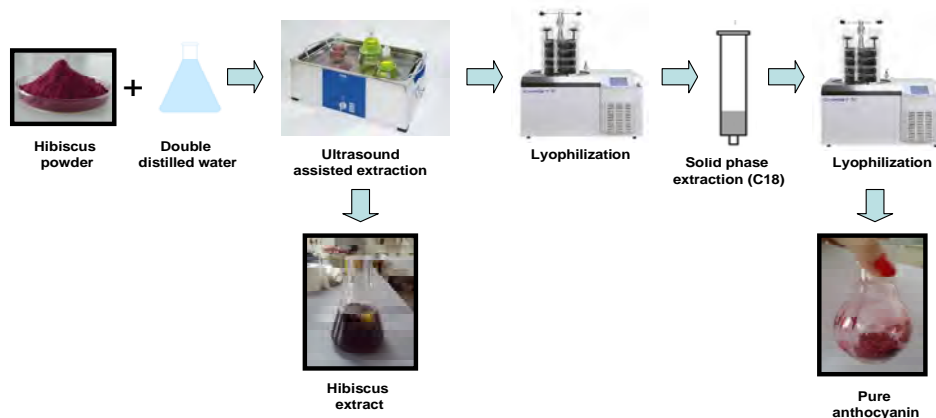


Figure 7. Schematic flowchart of anthocyanin extraction and separation from Hibiscus petals

The purified anthocyanin resulted from the above presented method will be denoted: AEH.

Preparation of berry extract with AOX effect by ultrasound-assisted extraction method

Fruits used in this method were bio-products deriving from a natural environment (Satu-Mare and Sălaj counties, Romania); during the ripening process, they were not treated with herbicides, nor insecticides, and were not contaminated with any pollutant. The following berries were used in this study: blueberry (*Vaccinium spp.*), hawthorn (*C. pinnatifida*), blackthorn (*Prunus spinosa L.*), and blackcurrant (*Ribes nigrum L.*). An amount of 0.5 g smashed berries was mixed with 30 ml of double distilled water in an Erlenmeyer flask. The flask was put in ultrasonic bath for 30 minutes at room temperature. The resulted solution was filtered by a vacuum filter. The filtrate containing anthocyanins and other compounds with possible AOX effect was kept in the refrigerator for 12 hours; after that the water excess was eliminated using a freeze-dryer.

The resulted extract contains different types of anthocyanins characteristic for each type of berry, other types of polyphenols and carbohydrates, and it will be hereinafter referred to as berry AOX mixture. The exact amount of extract yield from different types of berries is summarized in Table 6.

Table 6. Extracted amount of anthocyanins and polysaccharides (g) from different types of berries.

Berries	Extracted amount of anthocyanins and polysaccharides (g)/ 0.5 g smashed berries
Blueberry	0.374
Blackcurrant	0.357
Hawthorn	0.335
Blackthorn	0.257

Antioxidant effect measurements of the plant extract

In order to compare the antioxidant activity of the extract of berries and hibiscus, and that of pure anthocyanin separated from hibiscus, the BR analytical method was used. The measurements were performed in a 20 ml double-walled glass batch reactor connected to a FALC FA 90 thermostat (accuracy $\pm 0.1^\circ\text{C}$) in order to maintain a constant 20°C temperature. A FALC 60 magnetic stirrer at a constant stirring rate provided continuous stirring. Oscillations were monitored with a double-junction saturated calomel electrode (SCE) as a reference electrode, and a Pt electrode. They were connected to a computer through a PCI 6036 E data-acquisition interface. The oscillations were recorded through the LabView data-acquisition program and were processed by the means of Origin 9.0 program. Stock solutions of malonic acid (MA) (Aldrich, reagent grade, >99%), manganese (II) sulfate monohydrate (Reactivul, reagent grade, >99%), and potassium iodate (Merck, reagent grade, >99%) were made without further purification of the reagents using double-distilled water. H_2SO_4 (Merck, 96%) and H_2O_2 (Merck, 30%) were of analytical grade. Hydrogen-peroxide was standardized by permanganometric analysis. The BR mixtures were obtained by mixing the appropriate amounts of stock solutions in a way that finally resulted in the initial composition $[\text{KIO}_3] = 0.0268 \text{ M}$, $[\text{H}_2\text{SO}_4] = 0.0716 \text{ M}$, $[\text{MA}] = 0.04 \text{ M}$, $[\text{MnSO}_4] = 0.004 \text{ M}$, $[\text{H}_2\text{O}_2] = 0.52 \text{ M}$. The order of mixing was: malonic acid, MnSO_4 , H_2SO_4 , KIO_3 , and H_2O_2 . Oscillations start after the addition of the H_2O_2 . After the third oscillation 0.5 ml diluted raw juice was added to the reactor by using a micropipette.

Preparation of silica-substituted hydroxyapatite (HAP-Si)

HAP-Si was prepared by precipitation method, as described in previous studies [31, 32], under controlled conditions. The following materials were used: calcium nitrate tetrahydrate, diammonium phosphate, 25% ammonia solution (Alfa Aesar), and sodium-silicate. The resulted material (HAP-Si with 10 wt% Si) had 87 m²/g specific surface. The materials were not heat-treated, because based on previous studies [31], calcined materials were known to have lower retaining capacity.

Adsorption measurements

The adsorption process was monitored by a Jasco V650 spectrophotometer. In order to calculate the concentration of the extract, different dilutions of the extract were prepared (from a stock solution of 3 mg/l) and the absorbance at specific wavelength ($\lambda = 535$ nm) were plotted against the concentration of the extract. The adsorption measurements were carried out in thermostatic conditions (Falco FA90 thermostat), as follows: 0.05 g HAP-Si material was added to a 10 ml of berry solution with a concentration of 3 g/l (0.03 g extract + 10 ml water). The adsorption process was carried out in a brown beaker in order to avoid the degradation of anthocyanins caused by light. After 24 hours, the solution was centrifuged, separating the solid and liquid phase. The concentration was measured from the remaining solution using the UV-VIS spectrophotometer (V 530-Jasco) and then the adsorbed amount was calculated from the remaining anthocyanins in the solution. From this data, the adsorption capacity and adsorption rate were calculated, with the results presented in Table 4.

Adsorption capacity q_t (mg/g) and adsorption efficiency η (%) were calculated with equations (1) and (2), using the following formula:

$$q_t = \frac{m_{\text{adsorbed}}}{m_{\text{adsorbent}}} \quad (1)$$

$$\eta = \frac{c_i - c_f}{c_i} \cdot 100 = \frac{c_{\text{ads}}}{c_i} \cdot 100 \quad (2)$$

where: m_{adsorbed} – adsorbed substance quantity (g)
 $m_{\text{adsorbent}}$ – adsorbent material quantity (g)
 c_i – adsorbed substance initial concentration (g/L)
 c_f – adsorbed substance final concentration (g/L)
 c_{ads} – adsorbed substance concentration (g/L)

REFERENCES

1. J.A. Gomez del R yo, P.J. Morando, D.S. Cicerone, *Journal of Environmental Management*, **2004**, 71, 169.
2. H.Y. Xu, L. Yang, P. Wang, Y. Liu, M.S. Peng, *Journal of Environmental Management*, **2008**, 86, 319.
3. F. Fernane, M.O. Mecherri, P. Sharrock, M. Hadioui, H. Lounici, M. Fedoroff, *Materials Characterization*, **2008**, 59, 554.
4. H. Shi, H. Zhong, Y. Liu, J.Y. Deng, *Acta Geologica Sinica -English Edition*, **2007**, 81, 517.
5. E.S. Bogy , R. Barab s, L. Bizo, V. R. Dejeu, Proceedings of the 11th ECERS Conference, Krakow, **2009**, 1109.
6. L.G. Ranilla, Y.-I. Kwon, E. Apostolidis, K. Shetty, *Bioresource Technology*, **2010**, 101, 4676.
7. R. Nowak, M. Olech, N. Nowacka, "Polyphenols in Human Health and Disease", first ed., Academic Press, Elsevier, **2014**, chapter 9.
8. A.J. Gomes Castro, L.S.E.P. Will Castro, M.S. Nascimento Santos, M.G.C. Faustino, T.S. Pinheiro, C.M.P. Guerra Dore, I.G. Baseia, E. Lisboa Leite, *Biomedicine & Preventive Nutrition*, **2014**, 4, 121.
9. L.-L. Huang, C. Pan, L. Wang, L. Ding, K. Guo, H.-Z. Wang, A.-M Xu, S. Gao, *The Journal of Nutritional Biochemistry*, **2015**, 26, 841.
10. R. Fu, Y. Zhang, Y. Guo, T. Peng, F. Chen, *Journal of Functional Foods*, **2016**, 22, 73.
11. V.M. Navarro Garcia, G. Rojas, L.G. Zepeda, M. Aviles, M. Fuentes, A. Herrera, E. Jim nez, *Pharmaceutical Biology*, **2006**, 44, 297.
12. C. Zhang, Z. Gao, C. Hu, , J. Zhang, , X. Sun, C. Ronga, L. Jia, *International Journal of Biological Macromolecules*, **2017**, 95, 778.
13. L. Bravo, *Nutrition Reviews*, **1998**, 56, 317.
14. Y. Cai, Q. Luo, M. Sun, H. Corke, *Life Sciences*, **2004**, 74, 2157.
15. Z.L. Ke, Y. Pan, X.D. Xu, C. Nie, Z.Q. Zhou, *Journal of Food and Nutrition Research*, **2015**, 3, 341.
16. P. Rajendran, N. Nandakumar, T. Rengarajan, R. Palaniswami, E.N. Gnanadhas, U. Lakshminarasaiah, J. Gopas, I. Nishigaki, *Clinica Chimica Acta*, **2014**, 436, 332.
17. J. Yu, L. Wang, R.L. Walzem, E.G. Miller, L.M. Pike, B.S. Patil, *Journal of Agricultural and Food Chemistry*, **2005**, 53, 2009.
18. C. Grajeda-Iglesias, E. Salas, N. Barouh, B. Bar a, A. Panya, M.C. Figueroa-Espinoza, *Food Chemistry*, **2016**, 194, 749.
19. K.M. Schaich, X. Tian, J. Xie, *Journal of Functional Foods*, **2015**, 14, 111.
20. B. Du, B. Xu, *Bioactive Carbohydrates and Dietary Fibre*, **2014**, 3(1), 11.
21. N. Muntean, G. Szab , M. Wittmann, T. Lawson, J. F l p, Z. Noszticzius, L. Onel, *The Journal of Physical Chemistry A*, **2009**, 113, 9102.
22. R. Cervellati, K. H ner, S.D. Furrow, D. Stanley, C. Neddens, S. Costa, *Helvetica Chimica Acta*, **2001**, 84, 3533.

23. R. Cervellati, E. Greco, *Helvetica Chimica Acta*, **2016**, 99, 41.
24. N. Muntean, G. Szabó, *Studia UBB Chemia*, **2013**, LVII, 2, 175.
25. N. Muntean, G. Szabó, *Studia UBB Chemia*, **2015**, LX, 3, 273.
26. M. Li, G. Hu, Y. Chen, *Food Chemistry*, **2016**, 197, 987.
27. D. Skroza, I. Generalić Mekinić, S. Svilović, V. Šimat, V. Katalinić, *Journal of Food Composition and Analysis*, **2015**, 38, 13.
28. T. Kokubo, H. Takadama, *Biomaterials*, **2006**, 27, 2907.
29. T. Kokubo, S. Ito, M. Shigematsu, S. Sanka, T. Yamamuro, *Journal of Materials Science*, **1987**, 22, 4067
30. J. Oszmianski, C.Y. Lee, *American Journal of Enology and Viticulture*, **1990**, 41, 204.
31. E.S. Bogya, R. Barabás, V.R. Dejeu, Al. Csavdari, I. Bâldea, *Chemical Papers*, **2009**, 63, 568.
32. Al.-C. Dancu, R. Barabás, E.S. Bogya, *Central European Journal of Chemistry*, **2011**, 9, 660.

BEHAVIOR OF MULTISUBSTITUTED HYDROXYAPATITES IN WATER AND SIMULATED BODY FLUID

OANA CADAR^a, REKA BALINT^b, GHEORGHE TOMOAI^{c,d},
DIANA FLOREA^{b,e}, IOAN PETEAN^b, AURORA MOCANU^b,
OSI HOROVITZ^b, MARIA TOMOAI-COTISEL^{b,d*}

ABSTRACT. Nanostructured hydroxyapatite (HAP) and three multiple substituted HAPs, containing Mg, Zn, Sr and Si were synthesized by a wet precipitation method. The presence of the HAP lattice as unique crystalline phase was established by XRD and by FTIR spectroscopy. The chemical composition was confirmed by SEM-EDX. The TEM, SEM and AFM imaging showed the morphology of these biomaterials. The elements release in water and in simulated body fluid (SBF) was monitored in time from 1 to 90 days, by using inductively coupled plasma optical emission spectrometry (ICP-OES). The results are important for the future use of these hydroxyapatite biomaterials, as bone substitutes or coatings on metallic implants, able to release essential physiological elements, both in vitro and in vivo, with great impact in orthopedics and dentistry.

Keywords: multisubstituted hydroxyapatites, magnesium, zinc, strontium, silicon, ions release, water, SBF

INTRODUCTION

The increasing application of biomaterials based on synthetic hydroxyapatites (HAPs) as bone substitutes imposes the preparation of

^a INCDO INOE 2000, Research Institute for Analytical Instrumentation, 67 Donath Str., RO-400293, Cluj-Napoca, Romania

^b Babeş-Bolyai University, Faculty of Chemistry and Chemical Engineering, Department of Chemical Engineering, 11 Arany J. Str., RO-400028, Cluj-Napoca, Romania

^c Iuliu Hațieganu University of Medicine and Pharmacy, Orthopedics and Traumatology Department, 47 Mosoiu T. Str., RO-400132 Cluj-Napoca, Romania

^d Academy of Romanian Scientists, 54 Splaiul Independentei, RO-050094 Bucharest, Romania

^e Iuliu Hațieganu University of Medicine and Pharmacy, Faculty of Dentistry, 8 Babeş V. Str., Cluj-Napoca, 400012, Romania

*Corresponding author: mcotisel@chem.ubbcluj.ro

HAPs with a composition which imitates that of the mineral phase of natural bone [1-3]. Along with calcium and phosphorus, a series of other elements are important in the biological function of the bone

Magnesium is found in bones and teeth. It is implied in bone growth and remodelling by the activation of osteoblast cells [4], while its deficit is related to osteoporosis. *Zinc* inhibits the osteoclasts [5] and increases the response of osteoblasts [6]; anti-inflammatory [7] and antimicrobial effects [8] of HAP with Zn were also reported. *Strontium* is known to regulate bone turnover by increasing the activity of osteoblasts [9] and diminishing bone resorption [9] acting on the osteoclasts [10]. Strontium ranelate is increasingly used in the treatment of osteoporosis [11] *Silicon* is also implied in the bioactivity of osteoblasts [12,13].

Strontium can substitute calcium in HAP, $\text{Ca}_{10}(\text{PO}_4)_6(\text{OH})_2$ in any proportion, even up to 100% [14]. The substitution of Mg^{2+} for Ca^{2+} is more problematic, since the ionic radius of Mg^{2+} is much lower than that of Ca^{2+} , and the HAP lattice is distorted. There are contradictory assumptions about the limit of substitution of Ca by Mg. According to many authors, this limit is 2.46 wt% Mg (10 mol% of Ca substituted by Mg) [15-18], The Mg in excess would be located in the amorphous phase and/or on the crystallite surface, while for higher Mg content a mixture of phases is obtained [19]. For zinc substituted HAPs, the limit of substitution is considered to be 12.4 wt% Zn (20 mol% of Ca substituted by Zn) [20, 21]. As for silicon, the estimated theoretical limit of phosphorus substitution, with conservation of the HAP lattice, would be 5.8 wt% Si. But experimentally lower limits were found, from 5 down to 3 wt% Si [e.g. 22, 23].

In the present investigation, multiple substituted HAPs containing the above mentioned elements, were prepared and characterized, and the release of their elements in water, respectively their release and uptake in simulated body fluid (SBF) was studied

RESULTS AND DISCUSSION

Pure hydroxyapatite (HAP), a complex triple substituted hydroxyapatite, with Mg, Zn and Si (HAPc), and two tetrasubstituted complex hydroxyapatites, containing Mg, Zn, Si and Sr were prepared. Their compositions are given in Table 1. The theoretical formula in the table were calculated assuming that Mg^{2+} , Zn^{2+} and Sr^{2+} ions partially substitute for Ca^{2+} ions in the HAP lattice, while Si, as silicate SiO_4^{4-} ions substitutes some of the phosphate, PO_4^{3-} ions, with a corresponding diminution of the number of OH^- ions, in order to maintain the electroneutrality of the lattice, according to the general formula: $\text{Ca}_{10-x-y-z}\text{Mg}_x\text{Zn}_y\text{Sr}_z(\text{PO}_4)_{6-u}(\text{SiO}_4)_u$.

Table 1. Composition of HAP and complex HAPs

Name	Composition (wt%)						Theoretical formula
	Ca	P	Mg	Zn	Sr	Si	
HAP	39.89	18.50	0	0	0	0	$\text{Ca}_{10}(\text{PO}_4)_6(\text{OH})_2$
HAPc	37.71	18.47	1.5	0.2	0	0.2	$\text{Ca}_{9.36}\text{Mg}_{0.61}\text{Zn}_{0.03}(\text{PO}_4)_{5.93}(\text{SiO}_4)_{0.07}(\text{OH})_{1.93}$
HAPc-Sr5	34.34	17.97	1.5	0.2	5	0.2	$\text{Ca}_{8.76}\text{Mg}_{0.63}\text{Zn}_{0.03}\text{Sr}_{0.58}(\text{PO}_4)_{5.93}(\text{SiO}_4)_{0.07}(\text{OH})_{1.93}$
HAPc-Sr10	30.98	17.46	1.5	0.2	10	0.2	$\text{Ca}_{8.12}\text{Mg}_{0.65}\text{Zn}_{0.03}\text{Sr}_{1.20}(\text{PO}_4)_{5.93}(\text{SiO}_4)_{0.07}(\text{OH})_{1.93}$

Structural and morphological characterization

The HAP structure, as unique phase present in all samples, was confirmed by XRD investigations. As an example, the XRD pattern for HAPc-Sr5 is compared in Fig. 1 with the powder diffraction file (PDF) 74-056 for pure HAP. The mean size of crystallites in the samples is about 40 nm and the degree of crystallinity 40-50%, the highest for pure HAP, the lowest for HAPc.

The FTIR spectrum is also that characteristic for hydroxyapatites, with the absorption bands corresponding to the vibrations of P-O bonds in PO₄ and of the structural O-H group (Fig. 2 for the example of HAPc-Sr10). With increasing Sr content, the intensity of the OH bands decreases, and in the spectrum of HAPc-Sr10, the libration band at about 634 cm⁻¹ appears only as a shoulder (Fig. 2b).

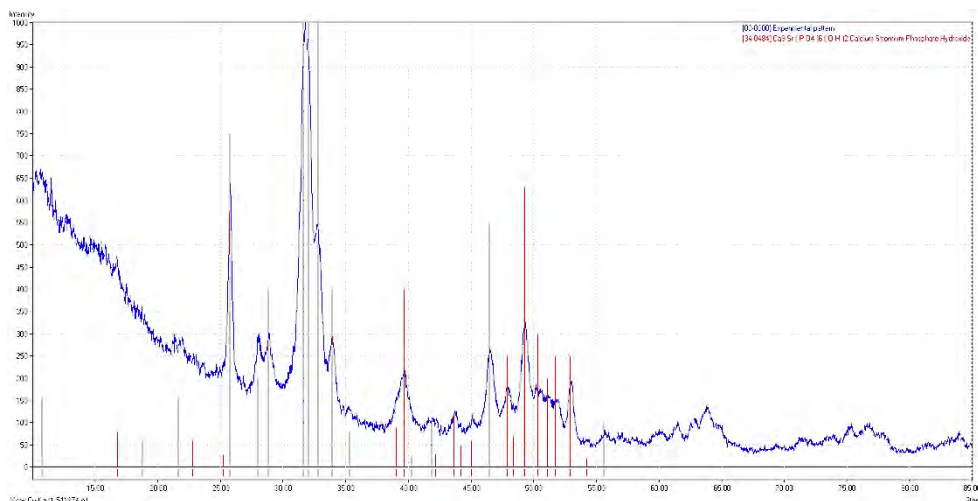


Figure 1. XRD patterns for HAPc-Sr5, compared with PDF 74-0566 for hydroxyapatite

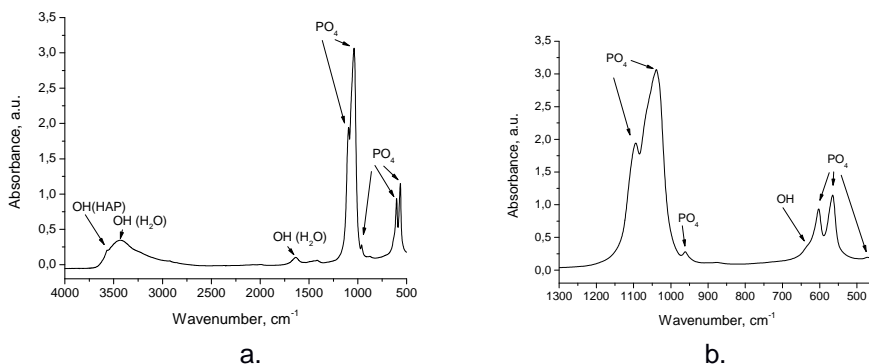


Figure 2. FTIR spectrum for HAPc-Sr10 (a), and detail (b).

The TEM (Fig. 3) and SEM (Fig.4a) images present the morphology of HAP particles. In the EDX spectrum of HAPc-Sr10 (Fig. 4b), the peaks for Ca, P, Mg, Zn, Sr and Si are all visible, along with peaks of gold, which was used to coat the hydroxyapatite particles for SEM imaging.

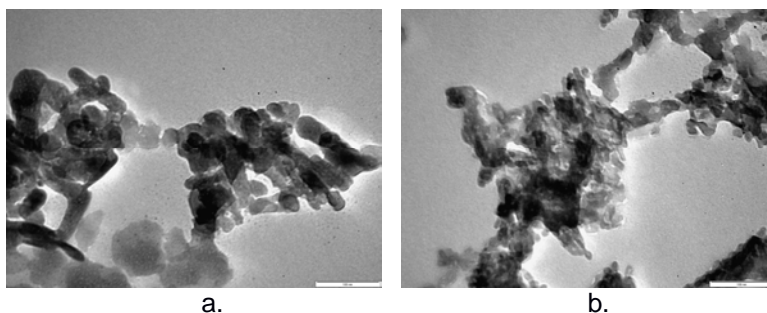


Figure 3. TEM images of HAP (a) and HAPc-Sr10 (b). The bars in the images are 100 nm.

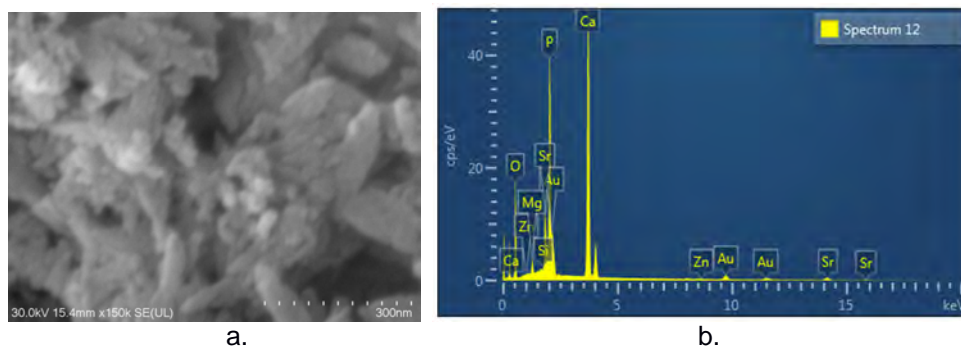


Figure 4. SEM image (a) and EDX spectrum (b) of HAPc-Sr10; the bar in image (a) is 300 nm.

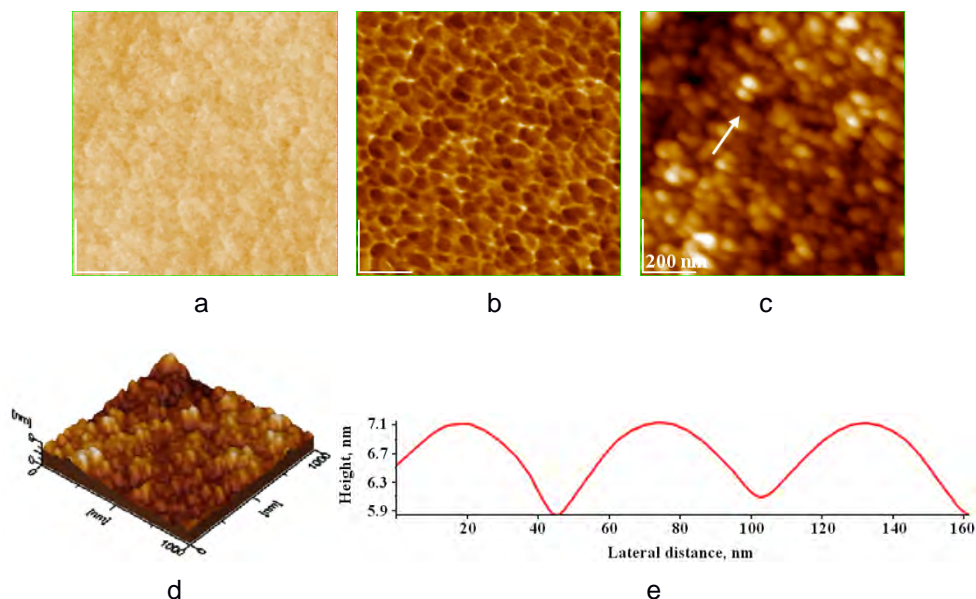


Figure 5. AFM images: 2D topography (a), phase (b), amplitude (c), 3D topography (d), cross section profile (e) for lyophilized HAPc-Sr5 powder, calcined at 300 °C, for 1h.

AFM images of lyophilized HAPc-Sr5 powders, calcined at 300 °C for 1h, as self-assembled layer on glass are shown in Fig. 5. As remarked in 2D topography (Fig. 5a), phase image (Fig. 5b), amplitude image (Fig. 5c) and 3D-topography (Fig. 5d), the shape of particles is almost spherical with an average diameter of 38 ± 3 nm, also visualized in cross profile (Fig. 5e).

The HAPc-Sr5 layer shows a rather low surface roughness, expressed as root mean square, RMS of 1.23 nm given on scanned area, and 0.37 nm on cross profile.

AFM images displayed, for all calcined lyophilized powders, the average size of particles in the nanoscale range, showing that these biomaterials are formed from nanoparticles in very good agreement with TEM and SEM data.

Behavior in water

The content of the elements (Ca, P, Mg, Sr, Si) which were released from the solid samples immersed in ultrapure water for 1 day to 90 days is represented in Fig. 6. The Zn content in the aqueous phase was below the limit of detection for all the samples.

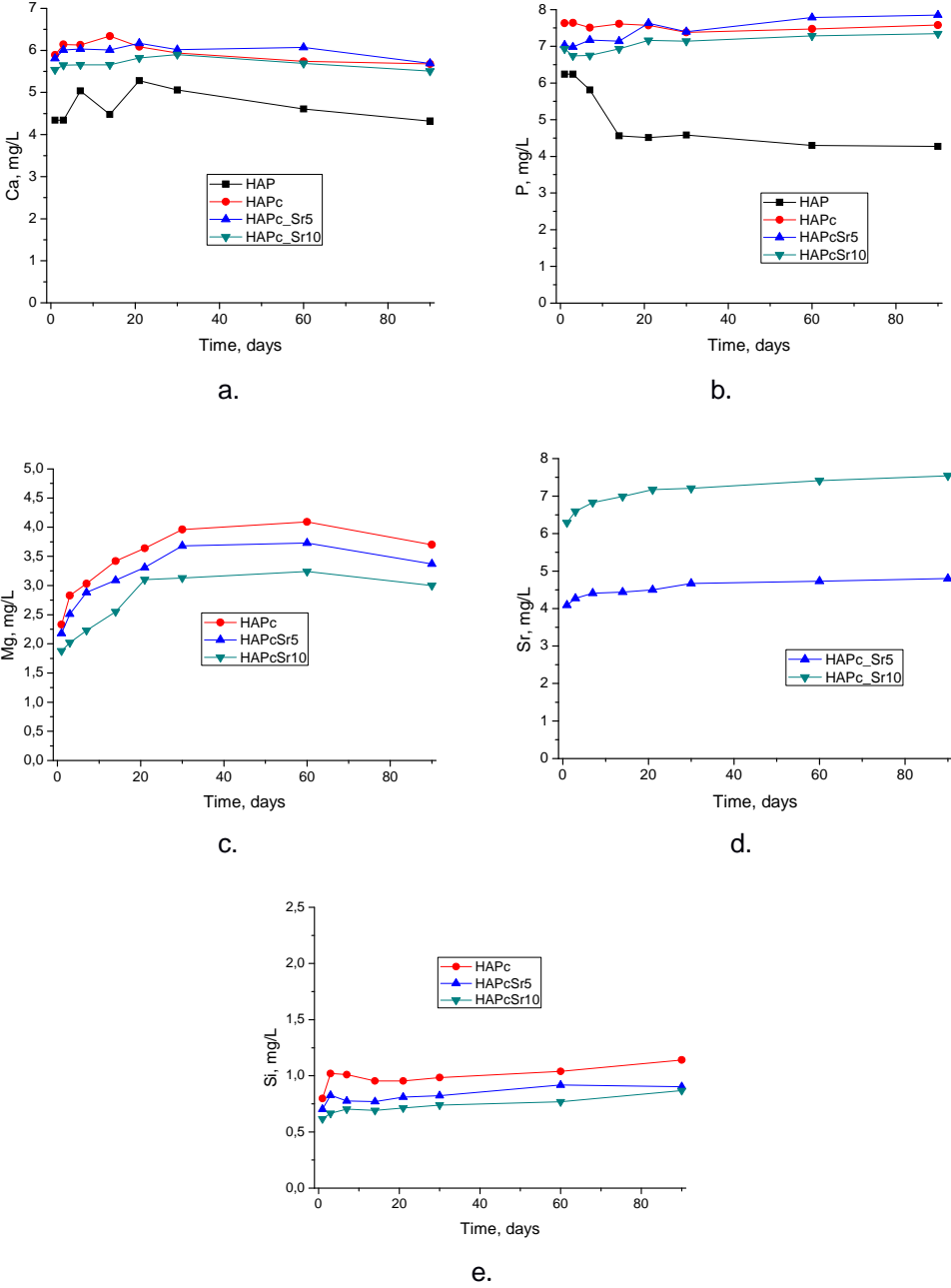


Figure 6. Calcium (a), phosphorus (b), magnesium (c), strontium (d), and silicon (e) release in water after immersion of HAPs samples for 1 – 90 days.

The calcium content in solution (Fig. 6a) is low, because of the little solubility of HAP in water; it is practically constant in time, and so after the 1st day the limit of solubility seems to be attained. For the substituted HAPs, the amount of Ca released is higher than from pure HAP, and very similar for all the complex HAPs.

The image is quite similar for P release in water (Fig. 6b), but the difference between substituted HAPs and pure HAP is larger (except for the first 3 days). The P/Ca ratio in solution is higher than in the solid samples, which points out an incongruent dissolution process [24, 25].

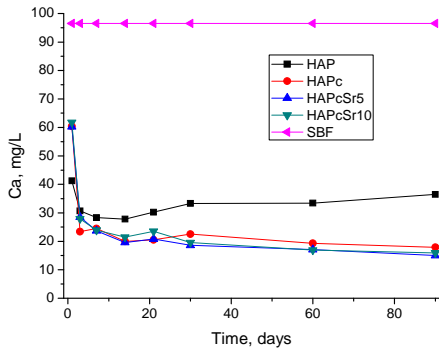
The Mg release (Fig. 6c) is increasing in time during the first 3-4 weeks, and then remains almost constant. The amount of Mg passed in the aqueous phase is disproportionately high as compared with its content in the solid samples. It is lower for the HAPc-Sr samples, denoting a stabilization of the complex HAP by the simultaneous presence of Mg and Sr [26].

The Sr release (Fig. 6d) is slowly increasing in time, and it is larger for a higher Sr content in the solid sample. Other investigations also showed that the solubility of Sr substituted HAPs increases continuously with increasing strontium content [27].

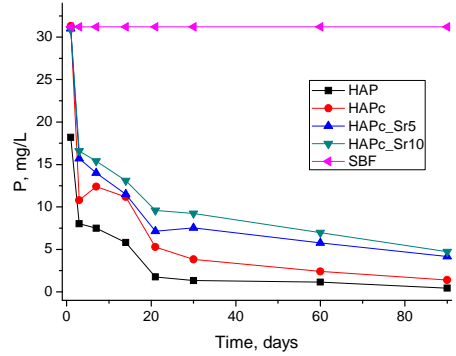
The Si content in the solution (Fig. 6e) is nearly constant in time after the first day; it is highest for HAPc and decreases with increasing Sr content. It is also higher than expected from the Si content in the samples.

Behavior in SBF is illustrated in Figures 7a-e

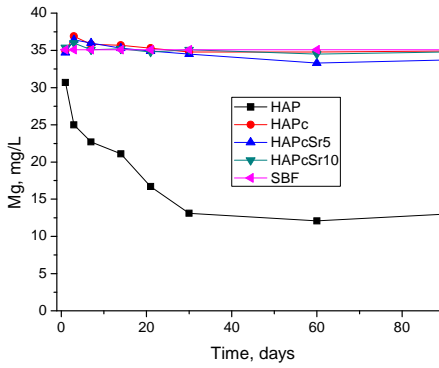
Ca (Fig. 7a) is initially removed from the SBF solution by the HAP and substituted HAP samples, but after the first days an equilibrium is established between solid HAP and solution. Two opposite processes determine the Ca²⁺ concentration in the solution, namely the uptake of Ca²⁺ ions to form a newly grown apatite lattice and the release of these ions. For complex HAPs the Ca content in the solution is lower than for simple HAP and continued to diminish slowly till the end of the testing period. This could be explained by an ionic exchange with the solution Ca²⁺ ions from SBF, which substitute Mg²⁺ and Sr²⁺ ions from the lattice.



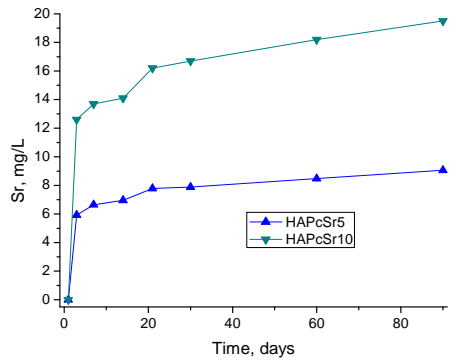
a.



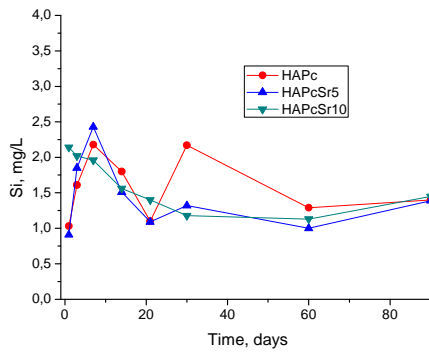
b.



c.



d.



e.

Figure 7. Calcium (a), phosphorus (b), magnesium (c), strontium (d), and silicon (e) contents in SBF after immersion of HAPs samples for 1 day to 90 days.

The phosphate content of the SBF (Fig. 7b) is almost totally used in the formation of new HAP lattice. For the substituted HAPs there is also a continuous diminution of the P content in the solution, but it remains above that in presence of pure HAP, probably due to their increased solubility, with phosphate ions release

While Mg content in SBF (Fig. 7c) decreased in presence of HAP to a constant value after a month, for substituted HAPs the Mg content in the solution remains nearly constant. There is an uptake of Mg^{2+} ions to the HAP lattice, but for the complex HAPs with 1.5 wt% Mg in the samples, this process is counterbalance by Mg release from the lattice and/or ionic exchange with the Ca^{2+} ions of SBF [28].

Sr (Fig. 7d) and Si (Fig. 7e) release in SBF present a similar trend as in water, but they are intensified, probably due to the ionic exchange with calcium, respectively phosphate ions from SBF. The increased release of Sr from HAPs in SBF was also observed in other samples [29].

CONCLUSIONS

The introduction of essential elements with important biological effects in nanostructured hydroxyapatite was proved by the physico-chemical investigations used in the present study. The multisubstituted HAPs presented an average degree of crystallinity and nanoparticle size pertaining to the nanoscale. The presence of Mg and Zn has a destabilizing effect on the HAP lattice, while the addition of Sr diminishes this effect. The release of their component elements was examined in aqueous solutions, as a model for biological liquids. The increased Sr concentration within HAP structure has significantly influenced the Sr release in both media: water and simulated body fluid. Notably, a different Ca, Mg and P profile is determined in both media, and the formation of a new biomimetic hydroxyapatite is apparently promoted in SBF. The long time release observed for the valuable physiological elements contained in multisubstituted hydroxyapatites evidences a promising future of these biomaterials for biomedical purposes.

EXPERIMENTAL SECTION

Samples preparation: A solution containing the cations, and one containing the anions were prepared. The 0.25 M cations solution contained Ca^{2+} , and additionally for the complex HAPs: Mg^{2+} , Zn^{2+} , and Sr^{2+} , according to the composition to be obtained. It was prepared by dissolving in ultrapure

water the nitrates: $\text{Ca}(\text{NO}_3)_2 \cdot 4\text{H}_2\text{O}$ (Merck), $\text{Mg}(\text{NO}_3)_2 \cdot 6\text{H}_2\text{O}$, $\text{Zn}(\text{NO}_3)_2 \cdot 6\text{H}_2\text{O}$ and $\text{Sr}(\text{NO}_3)_2$ (all from Sigma-Aldrich). The 0.15 M anions solution contained PO_4^{3-} , and (for the complex HAPs) SiO_4^{4-} ; it was obtained from diammonium hydrogen phosphate, $(\text{NH}_4)_2\text{HPO}_4$ (Sigma-Aldrich) and tetraethyl orthosilicate, TEOS, $\text{Si}(\text{OC}_2\text{H}_5)_4$ (98%, ALFA AESAR, Germany) in the adequate ratio. The working pH was 11.5, fixed by adding a 25% ammonia solution (Merck).

The solutions were quickly mixed (equal volumes) at room temperature 22°C, using a peristaltic pump and an impact reactor type “Y” for the two liquid flows [12, 14, 21, 30-34]. The obtained suspension was matured in two stages: at 22°C for 24 h, and at 70°C, for other 24 h, under intermittent stirring. The final precipitate was filtered and washed repeatedly with ultrapure water until nitrate free, at room temperature. It was dried by lyophilisation, and calcined at 300°C for one hour, and then disintegrated in a ball mill, to obtain a fine powder.

Samples characterization: X-Ray Diffraction (XRD) investigations were carried out using a DRON-3 diffractometer, in Bragg-Brentano geometry, equipped with a X-ray tube with cobalt K_α radiation, wavelength 1.79026 Å, 25 kV/20 mA. FTIR spectra were measured on KBr pellets, containing the sample powders with a FTIR spectrometer JASCO 6100 in the 4000-400 cm^{-1} range of wave numbers, with a 4 cm^{-1} resolution.

The HAPs aqueous dispersions needed for TEM and AFM imaging were homogenized *using* a high-intensity ultrasonic processor Sonics Vibra-Cell, model VCX 750, for 5 minutes, at room temperature, 22 °C. Transmission electron microscope: TEM JEOL–JEM 1010 was used to determine the shape and the size of the phosphates nanoparticles. The samples were dispersed in deionized water, and the resulted colloidal dispersion was adsorbed on the TEM grids. For the examination with the scanning electron microscope, SEM Hitachi SU-8230, operated at 30 kV was used. It is equipped with Oxford energy-dispersive X-ray spectrometer (EDS) for elemental analysis (EDX spectra). SEM grids are made of Cu, covered by a carbon layer of 10 to 20 nm thickness. SEM samples were prepared by deposition of HAP samples, as powder, in thin layers on SEM grids The samples were gold sputtered in the AGAR, Auto Sputter Coater.

Atomic force microscopy (AFM) images were obtained using the AFM JEOL 4210 equipment, operated in tapping mode, using standard cantilevers with silicon nitride tips, with resonant frequency in the range of 200-300 kHz and spring constant of 17.5 N/m [35-45]. The particles were adsorbed from their aqueous dispersion on optically polished glass support.

Elements release tests: The Ca, P, Si and Mg amounts were measured in the solutions after immersion of 0.15 g of each sample in 15 mL ultrapure water, respectively Kokubo simulated body fluid (SBF) and incubation at 37°C in separated closed flasks for each sample/day. SBF solution as

prepared according to *Kokubo's SBF* solution [46] having the composition (mmol/dm³): Na⁺ (142.0); K⁺ (5.0); Mg²⁺ (1.5); Ca²⁺ (2.5); Cl⁻ (147.8); HCO₃⁻ (4.2); HPO₄²⁻ (1.0); SO₄²⁻ (0.5), and buffered at the physiologic pH 7.40 at 37 °C, with tris(hydroxymethyl)amino methane and hydrochloric acid. After 1, 3, 7, 14, 21, 30, 60, and 90 days, the supernatant (after centrifugation) was filtered and Ca, Mg, P, Sr, Zn and Si contents in the filtrate were determined using an inductively coupled plasma optical emission spectrometer (ICP-OES) OPTIMA 3500 DV (Perkin-Elmer, USA). For calibration, multi-element standard solutions were prepared by the dilution of stock multi-element 1000 mg/L solutions Merck IV. All the experiments were performed in triplicate and the results were calculated as average values. The elements content in SBF solution without samples of hydroxyapatites was also measured in the same days, and the average value was calculated.

ACKNOWLEDGMENTS

Authors acknowledge the financial support from the Executive Agency for Higher Education, Research, Development and Innovation Funding (UEFISCDI) through grants no. 241 and no. 83.

REFERENCES

1. D. Tadic, M. Eppele, *Biomaterials*, (2004, 25, 987.
2. M. Figueiredo, J. Henriques, G. Martins, F. Guerra, F. Judas, H. Figueiredo, *Journal of Biomedical Materials Research*, 2009, 92B, 409.
3. M. Figueiredo, A. Fernando, G. Martins, J. Freitas, F. Judas, H. Figueiredo, *Ceramics International*, 2010, 36, 2383.
4. A. Bigi, E. Foresti, R. Gregorini, A. Ripamonti, N. Roveri, J.S. Shah, *Calcified Tissue International*, 1992, 50, 439.
5. B.S. Moonga, D.W. Dempster, *Journal of Bone and Mineral Research*, 1995, 10, 453.
6. T.J. Webster, E.A. Massa-Schlueter, J.L. Smith, E.B. Slamovich, *Biomaterials*, 2004, 25, 2111.
7. F. Velard, D. Laurent-Maquin, J. Braux, C. Guillaume, S. Bouthors, E. Jallot, J.M. Nedelec, A. Belaouaj, P. Laquerriere, *Biomaterials*, 2010, 31, 2001.
8. V. Stanic, S. Dimitrijevic, J. Antic-Stankovic, M. Mitric, B. Jokic, I.B. Plecas, S. Raicevic, *Applied Surface Science*, 2010, 256, 6083.
9. W. Querido, A.L. Rossi, M. Farina, *Micron*, 2016, 80, 122.

10. A.S. Hurtel-Lemaire, R. Mentaverri, A. Caudrillier, F. Cournarie, A. Wattel, S. Kamel, E.F. Terwilliger, E.M. Brown, M. Brazier, *Journal of Biological Chemistry*, **2009**, 284, 575.
11. A.L. Rossi, S. Moldovan, W. Querido, A. Rossi, J. Werckmann, O. Ersen, M. Farina, *Micron*, **2014**, 56, 29.
12. G. Tomoaia, A. Mocanu, I. Vida-Simiti, N. Jumate, L.D. Bobos, O. Soritau, M. Tomoaia-Cotisel, *Materials Science and Engineering: C*, **2014**, 37, 37.
13. A.F. Khan, M. Saleem, A. Afzal, A. Ali, A. Khan, A.R. Khan, *Materials Science and Engineering C*, **2014**, 35, 245.
14. P.T. Frangopol, A. Mocanu, V. Almasan, C. Garbo, R. Balint, G. Borodi, I. Bratu, O. Horovitz, M. Tomoaia-Cotisel, *Revue Roumaine de Chimie*, **2016**, 61, 337.
15. A. Bigi, G. Falini, E. Foresti, M. Gazzano, A. Ripmonti, N. Roveri, *Acta Crystallographica Section B*, **1996**, 52, 87.
16. S. Nsar, A. Hassine, K. Bouzouita, *Journal of Biomaterials and Nanobiotechnology*, **2013**, 4, 1.
17. I.V. Fadeev, L.I. Shvorneva, S.M. Barinov, V.P. Orlovskii, *Inorganic Materials*, **2003**, 39, 947.
18. I. Cacciotti, A. Bianco, M. Lombardi, L. Montanaro, *Journal of the European Ceramic Society*, **2009**, 29, 2969.
19. F. Ren, Y. Leng, R. Xin, X. Ge, *Acta Biomaterialia*, **2010**, 6, 2787.
20. E. Boanini, M. Gazzano, A. Bigi, *Acta Biomaterialia*, **2010**, 6, 1882.
21. C. Garbo, M. Sindilaru, A. Carlea, G. Tomoaia, V. Almasan, I. Petean, A. Mocanu, O. Horovitz, M. Tomoaia-Cotisel, *Particulate Science and Technology*, **2017**, 35, 29.
22. E.S. Thian, J. Huang, M.E. Vickers, S.M. Best, Z.H. Barber, W. Bonfield, *Journal of Materials Science*, **2006**, 41, 709.
23. S. Gomes, J.M. Nedelec, E. Jallot, D. Sheptyakov, G. Renaudin, *Crystal Growth and Design*, **2011**, 11, 4017.
24. A.N. Smith, A.M. Posner, J.P. Quirk, *Journal of Colloid and Interface Science*, **1974**, 48, 442.
25. H.W. Kaufman, I. Kleinberg, *Calcified Tissue International*, **1979**, 27, 143.
26. M.P. Moreira, G.D. de Almeida Soares, J. Dentzerc, K. Anselme, L.Á. de Sena, A. Kuznetsov, E. A. dos Santos, *Materials Science and Engineering C*, **2016**, 61, 736.
27. H.B. Pan, Z.Y. Li, W.M. Lam, J.C. Wong, B.W. Darvell, K.D.K. Luk, W.W. Lu, *Acta Biomaterialia*, **2009**, 5, 1678.
28. C. Stötzel, F.A. Müller, F. Reinert, F. Niederdraenk, J.E. Barralet, U. Gbureck, *Colloids and Surfaces B: Biointerfaces*, **2009**, 74, 91.
29. J. Beuvelot, Y. Mauras, G. Mabileau, H. Marchand-Libouban, D. Chapparda, *Digest Journal of Nanomaterials and Biostructures*, **2013**, 8, 207.
30. A. Mocanu, R. Balint, C. Garbo, L. Timis, I. Petean, O. Horovitz, M. Tomoaia-Cotisel, *Studia Universitatis Babeş-Bolyai, Chemia*, **2017**, 62(2), Tom 1, 95.
31. G. Tomoaia, A. Mocanu, L.-D. Bobos, L.-B. Pop, O. Horovitz, M. Tomoaia-Cotisel, *Studia Universitatis Babeş-Bolyai, Chemia*, **2015**, 60(3), 265-272.

32. A. Mocanu, G. Furtos, S. Răpunțean, O. Horovitz, C. Flore, C. Garbo, A. Dănișteanu, G. Răpunțean, C. Prejmerean, M. Tomoaia-Cotisel, *Applied Surface Science*, **2014**, 298, 225.
33. G. Tomoaia, O. Soritau, M. Tomoaia-Cotisel, L.-B. Pop, A. Pop, A. Mocanu, O. Horovitz, L.-D. Bobos, *Powder Technology*, **2013**, 238, 99.
34. G. Tomoaia, M. Tomoaia-Cotisel, L.B. Pop, A. Pop, O. Horovitz, A. Mocanu, N. Jumate, L.-D. Bobos, *Revue Roumaine de Chimie*, **2011**, 56, 1039.
35. A. Mocanu, R. Balint, C. Garbo, L. Timis, I. Petean, O. Horovitz, M. Tomoaia-Cotisel, *Studia Universitatis Babeș-Bolyai, Chemia*, **2017**, 62(2), Tom I, 95.
36. R.D. Pasca, G. Tomoaia, A. Mocanu, I. Petean, G.A. Paltinean, O. Soritau, M. Tomoaia-Cotisel, *Studia Universitatis Babeș-Bolyai, Chemia*, **2015**, 60(3), 257.
37. M.A. Naghiu, M. Gorea, E. Mutch, F. Kristaly, M. Tomoaia-Cotisel, *Journal of Material Science and Technology*, **2013**, 29(7), 628.
38. A. Danistean, M. Gorea, A. Avram, S. Rapuntean, G. Tomoaia, A. Mocanu, C. Garbo, O. Horovitz, M. Tomoaia-Cotisel, *Studia Universitatis Babeș-Bolyai, Chemia*, **2016**, 61 (3), 275.
39. G. Tomoaia, O. Horovitz, A. Mocanu, A. Nita, A. Avram, C.P. Racz, O. Soritau, M. Cenariu, M. Tomoaia-Cotisel, *Colloids and Surfaces B: Biointerfaces*, **2015**, 135, 726.
40. P.T. Frangopol. D.A. Cadenhead, G. Tomoaia, A. Mocanu, M. Tomoaia-Cotisel, *Revue Roumaine de Chimie*, **2015**, 60(2-3), 265.
41. G. Furtos, M.A. Naghiu, H. Declercq, M. Gorea, C. Prejmerean, O. Pana, M. Tomoaia-Cotisel, *Journal of Biomedical Materials Research Part B. Applied Biomaterials*, **2016**, 104, 1290.
42. M. Tomoaia-Cotisel, A. Mocanu, *Revista de Chimie (Bucharest)*, **2008**, 59, 1230.
43. O. Horovitz, G. Tomoaia, A. Mocanu, T. Yupsanis, M. Tomoaia-Cotisel, *Gold Bulletin*, **2007**, 40 (4), 295.
44. M. Tomoaia-Cotisel, A. Tomoaia-Cotisel, T. Yupsanis, G. Tomoaia, I. Balea, A. Mocanu, Cs. Racz, *Revue Roumaine de Chimie*, **2006**, 51 (12), 1181.
45. G. Tomoaia, A. Mocanu, L.D. Bobos, L.B. Pop, O. Horovitz, M. Tomoaia-Cotisel, *Studia Universitatis. Babeș-Bolyai, Chemia*, **2015**, 60 (3), 265.
46. T. Kokubo, H. Kushitani, S. Sakka, T. Kitsugi, T. Yamamuro, *Journal of Biomedical Materials Research*, **1990**, 24, 721.

EXPERIMENTAL STUDY OF SULFUR DIOXIDE ABSORPTION INTO CARBONATE SUSPENSIONS WITH SULFITES ADDITION

SIMION DRĂGAN^a

ABSTRACT. This paper presents the experimental results obtained by sulfur dioxide chemisorption into carbonate suspension with sulfites addition at different temperatures and concentration of the absorbent suspension. Presence of sulfites in the absorbent suspension has a positive influence on the global rate of the absorption process. The acceleration of SO₂ chemisorption process in the absorbent suspension containing MeSO₃ – MeCO₃ is determined by the higher concentration of ions in the liquid phase resulted from higher solubility of MeSO₃ comparative with MeCO₃. The addition of MeSO₃ at a concentration of 10% in the composition of the absorbent suspension determines a significant decrease of the time required for obtaining a high conversion.

Keywords: *wet desulfurization, carbonate suspension, sulfites addition.*

INTRODUCTION

The issue of environmental pollution is a consequence of industrial development. An industrial sector with a major environmental impact is the energy sector, which is a major source of pollution by combustion of fossil fuels [1-3]. Desulfurization of combustion gases is currently the subject of numerous experimental research and research projects that have proposed and developed numerous desulfurization processes: dry, semi-dry and wet [4-8].

Independent of the type of desulfurization process applied in a desulphurization plant, two main conditions are required:

^a *Babeş-Bolyai University, Faculty of Chemistry and Chemical Engineering, Department of Chemical Engineering, 11 Arany Janos str., RO-400028, Cluj-Napoca, Romania, sdragan@chem.ubbcluj.ro*

- the removal of sulfur dioxide from the waste gas with minimal investment and exploitation costs;
- the product must have storage capacity and can be reusable.

Researches in the field of combustion gases desulfurization are directed towards the development of technologies that produce sulfur compounds that can be fully utilized. A great prospect is the SO₂ absorption process into dolomite suspension thus reducing the amount of gypsum due to the fact that part of the sulfur is recovered as MgSO₄, compound with many practical uses [9].

The kinetic study of the SO₂ chemisorption process into dolomite-brucite suspensions revealed that the global process takes place according to the shrinking core model without crust or according to the unreacted core model with crust formation of the reaction products [9-10]. In the temperature range $T = 293-333\text{K}$ and the suspension concentration $C = 5-15\%$ limitative steps of the global absorption process are the diffusional processes. At low concentrations of the suspension and high temperatures, the diffusion through the liquid phase to the outer surface of the granule is the determining step. At low temperatures and high concentrations of the suspension, the limitative step is the diffusion through the crust of reaction product.

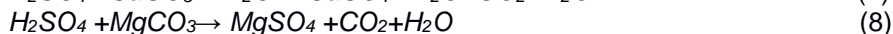
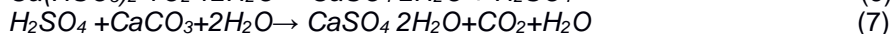
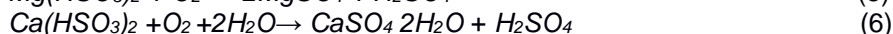
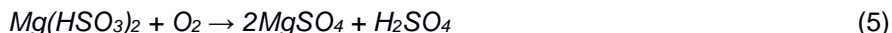
RESULTS AND DISCUSSIONS

The investigations present the influence of the suspension concentration and temperature on the global rate of the chemisorption process. Preparation of the suspension containing MeCO₃ and MeSO₃ can be achieved if the neutralization zone of the industrial absorber is comprised of two compartments:

I. Neutralization compartment - where the following reactions occur:



II. Oxidation-neutralization compartment - where the following reactions occur:



The $\text{MeSO}_3\text{-MeCO}_3$ suspension resulting from compartment I is recirculated in the absorption column and the slurry accumulated in compartment II is filtered and processed to recover CaSO_4 and MgSO_4 .

The experimental study of the absorption process showed that regardless of the temperature and concentration of the suspension there is a period at the beginning of the process where the chemisorption rate is lower. The duration of this induction period extends until the pH of the suspension decreases from $\text{pH}=6.7\text{-}7$ to $\text{pH}<5.5$. In the range of $\text{pH}=7\text{-}5.5$, thermodynamically stable are MeSO_3 neutral sulfites, which have a low solubility. When the pH of the suspension decreases to $\text{pH}<5.5$ the neutral sulfites MeSO_3 react with H_2SO_3 to form acid sulfites whose high solubility eliminates crust formation and so, the rate of chemisorption increases. This suggests the acceleration of the SO_2 chemisorption process into dolomite-brucite suspensions if the absorbent suspension also contains MeSO_3 in addition to MeCO_3 .

The intensification of the SO_2 chemisorption process in the absorbent suspension containing $\text{MeSO}_3\text{-MeCO}_3$ is determined by:

-the higher-concentration of ions HSO_3^- in the liquid phase resulting from the following reactions:



These reactions cause the increase of ion HSO_3^- diffusion to be by the liquid phase to the outer surface of the solid granule;

-the higher solubility by an order of magnitude of the CaSO_3 compared to CaCO_3 and for the MgSO_3 to 10^4 compared to the MgCO_3 [11], causing the chemisorption reactions at the outer surface of the solid granules and into volume of the solution;

- the increase of the contact surface of the reactants due to the dissolution of MgSO_3 , since the solid granules become more porous.

These were the theoretical bases that determined the SO_2 chemisorption to be performed in $\text{MeCO}_3\text{-MeSO}_3$ suspensions.

Based on the experimental results, the rate constants in the range $T = 293\text{-}333$ K and for three different concentrations of the suspension were calculated. The obtained results of the sulfur dioxide absorption into dolomite-sulfite ($\text{MeCO}_3\text{-MeSO}_3$) suspensions are presented in comparison with those obtained by absorption carried out only into dolomite (MeCO_3) suspensions.

The influence of the concentrations of $\text{MeCO}_3\text{-MeSO}_3$ suspensions on the rate of SO_2 chemisorption is shown in Figures 1-8.

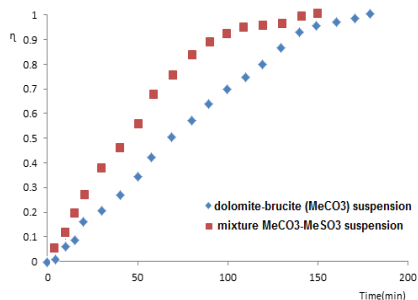


Figure 1. Absorption diagram of SO_2 into dolomite-brucite (MeCO_3) suspensions, $C_{\text{MeCO}_3} = 5\%$ and in mixture of dolomite-brucite-sulphite ($\text{MeCO}_3\text{-MeSO}_3$) with $C_{\text{MeCO}_3} = 5.54\%$, $C_{\text{CaSO}_3} = 5.62\%$, $C_{\text{MgSO}_3} = 4.33\%$, at $T = 293^\circ\text{K}$

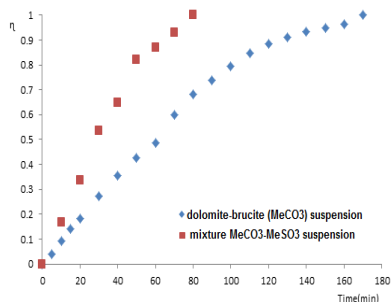


Figure 2. Absorption diagram of SO_2 into dolomite-brucite (MeCO_3) suspensions $C_{\text{MeCO}_3} = 10\%$ and in mixture of dolomite-brucite-sulphite ($\text{MeCO}_3\text{-MeSO}_3$) with $C_{\text{MeCO}_3} = 5.83\%$, $C_{\text{CaSO}_3} = 9.86\%$, $C_{\text{MgSO}_3} = 8.61\%$, at $T = 293^\circ\text{K}$

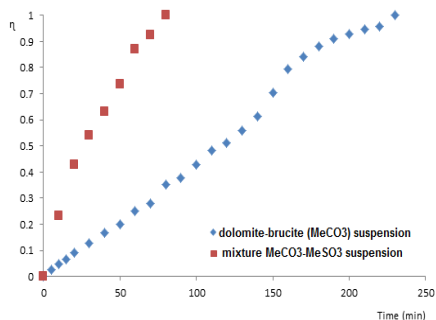


Figure 3. Absorption diagram of SO_2 into dolomite-brucite (MeCO_3) suspensions $C_{\text{MeCO}_3} = 15\%$ and in mixture of dolomite-brucite-sulphite ($\text{MeCO}_3\text{-MeSO}_3$) with $C_{\text{MeCO}_3} = 11.80\%$, $C_{\text{CaSO}_3} = 10.39\%$, $C_{\text{MgSO}_3} = 8.57\%$, at $T = 293^\circ\text{K}$

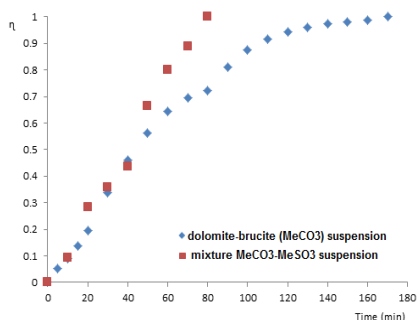


Figure 4. Absorption diagram of SO_2 into dolomite-brucite (MeCO_3) suspensions $C_{\text{MeCO}_3} = 5\%$ and in mixture of dolomite-brucite-sulphite ($\text{MeCO}_3\text{-MeSO}_3$) with $C_{\text{MeCO}_3} = 6.20\%$, $C_{\text{CaSO}_3} = 5.67\%$, $C_{\text{MgSO}_3} = 4.27\%$, at $T = 313^\circ\text{K}$

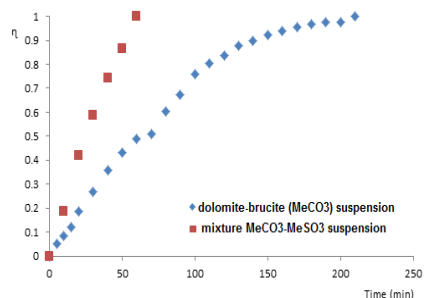


Figure 5. Absorption diagram of SO₂ into dolomite-brucite (MeCO₃) suspensions $C_{MeCO_3} = 10\%$ and in mixture of dolomite-brucite-sulphite (MeCO₃-MeSO₃) with $C_{MeCO_3} = 4.91\%$, $C_{CaSO_3} = 10.18\%$, $C_{MgSO_3} = 8.42\%$, at $T = 313^\circ K$

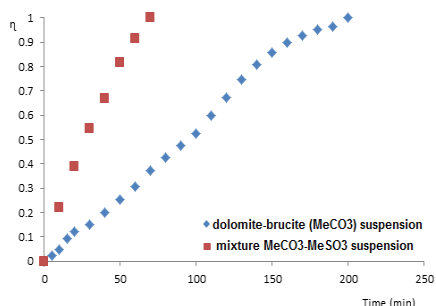


Figure 6. Absorption diagram of SO₂ into dolomite-brucite (MeCO₃) suspensions $C_{MeCO_3} = 15\%$ and in mixture of dolomite-brucite-sulphite (MeCO₃-MeSO₃) with $C_{MeCO_3} = 10.6\%$, $C_{CaSO_3} = 11.35\%$, $C_{MgSO_3} = 9.31\%$, at $T = 313^\circ K$

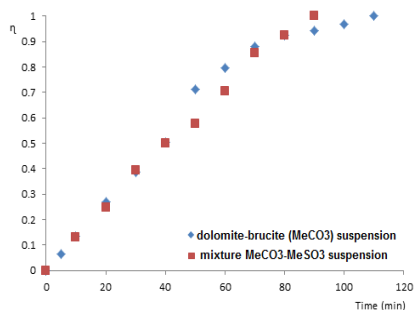


Figure 7. Absorption diagram of SO₂ into dolomite-brucite (MeCO₃) suspensions $C_{MeCO_3} = 5\%$ and in mixture of dolomite-brucite-sulphite (MeCO₃-MeSO₃) with $C_{MeCO_3} = 5.45\%$, $C_{CaSO_3} = 5.89\%$, $C_{MgSO_3} = 5.16\%$, at $T = 333^\circ K$

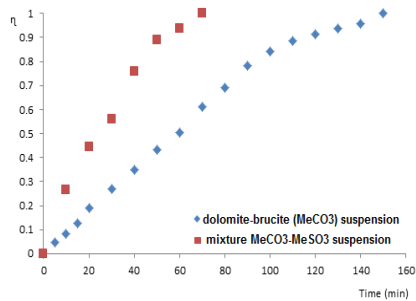


Figure 8. Absorption diagram of SO₂ into dolomite-brucite (MeCO₃) suspensions $C_{MeCO_3} = 10\%$ and in mixture of dolomite-brucite-sulphite (MeCO₃-MeSO₃) with $C_{MeCO_3} = 4.77\%$, $C_{CaSO_3} = 10.31\%$, $C_{MgSO_3} = 9.12\%$, at $T = 333^\circ K$

The analysis of the kinetic curves from figures 1-8, indicates that the process is very complex and is influenced by two important parameters: concentration and temperature. It can be seen that the chemisorption process takes place at a higher rate in (MeCO₃-MeSO₃) suspensions than in (MeCO₃) suspensions. The time corresponding at conversion $\eta \geq 0.95$ to absorption in the two types of suspension is shown in Table 1.

Table 1. Time limits required achieving conversions $\eta \geq 0.95$

Conc. Susp.	Temperature, K	Time, min	
		MeCO ₃	MeCO ₃ -MeSO ₃
5%	293	150	120
	313	120	80
	333	90	90
10%	293	135	75
	313	180	58
	333	128	60
15%	293	200	70
	313	180	62
	333	-	-

It is noted that the time required to achieve the conversions $\eta \geq 0.95$ is higher when the absorption is carried out into dolomite-brucite suspension (MeCO₃). The decrease in the time required to achieve values $\eta \geq 0.95$ in the case of the absorption of (MeCO₃-MeSO₃) suspensions is due to the high dissolution rate of the acid sulfites formed Me(HSO₃)₂. Based on the Arrhenius law, the values of the constants rate were determined. Table 2 shows the values of the rate constants for SO₂ absorption into MeCO₃ suspensions compared to values obtained when the absorption is carried out in a mixture of MeCO₃-MeSO₃ suspensions.

Table 2. The rate constants of the SO₂ chemisorption into MeCO₃ and MeCO₃-MeSO₃ suspensions

Concentration of dolomite-brucitic susp.	Temperature, K	Rate constant			
		MeCO ₃		MeCO ₃ -MeSO ₃	
		k ₁ , min ⁻¹	k ₂ , min ⁻¹	k ₁ , min ⁻¹	k ₂ , min ⁻¹
5%	293	0,0109	0,0359	0,0153	0,052
	313	0,0146	0,0388	0,016	0,055
	333	0,0166	0,0442	0,0169	0,0591
10%	293	0,0109	0,0244	0,0235	0,0512
	313	0,011	0,0315	0,0258	0,0562
	333	0,0112	0,0315	0,0283	0,0693
15%	293	0,0056	0,0278	0,0257	0,0667
	313	0,0068	0,0311	0,0267	0,0688
	333	0,0086	0,0351	-	-

It can be observed that for the concentration of the suspension 5% the rate constants have higher values at the beginning of the absorption process into mixture $\text{MeCO}_3\text{-MeSO}_3$ suspension compared to the corresponding absorption into suspension of MeCO_3 .

The high concentration of HSO_3^- in suspension determines a higher rate of the substance transformation and the transport processes. The acceleration of the absorption of SO_2 into $\text{MeCO}_3\text{-MeSO}_3$ suspension is more pronounced at concentrations of 10% and temperature of 313 K. In these conditions, the diffusional driving force and the dissolution rate of reaction product increase. The overall process is carried out according to the shrinking core model without crust formation. At the suspension concentrations greater than 10%, the saturation concentration of solution is rapidly reached, the $\text{Me}(\text{HSO}_3)_2$ formed is no longer dissolved, and so the overall rate of the process decreases.

The influence of temperature on the global absorption process is represented in Figures 9-11.

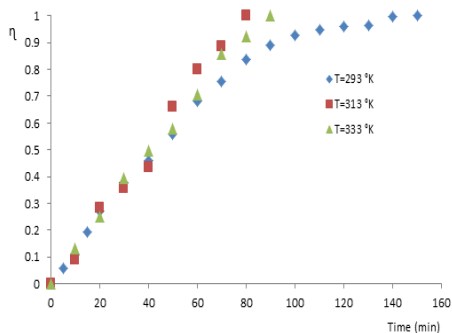


Figure 9. Influence of temperature on the SO_2 absorption into mixture of dolomite-brucite ($\text{MgSO}_3\text{-CaSO}_3$) suspensions at $C_{\text{MeCO}_3} = 5\%$

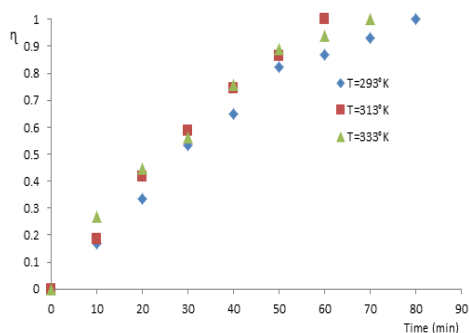


Figure 10. Influence of temperature on the SO_2 absorption into mixture of dolomite-brucite ($\text{MgSO}_3\text{-CaSO}_3$) suspensions at $C_{\text{MeCO}_3} = 10\%$

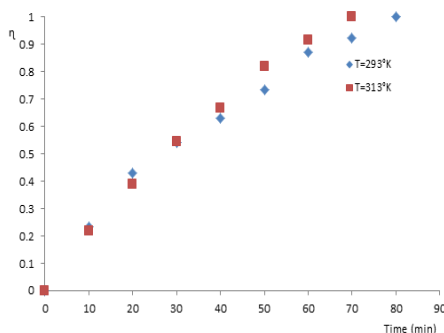


Figure 11. Influence of temperature on the SO_2 absorption into mixture of dolomite-brucite ($\text{MgSO}_3\text{-CaSO}_3$) suspensions at $C_{\text{MeCO}_3} = 15\%$

The diagrams from figures 9-11 show that for all three concentrations of the $(\text{MeCO}_3\text{-MeSO}_3)$ suspensions, the kinetic curves are very close at the start of the chemisorption process. Larger differences occur at low temperatures and the end of the process, when the conditions of formation of crust are met. These results confirm the transport of the HSO_3^- through the crust with lower velocity and the global absorption process according to the unreacted core model with crust formation of reaction products.

CONCLUSIONS

The experimental results showed the positive influence of sulfites MeSO_3 on the global rate of the studied process.

The rate constants of the chemisorption process were calculated for three different concentrations of the absorbent suspension. Comparative analysis of rate constants has shown values of these almost two times higher when absorption is performed in suspensions with sulfites addition.

The presence of MeSO_3 at a concentration of 10% in the composition of the absorbent suspension results in a significant reduction in the time required for a conversion $\eta \geq 0.95$.

EXPERIMENTAL SECTION

The experimental research was carried out in a cylindrical batch reactor (Figure 13), with the volume of 0.4 l at a overpressure of 98.1 Pa. To emphasize phenomenology of processes occurring in the liquid phase and eliminate the transfer of SO_2 in the gas phase, the experiment was carried out with pure SO_2 (99.9% of the Linde Company). Excess of SO_2 was absorbed in a solution of 15% NaOH . Stirring of the reaction mass was performed with a magnetic stirrer at a speed of $n = 200$ rpm.

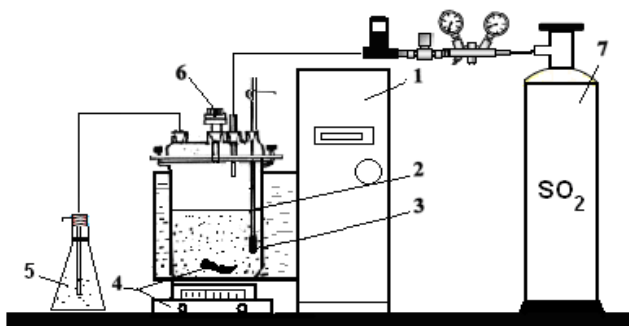


Figure. 12. The schematic of the experimental setup for SO_2 absorption study:
 1- ultra thermostat; 2- absorption reactor; 3- thermometer; 4 - magnetic stirrer;
 5-neutralization vessel for final gas; 6 - sampling device; 7-cylinder with sulfur dioxide

The evolution of the process was monitored by means of iodometric determination of the SO₂ in the slurry. In order to compare the rate of the chemisorption of SO₂ initially were prepared suspension of dolomite with concentration of 5%; 10%; 15%. The suspensions thus prepared were used for absorption of SO₂ to constant content of the suspension. In these suspensions, whose liquid contained Mg(HSO₃)₂ and Ca(HSO₃)₂ were added amounts of dolomite: 24 g suspension with initial concentration of 5%; 31 g for the suspension with the initial concentration of 10% and 45 g respectively for the suspension with the initial concentration of 15%. The suspensions thus obtained were stirred for 12 hours at room temperature until the pH of the slurry increased from pH=4-4.5 to pH=6.7-6.8. After neutralizing Me(HSO₃)₂, the reaction was maintained at operating temperatures of 293 K; 313 K; 333 K. When the temperature reaches the established values was made connection of the reactor with the source of SO₂. At various time intervals were taken samples and determined SO₂ by the iodometric method.

REFERENCES

1. K.J. Ladwig, G.M. Blythe, *Coal Combustion Products*, **2017**, 67.
2. R. del Valle-Zermeno, Formosa J. and Chimenos J.M., *Reviews in Chemical Engineering*, **2015**, 31 (4), 303.
3. I. Siminiceanu, S. Drăgan, A. Friedl, M. Harasek, *Environmental Engineering and Management Journal*. **2006**, 5 (3), 433.
4. Dou, W. Pan, Q. Jin, W. Wang, and Y. Li., *Energy Conversion and Management*, **2009**, 50 (10), 2547.
5. Mathieu Y, Tzanis L, Soulard M, Patarin J, Vierling M, Moliere M., *Fuel Process Technology*, **2013**, 114, 81.
6. Karatepe N., *Energy Source*, **2000**, 22, 197.
7. Hlincik T, Buryan P., *Fuel*, **2013a**, 104, 208.
8. Hlincik T, Buryan P., *Fuel Process Technology*, **2013b**, 111, 62.
9. S. Drăgan, Al. Ozunu, *Central European Journal of Chemistry*, **2012**, 10 (5), 1556.
10. S. Drăgan, Adina Ghirișan, *STUDIA Universitatis Babeș-Bolyai, Chemia*, **2011**, 56 (4), 143.
11. Masson, M.R., Lutz, H.D., Engelen, B., *Solubility Data Series, Sulfites, Selenites, and Tellurites*, Pergamon Press, Oxford, **1986**, 441.

MALACHITE GREEN DYE ADSORPTION FROM MODEL AQUEOUS SOLUTIONS USING CORN COB ACTIVATED CARBON (CCAC)

SILVIA BURCĂ^a, CERASELLA INDOLEAN^{a*}, ANDRADA MĂICĂNEANU^b

ABSTRACT. This paper presents a report on kinetics of malachite green (MG) dye removal from model aqueous solutions using a biomaterial formed by corn cob activated carbon (CCAC). The sorbent was characterized using specific surface area and pore size distribution (Brunauer–Emmett–Teller, BET) analysis. The BET analysis confirmed the macro-porosity of the adsorbent. Effects of initial concentration of MG dye and CCAC quantity, particle size and stirring rate on adsorption capacities and efficiency were monitored through pseudo first- and second-order models, intra-particle and film diffusion models to present adsorption rate parameters. The removal efficiency of MG increased with the adsorbent quantity and particle size.

Keywords: *corn cob biomass, activated carbon, malachite green, aqueous phase, characterization techniques, kinetics.*

INTRODUCTION

Urbanization and industrialization from recent years have generated, in a worrying rate, the environmental pollution. Water pollution (surface and groundwater) is one of the most undesirable environmental problems and requires rapid and efficient solutions. Among the inorganic and organic pollutants present in wastewater, dyes represent a strong threat because these contaminants are highly toxic, carcinogenic, mutagenic and teratogenic for human beings, fish species and microorganisms [1-3]. From literature, a series of physical,

^a Babeş-Bolyai University, Faculty of Chemistry and Chemical Engineering, Department of Chemical Engineering, 11 Arany Janos st., Cluj-Napoca, RO-400028, Romania.

^b Indiana University of Pennsylvania, Department of Chemistry, Indiana, PA 15705, USA

*Corresponding author: cella@chem.ubbcluj.ro

chemical and biological measures for the removal of dyes from effluents have been developed, such as adsorption [4-6], membrane separation [7], chemical coagulation [8,9], electrochemical method [10], or oxidative processes [11,12].

Adsorption has been demonstrated to be very effective physico-chemical method for removing dyes from aqueous effluents, in wastewater treatment [1,3,13]. Many adsorbents have been used for the removal of undesirable substances from aqueous solution [1,3,6,14-16]. Activated carbon is one of the most popular and extensively used adsorbent in wastewater treatment, because of its high porosity, adsorption capacity and efficiency [16,17]. So, production and commercialization of cheap and efficient activated carbon has become extremely necessary and of great applicative interest. Many agricultural and industrial waste materials, such as waste wood [18,19], pine cone [20,21], coffee husk [22], corn stalk [18], tea leaves [17] and waste tea [16,23], orange peel [24], coconut shell [1], etc. are used for low cost activated carbon obtaining. Malachite green (MG) is a cationic (basic) dye, used for the dyeing of cotton, paper, leather, silk, etc. Also, is produced for manufacturing of paints and printing inks [16]. MG is an anti-parasitic and antifungal agent in aquaristics [25].

This paper presents the MG adsorption behaviour onto activated carbon produced from an agricultural by-product, corn cob biomass (CCAC) and the study of some physico-chemical characteristics of this cheap and abundant material.

2. RESULTS AND DISCUSSION

2.1. Physical-chemical characterization of CCAC

The adsorption capacity of a porous material is correlated with some properties such as surface area, pore volume and porosity. These properties are specific to each material, depending on the nature of the feedstock and the activation method. Improvement of these specific properties could be achieved by activating crude material at high temperatures, in the absence of air or steam activation use. A typical analysis of corn cob, from literature data, was as follows: moisture, 4.3 wt%; volatiles, 78.7 wt%; fixed carbon, 16.1 wt%; ash, 0.9 wt% [26]. Elemental analysis of corn cob was as follows: C, 45.21 wt%; H, 6.12 wt%; N, 0.94 wt%; O, 47.73 wt%. The results reveal that corn cob has high carbon, but low ash content, which makes it a good precursor material for adsorbents

2.1.1 The assessment of real (volumetric mass) density, apparent density and porosity of CCAC

The **real density** of CCAC reflects the ratio of the mass of material to its volume, without taking into account pore volume.

The real (volumetric mass) density of CCAC obtained, with $\Phi=1.6-1.8$ mm (average particles diameter, particle size) was gravimetrically determined. In the first step, the empty and dry pycnometer was weighed on the analytical balance. Then, the pycnometer volume is determined by filling it with distilled water and weighing again. The density of ethanol were after measured by weighing the ethanol-filled pycnometer. The real CCAC density is determined by introducing 1-2 g of CCAC sample into the pycnometer, which will then be filled with ethanol and weighed on the analytical balance.

The real (volumetric mass) density is then calculated, with the formula (1) [27]:

$$\rho_{real\ CCAC} = \frac{m}{(m_3 + m) - m_4} \times \rho_{ethanol}, \text{ g/cm}^3 \quad (1)$$

where m – CCAC weight utilized, g

m_3 – empty and dry pycnometer weight, g

m_4 – pycnometer weight with CCAC and ethanol, g

$\rho_{real\ CCAC}$ – the real CCAC density, g/cm³

$\rho_{ethanol}$ – the ethanol density, g/cm³.

The **apparent density** of a material expresses the ratio of the mass of this material to its volume, including the volume of the pores.

The apparent density of CCAC obtained, with $\Phi=1.6-1.8$ mm, is also gravimetrically determined, using a wire basket and a graduated (measuring) cylinder. In the first step, the empty basket is sink into the cylinder filled with water, and the volume increase, due to the empty basket, is noted. Then, dry the basket in the oven, and in the empty basket, 1-2 g of CCAC will be added. The CCAC-filled basket is immersed in water and the increase in volume, caused by the CCAC adding, is noted.

The apparent density is calculated with the formula [27]:

$$\rho_{apparent} = \frac{m}{V_2 - V_1}, \text{ g/cm}^3 \quad (2)$$

where, m – CCAC weight utilized, g

V_2 – the volume increase caused by the CCAC-basket, ml.

V_1 – the volume increase caused by the empty basket, ml.

The **porosity** of an active carbon (CCAC) reflects the ratio between the pores volume and the total volume of material, and is determined by the formula [27]:

$$P = \frac{\rho_{\text{apparentCCAC}} - \rho_{\text{realCCAC}}}{\rho_{\text{realCCAC}}} \times 100, \% \quad (3)$$

2.1.2. Determination of the CCAC specific surface. BET surface

The establishing of CCAC specific surface area, with $\Phi = 1.6-1.8$ mm, is achieved by using the gravimetric method for the desorption isotherm determination. In the first step, it weigh the vial with cap on the analytical balance. Then, an amount of 0.4-1g of CCAC (sample) is introduced into the vial. With a pipette, ethanol is added to CCAC, until the drowning the sample bed. The sample is left at rest for few minutes to reach room temperature, then place it on the balance tray. Using a stopwatch, the rate of decreasing of vial mass with 0.002g will be determined. As long as the CCAC sample is coated with liquid, the rate of vial mass decreasing is constant, due to the evaporation process. When the liquid evaporation is replaced by desorption, the rate steadily decreases, with the vapor pressure decreasing at the CCAC surface. For the CCAC specific surface calculation it will be used the BET equation [27]:

$$\frac{x}{a(1-x)} = \frac{1}{a_m \bullet C} + \frac{C-1}{a_m \bullet c} \bullet x \quad (4)$$

2.1.3. Determination of ash content

The ash is the residual solid remaining after calcination of CCAC at $815 \pm 25^\circ\text{C}$ temperatures, to constant weight. The ash content is calculated as the ratio between the mass of the residue obtained after calcination and the sample mass before calcination, expressed as a percentage [27]. To determine the ash content for a sample ($\Phi = 1.6-1.8$ mm, particle size), obtained by impregnation with conc. H_2SO_4 , 98%, a quantity of 1-2 g CCAC is introduced into a melting pot (crucible). This is heated to $815 \pm 25^\circ\text{C}$, for 90 minutes and, after cooling, the residue remaining in the crucible is weighing. The ash content of the analysed sample is determined by the formula [27]:

$$A^a = \frac{m_3 - m_1}{m_2 - m_1} \times 100, \% \quad (5)$$

where, m_1 – the empty melting pot weigh, g
 m_2 – the weigh of melting pot with CCAC sample, g
 m_3 – the weigh of melting pot with CCAC sample, after calcination, g

The results for physic-chemical characterization of CCAC are presented in Table 1.

Table 1. Physical parameters for CCAC

S_{BET} (m^2/g)	Apparent density (g/cm^3)	Real density (g/cm^3)	Porosity (%)	Ash content (%)	Pore volume (cm^3/g)
142	1.151	0.7998	44.36	1.56	0.047

A defining feature of the adsorption process is the porosity of the CCAC. The higher it is its value, the higher is the adsorption capacity of material. The reduced CCAC ash content, obtained by impregnation with H_2SO_4 , is comparable to the literature results [28]. Excessive ash content reduces CCAC adsorption capacity.

2.2. Effect of MG initial concentration

Experiments were conducted using 100 mL MG aqueous solutions with the following concentrations: 74, 158, 183, 231, and 279 mg MG/L, in batch conditions, with magnetic stirring at 200 rpm, at room temperature ($T=296K$) and 1 g of CCAC.

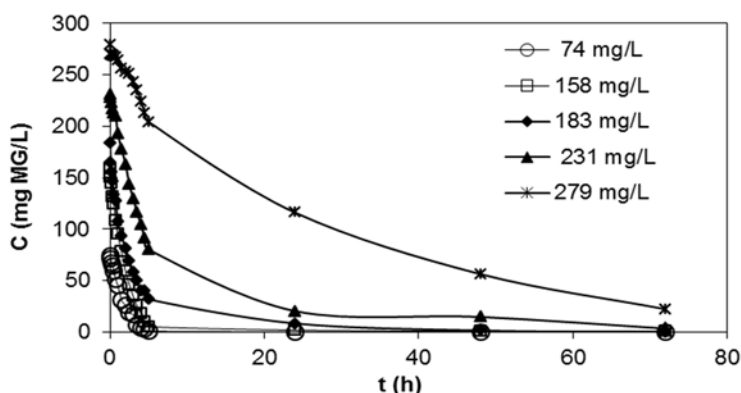


Figure 1. Influence of the initial MG concentration over the time evolution for dye adsorption onto CCAC ($C_0 = 74\text{--}279$ mg MG/L, 1 g CCAC, $\Phi=1.6\text{--}1.8$ mm, 296 K, $pH=6.3$, 200 rpm)

Regarding MG concentration time evolution during the adsorption process, it can be observed that the drop in concentration is very steep in the first 4.8-5.5 h for 279 and 231 mg MG/L, respectively, and approximately 5.8-5.9 h

for the rest initial MG concentrations utilized, and the equilibrium was reached in quite different time intervals, depending on the initial MG concentration. Thus, for the initial concentrations of 74 and 158 mg MG/L, the equilibrium was reached after about 24 h, for 183 mg MG/L the equilibrium has been achieved after approximately 48 h and, in case of 231 and 278 mg MG/L, the equilibrium was reached after about 70 and 72 h, respectively. The adsorption of MG is relatively fast in the first 4-5 h (first step), then the adsorption rate decreases and progresses much slower, until the equilibrium was achieved (second step). It is interesting to observe that in the first step, most of the MG quantity is retained on the CCAC surface (between 99 and 91%, for 74 and 231 mg MG/L, respectively, and 58% MG, for initial concentration of 279 mg MG/L). This shows that surface diffusion became rate-determining step due to particle agglomeration, which leads to difficult access to the adsorption sites, as the initial dye concentration increases.

2.3. Effect of sorbent quantity

The influence of CCAC quantity onto the MG sorption process was studied at room temperature, using 0.25, 0.5, 0.75, 1 and 1.5 g CCAC and 100 ml solution, 158 mg MG/L, in batch conditions, 200 rpm. The removal efficiencies of MG, at equilibrium are 55, 56, 79, 96 and 99% for 0.25, 0.5, 0.75, 1 and 1.5 g of adsorbent, respectively (Fig 2). This indicates that the best efficiencies will be obtained if 100 ml solution ($C_0=158$ mg MG/L) would be treated with 1 g and 1.5 g of CCAC. But, it is, probably, more efficient to use 1 g of CCAC for 100 ml solution, because the yield difference it is of only 3 units (96% for 1 g CCAC, compared to 99% for 1.5 g CCAC).

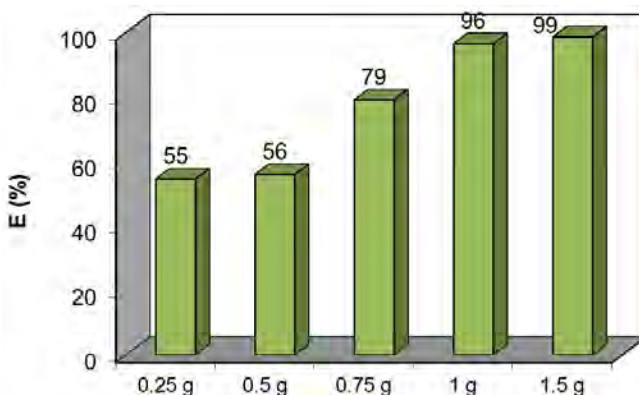


Figure 2. The effect of CCAC quantity on the maximum efficiency values for MG adsorption (296 K, $C_0=158$ mg MG/L, 100 mL solution, $\Phi=1.6-1.8$ mm, 200 rpm, pH = 6.3, 296 K, 24 h).

2.4. Effect of stirring rate

Depending upon the degree of agitation of the fluid particle system, the rate of the adsorption is controlled either by film diffusion or pore diffusion. From literature data, it can be asserted that at lower agitation speed, the fluid film around the particle is thicker and the film diffusion seems to be rate limiting step [29].

In order to understand the effect of stirring rates on the adsorption of MG dye onto CCAC, experiments were carried out in batch system, with different stirring rates changing from 200 to 1000 rpm (200, 400, 600, 800 and 1000 rpm). Obtained results are showed in Figure 3. It can be seen that the increase in stirring rate, from 200 to 1000 rpm, leads to a decrease in the amount of MG adsorbed, from 12.35 to 11.65 mg MG/g, respectively. This fact can be explained that due to the intense stirring, MG molecules are not able to reach the solid surface, therefore the adsorbed amount is going to be smaller for the same duration of the process (24 h). Such moderate speed gives probably, a good homogeneity for the mixture suspension in solution.

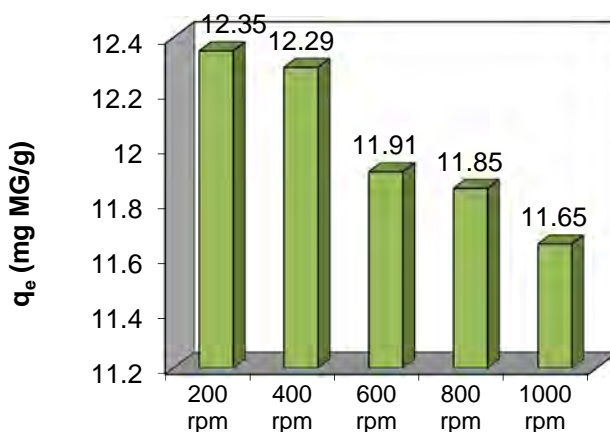


Figure 3. The effect of stirring rate over the amount of MG uptake onto CCAC adsorption ($C_0=158$ mg MG/L, 296 K, 100 mL solution, $\Phi=1.6-1.8$ mm, pH = 6.3, 296 K, 24 h)

2.5. Adsorption kinetics

The controlling mechanisms of adsorption process, such as chemical reaction, diffusion control or mass transfer coefficient are used to determine kinetic models [30]. In order to investigate the removal of MG from model

solutions presented, using CCAC material, the data obtained from adsorption kinetic experiments were simulated using four kinetic models, which are pseudo-first order, pseudo-second order reaction rate, Weber-Morris intra-particle diffusion and Boyd models.

The pseudo-first-order rate equation, or Lagergren equation, is derived on the assumption of one step reaction [17,31] and is expressed as:

$$\ln(q_e - q_t) = \ln q_e - k_1 t \quad (6)$$

where, q_e is the amount of dye adsorbed at equilibrium (mg/g),
 q_t is the amount of dye adsorbed at time t (mg/g),
 k_1 is the pseudo-first-order reaction rate constant (1/min).

For the pseudo-second order model, data were applied to the Ho and McKay's pseudo-second order chemisorption kinetic rate equation, which expressed as [17,32,33]:

$$\frac{t}{q_t} = \frac{1}{k_2 q_e^2} + \frac{t}{q_e} \quad (7)$$

where, k_2 is the pseudo-second order reaction rate equilibrium constant (g/mg·min).

In order to determine the rate constant and equilibrium uptake, the straight line plots of $\ln(q_e - q_t)$ against t , eq. (6), were made at different initial MG concentrations, figure 4.

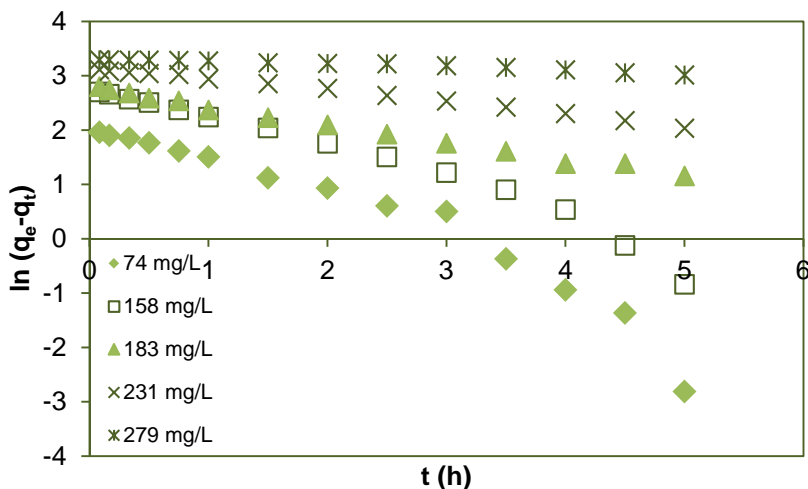


Figure 4. First order plots for different initial MG concentrations ($C_0=74, 158, 183, 231$ and 279 mg MG/L) using 1 g CCAC (200 rpm, 296 K, $\text{pH}=6.3$, 100 mL MG solution).

The coefficient of correlation (R^2), which represent the percentage of variability in the dependent variable (the variance about the mean) is employed to analyse the fitting degree of isotherm and kinetic models with the experimental data [34] and as is well known, may vary from 0 to 1. The values of k_1 and q_e calculated from the slope and intercept obtained from the linear plot of $\ln(q_e - q_t)$ vs. t , and the R^2 values of fitting the first-order rate model at the five concentrations are presented in Table 2.

Linear plot of t/q_t vs. t , figure 5, was used for calculating the q_e (cal) of pseudo-second order and k_2 , and these values are also shown in Table 2.

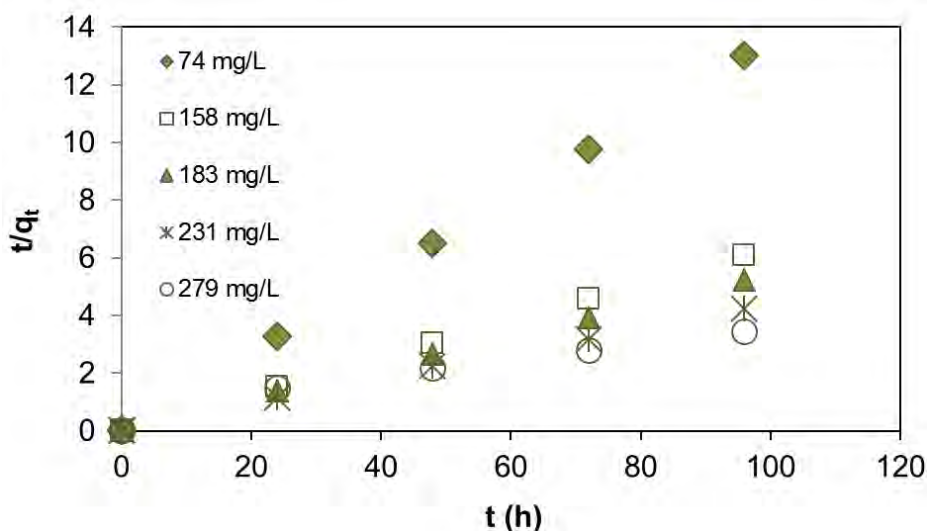


Figure 5. Second order plots for different initial MG concentrations ($C_0=74, 158, 183, 231$ and 279 mg MG/L) using 1 g CCAC (200 rpm, 100 mL MG solution, 296 K).

Table 2. First-order and second-order model rate coefficients for MG adsorption on CCAC, $C_0=74-279$ mg/L, 200 rpm, 296 K.

C_0 mg/L	q_{eexp} (mg/g)	First-order model			Second-order model		
		k_1 (1/min)	q_{ecalc} (mg/g)	R^2	k_2 (g/mg-min)	q_{ecalc} (mg/g)	R^2
74	7.381	0.825	9.932	0.93	18.360	7.380	1
158	15.803	0.640	15.906	0.96	2.356	15.797	1
183	18.343	0.327	18.096	0.99	0.341	18.348	0.99
231	22.760	0.214	23.492	0.99	0.115	22.675	0.99
279	27.940	0.053	27.678	0.95	0.014	27.727	0.99

Taking into consideration the correlation coefficient (R^2), which for the pseudo-second order is between 0.99 and 1 (Table 2), it can conclude that MG sorption on CCAC can be classified as pseudo-second order, fact confirmed by the literature scientific results [5,6,35]. In addition, based on the fact that pseudo-second-order equation is derived on the assumption of a two-step reaction, we concluded that MG adsorption takes place as a two-step reaction scheme.

Intra-particle and film diffusion models

In order to identify diffusion mechanism, Weber-Morris [36] and Boyd [37] models were employed.

The intra-particle diffusion model (Webber and Morris) can be written as follows [36,38]:

$$q_t = K_{ip} t^{1/2} \quad (8)$$

where: K_{ip} is the intra particle diffusion rate constant ($\text{mg/g min}^{-1/2}$).

If the intra-particle diffusion is rate-controlling step, the plot of q_t versus $t^{1/2}$ should be linear and pass through the origin, figure 6 [38]. Values of the intra particle diffusion constant, K_{ip} ($0.9227 \text{ mg/g min}^{-1/2}$ for the concentration 74 mg MG/L and $0.2431 \text{ mg/g min}^{-1/2}$ for the 279 mg MG/L) were obtained. The correlation coefficients (R^2) for the intra-particle diffusion model were between 0.908 and 0.980 (Table 3). These values indicate that intra-particle diffusion is not the rate-controlling step for MG adsorption onto CCAC.

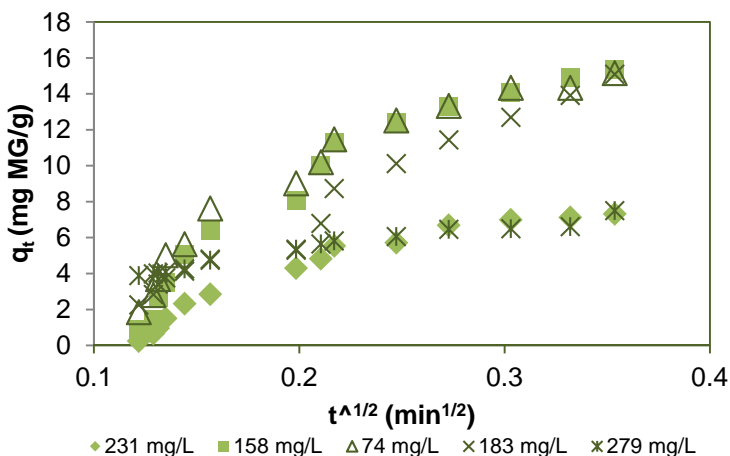


Figure 6. Weber-Morris intraparticle model plot for adsorption of initial MG concentrations, $C_0=74\text{-}279 \text{ mg MG/L}$, 200 rpm, 296K, 1 g CCAC, 100 ml MG solution.

The film diffusion model (Boyd) [37] is expressed as:

$$(1 - F) = -k_{fd} \cdot t \quad (9)$$

where F is the fraction attainment at equilibrium ($F = qt/q_e$), and k_{fd} is the liquid film diffusion rate constant (1/min).

If the obtained plots give straight lines passing through origin, film diffusion is considered to be rate determining step, figure 7. Also from the slope of these plots, film diffusion rate constants can be determined, Table 3. Very small values of the intercept in the case of extra particle diffusion model suggest that extra-particle (film) diffusion could be a rate determining step towards the end of the adsorption process.

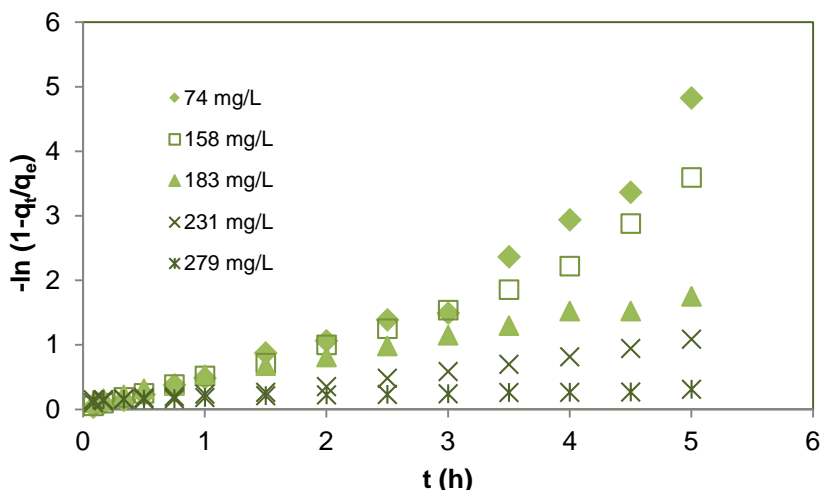


Figure 7. Fitting of the extra particle diffusion model, adsorption at $C_0=74-279$ mg mg/L, 200 rpm, 1 g CCAC, 100 ml MG solution.

Table 3. Intra-particle and external diffusion rate coefficients for MG adsorption on CCAC, $C_0=74-279$ mg/L MG, 200 rpm, 276 K.

C_0 (mg/L)	Intra-particle diffusion			External diffusion		
	K_{ip} (mg/g min ^{1/2})	Intercept	R^2	K_{fd} (min ⁻¹)	Intercept	R^2
74	0.9227	2.06	0.908	0.0138	0.209	0.930
58	0.9121	4.62	0.919	0.0106	0.136	0.960
183	0.8963	4.01	0.980	0.0054	0.141	0.993
231	0.5302	2.46	0.910	0.0031	0.057	0.978
278	0.2431	2.27	0.957	0.0005	0.050	0.967

CONCLUSIONS

The past ten years has seen a developing interest in the preparation of activated carbons from low-cost agro-industrial wastes as adsorbents for water and wastewater treatment processes.

Corn cob activated carbon (CCAC) was prepared through chemical activation using concentrated sulphuric acid (98%). The maximum adsorption capacity for CCAC was determined to be 12.35 mg/g ($C_0=158$ mg MG/L, 296 K, 100 mL solution, $\Phi=1.6-1.8$ mm, pH = 6.3, 296 K, 24 h, 200rpm). Pseudo-second order kinetic model was found to adequately describe the adsorption process.

The sorption diffusion mechanisms were determined from the intra-particle (Weber-Morris) and film diffusion (Boyd) models. It has been found that the adsorption of MG dye onto CCAC was mainly governed by film diffusion model.

These results indicated that corn cob could be a good and cheap precursor for the production of an effective activated carbon adsorbent and alternative to commercial-activated carbon.

EXPERIMENTAL SECTION

Materials

Collection and preparation of adsorbent material (CCAC)

Agricultural waste biomass (corn cob) was received freshly from farm fields from Transylvania, Cluj County, Romania. The material was initially washed with deionized water several times, to remove the dust particles, and then biomaterial was cut, crushed and grounded to get size fraction of $\Phi=1.6-1.8$ mm, dried at 95°C for 24h, then was impregnated with concentrated sulfuric acid (98%) for 24h, with an impregnation rate of H_2SO_4 : corn cob biomass = 1: 5. The carbonated material was neutralized with 2% sodium bicarbonate ($NaHCO_3$) solution, washed with distillate water, until the pH of the wash water reaches the pH of the distilled water (pH ≈ 6.3), dried at 105°C for 24 h. Acid impregnated CCAC was carbonized at a tube furnace under nitrogen atmosphere. It was heated from room temperature to 500°C (heating rate of 5°C/min) with 1h holding time at 100°C interval. After cooling to room temperature, the activated carbon was washed thoroughly with distilled water until the washing water became neutral and dried in oven at 105°C, for 12 h approximately. The resulted activated carbon (CCAC) was grinded, shived ($\Phi=1.6-1.8$ mm) and kept in a desiccator for further use.

Specific surface area, real and apparent density, calculated porosity (using gravimetric method), ash content and pore volume were determined for obtained carbon material [27, STAS 5628-73, STAS 10967-88, STAS 5265-86].

Malachite green (MG) oxalate ($C_{23}H_{25}N_2 \cdot C_2HO_4 \cdot 0.5C_2H_2O_4$, $M_W=463.5$) was purchased from Penta (Czech Republic) and used without further purification. 1000 mg MG/L of stock solution was prepared by dissolving the required amount of dye in distilled water. Other concentrations (74-279 mg MG/L) of MG were obtained by dilution of stock solution.

Adsorbent characterization

Elemental analysis (C, H, N, S) was performed using a CHN CARLO ERBA EA 1108 Elemental Analyzer. The oxygen percentage was estimated by difference.

Specific surface area and pore specific volume for the CCAC were determined by the Brunauer–Emmett–Teller (BET) method using a Sorptomatic ADP-nitrogen adsorption analyzer (Thermo Electron-Corp.). Prior to N_2 adsorption, samples were out gazed for 20h at 105°C.

Adsorption experiments

The MG adsorption process was studied using the batch technique, by contacting different quantities of adsorbent (0.25-1.5 g), magnetic stirring (200-1000 rpm), room temperature (296K) with 100 mL MG aqueous solutions with different initial concentrations ($C_0=74-279$ mg MG/L). The MG concentration in aqueous phase was determined using a double beam UV-visible spectrophotometer (GBC Cintra 202) at $\lambda = 618$ nm. The experiments were repeated three times and concentration values were calculated using averaged concentration values.

Data evaluation

The amount of dye (MG) adsorbed per gram of CCAC, q_e (mg MG/g CCAC), was calculated using the equation (11) [14,17]

$$q_e = \frac{(C_0 - C_e)}{m} \times \frac{V}{1000} \quad (11)$$

where:

- C_0 – is the initial MG concentration (mg/L)
- C_e – is the equilibrium MG concentration (mg/L)
- V – is the volume of MG solution used (mL)
- m – is the mass of CCAC used (g).

The percentage removal (or removal efficiency), E (%) of the MG, was calculated with formula (12) [14,17]:

$$E\% = \frac{(C_0 - C_e)}{C_0} \cdot 100 \quad (12)$$

Experimental data were used to establish which equilibrium and kinetic model describe better the adsorption process.

REFERENCES

1. A.M. Aljeboree, A.N. Alshirifi, A.F. Alkaim, *Arabian Journal of Chemistry*, **2017**, *10*, S3381.
2. B. Nagy, C. Manzatu, A. Măicăneanu, C. Indolean, L. Barbu-Tudoran, C. Majdik, *Arabian Journal of Chemistry*, **2017**, *10*, S3569.
3. D. Vuono, E. Catizzzone, A. Aloise, A. Policicchio, R.G. Agostino, M. Magliori, G. Giordano, *Chinese Journal of Chemical Engineering*, **2017**, *25*, 523.
4. Z. Li, Z. Jia, T. Ni, S. Li, *Journal of Molecular Liquid*, **2017**, *242*, 747.
5. J.R. Njimou, A. Măicăneanu, C. Indolean, C.P. Nanseu-Njiki, E. Ngameni *Environmental technology*, **2016**, *37(11)*, 1369.
6. A.M. Sacara, C. Indolean, L.M. Muresan, *Studia UBB Chemia*, **2016**, *61*, 183.
7. C. Bellona, J.E. Drewes, P. Xu, G. Amy, *Water Research*, **2004**, *38*, 2795.
8. S. Saravanan, T. Prakash, V.K. Gupta, A. Stephen, *Journal of Molecular Liquid*, **2014**, *193*, 160.
9. M. Davaraj, R. Saravanan, R.K. Deivasigamani, V.K. Gupta, F. Gracia, S. Jayadevan, *Journal of Molecular Liquid*, **2016**, *221*, 930.
10. C.H. Zhang, J.W. Tang, C. Peng, M.Y. Jin, *Journal of Molecular Liquid*, **2016**, *221*, 1145.
11. L. Ai, C. Zhang, L. Li, J. Jiang, *Applied Catalysis B: Environmental*, **2014**, *149*, 191.
12. A.R. Khataee, M. Fathinia, S. Aber, M. Zarei, *Journal of Hazardous Materials*, **2010**, *181*, 886.
13. F. Jiang, D.M. Dinh, Y.-L. Hsieh, *Carbohydrate Polymers*, **2017**, *173*, 286.
14. C. Majdik, S. Burca, C. Indolean, A. Maicaneanu, M. Stanca, S. Tonk, P. Mezey, *Revue Roumaine de Chimie*, **2010**, *55(11-12)*, 871.
15. C. Majdik, A.M. Török, E. Buta, C. Indolean, Sz. Tonk, L. Silaghi-Dumitrescu, *Acta Chimica Slovenica*, 2015, *62(2)*, 452.
16. E. Akar, A. Altinişik, Y. Seki, *Ecological Engineering*, **2013**, *52*, 19.
17. M. Goswami, P. Phukan, *Journal of Environmental Chemical Engineering*, **2017**, *5*, 3508.
18. D.C. W. Tsang, J. Hu, M.Y. Liu, W. Zhang, C.K. Lai, I.M. C. Lo, *Water Air and Soil Pollution*, **2007**, *184(1-4)*, 141.

19. J. Acharya, J.N. Sahu, B.K. Sahoo, C.R. Mohanty, B.C. Meikap, *Chemical Engineering Journal*, **2009**, 150, 25.
20. S. Dawood, T.K. Sen, C. Phan, *Water, Air & Soil Pollution*, **2014**, 225, 1818.
21. K. Li, S. Tian, J. Jiang, J. Wang, X. Chen, F. Yan, *Journal of Material Chemistry A*, **2016**, 4, 5223.
22. M. Concalves, M.C. Guerreiro, L.C.A. Oliveira, C. Solar, M. Nazarro, K. Sapag, *Waste and Biomass Valorization*, **2013**, 4(2), 395.
23. M. Auta, B.H. Hameed, *Chemical Engineering Journal*, **2011**, 171(2), 502.
24. M.E. Fernandez, G.V. Nunell, P.R. Bonelli, A.L. Cukierman, *Industrial Crops and Products*, **2014**, 62, 437.
25. C. Indolean, S. Burcă, A. Măicăneanu, *Acta Chimica Slovenica*, **2017**, 64, 513.
26. C.-F. Chang, C.-Y. Chang, W.-T. Tsai, *Journal of Colloid and Interface Science*, **2000**, 232, 45.
27. M. Stanca, A. Măicăneanu, C. Indolean, *Caracterizarea, valorificarea și regenerarea principalelor materii prime din industria chimică și petrochimică: îndrumar de lucrări practice*, **2007**, Presa Universitară Clujeană, Cluj.
28. C. Moreno-Castilla, F. Carrasco-Marin, F.J. Maldonado-Hódar, J. Rivera-Utrilla, *Carbon*, **1998**, 36(1-2), 145.
29. C. Djilani, R. Zaghdoudi, F. Djazi, B. Bouchekima, A. Lallam, A. Modarressi, M. Rogalski, *Journal of Taiwan Institute of Chemical Engineering*, **2015**, 53,112.
30. M.T. Yagub, T.K. Sen, S. Afroze, H.M. Ang, *Advances in Colloid an Interface Science*, **2014**, 209, 172.
31. S. Lagergren, B.K. Svenska, *Kungliga Svenska Vetenskapsakademiens Handlingar*, **1898**, 24(4), 1.
32. Y.S. Ho, G. Mckay, *Process Biochemistry*, **1999**, 34, 451.
33. Y.S. Ho, *Process Biochemistry*, **2006**, 136, 681.
34. K.Y. Foo, B.H. Hameed, *Chemical Engineering Journal*, **2010**, 156, 2.
35. H. Saygılı, F. Güzel, *Chemical Engineering Research and Design*, **2015**, 100, 27.
36. W. Weber, J. Morris, *Journal Sanitary Engineering Division Proceedings. American Society of Civil Engineers*, **1963**, 89(2), 31.
37. G.E. Boyd, A.W. Adamson, L.S. Myers Jr., *Journal of American Chemical Society*, **1947**, 69, 2836.
38. S. Burcă, A. Măicăneanu, C. Indolean, *Revue Roumaine de Chimie*, **2016**, 61(6-7), 541.

COMPARATIVE STUDY OF SPRAY-DRYING AND FREEZE-DRYING ON THE SOLUBLE COFFEE PROPERTIES

ADINA GHRIȘAN^a, VASILE MICLĂUȘ^{a*}

ABSTRACT. The paper presents a comparative study of some physical properties, microstructure and antioxidant capacity of soluble coffee obtained at laboratory scale using spray-drying (SD) and freeze-drying (FD) as dehydration techniques. SEM was used for monitoring structures and size of the coffee powder. The results of SEM show the difference in the microstructure with the used drying technique. SD dried coffee has only spherical shape, narrow distribution, with the particle mean size of about 10 μm and smooth surface. The FD dried coffee has spherical shape with the size of about 40 μm and flaky structure, non-spherical shape, with the dimensions between 10 x 20 μm and 30 x 90 μm . EPR was used for the determination of coffee antioxidant capacity. SD coffee powder shows a higher antioxidant activity in comparison with FD dried coffee.

Keywords: *soluble coffee, spray-drying, freeze-drying, physical properties, microstructure, antioxidant activity.*

INTRODUCTION

Soluble coffee, also called instant coffee or coffee powder, is obtained from freshly ground-roast coffee beans by extraction with hot water at high pressure in order to extract water-soluble compounds. This soluble material is then cooled and sometimes centrifuged, concentrated by heating, and dried to reduce moisture to approximately 5%. Alternatively, steam/water and/or oil may be used to rewet the surface of the instant coffee granules, followed by drying. This process is called agglomeration [1].

Manufacturers use different techniques to improve the appearance and taste of the final product. Ground-roast coffee generally consists of

^a Babeș-Bolyai University, Faculty of Chemistry and Chemical Engineering, Department of Chemical Engineering, 11 Arany Janos str., RO-400028, Cluj-Napoca, Romania

* Corresponding author miclaus@chem.ubbcluj.ro

Arabica species. Robusta coffee is often used at a high percentage or alone in blends designated for instant coffee production. Robusta seeds contain higher amounts of soluble solids, which increases yield extraction [2].

There are two basic methods available to convert the liquid coffee extract to the dried powder: spray-drying (SD) and freeze-drying (FD) or lyophilisation. By spray-drying the coffee liquid is pulverized into hot air, in spray dryer (atomizer). Through the heat the water evaporates during the downfall of coffee to the bottom of the spray dryer [3]. Freeze-drying is a gentle method used for sensitive products. The concentrated coffee liquid is first frozen and than water changed in ice crystals is removed as vapours by sublimation [4, 5].

Comparing these drying techniques, it is obvious that spray-drying is done at high temperature, affecting some characteristics of final product, but it is less costly and shorter times drying, and so, it allows larger scale economic production [6]. The freeze-drying provides a product with higher quality, overcoming the loss of flavor and aroma, but is energy intensive and expensive due to the low temperature and low-pressure operation [7]. Till now freeze-drying technology is only used at industrial scale to dry coffee, milk, spices, meats and other high-value foods.

In the present work, some physical properties and the antioxidant activity of coffee powder obtained by spray-drying (SD) and freeze-drying (FD) were determined.

Antioxidant activity is an important issue that must be followed during the technological process of producing soluble coffee. According to the literature, coffee is one of the food sources rich in antioxidants. Antioxidants are substances that through their action protect the body against oxidative stress, which unfortunately increase the risk of various diseases of which the most common are cancer, cardiovascular and neurological.

Antioxidant activity of coffee brews is related to chlorogenic, ferulic, caffeic, and *n*-coumaric acids contained in it [8]. Melanoidins (brown pigments) and phenylalanines showing strong antioxidant activity are synthesized during the roasting process when the Maillard reaction is produced [8,10-12].

RESULTS AND DISCUSSION

a. Moisture content of dehydrated materials plays an important role in the handling of soluble coffee powder. The moisture content (% wet basis) determined gravimetric by the mass loss on coffee powder shows higher moisture of freeze dried coffee (7.46 %) than spray dried coffee (4.72%). The lower moisture content of spray dried (SD) coffee, which means better preservation and stability, was expected due to the high temperature used by this technique comparative to freeze-drying process.

b. Microscopic structures, the shape, the surface morphology and the particles size of coffee powder, were examined by **Scanning Electron Microscopy (SEM)**. The results of SEM show the difference in the microstructure with the used drying technique (Figures 1 and 2).

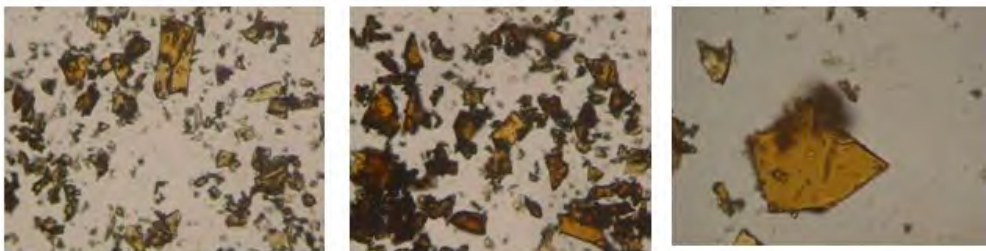
In the case of SD technique, the obtained dried particles have only spherical shape, monomodal with a mean size of about 10 μm , and smooth surface. As in other articles atomization seems to promote the formation of particles with narrow distribution and spherical shape [13].



Figure 1. SEM micrographs of spray dried coffee sample



a.



b.

Figure 2. SEM micrographs of freeze dried coffee sample:
a. first experiment, b. second experiment

In the case of powder obtained by FD, the particles show spherical and flaky structure with irregular shapes: spherical shape with the size of about 40 μm and flaky structure, non-spherical shape, with the dimensions of 20 x 50 μm and 30 x 90 μm , for first experiment and spherical particles with diameter of 40 μm , and flattened particles with the dimensions 10 x 20 μm și 20 x 30 μm , for the second experiment [14].

Scanning electron micrographs of freeze dried and spray dried coffee were realized at a magnification of 4x, 10x and 40x. Due to the smaller size of SD coffee particles it is expected an increase of specific surface area and in consequence the increase of solubility comparative with the FD powder, as in other articles has described [15, 16].

c. Bulk porosity

An other property which characterizes the soluble coffee is the bulk porosity. Bulk porosity was calculated by determining the ratio of particle density (ρ_p) and bulk density (ρ_b) using next equation [17]:

$$\varepsilon_b = 1 - \frac{\rho_b}{\rho_p}$$

The particle density (ρ_p) of soluble coffee was determined by pycnometer method. The bulk density of the coffee powder obtained from both drying techniques was measured following the procedure described in literature [16, 17]. The free bulk density of SD dried coffee was 0.324 g/cm^3 comparative to FD dried coffee it was 0.338 g/cm^3 . The higher values of FD powder bulk density can be due to its higher residual moisture content, and wider particle size distribution. The obtained values of porosity soluble coffee were: for SD powder $\varepsilon_{b(\text{SD})} = 0.640$ and for FD powder $\varepsilon_{b(\text{SF})} = 0.624$. In our case, the porosity of the SD powder containing smaller particles has a higher porosity than FD dried powder.

d. Antioxidant capacity

Roasting markedly affects the composition of the coffee polyphenols through the Maillard reaction and confers to coffee its pleasant taste and aroma [18]. The coffee beverage is the dietary source of potential antioxidants, such as caffeine, phenolic compounds (mainly chlorogenic acid), hydroxycinnamic acids and Maillard reaction products [19]. The antioxidant capacity of coffee is related to the presence of both natural constituents and compounds formed during its processing [20].

The antioxidant activity of obtained coffee powders was evaluated through their ability to reduce tempol free radical by EPR.

The tempol was used as solution of 0,01% mixed with dried coffee powder obtained by SD and FD techniques.

An overview on the fall time of the soluble coffee antioxidant activity obtained under laboratory conditions is shown in Figure 3: coffee_1 is SD dried coffee, coffee_2 the FD dried coffee (first experiment) and coffee_3 the FD dried coffee (second experiment). The antioxidant activity decreases after 30 minutes to half from the initial activity followed by a slower decline after that. It can be seen for all three samples that the antioxidant activity decreases at a rate of about 60-70% in the first 60 minutes. After that the decrease is slower, reaching zero value in about 400 minutes from the start of the experiment.

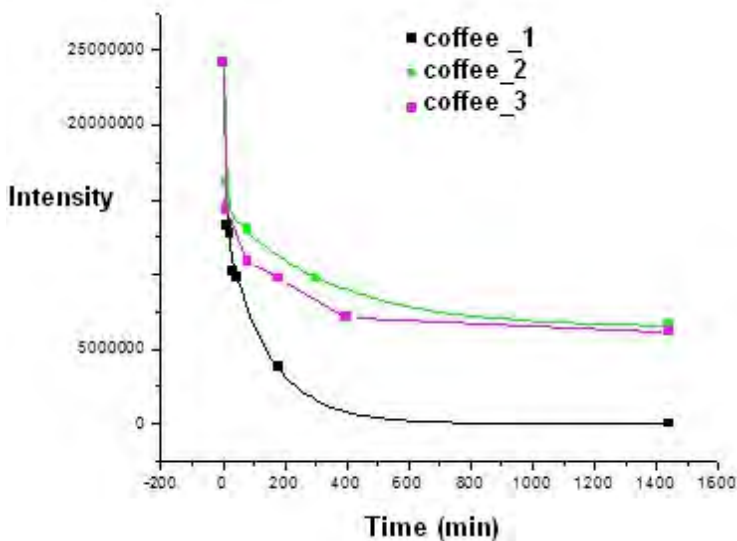


Figure 3. Antioxidant activity vs. time for: coffee_1 - SD dried (black), coffee_2 - FD dried sample 1 (green) , and coffee_3 - FD dried sample 2 (pink)

The results have shown that the FD dried coffee obtained by us has a lower antioxidant activity than SD dried coffee. The lower antioxidant activity of freeze dried coffee can be explained considering the duration of the drying method which is larger for freeze-drying (hours) comparative with the spray-drying (seconds). Similar conclusion was obtained when the antioxidant activity was analyzed as total phenolic content [21].

CONCLUSIONS

The physical properties and the microstructure of soluble coffee were affected by drying methods.

By spray-drying technique it was obtained a product with smooth and spherical shape and large number of smaller particles of about 10 µm diameter.

SD coffee powder has shown smaller free bulk density, higher porosity and higher total antioxidant activity in comparison with FD coffee powder, for the laboratory conditions mentioned in the presented study.

EPR analysis could be a useful method of coffee antioxidant activity evaluation during the drying.

On the basis of physical characteristics (residual moisture, particle size, microscopic structure, bulk porosity) and antioxidant activity we consider spray-drying a good technique which can be used to obtain soluble coffee.

EXPERIMENTAL SECTION

Materials

Coffee solution/liquid was prepared by adding 30 grinded coffee from Firma Tchibo Exclusiv (purchased from local market) to each 100 mL of distilled water. The obtained liquid was heated until it had foamed twice, allowed to settle and than decanted/filtrated. The concentrated solution was used in order to obtain soluble coffee through spray-drying and freeze-drying.

Spray-drying (SD)

SD was carried out in a single stage in the laboratory dryer (Atomizer Mini Spray Dryer BUCHI B-290, Suisse) with co-current drying configuration. Peristaltic pump was used to deliver the feed coffee solution to the atomizer. Ambient air with the flow rate 410 ± 5 L/h was electrical heated. The inlet air temperature was 145 °C. The outlet air temperature was maintained at 100 °C by the adjusted feed flow rate. Product was collected from the outlet chamber and stored in a desiccator at the ambient temperature.

Freeze-drying (FD)

The concentrated coffee solution, with layers of 7 mm placed in Petri dishes, was frozen for 1 hour at -80 °C in the freezer. Than the frozen samples were transferred inside the freeze dryer (ALPHA 1-2 LD_{Plus}, MARTIN CHRIST

Gefriertrocknungsanlagen GmbH, Germany) for a period of 7 hours under the pressure of 0.1 mbar (experiment 1) and 0.045 mbar (experiment 2) and a shelf temperature starting from 20 °C. The condenser temperature was kept to -50 °C. The obtained freeze dried coffee powder was stored in a desiccator at the ambient temperature.

Moisture content

The moisture content (% wet basis) was analyzed based on the gravimetric determination of the mass loss on drying. 1 g of the coffee sample was placed on the dish and heated at 95 °C for 4 h in the hot air oven. The analysis was performed in duplicates, and the mean value was calculated.

Scanning Electron Microscopy (SEM)

SEM was used to examine the shape, the surface morphology and the particles size of coffee powder samples. The equipment used in our research was *Nikon Eclipse E200* from Nikon GmbH Niederlassung Wien, Austria. The used resolution was 40x Binocular.

EPR spectra were recorded with a Bruker EMX spectrometer (Germany), operating in the X-band (9.1GHz – 9.6 GHz) equipped with a computer acquisition system.

REFERENCES

1. GEA Process Technology for Instant Coffee, Available on http://www.gea.com/global/en/binaries/GEA_Process
2. P. Patel, M. P. Patel, A. M. Suthar, *Indian Journal of Science and Technology*, **2009**, 2(10), 44.
3. G.R. Nireesha, L. Divya, C. Sowmya, N. Venkateshan, M. Niranjan Babu, V. Lavakuma, *International Journal of Novel Trends in Pharmaceutical Science*, **2013**, 3(4), 87.
4. C. Ratti, *Handbook of food powders: processes and properties*, **2013**, 57.
5. S. Khalloufi, J.L., Robert, C. Ratti, *Journal of Food Processing Engineering*, **2005**, 28(2), 107.
6. G.A. Reineccius, *Drying Technology*, **2004**, 22(6), 1289.
7. W. Suwelack, D. Kunke, *Process for freeze drying coffee extract*, **2002**, US 6,428,833 B1.

8. M.C. Nicoli, M. Anese, L. Manzocco, C.R. Lerici, *Lebensmittel Wissenschaft und Technology*, **1997**, 30, 292.
9. H. Steinhart, A. Luger, J. Piost, "Antioxidative Effect of Coffee Melanoidins. In Proceedings of the 19th International Scientific Colloque on Coffee", Trieste, Italy, 14–18 March, 2001.
10. A. Farah, C.M. Donangelo, *Brazilian Journal of Plant Physiology*, **2006**, 18, 23.
11. M.D. Del Castillo, J.M. Ames, M.H. Gordon, *Journal of Agricultural Food Chemistry*, **2002**, 50, 3698.
12. E. Nebesny, G. Budryn, *European Food Research and Technology*, **2003**, 217, 157.
13. S. Padma Ishwarya, C. Anandharamakrishnan, *Journal of Food Engineering*, **2015**, 149, 171.
14. A. Ghirişan (Miclăuș), S. Drăgan, V. Miclăuș, *STUDIA Universitatis "Babeş-Bolyai", Chemia*, **2017**, 62(1), 7.
15. G. Kaptay, *International Journal of Pharmaceutics*, **2012**, 430, 253.
16. O.A. Caparino, J. Tang, C.I. Nindo, S.S. Sablani, J.R. Powers, J.K. Fellman, *Journal of Food Engineering*, **2012**, 111, 135.
17. M.K. Krokida, Z.B. Maroulis, G.D. Saravakos, *International Journal of Food Science and Technology*, **2001**, 36, 53.
18. M. Richelle, I. Tavazzi, E. Offord, *Journal of Agriculture Food Chemistry*, **2001**, 49, 3438.
19. E. Nebesny, G. Budryn, *European Food. Research and Technology*, **2003**, 217, 157.
20. J.A. Vignoli, D.G. Bassoli, M.T. Benassi, *Food Chemistry*, **2011**, 124, 863.
21. A. Wilkowska, W. Ambroziak, A. Czyzowska, J. Adamiec, *Polish Journal of Food and Nutrition Sciences*, **2016**, 66(1), 11.

DETERMINATION OF HEAVY METALS AND LEAD-STROMTIUM ISOTOPE CHARACTERIZATION FROM MERLOT SOIL SAMPLES, DEALU BUJORULUI VINEYARD

FLORIN DUMITRU BORA^{a*}, ALINA DONICI^a, ANAMARIA CALUGAR^b,
IOAN VALENTIN PETRESCU MAG^c, EMESE GÁL^d,
CLAUDIU IOAN BUNEA^b

ABSTRACT. Contamination of vineyard soils with heavy-metals has been a worldwide concern, determination of these elements it is important for the wine industry. The aim of this research was to determine the concentration of different heavy metals (Cd, Pb, U, Hg, As, Sr, Co, Cu, Ni and Cr) from vineyard soil on different depths in an area of vineyard cultivation from Dealu Bujorului Galati County. In order to highlight the combination of different sources, natural or anthropogenic of heavy metals the isotopic ratios for $^{206}\text{Pb}/^{207}\text{Pb}$, $^{208}\text{Pb}/^{206}\text{Pb}$, $^{206}\text{Pb}/^{207}\text{Pb}$ and $^{87}\text{Sr}/^{86}\text{Sr}$ from soil were established. The highest concentrations for heavy metals were recorded on the surface, with increasing depth of the soil these concentrations decrease. Regarding of Pb sources (lithogenic or anthropogenic), the average $^{206}\text{Pb}/^{207}\text{Pb}$, $^{208}\text{Pb}/^{206}\text{Pb}$ and $^{206}\text{Pb}/^{204}\text{Pb}$ ratios in soil profile increase horizons followed the order: 1.13526 (0-10 cm $^{206}\text{Pb}/^{207}\text{Pb}$) > 1.13427 (10-20 cm $^{206}\text{Pb}/^{207}\text{Pb}$); 2.12626 (10-20 cm $^{208}\text{Pb}/^{206}\text{Pb}$) > 2.12472 (10-20 cm $^{208}\text{Pb}/^{206}\text{Pb}$) and 17.36201 (10-20 cm $^{206}\text{Pb}/^{204}\text{Pb}$) > 17.36128 (0-10 cm $^{206}\text{Pb}/^{204}\text{Pb}$). Statistically, in the case of $^{206}\text{Pb}/^{207}\text{Pb}$ and $^{208}\text{Pb}/^{206}\text{Pb}$ there are very significant differences between the analyzed variants while $^{206}\text{Pb}/^{204}\text{Pb}$ does not show any differences with in terms of distribution on the depth of the soil profile. Our results confirm that the

^a *Research Station for Viticulture and Enology Targu Bujor, 65 G-ral Eremia Grigorescu, RO-805200, Galați Country Romania*

^b *University of Agricultural Sciences and Veterinary Medicine, Department of Horticulture and Landscaping, 3-5 Mănăștur Street, RO-400372 Cluj-Napoca, Romania*

^c *University of Agricultural Sciences and Veterinary Medicine, Department of Agriculture, 3-5 Mănăștur Street, RO-400372 Cluj-Napoca, Romania*

^d *Babeș-Bolyai University, Faculty of Chemistry and Chemical Engineering, 11 Arany Janos str., RO-400028, Cluj-Napoca, Romania*

* *Corresponding author borafiorindumitru@gmail.com*

$^{207}\text{Pb}/^{206}\text{Pb}$, $^{208}\text{Pb}/^{206}\text{Pb}$, $^{204}\text{Pb}/^{206}\text{Pb}$ and $^{87}\text{Sr}/^{86}\text{Sr}$ isotope ratio can be used to track the geographical origin of wine, discriminate between wine production regions, and be used to characterize wine *terroirs* for forensic purpose.

Keywords: heavy metals, soil profile, $^{207}\text{Pb}/^{206}\text{Pb}$, $^{208}\text{Pb}/^{206}\text{Pb}$, $^{204}\text{Pb}/^{206}\text{Pb}$, $^{87}\text{Sr}/^{86}\text{Sr}$ isotope ratio.

INTRODUCTION

The soil conservation is an important and fundamental factor for sustainable development and preservation, biodiversity and balance of ecosystems. The main sources of different elements in soil are natural background (elements derived from parent rocks) and anthropogenic, which include agrochemicals, amendments, mineral fertilizer, irrigation, sewage sludge and also, the industrial wastes [1, 2]. Nevertheless, the concentration, the distribution and the bioavailability of chemical elements in the environment are influenced mainly by the climatic conditions, soil type, topography, geology, and erosive process [3, 4].

Between anthropic activities, agriculture is the main pollutant and contaminant of soil. Viticulture is an intensive practice, so the phytopharmaceuticals and chemical fertilizers are the main source of elemental pollution [5]. In vineyard areas, the use of fungicide based on Cu in their composition pollute the soil by accumulation in high concentrations in worldwide grapevine areas [6-9]. Vines and other plants have the capacity to tolerate Cu in excess. Plants differ in terms of their capacity to accumulate heavy metals depending on genotype, on the soil conditions and on the microorganism associated to the soil, which play the role of pollutants absorbers [10]. The most of the copper and other applied chemical tends to remain on the surface of soils [11]. Some European countries have banned the use or restricted the amount of copper-based fungicides, in response to environmental concerns over the accumulation of copper in agricultural soils and the potential impact on soil ecology [12].

Lead is an element found in the Earth's crust and soil and may be taken by plants (some species absorbing more than others, especially in certain parts) and grazing animals. The lead is evacuated in the atmosphere by different sources and can get directly into organism within the inspired air, or indirectly, after the depositing on the surface or soil, then water and food [13]. Nickel is an element found in soil and is highly dependent on the content of the parent rock material and climatic conditions, meaning that, in

soil of arid and semiarid regions, its amounts are higher [14]. The total content of Ni showed significant positive correlation with the organic matter from soil surface (0-20 cm depth) which indicate that the organic matter on the first layer of the cultivated soil contribute to Ni retention in the soil [9]. Nickel may be removed by some cultures or by leaching to deeper layer in the soil profile and this could justify the reduction of this element in some areas given its high mobility [15, 16]. Arsenic is a metalloid well-known for its toxicity and it is found in the environment from natural and anthropogenic sources (represented by mining, the use of pesticides in agriculture, industrial and municipal wastes discharging, burning of fossil fuels) [17].

Evaluation of natural abundance isotope ratios provides information on plant type or animal diet (carbon ratios) and geographical origin (lead, strontium, deuterium and oxygen isotopic ratios) [18]. Strontium is found in nature as three abundant isotopes: ^{86}Sr , ^{87}Sr , ^{88}Sr and ^{84}Sr as less abundant isotope [19–20]. Since the content of ^{87}Sr in soil varies with geological age and geographical location, the $^{87}\text{Sr}/^{86}\text{Sr}$ isotopic ratio can be used as a tracer for determining the geographical origin of grapes and wine [21]. Lead is found in nature as four abundant isotopes: ^{206}Pb , ^{207}Pb , ^{208}Pb and ^{204}Pb as less abundant isotope [22]. The Pb isotope of ore deposits and anthropogenic sources has their distinct isotopic ratios or signatures [23]. The Pb isotope ratio did not change in industrial or environmental processing and it's retained its characteristic ratio from source ore [24]. Each geologic substratum of vineyards is liable to have its own Sr isotope composition, which can potentially represent a fingerprint to trace the wine production provenance [25]. The use of $^{87}\text{Sr}/^{86}\text{Sr}$ in tracking wine regional provenances was among the most pioneering application of isotope geology to other sciences [26]. In most of the cases, however, the analytical uncertainty observed in Sr isotopes analyses of wines from literature is larger than most of the soil/rock isotopic variability, giving strong difficulties in matching data of wines with those from geologic substrata of the vineyards. Recently, high precision analytical method for determining $^{87}\text{Sr}/^{86}\text{Sr}$ has been provide enabling then direct comparison between data on wines with those of the pedological and geological substrata [27,28]. Long lived isotope ratios of heavy metals of geological interest, such as $^{87}\text{Sr}/^{86}\text{Sr}$, $^{206}\text{Pb}/^{204}\text{Pb}$, $^{207}\text{Pb}/^{204}\text{Pb}$, $^{208}\text{Pb}/^{204}\text{Pb}$, have in the last decades gained importance in tackling the issues of geographical food traceability as well as in solving issues related with archaeological, environmental, medical and also forensic sciences [29].

The purpose of this study was to determine the elemental composition (Cd, Pb, U, Hg, As, Sr, Co, Cu, Ni and Cr) from vineyard soil, on different depths (0-120cm) using the ICP-MS technique (method approved by

L'Organisation International du Vie et Vin) and also to complete the knowledge of the large-scale distribution of strontium ($^{87}\text{Sr}/^{86}\text{Sr}$) and lead ($^{206}\text{Pb}/^{204}\text{Pb}$, $^{207}\text{Pb}/^{204}\text{Pb}$, $^{208}\text{Pb}/^{204}\text{Pb}$) isotope ratios in soil from Dealu Bujorului Vineyard (Galati county).

RESULTS AND DISCUSSION

Heavy metals content from Merlot soil samples

In Table 1 are summarized the total contents of Cd, Pb, U, Hg, As, Sr, Co, Cu, Ni and Cr on the depth of the soil profile. The mean contents of Cd and Pb were 0.33 ± 0.05 mg/kg and 6.20 ± 0.57 mg/kg, in case of Cd the lowest concentrations were recorded in the surface of the soil profile [0.19 ± 0.02 mg/kg (10-20 cm)], while the highest concentration was recorded on the depth of the soil profile [0.61 ± 0.05 mg/kg (90-100 cm)]. Pb content in soil ranged from [10.46 ± 1.28 mg/kg (10-20 cm)] and [2.61 ± 0.73 mg/kg (110-120 cm)], the highest concentration was recorded on the surface of the soil profile. The results agree with other scientific papers [30] 0.30 mg/kg (Cd), 11.50 mg/kg (Pb); [31] 0.18 mg/kg (Cd) and significantly lower than those obtained by some authors [32] 7.38 mg/kg (Cd), 132.30 mg/kg (Pb) and [31] 36.00 mg/kg (Pb). The U concentration from soil was between [0.51 ± 0.10 mg/kg (0-10 cm)] and [0.25 ± 0.10 mg/kg (110-120 cm)] with an average of 0.35 ± 0.06 mg/kg. Regarding the distribution of U concentration on the depth of the soil profile, it can be observed that with increase of the depth the U concentration from soil decreases, as in the case of Pb. The results agree with Moragues-Quiroga et al. [33] 0.03 mg/kg (U); and significantly lower than those obtained by Saat et al. [34] 2.21 mg/kg (U).

The content of Hg, As Sr and Co found in Dealu Bujorului Vineyard agreed with literature data [33, 35-37]. The average values of these metals 0.076 ± 0.012 mg/kg (Hg), 1.31 ± 0.11 mg/kg (As), 34.44 ± 1.62 mg/kg (Sr) and 3.45 ± 0.25 mg/kg (Co) do not indicate soil pollution in Dealu Bujorului vineyard (Table 1).

In terms of Ni and Cr the highest concentration was recorded in the surface of the soil profile for both metals, Ni [9.17 ± 0.99 mg/kg (0-10 cm); 8.18 ± 1.00 mg/kg (10-20 cm)] and Cr [13.80 ± 1.33 mg/kg (30-40 cm); 13.08 ± 0.83 mg/kg (20-30 cm)] with an average value of 5.61 ± 0.23 mg/kg (Ni) and 10.81 ± 0.72 mg/kg (Cr) (Table 1). The results agree with literature data [30-37].

Concerning Cu concentration in soil, at the surface of the soil profile were recorded the highest concentration [546.01 ± 9.15 mg/kg (0-10 cm); 521.37 ± 4.59 mg/kg (10-20 cm)] with an average value of 371.25 ± 2.01 mg/kg,

these concentrations from far exceed the maximum allowed by the legislation (20 mg/kg). The data demonstrate strong pollution of vineyard soil by copper. Copper concentrations in the topsoil of Dealu Bujorului vineyard was between the values of 546.01 ± 9.15 mg/kg (0-10 cm) and 120.59 ± 1.15 mg/kg (80-90 cm) with an average value of 356.03 ± 4.36 mg/kg. The copper enrichment in different vineyard soil types reflects the period of copper-based pesticide application [39]. We consider the climate and application of elevated volumes of fungicide as the circumstantial factor for the high copper contamination in vineyards soil. Copper concentration in soil is significantly lower than the maximum value reported in literature (1500 mg/kg) [40]. Regarding the distribution of copper concentration on the depth of the soil profile, it can be observed that with increase of the depth the copper concentration from soil decreases. We assume that total copper distribution between vine lines mainly depends on certain technical operations, such as implemented spraying technical operations, foliage removing from midway zones or simply foliage and other organic debris redistribution in horizontal directions by winds, machine wheels, animals and/or humans [39].

The copper sulphate actually are used in all wine counties and also in Bordeaux, according to Mirlean et al. [39] mixture preparation contains: Zn 1309 mg/kg, Pb 95 mg/kg, Cr 19 mg/kg Ni 10 mg/kg and Cd 1.4 mg/kg. Therefore, we considered that copper-based pesticide is the principal source of established soil enrichment by heavy metals. Similar conclusions have reached also some authors in Serbia [32], Brasil [39], Italy [41], Romania [42], France [43] and Spain [44]. The results agree with Alagić et al. [32] 315.00 mg/kg (Cu), Couto et al. [45] 602.23 mg/kg (Cu), Romić et al. [46] 586 mg/kg (Cu), Chaignon et al. [47] 398 586 mg/kg (Cu) and significantly higher than those obtained by Rusjan et al. [48] 88.00 mg/kg (Cu).

Concerning factor which influences the distribution of metals on the soil profile, it can be seen as the depth factor had influenced very significant distribution Cd, Pb, U, As, Sr, Co, Cu, Ni and Cr, in case of Hg distribution on the soil profile depth factor had a lesser influence (Table 1).

Reporting the obtained results [Cd average 0.33 ± 0.05 mg/kg (1 mg/kg M.A.L = (maximum limit allowed); Pb average 5.82 ± 0.75 mg/kg (20 mg/kg M.A.L); Hg average 0.076 ± 0.012 mg/kg (0.1 mg/kg M.A.L); As average 1.31 ± 0.11 mg/kg (1 mg/kg M.A.L); Co average 3.45 ± 0.25 mg/kg (15 mg/kg M.A.L); Ni average 5.61 ± 0.23 mg/kg (1 mg/kg M.A.L) and Cr average 10.81 ± 0.72 mg/kg (30 mg/kg M.A.L)] to national and international legislation we can say that the soil from Dealu Bujorului vineyard falls within the limits set by the law, except the Cu average 356.03 ± 4.36 mg/kg concentration which exceeds this limit (20 mg/kg) (Table 1).

Table 1. Variation of the metal content in Merlot soil samples from Dealu Bujorului Vineyard (mg/kg)

Area	Type of soil	Depth (cm)	Cd	Pb	U	Hg	As	Sr	Co	Cu	Ni	Cr	
													M.A.L.
Dealu Bujorului Vineyard (Merlot plantation)	Normal Values	0-10	0.34±0.07 c	7.52±1.05 b	0.51±0.10 a	0.045±0.013 b	0.44±0.11 f	40.43±0.72 ab	2.66±0.53 de	546.01±50.15 a	9.17±0.99 a	12.62±0.77 ab	
		10-20	0.19±0.02 d	10.46±1.28 a	0.51±0.05 a	0.076±0.019 a	0.39±0.44 f	41.02±2.13 a	2.94±0.94 d	521.37±4.99 b	8.18±1.00 ab	12.02±1.89 b	
		20-30	0.25±0.07 cd	10.29±0.89 a	0.33±0.07 bcde	0.075±0.018 a	0.87±0.08 e	39.10±1.37 abc	3.16±0.16 d	516.10±7.85 bc	7.68±0.68 b	13.06±0.83 ab	
	Alert threshold	0-10	0.27±0.08 cd	9.41±9.26 a	0.35±0.09 bcde	0.064±0.017 ab	1.44±0.19 b	1.28±0.07 bc	39.71±1.52 abc	4.11±0.08 c	510.79±3.35 c	5.31±0.15 cde	13.90±1.33 a
		10-20	0.28±0.08 cd	8.03±0.51 b	0.42±0.07 abc	0.045±0.014 b	1.28±0.07 bc	36.18±1.76 abc	3.16±0.16 d	4.13±0.02 c	320.79±2.84 f	4.45±0.39 defg	12.48±0.44 ab
		20-30	0.18±0.06 d	4.18±0.80 cd	0.40±0.01 abc	0.062±0.012 a	1.38±0.14 b	32.18±1.04 d	4.41±0.13 bc	5.39±0.27 a	367.46±4.73 e	4.17±0.03 efg	9.88±0.39 cd
	Less Susceptible	0-10	0.24±0.07 cd	2.66±0.78 de	0.36±0.06 bcde	0.091±0.004 a	0.99±0.02 de	37.65±1.80 bc	5.39±0.27 a	400.73±1.93 d	5.20±0.10 cdef	3.67±0.93 g	10.53±0.52 c
		10-20	0.53±0.03 ab	3.70±0.88 cde	0.34±0.08 bcde	0.066±0.016 a	2.42±0.10 a	36.70±1.18 c	4.75±0.06 b	319.52±6.05 g	3.67±0.93 g	3.96±0.07 f	10.35±0.75 c
		20-30	0.44±0.05 b	2.76±0.35 de	0.26±0.07 cd	0.066±0.004 a	2.22±0.08 a	37.16±1.55 c	2.33±0.19 e	120.99±1.15 f	3.96±0.07 fg	3.96±0.07 fg	10.35±0.75 c
	Chemozem	0-10	0.61±0.05 a	3.71±0.26 cde	0.28±0.04 cde	0.083±0.007 a	1.47±0.27 b	26.49±2.01 e	2.38±0.38 e	121.18±3.47 i	4.47±0.12 defg	4.47±0.12 defg	7.58±0.55 e
		10-110	0.32±0.04 c	4.50±1.16 c	0.27±0.04 cde	0.070±0.022 ab	1.31±0.03 bc	241.82±1.99 f	2.23±0.11 e	316.28±6.19 g	6.32±1.47 c	6.32±1.47 c	8.76±0.32 de
		110-120	0.33±0.06 c	2.61±0.73 e	0.25±0.10 d	0.085±0.005 a	1.14±0.10 cd	22.81±2.36 f	2.95±0.51 d	213.41±0.31 j	5.35±0.79 cde	5.35±0.79 cde	8.58±0.32 de
	Average	Minimum Values	0.33±0.05	5.82±0.75	0.35±0.06	0.076±0.012	1.31±0.11	34.44±1.62	3.43±0.25	371.75±2.01	5.61±0.23	5.61±0.23	10.81±0.72
		Maximum Values	0.18±0.06	2.61±0.73	0.25±0.10	0.045±0.013	0.44±0.11	21.82±1.99	2.23±0.11	120.99±1.15	3.96±0.07	3.96±0.07	7.66±0.65
		Sig	0.61±0.05	10.40±1.28	0.51±0.10	0.082±0.012	2.42±0.10	41.02±2.13	5.39±0.27	546.01±50.15	9.17±0.99	9.17±0.99	13.90±1.33
Depth	F	16.320	21.062	4.356	2.987	68.951	114.565	54.123	2531.546	21.946	21.946	18.152	
	Sig	***	***	***	**	***	***	***	***	***	***	***	
	[1]	2.20	36.60			10.76±0.01			368.00	62.70	62.70	67.60	
	[2]	3.14±0.03	42.90						293.00	16.67±0.09	16.67±0.09		
	[3]	16.18±0.20	264.90						10.87±5.10	9.00	9.00	27.00	
[4]	26.00	264.90						3.60	165.30	165.30	54.10		
[5]	0.40	7.10							211.40	211.40			

Average value ± standard deviation (n = 3). Different letters are significantly different for $p \leq 0.05$ between depths. The difference between any two values, followed by at least one common letter, is insignificant. Order of the Ministry of Waters, Forests and Environmental Protection No.756/3 November 1997, approving the regulation on the assessment of environmental pollution, Bucharest, Romania; 1997. M.L.A.* (maximum limit allowed) = Normal Values.

$^{206}\text{Pb}/^{207}\text{Pb}$, $^{208}\text{Pb}/^{206}\text{Pb}$, $^{206}\text{Pb}/^{204}\text{Pb}$, $^{87}\text{Sr}/^{86}\text{Sr}$, isotope ratio from Merlot soil samples

The Pb isotope ratio for the selected soil (Table 2) varies in range between 1.13142-1.14205 ($^{206}\text{Pb}/^{207}\text{Pb}$), 2.12065-2.14153 ($^{208}\text{Pb}/^{206}\text{Pb}$) and 17.29604-17.42010 ($^{206}\text{Pb}/^{204}\text{Pb}$) with average 1.13418 ($^{206}\text{Pb}/^{207}\text{Pb}$), 2.12906 ($^{208}\text{Pb}/^{206}\text{Pb}$) and 17.36398 ($^{206}\text{Pb}/^{204}\text{Pb}$). The wide range of isotope ratio obtained suggest that Pb content in the soil is a product of the combination of different sources and not from a sole origin, natural or anthropogenic, and that it has also been accumulating over time since the massive use of Pb in fuel, pain [49]. The $^{206}\text{Pb}/^{207}\text{Pb}$ ratio is most commonly used in environmental studies because it can be determined precisely, and the abundances of these isotopes are relatively important [50]. The isotope ration $^{206}\text{Pb}/^{207}\text{Pb}$ revealed a different behaviour between soil profiles at each sampling site.

Regarding $^{206}\text{Pb}/^{207}\text{Pb}$ isotope ration based on analyses it can be concluded that the vineyard soil from Dealu Bujorului with an average values of 1.13418 $^{206}\text{Pb}/^{207}\text{Pb}$ come from automobile emissions (if $^{206}\text{Pb}/^{207}\text{Pb}=1.1000-1.1400$ [automobile emissions]) [51]. The values of $^{208}\text{Pb}/^{206}\text{Pb}$ and $^{206}\text{Pb}/^{204}\text{Pb}$ isotope ratio are between the ranges from 2.12065 to 2.14153 ($^{208}\text{Pb}/^{206}\text{Pb}$) and 17.29604 to 17.42010 ($^{206}\text{Pb}/^{204}\text{Pb}$) with an average values of 2.12906 ($^{208}\text{Pb}/^{206}\text{Pb}$) and 17.36398 ($^{206}\text{Pb}/^{204}\text{Pb}$). The highest values of $^{208}\text{Pb}/^{206}\text{Pb}$ and $^{206}\text{Pb}/^{204}\text{Pb}$ isotope ratio were registered on the depth of the soil profile from 70-80 cm [2.14153 ($^{208}\text{Pb}/^{206}\text{Pb}$)] followed by 80-90 cm [2.13417 ($^{208}\text{Pb}/^{206}\text{Pb}$)] and values recorded at 50-60 cm [17.42010 ($^{206}\text{Pb}/^{204}\text{Pb}$)] followed by 90-100 cm [17.41431 ($^{206}\text{Pb}/^{204}\text{Pb}$)] and 110-120 cm [17.39252 ($^{206}\text{Pb}/^{204}\text{Pb}$)]. The lowest values of $^{208}\text{Pb}/^{206}\text{Pb}$ and $^{206}\text{Pb}/^{204}\text{Pb}$ isotope ratio were recorded also on the depth of the soil profile 30-40 cm [2.21065 ($^{208}\text{Pb}/^{206}\text{Pb}$)] followed by 110-120 cm [2.12311 ($^{208}\text{Pb}/^{206}\text{Pb}$)], 10-20 cm [2.12472 ($^{208}\text{Pb}/^{206}\text{Pb}$)], 60-70 cm [2.12443 ($^{208}\text{Pb}/^{206}\text{Pb}$)], 90-100 cm [2.12512 ($^{208}\text{Pb}/^{206}\text{Pb}$)], 100-110 [2.12457 ($^{208}\text{Pb}/^{206}\text{Pb}$)].

Regardless of Pb sources (lithogenic or anthropogenic), the average $^{206}\text{Pb}/^{207}\text{Pb}$, $^{208}\text{Pb}/^{206}\text{Pb}$ and $^{206}\text{Pb}/^{204}\text{Pb}$ ration in soil profile horizons followed the order: 1.13526 (0-10 cm $^{206}\text{Pb}/^{207}\text{Pb}$) > 1.13427 (10-20 cm $^{206}\text{Pb}/^{207}\text{Pb}$); 2.12626 (10-20 cm $^{208}\text{Pb}/^{206}\text{Pb}$) > 2.12472 (10-20 cm $^{208}\text{Pb}/^{206}\text{Pb}$) and 17.36201 (10-20 cm $^{206}\text{Pb}/^{204}\text{Pb}$) > 17.36128 (0-10 cm $^{206}\text{Pb}/^{204}\text{Pb}$). Statistically, in the case of $^{206}\text{Pb}/^{207}\text{Pb}$ and $^{208}\text{Pb}/^{206}\text{Pb}$ there are very significant differences between the analyzed variants while $^{206}\text{Pb}/^{204}\text{Pb}$ does not show any differences with in terms of distribution on the depth of the soil profile.

These results demonstrate that Pb isotopic ratios were derived mainly from weathered parent material, except the $^{206}\text{Pb}/^{207}\text{Pb}$ uppermost horizons of soil profiles which come from automobile emissions. The more radiogenic $^{208}\text{Pb}/^{206}\text{Pb}$ and $^{206}\text{Pb}/^{207}\text{Pb}$ ratio in soil probably reflects the Pb derived from

weathered bedrock, and the isotopic composition of Pb is mostly influenced by the decay of U and Th content in the soil, weathering processes and original rock age, which provide a fingerprint used for different forensic and archeological purposes [52].

Concerning $^{87}\text{Sr}/^{86}\text{Sr}$ isotope ratio the values are between the ranges from 0.72316 to 0.72701, with an average value of 0.72514. The highest values were registered on the depth of the soil surface profile 60-70 cm (0.72701) followed by values recorded at 40-50 cm (0.72653) and 50-60 cm (0.72616), the lowest value of $^{87}\text{Sr}/^{86}\text{Sr}$ isotope ratio was registered on the depth of the soil at 70-80 cm (0.722316) (Table 2). In this case, these are no significant differences between the $^{87}\text{Sr}/^{86}\text{Sr}$ isotope ratio. These obtained values of $^{87}\text{Sr}/^{86}\text{Sr}$ isotope ratio can be attributed to a larger proportion of radiogenic (K and Rb rich) mineral due to the weathering of the most weatherable mineral, i.e. Ca-plagioclase, which is promoted by a strong decrease of the soil pH [53].

CONCLUSIONS

In this work the heavy metals concentration from Merlot plantation was studied in order to highlight the heavy metals composition of soil. In case of Cd (1 mg/kg), Pb (20 mg/kg), Hg (0.1 mg/kg), As (5 mg/L), Co (15 mg/kg), Ni (20 mg/kg) and Cr (30 mg/kg) metals in analysed soil samples were under Maximum Permissible Limits (MPL). Cu concentration in the soil exceeds the maximum admissible limit (20 mg/kg) having the average value of 371.25 mg/kg, this value is a common one for vineyards soils.

Regardless of Pb sources (lithogenic or anthropogenic), the average $^{206}\text{Pb}/^{207}\text{Pb}$, $^{208}\text{Pb}/^{206}\text{Pb}$ and $^{206}\text{Pb}/^{204}\text{Pb}$ ration in soil profile horizons followed the order: 1.13526 (0-10 cm $^{206}\text{Pb}/^{207}\text{Pb}$) > 1.13427 (10-20 cm $^{206}\text{Pb}/^{207}\text{Pb}$); 2.12626 (10-20 cm $^{208}\text{Pb}/^{206}\text{Pb}$) > 2.12472 (10-20 cm $^{208}\text{Pb}/^{206}\text{Pb}$) and 17.36201 (10-20 cm $^{206}\text{Pb}/^{204}\text{Pb}$) > 17.36128 (0-10 cm $^{206}\text{Pb}/^{204}\text{Pb}$). Statistically, in the case of $^{206}\text{Pb}/^{207}\text{Pb}$ and $^{208}\text{Pb}/^{206}\text{Pb}$ there are very significant differences between the analyzed variants while $^{206}\text{Pb}/^{204}\text{Pb}$ does not show any differences with in terms of distribution on the depth of the soil profile.

Our results confirm that the $^{207}\text{Pb}/^{206}\text{Pb}$, $^{208}\text{Pb}/^{206}\text{Pb}$, $^{204}\text{Pb}/^{206}\text{Pb}$ and $^{87}\text{Sr}/^{86}\text{Sr}$ isotope ratio can be used to track the geographical origin of wine, discriminate between wine production regions, and be used to characterize wine *terroirs* for forensic purpose.

Table 2. The $^{206}\text{Pb}/^{207}\text{Pb}$, $^{208}\text{Pb}/^{206}\text{Pb}$, $^{206}\text{Pb}/^{204}\text{Pb}$, $^{87}\text{Sr}/^{86}\text{Sr}$, isotope ratios obtained from soil samples on Dealu Bujorului Vineyard

Area	Type of soil	Depth (cm)	$^{206}\text{Pb}/^{207}\text{Pb}$	SD	RSD (%)	$^{208}\text{Pb}/^{206}\text{Pb}$	SD	RSD (%)	$^{206}\text{Pb}/^{204}\text{Pb}$	SD	RSD (%)	$^{87}\text{Sr}/^{86}\text{Sr}$	SD	RSD (%)	Pb (mg/kg)	Sr (mg/kg)
Dealu Bujorului Vineyard (Mielot plantation)	Chemozem	0-10	1.13526 b	0.00081	0.07094	2.12625 cde	0.00450	0.21164	17.36128 ab	0.00372	0.02144	0.72402 a	0.00127	0.7510	7.52±1.05 b	40.43±0.72 ab
		10-20	1.13427 bc	0.00179	0.15741	2.12472 de	0.00245	0.11508	17.36201 ab	0.04304	0.24790	0.72531 a	0.00300	0.41403	10.46±1.28 a	41.02±2.13 a
		20-30	1.13367 bcd	0.00244	0.19737	2.13431 bcd	0.00143	0.06723	17.36131 ab	0.10953	0.66295	0.72526 a	0.00203	0.28009	10.25±0.89 a	39.12±1.37 abc
		30-40	1.13514 b	0.00267	0.23493	2.12065 e	0.00664	0.31739	17.36118 ab	0.04951	0.28516	0.72420 a	0.00205	0.28206	9.41±0.26 a	35.71±1.52 abc
		40-50	1.13142 d	0.00114	0.10114	2.13304 bc	0.00231	0.10842	17.36735 ab	0.09673	0.55696	0.72653 a	0.00522	0.71860	8.03±0.51 b	36.18±1.76 abc
		50-60	1.13259 bcd	0.00048	0.04237	2.13010 bcd	0.00629	0.29552	17.42010 a	0.03343	0.19188	0.72616 a	0.00655	0.98984	4.19±0.89 cd	32.18±1.04 d
		60-70	1.14205 a	0.00051	0.04482	2.12443 de	0.00118	0.05573	17.29604 b	0.07263	0.41983	0.72701 a	0.00673	0.92568	2.66±0.78 de	37.65±1.90 bc
		70-80	1.13260 bcd	0.00016	0.01976	2.14153 a	0.00521	0.24325	17.33670 ab	0.03654	0.42661	0.72316 a	0.00260	0.35985	3.70±0.66 cde	36.70±1.18 c
		80-90	1.13375 bcd	0.00132	0.11695	2.13417 b	0.00153	0.07163	17.34712 ab	0.04841	0.27936	0.72498 a	0.00218	0.30032	2.76±0.35 de	37.16±1.95 c
		90-100	1.13330 bcd	0.00149	0.13186	2.12512 de	0.00264	0.12429	17.41431 a	0.10703	0.66160	0.72511 a	0.00353	0.48734	3.71±0.26 cde	26.49±2.01 e
		100-110	1.13222 cd	0.00040	0.03513	2.12457 de	0.00037	0.01750	17.34786 ab	0.03338	0.19243	0.72451 a	0.00227	0.31268	4.50±1.16 c	21.82±1.99 f
		110-120	1.13354 bcd	0.00165	0.14682	2.12978 bcd	0.00465	0.21854	17.39232 a	0.02353	0.13528	0.72541 a	0.00360	0.69581	2.61±0.73 e	22.81±2.38 f
Average	1.13418	0.00122	0.10775	2.12906	0.00327	0.15248	17.36398	0.03855	0.22211	0.72514	0.00293	0.40245	5.62±0.75	34.44±1.62		
Minimum Values	1.13142	0.00016	0.01376	2.12065	0.00037	0.01750	17.29604	0.00372	0.02144	0.72316	0.00127	0.28584	2.61±0.73	21.82±1.99		
Maximum Values	1.14205	0.00267	0.23493	2.14153	0.00664	0.31739	17.42010	0.09673	0.55696	0.72701	0.00673	0.92568	10.46±1.28	41.02±2.13		
Sig.																
[6]			1.17190	0.00004		2.09543	0.00013		18.31684	0.00160				9.00		
Tyszka et al. [88]			1.17300	0.01400		2.09500	0.01700							36.00		
Ayuso et al. [89]			1.19550						18.67900			0.72338		11.00		1.74
des Santos et al. [91]			1.17000	0.05000					17.96000	0.86000				13.55		
Reza et al. [92]			1.18390			2.46240						0.71008		6.20		
Sherman et al. [93]			0.84390			2.06200										
Vorster et al. [94]												0.71270				

Average value ± standard deviation (n = 3). Romans letters represent the significance of the variety difference (p ≤ 0.05). The difference between any two values, followed by at least one common letter, is insignificant. SD-standard deviation, RSD %-relative standard deviation. in = insignificant.

EXPERIMENTAL SECTION

Study area

Soil samples were harvested from Dealu Bujorului vineyard (45°52'10" N, 27°55'8"E), the scattered spreading territory of this vineyard corresponds almost entirely to the geographical subunit known as Colinele Covurluiului, in whose area is also the Dealu Bujorului vineyard. The vineyard is crossed by the parallel 46° latitude north, intersected by the 28° longitude meridian. Dealu Bujorului vineyard belongs to Galați country. The specificity of the transition area is highlighted by the predominance of deposits of clays and sands. Versants were made from clay deposits and sandy sands.

Soil sample collection

Soil sampling was carried out on the depth of the soil profile (0-10 cm, 10-20 cm, 20-30 cm, 30-40 cm, 40-50 cm, 50-60 cm, 60-70 cm, 70-80 cm, 80-90 cm, 90-100 cm, 100-110 cm and 110-120 cm). Soil samples were collected using stainless steel shovels and were stored in individual black plastic bags (darkness). All samples were taken in triplicates from the defined experimental plot. Soil samples have been brought first to sand-size material (< 2 mm) using a jaw crusher then mechanically split to obtain a representative samples and eventually pulverized to powder-size, grain-size smaller than 100 μ (< 400 mesh), using a ball mill. Agate ball mill is used in place of any other pulverization metal device to avoid possible trace element contamination [54]. Soil samples before splitting and pulverisation have been dried at 60 °C.

Reagents and solutions

Ten elements (Cd, Pb, U, Hg, As, Sr, Co, Cu, Ni and Cr) were determined in order to assess their ability to discriminate wines by geographical origin. The analysis was made using multielement analysis and ICP-MS technique, after an appropriate dilution, using external standard calibration method. The calibration was performed using XXICertiPUR multielement standard, and from individual standard solution of Cr and Hg. The working standards and the control sample were prepared daily from the intermediate standards that were prepared from the stock solution. The intermediate solutions stored in polyethylene bottles and glassware was cleaned by soaking in 10% v/v HNO₃ for 24 hours and rinsing at least ten times with ultrapure water (18.2 M Ω cm⁻¹ ultrapure water-Types 1). The

accuracy of the methods was evaluated by replicate analyses of fortified samples (10 µL-10 mL concentrations) and the obtained values ranged between 0.8-13.1 percent, depending on the element. The global recovery for each element was estimated and the obtained values were between 84.6-100.9% [21].

For quality control purpose, blanks and triplicates samples ($n = 3$) were analyzed during the procedure. The variation coefficient was under 5% and detection limits (ppb) were determined by the calibration curve method. Limit of detection (LoD) and Limit of quantification (LoQ) limits were calculated according to the next mathematical formulas: $LoD = 3SD/s$ and $LoQ = 10 SD/s$ (SD = estimation of the standard deviation of the regression line; s = slope of the calibration curve).

Table 3. Instrumental conditions for the determination of each element (ICP-MS technique)

Element	Correlation coefficient	LoD* (µg/L)	LoQ*** (µg/L)	BEC** (µg/L)
Cd	0.9999	0.0202	0.0673	0.027
U	0.9999	0.0253	0.0842	0.005
As	0.9999	0.2335	0.7776	0.538
Co	0.9999	0.0365	0.1215	0.152
Ni	0.9999	0.0591	0.1968	0.091
Pb	0.9999	0.0003	0.0010	0.002
Hg	0.9999	0.0417	0.1379	0.128
Sr	0.9999	0.1434	0.4775	0.955
Cu	0.9999	0.0402	0.1339	0.237
Cr	0.9999	1.6630	5.5378	0.636

*Detection limit; **Background equivalent concentration; ***Quantification limit.

For calibration and also to verify the achieved accuracy and precision, ten NIST-SRM 987 and NIST-SRM 982 analysis results were pooled together with the calculated relative standard deviation presented in Table 4. Based on the obtained results, it was verified that, applying quadrupole ICP-MS, relative standard deviation and reproducibility of approximately 0.5% for $^{87}\text{Sr}/^{86}\text{Sr}$, $^{206}\text{Pb}/^{207}\text{Pb}$ and $^{208}\text{Pb}/^{206}\text{Pb}$ are feasible. The results were in agreement with those reported by [21, 52].

Table 4. Lead isotopic ration and Lead isotopic ration determination precision and accuracy based on the NIST SRM 982 (Lead) NIST SRM 987 (Strontium) (n=10)

Replicate	$^{207}\text{Pb}/^{206}\text{Pb}$ (a)	RSD (%)	$^{208}\text{Pb}/^{206}\text{Pb}$ (b)	RSD (%)	$^{204}\text{Pb}/^{206}\text{Pb}$ (c)	RSD (%)	$^{87}\text{Sr}/^{86}\text{Sr}$ (d)	RSD (%)
1	0.46483	0.51	0.99891	0.67	0.00271	0.32	0.70493	0.31
2	0.47891	0.48	0.99452	0.61	0.00272	0.41	0.72046	0.45
3	0.46978	0.32	0.99794	0.55	0.00275	0.28	0.70325	0.63
4	0.47123	0.64	0.99688	0.64	0.00273	0.51	0.70634	0.48
5	0.46987	0.56	0.99726	0.48	0.00246	0.14	0.71478	0.36
6	0.46154	0.37	0.99647	0.56	0.00258	0.39	0.71245	0.59
7	0.47362	0.70	0.99969	0.34	0.00279	0.47	0.70987	0.46
8	0.45641	0.43	0.99744	0.58	0.00278	0.51	0.72326	0.42
9	0.41562	0.36	0.99576	0.59	0.00273	0.49	0.70845	0.68
10	0.45612	0.45	0.99874	0.61	0.00278	0.36	0.10789	0.47
Average	0.46179	0.48	0.99736	0.56	0.00270	0.41	0.71117	0.49

^aCertified value= $^{207}\text{Pb}/^{206}\text{Pb}$ (0.46707±0.00020);

^bCertified value= $^{208}\text{Pb}/^{206}\text{Pb}$ (1.00016±0.00036);

^cCertified value= $^{204}\text{Pb}/^{206}\text{Pb}$ (0.027219±0.00027);

^dCertified value= $^{87}\text{Sr}/^{86}\text{Sr}$ (0.71034±0.00026); RSD (%) = relative standard deviation.

Sample preparation for determination of heavy metals and isotopic ration from soil using ICP-MS

For the determination of heavy metals from soils samples were used an amount of 0.5 g soil and adjust 8 mL (7 mL HNO₃ 65%+1 mL H₂O₂) were placed in a clean Teflon digestion vessel, after 15-30 minutes the mineralization was performed using a microwave system Milestone START D Microwave Digestion System set in three steps: step I (time 10 min., temperature 220°C), step II (time 15 min., temperature 220°C) and step III (time 60 min., ventilation - temperature 35°C). After mineralization, samples were filtered through a 0.45 mm filter and brought to a volume of 50 mL. The Pb and Sr isotope ration in the analysed soil samples ($^{206}\text{Pb}/^{207}\text{Pb}$, $^{208}\text{Pb}/^{206}\text{Pb}$, $^{206}\text{Pb}/^{204}\text{Pb}$, $^{87}\text{Sr}/^{86}\text{Sr}$) were determined according to the methodology indicated by Mihaljevič *et al.* [51]; Geana *et al.* [21].

In order to confirm the best chosen conditions for soil digestion standard additions for checking accuracy of the microwave digestion and recoveries were calculated (Table 5). The digestion seemed visually completed in all of the combinations, but the spiked recoveries showed significant differences for total elements content ($p = 0.005$).

Table 5. Standard additions for checking accuracy of the microwave digestion ICP-MS method (n = 3)

Element	Certified Concentration (mg/kg)	Measured Concentration (mg/kg)
Cd	0.371±0.002	0.369±0.006
U	3.15±0.05	3.17±0.03
As	10.50±0.30	10.26±0.18
Co	130.00±9.00	129.32±0.36
Ni	85.00±2.00	83.65±1.89
Pb	0.00173±0.00001	0.00169±0.0002
Hg	0.90±0.20	0.91±0.21
Sr	239.00±6.00	238.02±1.56
Cu	33.90±0.50	33.96±0.53
Cr	130.00±9.00	130.15±0.78

Instrumentation

The determination of metals was performed on mass spectrometer with inductively coupled plasma, (ICP-MS) iCAP Q Thermo scientific model, based polyatomic species before they reach the quadrupole mass spectrometer, using a PFA micro flow concentric nebulizer. The argon used was of 99.99% purity (Messer, Austria). The instrument was daily optimized to give maximum sensitivity for M^+ ions and the double ionization and oxides monitored by the means of the ratios between Ba^{2+}/Ba^+ and Ce^{2+}/CeO^+ , respectively, these always being less than 2%. The experimental conditions were: argon flow on nebulizer (0.82 L/min.), auxiliary gas flow 0.80 L/min., argon flow in plasma 15 L/min., lens voltage 7.30 V; RF power in plasma 1100 W, spray chamber temperature ($2.50 \pm 1.00^\circ C$). Accuracy was calculated for the elements taken into consideration (0.5-5.0%).

Statistical analysis

The statistical interpretation of the results was performed using the Duncan test, SPSS Version 24 (SPSS Inc., Chicago, IL., USA). The statistical processing of the results was primarily performed in order to calculate the following statistical parameters: average and standard deviation. This data was interpreted with the analysis of variance (ANOVA) and the average separation was performed with the DUNCAN test at $p \leq 0.05$.

ACKNOWLEDGMENTS

This paper was published under the frame of the Romanian Ministry of Agriculture and Rural Development, project ADER no. 14.2.2. “Quantitative studies on assessment and monitoring contaminants, on the chain of viticulture and winemaking to minimize the amount of pesticides and heavy metals as principal pollutants”.

REFERENCES

1. Li, J.L., He, M., Han, W., Gu, Y.F., *Journal of Hazardous Materials*, **2009**, *164*, 976-981.
2. L.R.F. Alleoni, R.B. Borba, O.A. Camargo, *Topicos em Ciencia do Solo*, **2005**, *4*, 1-42.
3. J.F.G.P. Ramalho, N.M.B. Amaral Sobrinho, A.C.X. Velloso, *Pesquisa Agropecuaria Brasileira*, **2000**, *35*, 1289-1303.
4. A. Kabata-Pendias, “Trace elements in soils and plants”. 4th ed. Boca Raton: Chemical Rubber Company Press, **2011**.
5. A. Facchinelli, E. Sacchi, L. Mallen, *Environmental Pollution*, **2001**, *114* (3), 313-324.
6. M.C. Ramos, M. L´opez-Acevedo, *Advances in Environmental Research*, **2004**, *8* (3-4), 687-696.
7. M. Kom´arek, E. ˇCadek, V. Chrastn´y, F. Bordas, J. Bollinger, *Environment International*, **2010**, *36* (1), 138-151.
8. G.C.G. dos Santos, G.S. Valladares, C.A. Abreu, O.A. de Camargo, C.R. Grego, *Applied and Environmental Soil Science*, **2013**, Article ID790795, 1-10.
9. W. Preston, Y.J.A.B. da Silva, C.W.A. do Nascimento, K.P.V. da Cunha, D.J. Silva, H.A. Ferreira, *Geoderma Regional*, **2016**, *7*, 357-365.
10. C. Nicula, A. Peter, L. Mihaly-Cozmuta, A. Mihaly-Cozmuta, *Carpathian Journal of Food Science and Technology*, **2013**, *5* (1-2), 1-8.
11. G.R. Nachtigall, R.C. Nogueirol, L.R.F. Alleoni, M.A. Cambri, *Brazilian Archives of Biology and Technology*, **2007**, *50* (6), 941-948.
12. Q-Y. Wanga, D-M. Zhoua, L. Canga, *Soil Biology and Biochemistry*, **2009**, *41*, 1504-1509.
13. L. Bretan, O. Ketney, F. Boltea, *Carpathian Journal of Food Science and Technology*, **2010**, *2* (2), 8-12.
14. A. Kabata-Pendias, H. Kabata, “Trace elements in soils and plants”, 3rd edition CRC Press, Boca Raton, **2001**.
15. V. Antoniadis, C.D. Tsadilas, *Applied Geochemistry*, **2007**, *22*, 2375-2380.
16. E.V. Mellis, M.P. Cruz, J.C. Casagrande, *Scientia Agricola*, **2004**, *61* (2), 190-195.

17. M. Senila, T. Kotsev, E. Levei, M. Roman, V. Mladenov, Z. Cholakova, L. Senila, *STUDIA UBB CHEMIA LXI*, **2016**, 3, Tom II, 333-344.
18. S. Kelly, K. Heaton, J. Hoogewerff, *Trends in Science and Technology*, **2005**, 16, 555–567.
19. M. Berglund, M.E. Wieser, *Pure and Applied Chemistry*, **2011**, 83 (2), 397–410.
20. P. Martins, M. Madeira, F. Monteiro, *OIV*, **2013**, 48 (1), 21–29.
21. E.I. Geana, A. Marinescu, A.M. Iordache, C. Sandru, R.E. Ionete, C. Bala, *Food Analytical Methods*, **2017**, 10 (1), 63-73.
22. K.J.R. Rossman, P. D. P. Taylor, *International Union of Pure and Applied Chemistry*, **1998**, 70 (1), 217–235.
23. H. Cheng, Y. Hu, *Environmental Pollution*, **2010**, 158 (5), 1134-1146.
24. W.U. Ault, R.G. Senechal, W.E. Erlebach, *Environmental Science and Technology*, **1970**, 4, 305-313.
25. S. Marchionni, A. Bucciatti, A. Bollati, *Food Chemistry*, **2016**, 190, 777-785.
26. R.D. Di Paola-Naranjo, M. V. Baroni, N. S. Podio, *Journal of Agricultural and Food Chemistry*, **2011**, 59, 7854-7865.
27. M.R. Mercurio, E. Grilli, P. Odierna, V. Morra, T. Prohaska, E. Coppola, C. Grifa, A. Buondonno, A. Langella, *Geoderma*, **2014**, 230-231, 64-78.
28. C. Baschieri, L. Bertacchini, D. Bertelli, M. Cocchi, A. Marchetti, D. Manzini, G. Papotti, S. Sighinolfi, *Food Chemistry*, **2015**, 173, 557-563.
29. S. Voerkeluis, G.D. Lorenz, S. Rummel, C.R. Quéte, G. Heiss, M. Baxter, C. Brach-Papa, P. Deters-Itzelberger, S. Hoelzl, J. Hoogewerff, E. Ponzevera, M. van Bockstaele, H. Ueckermann, *Food Chemistry*, **2010**, 118, 933-940.
30. E. Mahmoudabadi, F. Sarmadian, R.N. Moghaddam, *International Journal of Environmental and Science Technology*, **2015**, 12 (10), 3283-3298.
31. F. Curran-Cournane, G. Lear, L. Schwendenmann, J. Khin, *Soil Research*, **2015**, 53, 306-315.
32. S.Č. Alagić, D.B. Tošić, M.D. Dimitrijević, M.A. Antonijević, M.M. Nujkic, *Environmental Science and Pollution Research*, **2014**, 22 (9), 7155-7175.
33. C. Moragues-Quiroga, J. Juilleret, L. Gourdol, E. Pelt, T. Perrone, A. Aubert, G. Morvan, F. Chabaux, A. Legout, P. Stille, C. Hissler, *Catena*, **2017**, 149 (1), 185-198.
34. A. Saat, A.S. Kamsani, W.N.A.N. Kamri, N.H.M. Talib, A.K. Wood, Z. Hamzah, *AIP Conference Proceeding*, **2015**, 1659 (1), 1-6.
35. H. Kailing, S. Zehanf, H. Yuanan Z. Xiangying; Y., Zhiqiang; C., Hefa, *Environmental Science and Pollution Research*, **2017**, 24, 9387-9398.
36. M. Laghlimi, *European Journal of Scientific Research*, **2015**, 129 (2), 167-178.
37. R.T. Ottesen, M. Birke, T.E. Finne, et al., *Applied Geochemistry*, **2013**, 33, 1-12.
38. M. Çolak, *Journal of Environment and Earth Science*, **2012**, 67, 695-712.
39. M. Mirlean, A. Roisenberg, J.O. Chies, *Environmental Pollution*, **2007**, 149, 10-17.
40. L.M. Flores-Veles, J. Ducaroir, A. M. Jaunet, M. Robert, *European Journal of Soil Science*, **1996**, 47, 523-532.

41. F. Pinamonti, G. Nicolini, A. Dalpiaz, et al., *Communications in Soil Science and Plant Analysis*, **1999**, *30*, 1531-1549.
42. F.D. Bora, C.I. Bunea, T. Rusu, et al., *Chemistry Central*, **2015**, *9*, 1-13.
43. E.I.B. Chopin, B. Marin, R. Mkougafoko, et al., *Environmental Pollution*, **2008**, *156*, 1092-1098.
44. S. Bravo, J.A. Amorós, C. Pérez-de-los-Reyes, et al., *Journal of Geochemical Exploration*, **2015**, *173*, 79-83.
45. R.R. Couto, L. Benedet, J.J. Comin, et al., *Environmental Earth Sciences*, **2014**, *73* (10), 6379-6386.
46. M. Romić, D. Romić, G. Ondrašek, *Agriculturae Conspectus Scientificus*, **2004**, 2-3, 35-41.
47. V. Chaignon, I. Sanchez-Neira, P. Herrmann, et al., *Environmental Pollution*, **2003**, *123*, 229-238.
48. D. Rusjan, M. Strlič, D. Pucko, et al., *Geoderma*, **2006**, *136*, 930-936.
49. I. Galušková, M. Mihaljevič, L. Borůvka, et al., *Journal of Geochemical Exploration*, **2014**, *147*, 215-221.
50. M. Komárek, V. Ettler, V. Chrastny, et al., *Environmental International*, **2008**, *34*, 562-577.
51. M. Mihaljevič, V. Ettler, O. Šebek, et al., *Journal of Geochemical Exploration*, **2006**, *88*, 130-133.
52. C.M.S. Almeida, A.C. Almeida, M.L.D.P. Godoy, et al., *Journal of the Brazilian Chemical Society*, **2016**, *27* (6), 1-6.
53. T. Drouet, J. Herbauts, W. Gruber et al., *European Journal of Soil Science*, **2007**, *58*, 302-319.
54. A. Takamasa, S. Nakai, *Geochemical Journal*, **2009**, *43*, 389-394.

MINERALOGICAL AND CHEMICAL CHARACTERIZATION OF THE SOIL FROM BÂRZAVA RIVER AREA

DELIA PIRȘAN^a, ANAMARIA TOROK^b, CLAUDIU TĂNĂSELIA^b,
PAULA PODEA^c

ABSTRACT Mineralogical and chemical characterization of soils is important in for the use of soils as agricultural land. The soil from downstream Bârzava River was characterized and existing geological features of this soil were presented and correlate with the size surfaces. pH measurements of soils samples collected from three different locations and from two different depths were performed. The soil samples were also analysed in order to assess the major and trace elements content. It is known that the pH and heavy metal concentrations are vital factors for plant growth and the obtained results could be use in future for elaboration of some soil bioremediation techniques.

Keywords: soil geological features, acidity control, metal concentration

INTRODUCTION

Acid soils occupy approximately 30% of the world's land area and restrain global agricultural production¹. Numerous factors can contribute to soil acidification, such as large inputs of inorganic fertilizers, high rainfall, acid deposition and greenhouse gas². As the concentration of H⁺ in the soil increases, it can inhibit root growth³, disrupt the functions of the plasma membrane⁴, cell wall⁵, or increase the Al³⁺ toxic levels⁶. Deficient levels of calcium (Ca), magnesium (Mg) and phosphorus (P) are also frequent under low pH conditions.

^a Technical University of Cluj-Napoca, Faculty of Materials and Environmental Engineering, Bd. Muncii Str., No. 103-105, RO-40064, Cluj-Napoca, Romania

^b INCDO-INOE 2000 Research Institute for Analytical Instrumentation ICIA, 67 Donath Str., RO-400293 Cluj-Napoca, Romania

^c Universitatea Babeș-Bolyai, Facultatea de Chimie și Inginerie Chimică, Kogălniceanu Str., No. 1, RO-400084, Cluj-Napoca, Romania

*Corresponding author: delia_pirsan@yahoo.com

Soil pH is widely accepted as a dominant factor that regulates soil nutrient bioavailability, vegetation community structure, plant primary productivity, and a range of soil processes including soil microbial community structure and activity⁷.

All the soil properties and the value of the soil pH can widely differ in reliance on soil type, topography, climate, vegetation, and anthropogenic activity, because all these factors influence the spatial variability of the observed soil types⁸. The value of soil pH is directly influenced by all five soil-forming factors (parent rock, climatic conditions, organisms, topography, and time) and further the value of soil pH is dependent on the season influence, way of management, tested soil horizon, soil water contents, and time limit of sampling for analysis⁹. In literature there are only some few studies regarding the correlation between soil acidity and agricultural plant cultures cultivated in Romania. Some studies and researches at national level have pointed out that there are relations of interdependence between plant cultivation technologies, the environment, the level of economic development and the quality of life^{10,11,12,13a,b,14}. Anthropogenic metals and metalloids in soils represent a potential risk for the environment. Accumulation of the heavy metals in agricultural soils and water resources poses a great threat for the living organism as well for the human health (due to high risk of their entry into food chain)¹⁵. Prolonged consumption of contaminated vegetables and cereals can lead to the disruption of numerous biological and biochemical processes in the human body¹⁶.

Taking into account all these, our paper presents eco-pedological research in the area of the Bârzava River, Caraș-Severin County, Romania, from a soil chemistry perspective, aiming at establishing improvement measures. The focus has been on soils characterization and determination of acidity and metal concentrations of soils samples. The characterization of soils, from this area, is important for the future studies regarding soils bioremediation.

RESULTS AND DISCUSSION

The study focussed on the lands downstream Bârzava River, Caraș-Severin County, Romania. The main soil types identified in the studied area, where soils with specific features have developed in close relationship with the variety of geomorphologic factors determining the existence of diversified relief units, of geolitic and hydrologic factors, and of different anthropogenic factors. Six soil samples were collected from three different locations in

Bârzava river area, two different samples (from 0-20 cm and 20-40 cm) from each location (Voiteni, Partoș, Banloc-Livezile) Samples were codified as A, B, C, D, E, F. (A soil sample from Banloc-Livezile pump station area (0-20 cm); B. soil sample from Partoș rice plantation area (0-20 cm); C. soil sample from Voiteni Farm of USAMVBT (0-20 cm); D. soil sample from wheat plantation area from Voiteni Farm of USAMVBT (20-40 cm); E. soil sample from Banloc-Livezile pump station area (20-40 cm); F soil sample from Partoș rice plantation area (20-40 cm)). Samples were mineralogical and chemical characterized, acidity and metal concentrations were determined.

Bârzava River is a river of 166 km long in Caraș-Severin County situated in south-west part of Romania. Location coordinates are 45°17'59"N 20°38'46"E.

In the low plain downstream Bârzava River, the soil type is gleic eutricambosoil, moderately gleized, moderately decarbonized (balticalcaric), medium sandy clay/medium clay, developed on medium fluvial carbonate materials.

Soil from downstream Bârzava River was characterized and main features of this soil were presented in Table 1.

The soil horizon or pedogenetic horizon is a layer approximately parallel to the soil surface, which has a number of properties resulting from the soil formation process, properties that differ from those of the above or underlying strata. The soil horizon is meant a component layer of the profile, characterized by the entire mass of the same properties (color, texture, structure, etc.). The Ao ocric horizon is a too bright or too bioaccumulative horizon in organic matter to be molluscic or shady, or which becomes massive and harsh during periods of drought. The AB horizon is a transition horizon between A and B, with horizon A properties and rock fragments, which are at least 30% altered. The Bvg2 horizon is a cambic surface horizon (change-over, modification), also known as the horizon of alteration of the parental material in situ, g2 signifies the degree of gleizing-weakness. BCg2 horizon is a transition horizon between B and C horizon, with the characters of the supracent B horizon and the underlying C being partially expressed, with a glearing degree (g2). Ckg3 horizon is underlying material, having a moderate (g3) degree of accumulation of carbonates. The Ckg4 horizon is underlying material, with a high degree (g4) of carbonate accumulations.

A moderate humus supply in the first 50 cm of soil and a low nitrogen level between 0-24 cm was observed. Also, highly acid soil between 43-64 cm, moderately acidic zone between 0-43 cm and 64-123 cm and low alkaline zone between depth of 123 and 165 cm was observed.

Table 1. Main soil features downstream Bârzava, Caraș-Severin County, Romania

Horizon	Ap	Ao	AB	Bvg2	BCg2	Ckg3	Ckg4
Depth (cm)	0-24	-43	-64	-96	-123	-148	-165
Coarse sand (2.0-0.2 mm) (%)	7.3	1.2	1.3	3.6	2.9	4.7	4.7
Fine sand (0.2-0.02 mm) (%)	60.5	60.8	58.3	53.5	59.9	69.8	73.4
Dust (0.02-0.002 mm) (%)	18.5	12.8	17.1	22.1	18.4	9.0	6.9
Colloidal clay (< 0.002 mm) (%)	13.5	25.2	23.3	20.8	18.8	16.5	15.0
Physical clay (< 0.01 mm) (%)	28.3	33.8	31.5	26.6	24.4	17.1	17.2
Texture	SM	LN	LL	LL	SF	SM	SM
Apparent density (Da) (g/cm ³)	1.4	1.5	1.6	1.6			
Specific density (Ds) (g/cm ³)	2.7	2.6	2.6	2.6			
Water pH	5.3	5.2	4.9	5.7	6.2	8.2	8.4
Carbonates(CaCO ₃) (%)						5.8	5.2
Humus (%)	2.4	1.4	1.1				
Nitrogen index (IN)	1.9						
Humus reserve (t/ha)	80.3	41.6	12.0	133.9			
Exchange bases (SB) (me/100)	7.4	8.9	12.0	19.1	21.6		
Exchange hydrogen (SH) (me/100)	4.6	4.6	4.4	3.3	1.9		
Cation exchange capacity (T) (me/100)	11.9	13.5	16.4	22.4	85.4		
Base saturation degree (V) (%)	61.8	66.2	73.0	85.4	91.5		

Legend: Ap-ploughed layer; Ao-ocric horizon; AB- horizon; Bvg2 horizon; BCg2 horizon; Ckg3 horizon; Ckg4 horizon; SM- sandy gray clay; LN - sandy clay; LL- middle clay; SF- sandy fine clay;

For soils characterization, agricultural surface with acidic soils distribution from downstream Bârzava River, were systematized from data obtained from administrative-territorial units of the studied area. As far as acid soils are concerned, they cover 47,297 ha of agricultural lands within the studied area (Table 2). These soils share a common feature; low pH values

(5.0-6.8), which groups them into two large groups depending on acidification and soil formation type: soils with a B argillic horizon (Bt) and soils with a B cambic horizon (Bv).

Table 2. Distribution of acidis soils in agricultural lands from downstream Bârzava river, Caras-Severin County, Romania

Commune/ Town	Total agricultural lands (ha)	Of which acid soils:		
		low pH: 5.8-6.8	moderate pH: 5.1-5.8	high- excessive < 5.1
Banloc(+Livezile)	15481	6337	1832	---
Denta	8414	4644	1712	---
Deta	2904	1702	484	---
Gătaia (+ Birda)	19496	9850	2724	83
Ghilad	10487	6023	1603	---
Giera	8556	4479	482	---
Voiteni	6523	3836	1506	---
Total	71861	36871	10343	83
%	66.0	51.3	14.4	0.1

Acidity, expressed as actual acidity (pH) and titratable acidity (exchange and hydrolytic) influences directly (through the root system) the process of nutrition in plants. Acidity influences deeply the process of metabolism by disturbing the formation of protein substances: this is the reason why nitrogen substances remain as amino acids in the root.

Some pH measurements were achieved, according the literature procedures^{17,18,19} from collected soils and results were presented in Table 3. From measurements we can observed that surface soil is more acidic.

Many studies reported that the soil pH and heavy metal concentrations are vital factors for plant growth^{20,21}. Therefore, in this study the six soil samples were analysed in order to assess the major and trace elements content. The obtained results are presented in the Table 4.

The metal content in collected soil samples was determined using an Inductively Coupled Plasma Mass Spectrometer. Over 50 different metals were identified. Some in higher concentration like Ca, Fe, Mg, Mn, Ba some in medium concentration like Sr, Na, Ti, Zn, Y, As, Co, Ni and some in low concentration, Sc, Ge, Rb, Zr, Cd. Some rare metals were detected but the concentration was under 0.01mg/Kg. Some lacticid metals were identified, the highest concentration was Ce, Nd, La, Gd, Dy.

Table 3. pH-values for soil samples obtained from Bârzava river, Caras-Severin County, Romania; (A soil sample from Banloc-Livezile pump station area (0-20 cm); B. soil sample from Partoș rice plantation area (0-20 cm); C. soil sample from Voiteni Farm of USAMVBT (0-20 cm); D. soil sample from wheat plantation area from the Voiteni Farm of USAMVBT (20-40 cm); E. soil sample from Banloc- Livezile pump station area (20-40 cm); F soil sample from Partoș rice plantation area (20-40 cm))

Soil samples	A	B	C	D	E	F
pH	5.3	5.6	5.4	6.1	5.9	6.1

Table 4. The total metal concentrations in soil samples collected from different areas: A. soil from Banloc-Livezile pump station area (0-20 cm); B. soil from Partoș rice plantation area (0-20 cm); C. soil from Voiteni Farm of USAMVBT (0-20 cm); D. soil from wheat plantation area from Voiteni Farm of USAMVBT (20-40 cm); E. soil from Banloc-Livezile pump station area (20-40 cm); F. soil from Partoș rice plantation area (20-40 cm)

Element	A. C _M =mg/kg	B. C _M =mg/kg	C. C _M =mg/kg	D. C _M =mg/kg	E. C _M =mg/kg	F. C _M =mg/kg
Li	1.63	0.88	2.07	1.95	0.97	1.19
Be	0.61	0.48	0.72	0.73	0.28	0.55
Na	29.65	75.91	54.87	70.39	15.72	71.89
Mg	3474.8	1796.4	2627.9	2487.2	1503.8	1793.6
Ca	8846.2	4338.5	6946.7	7063.1	3369.4	4843.1
Sc	0.64	0.94	0.65	0.62	0.30	0.98
Ti	14.76	8.23	12.69	12.93	6.15	9.23
V	23.38	19.32	15.96	14.16	10.29	21.07
Cr	4.17	2.51	4.12	3.53	2.15	3.22
Mn	307.03	112.57	477.34	379.92	128.59	132.31
Fe	320.78	3635.8	2560.7	2211.4	1363.6	283.87
Co	5.25	6.91	6.36	6.27	2.11	3.41
Ni	7.69	4.61	9.22	8.50	3.44	5.37
Cu	8.45	7.68	7.75	6.56	3.30	8.09
Zn	14.76	17.69	15.12	15.60	6.02	20.97
Ga	0.95	0.59	0.88	0.76	0.42	0.69
Ge	0.03	0.02	0.03	0.02	0.01	0.02
As	7.32	4.72	5.22	4.99	2.74	4.90
Se	<0.01	0.15	<0.01	<0.01	0.09	<0.01
Rb	0.43	0.25	0.43	0.47	0.16	0.25
Sr	24.17	16.32	20.61	19.51	9.48	18.45
Y	9.12	7.16	10.11	9.79	3.75	8.25
Zr	0.39	0.15	0.25	0.21	0.12	0.18

MINERALOGICAL AND CHEMICAL CHARACTERIZATION OF THE SOIL FROM BĂRZAVA RIVER AREA

Element	A. C _M =mg/kg	B. C _M =mg/kg	C. C _M =mg/kg	D. C _M =mg/kg	E. C _M =mg/kg	F. C _M =mg/kg
Nb	0.03	0.02	0.02	0.02	0.01	0.02
Mo	0.03	0.01	0.01	<0.01	<0.01	<0.01
Ru	<0.01	<0.01	<0.01	<0.01	<0.01	<0.01
Rh	<0.01	<0.01	<0.01	<0.01	<0.01	<0.01
Pd	<0.01	<0.01	<0.01	<0.01	<0.01	<0.01
Ag	0.06	0.06	0.04	0.04	0.02	0.06
Cd	0.14	0.20	0.13	0.11	0.05	0.22
In	<0.01	0.03	<0.01	<0.01	<0.01	0.03
Sn	0.04	0.04	0.02	0.02	<0.01	0.03
Sb	0.02	<0.01	<0.01	0.01	<0.01	<0.01
Te	<0.01	<0.01	<0.01	<0.01	<0.01	<0.01
I	0.01	<0.01	0.04	0.04	<0.01	<0.01
Cs	<0.01	<0.01	<0.01	<0.01	<0.01	<0.01
Ba	127.69	76.31	140.36	131.24	46.41	93.10
La	10.01	8.11	10.89	10.07	3.68	9.53
Ce	24.97	19.13	27.38	24.63	9.13	22.79
Pr	3.02	2.29	3.29	3.09	1.10	2.78
Nd	12.95	10.02	14.34	13.61	1.56	12.06
Sm	1.09	0.81	1.24	1.19	0.36	1.01
Eu	0.28	0.21	0.31	0.29	0.09	0.26
Gd	6.76	1.04	7.47	7.07	0.41	6.05
Tb	1.02	0.14	1.13	1.08	0.06	0.17
Dy	6.53	0.78	7.05	6.86	0.33	0.97
Ho	1.68	0.14	1.82	1.76	0.06	0.18
Er	0.53	0.40	0.56	0.55	0.17	0.49
Tm	0.07	0.06	0.08	0.07	0.02	0.07
Yb	0.50	0.39	0.52	0.50	0.16	0.47
Lu	0.08	0.06	0.08	0.08	0.02	0.07
Hf	0.01	0.01	0.01	0.01	<0.01	0.01
Ta	<0.01	<0.01	<0.01	<0.01	<0.01	<0.01
W	<0.01	<0.01	<0.01	<0.01	<0.01	<0.01
Re	<0.01	<0.01	<0.01	<0.01	<0.01	<0.01
Os	<0.01	<0.01	<0.01	<0.01	<0.01	<0.01
Ir	<0.01	<0.01	<0.01	<0.01	<0.01	<0.01
Pt	<0.01	<0.01	<0.01	<0.01	<0.01	<0.01
Au	<0.01	<0.01	<0.01	<0.01	<0.01	<0.01
Hg	<0.01	0.01	0.01	<0.01	<0.01	0.02
Tl	<0.01	<0.01	<0.01	<0.01	<0.01	<0.01
Pb	<0.01	<0.01	<0.01	<0.01	<0.01	<0.01
Bi	0.15	0.42	0.09	0.09	0.05	<0.01

CONCLUSIONS

Soil from downstream Bârzava River was characterized and main features were presented. The six soil collected samples were characterized and analysed and in order to assess the major and trace elements content and to determine the acidity of soils. The pH of soils was determined from different depths, the surface soil being more acidic. It was revealed that Ca, Fe, Mg, Mn, Ba were the most abundant elements in the studied soil samples. It is known that the pH and heavy metal concentrations are vital factors for plant growth and the obtained results could be use for elaboration of some soil bioremediation techniques.

EXPERIMENTAL SECTION

Material and methods

Six soil samples were collected from different areas, from lands downstream Bârzava River, Caraș-Severin County, Romania: A. soil sample from Banloc-Livezile pump station area (0-20 cm); B. soil sample from Partoș rice plantation area (0-20 cm); C. soil sample from Voiteni Farm of USAMVBT (0-20 cm); D. soil sample from wheat plantation area from Voiteni Farm of USAMVBT (20-40 cm); E. soil sample from Banloc-Livezile pump station area (20-40 cm); F soil sample from Partoș rice plantation area (20-40 cm).

The metal contents were determined by Inductively Coupled Plasma Mass Spectrometer (SCIEX Perkin Elmer Elan DRC II) using a semi-quantitative analysis. Merck ICP multi-element standard solution VI was diluted and used for factor response calibration, while the dynamic reaction cell was used in rf-only mode (no gas). Oxides and double charged ions were kept below 3%, plasma power was set at 1450 W and the instrument was optimised for lowest signal/noise raise before measurements.

All reactive and standards were purchased from Merck (Darmstadt, Germany).

Sample preparation and pH measurement

The soil samples were air-dried and grounded to 2 mm. Soil samples pH were measured in soil-water slurry (1:5, w/v) with a pH meter. The pH meter was calibrate according to manufacturer's instructions using buffer solutions (pH 4.0 - 10.0).The pH measurement was performed at room temperature (20°- 23°C).

Extraction and determination of metals from soil samples

The total metal content of the soil samples were determined on centrifugated extracts (0.5 g/mL) obtained from 5 g samples which were digested with 10 ml 1M HCl. The total metal determinations were conducted by Inductively Coupled Plasma Mass Spectrometer (SCIEX Perkin Elmer Elan DRC II).

ACKNOWLEDGMENTS

The authors thank for financial support from the National Authority for Scientific Research and Innovation (ANCSI) Core Program (Project No. 16.40.02.01).

REFERENCES

1. H.R. Uexküll, E. Mutert, *Plant and Soil*, **1995**, *171*, 1-15.
2. J.H. Guo, X.J. Liu, Y. Zhang, J.L. Shen, W.X., Han, W.F. Zhang, P. Christie, K.W.T. Goulding, P.M. Vitousek, F. S. Zhang, *Science*, **2010**, *327*, 1008-1010.
3. J. Polomski, N. Kuhn, "Root Research Methods. In: Waisel, Y., Eshel, A., Kafkafi U. and Dekker, M., Eds., *Plant Roots: The Hidden Half*" (third), New York, **2002**, 313-314.
4. V.A. Vitorello, F.R. Capaldi, V.A. Stefanuto, *Brazilian Journal of Plant Physiology*, **2005**, *17*, 129-143.
5. S.M. Alam, S.S.M. Naqvi, R. Ansari, "Impact of Soil pH on Nutrient Uptake by Crop Plants. In: Pessarakli, M.", Ed., *Handbook of Plant and Crop Stress*, New York, **1999**, 51-60.
6. J.F. Ma, *International Review of Cytology*, **2007**, *264*, 225-252.
7. A. Robson, *Soil Acidity and Plant Growth*, 1st Ed., Academic Press, **1989**, 318.
8. W.Y. Shi, H.B. Shao, M. Shao, S. Du, *Journal of Hazardous Materials*, **2009**, *170* (1), 1-6.
9. F.R. Troeh, L.M. Thomson, "Soils and soil fertility", Ed. Blackwell, **2005**, 489.
10. D. Țărău, Gh. Rogobete, A. Grozav, D. Dicu, A. Țărău, *Research Journal of Agricultural Science*, **2012**, *44* (3), 293-298.
11. Gh. Rogobete, D. Țărău, "Soils and their improvement", Ed. Marineasa, **1997**, Timisoara.
12. M. Dumitru, C. Ciobanu, R. Lacatusu, L. Latis, G. Gament, M. Dracea, St. Carstea, E. Dulvara, D. Plaxienco, B. Kovacsovics, R. Enache, M.D. Motelica, M. Alexandrina, N. Vranceanu "Protectia Mediului in Agricultura", Ed. Helicon, **2000**, p.16-42.

13. a) I. Nițu, C. Răuță, M. Drăcea, *Agropedoameliorative works*, vol I, Ceres Publishing House, **1988**, Bucharest; b) I. Nițu, C. Răuță, M. Drăcea, *Agropedoameliorative works*, vol II, Ceres Publishing House, **1990**, Bucharest.
14. I. Borza, D. Țărău, R. Jarabă, I. Țărău, "The impact of economical and social activities on soil quality and use of agricultural lands in the peri-urban area URUIOC STELA et al.: Evaluation of the degree of pollution with heavy metals of soils of Timisoara town", vol. XXXVII, Ed. Agroprint, Timișoara, **2005**, ISSN 1221-5279, 258-263.
15. N. Sarwar, Saifullah, S.S. Malhi, M.H. Zia, A. Naeem, S. Bibi, G. Farid, *Journal of the Science of Food and Agriculture*, **2010**, 90, 925.
16. A. Mahmood, R. Naseem Malik, *Arabian Journal of Chemistry*, **2014**, 7, 91.
17. A. Behnood, K. Van Tittelboom, N. De Belie, *Construction and Building Materials*, **2016**, 105, 176.
18. R.O. Miller, D.E. Kissel, *Soil Science Society of America Journal*, **2008**, 74, 310.
19. M. Hansen, T. Bang-Andreasen, H. Sorensen, M. Ingerslev, *Forest Ecology and Management*, **2017**, 406, 274.
20. M. Vítkov, S. Rakosov, Z. Michalkov, M. Komarek, *Journal of Environmental Management*, **2017**, 186, 268.
21. S. Willscher, L. Jablonski, Z. Fona, R. Rahmi, J.Wittig, *Hydrometallurgy*, **2017**, 168, 153.

STUDY OF (PB, BA) - CRT GLASS WASTE BEHAVIOUR AS A PARTIAL AGGREGATE REPLACEMENT IN CEMENT MORTARS

LILIANA HORNEA^a, MARIA GOREA^b, NICOLAE HAR^{a*}

Abstract: This study investigates the usability of the cathode ray tube (CRT) glass waste in a binder system. The raw materials – glass waste, river sand and cement were characterised. CRT waste was added in the amount of 30, 40 to 50 weight percent, as replacement for river sand. Glass chemical composition shows a high content in lead and alkaline oxides. Mortar prisms were prepared and kept under humid conditions. The mechanical properties were studied after 7, 28 and 90 days respectively. SEM with additional EDS was used in order to investigate the microstructure of the samples. All the samples containing glass waste achieved higher compressive strength than the control mortar. After 14, 28 and 42 days of maintaining the mortar in water no evidence of Pb was detected in the solutions.

Key words: *cement, mortar, CRT glass waste, compressive strength*

INTRODUCTION

It is well known that the process of recycling represents the trend of the modern world. This process is closely related to the quantity of products removed from the market [1-5]. The electronic and electro-technical fields go through changes every day since the beginning of rapid technological achievements [6]. Good examples are computer monitors and TV sets that are composed of cathode ray tube (CRT) glass. If 25 years ago, these products were recycled, being used to create new devices, at present, their market demand is non-existent, given the superiority of liquid crystal display (LCD) and light emitting diode (LED) technology [7].

^a Babeş-Bolyai University, Faculty of Biology and Geology, Kogălniceanu str., 1, RO-400084 Cluj-Napoca, Romania. E-mail: liliana.hornea@gmail.com; nicolae.har@bioge.ubbcluj.ro

^b Babeş-Bolyai University, Faculty of Chemistry and Chemical Engineering, 11 Arany Janos str., RO- 400028, Cluj-Napoca, Romania, mgorea@chem.ubbcluj.ro

*Corresponding author: nicolae.har@bioge.ubbcluj.ro

Introduction of glass waste as aggregate replacement in mortar and concrete has been studied for a long time. In the last 10 years this area has been intensely discussed by researchers due to high costs required for disposal but especially as a consequence of the new environmental regulations [8-11]. Electrical and electronic waste equipment involves serious environmental problems both due to their growing volume as well as to their toxicity caused by their content in Pb, Mn, Zn, Sn, Co etc., respectively. Eliminating CRT glass has become a worldwide environmental problem due to its high content in lead [12]. There are now plenty of ways to recycle this waste. One of them is to use it in the manufacturing of other monitors but the method becomes useless due to the low demand of CRT monitors [13]. Another method involve using these materials as flux in glass and ceramics industry [14-17]. These technologies limit the content of toxic oxides, mainly PbO. As a result, a separation of glass waste containing lead is required. This increases the price of the final product. Waste shredding and washing with acid to remove lead is also a complex process [4, 18]. Castro and Brito [19] review the main attempts regarding the feasibility of introducing glass waste in concrete as an aggregate. Promising results on lead immobilization from waste in a binder matrix (Portland cement, mixed silicate binders and other derived blender cements) would justify their use as a partial replacement of mineral aggregates in certain types of concrete [20].

The main aim of this study is to characterize the composition of CRT glass and to prepare the cement mortars in which the natural sand is partially replaced by these wastes. Also the microstructure characteristics correlated with the mechanical properties of hardened mortar are highlighted. Capacity of lead immobilization in the binder system is also studied.

RESULTS AND DISCUSSION

Characterization of raw materials

CRT glass waste aspect

Cathode ray tube glass waste used in this study represents a mix of funnel and screen glass obtained by the shredding of computer monitors. The computer monitors were scrapped; glass components were separated from the metal and plastic parts, then crushed and finally sieved below 4.00 mm particle size. The glass waste without any further chemical treatment was used. Particle size of river sand is in the range of 0 to 4.00 mm.

Macroscopic and microscopic aspect of the CRT glass waste is highlighted in Figure 1. The colour of waste is light grey. After the crushing process, the SEM image highlights angular fragments of glass, isometric or elongated in shape, with different sizes up to 4.00 mm.

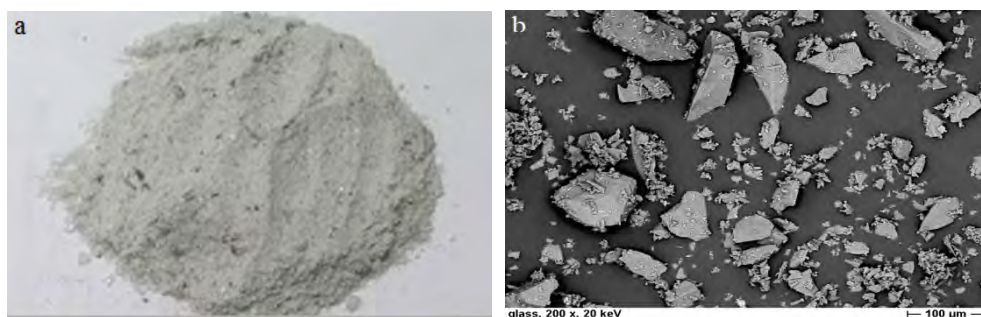


Figure 1. CRT glass waste with size less than 4 mm: a – macroscopic aspect; b - SEM image

Physical-chemical characterisation

The traditional river sand for mortar contains a high amount of silicon oxides besides small quantities of aluminium, calcium and alkaline oxides, respectively. The silicon oxide content is lower in CRT glass wastes than in river sand, about 46 wt%. The content of both fluxes oxides and earth and alkaline oxides, respectively is high and lead oxide is also present in high quantity, about 25 wt%.

The CRT glass composition is rich in lead oxide (25 wt %) which makes this waste difficult to store; hazardous oxides as BaO (2.23 wt%) and SrO (2,4 wt%) are also present. A high content of alkali and alkali-earth oxides Na₂O, K₂O, MgO, and CaO is observed. The sand contains a high amount of silica, about 89 wt % and aluminium oxide (3.95 wt%) and, in small proportions, alkali and alkali-earth oxides.

As expected, the glass waste shows a slow water absorption value of 0.04 wt%, smaller as compared with the sand, which is 1.93 wt%. Due to its vitreous texture, glass adsorbs less water than the other aggregate. This fact leads to a higher water amount in the mortar mixture, which involves a better workability.

As compared with sand density (2620 kg/m³), CRT glass has a higher density (3020 kg/m³), due to its content in heavy metal oxides BaO, SrO and PbO. This value is closed to the cement powder density (3150 kg/m³), providing a good blending of raw materials and avoiding aggregates segregation.

Regarding the size distribution of aggregates there are no relevant differences between river sand and CRT glass waste. Therefore, the mortar compactness is expected to be close for control and CRT studied samples.

The physical-chemical characteristics of materials are presented in Tables 1 and 2.

Table1. Physical-chemical characteristics of raw materials

Material/oxide	Portland Cement [wt%]	CRT glass waste [wt%]	Traditional river sand [wt%]
SiO ₂	20.39	46.10	88.97
Al ₂ O ₃	4.71	3.26	3.95
Fe ₂ O ₃	3.91	0.13	0.53
CaO	61.62	3.41	2.00
MgO	1.11	1.71	1.00
Na ₂ O	0.21	6.24	1.05
K ₂ O	0.72	7.40	1.26
TiO ₂		0.12	
SrO		2.40	
ZrO ₂		0.22	
BaO		2.23	
PbO		25.00	
SO ₃	2.74		
Cl ⁻	0.0049		
LOI		0.72	0.62
Physical Properties			
Density [kg/m ³]		3020	2620
Water absorption [wt%]		0.14	1.93

The different aggregates density in the cement mortar has to be close to each other and to the binder density. The CRT glass waste and river sand have an adequate density to avoid the aggregates sedimentation during the mixing. The water absorption of CRT glass waste is lower than of the river sand, so the mixture workability is not influenced.

Aggregate sizes

The size distribution of the aggregates is presented in Table 2. The size of both aggregates are similar. This fact involves a good homogenisation of aggregate fragments and of mortar mixtures.

Table 2. Aggregates sizes

Aggregate/Sieve size	[mm]	4.00	3.15	2.00	1.40	1.00	0.71	0.50
CRT glass waste	[wt%]	100.00	93.50	87.17	76.34	64.34	53.67	44.00
Traditional river sand	[wt%]	100.00	95.90	81.20	72.70	62.60	56.00	45.30

Alkali solubility of glass waste

The pH measurements show that the pH value of the glass solution has slight variations in the first two hours. In this time interval the highest value is 9.68 (Figure 2,a).

Following the pH evolution, in the 3rd day, the pH value increases to 10.15 then drops to 10.07. pH values remain almost constant starting with the 5th day (Figure 2, b). This pH value is recommended for the cement mortars.

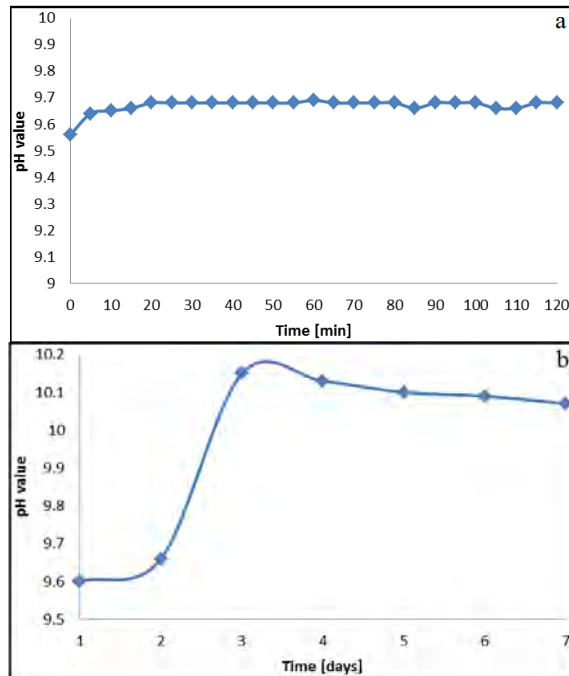


Figure 2. Evolution of pH solution of CRT glass waste during (a) 2 hours; (b) 7 days

Hydraulic activity of CRT waste

Hydraulic activity measures the reaction capacity of a substance/material with calcium hydroxide in the presence of water. The hydraulic activity of CRT glass waste was studied at two different maturation intervals of 8 and 16 days, respectively. Following the processing of the data obtained from solution titration, it can observe that the values of CRT glass hydraulic activity are above the saturation curve of CaO (Figure 3).

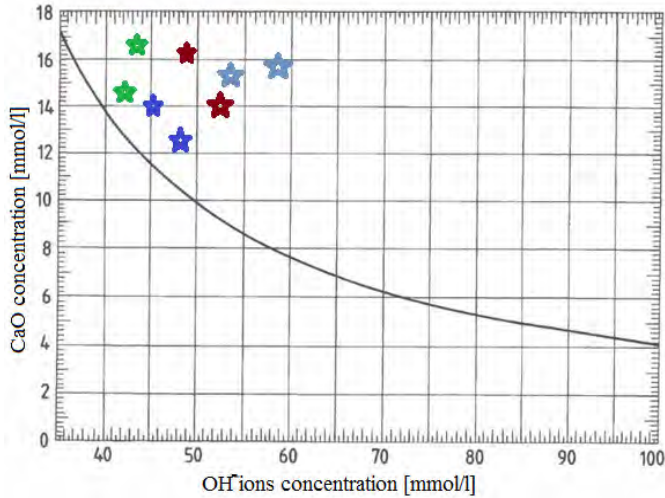


Figure 3. Distribution of sample concentrations on CaO saturation curve:
 ★ - control mortar, ★ - 30 wt% CRT waste mortar, ★ - 40 wt% CRT waste mortar,
 ★ - 50 wt% CRT waste mortar.

According to the convention regarding the hydraulic behaviour, the points above the saturation curve of CaO indicate a poor hydraulic activity. This encourages the use of cathode glass waste as aggregate in cement mortars.

Mortar Characterization

Cement mortars compositions

Four cement mortars compositions were prepared according to Table 3. The control mortar mixture (M1) is free of CRT glass waste, while the other three compositions have the river sand aggregates substituted by CRT glass waste in the proportions of 30 wt %, 40 wt %, and 50 wt % respectively. All the mixtures were prepared with water/cement ratio of 0.5 and with aggregate/cement ratio of 3.

Table 3. Experimental mortars mixtures

Sample / Component [wt%]	Portland cement	Aggregate	
		River sand	CRT glass
M1	25	75.00	-
M2	25	52.50	22.50
M3	25	45.00	30.00
M4	25	37.50	37.50

Mineralogical investigations

The mortar phases are well revealed by BSE images in Figure 4. As expected, grains of quartz (Q), feldspars (Fsp) and glass (G) appear in the cement matrix (M).

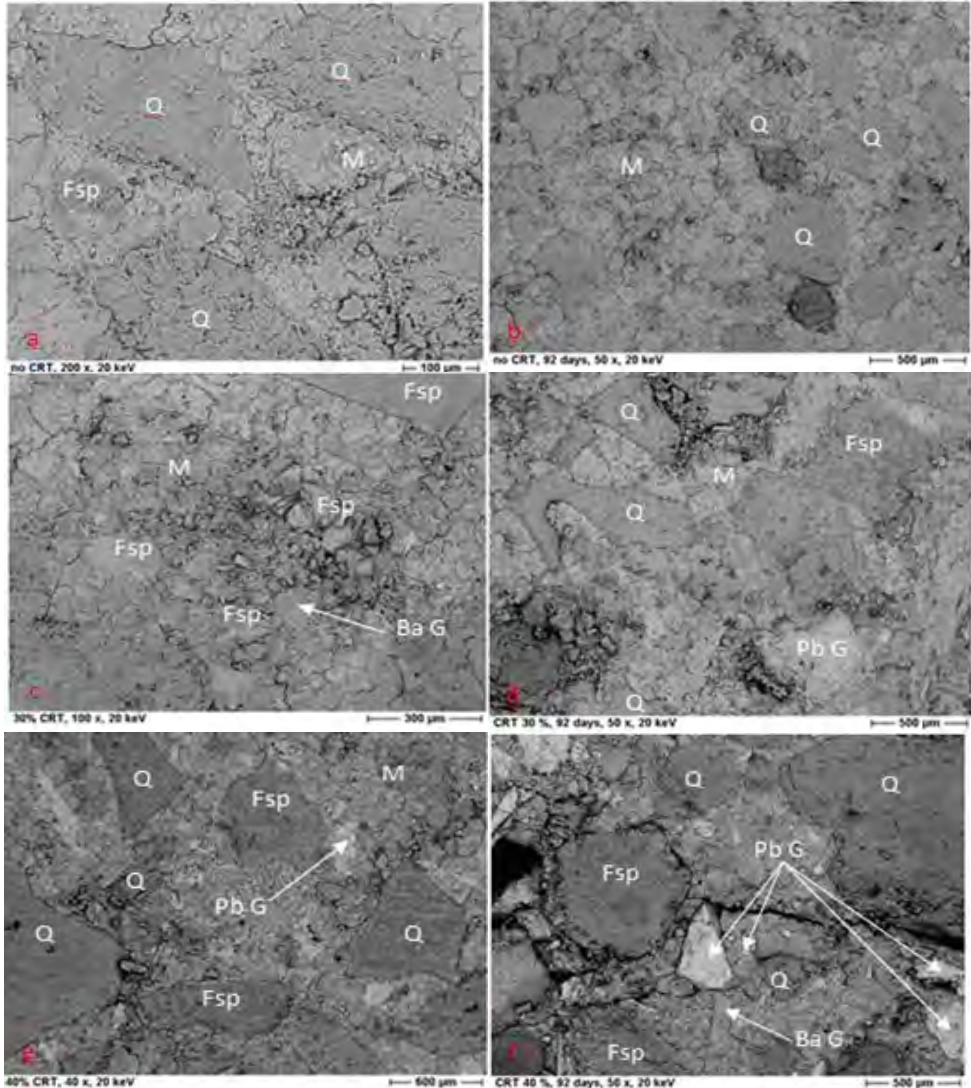


Figure 4. BSE images of mortars: a - control mortar 28 days, b - control mortar 90 days, c - 30% CRT mortar 28 days, d - 30% CRT mortar 90 days, e - 40% CRT mortar 28 days, f - 40% CRT mortar 90 days (quartz - Q, feldspars -Fsp, lead glass - PbG, barium glass – BaG and cement matrix - M)

The mortar control sample aspect is illustrated in Figure 4a and b. In each samples grains of quartz and feldspar with specific shapes and sizes from the aggregate in mortars are well observed. As expected, mortar samples are well blended, the aggregate grains are dispersed in the cement matrix and the mortar microstructure is compact. The cracks observed in the samples are the result of the mechanical tests and the dehydration processes which took place during sample preparation.

Quartz grains are bound in a matrix that consists of calcium silicate hydrates, calcium ferrite aluminat hydrates and also magnesium compounds. These components are hydrated and form a homogenous mixture. On the upper side of the sample, the carbonation process is present. Its appearance may have different explanations. It might be that the mortar samples were held in natural atmosphere, so the CO₂ could enter through the pores in the mortar structure. There, it would react with the portlandite resulted from calcium oxide hydration and form calcium carbonate - calcite. Another possible explanation could be the presence of limestone as additive in Portland cement type II A-LL.

The 30 wt% CRT mortar microstructure, in which the CRT glass (BaG – barium glass and PbG – lead glass) has angular shape with sharp edges as a result of the grinding process, is shown in Figure 4c and d. The same sharp boundaries of glass in the cement matrix can be observed on the 40 wt% CRT mortar microstructure – Figure 4e and f.

The composition of glass waste aggregates of mortar containing 50 wt% glass (sample M4) was investigated by BSE and EDS (Figure 5). Pieces of glass with high Pb content (spectrum b) and Ba content (spectrum a) are revealed.

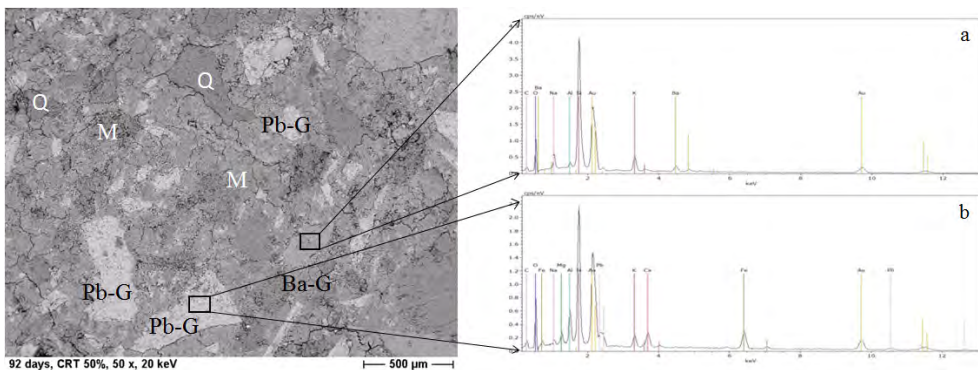


Figure 5. BSE image and EDS spectrum of the 50% CRT mortar after 90 days

EDS investigations reveals the same chemical elements found by the chemical analysis. Two types of glass are highlighted: one that contains Pb and one that is rich in Ba. This fact indicates the different sources of glass: computer pannel for Ba type and cathode for Pb type. The occurrence of Pb and Ba glass pieces in the mixture is rather random, no particular distribution is observed.

Density of the hardened mortar

The density of studied hardened mortars increases with the increase of CRT glass waste content in mortar compositions. The highest density is reached by the 50 wt% CRT glass containing mortar – 2286.29 kg/m³, while the control mortar has the lowest value - 2190.63 kg/m³ (Figure 6).

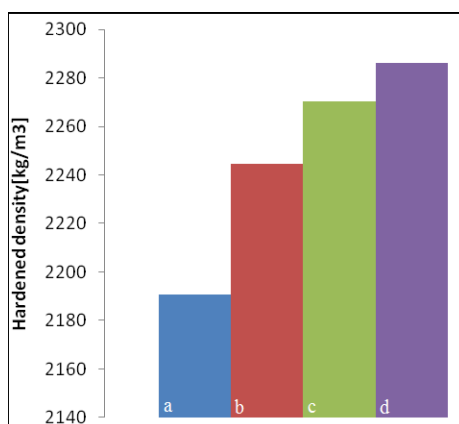


Figure 6. Density variation of studied mortars: a - control mortar, b – 30 wt% CRT mortar, c – 40 wt% CRT mortar, d - 50 wt% CRT mortar

The density of the glass containing hardened mortars (30 wt%, 40 wt%, and 50 wt%) presents an increase of 2.46 wt%, 3.64 wt%, respectively 4.37 wt% as compared to the control mortar. The high mortar density values can be correlated with the high glass density due to its content in heavy oxides.

Mortar porosity

According to the size distribution of both aggregates, there are no relevant differences between the size of CRT waste and river sand. As such, the mortar compactness should be close. The pore distribution, illustrated by blue colour, is presented in Figure 7. An uniform distribution and small size pores are present in both type of mortars, the control one and CRT waste mortar, respectively.

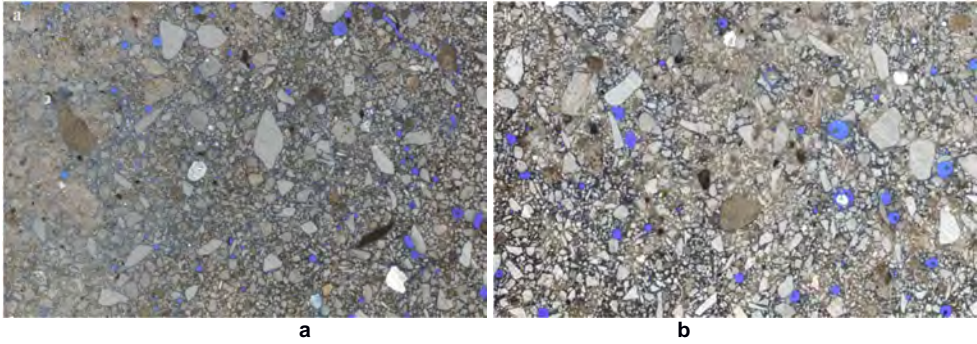


Figure 7. Porosity distribution of two studies samples: a - control mortar, b – 30 wt% CRT waste mortar

Compressive strength

Mechanical test reveals a better behaviour of the CRT glass containing mortars as compared to the control mortar (Figure 8). In each case, the glass has a positive influence on the mortar resistance. The compressive strength increases progressively with the decreasing of the river sand in favour of glass waste and with curing age.

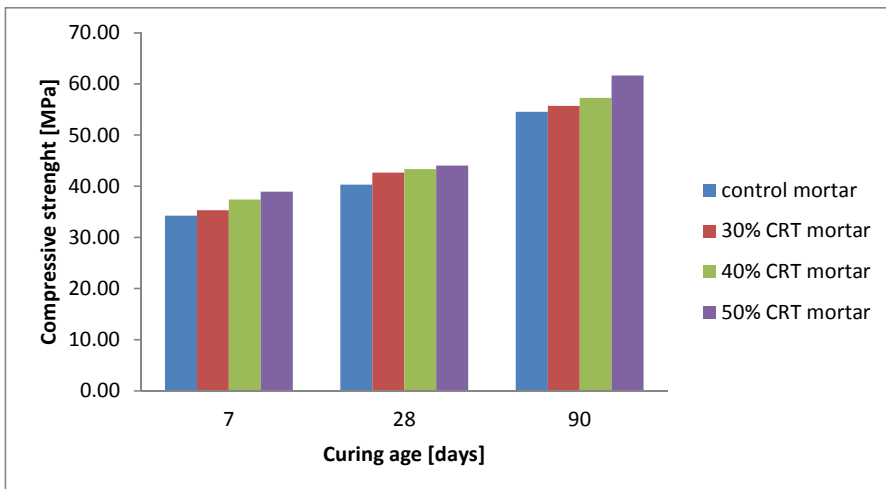


Figure 8. Compressive strength of studied mortars

The mortars with 50 wt% CRT glass content show the highest compressive strength at 90 days, 61.69 MPa. This represents about 113 % of control mortar strength at the same age. Romero [22] also demonstrates that the strength of mortars prepared with CRT glass waste in a lower amount (10 wt%, 20 wt% and up to 30 wt%) surpass that of the control mortars. The improved behaviour could be explained by the glass's low water absorption that facilitates workability, and reduces drying shrinkage. Maschio [23] supports the fact that mortar samples prepared with glass prove a more rapid increase of strength as compared to the control mortar in long-term ageing.

Leaching test

After each period of maintaining the mortar samples in water, the resulting solutions were analysed by AAS apparatus with absorption limits between 0.1-100 ppm.

No evidence of Pb was detected in the solutions in this range.

CONCLUSIONS

This study investigates the characteristics of CRT glass cement mortars and possibility of encapsulating hazardous metal oxides from scrap monitors in these mortars as aggregates. CRT glass waste, traditional river sand, cement and water were mixed in order to obtain mortars.

The density of CRT waste mortars show higher values than control mortar as the aggregate is enriched in PbO and BaO glass.

The pH data fits into standard values for cement mortars. The AAS analysis made on the solutions consisting of mortar samples and deionised water indicates no dissolution of Pb in the 0.1-100 ppm range. It can be presumed that lead and barium oxides are well embedded by the cement matrix.

An uniform distribution and small size of the pores both in control as well as in CRT waste mortar are evidenced.

Compressive strength of studied mortars increases when a high percent of river sand aggregate is replaced. The best value is recorded by composition M4, in which CRT glass waste to river sand ratio is 1:1. In each case, the control mortars strength is exceeded by that of the CRT glass mortars.

Despite of their angular shape this type of aggregate makes a good bond with the cement matrix, fact proved by the compressive strength of mortar samples.

In conclusion, the CRT glass waste could be used as aggregates in cement mortar for replacing the river sand.

EXPERIMENTAL

Materials and methods

Materials

In order to prepare the mortar samples, the cement, aggregate, and water as raw materials are necessary. A type II Cement A-LL 42.5 R was used for this study. Chemical composition of cement is presented in Table 1. Both traditional river sand and CRT glass waste as aggregates were used. River sand was sourced from the Cluj area and CRT glass was provided by Babeş-Bolyai University laboratory (scrap computers).

Mortar samples preparation

According to the standard EN-196-1-ASTM C305 three mortar prisms for each composition were prepared. The raw materials were mixed in a laboratory mixer. The mixture was immediately put into standard steel moulds (160x40x40 mm). The mortars were compacted using a shock table. After 24 hours they were removed from the moulds and kept in 70 wt% humidity atmosphere for 7, 28 and 90 days respectively.

Tests methods

Glass waste investigations

Alkali solubility was measured over a period of 7 days. 10g of glass waste were weighted into a plastic jar with 100 ml deionised water. The pH was determined with VERFAHREN pH –stat method (according to LAGA standard EW 98 P). The pH of the solution was measured every 5 minutes in the first 2 hours, then every 24 hours.

Mortars investigations

Compressive strength

Compressive strength of the hardened mortar was investigated after each setting time (7, 28, 90 days) using a CONTROLS Hydraulic Press 50-36V2 according to Romanian SR EN 196-1.

Chemical composition and surface phases

Chemical composition and surface phases of the samples were studied with JEOL 640 Electron Microscope (Scanning Electron Microscopy - SEM and Back Scattering Electron Microscope- BSE) coupled with Energy Dispersive Spectroscopy (EDS). The microstructure of prepared mortars was investigated at two different curing periods: 28 and 90 days. Presence of cracks in the images is common fact due to dehydration effects during sample preparation for SEM and BSE [21].

Leaching test

Lead solubility was determined at 14, 28 and 42 days. Pieces of mortars from mechanical tests are introduced in deionised water (1 part mortar in 2 parts water). After each period 10 ml solution was collected for Pb testing with an AVANTA PM GBC Atomic Absorption Spectrometer.

ACKNOWLEDGMENTS

The authors wish to thank to Prof. Dr. Herbert Pöllmann and Dr. rer. nat. Ronny Kaden from Institute of Geosciences and Geography at Martin Luther University of Halle-Wittenberg, Germany and to Interdisciplinary Research Institute of Bio-Nano-Sciences of Babeş-Bolyai University Cluj Napoca.

REFERENCES

1. Ruixue Wang, Zhenming Xu, *Waste Management*, 34, 8, **2014**, 1455
2. Qingbo Xu, Guangming Li, Wenzhi He, Juwen Huang, Xiang Shi, *Waste Management*, 32, 8, **2012**, 1566.
3. J.R. Mueller, M. W. Boehm, C. Drummond, *Waste Management*, 32, 8, **2012**, 1560.
4. Qingbo Xu, Mengjing Yu, A. Kendall, Wenzhi He, Guangming Li, J.M. Schoenung, *Conservation and Recycling*, 78, 9, **2013**, 92.
5. L. Rocchetti, F. Beolchini, *Waste Management*, 34, 2, **2014**, 468.
6. Ching-Hwa Lee, Chang-Tang Chang, Kuo-Shuh Fan, Tien-Chin Chang, *Journal of Hazardous Materials*, 114, 1–3, 18, **2004**, 93
7. M. Leet Socolof, J.G. Overly, J.R. Geibig, *Journal of Cleaner Production*, 13, 13–14, **2005**, 1281.
8. F. Méar, P. Yot, M. Cambon, M. Ribes, *Waste Management*, 26, 12, **2006**, 1468.
9. İ. B. Topçu, M. Canbaz, *Cement and Concrete Research*, 34, 2, **2004**, 267.
10. C. Meyer, S. Baxter, W. Jin, *Proceedings of 4th materials engineering conference: materials for the new millennium*. Reston, VA.: ASCE; **1996**, 1388.
11. Ching-Hwa Lee, Chang-Tang Chang, Kuo-Shuh Fan, Tien-Chin Chang, *Journal of Hazardous Materials*, 114, 1–3, 18, **2004**, 93.
12. C.S. Poon, *Waste Management*, 28, 9, **2008**, 1499.
13. Fangfang Xie, Lili Liu, Jinhui Li, *Environmental Sciences*, 16, **2012**, 585.
14. F. Andreola, L. Barbieri, A. Corradi, I. Lancellotti, *Journal of the European Ceramic Society* 27, **2007**, 1623.

15. F. Andreola, L. Barbieri, A. Corradi, I. Lancellotti, R. Falcone, S. Hreglich, *Waste Management* 27 (2), **2005**, 183.
16. M. Dondi, G. Guarini, M. Raimondo, C. Zanelli, *Waste Management*, 29, 6, **2009**, 1945.
17. J. Bartha, M. Gorea, *STUDIA UBB CHEMIA LX*, 4, **2015**, 35.
18. Tung-Chai Ling, Chi-Sun Poon, *Journal of Hazardous Materials*, 192, 2, 30, **2011**, 451.
19. Sarade Castro, Jorge de Brito, *Journal of Cleaner Production*, 41, 2, **2013**, 7.
20. A.M. Oancea, M. Georgescu, A. Badanoiu, E. Matei, *Romanian Journal of Materials*, **2012**, 42 (2), 152.
21. M. Schmidt, H. Poellmann, A. Egersdorfer, J. Goske, S. Winter, *ICMA*, **2011**.
22. D. Romero, J. James, R. Mora, C.D. Hays, *Waste Management*, 33, 7, **2013**, 1659.
23. S. Maschio, G. Tonello, E. Furlani, *Journal of Waste Management*, 2013, Article ID 102519, <http://dx.doi.org/10.1155/2013/102519>.

CORROSION INHIBITION OF LOW CARBON STEEL IN SIMULATED WASTEWATER FROM PETROLEUM INDUSTRY

JULIETA DANIELA CHELARU^a, DOVRAN AYLAKOV^a,
LIANA MARIA MUREȘAN^{a*}

ABSTRACT. The corrosion inhibition efficiency of three commercial inhibitors on low carbon steel was investigated by electrochemical methods (EIS and polarization curves). The efficiency of corrosion inhibitors was tested at different concentrations. Corrosion tests were carried out in a solution simulating a saline wastewater from petroleum industry (pH = 3) in order to find the best inhibitor for the protection of steel pipelines.

Key words: *steel, corrosion inhibitors, electrochemical impedance spectroscopy, polarization curves, inhibitor efficiency, synthetic wastewater from petroleum industry.*

INTRODUCTION

The corrosion of pipelines from petrochemical industry can lead to decreased production, economic losses and also security risks [1]. Pipelines corrosion can be caused by a wide variety of factors, including physical, chemical and biological ones [2]. Almost any aqueous environment can promote corrosion, which occurs under numerous complex conditions in oil and gas production, processing, and pipeline systems [3].

Water is frequently injected into wells to increase oil recovery. There is referred to as produced water, and is the largest volume by product stream in oil and gas production, having an adverse environmental impact due to its complex composition and high disposal costs. The cost of producing, handling, and disposing of the produced water often defines the economic lifetime of an oil field and the actual hydrocarbon reserves; therefore, understanding and predicting the aspects, behavior, and problems induced by the produced-water flow is important.

^a "Babeș-Bolyai" University, Department of Chemical Engineering, 11 Arany Janos St., 400028 Cluj-Napoca, Romania

*Corresponding author: limur@chem.ubbcluj.ro

The composition of produced water is complex. The major hydrocarbon groups present in produced water include alkanes, aromatics, polynuclear aromatics, hydrocarbon compounds containing oxygen, nitrogen and sulfur and unknown hydrocarbons (oil & grease) [4 - 6]. Produced water also contains high amounts of dissolved salts with predominant cations such as Na^+ , K^+ , Ca^{2+} and Mg^{2+} ; anions such as Cl^- and SO_4^{2-} , and silica (SiO_2) [6].

Due to its composition, produced water is a highly corrosive medium for the steel pipelines. In order to prevent their corrosion, the first priority is to find the factors that lead to corrosion and after that, to use the most appropriate methods of corrosion protection.

The use of inhibitors is one of the most practical methods for protecting metals or alloys from corrosion [7]. There is a wide variety of organic compounds used as corrosion inhibitors for steel in acid media: amines [8], compounds based on imidazoline [9], triazoles, pyridine [10], aromatic aldehydes, but also "green compounds" such as henna extract [11], *Justicia gendarussa* plant extract [12] etc., but to find new efficient corrosion inhibitors remains a challenge.

In this context, the aim of this paper is to investigate the corrosion of low carbon steel in synthetic solutions simulating wastewater from petroleum and oil industry (pH 3) in the absence and in the presence of two commercial phosphino succinic oligomer derivatives from Nalco Products, USA, (3DT177, 3DT179). They inhibit calcium carbonate scale formation and are used in a variety of cooling water applications in many industries. The effect of these inhibitors was compared with that of Galoryl IC20 (produced by ArrMazz Chemicals SAS, USA).

The protective effect of inhibitors at different concentrations was investigated by electrochemical methods (polarization measurements and electrochemical impedance spectroscopy).

RESULTS AND DISCUSSION

Polarization measurements

In order to characterize the protective effect of the inhibitors at different concentrations in the synthetic wastewater (pH = 3), electrochemical corrosion measurements were carried out.

The evolution of the open circuit potential (OCP) of the low carbon steel was recorded, in the absence and in the presence of corrosion inhibitors, during 1 hour (Fig. 1). Analyzing the data it can be observed a positive shift of OCP values in the presence of inhibitors, but no clear correlation was found between the OCP and the inhibitors concentration.

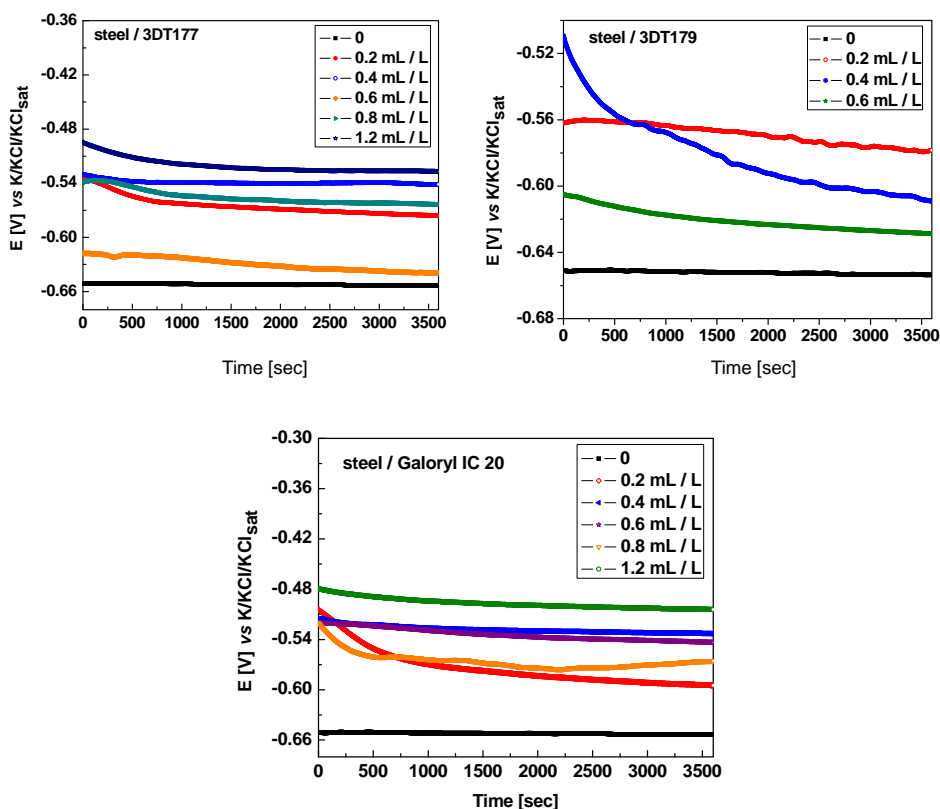


Figure 1. Open circuit potential measurements for the tested samples in the presence of corrosion inhibitors, immersed in corrosion solution, pH 3

Electrochemical impedance spectroscopy

Impedance spectra were recorded immediately after OCP monitoring in the simulated produced water in the presence of various concentrations of inhibitors and the results obtained were compared with those without inhibitors.

The Nyquist diagrams for steel corrosion in the presence of 3DT177 and Galoryl IC 20 are presented in Fig. 2. It can be observed that the impedance spectra exhibit a capacitive behaviour in the whole frequency domain. The experimental impedance spectra were analyzed for all cases by fitting to a 2RQ equivalent electrical circuit (Fig. 3). The parameters obtained for all samples by using the proposed equivalent electrical circuits are shown in Table 1. The quality of fitting procedure was evaluated by the chi squared (χ^2) values, which were of order 10^{-4} .

The equivalent electrical circuit from Fig. 3 consists of: the $R_{ct} - C_{dl}$ couple at high frequencies, representing the charge transfer resistance R_{ct} and the double layer capacity, C_{dl} , at the steel | electrolyte interface and a second couple ($R_F - C_F$) at low frequencies, where R_F represents the faradic resistance of the corrosion products accumulated at the interface and C_F , the faradic capacity due to an oxidation - reduction process taking place at the electrode surface, probably involving the corrosion products. R_e represents the electrolyte resistance. Coefficients n_{dl} and n_F represent the depressed feature of the capacitive loop in *Nyquist* diagram ($0 < n \leq 1$). The values of C_F and C_{dl} were calculated using the equation $C = (R^{1-n}Q)^{1/n}$, where Q is the constant phase element.

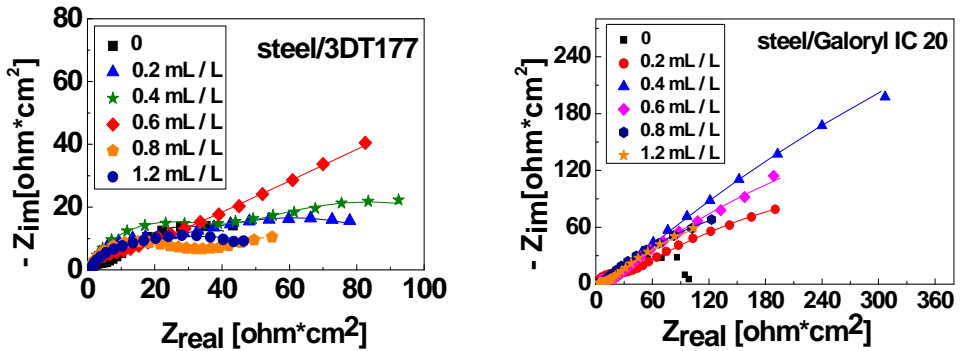


Figure 2. Nyquist impedance diagrams for the steel electrodes in synthetic wastewater (pH 3), at different concentrations of inhibitors; the lines represent fitted data

Analyzing the data from Table 1, it can be observed that, the value of the corrosion resistance depends on the concentrations of inhibitors, which influences the formation of the oxide film which inhibits the corrosion process on the surface of steel.

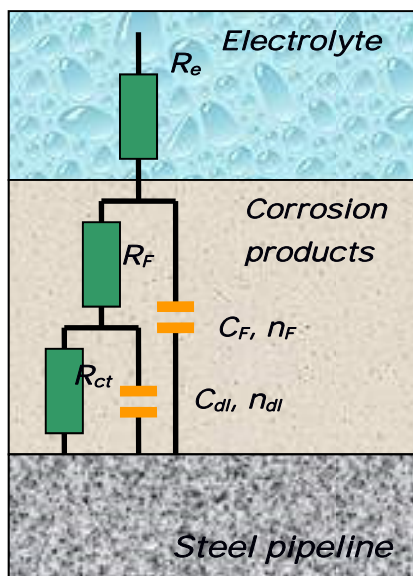


Figure 3. The equivalent electrical circuit used for fitting of the experimental results

Table 1. The electrochemical impedance parameters estimated by fitting the experimental impedance data from Figure 6.

	Concentration [mL / L]	R_e [Ω^*cm^2]	R_{ct} [Ω^*cm^2]	C_{dl} [$\mu F/cm^2$]	n_{dl}	R_F [Ω^*cm^2]	C_F [mF/cm ²]	n_F	R_p^* [Ω^*cm^2]
	0	1.55	11.15	215.5	0.804	97.9	19.23	0.648	109.03
3DT177	0.2	1.80	71.51	321.2	0.804	200.6	51.77	0.492	272.11
	0.4	1.56	27.90	165.9	0.775	289.8	52.55	0.501	317.70
	0.6	1.73	26.84	132.5	0.851	276.2	44.17	0.230	303.04
	0.8	1.67	35.08	177.6	0.884	179.2	21.60	0.435	214.28
	1.2	2.03	24.01	369.4	0.807	110.8	15.25	0.401	134.81
Galoryl IC 20	0.2	1.6	19.9	39.75	0.85	659.8	307.5	0.38	679.7
	0.4	2.93	10.11	18.52	0.79	2045	251.5	0.46	2055.11
	0.6	2.19	11.47	17.65	0.84	952.4	311	0.44	963.87
	0.8	1.10	3.63	2.72	0.65	466.8	263.9	0.45	470.43
	1.2	2.37	8.83	17.87	0.46	445.3	399.4	0.46	454.13

$$R_p^* = R_{ct} + R_F$$

The highest polarization resistance ($R_p = R_{ct} + R_F$), which is an indicator of corrosion resistance, was observed at the concentration of 0.4mL/L. From the three tested inhibitors, Galoryl IC 20 was proven to be the best. The results were confirmed by linear and potentiodynamic polarization measurements.

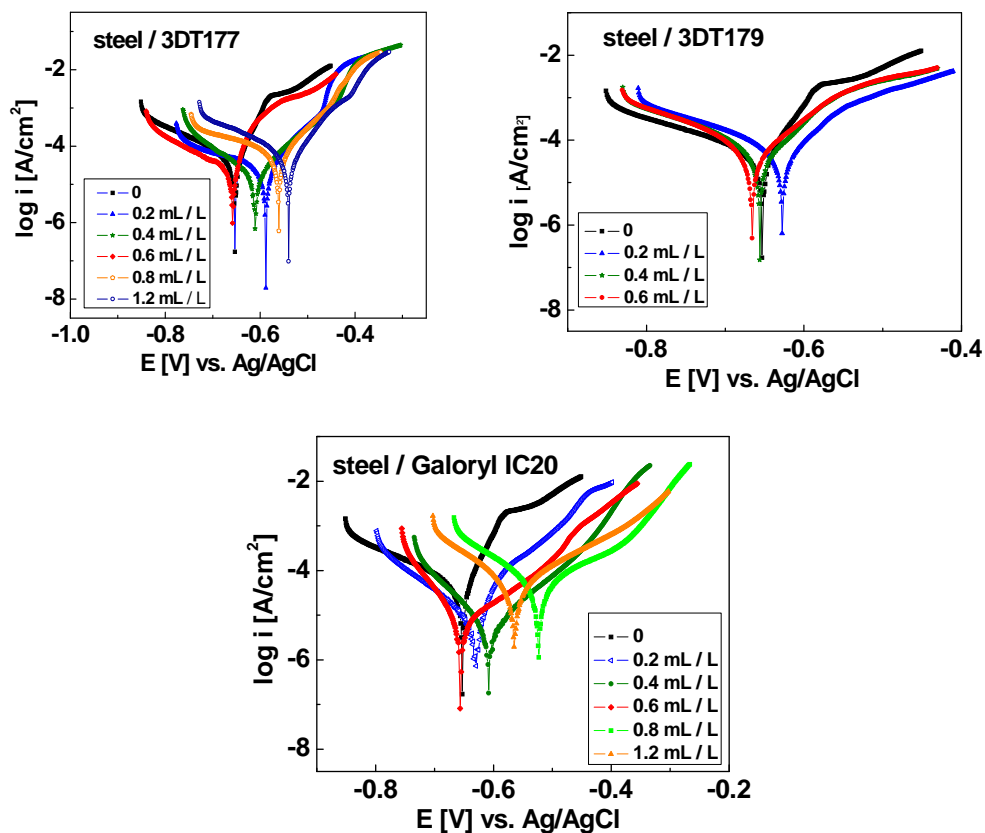


Figure 4. The polarization curves (± 200 mV vs. OCP) for the studied electrodes immersed in synthetic wastewater (pH = 3) at different concentrations of inhibitors; scan rate, 10 mV / min.

To determine the polarization resistance of the electrodes, linear polarization curves were recorded, in the potential domain of ± 20 mV vs. OCP. The polarization resistance (R_p) values, for each electrode, was calculated with the formula: $R_{p(\Delta E \rightarrow 0)} = \frac{\Delta E}{\Delta i}$, (1), and are shown in Table 2.

The protection efficiency of the inhibitors on steel was determined with the formula: $IE[\%] = \frac{R_p^{inh} - R_p^0}{R_p^{inh}} \cdot 100$, (2), where R_p^{inh} is the polarization resistance in presence of inhibitors and R_p^0 is the polarization resistance without inhibitors, respectively.

In order to determine the kinetic parameters of the corrosion process, potentiodynamic polarization curves were recorded in the potential range of ± 200 mV vs. OCP (Fig. 4). The Tafel interpretation of the polarization curves led to the results presented in Table 2.

Table 2. Corrosion process parameters for the examined samples

Inhibitor	Concentration [mL/L]	E_{corr} [mV]	i_{corr} [$\mu\text{A}/\text{cm}^2$]	$-\beta_c$ [mV]	β_a [mV]	R_p [$\Omega^*\text{cm}^2$]	IE [%]
-	0	-654.34	61.80	166.79	46.36	80	-
3DT177	0.2	-587.81	38.38	447.07	84.40	570	84.04
	0.4	-613.35	18.36	145.87	103.16	970	86.61
	0.6	-658.06	24.46	155.38	36.87	480	84.38
	0.8	-558.11	86.09	401.05	110.99	400	74.14
	1.2	-541.08	74.06	186.23	84.12	280	74
3DT179	0.2	-627.44	73.45	180.60	82.81	90	16
	0.4	-655.14	60.51	140.29	80.28	90	16
	0.6	-665.63	60.38	135.18	89.61	110	31.81
Galoryl IC 20	0.2	-628.58	7.18	105.54	48.00	450	83.33
	0.4	-607.73	5.75	78.75	132.13	580	87.07
	0.6	-636.34	9.59	62.81	114.91	380	80.26
	0.8	-521.64	48.86	115.87	142.83	340	77.94
	1.2	-564.22	49.2	118.57	149.49	260	75.80

β_a and β_c are the Tafel coefficients [mV]

The analysis of the data from Table 2 led to the conclusion that in case of 3DT177 and Galoryl IC 20 an increase of corrosion resistance takes place at all inhibitors concentrations. The highest corrosion resistance and the lowest corrosion current density were noticed at 0.4 mL/L concentration of inhibitors. This is in agreement with the results obtained from the EIS measurements.

In case of 3DT179, the increase of the corrosion resistance was not significant.

Adsorption isotherm

The polarization resistance values (Table 2), were used to calculate the degree of surface coverage (θ) with inhibitor molecules according to the

following equation: $\theta = \frac{R_p^{inh} - R_p^0}{R_p^{inh}}$, (3).

Since the corrosion inhibition process is based on the adsorption of corrosion inhibitor molecules on steel surface, it is important to elucidate their adsorption behaviour. Fig. 5 shows that the plot of $\frac{C_{in}}{\theta}$ versus C_{in} results in a straight line, confirming that the adsorption of both inhibitors (3DT177 and Galoryl IC20) on low carbon steel obeys Langmuir isotherm: $\frac{C_{in}}{\theta} = \frac{1}{K} + C_{in}$, (4) where K is the adsorption equilibrium constant and C_{in} is the inhibitor concentration.

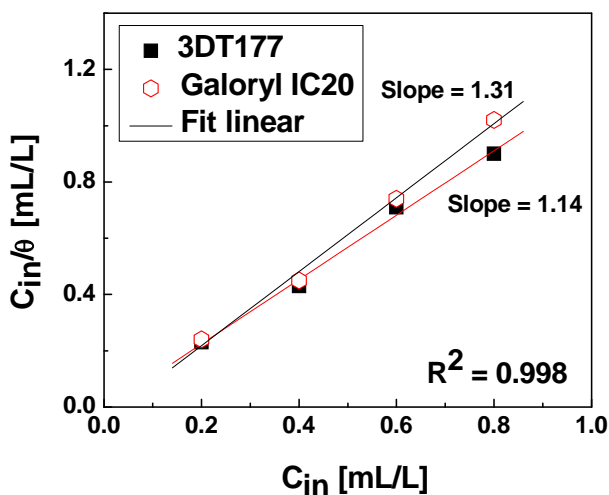


Figure 5. Langmuir isotherm for adsorption of 3DT177, Galoryl IC 20 on low carbon steel surface

The beneficial effect of Galoryl IC 20 can be seen also by naked eye, inspecting the steel electrodes surface after the corrosion tests. As can be observed from Fig. 6, in the absence of inhibitors, the surface is non-uniformly corroded. In the presence of 3DT177, the surface is covered with a uniform layer of corrosion products which may confer to steel a certain resistance to further corrosion. Best results were obtained in the case when Galoryl IC 20 was used, the electrode surface remaining clean and bright after the corrosion tests.

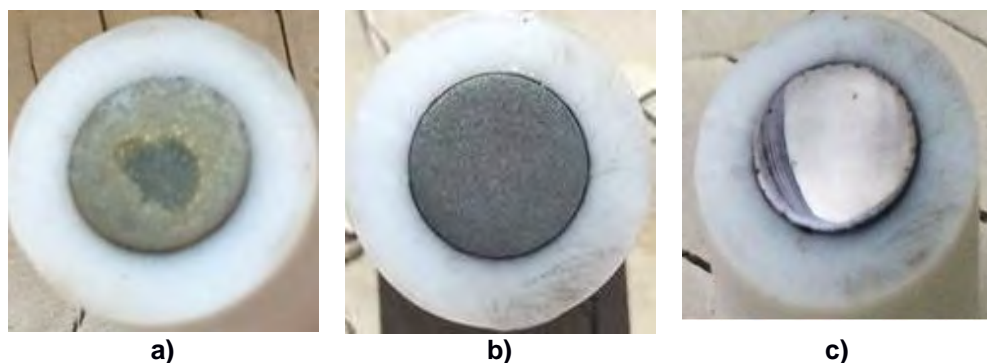


Figure 6. Surface of low carbon steel electrodes after corrosion tests: in the absence of inhibitors (a), in the presence of 3DT177 (b) / Galoryl IC 20 (c)

CONCLUSIONS

Electrochemical investigations (polarization and impedance measurements) have shown that two of the three inhibitors used exert a good protective effect against steel corrosion in simulated wastewater from petroleum and oil industry. The best anticorrosive effect was noticed when 0.4 mL inhibitor were used (PE = 86.61 % for 3DT177 and respectively PE = 87.07 % for Galoryl IC 20). With the increase of inhibitors concentration in corrosion solution, the anticorrosive effect in both cases decreases.

The corrosion behavior of the steel immersed in synthetic wastewater from petroleum and oil industry (pH 3) solution can be simulated with a 2RQ electric circuit.

Adsorption of both inhibitors (3DT177, Galoryl IC 20) on low carbon steel surface obeys Langmuir isotherm.

EXPERIMENTAL

Materials

The working electrodes used in this work were cut from an OL37 steel bar, with the chemical composition (wt. %): C (0.22), Mn (0.85), P (0.055), S (0.055) and Fe balance. The surface of the working electrodes exposed to the corrosive solution was disk - shaped, with a surface $S = 0.5 \text{ cm}^2$. The working electrodes were sealed by encapsulation in Teflon. For electrical contact, a copper rod was attached. Before the corrosion tests, the working surface of the electrodes was ground sequentially with emery papers from # 800 up to # 2000 grades, and degreased with acetone, washed with

distilled water and dried. The surface of the steel electrodes was examined by optical microscopy using an OLIMPUS GS 51 optical microscope. For this purpose, the electrodes were polished on the sample polishing machine with alumina paste, after which the surface was attacked with nital for a few seconds. The microstructure of the steel contained ferrite and pearlite (Fig. 7).

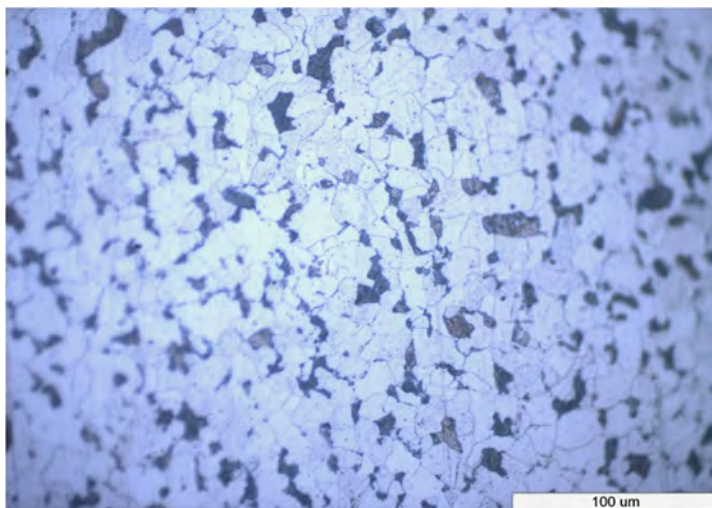


Figure 7. Microscopic structure of low carbon steel used for electrochemical studies X500

Corrosion inhibitors

The inhibitors used in the experiments were:

(i) 3DT177, 3DT179 (Nalco Products)

Physical Chemical Properties:

- clear, light yellow liquid
- slight acidic odor
- miscible in water
- pH 3.1
- vapor pressure 15.6 mm Hg at 100 °F / 20 °C

(ii) Galoryl IC 20 EU is an aqueous anionic solution of organic and inorganic additives specifically developed as a corrosion inhibitor in fertilizer industries.

Typical properties:

- physical appearance, yellow liquid
- pH 9.0
- specific gravity (25 °C), 1.03

The inhibitors were dissolved in the corrosive solution at different concentrations: 0.2 mL / L, 0.4mL / L, 0.6 mL / L 0.8 mL / L, 1.2 mL / L.

Experimental investigation

The electrochemical corrosion measurements were performed on a PC – controlled electrochemical analyzer PAR 2273 (Princeton Applied Research, USA) using a three electrodes cell containing a working electrode (steel), a saturated calomel electrode (ECS) as reference electrode and a platinum counter electrode. The electrolyte solution for corrosion measurements prepared conform Table 3, was acidic (pH = 3) and had high salinity.

Table 3. The composition of the “produced water” used in corrosion tests (pH = 3)

Conc.	Fe ³⁺	Ni ²⁺	Cu ²⁺	Na ⁺	K ⁺	SO ₄ ²⁻	NO ₃ ⁻	Cl ⁻
g / L	0.02	0.006	0.1·10 ⁻³	50	5.4	6.64	0.27·10 ⁻³	77.09

The open circuit potential for steel immersed in the corrosive solution was monitored during 1 hour. The EIS was then measured in the frequency range from 10 kHz to 10 mHz at 30 points with a disturbance voltage of ± 10 mV. The impedance data were fitted with a 2RQ equivalent electrical circuit, using the ZSimpWin V3.21 software.

After the EIS measurement was finished, polarization curves were recorded immediately by scanning in a potential range of ± 20 mV and of ± 200 mV vs. open circuit potential, with a scan rate of 10 mV / min. The testing temperature was kept at 20 °C.

REFERENCES

1. Y. Liu, B. Zhang, Y. Zhang, L. Ma, P. Yang, *Engineering Failure Analysis*, **2016**, 60, 307.
2. T. Liu, Y. F. Cheng, M. Sharma, G. Voordouw, *Journal of Petroleum Science and Engineering*, **2017**, 156, 451.
3. S.S.M. Tavares, J.M. Pardal, F.B. Mainier, H.R. da Igreja, E.S. Barbosa, C.R. Rodrigues, C. Barbosa, J.P. Pardal, *Engineering Failure Analysis*, **2016**, 61, 100.
4. H. Gao, Q. Li, Y. Dai, F. Luo, H.X. Zhang, *Corrosion Science*, **2010**, 52, 1603.
5. Y. Liu, Y. Zhang, J. Yuan, *Engineering Failure Analysis*, **2014**, 45, 225.

6. A. Venkatesan, P.C. Wankat, *Desalination*, **2017**, 404, 328.
7. M. Finšgar, J. Jackson, *Corrosion Science*, **2014**, 86, 17.
8. M.L. Walker, Method and Composition for Acidizing Subterranean Formations, in: US Patent 5,366,643, Halliburton Company, Duncan, Okla, **1994**.
9. P.C. Okafor, X. Liu, Y.G. Zheng, *Corrosion Science*, **2009**, 51, 761.
10. D.A. Williams, P.K. Holifield, J.R. Looney, L.A. McDougall, Method of Inhibiting Corrosion in Acidizing Wells, in: US Patent 5,200,096, Exxon Chemicals Patents, Inc., Linden, N.J., **1993**.
11. A. Ostovari, S.M. Hoseinie, M. Peikari, S.R. Shadizadeh, S.J. Hashemi, *Corrosion Science*, **2009**, 51, 1935.
12. A.K. Satapathy, G. Gunasekaran, S.C. Sahoo, K. Amit, P.V. Rodrigues, *Corrosion Science*, **2009**, 51, 2848.

THE STUDY OF DISSOLVING UREA GRANULES BASED ON THE GENERALISED DIMENSIONAL ANALYSIS

MISCA B.R.H.^{a*}, CHIRA G.C.^b

ABSTRACT. This paper work contains the study of non-stationary dissolution of individual urea granules used as fertilizers. The present study is based on The Generalized Dimensional Analysis and includes comments about the fundamental factors, the important factors, the secondary factors and about the unimportant factors which can control the phenomenon. It also contains experimental determinations on simple and filmed urea granules that lead to a general equation for the dissolving process.

Keywords: *Generalized Dimensional Analysis, non-stationary dissolution, pure and filmed urea granules, mathematical equations for non steady-state dissolution.*

INTRODUCTION

Starting with The Generalized Dimensional Analysis Method (GDAM), defined by Prof. Dr. Eng. Staicu C-tin, [1] and later developed by others, [2], we tried to study the dissolution of urea granules utilized as fertilizers. According to the methodology, we established the list of variables, that can influence the process. The list is presented below:

$$\| \tau, D, d, c_{\text{sat}}, m, d, V, g, \rho, \eta, \nu \|$$

where:

- L, M, T - the symbols of the measuring units for Length, Mass and Time;
- $Fo_d = (\tau D_{di})/d^2$ - the Fourier criteria for diffusion, [-];
- $Sc = (\nu/D_{di})$ - the Schmidt criteria, [-],
- $k_1, k_2, k_3, k_4, \dots$ - the numerical coefficients of the monomial relation, [-].

^a Babeş-Bolyai University, Faculty of Chemistry and Chemical Engineering, 11 Arany Janos str., RO-400028, Cluj-Napoca, Romania

^b S. A. Azomures, Târgu-Mures

* Corresponding author: miscar@chem.ubbcluj.ro

Table 1. The parameter's exponent of variables

The parameter's exponent	The parameter, (variable)
a	τ , - dissolution time, [s];
h	D_{di} , - diffusion coefficient, [m ² /s];
b	c_{sat} , - concentration at saturation, [kg/m ³];
e	m, - the mass of particle, [kg];
i	d, - the diameter of particle, [m];
f	V, - the volume of particle, [m ³];
p	g, - the gravitational acceleration, [m/s ²];
t	ρ , - the solvent's density, [kg/m ³];
r	η , - dynamic viscosity, [kg/m·s];
s	ν , - kinematic viscosity, [m ² /s];

The working procedure is detailed in the bibliographical references [1, 2] and in others as well [3, 4, 5]. The linear matrixes of the minimum parameters that can influence the variables with direct action over the process are separated by the variables that have a reverse action over the process. The undetermined dimensional system of the variables exponents is attached to this linear matrix. This truncated system is resolved by the progressive homogenization method. The solution to this system must be: minimal, integer, positive and nonzero. The variables are introduced one by one and the computation procedure is repeated for each case. The numeric value of the parameters exponent and the number of solutions accepted by the GDAM establish the level of hierarchization of the parameter, from fundamental to unimportant. The monomial expression of the distributed variables is formed with the numeric value identified for each parameter's exponent. In order for a monomial expression to be correct it must be dimensionally homogenous and the numeric value of the monomial's coefficient must be constant. Through common mathematical operation the similitude criteria or simplexes can be obtained, offering new possibilities for interpretation to each parameter's importance.

a) The study starts with the minimum number of variables that can possibly influence the dissolving process. The linear matrix with dimensional matrix of the variables attached to it is:

$$\begin{array}{l}
 \mathbf{L} \\
 \mathbf{M} \\
 \mathbf{T}
 \end{array}
 \begin{array}{l}
 || \tau,^a \\
 \mathbf{0} \\
 \mathbf{0} \\
 \mathbf{1}
 \end{array}
 \begin{array}{l}
 c^{b_{sat}, ;} \\
 -\mathbf{3} \\
 \mathbf{1} \\
 \mathbf{0}
 \end{array}
 \begin{array}{l}
 m^e, || \\
 \mathbf{0} \\
 \mathbf{1} \\
 \mathbf{0}
 \end{array}$$

The undetermined system of variable's exponents is:

$$\begin{array}{rcl} L & & -3b = 0 \\ M & & b = e \\ T & & a = 0 \end{array}$$

This system doesn't follow the type of solution accepted by the method: integer, positive, minimum and nonzero, two of the exponents, a and b, being equal to zero.

b) The parameters are replaced with others circular permutations and the result we get are two other linear matrixes:

$$\begin{array}{rcl} & || \tau,^a & c^{b_{sat}}; V^f, || \text{ and} & & || \tau,^a & c^{b_{sat}}; d^i, || \\ L & 0 & -3 & 3 & L & 0 & -3 & 1 \\ M & 0 & 1 & 1 & M & 0 & 1 & 1 \\ T & 1 & 0 & 0 & T & 1 & 0 & 0 \end{array}$$

Neither one nor the other matrixes follow the type of solution accepted by the method, because a = 0 in both cases.

Commentary: These parameters are not sufficient for describing the process.

The fact that linear dimensions, V and d, are closer to an accepted solutions can be remarked.

c) The process is repeated with the following linear matrixes:

$$|| \tau,^a D^{h_{di}}; m^e, || \quad || \tau,^a D^{h_{di}}; V^f, || \quad || \tau,^a D^{h_{di}}; d^i, ||$$

The solutions are:

$$a = 1; h = 1; e = 0; \quad a = 1; h = 1; f = 2/3; \quad a = 1; h = 1; i = 2;$$

One of the above matrixes generates a solution accepted by the method, containing the diameter of the granule.

The monomial expression is:

$$\tau = k_1 \cdot (d^2/D_{di}), [s] = [s];$$

it is dimensionally homogeneous and can be rewritten as:

$$(\tau \cdot D_{di} / d^2) = k_1 = (Fo_d).$$

Conclusion: The fundamental parameters for the process are: τ , D_{di} , and d, parameters also encountered in the Fourier criteria for diffusion for mass transfer.

d) The simultaneous introduction of the variables that describe the general processes of mass transfer: c_{sat} and D_{di} generate the following linear matrixes:

$$\| \tau,^a c^{b_{\text{sat}}}, D^{h_{\text{di}}}, ; m^e, \| \quad \| \tau,^a c^{b_{\text{sat}}},, D^{h_{\text{di}}}, ; V^f, \|$$

$$\| \tau,^a c^{b_{\text{sat}}}, D^{h_{\text{di}}}, ; d^i, \|$$

None of them contains solutions accepted by the method.

Conclusion: It is very likely for the parameter concentration to have a secondary or reduced importance.

e) Introducing the variable gravitational acceleration, in all the possible permutations, nine in total, does NOT generate solutions accepted by the method.

Conclusion: The parameter gravitational acceleration is a secondary parameter or has a reduced influence on the dissolving process.

f) By introducing the variable dynamic viscosity, in all permutation, nine in total, we do not obtain any solutions accepted by the method.

Conclusion: It is very likely that the parameter dynamic viscosity to have a secondary or reduced importance on the dissolving process.

g) Introducing the kinematic viscosity as a variable, in all possible permutations, nine in total, we obtain only one solution accepted by the method.

	$\ \tau,^a$	$D^{h_{\text{di}}}, ;$	$d^i,$	$v^s \ $
L	0	2	1	2
M	0	0	0	0
T	1	-1	0	-1

The system solution is: $a = 1$; $s = 1$; $h = 2$; $i = 2$, and the monomial expression is:

$$\tau = k_2 \cdot (d^2 \cdot v / D^2_{\text{di}})$$

and can be rewritten as:

$$(\tau \cdot D_{\text{di}}) / d^2 = k_2 \cdot (v / D_{\text{di}}) \quad \text{or} \quad \text{Fo}_d = k_2 \cdot (\text{Sc}).$$

Conclusion: Kinematic viscosity is a secondary parameter or has a very little influence on the dissolving process.

This unic result accepted leads to the idea of verifying the solution's density as a working parameter.

h) By introducing the variable solution's density, in all permutations, nine in total, we obtain a single solution accepted by the method.

	$\ \tau,^a$	$c^{b_{\text{sat}}},$	$D^{h_{\text{di}}}, v^s, ;$	$d^i,$	$\rho^t,$	$\eta^r, \ $
L	0	-3	2 2	1	-3	-1
M	0	1	0 0	0	1	1
T	1	0	-1 -1	0	0	-1

The system's solution is: $a = 1$; $s = 1$; $h = 1$; $i = 2$; $t = 1$; $r = 1$; $b = 2$, and the monomial:

$$\tau = k_3 \cdot (d^2 \cdot \rho \cdot \eta)(c_{\text{sat}}^2 \cdot D_{\text{di}} \cdot v),$$

or rearranged:

$$(\tau \cdot D_{\text{di}}/d^2) = k_3 \cdot (\rho \cdot \eta) \cdot (c_{\text{sat}}^2 \cdot \tau) = k_5 \cdot (\rho^2)/(c_{\text{sat}}^2);$$

$$Fo_d = k_3 \cdot (\rho^2)/(c_{\text{sat}}^2).$$

Conclusion: Obtaining a simplex of similitude, dependent on the solution's density and the concentration at saturation shows that in addition to Fourier's criteria, an essential criteria in the non-steady-state dissolving process, both of the variables can be accounted in some cases, for example when the quantity of solution is considerably higher than the quantity of solid or in the case of reaching the saturation concentration, cases that can not be met when dissolving urea granules in the soil.

i) If the following variables are considered:

τ, a	c_{sat}^b	D_{di}^h	v^s	d^i	m^e	\parallel
L	0	-3	2	2	1	0
M	0	1	0	0	0	1
T	1	0	-1	-1	0	0

The system's solutions is: $a = 2$; $s = 1$; $h = 1$; $i = 1$; $t = 1$; $e = 1$; $b = 1$, and the monomial expression is:

$$\tau^2 = k_4 \cdot (d \cdot m)(c_{\text{sat}} \cdot D_{\text{di}} \cdot v), \quad \text{or rearranged:}$$

$$(v \cdot D_{\text{di}}/d^2)^2 = k_4 \cdot (D_{\text{di}}/v) \cdot (m/c_{\text{sat}} \cdot d^3);$$

$$Fo_d^2 \cdot Sc = k_4 \cdot (m) \cdot (c_{\text{sat}} \cdot d^3); \quad \text{or:}$$

$$Fo_d^2 \cdot Sc = k_4 \cdot (C_{\text{particule}})/(c_{\text{sat}}).$$

Conclusion: By introducing the variable mass of granule, it was obtained a single solution accepted by the method.

The generation of a new simplex of similitude, dependent on the density of the particle, (which represent the concentration of the solid, m/V , or density of particle, ρ , as well) and the concentration of saturation, shows that in addition to Fourier's criteria, we obtain Schmidt's criteria, Sc , and both variables can be accounted for in some cases, for example when the solid is not pure, or when the concentration at saturation is reached, cases not met when dissolving the granule in soil.

RESULTS AND DISCUSSION

The evolution of dissolving pure and filmed urea granules are presented below:

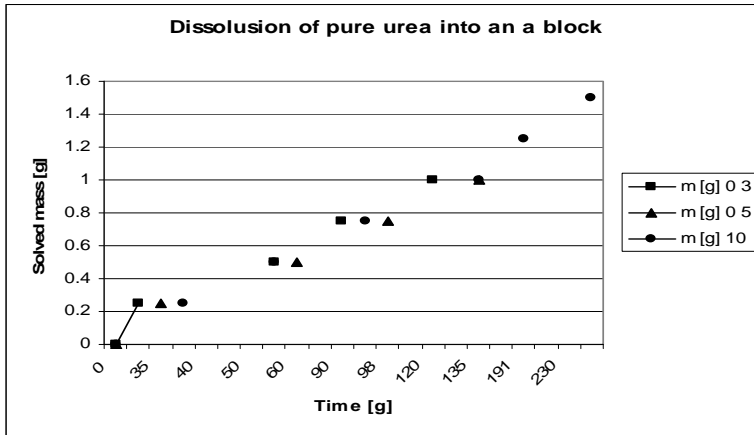


Figure 1. Dissolution of pure urea into block granules

For each determination, the average slope of measures, meaning the average dissolving speed is:

- for 3 [g]; $1/120 = 0.00083$ [g/s];
- for 5 [g]; $1/125 = 0.00080$ [g/s];
- for 10 [g]; $2/326 = 0.00061$ [g/s].

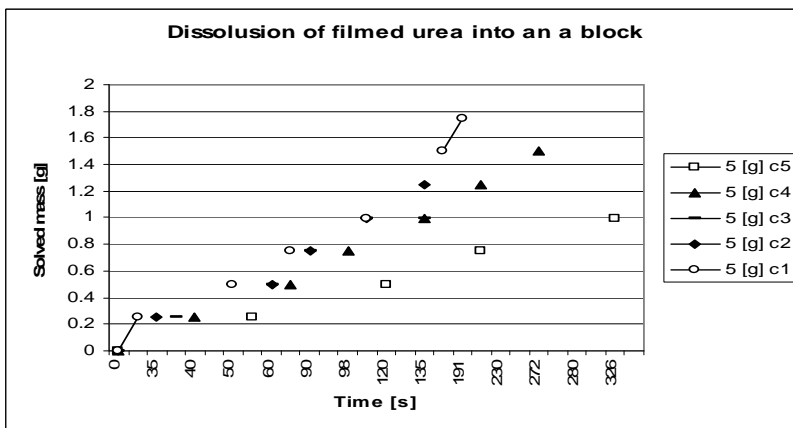


Figure 2. Dissolution of filmed urea into block granules

For each concentration of the varnish, we found values of the dissolving speeds in the following manner:

- c 5) - between 0 and 120 [s]: $0.5/120 = 0.004$ [g/s];
 - between 120 and 326 [s]: $0.5/(326-120) = 0.00243$ [g/s].
- c 4) - between 0 and 75 [s]: $1.0/75 = 0.0066$ [g/s];
 - between 75 and 272 [s]: $0.5/(272 - 75) = 0.005$ [g/s].
- c 3) -between 0 and 60 [s]: $0.5/60 = 0.0083$ [g/s];
 - between 60 and 135 [s]: $0.5/(135 - 60) = 0.0066$ [g/s].
- c 2) - between 0 and 135 [s]: $0.5/75 = 0.0066$ [g/s].
- c 1) - between 0 and 109 [s]: $1.0/109 = 0.0092$ [g/s];
 - between 109 and 162 [s]: $0.5/(162 - 109) = 0.0094$ [g/s];
 - between 162 and 191 [s]: $0.25/(191-162) = 0.0086$ [g/s].

From the graphs and computation results, we noticed a different behavior at dissolving between pure and filmed granules, fact expected to manifest due to the presence of the polymeric film.

The pure granules have a linear and higher dissolving speed than the filmed granules. The film, depending on the concentration of the varnish, meaning the thickness of the film, modifies the behavior of dissolving process.

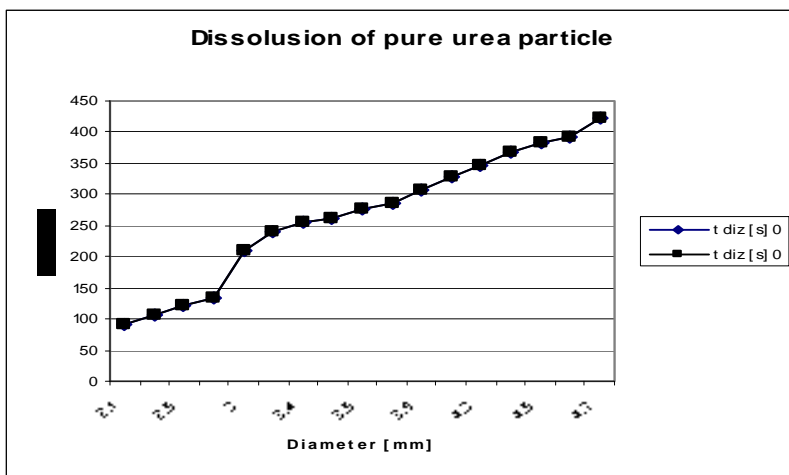


Figure 3. Dissolution of pure urea single particle

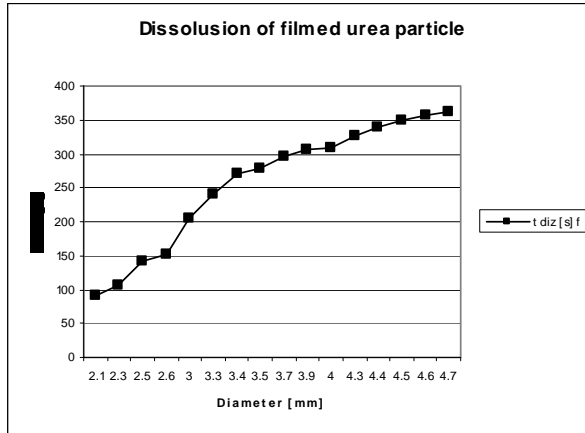


Figure 4. Dissolution of filmed urea single particle

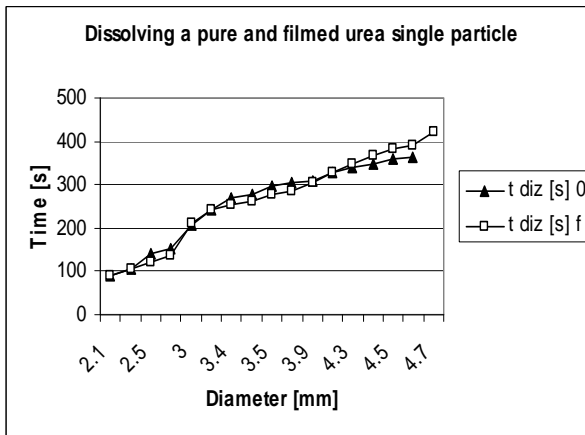


Figure 5. Dissolution of pure and filmed urea single particle

In order to verify the speed determining phase, the classic relations and the relation resulted from the generalized dimensional analysis were tested:

$$(t_1/t_2) = (d_1/d_2)^x, [6];$$

- if $x = 2$ determinant phase is internal diffusion;
- if $x = 1$ determinant phase is dissolution;
- if $x = (1.5 - 2.5)$ determinant phase is external diffusion.

The equation is solved by applying the logarithm:

$$\log(t_1/t_2) = x \cdot \log(d_1/d_2) \quad x = [\log(t_1/t_2)/\log(d_1/d_2)].$$

For pure urea granules the results are presented in Table 1. The values obtained are close to 1, which means that the determining speed step is the dissolution, a fact that is normal and was expected, because the process studied was the dissolution.

Table 1 Dimensional analysis results

Pure urea granules	Filmed urea granules	Ratio	
$x \cdot 2,1/d_i$	$x \cdot 2,1/d_i$	$p \cdot t/d^2$	$f \cdot t/d^2$
0.934479	1.711885	20.45351	20.43084
0.937766	3.472922	19.92439	19.96219
0.941538	1.90115	22.528	19.584
0.74215	2.11096	22.44083	20.0
0.962214	1.665457	22.8	23.35556
0.969388	3.912924	22.08448	22.06612
0.999258	0.931743	23.38235	22.09343
0.947109	1.178802	22.66939	21.72642
1.028271	0.617695	21.65814	22.67755
0.98282	0.397741	20.13807	20.86194
0.958663	0.790347	19.3375	20.13807
1.013165	1.385157	17.71769	20.48125
0.967862	1.360509	17.46901	18.80476
0.97803	1.146694	17.21975	18.9876
1.003171	0.619985	16.89981	18.98272
			19.09914

For filmed urea granules the results are presented in Table 1.

The values presented show a high fluctuation of exponents. If the higher values, at the initial phase of the process, close to '2', show the influence of the polymer film, the external diffusion being the determinant speed phase, in final, the exponent gets close to value '1', so the destroyed film has a smaller influence, and the process gets closer to pure dissolution.

From the generalized dimensional analysis method results that the monomial which describes dissolution, $\tau = k_1 \cdot (d^2/D_{dif})$, can be verified by the experimental data presented above. In order to do so, we formed the ratio: $(\tau/d^2) = k_1 \cdot (1/D_{dif})$, or $(\tau/d^2) = \text{const}$, a plausible fact, considering that the diffusion coefficient is constant at the same temperature. The value of this ratio for pure, (p) and filmed, (f), granules are presented Table 1.

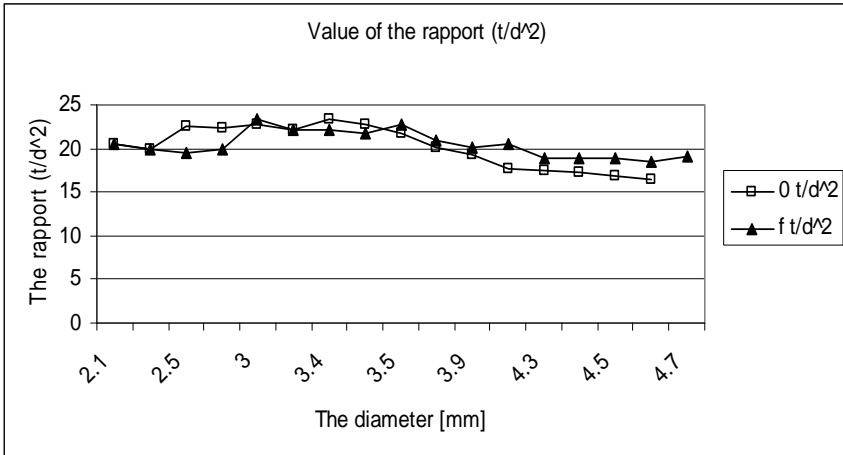


Figure 6. Verifying the monomial constant

In both cases the same effects appear:

- for pure granules, the particle with a diameter between 2.5 and 3.7 [mm] have a different behavior than the rest of diameters studied, 2.1 ÷ 2.3 and respectively 3.9 ÷ 4.7 [mm]. The arrangement of diameters is the same:

2.1 ÷ 2.3 [mm] 2.5 ÷ 3.7 [mm] 3.9 ÷ 4.7 [mm]

- for filmed granules, the evolution is the same, only the diameters differ:

2.1 ÷ 2.6 [mm] 3.0 ÷ 4.0 [mm] 4 ÷ 4.7 [mm].

The nonlinear evolution is in contradiction with the generalized dimensional analysis, where the constant numeric coefficient is stated from the monomial. I put this evolution on the experimental errors, the inaccuracy of measures to both the diameter and the final time of dissolution. Small errors can generate high errors of computation and that is the reason why the values of speed for instantaneous dissolution are not presented here. Getting a relatively narrow interval for the values, 4 units for pure urea, and 8 units for filmed urea, is a reason to continue further measuring of these parameters but in higher accuracy conditions.

CONCLUSIONS

We applied the generalized dimensional analysis method to the dissolving of granules without stirring in liquid.

The main parameters of the process are: the time τ , the diameter of granule d , and the diffusion coefficient D_{dif} .

Kinematic viscosity is a secondary parameter.

The results of the mathematical analysis lead to the following relations:

- the minimum one: $\tau = k_1 \cdot (d^2/D_{\text{dif}})$, or $(\tau \cdot D_{\text{dif}}/d^2) = k_1 = (Fo_d)$.

- the extended one:

$\tau = k_2 \cdot (d^2 \cdot v/D_{\text{dif}}^2)$, $(v \cdot D_{\text{dif}})/d^2 = k_2 \cdot (v/D_{\text{dif}})$ or $Fo_d = k_2 \cdot (Sc)$.

A device for measuring the time of dissolution of a granules quantity was improvised. The speed and the dissolving time depend on the quantity of solid, which is a secondary parameter.

The time or the speed of dissolutions depends on the nature of the solid, pure or filmed. The time increases with the thickness of the film.

The verification of the speed determinant phase for the process lead to a value of 1 for the exponent, meaning that dissolution is the main phase for pure granules and a value close to 2 for filmed granules.

The verification of the numeric coefficient generated by the generalized dimensional analysis method lead to an interval of values higher for the pure solid, 8 units, and a narrower interval for the filmed granules, 4 units.

EXPERIMENTAL SECTION

The objective of the experimental part is the practical determination of pure and filmed urea granule's behavior at dissolution. Filmed urea granules refer to the granules covered in a polymeric compound that generates a thin membrane on the surface of the granule.

For the experimental part of the study of urea without stirring, two sets of experiments were conducted:

1. The dissolution of a set of granules;
2. The dissolution of individual granules.

Materials, tools and methods

- urea granules;
- varnish solutions of various concentrations;
- tap water;
- Berzelius glass, weights, chronometer, calipers.

For the dissolution of a set of granules an experimental device, based on Archimedes's principle was elaborated and applied by the Mohr – Westphal balance. As working principle: the nacelle containing the urea granules is immersed in the glass containing water and then the balance is set to `0`. A determined quantity of granules is then introduced in the nacelle and the balance is set again to the zero value. From this moment, considered `0' as well, the time necessary

to a 0.25 [g] weight to readjust the balance to zero is measured. Then another 0.25 [g] weight is added and the time necessary to readjust the balance is measured. This process is repeated until the granules are completely dissolved and the balance becomes immobile.

The filming of the granules was performed by immersing the granules into a varnish with different concentrations, draining the excess varnish and drying the granules through continuous stirring in the vase, at atmospheric conditions, until complete drying. The stirring was performed through continuously rotating the recipient in order to avoid the granules to stick to each other during drying.

The varnish concentration was determined in the following manner:

- a quantity of varnish of 38.4 [g] was left in a capsule until reaching a constant mass. The quantity of solid resulted was 0.82 [g]. The initial concentration of the varnish is 2.135 [%].

- the solution was gradually diluted to double, resulting the following working concentrations:

5) 2.135 [%]; 4) 1.068 [%]; 3) 0.534 [%];
2) 0.267 [%]; 1) 0.133 [%].

- for each determination 500 [ml] of water were used, in order to get closer to an infinite dilution, but mostly for providing enough space for the nacelle to travel vertically during the determination.

- quantities of 3, 5, and 10 [g] of pure granules and 5 [g] of filmed granules were used.

- the working temperature was room temperature, 20 [°C].

For the dissolutions of individual granules, the method was simple: the diameter of granule was measured, then the time it passed from the moment of immersing it in 500 [ml] of water and it's visual desperation.

REFERENCES

1. C. Staicu, Analiza dimensională generală, *Ed. Tehnică*, București, **1976**.
2. B.R.H. Mișca, Teză de doctorat, UBB Cluj-Napoca, **1998**.
3. B.R.H. Mișca, An interpretation of solid-liquid extraction using the general dimensional method; *Studia UBB Chemia*, **2014**, LIX(3), 139 – 152.
4. B.R.H. Mișca, A. Ozunu, C. Paisz, D. Manciula, A view point upon the droplets formation; *The 30th Conference SSCHE, Proceedings on CD ROM, Tatranske Matliare, SK, 26 – 30 May, 2003, ISBN 80-227-2052-2*.
5. B.R.H. Mișca, A. Ozunu, I. Marian, The General Dimensional Analysis applied to the Microwave Drying of Materials; *The 31th Conference SSCHE, Proceedings on CD ROM, Tatranske Matliare, SK, 24 – 28 May, 2004, ISBN 80-227-2052-2*.
6. R. Mihail, C. Cârloganu, Reactoare în ingineria chimică, *Ed. Tehnică*, București, **1963**, 358 – 368.

NEW FUNCTIONALIZED GLASS FIBERS EMPLOYING CALIXARENIC SYSTEMS

RALUCA ANAMARIA SEPTELEAN^a, MYRAT VELNAZAROV^a,
DOINA PRODAN^b, IOANA PERHAITA^b, OVIDIU NEMES^{c*},
MARIOARA MOLDOVAN^{b*}

ABSTRACT. New precursors for functionalized glass fibres were obtained through deposition of functionalized calix[4]arenes on G14 short glass fibers. The methods employed for the preparation as well as the characterization by thermal analysis, FT-IR spectroscopy, TEM and SEM microscopy of the newly obtained materials is presented.

Keywords: *calixarenes, functionalized glass fibers, thermal analyses, electronic microscopy*

INTRODUCTION

Calix[n]arenes macrocyclic compounds obtained by the condensation of para- substituted phenol with formaldehyde or para-formaldehyde, [1] can be functionalized with a large number of organic or organometallic groups [2,3], at both the *lower* rim (the hydroxyl groups) or the *upper* rim (the *para* position of the phenyl rings) leading to an important class of organic compounds. Their characteristic structure, namely the existence of a hydrophobic cavity which can be tuned in size by the number of phenolic units ($n = 4-20$) as well as the type of the functional groups grafted onto the aromatic rings, makes this class of compounds versatile in a large number of applications ranging from host-guest interactions [4] with metallic ions [5] and neutral molecules to biomedical research [6,7], chromatography [8], electrochemical and luminescent sensors [9,10,11] and catalysis [12].

^a *Facultatea de Chimie și Inginerie Chimică, Universitatea Babeș-Bolyai Cluj-Napoca, Str. Arany Janos, nr 11, RO-400028.*

^b *Institutul de Cercetări în Chimie Raluca Ripan, Universitatea Babeș-Bolyai Cluj-Napoca Str. Fântânele, nr. 30, Cluj-Napoca RO-400294, *marioara.moldovan@ubbcluj.ro*

^c *Facultatea de Ingineria Materialelor și a Mediului, Universitatea Tehnică din Cluj-Napoca, Bulevardul Muncii 103-105, RO-400641, *ovidiu.nemes@sim.utcluj.ro*

A new and exciting field in which calixarenes have recently shown their potential is their use as interfaces towards new materials [13,14,15]. The use of calixarenes as coupling agents assures a better binding to the inorganic material due to multiple connection sites and could increase their elasticity by concurrently taking over the stress on all four connectivity points [16,17].

This work presents a new functionalization method of short glass fibers with substituted calix[4]arene as well as the thermal behavior of the new product and their precursors together with the characterization of the studied systems.

RESULTS AND DISCUSSION

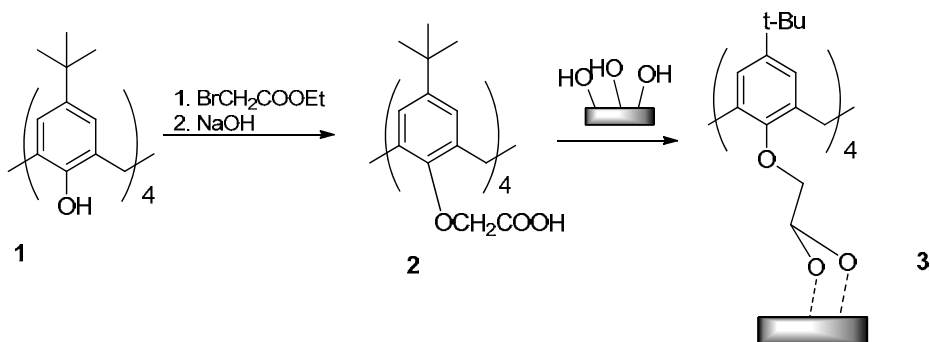
New inorganic based materials were prepared by the deposition of lower rim tetracarboxyl functionalized para-tertbutyl-calix[4]arene **2** onto short glass fibers of G14 type. Calix[4]arene systems were chosen for their relative good solubility when compared to their larger analogues and their preference to adopt a cone conformation, which is more favorable for their study as coupling agents.

The preparation of the organic macrocycle **2** (Scheme 1), was achieved through the methods described in the scientific literature, starting from the commercially available para-tert-butyl calix[4]arene **1**. Derivative **2** was obtained in a two step reaction, and after the purification and separation of the obtained solid, its structure was confirmed by ¹H NMR, FT-IR and MS studies, giving results similar to those already described in the literature [18,19,20].

The new product glass fibers-tetracarboxyl functionalized para-tertbutyl-calix[4]arene **3** (Scheme 1) was obtained by the deposition of calixarenic coupling agent **2** in dilute solutions of ethanol and acetone on short glass fibers type G14.

The methods employed for this deposition consists in the preparation of dilute solutions of functionalized calixarene **2** (5%) in acidified ethylic alcohol **3a** (method 1) or acetone **3b** (method 2). Fine grinded type G14 glass fibers were added to the prepared solutions and the obtained mixture was stirred at room temperature.

After drying, washing and thermal treatment, the resulted products were granulometrical sorted and characterized by means of FT-IR spectroscopy, thermogravimetric analysis and electron microscopy (SEM and TEM).



Scheme 1

In order to fully comprehend the thermal behaviour of the products **3a** and **3b**, their thermograms, together with the ones of the non-modified glasses, calix[4]arene **1** and functionalized calix[4]arene **2** have been recorded (Figure 1).

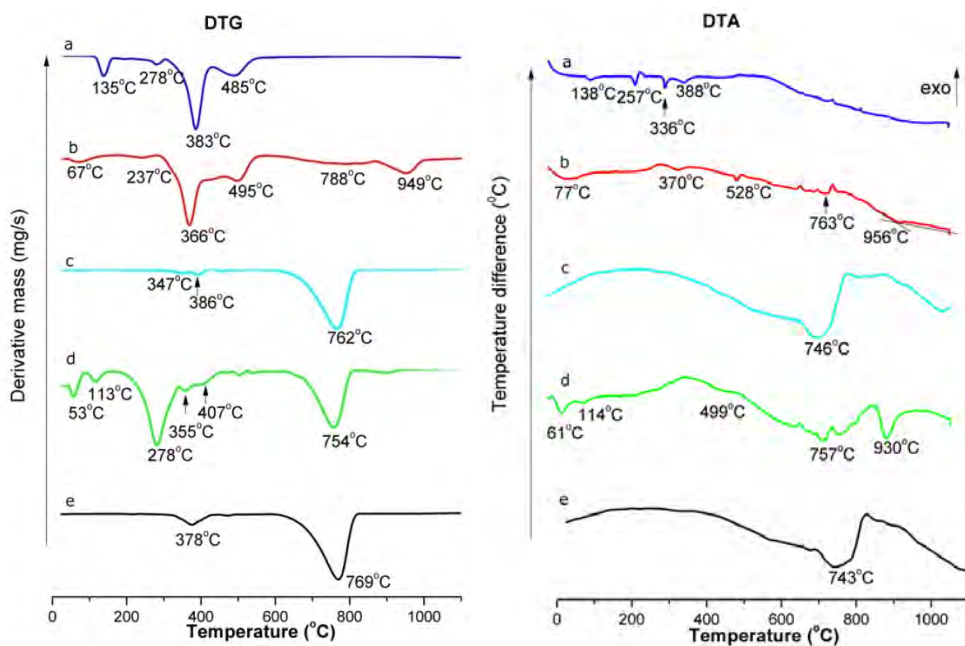


Figure 1. DTG and DTA plots for (a) para-tert-butylcalix[4]arene **1**, (b), para-tert-butylcalix[4]arene acetic acid **2**, (c) glass fibers, (d) product **3a** (glass fiber – functionalized calixarene) in alcohol, (e) product **3b** (glass fiber – functionalized calixarene) in acetone.

Analysing the recorded thermograms, for products **3a** and **3b**, it is clearly to notice a better deposition onto glass fibers by the use of an acidulated solution of ethanol (method 1, Figure 1d). For product **3a**, two important weight loss intervals can be evidenced: 16.1% in the temperature range of 160-340°C, corresponding to the decomposition of the tetraacid calix[4]arene **2** [21], and a second mass loss of 15.0% in the 540-1100°C range, which clearly represents the decomposition of the G14 type glass fibers. For the functionalized tetraacid calix[4]arene **2** (Figure 1b) the first significant weight loss of 38.1% in the 280-460°C temperature range correlates to the similar decomposition observed in case of product **3a**. The fact that the peak temperature for the decomposition in case of **3a** (278°C) is substantially lower than in case of functionalized calixarene **2**, denotes the functionalization of the glass fibers. The thermal stability of the functionalized calixarenes decreased [21,22] if the functional groups grafted at the lower rim of the macrocycles are connected to the inorganic substrate [23].

On the other hand, analyzing the recorded DTG and DTA of the system **3b** (Figure 1e), the obtained plot is almost identical to the starting glass fibers, which suggests that the deposition of the calixarenic coupling agent from acetone solution did not occur as expected, and if it did, it was to a very small extent.

The FT-IR spectra (Figure 2) confirm the results of the thermogravimetric analysis previously discussed. The spectra measured for compounds **3a** and **3b** suggest furthermore that the deposition of the calixarenic coupling agent in alcohol gives the expected results. The broad bands specific to the -OH functional groups around 3500 cm⁻¹ for compound **2** are less significant in the spectrum of product **3a**, suggesting their involvement in the interactions with the surface of the inorganic substrate. The characteristic bands for the organic moieties of calixarenic macrocyclic are situated in the specific range, accordingly with the literature [1, 24, 25].

For a complete characterization of the product **3a** and **3b**, a morphological study using scanning electron SEM (Figure 3) and transmission electron microscopy TEM (Figure 4) respectively was realized.

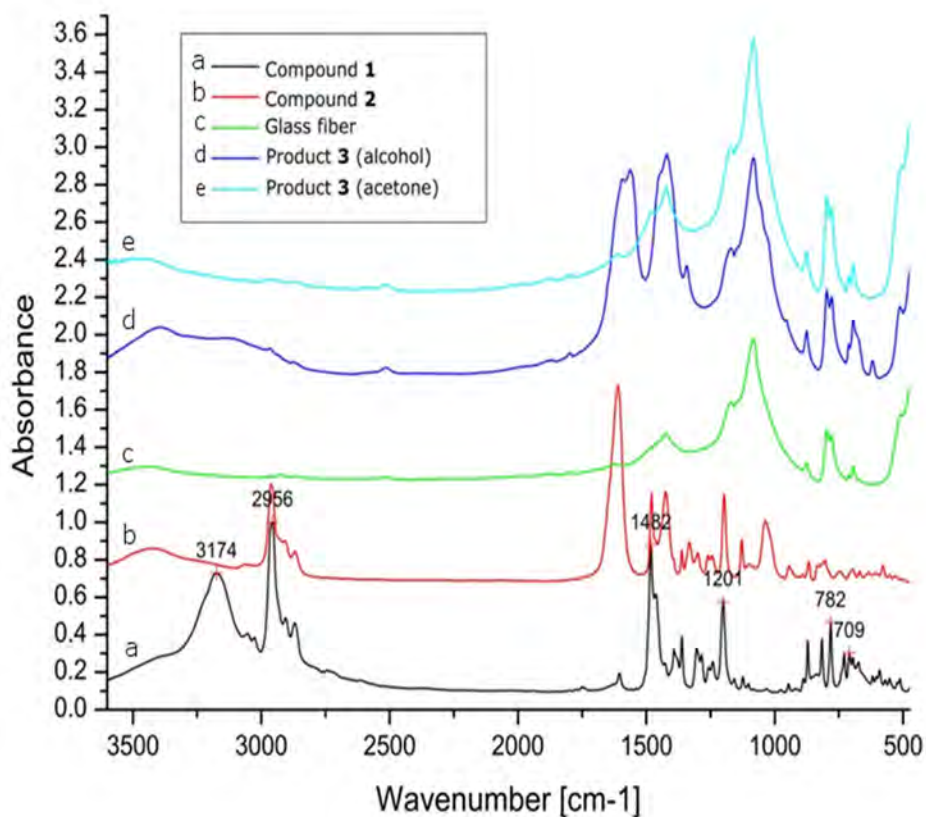
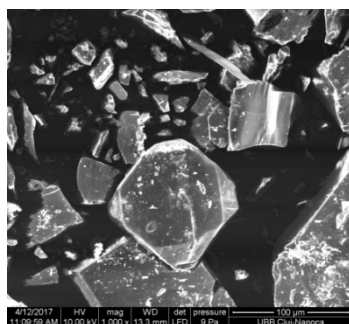
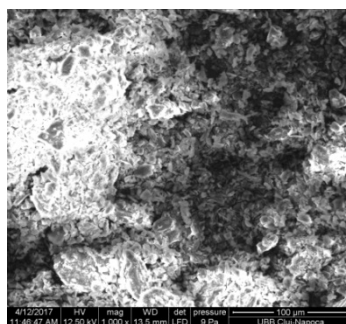


Figure 2. IR spectra of para-tert-butylcalix[4]arene **1** (a), para-tert-butylcalix[4]arene acetic acid **2** (b), glass fibers (c), system **3a** (glass fiber – functionalized calixarene) in alcohol (d), system **3b** (glass fiber – functionalized calixarene) in acetone (e).

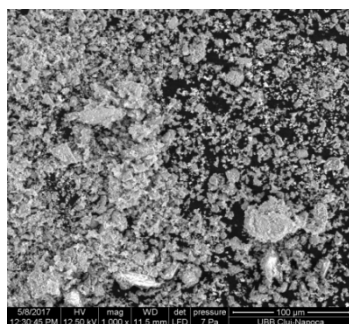
SEM images suggest that, in the case in which the functionalization of the glass fibers has been achieved in acidulated solution of alcohol, the deposition of the functionalized calixarene **2** is much more efficient than if the process is undertaken in acetone (Figure 3).



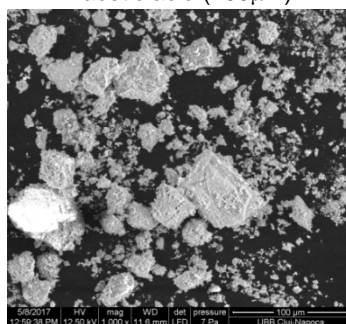
Glass particles (100 μ m)



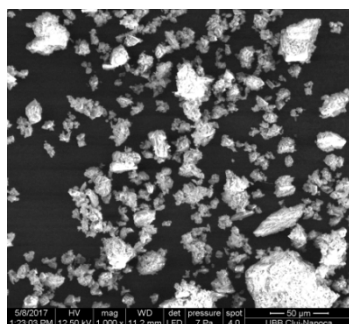
Para-tert-butylcalix[4]arene acetic acid (100 μ m)



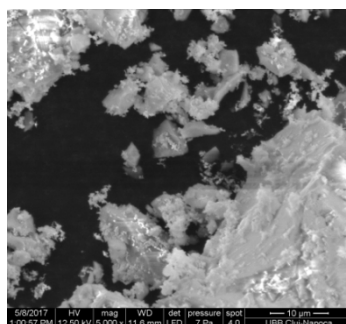
Product **3a** (100 μ m)



Product **3b** (100 μ m)



Product **3a** 50 μ m



Product **3b** 10 μ m

Figure 3. SEM images of used glass fibers, acid functionalized calixarene **2** and the products **3a** and **3b**.

The SEM images of the precursors suggest a clean flat surface in the case of the glass fibers while the acid functionalized calix[4]arene **2** shows a needle-like surface sharp form **3a**. The images recorded for **3a** show the deposition of a continuous layer of coupling agent on the glass surface, while for the product **3b**, the changes of the glass surface are less obvious.

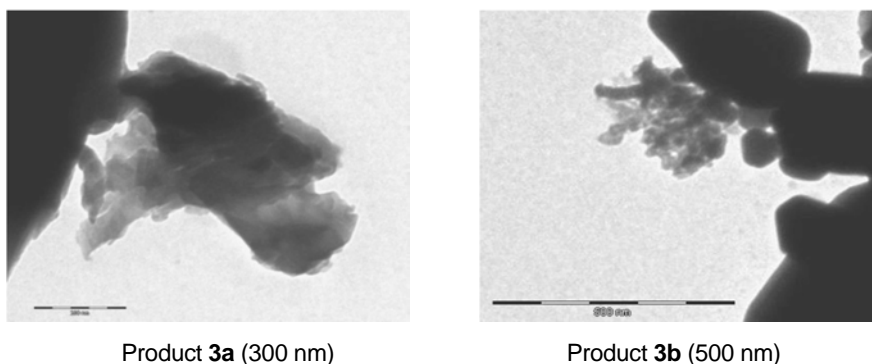


Figure 4. TEM images of product glass fiber – functionalized calixarene.

The results obtained by SEM are supported by TEM analysis, in which a more uniform deposition in the case of **3a** compared to **3b** can be observed (Figure 4).

The complex morphostructural analysis carried out show that the new material has been formed.

CONCLUSIONS

This work presents the successful binding of tetraacetyl functionalized calix[4]arene to short glass fibers of type G14. The deposition of the macrocycle to the glass surface has been done through a novel method, in acidified alcohol solution. The new system together with his precursors were characterized by specific methods including FT-IR, DTG, SEM and TEM, which prove the presence of interactions of the functionalized calixarenic macrocycle system on the inorganic substrate.

EXPERIMENTAL

All the chemicals were used as purchased without any further purification with the exception of THF which was distilled from Na/benzophenone before using.

The ^1H NMR spectra were recorded on a Bruker Avance 400 MHz spectrometer in CDCl_3 , with TMS as reference at a frequency of 400.13 MHz.

The thermal behavior of the samples was investigated by thermogravimetry (TG) differential thermal analysis (DTA) and derivative thermogravimetry (DTG) using a Mettler Toledo TGA/SDTA851 instrument in alumina crucible, with a heating rate of 10 C min^{-1} under nitrogen flow of 50 mL min^{-1} .

The scanning electron microscopy experiments were performed on an Inspect S microscope (FEY Company). The TEM images were obtained using a Hitachi Automatic TEM H7650 system (accelerating voltage 40-120 kV, zoom 200x-600000x)

Synthesis of product 2

Step 1: 3.40 mL of ethyl bromoacetate (5.029 g, 30.11 mmol) were added to a suspension of 1 g (1.54 mmol) of *para*-tert-butylcalix[4]arene and 1.655g (69 mmol) NaH in 30 ml of THF. The resulting mixture was refluxed for one hour, quenched in water after cooling and filtered to yield 1.37 g of tetraethyl calix[4]arene acetic ester (95% yield). The obtained ester was characterized by ¹H NMR giving resonance signals in the ranges described by the literature. [19]

Step 2: A Mixture of 1.37 g brute tetraethyl calix[4]arene acetic ester (1.381 mmol), 25 mL of methanol and 600 mg of NaOH (5.524 mmol) dissolved in 10 mL of water was refluxed for an hour. After cooling, water was added to the reaction mixture. The off-white waxy solid was filtered and washed with several portions of acetone (5 x 10 mL) to yield **2** as a white powder. The derivative was characterized by ¹H NMR, MS and FT-IR giving similar results to those reported in the literature.[20]

Deposition of the organic coupling agent on the glass fibers

The functionalized calix[4]arene was deposited on the glass fibers by dissolving into an alcoholic solution (90 ethanol and 10% distilled water) acidified to a pH of 3.5-4 by means of glacial acetic acid. Due to the low solubility of the macrocycle, a 5% (in weight) solution was used for the deposition. 10 mL of this solution was added to 2 g of finely grinded G14 glass fibers. The mixture was vigorously stirred for 1 hour at room temperature. The thick white paste thus obtained was allowed to dry, in air. After 2 days at room temperature, the resulted product was fixated by thermal treating at 70 °C, in a 1 cm layer for 7 hours. The final product was obtained after sieving through a vibrating sieve (50 μm). The deposition in acetone was achieved in the same manner by dissolving the functionalized calix[4]arene in acetone (5% weight solution) and following the same working procedure.

ACKNOWLEDGMENTS

O.N. thanks for financial support to UEFISCDI by project number PN-III-P2-2.1-96BG-2016. M.M. thanks UEFISCDI for partial financial support by project 101-PED-2017. The authors would like to thanks Dr. Gabriel Katona for recording the TEM images.

REFERENCES

1. C.D. Gutsche, J.F. Stoddart, "Calixarenes Revisited", The Royal Society of Chemistry, Cambridge, **1998**.
2. C. Wieser, C.B. Dieleman, D. Matt, *Coordination Chemistry Reviews*, **1997**, 165, 93.
3. L. Baldini, A. Casnati, F. Sansone, R. Ungaro, *Chemical Society Reviews*, **2007**, 36, 254.
4. J. Rebek, *Chemical Communications*, **2000**, 8, 637.
5. F. Zhang, Y. Sun, D.M. Tian, W.S. Shin, J.S. Kim, H.B. Li, *Chemical Communications*, **2016**, 52, 12685.
6. M.A. Hussain, M.U. Ashraf, G. Muhammad, M.N. Tahir, S.N.A., *Current Pharmaceutical Design*, **2017**, 23, 2377.
7. E.V. Ukhatskaya, S.V. Kurkov, S.E. Matthews, T. Loftsson, *Journal of Pharmaceutical Sciences*, **2013**, 102, 3485.
8. M. Sliwka-Kaszynska, *Critical Reviews in Analytical Chemistry*, **2007**, 37, 211.
9. C.P. Han, H.B. Li, *Analytical and Bioanalytical Chemistry*, **2010**, 397, 1437.
10. J.S. Kim, D.T. Quang, *Chemical Reviews*, **2007**, 107, 3780.
11. D. Diamond, M.A. McKervey, *Chemical Society Reviews*, **1996**, 25, 15.
12. S.Y. Li, Y. W. Xu, J.M. Liu, C.Y. Su, *International Journal of Molecular Sciences*, **2011**, 12, 429.
13. J. Kulesza, B.S. Barros, S. Alves, *Coordination Chemistry Reviews*, **2013**, 257, 2192.
14. S. Hutchinson, G.A. Kearney, E. Home, B. Lynch, J.D. Glennon, M.A. McKervey, S.J. Harris, *Analytica Chimica Acta*, **1994**, 291, 269.
15. S. Friebe, S. Gebauer, G.J. Krauss, G. Goermer, J. Krueger, *Journal Of Chromatographic Science*, **1995**, 33, 281.
16. O. Gezici, M. Bayrakci, *Journal of Inclusion Phenomena and Macrocyclic Chemistry*, **2016**, 83, 1.
17. R. Ranete, P.M. Petrar, R. Septelean, I. Perhaita, G. Nemes, *Studia Universitatis Babeş-Bolyai Chemia*, **2015**, 60, 15.
18. A. Arduini, A. Pochini, S. Reverberi, R. Ungaro, *Journal Of The Chemical Society-Chemical Communications*, **1984**, 15, 981.
19. K. Iwamoto, S. Shinkai, *Journal of Organic Chemistry*, **1992**, 57, 7066.
20. W. Wang, S. Gong, Y. Chen, J. Ma, *New Journal of Chemistry*, **2005**, 29, 1390.
21. A. Saponar, E.-J. Popovici, I. Perhaita, G. Nemes, A.-I. Cadis, *Journal of Thermal Analysis and Calorimetry*, **2012**, 110, 349.
22. H. Deligoz, O. Ozen, G.K. Cilgi, H. Cetisli, *Thermochimica Acta*, **2005**, 426, 33.
23. S. Ozkinali, H. Kocaokutgen, *Journal of Molecular Structure*, **2013**, 1031, 70.
24. A. Saponar, E.-J. Popovici, N. Popovici, E. Bica, G. Nemes, P. Petrar, I. Silaghi-Dumitrescu, *Revista de Chimie*, **2009**, 60, 278.
25. V.L. Furer, E.I. BorisoGlebskaya, V.I. Kovalenko, *Spectrochimica Acta Part A*, **2005**, 61, 355.

QUANTITATIVE MEASUREMENT OF THE LEATHER DEGREE OF SWELLING

SIMONA POPA^a, SORINA BORAN^{a,*}

ABSTRACT. In this paper are presented the experimental results obtained in assessing the degree of swelling of the leather by means of shrinkage temperature. The moisture content of the skin was determined in its various processing steps, correlated with the leather shrinkage value.

Keywords: *drying process, skin type, shrinkage temperature*

INTRODUCTION

During processing of the animal skin there are stages that change the internal protein structure of the collagen fibers [1-5]. Rheology of collagen films is presented in [6].

Some of the stages have a pollutant effect on the environment. To reduce the negative effects of industrial activities on the environment can be used the following solutions: recycling some of the polluting materials [7-9], obtaining other useful products by reusing wastes [10-11] or to immobilize other hazardous waste [12-13].

In industrial technologies, for assessing the degree of leather processing, there are still only qualitative assessments, such as: craving, elasticity, softness etc. [1-4]

From the best of our knowledge, the introduction of quantitative parameters for characterizing the different stages of the process is not yet accomplished.

The present paper attempts to explore one of the few quantitative parameters for characterizing the degree of leather licking, namely: the shrinkage temperature, using the drying operation.

^a Faculty of Industrial Chemistry and Environmental Engineering, University Politehnica Timisoara, Victoriei Sq.2, 300006 Timisoara, Romania

* Corresponding author: sorina.boran@upt.ro

Drying of colloidal materials is a process of heat and mass transfer, usually accompanied by the deformation processes of the material [14].

The shrinkage temperature characterizes the degree of crosslinking of the collagen fibers, by determining the resistance of the dermal tissue to the heat and humidity action. It represents the temperature at which the shortening of the dermal tissue fibers begins to occur in the aqueous medium when raising the temperature [4].

The shrinkage temperature of the finished skins is influenced by several factors, including the water content of the skin.

Quantatively, it is expected that the contraction temperature will vary inversely with the degree of swelling of the skin, with its non-reticulation. The moisture content of the skin may be calculated using the following relationship [15-17]:

$$U, \% = \frac{m_i - m_d}{m_d} \cdot 100$$

where: m_i – initial leather mass, g
 m_d – dried leather mass, g

The aim of the paper is to correlate the degree of swelling of the dermis expressed by the shrinkage temperature with the moisture content using the drying process of the skin samples from different stages of leather production.

RESULTS AND DISCUSSION

By drying in an oven at 100°C of the skins, their weight will decrease over time. In Table 1 are presented the weight of the skins at different stages of processing at different drying times

Table1. The weight of the skins at different stages of processing at different drying times

No.	Time, min	Weight depending on skin type, g			
		Soaked	Gelatine	Pickled	Tanned
1	0	23.8	23.8	23.8	23.8
2	60	15.1	7.6	10.47	8.23
3	120	10.9	4.43	6.95	4.7
4	180	7.2	2.95	5.48	4.7
5	240	7	2.8	5.4	4.7
6	300	7	2.8	5.4	4.7

Analysing these values it is found that the drying processes of different skin types have a similar evolution. The most water is eliminated by drying at the beginning of the process, this being the existing water between the fibers, then by diffusion from the inside of the fibers outwards, and eventually the removing it completely from the skin.

The gel material, i.e. the soaked skin, gelatin and pickled ones, dries slower because the water is strongly retained inside it. The fastest drying process appears for the tanned skin (the fibrous body).

The equations of the mass loss curves of the skins at different stages of processing at different drying times are presented in Table 2.

Table 2. The equations of the mass loss curves of the skins at different stages of processing at different drying times

Skin type	$y = ax^2 - bx + c$	R^2
Soaked	$y = 0,0003x^2 - 0,1419x + 23,375$	0.992
Gelatine	$y = 0,0004x^2 - 0,1714x + 22,133$	0.939
Pickled	$y = 0,0005x^2 - 0,1874x + 21,524$	0.896
Tanned	$y = 0,0005x^2 - 0,1961x + 21,571$	0.918

On the basis of these results it was possible to determine the decrease in time of the water content for the respective skins, values shown in Table 3.

Table 3. The water content at different stages of processing at different drying times

No.	Time, min	The water content at different stages of processing, %			
		Soaked	Gelatine	Pickled	Tanned
1	0	70.6	88.23	77.31	80.25
2	60	34	20.2	21.3	14.8
3	120	16.4	2.65	6.51	0
4	180	0.84	0.63	0.34	0
5	240	0	0	0	0

The equations of the water content of the skins at different stages of processing and different drying times are presented in Table 4.

Table 4. The equations of the water content curves of the skins at different stages of processing at different drying times

Skin type	$y = ax^2 - bx + c$	R^2
Soaked	$y = 0,0013x^2 - 0,5895x + 68,606$	0.987
Gelatine	$y = 0,003x^2 - 1,0426x + 83,024$	0.957
Pickled	$y = 0,0024x^2 - 0,8642x + 73,319$	0.967
Tanned	$y = 0,0029x^2 - 0,986x + 74,884$	0.946

By determining the shrinkage temperature in the skins of the various manufacturing steps, the results presented in Table 5 are obtained.

Table 5. The skin shrinkage temperature of the different stages of manufacture

No.	The shrinkage temperature of different skin type, °C			
	Soaked	Gelatine	Pickled	Tanned
1	62.5 - 66.5	52 - 58	49.5 - 53	89 - 92

It is found that the highest shrinkage temperature occurs in tanned leather, which is a fibrous material.

The other forms of leather processing (soaked, gelatin, and pickled) refer to gel bodies, which can be transformed by incorporating water to the sol-gel.

This also explains the variation in the shrinkage temperature of these skins depending on their moisture content, which also results from the analysis of the graph in Figure 1.

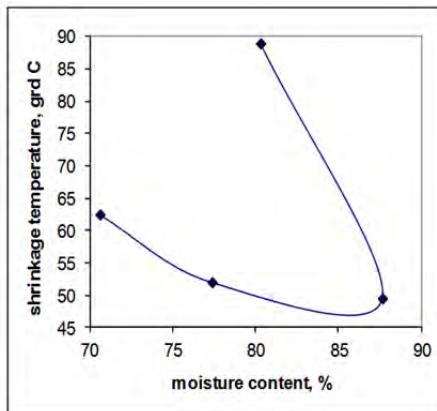


Figure.1. Dependence of shrinkage temperature on skin moisture content

CONCLUSIONS

As the skin sprouting progresses, the gelling components are eliminated, leaving only the fibrous material (collagen fibers) which is more resistant and determines the characteristics of the leather, in our case, the shrinkage temperature, which is the greatest for the tanned skin.

The works have shown that the shrinkage temperature cannot alone assess the state of the fibrous material, due to the massive gel matrix at the beginning of the processing.

Determinations made on various processed materials indicate a qualitative correlation between the shrinkage temperature and the degree of crosslinking of the collagen material, which gives mechanical strength to the leather.

EXPERIMENTAL SECTION

In order to determine skin moisture, STAS 8574/70 was worked out, taking skin samples of the same weight from different skin processing steps, namely: soaked skin, gelatin skin, pickled skin and tanned leather.

They were placed in the oven at 100°C for water evaporation, weighing periodically until a constant mass was reached.

Determination of the shrinkage temperature is performed, according to STAS 5053/70, by means of a device which allows tracking of the moment when the skin contraction occurs on a graduated dial.

The temperature at which the indicator needle deviation occurs is the skin's shrinkage temperature. Usually there is a temperature range in which the skin contraction occurs.

REFERENCES

1. F.O'Flaherty, W.T. Roddy, R.M. Lollar (Ed.), „The Chemistry and Technology of Leather”, Vol.I., Krieger Publishing Company, Malabar, Florida, **1979**.
2. K. Bienkiewicz, „Physical Chemistry of Leather Making”, R.E. Krieger Publishing Company, Malabar, Florida, **1983**.
3. G. Chiriță, „Tehnologia Pieilor și Blănurilor”, Vol.I, Ed.Tehnică, București, **1985**.
4. E. Heidemann, „Fundamentals of Leather Manufacture”, Roetherdruck, Darmstadt, **1993**.

5. J.H. Sharphouse, „Leather Technician's, Handbook”, Leather Producers' Association, Northhampton, **1995**.
6. S. Popa, S. Boran, V. Simulescu, *Materiale Plastice*, **2017**, 54, 359.
7. G. Mosoarca, P. Negrea, M. Motoc, M. Craciunescu, M. Anghel, D. David, *Rev. Chim.* **2009**, 60, 636.
8. G. Mosoarca, V. Pode, *Rev. Chim.* **2009**, 60, 836.
9. G. Mosoarca, P. Negrea, *Journal of Environmental Protection and Ecology*, **2012**, 13, 198.
10. I. Lazau, C. Vancea, *Romanian Journal of Materials*, **2012**, 42, 270.
11. C. Vancea, I. Lazau, *Central European Journal of Chemistry*, **2014**, 12, 804.
12. I. Lazau, C. Vancea, G. Mosoarca, *Romanian Journal of Materials*, **2013**, 43, 210.
13. C. Vancea, G. Mosoarca, A. Negrea, A. Latia, R.M. Jurca, *Romanian Journal of Materials*, **2016**, 46, 296.
14. V.A. Sychevskii, *International Journal of Heat and Mass Transfer*, **2015**, 85, 740.
15. E.A. Bratu, „Operații unitare în ingineria chimică”, vol.II., Ed. Tehn., București **1985**.
16. A. Dăscălescu, „Uscarea și aplicațiile ei industriale”, Ed. Tehn., București **1974**.
17. F. Vitan, N. Badea, M. Macoveanu, I. Iacomi, „Ingineria proceselor în textile și pielărie”, Casa de presă și Editura Cronica, Iași **1992**.

THE INFLUENCE OF MINERALS AND LACTOSE CONTENT ON THE STABILITY OF WHEY PROTEIN POWDERS

DOINA PRODAN^a, MIUȚA FILIP^a, IOANA PERHAIȚA^a,
MIHAELA VLASSA^a, VIOLEȚA POPESCU^b, IOAN MARCUS^c,
MARIOARA MOLDOVAN^{a,*}

ABSTRACT. The aim of this paper was to determine the minerals and lactose from a Zonar lactoserum concentrate (L-ZS) obtained by lyophilization as compared to other two commercial powders: a bio whey concentrate (BWP) and a whey protein isolate (IWP), in order to investigate the influence of the mineral and lactose concentration on the protein denaturation temperature. The BCAA content from protein hydrolysates and surface structure of whey powder samples have been also investigated. Lactose content of samples was: 47.4 g/100g for L-ZS, 46.4 g/100g for BWP, 0 g/100g for WPI. The highest concentrations of minerals Ca, K, Mg, Na and P has been found in BWP, followed by, L-ZS and IWP powders. The fact that L-ZS sample shows a peak temperature (Tp) with 15.82 °C higher than in the case of BWP sample, makes it more resistant to denaturation. The IWP powder has Tp of 87.25 °C, because contains the high quantity proteins that are more resistant to unfolding (denaturation) than the other two samples. Loss of calcium ions leads to partial protein unfolding. The lower mineral content increases the stability of whey protein. A high lactose content leads to the protein aggregation; the functional properties of powder is changes by protein crosslinking. Branched-chain amino acids content in studied samples is in accordance with whey proteins powders type.

Keywords: *lactoserum Zonar, bio whey concentrate, whey, protein isolate, lactose, BCAA, minerals, DSC, SEM*

^a Babeș-Bolyai University, Raluca Ripan Institute for Research in Chemistry, 30 Fântânele street, RO-400294, Cluj-Napoca, Romania

^b Technical University of Cluj-Napoca, Faculty of Materials and Environment Engineering 103-105 Muncii Avenue 400641 Cluj-Napoca, Romania

^c University of Agricultural Sciences and Veterinary Medicine Cluj-Napoca; Faculty of Veterinary Medicine, 3-5 Mănăștur Street, 400372, Cluj-Napoca, Romania

* Corresponding author: mmarioara2004@yahoo.com

INTRODUCTION

Sweet whey is the liquid left after extraction of casein and milk fat in the cheese making process. This contains a large proportion of milk salts, lactose and water-soluble proteins. The most important whey proteins are alpha-lactalbumin (α -la), beta-lactoglobulin (β -lg), bovine serum albumin, immunoglobulins and protease peptones [1]. The whey composition varies according to the milk composition, the cheese type from which it derives, the heat treatment and other factors. The name of sweet whey protein is due to the fact that it is derived from the production of matured cheeses (like swiss, cheddar, provolon, etc.) and its pH (6.2 - 6.6) is slightly lower than that of fresh milk [2].

The current industrial processes for the production of whey protein concentrates are based on the following processing steps: the whey that containing only about 0.5-0.7 % protein is pasteurized; is concentrated by ultrafiltration (UF) to obtain a fold protein concentration of 20-25; UF retentate being very thick after ultrafiltration is diluted and filtered once more (diafiltration); UF retentate is concentrated by vacuum evaporation; and the UF retentate is concentrate by spray-dried [3].

By the ultrafiltration process is reduced the concentration of lactose and whey minerals. Some of the mineral components can bind to proteins by hydrogen bonding or other attraction forces and can be retained with them. Calcium from whey can prevent or reduce the flow rate of water through the membranes. Techniques such as heating and the pH adjusting of the whey to avoid the problem of water flow rate through the filtration membranes are pre-treatments having an effect by the final mineral content [2].

According to published data [4] "protein denaturation is any modification in secondary, tertiary or quaternary conformation that is not accompanied by the rupture of peptide bonds involved in the primary structure" and "the terms aggregation refer to unspecified protein-protein interactions that result in the formation of large complexes with higher molecular weights" [4]. A biomolecule is in equilibrium in solution between native conformation (folded) and its denaturated (unfolded) state. The temperature at which 50% of biomolecules are unfolded is named intermediate transition point (T_m). Higher T_m corresponds to more stable molecules [5,6]. Transition of proteins from native form to denaturated conformation is accompanied by breakage of inter and intramolecular bonds. DSC allows the determination of the denaturation temperature of the protein [5]. In [7] these transitions explain that the gelation phase of whey globular proteins in heating involves two separate stages. In the first stage there is a partial (denaturation) of the native global structure involving a breakdown of intramolecular (non-

covalent, disulfide) bonds leading to an endothermic process. In the second step an intermolecular aggregation involves the formation of new bonds between the protein molecules and therefore an exothermic DSC process is expected.

Dairy protein hydrolysates contain bioactive peptides with anti-inflammatory properties but also some amino acids. Amino acid profile differs between caseins and whey proteins; caseins contain a large proportion of glutamine and proline residues and minor proportions of arginine, while whey proteins contain branched-chain amino acid (BCAA) residues [8]. BCAAs are so called because of their structure, which includes a side chain of one carbon atom and three hydrogen atoms.

The BCAA are three of the nine essential amino acids respectively leucine (Leu), isoleucine (ILeu) and valine (Val). They are important precursor for muscle protein synthesis [9]. The high level of BCAA and their good digestibility from whey proteins, in particularly Leu, confer those proteins a good nutritional profile for sports nutrition [10].

The proposal of this study is to investigate a powder obtained by lyophilisation of a commercial whey formula (lactoserum namely Zonar) (L-ZS) and to compare it with other two commercial powders, bio whey concentrate (BWP) and whey protein isolate (IWP) in order to correlate influence of the minerals and lactose concentrations upon protein denaturation temperature. The BCAA content from protein hydrolysates and surface structure of studied samples have been investigated.

RESULTS AND DISCUSSION

At present, there are a large variety of applications of milk whey, especially in medicine and in the food industry, depending on the characteristics of each type of whey. The Zonar lactoserum, produced and distributed by S.C. EmbryoOm Capital investment S.R.L., (Satu-Mare, Romania) is obtained from cow's milk and intended to use in curative purposes, at nutritional therapies, or as an adjuvant in the treatment of various diseases such as obesity or type II diabetes [11]. Two commercial powders, from the Romanian market, a bio whey concentrate (distributed by SC Deco Italia SRL, Suceagu, Romania) and a whey protein isolate (distributed by S.C. Way Better Nutrition from Cluj-Napoca) were also investigate.

Quantification of minerals and trace elements in the whey powders

The concentrations of minerals (Ca, K, Mg, Na, P) and trace elements (Cu, Fe, Pb, Zn) in studied whey powders are shown in Figure 1 and 2.

In Figure 1 it can be observed high concentrations of Ca, K, Mg, Na and P in BWP sample compared with L-ZS and IWP samples.

The sodium concentration, of 0.45 mg / kg in L-ZS sample is lower by compared with 570 mg / kg in BWP sample and 166.91 mg / kg in IWP sample. The calcium concentration is 3134 mg / kg in L-ZS sample while in BWP sample is 4220 mg / kg and in IWP sample is the lowest 2376 mg / kg. The high content of calcium in the BWP sample is an important reason for a lower stability of the protein compared to the L-ZS sample due to hydrophobic interactions that favoring the formation of a very little hydrated gel. [12]. The potassium concentration in L-ZS sample is 7880 mg / kg, but the largest amount was found in BWP sample of 10340 mg / kg, while in IWP sample is the 1380 mg / kg. The magnesium concentrations are 799 mg / kg in L-ZS sample, 1060 mg / kg in BWP sample and 594 mg / kg in IWP sample. Phosphorus is an essential component in many biological molecules, proteins, carbohydrates and nucleic acids. Phosphorus concentration found in L-ZS sample is 4900 mg / kg comparative with 5440 mg / kg in BWP sample and 1770 mg / kg in IWP sample.

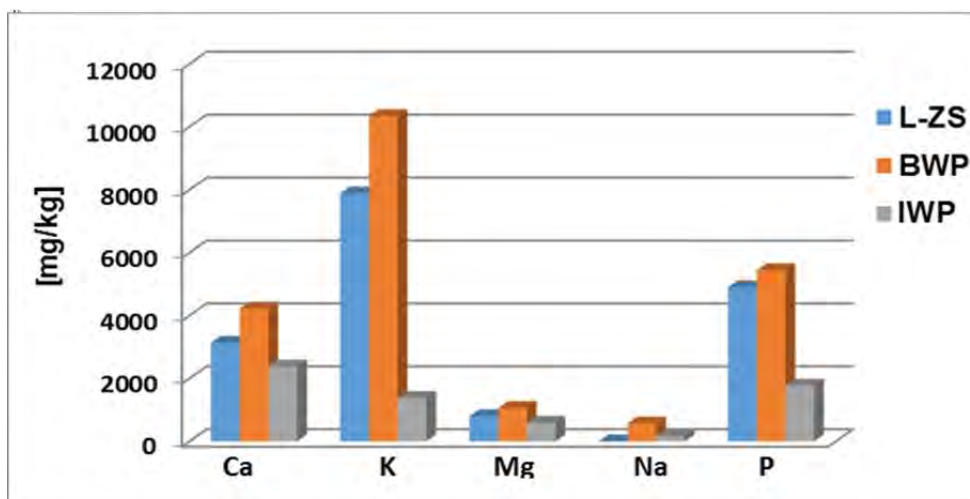


Figure 1. The minerals distribution in the studied whey powders (L-ZS is *Zonar lactoserum concentrate*, BWP is *bio whey concentrate*, IWP is *whey protein isolate*).

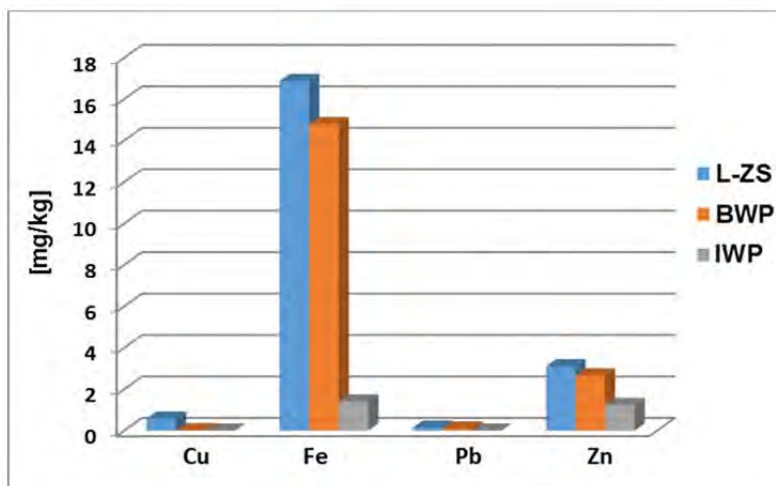


Figure 2. Distribution of the trace elements in the studied whey powders.

The Figure 2 shows that the L-ZS sample contains the highest iron concentration, of 16.87 mg / kg, while the BWP sample contains of 14.79 mg / kg and the IWP sample contains of 1.405 mg / kg .

In the immune system the zinc have a lot of functions like produce energy, to synthesize proteins, to stabilize membranes against bacterial endotoxins, to produce antioxidant enzymes and to produce antibodies [13]. The L-ZS sample also contains a higher concentration of zinc of 3.1 mg / kg while the BWP sample contains 2.66 mg / kg and IWP sample contains 1.23 mg / kg. Concerning the cooper and lead concentrations, these are below 1 mg / kg in all investigated samples.

The concentrations of the investigated elements may varies, depending on the milk type (from cow or goat), the animals feeding, the whey obtaining method and not the least, the analysis method used for whey characterisation [14].

Determination of lactose in the whey powders by HPLC

Lactose affects the whey protein powders stability, protecting the proteins against thermal denaturation during drying. If the lactose content of the powder is lower, then the amount of denatured protein is greater. Lactose from the studied powders affects the aggregation of thermally denatured proteins as well as the characteristics of these aggregates; Also it has the ability to replace the water molecules in hydrophobic areas and to prevent complet unfolding of protein [15].

Determination of lactose in the whey powders was performed by high performance liquid chromatography with reflectance index detector (HPLC-RI). Figure 3 shows the chromatograms of lactose standard and studied samples.

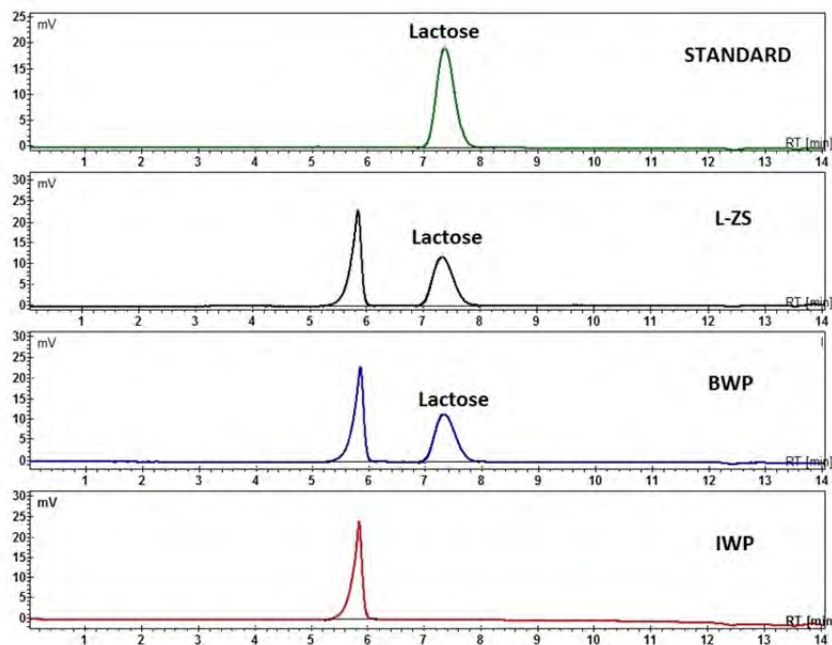


Figure 3. HPLC-RI chromatograms of lactose standard (RT = 7.24 min) and *Zonar* lactoserum concentrate (L-ZS), whey bio concentrate (BWP) and whey protein isolate (IWP) samples.

The lactose concentrations in studied samples are: L-ZS sample contain 47.4 g lactose / 100 g powder and BWP sample contain 46.4 g lactose/100g powder. The IWP sample do not contains the lactose because this is a powder of isolate in proteins and not a concentrate in proteins.

Because the lactose contain in the L-ZS sample is highest, this sample is more stable at unfolding of proteins, than BWP sample.

Determination of branched-chain amino acids in whey protein hydrolysates by OPLC

Proteins are macromolecules made up of amino acid chains. To be absorbing in the body, these protein chains it break by means of enzymes. Determination of branched-chain amino acids (BCAA) in whey protein

hydrolysates was performed by Overpressured Layer Chromatography (OPLC) technique. The prepared solutions of whey protein hydrolysates were submitted to the OPLC chromatographic separation for determination of BCAA according to previously reported procedure [16].

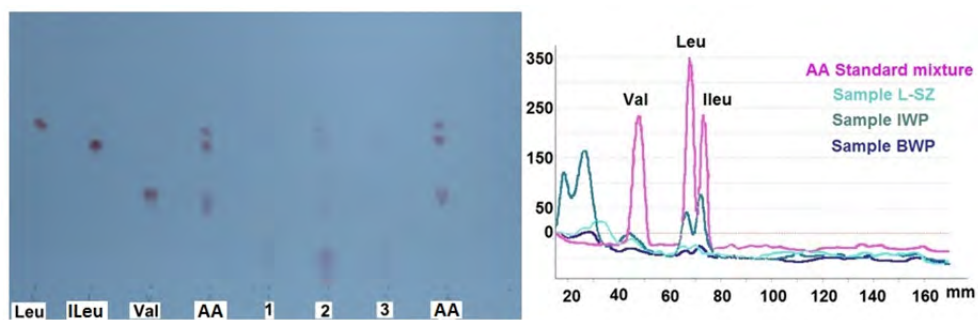


Figure 4. OPLC Chromatoplate and overlay densitograms of the studied samples. Leu, lLeu, Val are individual standards (1 mg ml^{-1} each); AA is amino acids standards mixture (0.333 mg ml^{-1}); samples: 1 (L-SZ); 2 (IWP); 3 (BWP).

The obtained results are presented In Table 1.

Table 1. The content of whey protein hydrolysates samples in BCAAs

Sample	Val [g/100g]	lLeu [g/100g]	Leu [g/100g]	Total BCAA[g/100g]
L-SZ	1.36	0.536	1.28	3.176
IWP	6.26	6.407	16.27	28.937
BWP	0.233	0.401	1.69	2.324

The OPLC analysis of the BCAAs in hydrolysates samples (whey concentrates, L-SZ and BWP) show that the L-SZ sample contains a larger quantity of BCAAs total than the BWP sample.

Regarding the IWP sample, this contains the higher quantity of BCAAs total is due to that the whey protein isolate is a isolate in whey protein, so it contains more proteins.

Whey powders surface structure investigation by SEM

The surface structure investigation of studied powders was performed by Scanning Electron Microscopy (SEM) using a magnification of 1000. In Figure 5 are shown the structure of studied powders: L-SZ, BWP and IWP.

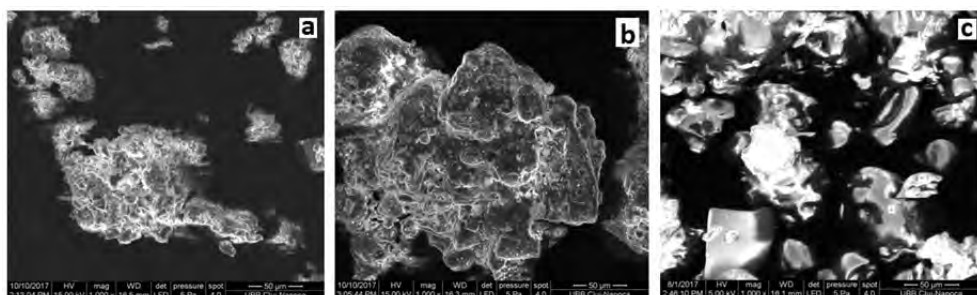


Figure 5. The SEM micrographs with 1000 magnification of: a) *Zonar* lactoserum concentrate (L-ZS), b) bio whey protein concentrate (BWP) and c) whey protein isolate (IWP).

From the micrographs a) and b) one can observe a similar structure of the surfaces of the two powders, with agglomerations of particles of different shapes. In the case of microscopy c) crystalline agglomerations with glowing particles of round or irregular shape, characteristic image for the whey protein isolate are observed.

Concerning the powder obtained by lyophilization, the powder surface it should be porous due to the removal of the ice during the lyophilization process, but this was not observed in the case of the L-SZ powder Figure 6 a).

At a larger magnification, at x 5000 (Figure 6), in the case of L-ZS, and BWP samples, a wrinkled structure of the sample surfaces with particles of 1-10 μm , more or less rounded, is observed. These are characteristic micrographs of powders with lactose, as whey protein concentrates

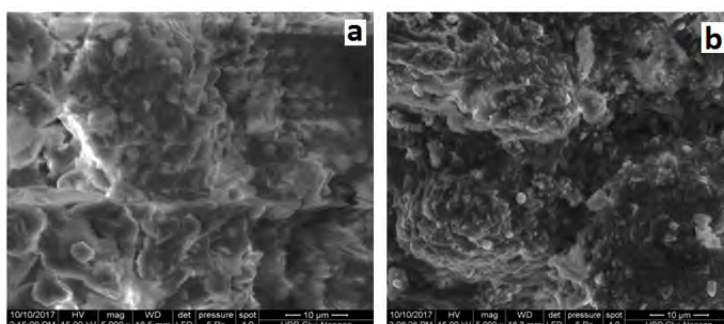


Figure 6. The SEM micrographs with 5000 magnification of: a) *Zonar* lactoserum concentrate (L-ZS), b) bio whey protein concentrate (BWP)

In conclusion, from, a clear difference can be observed (Figures 5 and 6) between the lactose free sample surface (IWP) and the samples surface with lactose content (L-ZS) and (BWP) respectively

Protein denaturation of whey powders by DSC

In differential scanning calorimetry (DSC), one or more peaks or inflection points may occur that reflect heat-induced transitions. Depending on the transition that takes place with heat absorption (endotherm) or with heat release (exotherm), the direction of the peak recorded on the thermograms differs. While solids melting and protein denaturation are endothermic processes, the crystallization of carbohydrates and the aggregation of proteins are manifested as exothermic processes [17].

In Figure 7 can see the protein denaturated temperatures of the investigated samples: L-ZS, BWP and IWP.

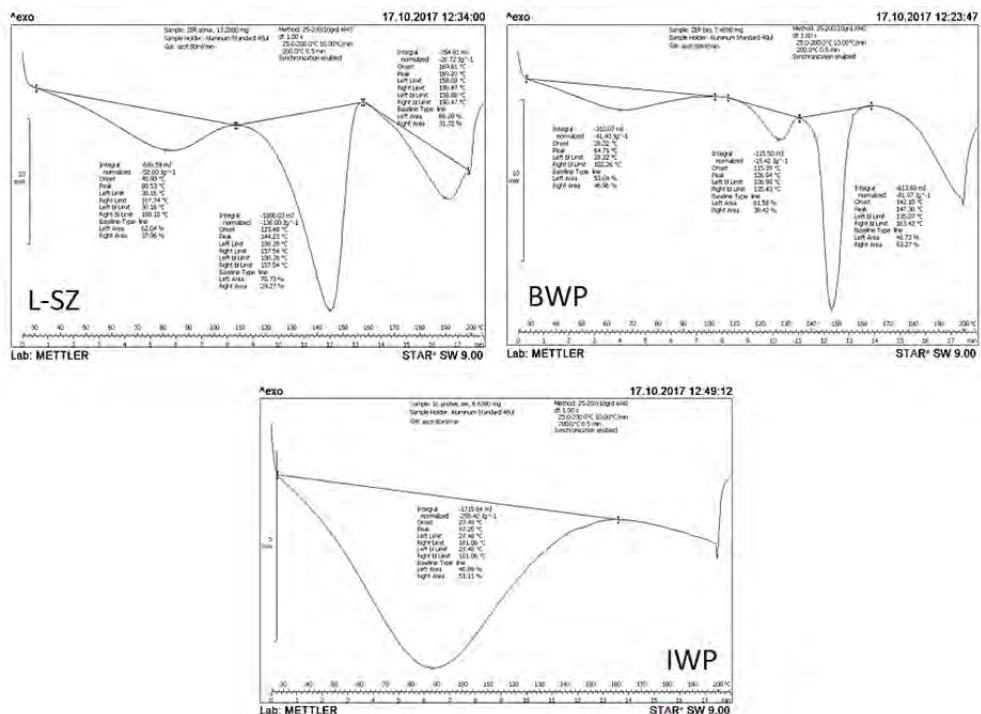


Figure 7. DSC analyses of: L-ZS - Zonar lactoserum concentrate, BWP - bio whey protein concentrate and IWP - whey protein isolate.

In this study, it is noted that and in other previous studies on the thermal gelation of whey protein, carried out on conventional scanning systems (typical sample mass ~ 15-50 mg), appears only endothermic transitions [7].

In Figure 7 has been observed that L-ZS sample and BWP sample have transition endotherms at the temperatures of 80.53 °C and 64.71 °C, respectively, representing the unfolded of the two major whey proteins α -lg and β -lg. The fact that L-ZS sample shows a peak temperature (T_p) of 15.82° C higher than in the case of BWP sample, makes it more resistant to denaturation. The IWP sample has a T_p of 87.25 °C, so it contains proteins in higher quantity and is more resistant to distortion than the other two.

Wit and Klarenbeek (1981) [19,20] analyzed by DSC the thermal behavior of major whey protein to 150 °C and observed two distinct heat effects: up to 70 °C the effect is attributed to denaturation and near 130 °C is attributed to the denaturation of the remaining protein structure. Regarding to the second transition isotherm, after Wit and Fitzsimons [7, 18,19] this can be attributed over 100 °C, to β -lg, and the breakdown of disulfide bonds, which have a very important role in stabilizing the spatial architecture of the protein molecule, followed by protein denaturation.

In Figure 7 we can see an isothermal transition in the case of the L-ZS sample having T_p of 144.23 °C and BWP sample with T_p of 126.94 °C. It is observed in the BWP sample a third isothermal transition to T_p of 147.3 °C which could be attributed to possible denaturation of other proteins unfolded yet. For a higher ratio of β -lg / α -lg, the denaturation temperature increases and this increase is more pronounced when the overall protein concentration is lower, probably due to the lower amount of protein that is unfolding [5].

From a biological point of view, α -lg is small protein, compact, has a more or less spherical shape and behaves like a coenzyme in lactose synthesis. The Ca ions are strongly bound and stabilize protein conformation. Loss of Ca ions at an acidic pH leads to partial protein unfolded; in this case, even at a low temperature, irreversible degradation of the protein takes place. However, the β -lg protein, the major serum protein, with properties that tend to dominate in particular the thermal treatment reactions. The β -lg protein shows secondary and tertiary structures, having two -S-S bonds and a free sulfhydryl group. The tertiary or quaternary protein is subject to a series of changes depending on the pH or temperature changes [20].

CONCLUSIONS

Loss of calcium ions leads to partial protein unfolding. The lower mineral content increases the stability of whey protein. A high lactose content leads to the protein aggregation and the functional properties of powder is changes by protein crosslinking. The present of BCAAs (leucine, isoleucine and valine) in studied samples were quantified in order to establish the quality of protein source.

EXPERIMENTAL SECTION

Materials, reagents

The studied samples were three powders of *Zonar* lactoserum concentrate (L-ZS), bio whey protein concentrate (BWP) and whey protein isolate (IWP). All chemicals used were analytical-grade from commercial sources and used as received.

Equipments and sample preparation

ICP-OES analysis

A quantity of 5 grams of each studied sample were used to determine the concentration of mineral and trace element. Three parallel determinations of each sample were made. The sample crucibles were introduced into a thermostated electric furnace, raising the temperature gradually from 50 °C to 50 °C (maintaining the temperature one hour on each level) to a temperature of 550 °C where it was maintained for 7 hours. After the samples were removed from the oven, they were treated with a mixture of concentrated HNO₃ (65%) and H₂O₂ (30%) in a ratio of 1:0.6, v/v successively added to each sample. After addition of HNO₃, the sample crucibles were placed on a sand bath to evaporate gradually. After cooling, H₂O₂ was added to the samples and heating was continued on the sand bath until the samples were again brought to dryness. The operation was repeated two more times. Determination of mineral and trace element from the clear solutions, was done with the Optima 2100- Perkin Elmer inductively coupled plasma-optical emission spectrometer (ICP-OES) connected to a computer.

HPLC analysis

Determination of the lactose content was performed by high-performance liquid chromatography (HPLC). Lactose was purchased from Aldrich (Milwaukee, USA). HPLC Sample preparation: 1 mL of milk-serum sample was diluted with 4 mL water. To 1 mL of this diluted solution 4 mL of

70% of acetonitrile were added, leading to protein precipitation; the solution was passed through a 0.45 μm filter and injected in the HPLC system. A HPLC Jasco Chromatograph (Japan) with a refractive index detector (RI) was employed. The data were processed with the ChromPass software. Separation was carried out on a CARBOsep column at 70°C column temperature. The mobile phase was a Milipore ultrapure water and the flow rate was 0.5 mL min^{-1} and the injector volume was 20 μL [21].

OPLC analysis

The acidic hydrolysis of the protein samples was performed in a hydrolysis tube: a protein mass of about 5-10 mg was treated with 1mL of 6M HCl, and heated at 110 °C for 24 h. The acid-hydrolyzed solutions were neutralized at pH 7 and then filtered on Munktell quantitative filter paper grade 389 (Munktell & Filtrak GmbH, Barenstein, Germany). The filtrate of each sample was collected in a volumetric flask of 10 mL and brought to volume with water. OPLC analysis was performed with the Personal OPLC 50 chromatograph (OPLC-NIT, Budapest, Hungary) on 20 cm \times 20 cm. OPLC plates precoated with 5- μm particle silica gel F254 (LA001; OPLC-NIT). The standards and the samples were applied on the plate with micropipettes in quantities of 2 μL .

SEM analysis

For surfaces analysis of the samples an INSPECT S (FEI Co) microscope was used.

DSC analysis

Differential scanning calorimetry (DSC) was performed using a Mettler Toledo DSC 823e/700 °C. The measurements were carried out in the 25-200 °C temperature range, in aluminum crucibles, under nitrogen flow (80 mL \cdot min $^{-1}$) with a heating rate of 10 °C \cdot min $^{-1}$. The sample weight was in the range of 7 -13 mg. The variation of the heat flow transmitted through the sample relative to a reference (empty crucible) is recorded.

ACKNOWLEDGMENTS

This work was funded by the Romanian Ministry of Education and Research, National projects: PNIII-P2-2.1-BG-2016-0204, 112 BG/2016; PNIII-P2-2.1-BG-2016-0335, 28BG/2016.

REFERENCES

1. K.J. Kimberlee Burrington, Dairy Research Institute, Technical Report: "Whey Protein Heat Stability".
2. N. Erdogdu, Z. Czuchajowska, Y. Pomeranz, *Cereal chemistry*, **1995**, 72(1), 70.
3. III-Dairy-G-Whey Products-5, <https://nzic.org.nz/ChemProcesses/dairy/3G.pdf>.)
4. H. Patel, S. Patel, "Technical Report: Understanding the Role of Dairy Proteins in Ingredient and Product Performance", USA Dairy Export Council, Edited by Robert Beausire, **2015**.
5. T. Vieira Arriaga, "Controlled and tailored denaturation and aggregation of whey proteins, dissertation", Technical University of Lisbon, 2011.
6. <https://www.malvern.com/en/products/technology/differential-scanning-calorimetry>.
7. S.M. Fitzsimons, D.M. Mulvihill, E.R. Morris, *Food Hydrocolloids*, **2007**, 21(4), 638.
8. M.S. Da Silva, C. Bigo, O. Barbier, I. Rudkowska, *Nutrition Research*, **2017**, 38, 43.
9. R.R. Wolfe, *Journal of the International Society of Sports Nutrition*, **2017**, 14, 30.
10. A.B. Nongonierma, R. J. FitzGerald, *Peptides*, **2015**, 73, 20.
11. <https://zonar.ro>
12. P. Walstra, J.T.M. Wouters, T.J. Geurts, "Dairy Science and Technology" Second Edition, Taylor & Francis Group, LLC, 2006.
13. M.W. Sawyer, Controlling the Mineral Content of Sweet Whey Powder in an Industrial Setting A Senior Project presented to the Faculty of the Dairy Science Department California Polytechnic State University, San Luis Obispo In Partial Fulfillment of the Requirements for the Degree Bachelor of Science, **2010**.
14. Imre Mucsi, Nutrients in whey and nutritional Properties of whey in Whey Every Aspect, Whey Handbook For The Dairy Sector, Edited by Kemal Çelik, pg. 69-90.
15. M.A. Haque, P. Aldred, J. Chen, C.J. Barrow, B. Adhikari, *Food chemistry*, **2013**, 141(2), 702-711.
16. M. Vlassa, V. Coman, M. Filip, F. Copaciu, A. Mocanu, M. Tomoaia-Cotișel, *Journal of Planar Chromatography*, **2013**, 26, 165-171.
17. <https://www.malvern.com/en/products/technology/differential-scanning-calorimetry>
18. J.N. de Wit, *Neth. Milk Dairy Journal*, **1981**, 35, 47.
19. J.N. de Wit, Klarenbeek, G. *Journal of Dairy Research*, **1981**, 48, 293.

20. P. Walstra, J.T.M. Wouters, T.J. Geurts "Dairy Science and Technology - Second Edition", Taylor & Francis Group, LLC, 2006.
21. D. Prodan, M. Moldovan, I. Perhaita, M. Filip, C. Sarosi, M. Vlassa, L. Silaghi-Dumitrescu, Physicochemical Characterization of Four "ZONAR" WHEY Samples, *International UAB - BENA Conference Environmental Engineering and Sustainable Development*, 25-27 mai, 2017, Alba Iulia, Romania.

NEW PHOSPHORUS CONTAINING BIS-SULFONE LIGANDS

NOÉMI DEAK^{a,b}, SONIA MALLET-LADEIRA^c,
LUMINITA SILAGHI-DUMITRESCU^a, DAVID MADEC^{b*},
GABRIELA NEMES^{*a}

ABSTRACT. Derivatives of bis-sulfone 1,3-bis(*p*-tolyl)SO₂-5-*tert*-butylbenzene **1**, containing P(III) and P(V) were obtained and characterized in solution by multinuclear NMR spectroscopy. For two of the compounds ([2,6-*p*-tolyl)SO₂]₂4-*t*-Bu-C₆H₂]PCl₂ **2** and [2,6-*p*-tolyl)SO₂]₂4-*t*-Bu-C₆H₂]P(O)(H)OEt **4** the crystal and molecular structures in solid state were also determined by single crystal X-ray diffraction.

Keywords: bis-sulfone, phosphorus derivatives, dichlorophosphine

INTRODUCTION

The study of phosphorus containing organic and organometallic derivatives has been a topic of interest for a long time, continuously expanding with numerous interesting results surfacing regularly. In the last decades, the chemistry of phosphines and low valent phosphorus containing compounds also came in focus. In the case of all these species the organic moieties play a very important role in the stabilization and the particular properties. Several types of ligands used to obtain low valent phosphorus derivatives are described in the literature,[1–4] like bulky organic groups (Mes, Mes*, Tip, etc),[1,5] or ligands containing electron donating heteroatoms (N, O, etc).[3] The synergic effect of both the bulkiness of the ligand and its electron donating properties was also proven several times.[1,2,5,6].

^a *Universitatea Babeş-Bolyai, Facultatea de Chimie și Inginerie Chimică, str. Arany Janos, nr. 11, RO-400028, Cluj-Napoca, Romania.*

^b *Université de Toulouse, UPS, LHFA, 118 Route de Narbonne, F-31062 Toulouse, France, CNRS, LHFA, UMR 5069, F-31062 Toulouse Cedex 9, France.*

^c *Institut de Chimie de Toulouse, FR2599, Université Paul Sabatier, UPS, 118 Route de Narbonne, F-31062 Toulouse Cedex 9, France.*

* *Corresponding to: gabriela.nemes@ubbcluj.ro, madec@chimie.ups-tlse.fr*

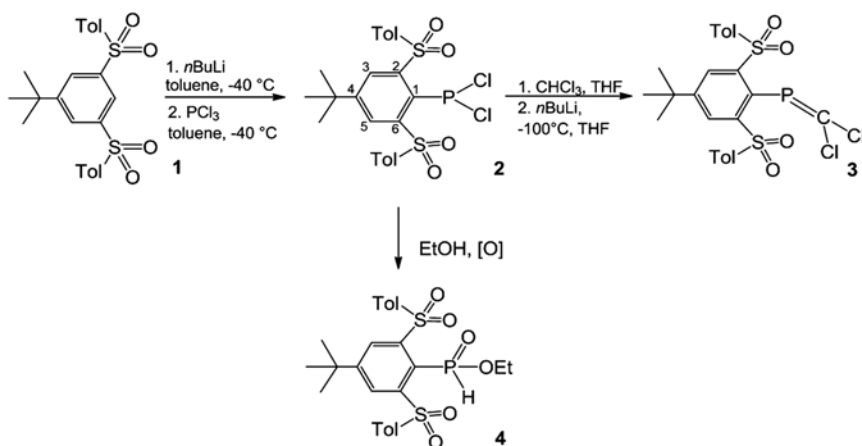
Since the stabilization of the first species containing low valent phosphorus atoms [7–9] the chemistry of these derivatives experienced a great development, becoming a versatile field of study. A large number of studies were reported over the years on the stability, reactivity and applications of P(III) containing derivatives, where the importance of these compounds was highlighted for their role as ligands in organometallic chemistry [1,3,10,16], in catalytic processes,[3] or compounds containing p-block elements.[5,6] The investigation of some derivatives containing phosphalkenyl $-P=C<$ moieties, their synthesis, characterisation and applications in organometallic and coordinative compounds, represents one of our research interests. [6,10–15]

In this study we investigated the connecting behaviour of the bis-sulfone 1,3-bis((4-methylphenyl)sulfonyl)-5-*tert*-butylbenzene **1** as a ligand towards phosphorus *tri*-chloride PCl_3 in order to obtain new derivatives that can be used as building blocks in today's chemistry. The importance of bis-sulfone as ligands was recently highlighted as they function as pincer-type ligands for the stabilization of metallylenes and have an important effect in their reactivity.[17–19]

RESULTS AND DISCUSSIONS

Based on the good results obtained with the bis-sulfone **1** in the stabilization of low valent group 14 elements and their reactivity,[18,19] the synthesis of phosphorus containing derivatives was also realised. A new dichlorophosphine was obtained with bis-sulfone **1**, as shown in Scheme 1, using a slightly modified method from literature.[7,20,21]

Tri-chlorophosphine was added at low temperature to the carbanion of the bis-sulfone **1**, obtained according to previously described methods.[18]



Scheme 1. Synthesis of phosphorus containing derivatives

The new (1,3-bis{(4-methylphenyl)sulfonyl}-5-*tert*-butylphenyl)-dichlorophosphine **2** was characterized in solution by NMR spectroscopy. The singlet signal in the ^{31}P NMR spectrum at 139 ppm (C_6D_6) confirms the formation of derivative **2**, the value of the chemical shift being in the range of chemical shifts characteristic for organo-dichlorophosphines.[22,23] In the ^1H NMR spectrum of compound **2** the disappearance of the multiplet signal at 8.90 ppm (C_6D_6 , $^4J_{\text{HH}} = 1.64$ Hz), assigned for H1 of bis-sulfone **1**, can be observed, that confirms the connection of the $-\text{PCl}_2$ fragment to the C1 atom (see Scheme 1). The downfield shift of the *meta* protons H3 and H5 on the central aromatic ring from 8.25 ppm (in bis-sulfone **1**, C_6D_6 , d, $^4J_{\text{HH}} = 1.64$ Hz) to 8.47 ppm (C_6D_6 , d, $^4J_{\text{HH}} = 1.74$ Hz) also suggests the formation of the new compound. The signal for the C1 atom in the ^{13}C NMR spectrum of compound **2** appears at 137.3 as a doublet ($^1J_{\text{C-P}} = 104.3$ Hz), because of the bonding with the phosphorus atom, with a downfield shift from 124.6 ppm for bis-sulfone **1**, characteristic shift and coupling constant for such derivatives.[22,24]

The structure of the bis-sulfone-dichlorophosphine **2** was confirmed in solid state by single crystal X-ray diffraction; the molecular structure together with some important geometrical parameters is presented in Figure 1.

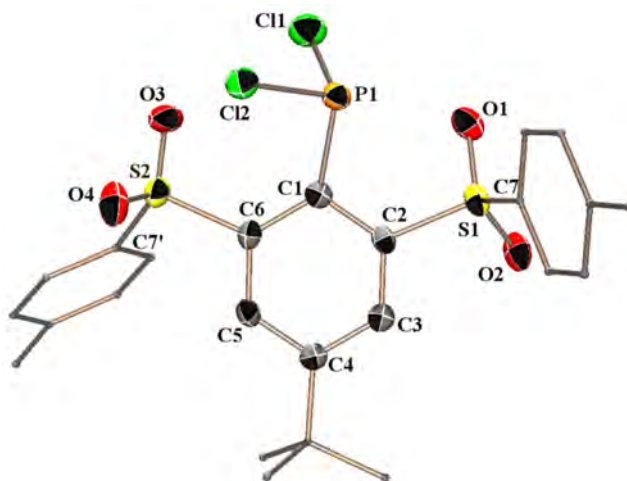


Figure 1. Molecular structure of compound **2** the solid state (50 % probability level for the thermal ellipsoids). For clarity, hydrogen atoms are omitted, tolyl and *t*-butyl groups are simplified. Selected bond distances [Å] and bond angles [deg]: S1-O1 1.441(3), S1-O2 1.435(3), S2-O3 1.434(3), S2-O4 1.432(3), P1-C1 1.859(3), Cl1-P1 2.050(1), Cl2-P1 2.057(1), C1-P1-Cl1 104.37(11), C1-P1-Cl2 99.57(11), C1-P1-Cl2 102.80(6), C6-S2-C7' 102.91(16), C2-S1-C7 106.64(15), P1-C1-C2 115.1(2), P1-C1-C6 129.1(3)

The solid state molecular structure of compound **2** shows that the phosphorus atom adopts a pseudo-tetrahedral geometry, considering the lone pair of electrons, with the angles C1-P1-Cl1 of 104.37(11)°, C1-P1-Cl2 of 99.57(11)° and Cl1-P1-Cl2 of 102.80(6)°. The C1-P1 bond length of 1.859(3) Å and P-Cl bond lengths of 2.050(1) and 2.057(1) Å, are close to values found in the literature for other organo-dichlorophosphines.[20,25] The tolyl groups are situated on opposite sides of the central aromatic ring; the S=O bonds are close to values observed in the case of the previously reported metallylenes with bis-sulfone ligands.[17–19] The O1-P1 distance in the dichlorophosphine **2** is of 2.754(3) Å, value between the sum of the covalent radii (1.73 Å)[26] and the sum of the van der Waals radii (3.38 Å),[27,28] while the O3-P1 distance of 3.367(3) Å is almost equal to the sum of the van der Waals radii (3.38 Å).[27,28] The orientation of the sulfonyl groups (the O1, O3) and the phosphorus atom does not make possible an interaction, moreover, in the case of the phosphorus(III) atom, the presence of the lone pair of electron could lead to repulsions with the lone pair of electron on the oxygen atom. However, the bulkiness of the bis-sulfone ligand **1** makes possible the stabilization of the dichlorophosphine **2**. It is to note, that in the literature there are only a few examples for phosphines stabilized by pincer ligands.[21,29–32]

The bis-sulfone-dichlorophosphine **2** was also used as precursor in the synthesis of the (1,3-bis{(4-methylphenyl)sulfonyl}-5-*tert*-butylphenyl)-dichlorophosphaalkene **3**. The formation of compound **3** was evidenced in solution by NMR spectroscopy, mainly through the ³¹P NMR, where the presence of a singlet signal at a the chemical shift 201.6 ppm, downfield shifted compared to the dichlorophosphine **2**, is characteristic for derivatives containing the –P=C< moiety.[3,8,10-12,33] The ¹H and ¹³C NMR spectra also confirm the formation of the expected compound **3**, data are presented in experimental part. The dichlorophosphaalkene **3** is stable under inert atmosphere, and presents low stability at air, after a few days decomposition can be observed with the formation of the bis-sulfone ligand **1**.

The reactivity of the derivative **2** was also tested in the presence of ethanol and oxygen, the oxidation state of phosphorus atom switch from P(III) to P(V), together with the substitution of the chlorine atoms, the formation of ethyl(1,3-bis{(4-methylphenyl)sulfonyl}-5-*tert*-butylphenyl)-phosphinate **4** was observed, as shown in Scheme 1.

The ³¹P NMR spectra of derivative **4** exhibits a doublet signal at 12.60 ppm (¹J_{PH} = 615.4Hz), with an upfield shift compared to dichlorophosphine **2** (139 ppm), found in the characteristic region for P(V) phosphorus atom containing derivatives.[10,13,22] The coupling constant of 615 Hz suggests the presence of a hydrogen atom linked to the phosphorus atom.[22] In the ¹H NMR spectrum of compound **4** slight downfield shifts can be observed for

the signals for the methyl and *tert*-butyl group and the aromatic protons of the bis-sulfone ligand compared to the compound **2**. At 1.11 ppm a triplet and at 4.13-4.35 ppm multiplet signals can be seen for the ethoxy group linked to the phosphorus atom.

Single crystals, suitable for X-ray analysis, were obtained and the molecular structure of compound **4** in solid state is presented in Figure 2 as well as some representative geometrical parameters.

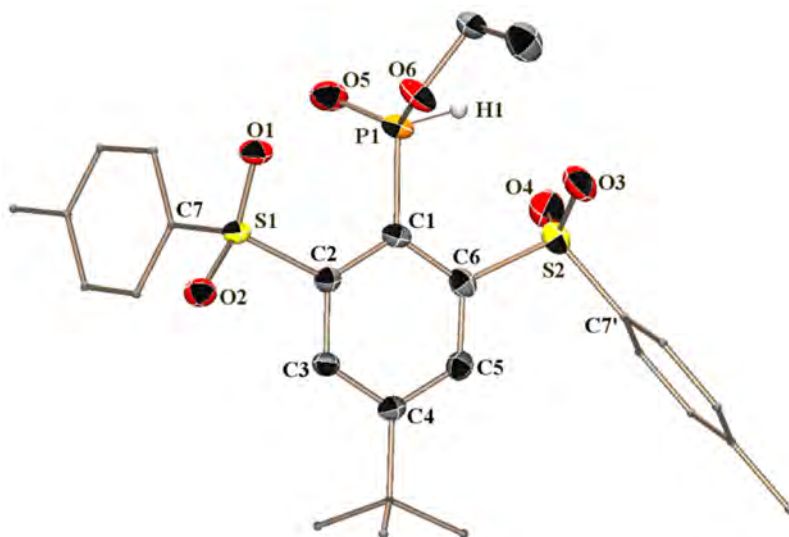


Figure 2. Molecular structure of compound **4** the solid state (50 % probability level for the thermal ellipsoids). For clarity, hydrogen atoms are omitted, tolyl and *t*-butyl groups are simplified. Selected bond distances [Å] and bond angles [deg]: S1-O1 1.434(1), S1-O2 1.442(1), S2-O3 1.439(1), S2-O4 1.438(1), P1-C1 1.828 (1), P1-O5 1.458(1), P1-O6 1.572(1), P1-H1 1.295(18), C1-P1-O5 113.55(6), C1-P1-O6 102.53(6), C1-P1-H1 106.9(8), P1-C1-C2 123.15(10), P1-C1-C6 121.67(10).

The solid state molecular structure of compound **4** shows a similar geometrical arrangement to derivative **2**. The tolyl groups are situated on opposite sides of the central aromatic ring. The O1-P1 distance is of 3.195(1) Å, the O3-P1 is 2.924(1) Å, values between the sum of the covalent radii (1.73 Å)[26] and the sum of the van der Waals radii (3.38 Å).[27,28] The P-O5 and P-O6 distances are in the range of values found in the literature for P=O bonds.[35]

Compound **4** is stable in the presence of moisture and oxygen.

CONCLUSIONS

The synthesis and characterization of three new organophosphorus derivatives containing bis-sulfone ligand **1** is presented. All compounds were characterized in solution by multinuclear NMR spectroscopy; for compounds **2** and **4** the solid state molecular structure was also determined by single crystal X-ray diffraction.

The P(III) containing derivatives show good stability under inert atmosphere of argon, while the P(V) containing derivative proved to be stable under air too.

The newly obtained organophosphorus derivatives are good candidates as precursors for organometallic compounds because of the stability of these derivatives under controlled atmosphere and the existence of multiple connecting points: lone pair of electrons of the phosphorus atom in compound **2**, P=C double bond in compound **3**, oxygen atom of the P=O bond in compound **4** and the oxygen atoms of the bis-sulfone ligand in all the cases.

EXPERIMENTAL SECTION

All syntheses were realized under dry and oxygen free argon atmosphere by using Schlenk-line and glove-box techniques; all solvents were purified using MBRAUN SBS-800 purification system. Bis-sulfone **1** was prepared according to literature procedures.[18] The NMR spectra were recorded with a Bruker Avance II 300 MHz apparatus: ^1H (300.13 MHz, reference TMS), ^{13}C (75.48 MHz, reference TMS), ^{31}P (121.51 MHz, reference H_3PO_4) at 298 K and Bruker Avance 400 MHz apparatus: ^1H (400.13 MHz, reference TMS), ^{13}C (100.61 MHz, reference TMS), ^{31}P (161.92 MHz, reference H_3PO_4) at 298 K. The signals in the ^1H and ^{13}C NMR spectra were assigned by COSY (^1H), HSQC (^1H - ^{13}C), and HMBC (^1H - ^{13}C) experiments. The X-ray data were collected at 193(2) K on a Bruker - AXS PHOTON100 D8 VENTURE diffractometer using MoK α radiation (wavelength = 0.71073 Å). Phi- and omega- scans were used. The data were integrated with SAINT[36] and an empirical absorption correction with SADABS[36] was applied. The structures were solved by direct methods with SHELXS-97[37] or by intrinsic phasing method (SHELXT)[38] and refined using a least-squares method on F^2 . [37] All non-H atoms were refined with anisotropic displacement parameters. CCDC 1587350 (**2**), CCDC 1587350 (**4**) contain the supplementary crystallographic data for this paper. These data can be obtained free of charge from The Cambridge Crystallographic Data Centre via www.ccdc.cam.ac.uk/data_request/cif.

Synthesis of compound 2

To a solution of bis-sulfone **1**[18] (300 mg, 0.678 mmol) in 12 mL of toluene cooled to -40°C , *n*-butyl lithium (0.44 mL, 0.711 mmol, 1.6 M in hexane) was added dropwise. The deep red solution was stirred 20 minutes at this temperature then was added over a solution of freshly distilled PCl_3 (0.118 mL, 1.356 mmol, 2eq) in 2 mL of toluene at -40°C . The dark red reaction mixture slowly turned white while it was allowed to warm to room temperature then it was stirred for 18 hours. After the evaporation of the volatiles, the solid was extracted with Et_2O and the lithium salts were eliminated by centrifugation in toluene. The compound was obtained as a white powder (185 mg, yield=50%). Colourless crystals suitable for X-ray analysis were obtained in toluene solution.

^1H NMR (C_6D_6) δ = 0.86 (s, 9H, *t*-Bu), 1.78 (s, 6H, Me), 6.67 (d, 4H, $^3J_{\text{HH}}$ = 7.97 Hz, *m*-CH Tol), 7.78 (d, 4H, $^3J_{\text{HH}}$ = 8.17 Hz, *o*-CH Tol), 8.47 (d, 2H, $^4J_{\text{HH}}$ = 1.74 Hz, *m*-CH Ph).

^{13}C NMR (C_6D_6) δ = 21.2 (Me), 30.1 (*t*-Bu), 35.3 (C *t*-Bu), 128.3 (d, $J_{\text{C-P}}$ = 4.47 Hz, *o*-CH Tol), 130.0 (*m*-CH Tol), 132.2 (*m*-CH Ph), 137.3 (d, $^1J_{\text{C-P}}$ = 104.3 Hz, C1), 140.1 (*ipso*-Tol), 144.5 (*p*-Tol), 149.0 (d, $J_{\text{C-P}}$ = 22.7 Hz, C2, C6) 157.1 (C4).

^{31}P NMR (C_6D_6) δ = 139.1

Note: The numbering for carbon atoms in all compounds is according to Scheme 1.

Synthesis of compound 3

To a solution of bis-sulfone **1** (300 mg, 0.678 mmol) in 12 mL of toluene cooled to -40°C , *n*-butyl lithium (0.44 mL, 0.711 mmol, 1.6 M in hexane) was added dropwise. The deep red solution was stirred 20 minutes at this temperature then was added over a solution of freshly distilled PCl_3 (0.118 mL, 1.356 mmol, 2eq) in 2 mL of toluene at -40°C . The dark red reaction mixture slowly turned white while it was allowed to warm to room temperature then it was stirred for 18 hours. All volatiles were evaporated, the white solid was solubilized in 12 mL of THF and freshly distilled CHCl_3 (55 μL , 0.678 mmol) was added to this solution. The mixture was cooled down to -100°C and *n*-BuLi (0.89 mL, 1.42 mmol, 2eq, 1.6 M in hexane) was added dropwise. The red reaction mixture was allowed to warm to room temperature, and slowly became transparent. The mixture was stirred 18 hours at room temperature. After evaporating all volatiles the compound was washed with pentane and obtained as a white solid.

^1H NMR (CDCl_3) δ = 1.46 (s, 9H, *t*-Bu), 2.37 (s, 6H, Me), 7.26 (d, 4H, J = 8.08 Hz, *m*-CH Tol), 8.54 (s, 4H, *m*-CH Ph), 7.71 (d, 2H, J = 8.31 Hz, *o*-CH Tol).

^{13}C NMR (CDCl_3) δ = 21.8 (Me), 31.1 (*t*-Bu), 35.9 (C *t*-Bu), 128.9 (*o*-Tol), 129.9 (*m*-Tol), 131.7 (*m*-CH Ph), 137.0 (*ipso*-Tol and C2, C6), 136.3 and 144.9 (*p*-Tol), 146.3 (d, $J_{\text{C-P}}$ = 3.06 Hz, C1), 156.0 (C4), C=P not seen.

^{31}P NMR (C_6D_6) δ = 201.6

Characterization of compound **4**

To a solution of dichlorophosphine **2** in C_6D_6 , 10 μL distilled EtOH was added. Transparent crystals were obtained in C_6D_6 and separated through filtration.

^1H NMR (C_6D_6) δ = 0.94 (s, 9H, *t*-Bu), 1.76 (s, 6H, Me), 1.11, (t, 3H, $^3J_{\text{HH}}$ = 6.96 Hz -O-CH₂-CH₃), 4.13 and 4.35 (m, 2H, -O-CH₂-CH₃) 6.71 (d, 4H, $^4J_{\text{HH}}$ = 7.90 Hz, *m*-CH Tol), 8.02 (d, 4H, $^4J_{\text{HH}}$ = 7.82 Hz, *o*-CH Tol), 8.89 (d, 2H, $^1J_{\text{HH}}$ = 2.62 Hz, *m*-CH Ph).

^{31}P (C_6D_6) δ = 12.6 (d, $^1J_{\text{P-H}}$ = 615.4 Hz)

$^{31}\text{P}\{\text{H}\}$ (C_6D_6) δ = 12.6

ACKNOWLEDGEMENTS

This work was supported by the Babeş-Bolyai University of Cluj-Napoca, by a grant of Ministry of Research and Innovation, CNCS - UEFISCDI, project number PN-III-P4-ID-PCE-2016-0351, within PNCDI III, by the Centre National de la Recherche Scientifique (CNRS) and the Université de Toulouse (UPS).

REFERENCES

1. J.T. Fleming and L. J. Higham, *Coordination Chemistry Reviews*, **2015**, 297–298, 127.
2. J.I. Bates, J. Dugal-Tessier and D.P. Gates, *Dalton Transactions*, **2010**, 39, 3151.
3. P.W.N.M. van Leeuwen and P.C.J. Kamer, *Phosphorus(III) Ligands in Homogeneous Catalysis: Design and Synthesis*, John Wiley & Sons, Ltd, Chichester, UK, **2012**.
4. D.W. Allen, D. Loakes and J.C. Tebby, Eds., *Organophosphorus Chemistry*, Royal Society of Chemistry, Cambridge, **2017**, vol. 46.
5. M. Yoshifuji, *European Journal of Inorganic Chemistry*, **2016**, 2016, 607.
6. J. Escudié and G. Nemeş, *Comptes Rendus Chimie*, **2010**, 13, 954.
7. M. Yoshifuji, I. Shima, N. Inamoto, K. Hirotsu and T. Higuchi, *Journal of the American Chemical Society*, **1981**, 103, 4587.

8. S.J. Goede and F. Bickelhaupt, *Chemische Berichte*, **1991**, 124, 2677.
9. T.C. Klebach, R. Lourens and F. Bickelhaupt, *Journal of the American Chemical Society*, **1978**, 100, 4886.
10. R. Septelean, G. Nemes, J. Escudié, I. Silaghi-Dumitrescu, H. Ranaivonjatovo, P. Petrar, H. Gornitzka, L. Silaghi-Dumitrescu and N. Saffon, *European Journal of Inorganic Chemistry*, **2009**, 2009, 628.
11. D. Matioszek, T.-G. Kocsor, A. Castel, G. Nemes, J. Escudié and N. Saffon, *Chemical Communications*, **2012**, 48, 3629.
12. P.M. Petrar, R. Şeptelean, N. Deak, H. Gornitzka and G. Nemeş, *Journal of Organometallic Chemistry*, **2015**, 787, 14.
13. R. Septelean, H. Ranaivonjatovo, G. Nemes, J. Escudié, I. Silaghi-Dumitrescu, H. Gornitzka, L. Silaghi-Dumitrescu and S. Massou, *European Journal of Inorganic Chemistry*, **2006**, 2006, 4237.
14. T.-G. Kocsor, G. Nemes, N. Saffon, S. Mallet-Ladeira, D. Madec, A. Castel and J. Escudié, *Dalton Trans.*, **2014**, 43, 2718.
15. S. Ito, H. Miyake and M. Yoshifuji, *Phosphorus, Sulfur and Silicon and the Related Elements*, **2009**, 184, 917.
16. J. Escudié, H. Ranaivonjatovo, M. Bouslikhane, Y. El Harouch, L. Baiget and G. Cretiu Nemes, *Russian Chemical Bulletin*, **2004**, 53, 1020.
17. M. El Ezzi, R. Lenk, D. Madec, J.M. Sotiropoulos, S. Mallet-Ladeira and A. Castel, *Angewandte Chemie - International Edition*, **2015**, 54, 805.
18. N. Deak, P.M. Petrar, S. Mallet-Ladeira, L. Silaghi-Dumitrescu, G. Nemeş and D. Madec, *Chemistry - A European Journal*, **2016**, 22, 1349.
19. N. Deak, I.-T. Moraru, N. Saffon-Merceron, D. Madec and G. Nemes, *European Journal of Inorganic Chemistry*, **2017**, 4214.
20. C. Overländer, J.J. Tirrée, M. Nieger, E. Niecke, C. Moser, S. Spirk and R. Pietschnig, *Applied Organometallic Chemistry*, **2007**, 21, 46.
21. D.A. Atwood, A.H. Cowley and J. Ruiz, *Inorganica Chimica Acta*, **1992**, 198–200, 271.
22. O. Kühl, *Phosphorus-31 NMR Spectroscopy*, Springer Berlin Heidelberg, Berlin, Heidelberg, **2009**.
23. A.N. Tavtorkin, S.A. Toloraya, E.E. Nifant'Ev and I.E. Nifant'Ev, *Tetrahedron Letters*, **2011**, 52, 824.
24. L. Baiget, M. Bouslikhane, J. Escudie, G.C. Nemes, I. Silaghi-Dumitrescu and L. Silaghi-Dumitrescu, *Phosphorus, Sulfur, and Silicon and the Related Elements*, **2003**, 178, 1949.
25. B. Buster, A.A. Diaz, T. Graham, R. Khan, M.A. Khan, D.R. Powell and R.J. Wehmschulte, *Inorganica Chimica Acta*, **2009**, 362, 3465.
26. B. Cordero, V. Gómez, A.E. Platero-Prats, M. Revés, J. Echeverría, E. Cremades, F. Barragán and S. Alvarez, *Dalton Transactions*, **2008**, 2832.
27. M. Mantina, A.C. Chamberlin, R. Valero, C.J. Cramer and D.G. Truhlar, *The Journal of Physical Chemistry A*, **2009**, 113, 5806.
28. A. Bondi, *The Journal of Physical Chemistry*, **1964**, 68, 441.
29. J. Bezombes, F. Carré, C. Chuit, R.J.P. Corriu, A. Mehdi and C. Reyé, *Journal of Organometallic Chemistry*, **1997**, 535, 81.

30. T. Řezníček, L. Dostál, A. Růžička and R. Jambor, *Journal of Organometallic Chemistry*, **2012**, 718, 38.
31. D.E. Herbert, A.D. Miller and O.V. Ozerov, *Chemistry - A European Journal*, **2012**, 18, 7696.
32. T. Řezníček, L. Dostal, A. Růžička and R. Jambor, *Main Group Metal Chemistry*, **2012**, 35, 129.
33. S. Ito, T. Nakagawa and K. Mikami, *Chemical Communications*, **2013**, 49, 9221.
34. T.G. Kocsor, D. Matioszek, G. Nemeş, A. Castel, J. Escudie, P.M. Petrar, N. Saffon and I. Haiduc, *Inorganic Chemistry*, **2012**, 51, 7782.
35. S. El Kettani, J. Escudie, C. Couret, H. Ranaivonjatovo, M. Lazraq, M. Soufiaoui, H. Gornitzka and G. Nemes, *Chemical Communications*, **2003**, 1662.
36. SAINT and SADABS, Bruker AXS Inc., Madison, Wisconsin, USA.
37. G.M. Sheldrick, *Acta Crystallographica*, **2008**, A64, 112.
38. G.M. Sheldrick, *Acta Crystallographica*, **2015**, A71, 3.

ELECTROCHEMICAL DEPOSITION AND DISSOLUTION OF THALLIUM OXIDE (III)

GULZIYA A. SEILKHANOVA^{a*}, ANDREY P. KURBATOV^a,
YENLIK ZH. USSIPBEKOVA^a, ANDREY V. BEREZOVSKIY^a,
MICHAEL K. NAYRYZBAEV^a

ABSTRACT. The regularities of precipitation and dissolution of thallium (III) oxide were studied by using cyclic and linear voltammetry. It is established that at 1.5V potential, a peak corresponding to the process of oxidation of monovalent to trivalent thallium is observed, according to: $Tl^+ \rightarrow Tl^{3+} + 2e^-$. Two peaks are observed in the cathode region, at 0.65V and -0.17V potential values. At $E = -0.17V$, the thallium oxide Tl_2O_3 dissolves, as at $E = 0.65V$, the intermediate products of the hydrolysis of trivalent thallium ($Tl(OH)^{2+}$, $Tl(OH)^{2+}$) are probably recovered. It was found that with increase of solution pH, the dissolution processes of thallium oxide intensified, while the optimum pH value was 11, also activation energy of the electrodeposition of thallium(III) oxide were calculated.

Keywords: thallium, thallium(III) oxide, electrolysis, voltammetry, precipitation, dissolution/solution.

INTRODUCTION

Today it is difficult to call the field of technology that would not use rare metals, their alloys and various compounds. Due to its physical-chemical properties, thallium, as well as its compounds of high purity, is widely used in many fields of science and technology. In particular, metal thallium is used to obtain bearing and low-melting alloys, in semiconductors, as a source of β -radiation it is used in radioisotope devices [1-3]. Alloys containing thallium have increased resistance, inertness with respect to acids, low melting point.

^a Al-Farabi Kazakh National University, Faculty of Chemistry and Chemical Technology 71 Al-Farabi av., 050040 Almaty, Kazakhstan,

* Corresponding author g_seilkhanova@mail.ru

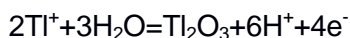
It is known that thallium is used as a catalyst in the obtaining of special alloys, optical lenses, jewelry, and the creation of low temperature thermometers. Thallium compounds are also used as medicines against rodents and insecticides [4-6]. It should be noted that the high toxicity and volatility of thallium compounds are not fundamental obstacles for the use of compositions based on it in engineering. In modern production and technology, the obtaining and use of particularly pure and ultrapure substances play an important role. Obtaining thallium of high purity is a complex technological task requiring the use of complex technological schemes, including both physical and chemical methods of purification. To determine the amount of impurities or the detection of traces of foreign matter in various materials, it is possible to successfully apply electrochemical methods, in particular, the method of electrochemical refining [7]. Therefore, the physical-chemical study of processes in the refining of thallium is very relevant.

This is characterized by the simplicity of appliance design and the possibility of effectively conducting the process at medium temperatures and pressures, yet with high performances. However, it is quite difficult to obtain high-purity thallium by electrolysis due to the similarity of chemical properties and very close position of electrode potentials of thallium and other metal impurities. The authors demonstrated previously [8-12] the principles of possible electrochemical thallium refining through the dissolution stage of anodically-deposited thallium(III) oxide.

As a result, this work aimed the establishing the regularities during precipitation and dissolution of thallium(III) oxide, for the selective electrochemical deposition of a rare metal.

RESULTS AND DISCUSSION

In order to optimize the purification process of rough thallium, the studies were carried out in a volumetric electrolysis cell with a potential of 1.5 V. A glassy carbon plate was used as cathode, platinum served as anode, and a silver chloride electrode as reference, respectively. In addition to the deposition of thallium ($Tl^+ + 1e^- \rightarrow Tl^0$) on the cathode, the platinum plate at the anode was covered at $pH > 2$ with a dark brown precipitate that corresponds to the trivalent thallium oxide [13]. Thus, the following process takes place on the anode:

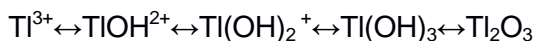


Higher impurity contents (such as Pb, Cu, Cd) are observed in the cathode sediments, because of their close or more positive electrode potentials [8]. The anode's precipitate, thallium oxide Tl_2O_3 , is purer. The only impurity which precipitates along with thallium oxide, due to the close pH of hydrate formation, is iron hydroxide. The purity of the anode sediment is 99.6%. The fact of formation of purer thallium(III) oxide on the anode can be used for refining the rough metal. Results in the literature [14] indicate the possibility of selective precipitation of thallium by using an anode precipitate - Tl_2O_3 , while the purity of rare metal is 99.98%.

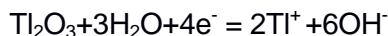
To establish the regularities of electrochemical deposition and dissolution of Tl_2O_3 , cyclic polarization curves were taken at different scanning rates, electrolyte stirring rates and temperatures.

Figure 1 shows cyclic volt-ampere curves at different scanning speeds. In the anode region, where the potential equals 1.5 V, a peak corresponding to the process of oxidation of monovalent to trivalent thallium ($Tl^+ - 2e^- = Tl^{3+}$) is observed.

After that, the oxide formation takes place according to the following scheme:

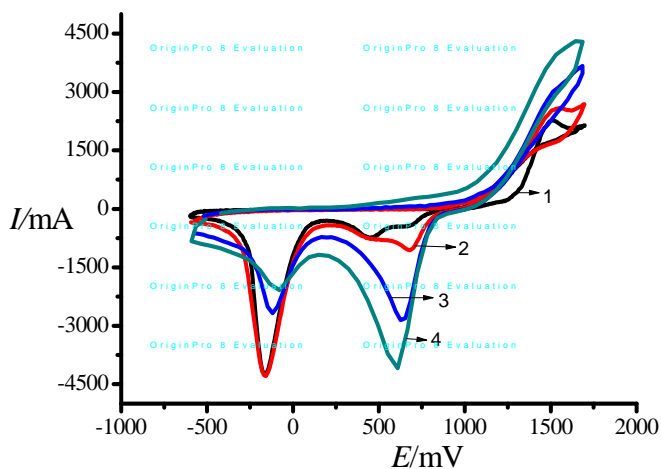


In the cathode region, two peaks are observed with potentials equaling 0.65 V and -0.17 V, respectively. At -0.17 V, Tl_2O_3 dissolves according to the reaction:



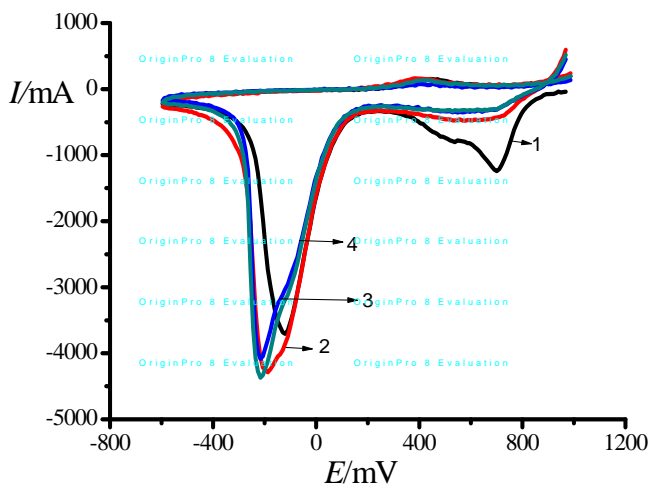
At 0.65V potential, the intermediate products of the hydrolysis of trivalent thallium ($TlOH^{2+}$, $Tl(OH)_2^+$) are probably recovered. With a decrease scanning speeds of the amount of electricity spent on the reduction process, presumably intermediate hydrolysis products, quantitatively goes into the amount of electricity spent to dissolve thallium oxide.

This indicates that the intermediate products of hydrolysis are not very stable and eventually transform into Tl_2O_3 . To confirm this fact, Tl_2O_3 was precipitated in potentiostatic mode, at $E = 1.5V$, for 30 seconds. The cathode polarization curves were registered immediately after precipitation, and furthermore after every 5, 10, 15 seconds. These are presented in Fig. 2.



1-10 mV/s; 2-20 mV/s; 3-50 mV/s; 4-100 mV/s.

Figure 1. Cyclic polarization curves of thallium on a glassy carbon electrode ($c = 10^{-2}$ M) at different scanning speeds



1-0 s; 2-5 s; 3-10 s; 4-15 s.

Figure 2. Cathode polarization curves on glass carbon electrode at different holding times, after precipitation of thallium oxide, at a potential of 1.5 V

Table 1. Amount of electricity, %, spent on cathodic processes at potentials of 0.65 and -0.17 V, respectively.

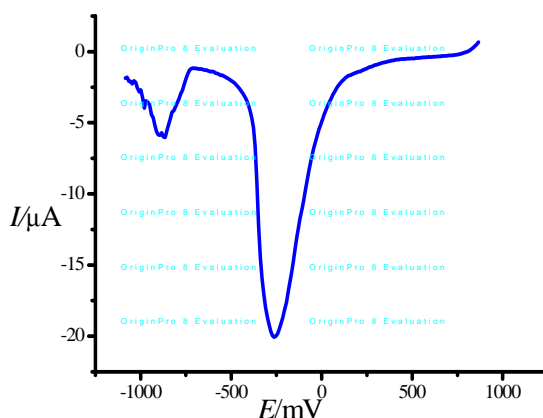
E (V)	Amount of electricity, %, (0 sec)	Amount of electricity, % (5 sec)	Amount of electricity, % (10 sec)	Amount of electricity, % (15 sec)
0.65	32.1±0.28	11.9 ±0.13	9.5±0.11	4.8±0.06
-0.17	67.9±0.70	88.1±0.91	91.5±0.94	95.2±0.97

As can be seen from figure 2 and table 1, over time of the amount of electricity spent on the reduction process, presumably intermediate hydrolysis products, quantitatively goes into the amount of electricity spent to dissolve thallium oxide, which gives the possibility of complete electrochemical dissolution of the oxide when potential equal to -0.17 V.

In order to prove the fact that thallium oxide dissolves with the formation of monovalent thallium, Tl_2O_3 was precipitated in potentiostatic mode ($E = 1.5V$) during the 5 minutes. Further, cathode polarization curves were registered to study the cathode peaks (Fig. 3). As can be seen from Fig. 3, two peaks are observed on the graph, indicating a two-stage dissolution mechanism of Tl_2O_3 . At $E = -0.25V$, thallium(III) oxide is recovered in a monovalent state:



Further, at $E = -0.86V$, the recovery of the monovalent to metallic thallium takes place [15]: $Tl^+ + e^- = Tl^0$

**Figure 3.** Cathode polarization curve on glass carbon electrode of deposited thallium oxide after precipitation during 5 minutes.

The dependence of the magnitude of the thallium peak amperage on the potential sweep speed is analyzed. As can be seen from Figure 4, an increase of the sweeping speed increases the amperage's peak. This may indicate a diffusion mode of the electrode process, because with an increase of the sweep rate, a linear dependence of the amperage density in the anode processes on the square root of the sweep speed is observed. In cathode processes, it is impossible to draw unambiguous conclusions through this parameter, because the processes of recovering intermediate products of trivalent thallium hydrolysis interfere with voltammograms.

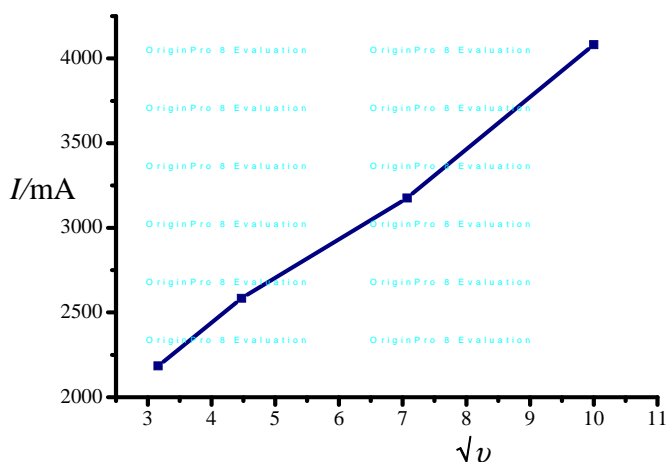
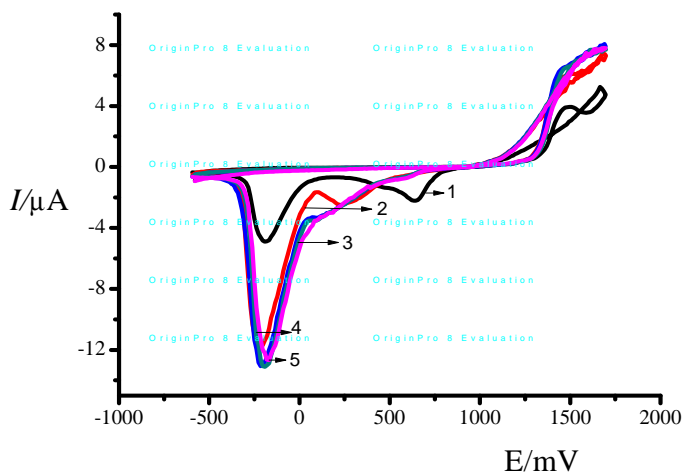


Figure 4. The amperage density dependence of the anode peaks on \sqrt{v} , where v is the sweep speed (Tl_2SO_4 , $c = 10^{-2}$ mole/L)

In order to determine the nature of the limiting stage of the process of precipitation and dissolution of Tl_2O_3 , cyclic polarization curves were taken at different rates of electrolyte mixing (Fig. 5).

It can be seen from the Figures 5 and 6 that the speed of the anode and cathode processes increases till $\omega = 500$ rev/min and does not change further, which indicates insignificant contribution of the mass transfer rate to the rate of electrochemical processes. On the other hand, the process can be limited by diffusion to a large extent till stirring speed reaches 500 rev/min.

ELECTROCHEMICAL DEPOSITION AND DISSOLUTION OF THALLIUM OXIDE (III)



1- 0 rev/min, 2- 250 rev/min, 3- 500 rev/min, 4- 750 rev/min, 5- 1000 rev/min
Figure 5. Cyclic polarization curves of Tl_2SO_4 on the glass carbon electrode at different mixing rates of the solution, $u = 20$ mV/s, $c = 10^{-2}$ mole/L

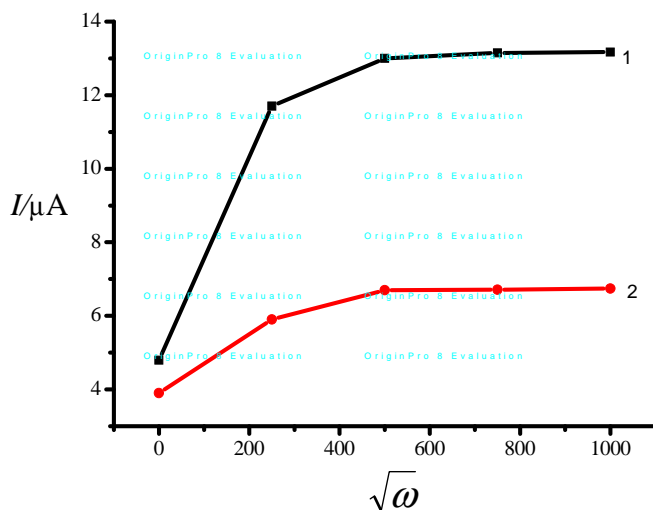


Figure 6. The amperage density dependence of cathode (1) and anode (2) peaks on $\sqrt{\omega}$, where ω is the mixing rate (Tl_2SO_4 , $c = 10^{-2}$ mole/L)

In order to determine the effect of temperature on the precipitation and dissolution of thallium oxide, cyclic polarization curves were taken at different temperatures, without and with ($\omega = 500$ rev/min) sweep rate of solution (Fig. 7).

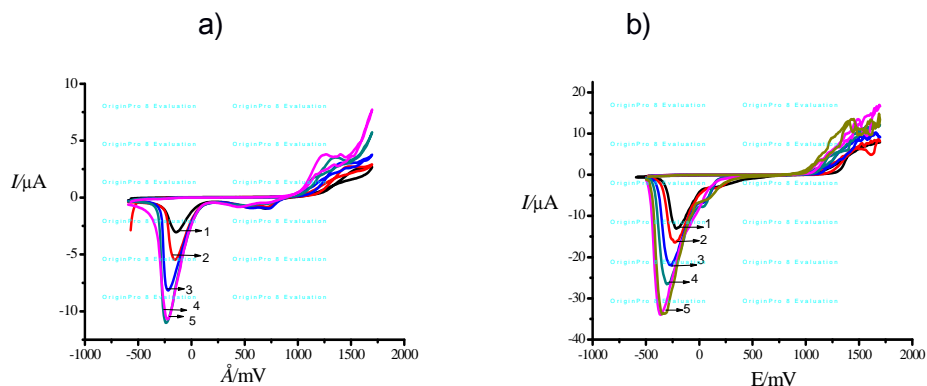


Figure 7. Cyclic polarization curves on the glassy carbon electrode at different temperatures, without sweep rate of solution (a) and $\omega = 500$ rev/min (b), Tl_2SO_4 , $c = 10^{-2}$ mole/L. 1- 20; 2- 30, 3- 40; 4- 50, 5- 60 °C

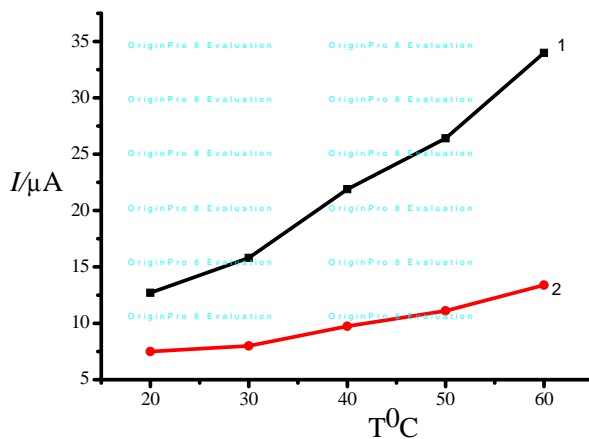


Figure 8. The amperage density dependence of cathode (1) and anode (2) peaks on temperature (Tl_2SO_4 , $c = 10^{-2}$ mole/L)

Graphs 7 and 8 show that a linear increase of the speed of the cathode and anode processes occurs with the increase of temperature up to 60°C. Further, the speed maintains the same level and does not change. Therefore, it means that $\omega = 500$ rev/min and $T = 60^\circ\text{C}$ can be considered as optimal conditions for the precipitation and dissolution of thallium oxide. In Table 2, the activation energies for the cathode and anode process were calculated with and without stirring the electrolyte.

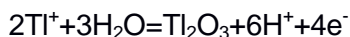
Table 2. The value of activation energy of cathode and anode processes

Process	W, rev/min	Number of points	Correlation coefficient	E_a , kJ/mole
cathode	0	5	0,90	11,7±0,13
anode	0	5	0,97	33,4±0,35
cathode	500	5	0,99	6,5±0,08
anode	500	5	0,97	11,8±0,13

The values of the activation energies lead to the following conclusions: the anode process of thallium oxide precipitation is limited by the rate of supply of the Tl^+ ion to the electrode surface. It is also evident that with stirring, the activation energy increases, indicating the transition to the internal-diffusion region of the precipitation process. It means that the process is limited by the rate of charge transfer through the film formed by Tl_2O_3 .

The anode process, even without stirring the electrolyte, is characterized by a high activation energy. At electrolyte mixing rates equal to 500 rpm, the activation energy significantly reduces. This can be explained by the fact that without mixing, the process of dissolution of Tl_2O_3 is limited by mixed-diffusion kinetics: the thallium transfer process through the oxide film and the Tl^+ withdrawal process from the electrode surface to the solution volume. When the solution is stirred, the cathode process is limited by the rate of charge transfer through the oxide film.

It is also found that with the increase of temperature, the formation of trivalent thallium intensifies, which can lead to acceleration of the formation of thallium oxide in the anode's space:



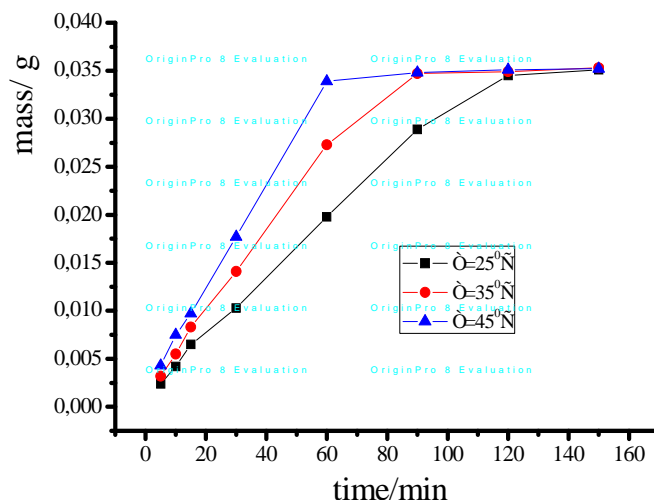


Figure 9. The deposited thallium oxide(III) mass dependence on time at different temperatures

To confirm this fact, the oxide of thallium(III) was deposited on the anode at different temperatures and at various times. The results are shown in Fig. 9. It can be observed that the increase of temperature contributes to achievement of a constant mass of oxide at lower electrolysis time. From the obtained data, values of the rate and activation energy of the electrodeposition processes of Tl_2O_3 , were calculated.

CONCLUSIONS

Thereby, there has been established that intermediate products are formed when Tl_2O_3 precipitates, presumably: $TlOH^{2+}$, $Tl(OH)_2^+$. However, over time they transfer into Tl_2O_3 , which should allow complete dissolution of obtained thallium oxide at potential values equal to -0.17 V. It has been established that the process of dissolution of thallium(III) oxide is a two-step process, the optimal background electrolyte is 1 mole/L Na_2SO_4 , the optimum pH value is 11, $\omega = 500$ rev/min and $T = 60^\circ C$. The results of the work indicate the possibility of selective precipitation of thallium via anode precipitation of Tl_2O_3 . The obtaining thallium can be used for further purification, in particular by zone melting. It is known that the purer the metal enters for refining by the zone melting method, the higher the degree of its purity. High-purity rare metals, in particular thallium, are used in semiconductor technology.

ACKNOWLEDGMENTS

The work was carried out within the framework of the program "Fundamental Foundations of Processes Based on Electrochemical Transformations", on the topic "Physicochemical regularities of cathode and anode processes in systems involving thallium".

EXPERIMENTAL

Materials and methods

Electrochemical measurements were performed on an AUTOLAB-30 potentiostat - galvanostat with a computer control station in its potentiostatic mode, in 0.01 mole/L Tl_2SO_4 solutions. The background electrolyte was of 0.5 mole/L Na_2SO_4 . The area of the working electrode was 1 cm^2 , platinum was used as an auxiliary electrode, and a silver chloride electrode served as reference. Preparation of electrodes was carried out by mechanical and chemical cleaning.

Mechanical treatment was carried out in order to remove visible contaminants. Chemical cleaning contributed to the dissolution of various compounds from the electrodes' surface. Concentrated solution of nitric acid (HNO_3) was used for this. Nitrate, sulfate, and sodium acetate were used as background electrolytes. Cyclic polarization curves were obtained in the temperature range of 20-60 $^{\circ}C$ and at potential sweep rates of 5-50 mV/s.

In order to establish the limiting stage of the electrochemical process, experiments were carried out at solution stirring rates equal to 0-1000 rev/min. All quantitative measurements were carried out in at least three replicates and processed statistically. Electrochemical calculations were performed by using Microcal Origin 8. Quantitative analysis of the composition of the precipitates was carried out by using an ICP OES 8000 optical emission spectrometer (Perkin Elmer) with the WinLab 5 software.

REFERENCES

1. Korovina S.S Rare and Scattered elements. Chemistry and technology. V. 1. M: MISiS, **1996**, 375 (in Russian).
2. Zelikman A.N., Korshunov B.G. Metallurgy of rare metals: textbook for high school. – 2nd edition, elaboration and edition - M.: Metallurgy, **1991**, 432 (in Russian).

3. Bolshakov K.A. Chemistry and technology of rare and scattered elements. – M.: High school, **1976**, 1, 295 (in Russian).
4. Maher J.P. Aluminium, gallium, indium, and thallium // Annu. Rep. Prog. Chem., Sect. A, **2003**, 99, 43–62.
5. Busev A.I., Tipzova V.G. Analytic chemistry of thallium. Success of chemistry. – M: Nauka, **1960**, 29, 8, 1011.
6. Kuketaev T. A. Optic and nuclear properties of KDP, activated by thallium ions // Khabarshy (Herald), **2008**, 69(in Russian)
7. Damaskin B.B., Petry O.A., Zirlina G.A. Electrochemistry. – 2 ed., edited and added — M.: Chemistry, Kolos, **2006**, 672 (in Russian).
8. Ussipbekova Ye. Zh., Seilkhanova G.A., Scholz F., Kurbatov A.P., Berezovskiy A.V., Nauryzbaev M.K. Electrochemical refining of thallium in the neutral space// News NAN RK.Chemical Serias. № 5 (407), **2014**, 64 – 69 (in Russian).
9. Eremin V.V., Kargov S.I., Uspenskaya I.A., Kuzmenko N.E., Lunin V.V. The basis of physical chemistry. Theory and problems. – M.: Exam, **2005**, 480 (in Russian).
10. Gorbachev S.V. Influences of temperature on electrolysis, as kinetic research methods of the nature of electrochemical processes//the 4th session on electrochemistry. Collection of scientific papers – M.: AN USSP, **1959**, 61-71 (in Russian).
11. Keshe G. Corrosion of metals. Physic-chemical principles and relevant problems // M. : Metallurgy, **2004**, 400 (in Russian).
12. Seilkhanova G.A., Ussipbekova Ye.Zh., Jeyabhrathi Ch., Scholz F., Kurbatov A.P., Nauryzbaev M.K., Berezovskiy A.V. Electrochemical deposition and dissolution of thallium from sulfate solutions // Internatoinal journal of analytical chemistry. vol. **2015**, doi:10.1155/2015/357514.
13. Zirlina G.A. Electro catalysis via thallium oxide anodes // Electrochemistry. **1995**, 31, 2, 219-221 (in Russian).
14. Utility patent model № 1514 Electrochemical methods of obtaining pure thallium, authors Seilkhanova G.A., Kurbatov A.P., Nauryzbaev M.K., Ussipbekova Ye.Zh., Berezovskiy A.V., Uteshova A.A. – published. 30.06.**2016**; Bulletin. - № 66 (in Russian).
15. Seilkhanova G.A., Kurbatov A.P., Ussipbekova Ye.Zh., Berezovskiy A.V., Elechthrochemical behavior of thallium in various electrololytes // "KazNU herald" Chemical serials, **2014**, 2, 41 - 48 (in Russian).

DIETHYLENE GLYCOL BASED DEEP EUTECTIC SOLVENTS AND THEIR PHYSICAL PROPERTIES

RUSUL KHALEEL IBRAHIM^a, MAAN HAYYAN^{b,c*},
MOHAMMED ABDULHAKIM ALSAADI^{b,d}, SHALIZA IBRAHIM^a,
ADEEB HAYYAN^{b,d*}, MOHD ALI HASHIM^{b,e}

ABSTRACT. In this study, diethylene glycol (DEG), as a hydrogen bond donor (HBD), was mixed with three ammonium based salts, namely N,N-diethylethanolammnium chloride, tetra-n-butylammonium bromide and choline chloride, as well as two phosphonium based salts, namely benzyl-triphenylphosphonium chloride and methyltriphenylphosphonium bromide, to prepare five different deep eutectic solvents (DESs) series. The DESs freezing points and functional groups were investigated. In addition, the physical properties viscosity, density, conductivity and surface tension were determined as function of temperature in the particular temperature range of 293.15- 353.15 K. It is worth mentioning that all examined DESs were stable and in liquid phase at room temperature which emphasize their promising potential to be utilized as inexpensive environment-friendlier solvents. Owing to their low recorded freezing points and viscosities, DEG based DESs can be effortlessly processed without any further heating required in diverse industrial applications.

Keywords: *deep eutectic solvents; ionic liquids; diethylene glycol; physical properties; chemical processes; industrial applications.*

^a Department of Civil Engineering, University of Malaya, Kuala Lumpur 50603, Malaysia

^b University of Malaya Centre for Ionic Liquids (UMCIL), Department of Chemical Engineering, University of Malaya, Kuala Lumpur 50603, Malaysia

^c Department of Chemical Engineering, Faculty of Engineering, Sohar University, P.O. Box 44, Sohar P.C. 311, Sultanate of Oman

^d Nanotechnology & Catalysis Research Centre (NANOCAT), University of Malaya, Kuala Lumpur 50603, Malaysia

^e Department of Chemical Engineering, University of Malaya, Kuala Lumpur 50603, Malaysia

* Corresponding author: maan_hayyan@yahoo.com; adeeb.hayyan@yahoo.com

INTRODUCTION

Owing to their distinctive physiochemical properties, ionic liquids (ILs) have served various purposes and gained a considerable attention in different academic and industrial fields. For instance, ILs have been used in metal extraction, in polymeric electrolyte membrane fuels cells, in Solar Cells and in biological applications such as drug delivery and activation of enzymes, as well as they have been applied as electrolytes in batteries and as reaction media for organics synthesis and biochemical reactions [1]. However, many studies have underlined the limitations of ILs, which restrain their applications on large scale in commerce, including their poor sustainability and biodegradability [2], their high toxicity to human and environment and the high required cost for their complicated synthesizing process [3, 4]. Therefore, the emergence of deep eutectic solvents (DESs) as inexpensive solvents with easier preparation and better biodegradability [5], has enlightened the opportunities of their exploitations as appealing alternatives to maintain the useful characteristics of ILs and to overcome the challenges that hinder ILs applications [6, 7]. Generally, the formation of DES can be easily obtained by mixing two or more of cheap and biodegradable components, namely, hydrogen bond acceptor (HBA) and hydrogen bond donor (HBD), which are connected with each other by hydrogen bond interactions [8]. DES is well characterized by its freezing point which is usually lower than that of its individual components. The main reason behind the depression of the eutectic mixture freezing point, is the delocalization of the charge occurring through hydrogen bonding between the halide anion and the HBD [9, 10].

Besides of having low production cost and having a good biocompatibility [11], DESs have been reported to own remarkable properties such as high viscosity, high thermal stability and low vapor pressure [12]. Therefore, many studies have been widely investigating the possibility of employing DESs in different applications [13]. For instance, DESs have shown interesting potentials in the electrochemistry technology, such as surface cleaning and metallurgy, due to their capability of donating or accepting electrons or protons to form hydrogen bonds which makes them of a great interest for dissolution of metal oxides [14]. The solubility of CuO in a choline chloride (ChCl) –urea (U) eutectic mixture was first studied by Abbott et al. [15]. Another example, DESs have been used to remove air pollutants from gas emissions, due to their physiochemical properties which make them superior substitutes for volatile organic compounds. Yang et al. [16] explored the removal of Sulfuric dioxide (SO₂) by (ChCl)-glycerol DESs. The results revealed the high absorption efficiency of SO₂ by the eutectic mixture and which was increased by decreeing the temperature, moreover, the absorbed

SO₂ could be easily stripped out from the DES by bubbling nitrogen through the eutectic mixture [16]. In addition, the effect of different temperatures and different DES molar ratio on the solubility of carbon dioxide (CO₂) was investigated by Han and co-workers using ChCl-U DES [17]. In like manner, Wong and co-workers explored the effect of water content on the absorption of CO₂ by using ChCl-U-H₂O [18]. These studies are considered of great concern for the development the separation and gas purification technology using DESs. Furthermore, Morison et al. [19] examined the potentials of ChCl-U and ChCl-malonic acid DESs for the drug solubilization, Hayyan et al. [20] studied the application of ChCl-glycerol based DESs in fuel purification by extracting glycerol from palm oil-derived biodiesel, and Abbott et al. used ChCl-Ethylene glycol (EG) as dispersant for electrodeposition of Ag and formation of Ag/ SiC/Al₂O₃ nanocomposite film [21].

DESs have been reported to have a promising industrial application [22]. Therefore, in order to suggest further application and design green technologies involving DESs, many studies have extensively been attempting to cover and understand the unique and common properties of DESs followed by applying them in different chemical researches. For example, Shahbaz et al. [23, 24] had successfully predicted the density and the surface tension of different DESs, and the effect of salt to HBD molar ratio on the predicted DESs densities was investigated. Also, Yadav et al. [25] investigated the densities and the dynamic viscosities of (ChCl:Gl) DES at a temperature range of (283.15–363.15 K). Similarly, the main purpose of this study is to document the physical properties as function of temperature (e.g. freezing point, FTIR analysis, density, surface tension, viscosity, conductivity) of five DES systems prepared by mixing five different salts, namely N,N-diethylethanolammnium chloride, benzyltriphenylphosphonium chloride, choline chloride, methyltriphenylphosphonium bromide and tetra-n-butylammonium bromide, and diethylene glycol (DEG) as HBD. DEG is an aliphatic compound which is widely used as solvent, antifreeze, chemical feedstock, and it can be found in automotive products and wallpaper stripper [26, 27]. For our best knowledge, there are no recorded data in literature concerning the physical properties of DEG based DESs.

RESULTS AND DISCUSSION

FREEZING POINT

The selected series of DESs are in liquid form under room-temperature conditions, which facilitate their exploitations in different industrial applications. Abbott et al. [28] stated that the freezing point of DES can be partially

measured by the melting points of the pure components parts, and it is dependent on the entropy changes, lattice energy and on the way of interaction between cation and anion components [28, 29]. The melting points of the salts used in this study, i.e., BTPC, MTPB, ChCl, DAC, and TBAB, are 603.15, 507.15, 575.15, 409.15, and 376.15 K, while the freezing point of DEG is 264.15 k. Table 1 displays the freezing points of the five studied DESs and their composition and abbreviations. It is clear that all the values are in agree with the general definition of DES that characterize the DES mixture with a lower freezing point than that of its individual constituents. As can be concluded from the data, the freezing points range between 247.92- 262.39 K, with the highest freezing point for [DAC:DEG] while the lowest freezing point for [TBAB:DEG]. All the recorded freezing points were below 323.15 K, and as reported by Zhang et al. [30], DESs with freezing points lower than 323.15 K are more attractive to be employed as cheap and safe ambient temperature solvents in many different fields.

Table 1. Composition, abbreviations and freezing point for the studied DESs.

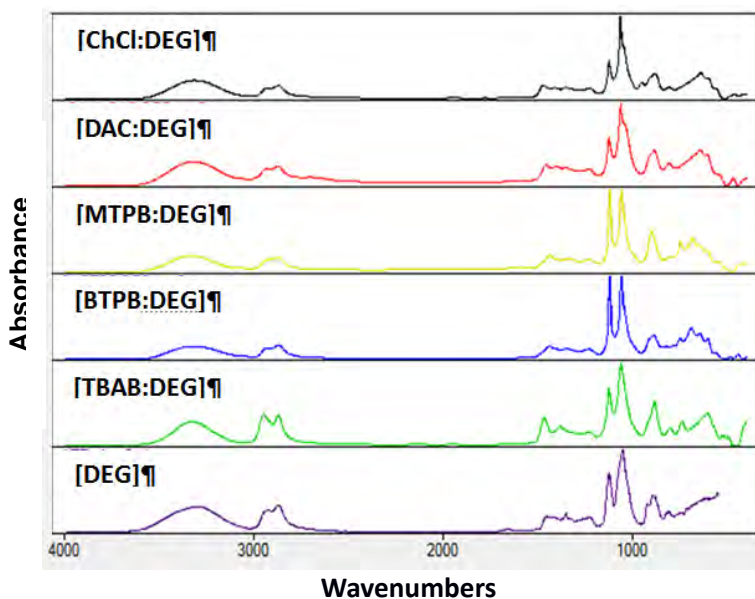
Salt*	Salt Molar ratio	HBD	HBD Molar ratio	DES Abbreviation	DES molecular weight	Freezing point. ^a (Tf /K)
ChCl	1	DEG**	2	[ChCl:DEG]	117.288	260.52
DAC	1		3	[DAC:DEG]	118.002	262.39
TBAB	1		2	[TBAB:DEG]	178.202	247.92
BTPC	1		7	[BTPC:DEG]	141.463	248.52
MTPB	1		4	[MTPB:DEG]	156.340	248.39

a Freezing point value represents the average point between the first crystal appearance and the last liquid drop disappearance. All freezing point data are reported at pressure of 0.1 MPa. *ChCl: choline chloride, DAC: N,N-diethylethanolammonium chloride, TBAB: tetra-n-butylammonium bromide, BTPC: benzyltriphenylphosphonium chloride, MTPB: methyltriphenylphosphonium bromide. ** DEG: diethylene glycol.

FTIR

The result of FTIR analysis is shown in Figure 1 indicates that the pure constituents of DESs (salt-HBD) have obvious effects on the structure of the DESs. The effect of DEG as HBD can be noticed in all DESs spectrums at peaks between 3500-3200 cm^{-1} , representing the O–H stretching bond [31-34]. Moreover, due to the utilization of DEG as HBD in the current DESs synthesizing process, the spectral peaks of the examined DES systems are virtually alike.

On the other hand, the effect of salts can be inferred from the existence of the P–H bonds in the structure of phosphonium based DESs, which could be overlapped with C–H bands at the region between $3000\text{--}2800\text{ cm}^{-1}$ [31, 33, 34]. In addition, the effect of salts on ammonium based DESs assimilated in the presence of ammonium structures between $3200\text{--}2400\text{ cm}^{-1}$, mainly N–H stretch at 2870 cm^{-1} [33–36]. For all examined DESs, the intense absorption bands at ($800\text{--}700\text{ cm}^{-1}$) and ($700\text{--}600\text{ cm}^{-1}$) were assigned to aliphatic organohalogen compounds with stretching bonds (C–Cl) and (C–Br) respectively [32]. Furthermore, the strong bonds ranging from ($1200\text{--}1050\text{ cm}^{-1}$), ($1600\text{--}1800\text{ cm}^{-1}$), and ($1400\text{--}1340\text{ cm}^{-1}$) are assigned to C–O, C=O and N–O correspondingly. The stretch $\text{PO}_4\text{--}3$ at ($1100\text{--}1000\text{ cm}^{-1}$) [32, 34] was strong and broad in [MTPB:DEG] and [BTPC:DEG] while peaks at ($1310\text{--}1230\text{ cm}^{-1}$) [32, 34] representing C–N stretch, were explicit in [ChCl:DEG], [DAC:DEG], and [TBAB:DEG].



Density

The density values of the five selected DESs as function of temperature are illustrated in Figure 2. At room temperature, [MTPB:DEG] attained the highest density of 1.209 g.cm^{-3} , whereas [TBAB:DEG] attained the lowest density of 1.078 g.cm^{-3} . At 293.15 K , the density of [ChCl:DEG] (1.1216 g.cm^{-3}) was found to be similar to that of [ChCl: ethylene glycol] (1.12 g.cm^{-3}) [37, 38], and

lower than that of [ChCl:urea] (1.25 g.cm^{-3}) [39-41]. Additionally, [MTPB:DEG] had a density value of 1.209 g.cm^{-3} which was lower than the reported density for [MTPB:glycerol] (1.30 g.cm^{-3}) [42], and slightly higher than that reported for [MTPB: triethylene glycol] (1.19 g.cm^{-3}) [43]. For further comparison purposes, Table 3 is arranged to compare the densities of the studied DESs with those of some reported ILs in literature.

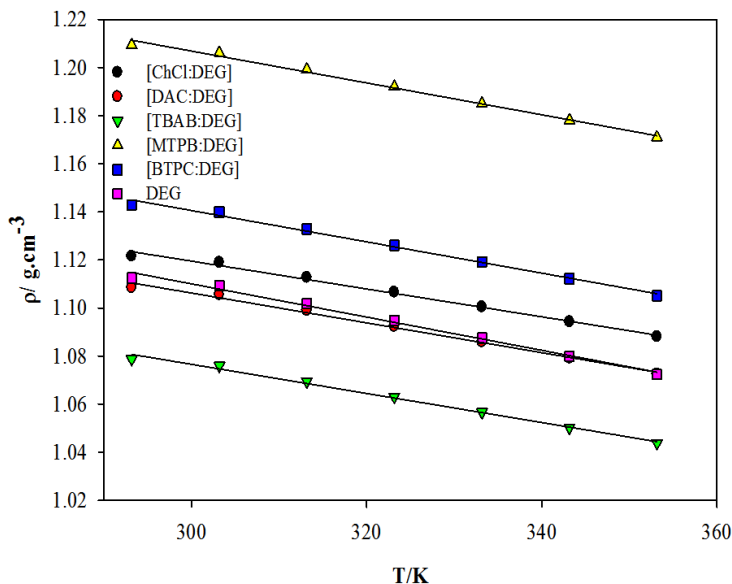


Figure 2. Densities for DEG based DESs as a function of temperature.

The calculated densities using the simple mixing rule (Eq 1) [44] were found to be incompatible with the recorded experimental densities and that indicates the interaction of both components molecules and confirms the hydrogen bonding formation which reduces the molecular distance between the salt and HBD.

$$\frac{1}{\rho_m} = \sum_i \frac{x_i}{\rho_i} \quad (1)$$

where ρ_m is the density of DES mixture (gm.cm^{-3}), x_i is mass fraction of component i , and ρ_i is the density of component i (gm.cm^{-3}).

Moreover, the densities of the examined DESs series decreased with the increase of temperature due to the effects of the increased internal energy on the mobility of DES molecule resulting in increasing the thermal expansion of DES volume [45].

Table 3. Comparison between the physical properties of the five studied DESs and the physical properties of some reported conventional ILs.

[Chol:DEG]	Examples of ILs		REF
μ (cP)	1-Butyl-3-methylimidazolium bis(trifluoromethyl)sulfonylimide	μ (cP)	52 (293.15 K) [53]
ρ (g.cm ⁻³)	1-Butyl-3-methylimidazolium tetrafluoroborate	ρ (g.cm ⁻³)	1.12 (298.15 K) [54, 55]
σ (mN m ⁻¹)	1-Butyl-3-methylimidazolium hexafluorophosphate	σ (mN m ⁻¹)	48.8 (298.15 K) [56]
[DAC:DEG]	Examples of ILs		REF
μ (cP)	1,3-Diallylimidazolium 3-(trifluoroborate)-butylnitrile	μ (cP)	56 (293.15 K) [57]
ρ (g.cm ⁻³)	1-Octyl-3-methylimidazolium tetrafluoroborate	ρ (g.cm ⁻³)	1.11 (298.15 K) [58]
σ (mN m ⁻¹)	2-Hydroxyethylammonium formate	σ (mN m ⁻¹)	65 (300.1 K) [59, 60]
[TBAB:DEG]	Examples of ILs		REF
μ (cP)	1,3-Dibenzylimidazolium dicyanoamide	μ (cP)	202 (293.15 K) [61]
ρ (g.cm ⁻³)	1-Ethyl-3-methylimidazolium dicyanoamide	ρ (g.cm ⁻³)	1.08 (293.15 K) [62]
σ (mN m ⁻¹)	1-Ethyl-3-methylimidazolium tetrafluoroborate	σ (mN m ⁻¹)	54.4 (298.15 K) [63]
[BTPC:DEG]	Examples of ILs		REF
μ (cP)	[Bis(bis-hexyl-amino)-methylene] dimethyl-ammonium bis(trifluoromethyl)sulfonylimide	μ (cP)	124 (333.15 K) [64]
ρ (g.cm ⁻³)	1-[2-(2-Methoxyethoxy)ethyl]-3-methylimidazolium chloride	ρ (g.cm ⁻³)	1.14 (298.15 K) [65]
σ (mN m ⁻¹)	2-Hydroxyethylammonium formate	σ (mN m ⁻¹)	65 (300.1 K) [59, 60]
[MTPB:DEG]	Examples of ILs		REF
μ (cP)	Tri-n-octylammonium 4,4,4-trifluoro-1-(2-furyl)-1,3 butanedionate	μ (cP)	140.2 (298.15 K) [66]
ρ (g.cm ⁻³)	N,N-methyl-N-ethyl-N-(2-methoxyethyl) ammonium tetrafluoroborate	ρ (g.cm ⁻³)	1.21 (298.15 K) [67]
σ (mN m ⁻¹)	2-Hydroxyethylammonium formate	σ (mN m ⁻¹)	65 (300.1 K) [59, 60]

For all examined DESs, the density-temperature relationship was fitted linearly using Eq 2 with regression values R^2 of 0.99.

$$\rho = a + bT \quad (2)$$

where ρ is the density, T is temperature in Kelvin, and a and b are constants and their values are listed in Table 4.

Table 4. Density- temperature model parameters.

DES	a	b	R ²
[ChCl:DEG]	1.2932	-0.0006	0.99
[DAC:DEG]	1.2922	-0.0006	0.99
[TBAB:DEG]	1.2581	-0.0006	0.99
[BTPC:DEG]	1.3358	-0.0007	0.99
[MTPB:DEG]	1.4055	-0.0007	0.99

Viscosity and conductivity

The values of viscosity and conductivity are the prominent attributes of DESs to be utilized as significant candidates as an electrolyte in electrochemical applications such as batteries, electroplating, and electrolysis. Figure 3 and Figure 4 elucidate the effect of temperature on the viscosity and the electrical conductivity of the studied DESs, respectively. For all selected DESs, the noted values of viscosity and conductivity were determined at temperature range of (293.15-353.15 K), and both of these physical properties for DESs were higher than those for DEG. At room temperature, the deliberated DESs series had the following viscosity sequence: [TBAB:DEG] > [MTPB:DEG] > [BTPC:DEG] > [DAC:DEG] > [ChCl:DEG]; while their conductivity order was as following: [ChCl:DEG] > [DAC:DEG] > [MTPB:DEG] > [BTPC:DEG] > [TBAB:DEG]. It is noticeable that DES with the highest viscosity attained the lowest conductivity value due to the extreme high consistency of DES mixture that constrained the transmission of the electrical current through the mixture. Another significant factor that has a perceptible impact on the viscosity and conductivity values is the ratio of salt in the DES mixture. Table 5 depicts that although [MTPB:DEG] has a higher viscosity than that of [BTPC:DEG], it recorded a

higher electrical transmission ability due to its high salt ratio content; moreover, it can be concluded from Table 5 that DES viscosity data is relatively proportional to the ratio of salt in DESs. It is noteworthy, that the temperature has an adverse influence on the viscosity because of the energetic motion gained by DESs molecules when the temperature increases, resulting in reducing the strength of intermolecular forces, decreasing the mixture viscosity and consequently increasing its conductivity.

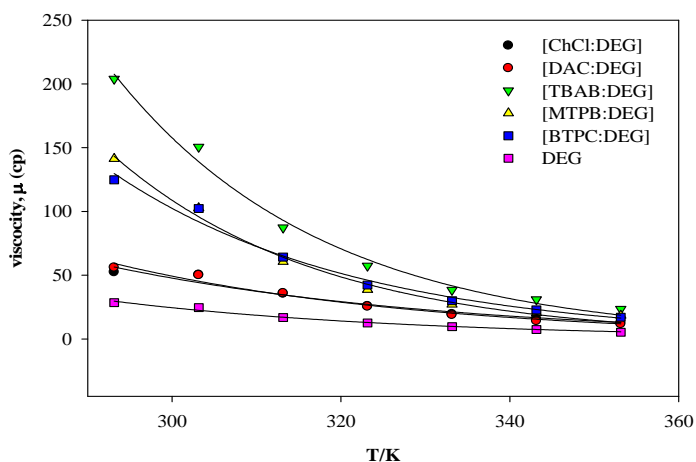


Figure 3. Viscosities for DEG based DESs a function of temperature

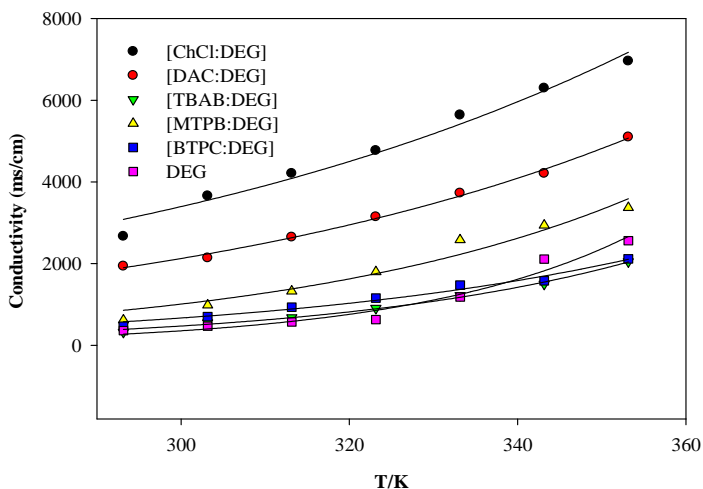


Figure 4. Conductivities for DEG based DESs as a function of temperature

Comparing the current considered DES systems with previous works, reveals that [ChCl:DEG] had a viscosity value of (52.49 cP at 293.15 K) higher than that of [ChCl: ethylene glycol] (37.0 cP at 298.15 K) [46], lower than that of [TBAC:EG] (>200 cP at 293.15 K) [45] and extremely lower than that of [ChCl: zinc chloride] (85000 cP at 298.15 K) [47]. Also, the viscosity of [MTPB:glycerol] was reported to be very high (2775.9 cP) at 298.15 K [48], while the viscosity of [MTPB:DEG] in this study was found to be comparatively low (141.3 cP) at 293.15 K. All the recorded viscosities of the concerned DESs at 353.15 K were much lower than the lowest viscosities values reported for triethylene glycol (TEG) based DESs [35].

Table 5. Salt ratio effect on the viscosity and conductivity (At 293.15 K).

DES	Salt ratio	μ (cP)	S ($\mu\text{S}/\text{cm}$)
[ChCl:DEG]	30.49	52.49	2670
[DAC:DEG]	32.55	56.09	1940
[TBAB:DEG]	60.3	203.9	325
[BTPC:DEG]	34.36	124.8	466
[MTPB:DEG]	45.7	141.3	618

Additionally, Table 3 presents a simple comparison between the viscosities of the studied DESs with some reported ILs. On the other hand, the conductivity of [DAC:DEG] ($2040 \mu\text{S}\cdot\text{cm}^{-1}$) at 298.15 K was found to be higher than that of [DAC: malonic acid] ($1130 \mu\text{S}\cdot\text{cm}^{-1}$) and much lower than that of [DAC: zinc nitrate] ($7050 \mu\text{S}\cdot\text{cm}^{-1}$) [49]. The conductivity of [ChCl:DEG] at 293.15 was found to be ($2670 \mu\text{S}\cdot\text{cm}^{-1}$) which is higher than that of [ChCl: 1,4-butanediol] ($1654 \mu\text{S}\cdot\text{cm}^{-1}$) [50] and that of [ChCl: triethanolamine] ($650 \mu\text{S}\cdot\text{cm}^{-1}$) [49]. It is worth mentioning that in this study ChCl salt based DES had attained the lowest viscosities and the highest conductivities among all DESs and that was similar to the reported case of ChCl salt based DES with glycerol (GLY) as HBD [48].

The trend of viscosity-temperature can be expressed with a regression value (R^2) higher than 0.97 for all DESs by the following Arrhenius-like equation, Eq 3 [51]:

$$\mu = \mu_0 e^{\left[\frac{E_\mu}{RT}\right]} \quad (3)$$

where μ is the viscosity, μ_0 is a pre-exponential factor, E_μ is the viscosity activation energy, R is them gas constant and T is temperature in K.

The model parameter values are listed in Table 6.

Table 6. Viscosity- temperature model parameters.

DES	μ_0	$(E_\mu R^{-1})$	R^2
[ChCl:DEG]	7×10^{-3}	2654.02	0.97
[DAC:DEG]	3×10^{-3}	2908.94	0.98
[TBAB:DEG]	4×10^{-4}	3892.81	0.99
[BTPC:DEG]	6×10^{-4}	3599.62	0.99
[MTPB:DEG]	3×10^{-4}	3784.48	0.98

The trend of conductivity-temperature is similar to that of viscosity-temperature but in the opposite direction and it can also be fitted using the following Arrhenius model, Eq 4 [52]:

$$S = S_0 e^{\left[\frac{-E_s}{RT}\right]} \quad (4)$$

where S is the conductivity in ($\mu\text{s}/\text{cm}$), S_0 is pre-exponential factor, E_s is the activation energy of electrical conduction, R is the gas constant, and T is the temperature in K. The model parameter and the regression coefficient values for all five DESs are arranged in Table 7.

Table 7. Conductivity- temperature model parameters.

DES	S_0	$(E_s R^{-1})$	R^2
[ChCl:DEG]	6×10^5	-1584.26	0.98
[DAC:DEG]	6×10^5	-1697.13	0.99
[TBAB:DEG]	1×10^7	-3010.37	0.99
[BTPC:DEG]	2×10^6	-2461.27	0.98
[MTPB:DEG]	2×10^7	-2960.37	0.98

Surface tension

The surface tension is one of the important properties that affects the reactivity of DESs and it is one of the crucial liquid characterization that is required in many industries. Figure 5, represents the surface tension of the studied DESs as function of temperature.

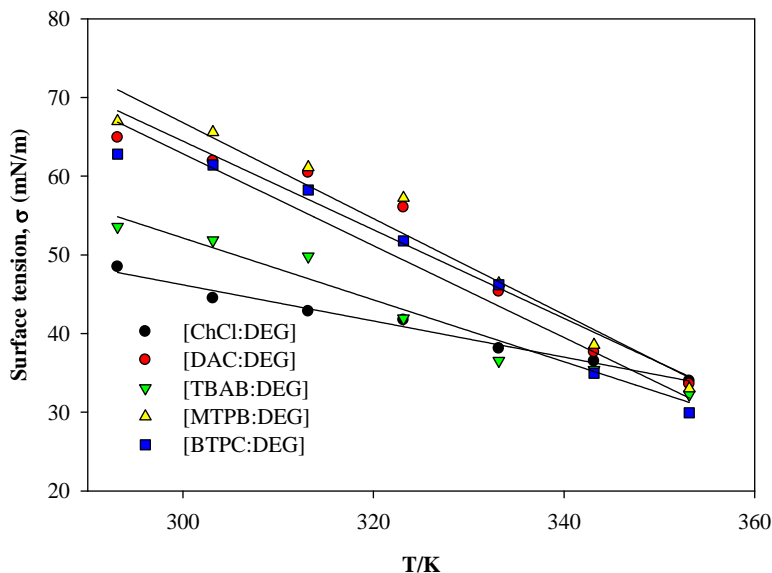


Figure 5. Surface tension for DEG based DESs as a function of temperature

At 293.15 K, the highest surface tension value was 66.98 mN m^{-1} for [MTPB:DEG], while the lowest surface tension value was 48.49 mN m^{-1} for [ChCl:DEG]. At 353.15 K, the surface tension of [MTPB:DEG], [ChCl:DEG] and [DAC:DEG] were almost the same with a value of 33.0 mN m^{-1} . Comparatively, at 313.15 K, the surface tension of [ChCl:DEG] (42.82 mN m^{-1}) was higher than that of [ChCl: 2,2,2-trifluoroacetamide] (35.9 mN m^{-1}) [40]. Meanwhile, at 293.15 K, [ChCl:DEG] had a surface tension value (48.49 mN m^{-1}) higher than that of [ChCl: 1,4-butanediol] (47.6 mN m^{-1}) and lower than that of [ChCl:Glycerol] (50.8 mN m^{-1}) [30]. More comparison examples between the studied DESs and ILs are listed in Table 3.

As expected, the trend of the surface tension-temperature is similar to that of viscosity-temperature, since both of the properties are highly dependent on the strength of the molecular interaction that rules the formation of DES mixture [30]. As can be simplified from Figure 5, when the temperature increases, the surface tension of DES decreases because of the reduced effects of the cohesive forces between the surface molecules which is resulted from the vibrant motion of molecules due to the thermal expansion [45]. The surface tension-temperature relationship was linearly fitted according to Eq 5:

$$\sigma = a + bT \quad (5)$$

where σ is the surface tension, T is the temperature in K, and a and b are constants. The model parameters along with the regression coefficient values (R^2) are shown in Table 8.

Table 8. Surface tension-temperature model parameters.

DES	a	b	R2
[ChCl:DEG]	115.0892	-0.2297	0.98
[DAC:DEG]	233.3722	-0.5631	0.94
[TBAB:DEG]	170.1202	-0.3932	0.95
[BTPC:DEG]	238.0510	-0.5840	0.95
[MTPB:DEG]	249.7380	-0.6098	0.95

CONCLUSIONS

The physical properties of the five DES systems were obtained at a temperature range of 293.15- 353.15 K. At 293.15 K, [TBAB: DEG] attained the highest viscosity with a value of 203.9 cP and the lowest conductivity with a value of 325 $\mu\text{s}\cdot\text{cm}^{-1}$. Both surface tension and density data decreased with the increase of temperature and their temperature trends were fitted linearly. By contrast, the temperature trends for the conductivity and viscosity were exponential growth and exponential decay, respectively, and both of the trends were successfully fitted to Arrhenius-like model. The freezing points of all considered DESs series were below 323.15 K, and compatible with the general definition of DES. The FTIR analysis revealed the existence of P–H bonds in the structure of phosphonium salts based DESs, and the presence of N–H in the structure of ammonium based salts DESs. The physical properties of DEG based DESs were found to be similar to those of some reported ILs. The variation in the temperature, and/or the DESs individual components, and/or the ratio of salt to HBD are of a considerable concern to obtain a eutectic mixture with adaptable physical characterizations to a specific type of application, which consequently contributes in widening the horizon of DESs employment as ILs alternatives.

EXPERIMENTAL

N,N-diethylethanolammonium chloride (DAC), tetra-n-butylammonium bromide (TBAB), methyltriphenylphosphonium bromide (MTPB), benzyltriphenylphosphonium chloride (BTPC), and diethylene glycol (DEG) were all supplied by Merck, while choline chloride (ChCl) was supplied by sigma Aldrich. All chemicals were supplied with purity ($\geq 98.0\%$) except ChCl and TBAB their purity was ($\geq 99.0\%$). The chemicals were dried in a vacuum oven for 3 h before conducting any experiments to prevent the adverse effects of moisture content on the physical properties measurements. Figure 6 displays the chemical structure and molecular formula of the chemicals used in this work.

The optimum DES composition ratio, at which DES is homogeneous and stable, was determined by carrying out an incipient screening where different ratios of salt to HBD were stirred at 180 rpm and 343.15 K for 120 min. The five selected DESs along with their relevant optimum ratios are listed in Table 1 were prepared at atmospheric pressure in moisture controlled environment followed by measurements of their physical properties as function of temperature in the range 293.15-353.15 K.

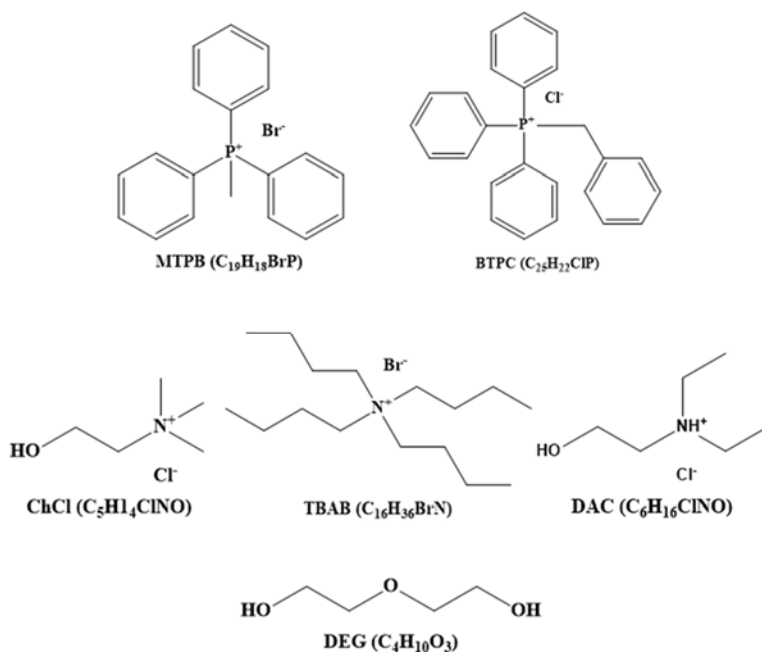


Figure 6. The chemical structure and molecular formula of DESs components

The functional groups were identified using spectrum 400 FT-IR spectrometer. Freezing points of the five selected DESs were measured using differential scanning calorimetry (DSC) METTLER TOLEDO, Figures 6S to 10S. A density meter (DM 40) METTLER TOLEDO, a Brookfield R/S Rheometer and an automated tensiometer Krüs K10ST classification B with Du Noüy ring method were utilized to determine densities, viscosities and surface tensions correspondingly. The conductivity of selected DESs was measured using Eutech Cyberscan Con 11 hand-held meter and the variation in the temperature range was controlled using an external water circulator (Techne-Tempette TE-8A). The standard uncertainties in measurements of each studied physical property are listed in Table 9.

Table 9. Standard uncertainties of measurements.

Measurements	Estimated uncertainties
Density ($\text{g}\cdot\text{cm}^{-3}$)	± 0.0001
Viscosity (cP)	(3-5) %
Surface tension (mN m^{-1})	± 0.1
Conductivity ($\mu\text{s}/\text{cm}$)	± 18
Freezing point (K)	± 0.01

ACKNOWLEDGMENTS

The author would like to acknowledge financial support from the UMRP grant RP019C-13AET for research assistantship (RKI) and materials. University of Malaya HIR-MOHE (D000003-16001) is also acknowledged for use of analytical instruments.

REFERENCES

1. Patel, D.D. and J.M. Lee, *The Chemical Record*, **2012**, 12, 329.
2. Paiva, A., R. Craveiro, I. Aroso, M. Martins, R.L. Reis, and A.R.C. Duarte, *ACS Sustainable Chemistry & Engineering*, **2014**, 2, 1063.
3. Hou, Y., Y. Gu, S. Zhang, F. Yang, H. Ding, and Y. Shan, *Journal of Molecular Liquids*, **2008**, 143, 154.

4. Dai, Y., J. van Spronsen, G.-J. Witkamp, R. Verpoorte, and Y.H. Choi, *Analytica chimica acta*, **2013**, 766, 61.
5. Lee, Y.R. and K.H. Row, *Journal of Industrial and Engineering Chemistry*, **2016**.
6. Durand, E., J. Lecomte, and P. Villeneuve, *European Journal of Lipid Science and Technology*, **2013**, 115, 379.
7. Tang, B. and K.H. Row, *Monatshefte für Chemie-Chemical Monthly*, **2013**, 144, 1427.
8. Pena-Pereira, F. and J. Namieśnik, *ChemSusChem*, **2014**, 7, 1784.
9. Carriazo, D., M.C. Serrano, M.C. Gutiérrez, M.L. Ferrer, and F. del Monte, *Chemical Society Reviews*, **2012**, 41, 4996.
10. Hayyan, M., M.A. Hashim, M.A. Al-Saadi, A. Hayyan, I.M. AlNashef, and M.E. Mirghani, *Chemosphere*, **2013**, 93, 455.
11. Hayyan, M., M.A. Hashim, A. Hayyan, M.A. Al-Saadi, I.M. AlNashef, M.E. Mirghani, and O.K. Saheed, *Chemosphere*, **2013**, 90, 2193.
12. Maugeri, Z. and P.D. de María, *Green Chem*, **2011**, 13, 82.
13. Hayyan, M., C.Y. Looi, A. Hayyan, W.F. Wong, and M.A. Hashim, *PLoS one*, **2015**, 10, e0117934.
14. Abbott, A.P., G. Frisch, J. Hartley, and K.S. Ryder, *Green Chemistry*, **2011**, 13, 471.
15. Abbott, A.P., D. Boothby, G. Capper, D.L. Davies, and R.K. Rasheed, *Journal of the American Chemical Society*, **2004**, 126, 9142.
16. Yang, D., M. Hou, H. Ning, J. Zhang, J. Ma, G. Yang, and B. Han, *Green Chemistry*, **2013**, 15, 2261.
17. Li, X., M. Hou, B. Han, X. Wang, and L. Zou, *Journal of Chemical & Engineering Data*, **2008**, 53, 548.
18. Su, W.C., D.S.H. Wong, and M.H. Li, *Journal of Chemical & Engineering Data*, **2009**, 54, 1951.
19. Morrison, H.G., C.C. Sun, and S. Neervannan, *International journal of pharmaceuticals*, **2009**, 378, 136.
20. Hayyan, M., F.S. Mjalli, M.A. Hashim, and I.M. AlNashef, *Fuel Processing Technology*, **2010**, 91, 116.
21. Abbott, A.P., G. Capper, K.J. McKenzie, and K.S. Ryder, *Journal of Electroanalytical Chemistry*, **2007**, 599, 288.
22. Guo, Z. and X. Lin, *Journal of Electroanalytical Chemistry*, **2005**, 576, 95.
23. Shahbaz, K., F. Mjalli, M. Hashim, and I. AlNashef, *Thermochimica acta*, **2011**, 515, 67.
24. Shahbaz, K., F. Mjalli, M. Hashim, and I. AlNashef, *Fluid phase equilibria*, **2012**, 319, 48.
25. Yadav, A., S. Trivedi, R. Rai, and S. Pandey, *Fluid Phase Equilibria*, **2014**, 367, 135.
26. Manfra, L., A. Tornambè, F. Savorelli, A. Rotini, S. Canepa, M. Mannozi, and A. Cicero, *Journal of hazardous materials*, **2015**, 284, 130.
27. Marruffa J.M., Diethylene Glycol, in: Wexler P., eds., *Encyclopedia of Toxicology* (Third Edition), Academic Press, Oxford, **2014**, 140.

28. Abbott A.P., Boothby D., Capper G., Davies D.L., Rasheed R.K., *J. Am. Chemical Society*, **2004**, 126, 9142.
29. Liu, Y.-T., Y.-A. Chen, and Y.-J. Xing, *Chinese Chemical Letters*, **2014**, 25, 104.
30. Zhang, Q., K.D.O. Vigier, S. Royer, and F. Jérôme, *Chemical Society Reviews*, **2012**, 41, 7108.
31. Stuart, B., *Infrared spectroscopy*. **2005**: Wiley Online Library.
32. Coates, J., *Encyclopedia of analytical chemistry*, **2000**.
33. Roeges, N.P., *A guide to the complete interpretation of infrared spectra of organic structures*. **1994**: Wiley.
34. Smith, B., *Boca Raton*, **1999**.
35. Hayyan, M., T. Aissaoui, M.A. Hashim, M.A. AlSaadi, and A. Hayyan, *Journal of the Taiwan Institute of Chemical Engineers*, **2015**, 50, 24.
36. Luo, J., O. Conrad, and I.F. Vankelecom, *Journal of Materials Chemistry*, **2012**, 22, 20574.
37. Abbott, A.P., R.C. Harris, K.S. Ryder, C. D'Agostino, L.F. Gladden, and M.D. Mantle, *Green Chemistry*, **2011**, 13, 82.
38. Shahbaz, K., S. Baroutian, F. Mjalli, M. Hashim, and I. AlNashef, *Thermochimica Acta*, **2012**, 527, 59.
39. Abbott, A.P., G. Capper, D.L. Davies, R.K. Rasheed, and V. Tambyrajah, *Chemical Communications*, **2003**, 70.
40. Abbott, A.P., G. Capper, and S. Gray, *ChemPhysChem*, **2006**, 7, 803.
41. Abbott, A.P., J.C. Barron, K.S. Ryder, and D. Wilson, *Chemistry—A European Journal*, **2007**, 13, 6495.
42. Kareem, M.A., F.S. Mjalli, M.A. Hashim, and I.M. AlNashef, *Journal of Chemical & Engineering Data*, **2010**, 55, 4632.
43. Shahbaz, K., F. Mjalli, M. Hashim, and I. AlNashef, *Energy & Fuels*, **2011**, 25, 2671.
44. Williams, J.D., W. Svrcek, and W. Monnery, *Developments in Chemical Engineering and Mineral Processing*, **2003**, 11, 267.
45. Mjalli, F.S., J. Naser, B. Jibril, V. Alizadeh, and Z. Gano, *Journal of Chemical & Engineering Data*, **2014**, 59, 2242.
46. Abo-Hamad, A., M. Hayyan, M.A. AlSaadi, and M.A. Hashim, *Chemical Engineering Journal*, **2015**, 273, 551.
47. Abbott, A.P., G. Capper, D.L. Davies, and R. Rasheed, *Inorganic chemistry*, **2004**, 43, 3447.
48. AlOmar, M.K., M. Hayyan, M.A. Alsaadi, S. Akib, A. Hayyan, and M.A. Hashim, *Journal of Molecular Liquids*, **2016**, 215, 98.
49. Bahadori, L., M.H. Chakrabarti, F.S. Mjalli, I.M. AlNashef, N.S.A. Manan, and M.A. Hashim, *Electrochimica Acta*, **2013**, 113, 205.
50. Abbott, A.P., R.C. Harris, and K.S. Ryder, *The Journal of Physical Chemistry B*, **2007**, 111, 4910.
51. Giap, S.G.E., *Journal of Physical Science*, **2010**, 21, 29.
52. Vila, J., P. Gines, J. Pico, C. Franjo, E. Jimenez, L. Varela, and O. Cabeza, *Fluid Phase Equilibria*, **2006**, 242, 141.

53. Gan, Q., D. Rooney, M. Xue, G. Thompson, and Y. Zou, *Journal of Membrane Science*, **2006**, 280, 948.
54. Zhou, Z.B., H. Matsumoto, and K. Tatsumi, *Chemistry—A European Journal*, **2004**, 10, 6581.
55. Nishida, T., Y. Tashiro, and M. Yamamoto, *Journal of Fluorine Chemistry*, **2003**, 120, 135.
56. Huddleston, J.G., A.E. Visser, W.M. Reichert, H.D. Willauer, G.A. Broker, and R.D. Rogers, *Green chemistry*, **2001**, 3, 156.
57. Zhao, D., Z. Fei, C.A. Ohlin, G. Laurenczy, and P.J. Dyson, *Chemical communications*, **2004**, 2500.
58. Berthod, A., M. Ruiz-Angel, and S. Carda-Broch, *Journal of Chromatography A*, **2008**, 1184, 6.
59. Greaves, T.L., A. Weerawardena, C. Fong, I. Krodkiewska, and C.J. Drummond, *The Journal of Physical Chemistry B*, **2006**, 110, 22479.
60. Greaves T.L., Weerawardena A., Fong C., Drummond C.J., *Langmuir*, **2007**, 23, 402.
61. Kulkarni, P.S., L.C. Branco, J.G. Crespo, M.C. Nunes, A. Raymundo, and C.A. Afonso, *Chemistry—A European Journal*, **2007**, 13, 8478.
62. Yoshida, Y., K. Muroi, A. Otsuka, G. Saito, M. Takahashi, and T. Yoko, *Inorganic chemistry*, **2004**, 43, 1458.
63. Zhou, Z.B., H. Matsumoto, and K. Tatsumi, *ChemPhysChem*, **2005**, 6, 1324.
64. Mateus, N.M., L.C. Branco, N.M. Lourenço, and C.A. Afonso, *Green Chemistry*, **2003**, 5, 347.
65. Branco, L.C., J.N. Rosa, J.J. Moura Ramos, and C.A. Afonso, *Chemistry—A European Journal*, **2002**, 8, 3671.
66. Gupta, O.D., B. Twamley, and M.S. Jean'ne, *Tetrahedron letters*, **2004**, 45, 1733.
67. Zhou, Z.-B., H. Matsumoto, and K. Tatsumi, *Chemistry Letters*, **2004**, 33, 886.

DETERMINATION OF HLB VALUES OF SOME NONIONIC SURFACTANTS AND THEIR MIXTURES

RÉKA KOTHENCZ^{a*}, ROLAND NAGY^a, LÁSZLÓ BARTHA^a

ABSTRACT. Advanced analytical and impact assessment methods are needed for the development of modern surfactants, so the composition, the effect and other properties of surfactants are examined by analytical tools which may be suitable for the quality testing of the raw materials, the intermediates and the final products. The HLB values of non-ionic surfactants and their mixtures were determined by three different methods: theoretical HLB based on the chemical structure and the given HLB of surfactants, the Greenwald method and an improved, titrimetric method. Our aim was to investigate if the new method to determine the water number and HLB value is suitable for this type of commercial surfactants and their mixtures. The particle size and the turbidity of micelles formed in surfactant solutions were also measured and evaluated.

Keywords: *surfactant, surfactant mixtures, theoretical HLB value, experimental HLB value*

INTRODUCTION

Surfactants in science and industry are widely used, ranging from primary production processes such as the recovery and purification of raw materials in the mining and petroleum industries, to enhancing the quality of finished products such as paints, cosmetics, pharmaceuticals, and foods. Polyethoxylated ester (POE) non-ionics, such as Tween product family, are generally excellent dispersing agents [1]. Sodium dodecylbenzenesulfonate (SDBS) is an anionic surfactant which is the major component of laundry detergents [2].

^a *University of Pannonia, Institutional Department of MOL Hydrocarbon and Coal Processing, 10 Egyetem str., HU-8200, Veszprém, Hungary*

* *Corresponding author: kothenczr@almos.uni-pannon.hu*

The capacity of the emulsification, the solubility and other surfactant properties depend on the HLB value of a given non-ionic surfactant which information is necessary for its practical application. The HLB (hydrophilic-lipophilic balance) concept was introduced by Griffin [3]. The HLB of an emulsifier is a number which expresses the mass ratio of water-soluble and oil-soluble groups in the surfactant molecule. The HLB value can be a critical factor in the development of new emulsions and in surfactant synthesis. The number of experiments can be reduced during the formulation screening stage and can be used as an important parameter for quality control [4].

The present work aimed to investigate if the new method to determine the water number and HLB value is suitable for this type of commercial surfactants and their mixtures. The difference between the HLB values determined by different methods was examined, the particle size and the turbidity of their aqueous solution was also investigated.

RESULTS AND DISCUSSION

Investigation of non-ionic surfactants

The HLB of POE surfactants was determined by conventional analytical method (Greenwald et al) [6] and by our improved method then it was compared with the HLB given by the manufacturer (Table 1, Figure 1). No information was provided about the HLB measurement method of the manufacturer.

Table1. The HLB values of Tween non-ionic surfactants

Product name	HLB (given by manufacturer)	HLB (Greenwald)	HLB (improved method)
Tween 20	16.7	20.4	16.0
Tween 40	15.6	18.9	16.0
Tween 60	14.9	16.1	14.7
Tween 80	15.0	16.6	14.4
Tween 85	11.0	14.9	10.6

The HLB values determined by our new developed method approximates better the given HLB values, than the HLB values of Greenwald method [7].

The hydrodynamic size of each surfactant was determined by dynamic light scattering method and the turbidity by fiber-optic spectrophotometer (Table 2).

The average size of the surfactant micelles was between 11.4 nm and 90.4 nm. It can be explained by the different micelle formation because of the diverse structure of surfactants.

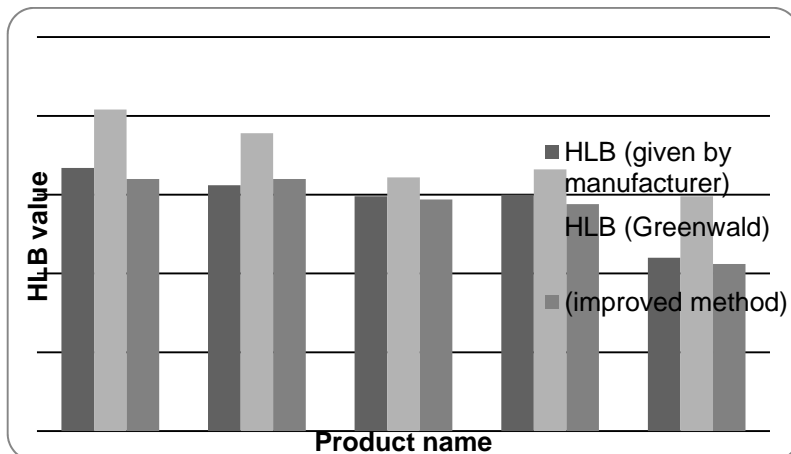


Figure 1. Difference between the HLB values determined by different methods

Table 2. Hydrodynamic size and turbidity of POE and SDBS surfactant solutions

Product name	Hydrodynamic size (nm)	Turbidity (%)
Tween 20	44.3	62
Tween 40	61.4	58
Tween 60	56.2	52
Tween 80	11.4	7
Tween 85	90.4	77

Investigation of surfactant mixtures

The surfactants are usually applied as surfactant mixtures [10] thus our aim was to determine their HLB value by our improved, titrimetric method described in the previous chapter.

No experimental results were published about the determination of HLB values of surfactant mixtures by Greenwald et al [11].

The HLB of surfactant mixtures was determined as follows (Table 3):

- weighted regarding the mixing ration (50 w/w% anionic, 50 w/w% non-ionic surfactant), the following HLB values were considered for the calculation [12, 13]:

- anionic surfactant: HLB calculated by the chemical structure,
- non-ionic surfactant: HLB given by the manufacturer.
- conventional analytical method (Greenwald method),
- the improved method.

The HLB value of SDBS was 19.9 and it was calculated based on its chemical structure.

Table 3. The HLB values of surfactant mixtures

Surfactant mixture	HLB (theoretical)	HLB (Greenwald)	HLB (improved method)
T-1	18.25	19.70	18.25
T-2	17.70	19.20	17.58
T-3	17.35	19.10	17.41
T-4	17.40	19.30	18.00
T-5	15.40	16.90	15.20

It was found that our improved method is suitable to determine also the HLB of this type of surfactant mixtures.

The difference between HLB values determined by different methods is shown in Figure 2.

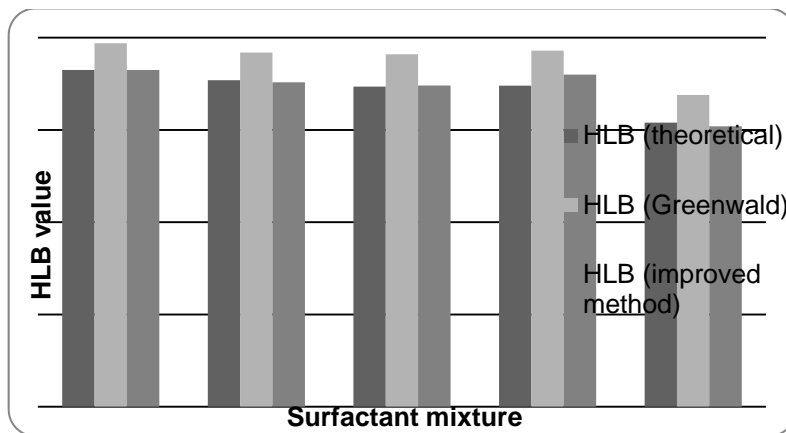


Figure 2. The difference between HLB values of surfactant mixtures determined by different methods

The HLB measured by our improved method approximates better the calculated theoretical HLB based on the chemical structure. Adding SDBS to the surfactant mixtures has resulted higher HLB values, thus the solubility in water has increased.

The average size of the surfactant micelles was between 123 nm and 910 nm and the turbidity was between 7-57%. The higher HLB value of surfactant mixtures has shown lower turbidity. However based on the measured particle size it was obtained that the formed micelles are bigger which require more detailed structural analysis.

Table 4. The particle size of the micelles and the turbidity of surfactant mixture solutions

Surfactant mixture	Particle size (nm)	Turbidity (%)
T-1	384	52
T-2	624	48
T-3	684	53
T-4	910	7
T-5	123	57

No correlation was found between the HLB value and the average particle size. The HLB value of the surfactant mixture can provide information about the hydrophilic or lipophilic nature but not about the ability of association or the colloidal properties of the surfactant mixture. Thus the HLB can be applied for the classification of surfactants which is important in terms of use.

CONCLUSIONS

The HLB values of non-ionic surfactants and their mixtures, the turbidity of their aqueous solution and the average size of micelles formed in aqueous solution of non-ionic surfactants and their mixtures were analyzed. The new experimental results can be summarized as follows.

- Based on the experimental data a more accurate method was developed for the determination of HLB which is applicable to POE type non-ionic surfactants.
- The improved method is suitable for the determination of HLB of this type of surfactant mixtures.
- In both case (nonionic and anionic surfactant alone or in their mixtures) the HLB value determined by our method approximates better the HLB value calculated by chemical structure.
- The particle size of surfactant association of the components not depends on the HLB value, but depends on the structure of surfactants. Further developments could contribute significantly to the formulation of the surfactant mixtures.

EXPERIMENTAL

Materials

Polyethoxylated sorbitan esters, environmentally friendly non-ionic surfactant family marketed under the Tween product name were used in the measurements. A polyethoxylated monoester of 3,6-sorbitan is represented in figure 3. POEs are hydrophilic in nature and are soluble or dispersible in water and dilute solutions of electrolytes [5]. The chemical identity of Tween products is shown in Table1.

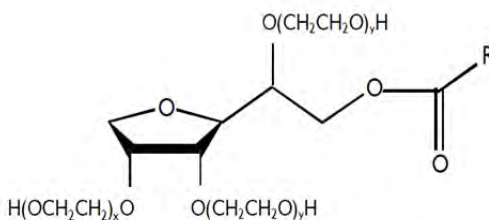


Figure 3. Chemical structure of a polyethoxylated monoester (R: alkyl group of fatty acid where (x+y) is the total number of moles of ethylene oxide)

Table 5. Chemical identity of Tween products

Product name	Chemical identity
Tween 20	PEG-20 sorbitan monolaurate
Tween 40	PEG-20 sorbitan monopalmitate
Tween 60	PEG-20 sorbitan monostearate
Tween 80	PEG-20 sorbitan monooleate
Tween 85	PEG-20 sorbitan trioleate

Sodium dodecylbenzenesulfonate (SDBS) is a member of the linear alkylbenzenesulfonates, the dodecyl group is unbranched. This dodecyl chain is attached at the 4-position of the benzenesulfonate group.

The composition of the surfactant mixtures is shown in Table 6. The mixtures contained 50 w/w% of non-ionic and 50 w/w% of anionic surfactants.

For preparing the surfactant solutions, the surfactants were dissolved in distilled water in 1 w/w% of total concentration.

Methods

Water Number and HLB determination

The method developed by Greenwald, Brown and Fineman [6] is suitable to determine the hydrophilic-lipophilic nature of the surfactants. It can provide information about the possible effectiveness of the emulsifiers.

Table 6. The composition of the surfactant mixtures

Surfactant mixture	Non-ionic surfactant component	Anionic surfactant component
T-1	Tween 20	SDBS
T-2	Tween 40	SDBS
T-3	Tween 60	SDBS
T-4	Tween 80	SDBS
T-5	Tween 85	SDBS

The surfactant is dissolved in benzene-dioxane mixture and the solution is titrated with distilled water until its permanent turbidity according to Greenwald et al [6]. Our method was developed to avoid the use of the highly toxic benzene. In our new process of sample preparation the test materials are dissolved in the mixture of cyclohexane-dioxane (with 4% cyclohexane content). The distilled water is added to the solution of surfactant until it becomes permanently cloudy and the transmittance cannot be decreased radically by the further addition of water. The transmittance is measured by fiber-optic spectrophotometer. The current transmittance values are represented as a function of distilled water volumes. The equivalence point of the obtained curve is the volume which corresponds to the Water Number (WN) of the surfactant [6]. The HLB value can be calculated from the Water Number, the equation of the improved method was created by linear regression.

Equation 1 can be applicable for non-ionic surfactants [7] and Equation 2 for surfactant mixtures [8].

$$HLB = \frac{WN}{0.6524} - 0.6339 \quad (1)$$

$$HLB = \frac{WN}{1.206} - 10.5 \quad (2)$$

Solubility in water

1 w/w% of surfactant is dissolved in distilled water. The turbidity is measured by spectrophotometer. The solubility in water is characterized by the transmittance (T) value (0% completely cloudy, 100% transparent). The turbidity of the diluted surfactants was calculated as [9]:

$$\text{Turbidity} = 100 - T(\%) \quad (3)$$

Particle size analysis

The average particle size and the distribution of the surfactants were measured by dynamic light scattering using Malvern Zetasizer Nano ZS instrument. The hydrodynamic radius determined by photon correlation spectroscopy (i. e. dynamic light scattering) and is estimated from the particles' diffusivity using the Stokes–Einstein relationship (Equation 4). The peak values of particle diameter (nm) for the different samples were obtained as an average of the data. In this work particle size means the size of surfactant associations formed in the aqueous solution.

$$D_0 = \frac{kT}{3\pi\eta d} \quad (4)$$

where:

- D₀ : diffusion coefficient
- k: Boltzmann constant
- T: temperature
- η: dynamic viscosity
- d: particle diameter

REFERENCES

1. M.J. Rosen, J.T. Kunjappu, „Surfactants and interfacial phenomena”, John Wiley and Sons, **2012**, chapter 1.
2. D. Myers, „Surfactant science and technology”, Wiley-Interscience, **2006**, chapter 2.
3. C.W. Griffin, *Journal of the Society of Cosmetic Chemists*, **1949**, 1(5), 311.
4. C.P. Fernandes, M.P. Mascarenhas, F.M. Zibetti, B.G. Lima, R.P.R.F. Oliveira, L. Rocha, D.Q Falcao, *Revista Brasileira de Farmacognosia* **2013**, 23(1), 108.
5. „The HLB SYSTEM, a time-saving guide to emulsifier selection”, ICI Americas Inc., **1994**.
6. P. Becher, “Emulsions: Theory and Practice”, Reinhold Publishing Corp., **1965**, chapter 6.
7. R. Kothencz, R. Nagy, L. Bartha, *Nano, Bio and Green- Technologies for a Sustainable Future*, 16th International Multidisciplinary Scientific Geoconference SGEM, **2016**, 6(3), 45.
8. R. Nagy, R. Kothencz, L. Bartha, *XXII. International Conference on Chemistry*, Timisoara, Romania, **2016**, 102.
9. R. Nagy, R. Kothencz, R. Sallai, L. Bartha, *International Journal of Scientific and Engineering Research*, **2015**, 6(3), 580.
10. S.P. Current, *US5110487*, **1992**.
11. X. Guo, Z. Rong, X. Ying, *Journal of Colloid and Interface Science*, **2006**, 298, 441.
12. “HLB & Emulsification, Description of Hydrophile, Lipophile Balance and use of HLB in Producing Emulsions”, Akzo Nobel Surface Chemistry LLC, **2008**.
13. R.C. Pasquali, M.P. Taurozzi, C. Bregni, *International Journal of Pharmaceutics*, **2008**, 356, 44.

AN EXPERIMENTAL AND MODELING INVESTIGATION ON DRYING OF CHICKEN MEAT IN CONVECTIVE DRYER

OSMAN ISMAIL^a

ABSTRACT. This work reported a theoretical and experimental study on the thin layer drying kinetics of chicken meat samples under different air drying conditions. Experimental drying curves of chicken meat were performed under different drying air conditions (three air temperatures: 40, 50 and 60 °C, air velocities: 1 ms⁻¹, and at atmosphere humidity). The drying rate was found to increase significantly with increase in temperature. The duration of constant rate period was found to be insignificant considering the total duration of drying and the entire drying period was considered to follow falling rate period. The experimental moisture ratio data was fitted to eight thin layer drying models. The Midilli et al. model showed the best fit in all drying conditions. The effective moisture diffusivity has been found to be varying between 4.39 x 10⁻¹⁰ and 9.96 x 10⁻¹⁰ m²s⁻¹ and activation energy was 27.85 kJ mol⁻¹.

Keywords: *Chicken meat, mathematical modeling, diffusion, activation energy*

INTRODUCTION

Increasing life standards impose people to change their eating habits and promote them to consume. With population growth and increasing income, the consumption of meat is expected to grow by 73% by 2050 [1]. U.S. Department of Agriculture (USDA) statistical data showed that the production of chicken meat world-wide is about 84 million tons; the major producer countries are USA, China, Brazil, European union etc. and Turkey. Turkey produced 1.7 million tons in 2013 [2]. From a nutritional perspective, chicken consists of high-quality protein (that is, protein that contains the eight essential amino acids), low in cholesterol and a relatively

^{a*} *Yildiz Technical University, Davutpasa Campus, Faculty of Chemical and Metallurgical Engineering, Department of Chemical Engineering, Davutpasa , 34210 Esenler, Istanbul, Turkey. E-mail: ismail@yildiz.edu.tr*

low amount of fat. Thus, chicken is often recommended by physicians and nutrition counselors as an alternative to red meat [3].

It is seen that the amount of meat production and consumption is associated with a special occasion and meat is consumed in large quantity for a limited period. The excess meat should be preserved for future consumption. A major problem associated with traditional or sun drying of meat is the infestation of the product by the fly and insect larvae during drying and storage and products are deteriorated before consumption. Recently some drying techniques have been developed to prevent this. One of these techniques is the convection drying method. Hot air drying is widely used for centuries to preserve food products and it allows their availability regardless the season of the year [4].

Drying is one of the oldest food preservation methods for decreasing available water in food materials and increasing shelf life of foods. In other words, drying of meat or any food material reduces the availability of water in meat and thus also water activity to a level where microbes cannot survive and thus meat is preserved. Moreover, volume and weight of the product decreases significantly resulting in lower costs and making easy the transport and the storage of the dried products comparing to the fresh ones [5] This process involves simultaneous heat and mass transfer, however due to the complexity of this process, some researchers developed semi-theoretical and empirical models derived from Fickian diffusion approach to explain the water movement within the solid food materials [6]. The semi-theoretical and empirical models have been applied and found best at describing the drying process and predicting the drying kinetics of numerous agricultural foods. Thin layer convective hot air drying technique enables the effective control and uniform distribution of drying air and temperature conditions over the material, thereby improving the overall quality of the final product. Decreasing the relative humidity and increasing the drying temperature is a potential way of shortening the process of producing dry cured meat products [7] and has been successfully applied to shorten the drying period of raw and cooked chicken meats [8].

Knowledge of the drying kinetics is essential for a good modeling of the drying process. Some studies have been conducted on the drying kinetics of chicken meat [7-9] which have mainly covered the effect of the drying air parameters and the modeling of this kinetics.

The objectives of this study, is to determine the drying mechanism of chicken meat with increasing drying temperature. Also thin layer drying modeling of the drying process to predict and simulate the drying behavior of chicken meat has been studied. For this purpose, eight different thin layer drying models were fitted to experimental drying data and applicability

of the models was compared according to statistical parameters. In addition, the diffusion coefficient and the activation energy of the samples were also calculated.

RESULT AND DISCUSSION

Chemical composition of fresh chicken meat samples

Initial moisture content, protein, fat and ash were determined using the method of AOAC [10]. The initial moisture content, ash, protein and fat percentage of fresh chicken meat samples are shown in Table 1.

Table 1. Composition of the fresh chicken samples

Moisture content	Protein	Fat	Ash
73.96 ± 0.04	22.38 ± 0.16	2.39 ± 0.15	1.22 ± 0.04

The initial moisture content and dry matter were 73.96% and 26.04% respectively. As seen from the table, protein is the major component of chicken samples other than water. The protein, fat and ash content of chicken samples was 22.38%, 2.39% and 1.22%, respectively. Our findings are consistent with the literature in which it was reported that chicken meat tissue consists of approximately 74.71% water, 25.29% dry matter, 21.86% protein, 1.75% fat and 1.13% ash [11].

Drying curves

Drying rates (*DR*) were determined by using the forward finite difference method according to Equation 1 [8].

$$DR = \frac{M_{t+\Delta t} - M_t}{\Delta t} \quad (1)$$

where: $M_{t+\Delta t}$ is the moisture content of samples at $t + \Delta t$ ($g_{\text{water}}/g_{\text{dry matter}}$), t is the time (min).

Drying rate is defined as the amount of water removed and time is shown in Figure 1 for chicken samples during thin layer drying at 40, 50 and 60 °C.

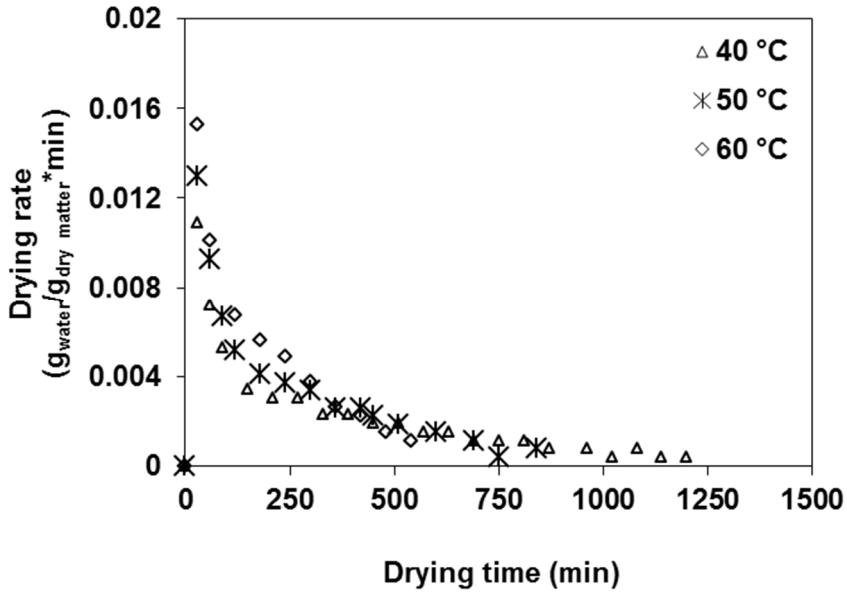


Figure 1. Variation of drying rate with drying time of chicken meat samples at different temperatures

Modelling of the thin-layer drying characteristics

The experimental drying data resulting from hot-air drying of chicken samples at different temperatures were fitted to eight different thin-layer drying models shown in Table 2.

Table 2. Mathematical models for drying curves

Model Name	Equation	Reference
Newton	$MR = \exp(-kt)$	[14]
Page	$MR = \exp(-kt^n)$	[14]
Henderson and Pabis	$MR = a \exp(-kt)$	[15]
Logarithmic	$MR = a \exp(-kt) + b$	[11]
Aghbashlo et al.	$MR = \exp((-k_1t)/(1+k_2t))$	[16]
Wang and Singh	$MR = 1 + bt + at^2$	[11]
Midilli et al.	$MR = a \exp(-kt^n) + bt$	[17]
Alibas	$MR = a \exp((-kt^n) + bt) + g$	[18]

The moisture content of a drying sample at any time t can be expressed as moisture ratio (MR) as follows:

$$MR = \frac{M_t - M_e}{M_o - M_e} \quad (2)$$

where: M_t , M_e and M_o are the moisture content at selected time, at equilibrium and the initial value in $g_{water}/g_{dry\ matter}$.

The obtained drying data was evaluated using nonlinear least squares regression analysis. The regression analysis was performed using the 6.0 program software (Statsoft Inc., Tulsa, OK) computer program. The correlation coefficient (R^2), reduced chi-square (χ^2) and root mean square error ($RMSE$) were used as the primary criteria for selection of the best model to define the drying curves [19]. These statistical values can be determined using the following equations:

$$RMSE = \left[\frac{1}{N} \sum_{i=1}^N (MR_{pre,i} - MR_{exp,i})^2 \right]^{1/2} \quad (3)$$

$$\chi^2 = \frac{\sum_{i=1}^N (MR_{exp,i} - MR_{pre,i})^2}{N - z} \quad (4)$$

where MR_{exp} and MR_{pre} represent experimental and predicted values of moisture ratios, respectively. N is the total number of experiments, and z is the number of constants in the drying model. The best model was selected with based on the highest R^2 and the lowest χ^2 , and the lowest $RMSE$ values. The curve fitting criteria or statistical calculation results for these models are shown in Table 3.

As seen from the tables, R^2 values higher than 0.98 indicating a good fit since R^2 value close to unity implies that the predicted drying data is close to the experimental drying data. This means that all established models successfully described the relation between time and MR . Another statistical parameters calculated to compare the model's accuracy were χ^2 and $RMSE$ values, which represent the differences between the predicted and experimental values. Therefore, the fact that χ^2 and $RMSE$ values are close to zero is desired. Among the thin-layer drying models, the Midilli et al. model was found to represent the drying kinetics of chicken samples with high R^2 values and low χ^2 and $RMSE$ values for all temperatures. It is clear that the R^2 , χ^2 and $RMSE$ values of this model were changed between 0.9992 and 0.9998, 0.000019 and 0.000121, 0.004006 and 0.010466, respectively. Variation of experimental

and predicted moisture ratio by Midilli et al. model with drying time are shown in Figure 2. As can be observed in this figure, good agreement between the former variables is observed.

Table 3. Curve fitting criteria for the thin layer drying models for drying of chicken meat samples

Models	Drying temperature (°C)	R^2	χ^2	RMSE
Newton	40	0.9987	0.000178	0.013191
	50	0.9957	0.000596	0.023992
	60	0.9954	0.000670	0.02519
Page	40	0.9988	0.000171	0.012762
	50	0.9961	0.000549	0.022634
	60	0.9972	0.000428	0.019563
Henderson and Pabis	40	0.9991	0.000128	0.011064
	50	0.9967	0.000460	0.020721
	60	0.9971	0.000438	0.019798
Logarithmic	40	0.9992	0.000128	0.010479
	50	0.9980	0.000445	0.020012
	60	0.9973	0.000443	0.019304
Aghbashlo et al.	40	0.9987	0.000182	0.013179
	50	0.9957	0.000615	0.02395
	60	0.9963	0.000573	0.022636
Wang and Singh	40	0.9904	0.001368	0.036114
	50	0.9872	0.001816	0.041147
	60	0.9834	0.002547	0.047728
Midilli et al.	40	0.9992	0.000121	0.010466
	50	0.9998	0.000019	0.004006
	60	0.9997	0.000041	0.005680
Alibas	40	0.9992	0.000124	0.010468
	50	0.9998	0.000024	0.004539
	60	0.9996	0.000073	0.007322

As seen in Figure 2, chicken meat drying curves were obtained using a convective tray drier at different temperatures of 50, 60 and 70 °C requiring of 1260, 870 and 540 min, respectively, to reach dry basis moisture content of about 14%.

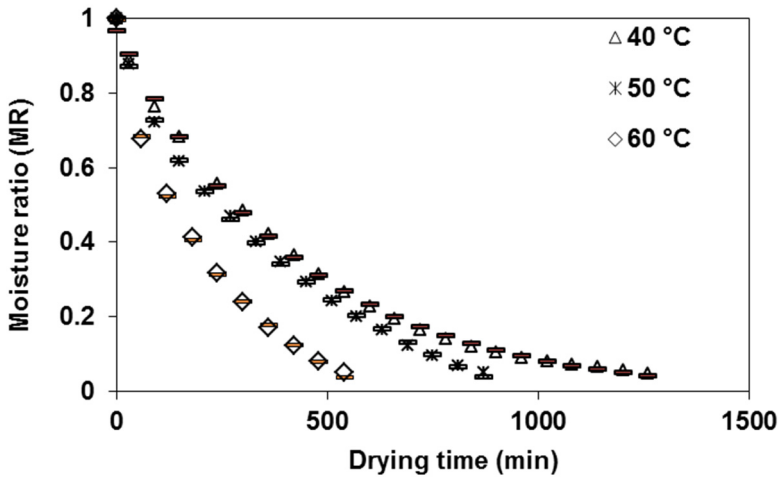


Figure 2. Variation of experimental and predicted moisture ratio by Midilli et al. model with drying time at different drying temperatures

Determination of the effective moisture diffusivity and activation energy

Effective moisture diffusivity (D_{eff}) was determined according to the general solution of Fick's second law equation for slab geometry (where L half thickness) in Equation 5 and only the first term of the equation was used [20].

$$MR = \frac{M_t - M_e}{M_0 - M_e} = \frac{8}{\pi^2} \exp\left[-\frac{\pi^2 D_{eff} t}{4L^2}\right] \quad (5)$$

where, D_{eff} is the effective moisture diffusivity (m^2/s) and L is the half thickness of chicken samples (m).

The variation in $\ln(MR)$ and drying time (t) at different temperatures have been plotted to obtain the slope Equation 5 which can give the effective moisture diffusivity.

$$S = \frac{\pi^2 D_{eff}}{4L^2} \quad (6)$$

By the help of the slope Equation 6, effective moisture diffusivity of chicken meat samples were calculated and shown in Table 4.

Table 4. Effective moisture diffusivity values for chicken meat samples at different temperatures

Drying Temperature (°C)	Effective moisture diffusivity (m ² /s)
40	4.39 x 10 ⁻¹⁰
50	6.08 x 10 ⁻¹⁰
60	9.96 x 10 ⁻¹⁰

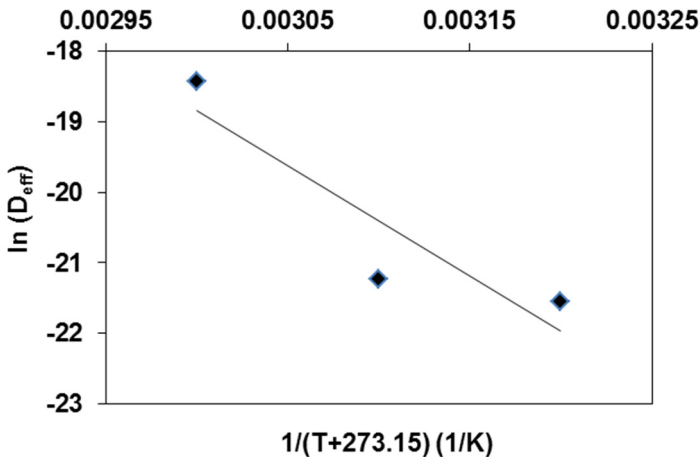
As seen in Table 4, it was observed that D_{eff} values increased with increasing air temperature. This phenomenon might be due to the fact that effective moisture diffusivity (D_{eff}) depends on the drying air temperature, cultivar, and composition of the drying samples [21]. The effective moisture diffusivity of chicken samples was 4.39×10^{-10} , 6.08×10^{-10} and 9.96×10^{-10} m²/s at 40, 50 and 60 °C, respectively. D_{eff} values for different food and agricultural products usually varied between 10^{-11} – 10^{-9} m²/s [21].

The Arrhenius equation was developed to relate the effective moisture diffusivity values to temperatures Equation 7.

$$D_{eff} = D_o \exp\left(-\frac{E_a}{RT}\right) \quad (7)$$

where D_o is the pre-exponential factor of Arrhenius equation or is the diffusivity for infinite temperature (m²/s), E_a is the activation energy (J/mol), R is the gas constant (8.31451 J/mol K) and T is the drying temperature (Kelvin).

Values of $\ln(D_{eff})$ plotted against $1/(T+273)$ for calculated activation energy are shown in Figure 3.

**Figure 3.** Arrhenius-type relationship between effective moisture diffusivity and temperature.

The activation energy is a sign of the required energy to delete moisture from a solid matrix. Higher E_a value indicates greatest temperature sensitivity of diffusion coefficient. The E_a value for chicken meat samples was found 27.85 kJ/mol. The values of the activation energy lie from 12.7 to 110 kJ/mol for most food materials [22]. Hii et al. [8] reported this value varying from 16.3 and 22.8 kJ/mol for for the raw and cooked chicken meat samples.

CONCLUSIONS

In this study, thin layer drying kinetics of chicken meat was studied at drying air temperatures of 40, 50 and 60°C. In conclusion, drying of chicken meat in the convective dryer was only described by the falling rate period. Drying air temperature were influencing factor to drying kinetics. Both the drying rate and moisture ratio decreased with time. Effective moisture diffusivity increased with increasing air temperature, and varied from 4.39 to 9.96 $\times 10^{-10}$ m²/s over the temperature range investigated, with activation energy equal to 27.85 kJ/mol. Eight selected thin layer drying models showed that the Midilli et al. model resulted in an excellent fit for all drying temperatures. These results clearly show that the Midilli et al. model was most suitable for predicting the drying curve of chicken meat. The Midilli et al. model was further validated by comparing the predicted moisture ratio against the experimental moisture figures. Therefore, the Midilli et al. model could be applied in describing the drying behavior and predicting the drying kinetics of chicken meat.

EXPERIMENTAL SECTION

Sample preparation

Chicken breast, used as raw material in the present study, was obtained from a butcher in Istanbul, Turkey. Chicken breast meat was obtained from the broiler chicks (Ross 308) at 45 days (Banvit A.Ş., Bandırma, Turkey). The chicken breasts were cut to a size of 6 cm \times 4 cm \times 1 cm (24 \pm 0.5 g). In order to preserve its original quality, they were stored in a Arcelik 1050 model refrigerator (Arcelik, Eskisehir, Turkey) at 4 °C until drying experiments were conducted.

Drying equipment and drying procedure

Drying experiments were performed in a cabinet laboratory type dryer (API & PASILAC Limited of Carlisle, Cambria, UK). In each experiment, 95 \pm 2 g of chicken samples was used. The chicken meat samples, was uniformly spread in a square basket in a single layer after the desired drying conditions

had stabilized. In order to prevent sticking and to facilitate easy removal of the sample after drying, the tray was lined with 80 µm thick polyethylene sheet. The dryer was installed in an environment with the relative air humidity of about 40–50% and the ambient air temperature about 18–25 °C. Drying experiments of chicken samples were conducted at three temperatures, 40, 50 and 60 °C, at a constant air velocity (1.0 m/s). To record the moisture loss during drying the trays were taken out of the dryer at regular intervals, weighed at 30 minute intervals by using an Ohaus PA214C digital balance which has an accuracy of 0.001 g (Ohaus, NY, USA) and quickly replaced inside the dryer. It was assumed that brief interruptions (less than 20 s) did not interfere with the drying process. The drying process was continued until the weight of the sample was reduced by the initial moisture content of about $0.14 \pm 0.03 \text{ g}_{\text{water}}/\text{g}_{\text{drymatter}}$ at air temperatures of 40, 50 and 60 °C, respectively.

Statistical analysis

All experiments and analyzes were repeated three times and data sets were subjected to analysis of variance using the general linear models. Significant differences between the samples means were determined at the $p < 0.05$ levels by ANOVA.

REFERENCES

1. FAO, Food and Agriculture Organization. Livestock in the balance Part 1. The state of food and agriculture report, 24, **2009**.
2. USDA, U.S. Department of Agriculture, www.usda.gov Accessed Jun 24, **2014**.
3. K.E. Charlton, Y.C. Probst, L.C. Tapsell, P.J. Blackhall, *Journal of the Home Economics Institute of Australia*, **2008**, 15, 5.
4. X.D. Chen, A.S. Mujumdar, "Drying Technologies in Food Processing". Blackwell Publishing Ltd., Oxford, UK, **2008**.
5. A.S. Mujumdar, S. Devahastin, "Fundamental principles of drying", In Devahastin (ed.), *Mujumdar's Practical Guide to Industrial Drying*, Exergex Corp., Montreal, Canada, **2000**, pp. 1.
6. Z. Erbay, F. Icier, *Critical Reviewers in Food Science and Nutrition*, **2010**, 50, 441.
7. J. Arnau, X. Serra, J. Comaposada, P. Gou, M. Garriga, *Meat Science*, **2007**, 77, 81.
8. C.L. Hii, C.E. Itam, S.P. Ong, *Drying Technology*, **2014**, 32, 1304.
9. H. Çakmak, S. Kumcuoğlu, Ş. Tavman, *Gıda*, **2014**, 39, 131.

10. AOAC, Official Methods of Analysis of AOAC International. 16th ed. Gaithersburg, Maryland, USA, **1998**.
11. M. Başlar, M. Kılıçlı, O.S. Toker, O. Sağdıç, M. Arici, *Innovative Food Science and Emerging Technologies*, **2014**, 26, 182.
12. S. Nag, K.K. Dash, *International Food Research Journal*, **2016**, 23, 2594.
13. P.S. Madamba, R.H. Driscoll, K.A. Buckle, *Journal of Food Engineering*, **1996**, 29, 75.
14. T. Ahmat, M. Barka, A.W. Aregba, D. Bruneau, *Journal of Food Processing and Preservation*, **2015**, 39, 2581.
15. S.M. Henderson, S. Pabis, *Journal of Agricultural Engineering Research*, **1961**, 6, 169.
16. M. Aghbashlo, M.H. Kianmehr, S. Khani, M. Ghasemi, *International Agrophysics*, **2009**, 23, 313.
17. A. Midilli, H. Kucuk, Z. Yapar, *Drying Technology*, **2002**, 20, 1503.
18. I. Alibas, *Journal of Agricultural Sciences*, **2012**, 18, 43.
19. H. Darvishi, M. Azadbakht, A. Rezaeiasl, A. Farhang, *Journal of the Saudi Society of Agricultural Sciences*, **2013**, 12, 121.
20. M.R. Okos, G. Narsimhan, R.K. Singh, A.C. Weitnauer, "Food Dehydration in Handbook of Food Engineering", Edited by Heldman D. R. and Lund D. B. Marcel Dekker Inc., **1992**.
21. R.A. Chayjan, M. Kaveh, S. Khayati, *Food Measure*, **2017**, 11, 12.
22. E. Mirzaee, S. Rafiee, A. Keyhani, Z. Emam-Djomeh, *Research in Agricultural Engineering*, **2009**, 55, 114.

CARBON DIOXIDE REMOVAL USING AMMONIA IN BIOGAS UPGRADING AND PURIFICATION

O. I. MAILE^{a*} AND E. MUZENDA^{a, b}

ABSTRACT. An alternative source of energy like biogas has become of interest to reduce the dependence on depleting fossil fuels for the source of energy. It is environmentally friendly and can be generated from various biomass wastes. It consists of CH₄ (55%- 65%) and CO₂ (35%- 45%) with a calorific value of 22 000- 25 000 kJ/m³ when raw and after CO₂ is removed, the methane gas has a calorific value up to 39 000 kJ/ m³ and is referred to as biomethane. Ammonia is used as an absorbent in chemical scrubbing to remove CO₂ from biogas. A continuous system consisting of 1L digester was used for biogas production which was bubbled through an absorbent in 500mL gas washing bottle at a constant temperature in a water bath. The obtained biomethane potential was found to be 0.387 m³ CH₄/ kg VS which simply means that more methane gas can be obtained when using ammonia for absorption. An increase in the gas flow rate leads to an increase in the mass transfer coefficient resulting in an increase in the rate of absorption. The initial CO₂ concentration affects the removal efficiency because more work needs to be done for biogas with a high initial concentration of CO₂. NH₃ has better absorption capacity because higher biogas purity was achieved at lower NH₃ concentration. The removal efficiency for NH₃ increased from 69%-79% on average with CH₄ concentration reaching over 85% vol. This is equivalent to a calorific value ranging from 25- 33.5 MJ/Nm³ which is promising in terms of the gas ability to run in an automobile engine.

Keywords: *absorption, concentration, efficiency, energy, fuel*

^a University of Johannesburg, Faculty of Engineering and Built Environment, Department of Chemical Engineering.

^b Botswana International University, Faculty of Engineering and Technology, Department of Chemical and Metallurgical Engineering.

* Corresponding author: ireenmaile@yahoo.com

INTRODUCTION

Energy is an important part of our daily lives. As a result, the world is facing energy crisis due to depleting oil reserves, emissions from this energy source and unstable prices among other several negative factors. An alternative source of energy like biogas has become of interest as it is environmentally friendly in addition to other several advantages.

Raw biogas as generated from various biomass wastes consists of CH_4 (55%- 65%) and CO_2 (35%- 45%). Its calorific value when raw is 22 000-25 000 kJ/m^3 and after CO_2 is removed, the methane gas has a calorific value of up to 39 000 kJ/m^3 and is referred to as biomethane [1, 2]. Ammonia has potential to yield purified gas of over 95% vol. CH_4 which is considered as biomethane and can be used for similar applications as natural gas.

Ammonia is used as an absorbent in chemical scrubbing to remove CO_2 from biogas. Though amines like MEA are primarily used, ammonia has number of advantages: higher CO_2 loading capacity, no solvent degradation, and equipment corrosion, has low regeneration heat requirements, it has a potential to simultaneously remove CO_2 , SO_2 and NO_x , suitable for large-scale applications, [3-9], it has good oxidative and thermal stabilities [10-13].

Solvent slippage is defined as the amount of liquid solvent that vaporises and is collected with the biomethane. Solvent slippage depends on the volatility of the solvent and the volatility depends largely on the operating temperature [14]. The MEA and NH_3 have a high slippage compared to the hydroxides at 22 °C. This means that for the same amount of biogas collected for every digester, the solvent composition is highest for NH_3 . This also means that the quality of the gas is compromised by the added solvent vapour.

Ammonia is a promising solvent that has been under investigation for carbon capture systems. However, it has a challenge of volatility which may result in solvent slippage. This occurs when some amount of liquid solvent vaporises and collected with the biomethane. The operating temperature plays a huge role as it affects the volatility of the solvent. Alleviating the temperature can limit the slippage of ammonia into the gaseous phase during CO_2 absorption [14].

Despite the fact that ammonia is gaining strength and recognition as an absorbent for removing acidic gases from flue gas and also biogas, it has high volatility and low carbon dioxide absorption rate [8, 11]. Promoters are often added to the aqueous ammonia solution to increase the absorption rate. The use of ammonia for removing impurities such as acidic gases from biogas has been researched by other researchers, however higher concentrations have not been extensively studied and this research seeks to address this aspect.

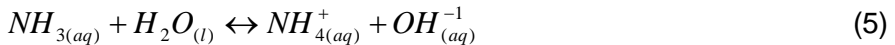
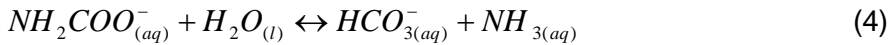
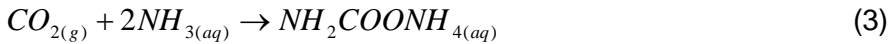
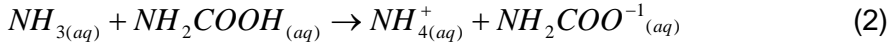
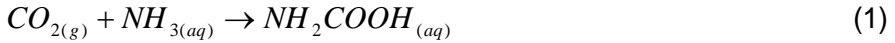
Table 1. Comparison of different absorption units

Absorption Unit	Dimensions	Operating Conditions	Removal Efficiency	Source
This study: Buchner flask	500 ml	Total Pressure Atmospheric ~1atm Temperature 293-333 K Absorbent: 5-15 wt.% ammonia CO ₂ concentration: 46 vol.%	22-79%	
Microchannel reactor	60 x 0.5 x 0.5 mm ³	Total pressure: 141- 401 kPa Temperature: 283- 303 K Absorbent: 4-10 wt.% ammonia CO ₂ concentration: 10 vol.% Gas flow rate: 0.0285 m ³ h ⁻¹ Liquid flow rate: 0.00012- 0.0003 m ³ h ⁻¹	72-97%	[15]
Packed column	600 mm in height, 100 mm in diameter	CO ₂ partial pressure: 5- 15 kPa Temperature: 293-328 K Absorbent: 2- 16 wt.% ammonia CO ₂ concentration: 5- 15 vol.% Gas flow rate: 0.6- 1.68 m ³ h ⁻¹ Liquid flow rate: 0.008- 0.024 m ³ h ⁻¹	52-99%	[22]
Spray tower	350 mm in height, 55 mm in diameter	Total pressure: 0.1 MPa Temperature: 293-323 K Absorbent: 1- 7 wt.% ammonia CO ₂ concentration: 10- 20 vol.% Gas flow rate: 0.2- 0.4 m ³ h ⁻¹ Liquid flow rate: 0.09- 0.18 m ³ h ⁻¹	-	[17]
Bubble column	305 mm in height, 42 mm in diameter	Total pressure: 100 kPa Temperature: 283- 313 K Absorbent: 0- 9 wt.% ammonia CO ₂ concentration: 0- 15 vol.% Gas flow rate: 0.06 m ³ h ⁻¹ Liquid volume: 0.15 L	-	[16]
Multistage spraying tower	540 mm in height, 50 mm in diameter	Total pressure: 0.7- 1 MPa Temperature: 293 K Absorbent: 10- 20 wt.% ammonia CO ₂ concentration: 10- 20 vol.% Gas flow rate: 1.8- 3.6 m ³ h ⁻¹ Liquid flow rate: 0.0696- 0.1296 m ³ h ⁻¹	72-87%	[23]

The absorption process is affected by the type of absorption unit and mechanism used. The types of columns include; packed column, bubble column, spray tower, multi-stage spraying tower, and microchannel reactor [15-19]. The type of packing also plays a role in the performance of the column; packings can either be random or structured [20]. Experimental flowsheet of a wetted-wall column was previously described [21].

Chemical reactions of the absorption process

Ammonia reacts with carbon dioxide to form ammonium carbonate in the liquid phase. Reaction 1 and 2 are intermediate reactions which are summarized by reaction 3. The reactions occurring in the absorption column are shown below:



RESULTS AND DISCUSSION

Ammonia was used to absorb carbon dioxide from biogas, concentrations were varied, and temperature effect was studied and discussed. The concentration studied were 10, 15, and 20% as shown in Table 1. The removal efficiency was also calculated and included in Table 1. It is observed that the absorption rate increases with increasing ammonia concentration, which is in agreement with the findings of [22].

Ammonia is a good carbon dioxide absorber and it is potent to remove the carbon dioxide from the biogas to produce methane rich gas. The cumulative methane yield was realized to be increasing with increasing aqueous ammonia concentration [22, 24, 25]. The obtained biomethane potential was found to be 0.387 m³ CH₄/ kg VS which simply means that more methane gas can be obtained when using ammonia for absorption.

A. The effect of solvent concentration on absorption

The results obtained from the tests that were done are also represented graphically in Figure 2 to Figure 4. An overall observation from the above graphs is that the absorption of carbon dioxide didn't occur steadily. This can be

attributed to the gas flow rate in the system which affects the rate of absorption. An increase in the gas flow rate leads to an increase in the mass transfer coefficient resulting in an escalation in the speed of the absorption process. Thus, it can be said that the days the absorption was higher the gas flow rate was high also because an increase in the gas flow rate improves the absorption rate and the opposite is true for the days the absorption was low.

The surface/contact area which is the gas-liquid interphase plays a huge role in the overall absorption rate and the mass transfer coefficient. The tests yielded an average methane content in the gas of 75%, 79%, and 83% for the 10%, 15%, and 20% ammonia concentration respectively. This can be a result of an increase in the active ammonia present in the solution due to an increase in concentration which is able to diffuse in the gas-liquid interface reacting with the carbon dioxide. This further leads to a decrease in the mass transfer resistance resulting in increased absorption rate.

B. Effect of liquid phase temperature on absorption

The effect of the solvent temperature on the absorption process was studied. The investigated temperatures were room temperature, 30 °C and 40 °C. Figure 5 shows the results obtained by comparing the gas quality from the different temperatures. The methane composition and yield increased with increasing temperature.

The results are further summarised in Table 4. The increase in CH₄ composition between room temperature and 30 °C is not significant, however, there is an improvement in the 40 °C study. The CH₄ composition recorded the highest at 40 °C. Furthermore, temperature helps in reducing the viscosity of the solvent to improve the absorption performance. However, the temperature of ammonia solvent and the absorption column should not be high above 60 °C in order to avoid slippage. In addition, higher temperatures also lead to decomposition of the ammonium bicarbonate salt at a temperature above the acceptable range of 20 °C to 40 °C. This is due to the reversibility of the reaction of carbon dioxide and ammonia, in which increases in temperature favours the forward reaction [26]. However, a further increase beyond 40 °C shifts the equilibrium to the reverse reaction.

C. Effect of solvent concentration on removal efficiency

The CO₂ removal efficiency for ammonia was calculated using Eq. 6 and the results are represented in Figures 6 and 7. The removal efficiency is influenced by many factors including, the concentration of aqueous ammonia, gas flow rate, and the ammonia to carbon dioxide molar ratio. The highest removal efficiency recorded was 66% which is contrary to what was obtained by reference [27]. It could be attributed to the process setup as a spray column

was used and it provides a good gas-liquid interface for the contact and thus resulting in high removal efficiency. It can be observed that the gas flow rate also plays a role in CO₂ removal. However, an increase in the gas flow rate leads to an increase in the removal efficiency. The molar ratio can either improve the efficiency or reduce it, hence it needs to be cautiously kept at an appropriate point.

$$\eta_{CO_2} = \left(1 - \frac{CO_{2\text{pur}}}{CO_{2\text{raw}}}\right) \times 100\% \quad (6)$$

Where:

η_{CO_2} - carbon dioxide removal efficiency

CO_{2pur}- carbon dioxide content of the purified sample

CO_{2raw}- carbon dioxide of the raw sample

The experimental configuration and type of absorber affect the carbon dioxide removal efficiency. This is illustrated in Table 1, where the removal efficiency for a packed column had a higher removal efficiency. Although high removal efficiencies were obtained by the other studies, it can be attributed to the operating conditions and initial concentration of carbon dioxide which was low in their case. Furthermore, the increase in concentration may lead to a decline in the removal efficiency as it leads to increase in viscosity which may contribute to the solvent loss.

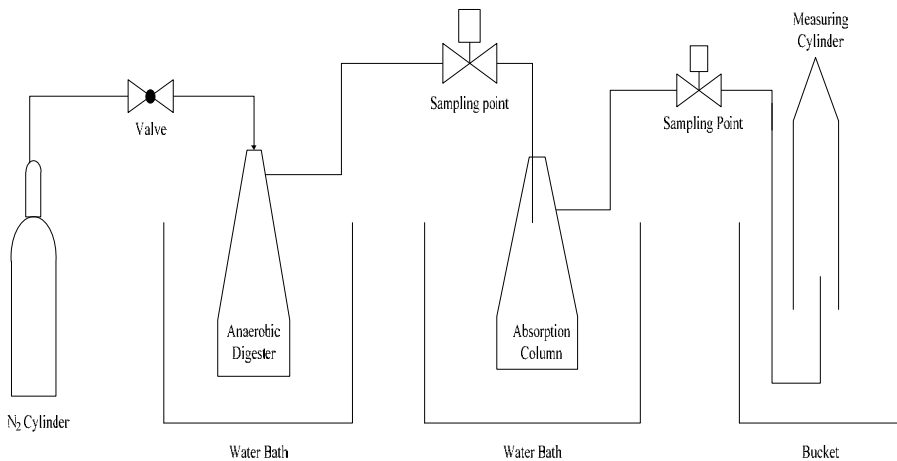


Figure 1. Schematic diagram of laboratory set up for absorption in aqueous ammonia

CARBON DIOXIDE REMOVAL USING AMMONIA IN BIOGAS UPGRADING AND PURIFICATION

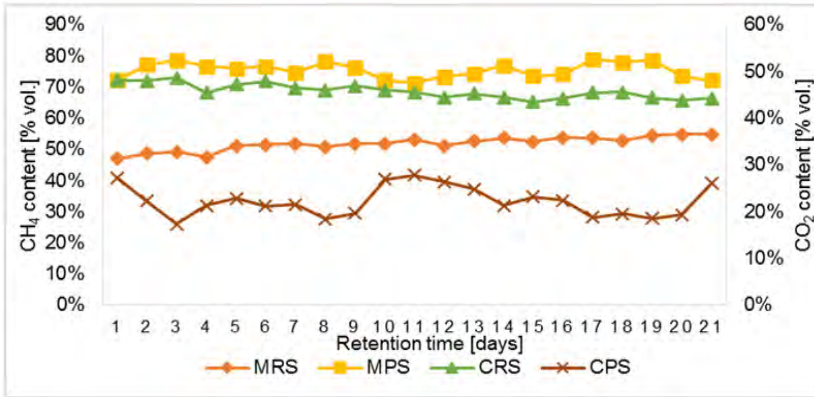


Figure 2. Absorption of CO₂ with NH₃ at 10% concentration.

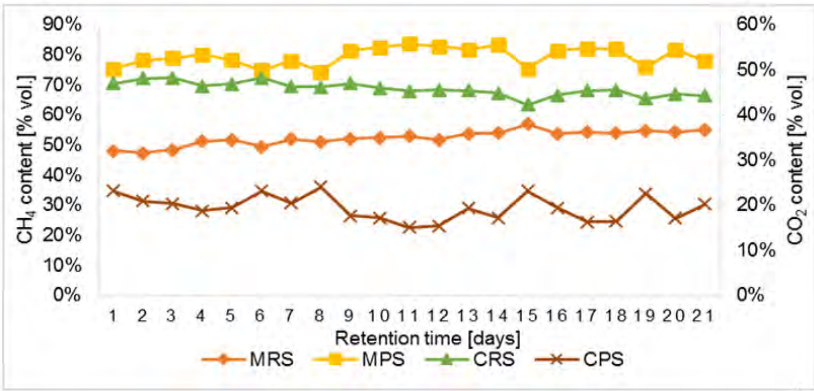


Figure 3. Absorption of CO₂ with NH₃ at 15% concentration.

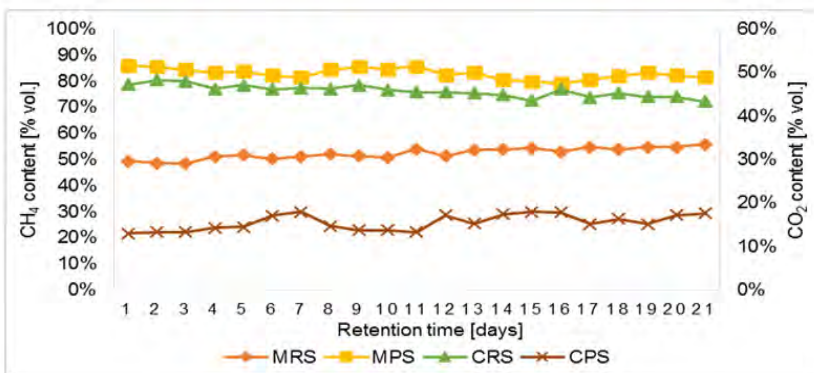


Figure 4. Absorption of CO₂ with NH₃ at 20% concentration.

Table 2. Notation table for Figures 2-4

Acronym	Meaning
MRS	Methane (CH ₄) content of the raw sample
MPS	Methane (CH ₄) content of the purified sample
CRS	Carbon dioxide (CO ₂) content of the raw sample
CPS	Carbon dioxide (CO ₂) of the purified sample

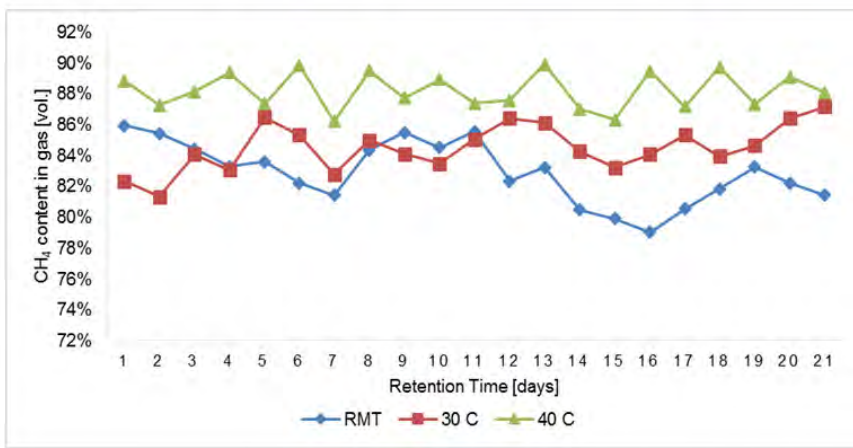


Figure 5. The effect of temperature on methane content in biogas purification

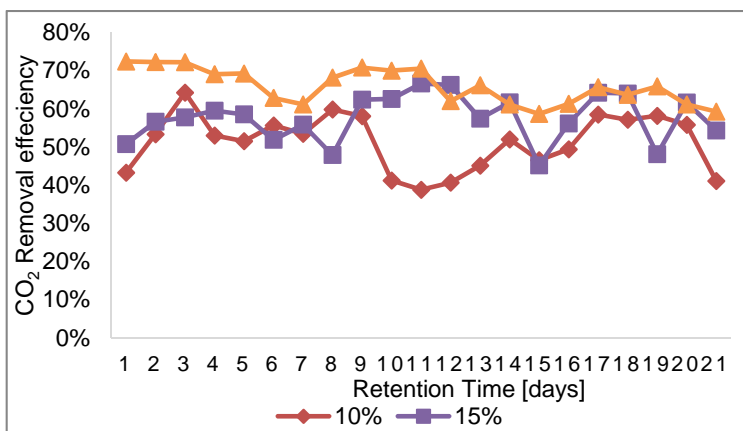


Figure 6. Effect of concentration on carbon dioxide removal efficiency

CARBON DIOXIDE REMOVAL USING AMMONIA IN BIOGAS UPGRADING AND PURIFICATION

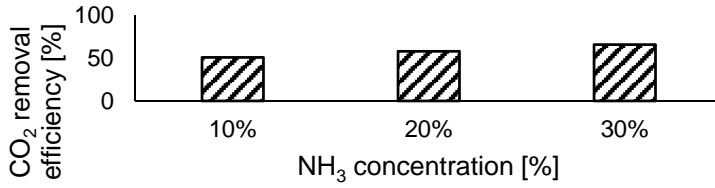


Figure 7. Carbon dioxide removal efficiency

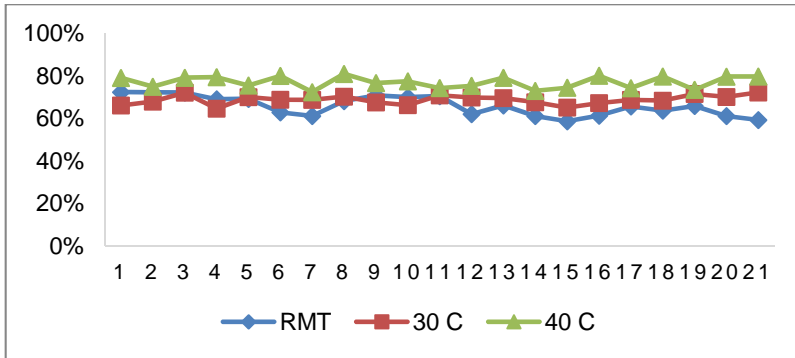


Figure 8. Effect of temperature on carbon dioxide removal efficiency

Table 3. Performance of NH₃ in CO₂ absorption

Gas	Composition	Raw Biogas	10%	15%	20%
CH ₄	%	52	75	79	83
CO ₂	%	46	22	19	16
η	%	-	51	58	66

Table 4. Summary of results on temperature variation

Parameter	RMT	30 °C	40 °C
CH ₄	83	85	88
CO ₂	16	14	11
η	66	69	77

CONCLUSIONS

Chemical absorption technique has been widely used to remove impurities from biogas as it is deemed to be cheap and effective. An increase in the concentration of ammonia enhanced the rate of absorption, which was mainly because the concentration of the reacting ions in the aqueous ammonia solution increases and contact between the gas-liquid interface is increased. The raw biogas had on average 52% CH₄ vol. which improved to 83% CH₄ vol. after absorption. The CO₂ removal efficiency improved from 22% to 66%. The initial CO₂ concentration affects the removal efficiency because more work needs to be done for biogas with a high initial concentration of CO₂. NH₃ has better absorption capacity because higher purity was obtained using even lower absorbent concentration.

The absorption rate also improved with an increase in temperature. The removal efficiency for NH₃ increased from 69%-79% on average with CH₄ concentration reaching over 85% vol. This is equivalent to a calorific value ranging from 25- 33.5 MJ/Nm³ which is promising in terms of the gas ability to run in an automobile engine. The less the impurities in the gas the more or easily combustible it becomes. Ammonia has high absorption capacity and can also be regenerated with ease, it also has an advantage of the use of ammonium carbonates as inorganic fertilizers.

EXPERIMENTAL SECTION

A continuous system was used according to literature data [15]. 1L digester was used for biogas production which was bubbled through an absorbent in 500mL gas washing bottle. The digester was kept in a water bath to maintain a constant operating temperature throughout the experiment. To study the effect of temperature on absorption the absorption column was also kept in a water bath and the temperature varied accordingly. Nitrogen gas was used to purge and create anaerobic conditions in the system. A valve is used to let the N₂ gas into the digester and closed after purging is done. Two sampling points in a form of T's closed with a septa between the processes, for the raw biogas and the purified gas. The gas exiting the absorption unit goes to 1L measuring cylinder for volume capturing using downward displacement.

Ammonia was used as an absorbent supplied by Sigma-Aldrich (South Africa). 10 – 20 %wt solution was used for the purification in a 500mL vessel which was kept at constant temperature. The gas exiting the absorption column was analysed using Gas Chromatography (SRI 8610C GC) equipped with FID and TCD detectors, packed with 6' Hayesep-D/ 6' Molecular Sieve-13 X. 1 mL SGE gas tight syringe was used to draw the gas for sampling from the septa.

ACKNOWLEDGMENTS

The authors are indebted to late Dr. Habtom Tesfagiorgis who supervised the Masters studies of the first author and research activities where this current work is drawn from. The Botswana International University of Science and Technology, the South African National Energy Development Institute (SANEDI), Global Excellence Scholarship (GES), the City of Johannesburg (CoJ), the department of Chemical Engineering and the Process Energy and Environmental Technology Station (PEETS) at the University of Johannesburg acknowledged for supporting this research.

REFERENCES

1. Yin, B., L.M. Chen, and Q.P. Kong, *Modern Chemical Industry*, **2009**, 29(11): p. 28.
2. Xiao, Y., et al., *CO₂ Chinese Journal of Chemical Engineering* **2014**, 22, 950.
3. Zhao, Z., H. Dong, and X. Zhang, *Chinese Journal of Chemical Engineering*, **2012**, 20(1), 120.
4. Zhang, M.K. and Y.C. Guo, *International Journal of Greenhouse Gas Control*, **2013**, 16, 61.
5. Puxty, G., R. Rowland, and M. Attalla, *Chemical Engineering Science*, **2010**, 65, 915.
6. Mores, P., N. Scenna, and S. Mussati, *International Journal of Greenhouse Gas Control*, **2012**, 6, 21.
7. M S Chen, S. Huihui, Z. Bin, C. Gongda, *Chemical Engineering Research and Design*, **2013**, 91, 2775.
8. V. Darde, W.J.M. van Well, P.L. Fosboel, E.H. Stenby, K Thomsen, *International Journal of Greenhouse Gas Control* **2011**, 5, 1149.
9. V. Darde, B. Maribo-Mogensen, W.J.M. van Well, E.H. Stenby, K. Thomsen, *International Journal of Greenhouse Gas Control*, **2012**, 10, 74.
10. F. Qin, S. Wang, I. Kim, H.F. Svendsen, C. Chen *International Journal of Greenhouse Gas Control* **2011**, 5, 405.
11. M. Fang, Q. Xiang, X. Zhou, Q. Ma, Z. Luo, *Energy Procedia* **2014**, 61, 2284.
12. P.W.J. Derks, G.F. Versteeg, *Energy Procedia*, **2009**, 1139.
13. H. Bai, A.C. Yeh, *Industrial Engineering Chemical Research*, **1997**, 36, 2490.
14. W.M. Budzianowski, *CO₂ Environment Protection Engineering*, **2011**, 37, 5.
15. N. Kittiampon, A. Kaewchada, A. Jaree, *International Journal of Greenhouse Gas Control*, **2017**, 63, 431.
16. S. Ma, G. Chen, S. Zhu, T. Han, W. Yu *Applied Energy*, **2016**, 162, 354.
17. S. Ma, H. Song, M. Wang, J. Yang, B. Zang, *Chemical Engineering Research and Design*, **2013**, 91(7), 1327.

18. S. Ma, B. Zang, H. Song, G. Chen, J. Yang, *International Journal of Heat and Mass Transfer*, **2013**, 67, 696.
19. L.S. Tan, A.M. Shariff, K.K. Lau, M.A. Bustam, *Journal of Industrial and Engineering Chemistry*, **2012**, 18(6), 1874.
20. B. Zhao, Y. Su, W. Tao, L. Li, Y. Peng, *International Journal of Greenhouse Gas Control*, **2012**, 9, 355.
21. J. Liu, S. Wang, B. Zhao, H. Tong, C. Chen, *Energy Procedia*, **2009**, 1(1), 933.
22. Q. Zeng, Y. Guo, Z. Niu, W. Lin, *Fuel Processing Technology*, **2013**, 108, 76.
23. B. Zhao, Y. Su, G. Cui, *Energy*, **2016**, 102, 106.
24. P.S. Nair, P.P. Selvi, *International Journal of Scientific and Research Publications*, **2014**, 4(4), 1.
25. C.H. Hsu, H. Chu, C.M. Cho, *Journal of Air & Waste Management Association*, **2012**, 53, 246.
27. A. McLeod, B. Jefferson, E.J. McAdam, *Water Research*, **2014**, 67, 175.
28. Z.Q. Niu, Y.C. Guo, W.Y. Lin, *Science China Technological Sciences*, **2010**, 53, 117.

METHOD DEVELOPMENT FOR THE ELEMENTAL ANALYSIS OF ORGANIC RICH SOIL SAMPLES BY MICROWAVE PLASMA ATOMIC EMISSION SPECTROMETRY

CSILLA NOÉMI TÓTH^{a*}, SÁNDOR HARANGI^b, ANIKÓ KÁROLYI^c,
ISTVÁN FÁBIÁN^c, EDINA BARANYAI^a

ABSTRACT. In this study, the method development is described for the multi elemental determination of organic rich soil reference material (BCR 700) by the new microwave plasma atomic emission spectrometry (MP-AES). Two sample preparation methods were compared (open vessel digestion on a hot plate and closed vessel microwave assisted digestion) for the BCR sample and EDTA extraction was carried out. The recoveries were tested by MP-AES and inductively coupled plasma optical emission spectrometry (ICP-OES) method to investigate whether the more cost-effective nitrogen supplied microwave plasma is appropriate for the elemental determination of digested organic rich soil samples. The BCR 700 sample was not certified for digestion methods yet similar sample pretreatment is present in the literature with which a good agreement was found. Our results also correlated with the values provided in the certification of the BCR 700 material for EDTA extraction. It was found that the microwave plasma is an effective and low-cost alternative of ICP-OES for soil analysis and with the convenient atmospheric digestion even the organic rich soil samples can be prepared prior to the elemental determination. However, the microwave assisted digestion is faster and easier to conduct. The limit of detection values of the measured elements by MP-AES are sufficiently low for the micro element determination of soils (Cd 70 $\mu\text{g kg}^{-1}$, Cr 5 $\mu\text{g kg}^{-1}$, Cu 25 $\mu\text{g kg}^{-1}$, Mn 12.5 $\mu\text{g kg}^{-1}$, Ni 45 $\mu\text{g kg}^{-1}$, Pb 220 $\mu\text{g kg}^{-1}$, Zn 155 $\mu\text{g kg}^{-1}$).

Keywords: *microwave plasma, inductively coupled plasma, atomic emission spectrometry, soil analysis, sample preparation*

^a University of Debrecen, Department of Inorganic and Analytical Chemistry, Agilent Atomic Spectroscopy Partner Laboratory, Egyetem square 1. H-4032, Debrecen, Hungary

^b University of Debrecen, Department of Ecology, P.O. Box 71, H-4010 Debrecen, Hungary

^c University of Debrecen, Department of Inorganic and Analytical Chemistry, Egyetem square 1. H-4032, Debrecen, Hungary

* Corresponding author: toth.csilla.noemi@science.unideb.hu

INTRODUCTION

Atomic spectrometry provides several tools for elemental analysis [1-3]. The most widely applied technique is inductively coupled plasma optical emission spectrometry (ICP-OES), which is nowadays a routine method for the quantitative determination of elements from solutions [4]. Nearly together with the ICP, in the 1970s, the microwave excitation sources had been developed and tested [5, 6], which application possibilities were discussed in several papers so far [7-11]. The conventional MIP instruments operate on a lower electric capacity and gas flow compared to the ICPs, and their analytical performance is lower due to the lower thermal stability and matrix tolerance of the applied emission source [12]. For these disadvantages it did not become commercially available, however the development of stable MIP sources continuously stayed in the focus of researchers [7, 8, 13 -18].

The new method has already been applied for several purposes yet many fields of application is still open to the MP-AES technique [19]–[22].

Soil is one of the most important energy source of ecosystem, which quality must be monitored and preserved. The biological components are the most sensitive to the environmental change and tend to degrade upon human activity [19-24]. The chemical composition of soil is also an important parameter and can indicate pollution both from natural and anthropogenic origin. Several essential elements are present in soil which are vital for the terrestrial flora and fauna (such as Co, Cu, Fe, Mn, Zn) however, above the threshold limit, they have a toxic effect [25-28]. There are also toxic elements which have no essential functions to living organisms (such as Al, Pb, Cd, Hg) therefore considered as pollutants in soils [19, 24, 29-33]. The elemental analysis of soil samples is of high importance to determine the amount of either essential trace metals or the quality and quantity of elemental contaminants. Atomic spectrometric methods are widely applied for this purpose and continuous development is required to meet the environmental principles.

The aim of this paper is to investigate the multi elemental determination of organic rich soil and the new method MP-AES was developed for trace element analysis by measuring a CRM soil (BCR 700) sample for Cd, Cr, Cu, Ni, Pb and Zn.

RESULTS AND DISCUSSION

The organic rich BCR sample was pre-treated by open vessel digestion on a hot plate and closed vessel microwave assisted digestion with the mixture of nitric acid and hydrogen peroxide. The effectiveness of the digestion methods was investigated with internal standards of Bi (added prior to the sample preparation process) and Y (added prior to the elemental analysis).

Since the applied multi element stock solution originally contained Bi, the experiment can be considered as a standard addition procedure. As seen in *Figure 1* a good recovery was obtained, since the added Bi concentration was gained in a good agreement and with a low standard deviation.

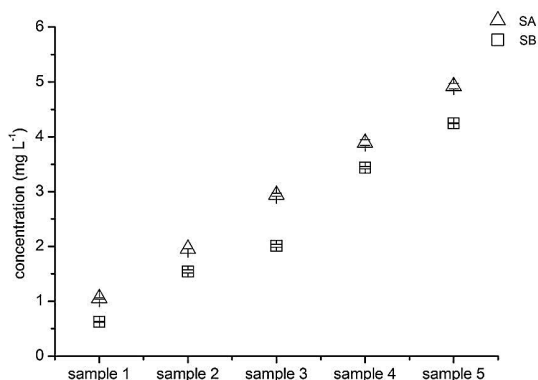


Figure 1. The Bi concentration of the digested SA (multi element stock solution + nitric acid + hydrogen peroxide) and SB (SA + BCR700 soil sample + Bi internal standard+ Y internal standard) ($\text{mg L}^{-1} \pm \text{SD}$, $n=3$)

The analysis results for Y is indicated in *Figure 2*. It was observed that a 14.02% more than the originally added Y concentration was found in the digested samples, respectively, while in the blank samples the expected value was found. It suggests that the reference material contained Y however its level was under the limit of detection of the MP-AES method. Therefore, it was not detected from the soil samples before its addition.

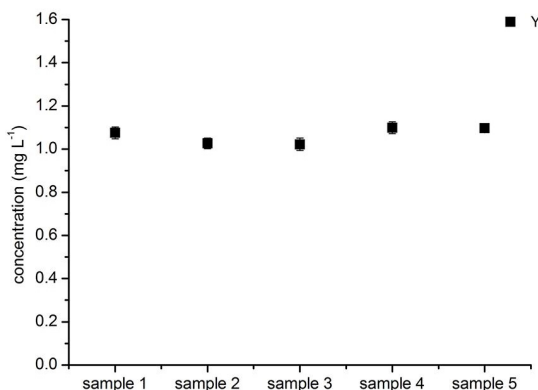


Figure 2. The Y concentration of the digested SB sample (SA + BCR700 soil sample + Bi internal standard + Y internal standard) ($\text{mg L}^{-1} \pm \text{SD}$, $n=3$)

The two internal standards proved that no sample loss occurs during the open vessel sample preparation process. The optimization of the sample pre-treatment was continued with the comparison of the open vessel digestion on a hot plate and closed vessel microwave assisted digestion, with two different initial sample masses (0.2 g and 0.5 g). *Figure 3* shows the MP-AES results for the measured elements (Cd, Cr, Cu, Mn, Ni, Pb and Zn) of the BCR 700 sample in case of the two digestion techniques.

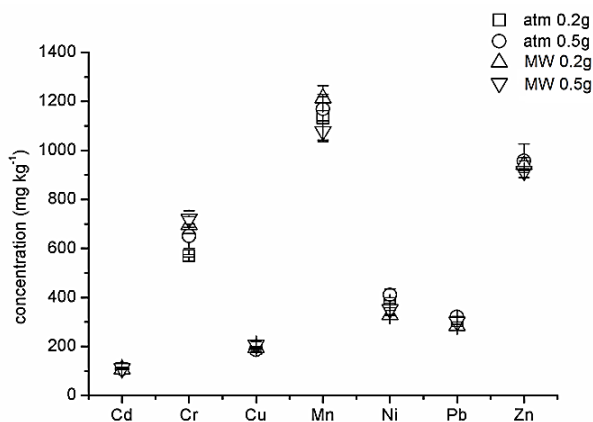


Figure 3. The elemental analysis results of soil samples (BCR700) prepared by open vessel (atm) and microwave assisted (MW) digestion with 0.2g and 0.5g of initial sample masses ($\text{mg kg}^{-1} \pm \text{SD}$, $n=3$)

The concentrations gained after both open vessel digestion on a hot plate and closed vessel microwave assisted digestion provided similar concentration results regardless the initial masses ($p>0.05$). It indicates that both methods are appropriate for the elimination of the organic matter from the organic rich BCR 700 sample and 0.2 grams is enough to carry out the quantitative analysis. However, the microwave assisted method is faster and requires less attention during operation.

The measurement of Cd, Cr, Cu, Mn, Ni, Pb and Zn was carried out by ICP-OES and MP-AES, respectively. Limit of detection (LOD) values were determined for the measured elements by both techniques and are compared in terms of the applied wavelengths in *Table 1*. We can conclude that the MP-AES method is sufficient regarding the LOD data for soil analysis. In some cases, similar LOD results were gained compared to ICP-OES suggesting that the lower temperature plasma source is enough for the excitation of the measured elements.

Table 1. The limit of detection values together with the applied wavelengths for ICP-OES and MP-AES methods

Element	Wavelength (nm)	MP-AES LOD ($\mu\text{g L}^{-1}$)	MP-AES LOD ($\mu\text{g kg}^{-1}$)	Wavelength (nm)	ICP-OES LOD ($\mu\text{g L}^{-1}$)	ICP-OES LOD ($\mu\text{g kg}^{-1}$)
Cd	228.802	1.4	70	228.802	0.04	2
Cr	425.433	0.1	5.0	267.716	0.20	10
Cu	324.754	0.5	25	324.754	0.15	7.5
Mn	403.076	0.25	12.5	257.61	0.03	1.5
Ni	352.454	0.9	45	231.604	0.70	35
Pb	405.781	4.4	220	220.353	1.10	55
Zn	213.857	3.1	155	213.857	0.10	5

Table 2 indicates the detailed experimental results of BCR 700 analysis comparing ICP-OES and MP-AES data as well as the applied sample pre-treatment techniques. The used organic rich reference material is only certified for elemental analysis after EDTA extraction, but Begum et al. (2012) studied its composition after wet digestion [38]. Thus, in the table concentration results gained by digestions are compared with literature data. A good correlation was found between the two atomic spectrometric methods and no significant difference occurred between them according to the statistical analysis. These results prove that the microwave plasma is suitable for the elemental analysis of organic rich soil samples providing a satisfactory multi elemental alternative to ICP-OES.

The excitation source of newly released MP-AES instrument is supported by nitrogen gas instead of argon which price is significantly lower. Also, a nitrogen generator can be applied producing nitrogen gas from air making the system even more cost-effective during operation. However, as found in this study, the emission line of Zn for example is in the ultraviolet range (213.857 nm) which requires the continuous gas purge of the optical system to avoid the absorption caused intensity decrease. The nitrogen generator of MP-AES cannot produce enough gas for purging thus an externally connected nitrogen gas cylinder is suggested to purge the optics.

In case of the EDTA extracted soil samples better recoveries were gained by ICP-OES compared to MP-AES (*Table 3*). Although both methods proved to be accurate we assume that the applied EDTA concentration was high and loaded the lower temperature microwave plasma thus further experiments are required to find the right concentration of the extraction solution that can be directly introduced to the microwave plasma without causing interferences.

Table 2. The elemental analysis results of BCR 700 by MP-AES and ICP-OES after open vessel digestion on a hot plate and closed vessel microwave assisted digestion (n.d.: no data is available)

Sample	Element (mg kg ⁻¹)									
	Cd	RSD%	Cu	RSD%	Ni	RSD%	Pb	RSD%	Zn	RSD%
MP-AES c (mg kg ⁻¹)										
ATM_0.2g	111±0.1	0.08	192±4	2.16	389±11	2.79	305±15	4.78	947±24	2.53
ATM_0.5g	108±2	1.65	186±4	2.36	411±24	5.83	321±2	0.58	958±69	7.17
MW_0.2g	105±0.8	0.70	196±5	2.57	328±2	0.55	285±4	1.46	941±16	1.70
MW_0.5g	111±5	4.79	207±14	6.66	352±5	1.47	300±0.6	0.20	914±5	0.50
ICP-OES c (mg kg ⁻¹)										
ATM_0.2g	107±0.6	0.57	158±4	2.35	259±0.7	0.27	233±0.3	0.13	1342±3	0.22
ATM_0.5g	104±1	0.95	158±2	1.05	299±4	1.38	224±5	2.14	1346±11	0.79
MW_0.2g	89±1	1.18	157±2	1.07	329±10	3.06	239±4	1.68	1343±25	1.86
MW_0.5g	93±0.4	0.40	158±4	2.51	221±7	3.35	232±0.8	0.35	1325±58	4.39
Begum et al., 2012 [34]	132±2	n.d.	169±4	n.d.	373±6	n.d.	288±3	n.d.	1584±22	n.d.

Table 3. The MP-AES and ICP-OES results of EDTA extracted BCR700 compared to the certified values (recoveries are expressed in percentage difference)

Element	BCR 700 certified values (mg kg ⁻¹)	ICP-OES (mg kg ⁻¹)	Recovery (%)	MP-AES (mg kg ⁻¹)	Recovery (%)
Cd	65.2±3.5	67.2±1.5	3.02	76±0.5	16.4
Cr	10.1±0.9	27.8±0.5	63.6	35.4±0.6	250
Cu	89.4±2.8	85.7±0.7	-4.3	108.9±0.9	21.8
Ni	53.2±2.8	65.4±0.4	18.6	86.6±0.2	62.7
Pb	103±5	110±2.1	6.75	119±2.5	15.1
Zn	510±17	503±18	-1.31	577±19	13.1

CONCLUSIONS

The new microwave plasma atomic emission method was tested for the elemental analysis of organic rich soil (BCR 700) certified reference material. It was found that no significant difference occur between the open vessel digestion on a hot plate and closed vessel microwave assisted wet

digestion. Both sample preparation techniques are suitable for the pre-treatment of organic rich soil samples, however the microwave digestion is faster and easier to conduct.

The MP-AES method proved to be appropriate for the determination of Cd, Cr, Cu, Mn, Ni, Pb and Zn after the digestion procedure. However, the EDTA level present in the extracted soil samples loaded the microwave plasma and better recoveries were gained by ICP-OES. The EDTA content should be reduced or completely removed prior to the MP-AES determination to avoid the matrix effects or external oxygen should be applied among nitrogen to elevate the robustness of the excitation source.

EXPERIMENTAL SECTION

Sample preparation

The BCR 700 certified reference material of organic rich soil was homogenized then dried until constant weight at 105°C in drying cabinet.

For the open vessel digestion, on a hot plate, 0.5 grams of the dried sample was weighed on analytical balance (Precisa 240A) into glass beakers and was digested on an electric hot plate along with 4 ml 65 % (m/m) nitric acid (analytical grade VWR) and 0.50 ml of 30 % (m/m) hydrogen peroxide (reagent grade Scharlau). After the heating, samples were transferred without loss into volumetric flasks and filled up until 25 ml with 0.1 M nitric acid prepared in ultrapure water (MilliQ A10, Millipore). The sample pretreatment was carried out with a reduced, 0.2 grams of initial sample mass as well. The preparation was carried out in triplicate.

The closed vessel microwave assisted digestion was carried out in an ETHOS UP system from Milestone. Digestion parameters and the thermal program are indicated by *Table 4*. The same amount of dried soil sample (0.2 g and 0.5 g) and chemicals were applied as well as the final volume of the gained solutions was 25 ml - similarly to the atmospheric digestion process.

Table 4. Digestion parameters of the EHOS UP (Milestone)

MW program "BCR 700"			
Nr	t	T1	E
1	0:15:00	200°C	1800W
2	0:20:00	200°C	1800W

In order to verify the digestion steps internal standards were used. Prior to the sample pretreatment a known concentration of Bi stock solution was applied since according to our preliminary measurements Bi was present under the limit of detection in the BCR material. Two sample series were prepared:

- SA - containing a multi element standard stock solution (Merck IV) nitric acid and hydrogen peroxide,
- SB - SA + BCR 700 and Bi.

The prepared 5 samples contained the multi element solution in an increasing order from 1 mg L⁻¹ to 5 mg L⁻¹. After the atmospheric digestion a known concentration (1 mg L⁻¹) of Y standard solution was also added to SB samples. The detailed compositions of the model samples are indicated in *Table 5*.

Table 5. The composition of the model samples, the volume and concentration of the applied internal standards and digestion chemicals

SA	multi element standard 1000 mg L ⁻¹	BCR 700 (g)	Bi 100 mg L ⁻¹	Y 100 mg L ⁻¹	reagent	final volume (ml)
1. atm	0 µl	-	-	-	4ml 65 % HNO ₃ + 30 % 0.5ml H ₂ O ₂	25
2. atm	250 µl	-	-	-	4ml 65 % HNO ₃ + 30 % 0.5ml H ₂ O ₂	25
3. atm	500 µl	-	-	-	4ml 65 % HNO ₃ + 30 % 0.5ml H ₂ O ₂	25
4. atm	750 µl	-	-	-	4ml 65 % HNO ₃ + 30 % 0.5ml H ₂ O ₂	25
5. atm	1000 µl	-	-	-	4ml 65 % HNO ₃ + 30 % 0.5ml H ₂ O ₂	25
6. atm	1250 µl	-	-	-	4ml 65 % HNO ₃ + 30 % 0.5ml H ₂ O ₂	25
SB						
7. atm	0 µl	0.2000	250 µl	250 µl	4ml 65 % HNO ₃ + 30 % 0.5ml H ₂ O ₂	25
8. atm	250 µl	0.2000	250 µl	250 µl	4ml 65 % HNO ₃ + 30 % 0.5ml H ₂ O ₂	25
9. atm	500 µl	0.2000	250 µl	250 µl	4ml 65 % HNO ₃ + 30 % 0.5ml H ₂ O ₂	25
10. atm	750 µl	0.2000	250 µl	250 µl	4ml 65 % HNO ₃ + 30 % 0.5ml H ₂ O ₂	25
11. atm	1000 µl	0.2000	250 µl	250 µl	4ml 65 % HNO ₃ + 30 % 0.5ml H ₂ O ₂	25
12. atm	1250 µl	0.2000	250 µl	250 µl	4ml 65 % HNO ₃ + 30 % 0.5ml H ₂ O ₂	25

The BCR 700 material is certified for EDTA extraction. On analytical balance 5 grams of dried BCR sample was measured and 50 ml of 0.05 M EDTA (Merck) was added to it in Erlenmeyer flasks. Ultrasound bath (Transsonic 460/H) was used for one hour. Then extracted soil samples were filtered (Schleicher & Schuell 595 ½ 1.4 µm) into 50 ml volumetric flasks. In *Table 6* the conditions of sample preparation applied for BCR 700 reference material are summarized.

Table 6. The sample preparation parameters of the organic rich soil (BCR 700) reference material

digestion	BCR 700 (g)	reagent	final volume (ml)
atm.	0.5000	4ml 65 %HNO ₃ + 30 % 0.5ml H ₂ O ₂	25
MW	0.5000	5ml 65 %HNO ₃ + 30 % 0.5ml H ₂ O ₂	25
atm.	0.2000	4ml 65 %HNO ₃ + 30 % 0.5ml H ₂ O ₂	25
MW	0.2000	5ml 65 %HNO ₃ + 30 % 0.5ml H ₂ O ₂	25
extraction	5.0000	0.05M EDTA	50

Instrumentation

The BCR soil samples were determined for Cd, Cr, Cu, Ni, Pb and Zn by inductively coupled plasma optical emission spectrometry (ICP-OES 5100 Agilent Technologies) and microwave plasma atomic emission spectrometry (MP-AES 4200, Agilent Technologies) after the open vessel digestion on a hot plate and closed vessel microwave assisted digestion as well as the EDTA extraction. A 5 points calibration was applied (Merck ICP IV) and the purity of chemicals were verified by measuring blank samples.

The first commercially available microwave plasma atomic emission spectrometer (MP-AES) was released in 2011, which applies a robust excitation source for stable and continuous measurements. The magnetron generates electromagnetic wavelengths at 2.5 GHz and the magnetic field is focused axially around the torch. Plasma is supplied with nitrogen produced by a generator from air which makes the technique the most cost-effective one in the field of atomic spectrometry. The excitation source has a lower temperature (approx. 5000-6000 K) to that of the inductively coupled ones (approx. 8000-10000 K) and the interferences occurring in the plasma is less studied so far.

Measuring parameters together with the applied wavelengths are indicated in *Table 7*. The MP-AES software provides less parameters to be adjusted by the user since the microwave plasma provides robust in a narrower range compared to the inductively coupled one. Thus, values of nitrogen flow are fixed however the nebulizer pressure can be adjusted per the measured elements.

The viewing position in case of both instruments was zero. In MP-AES automatic background correction was applied while in ICP-OES measurements fitted correction was used - both offered by the Agilent Spectra software. Solutions were measured in analyte type except the standards of calibration. Double pass spray chamber and sea spray nebulizer was used for sample introduction along with SPS3 (Agilent Technologies) autosampler.

Table 7. The measurement parameters of MP-AES and ICP-OES

MP-AES measurement conditions			ICP-OES measurements conditions		
Elements (nm)	Read time (s)	Nebulizer pressure (kPa)	Fixed values*	Read time (s)	Nebulizer flow (L/min)
Ni (352.454)	5	240	Nitrogen (L/min): 22.5	5	0.70
Cd (228.802)	5	140	Air (L/min): 25	RF power (kW): 1.20	Plasma flow (L/min): 12.00
Cu (324.754)	2	240	Intermediate (L/min): 170	Stabilization time (s): 10	Aux flow (L/min): 1.00
Mn (403.076)	2	240	Outer (L/min): 170	Viewing mode: SVDV	Make up flow (L/min): 0.00
Pb (405.781)	5	240		Viewing height (mm): 8	
Cr (425.433)	3	240	*Fixed values cannot be adjusted by the users		
Bi (306.772)	5	140			
Y (371.029)	2	140			
Al (396.152)	2	240			
Zn (213.857)	3	140			
Fe (371.993)	3	120			

Evaluation of data

Statistical analysis was applied to compare the elemental analytical results gained by ICP-OES and MP-AES method. General Linear Model (ANOVA) was used (SPSS IBM 22) where the homogeneity of the groups was tested by Levene's test and the significant differences were evaluated by Tukey's Multiple Comparison test.

ACKNOWLEDGMENTS

The research was supported by the EU and co-financed by the European Regional Development Fund under the project GINOP-2.3.2-15-2016-00008. We would like to highly acknowledge Agilent Technologies (Novo-Lab Ltd.) for providing the MP-AES 4200 and ICP-OES 5100 instruments and Milestone (Novo-Lab Ltd.) for the ETHOS UP microwave digestion system.

REFERENCES

1. B. Welz and M. Sperling, Eds., *Atomic Absorption Spectrometry*. Weinheim, Germany: Wiley-VCH Verlag GmbH, **1998**.
2. B. Welz, H. Becker-Ross, S. Florek, and U. Heitmann, *High-Resolution Continuum Source AAS: The Better Way to Do Atomic Absorption Spectrometry*. Weinheim, FRG: Wiley-VCH Verlag GmbH & Co. KGaA, **2005**.
3. R. Cornelis, Ed., *Handbook of elemental speciation: techniques and methodology*. Chichester, West Sussex, England ; Hoboken, NJ: Wiley, **2003**.
4. E. Frahm, G.F. Monnier, N.A. Jelinski, E.P. Fleming, B.L. Barber, and J.B. Lambon, *Journal of Archaeological Science*, **2016**, *75*,115.
5. H.P. Broida and M.W. Chapman, *Analytical Chemistry*, **1938**, *30*, 2049.
6. N.S. Ham and A. Walsh, *Spectrochimica Acta*, **1958**, *12*, 88.
7. J.A.C. Broekaert and U. Engel, "Microwave-Induced Plasma Systems in Atomic Spectroscopy," in *Encyclopedia of Analytical Chemistry*, R.A. Meyers, Ed. Chichester, UK: John Wiley & Sons, Ltd, **2000**.
8. J.A.C. Broekaert and V. Siemens, *Spectrochimica Acta Part B Atomic Spectroscopy*, **2004**, *59*, 1823.
9. S. Greenfield, H.M. Mcgeachin, and P.B. Smith, *Talanta*, **1975**, *22*, 3.
10. P.C. Uden, American Chemical Society, and American Chemical Society, Eds., *Element-specific chromatographic detection by atomic emission spectroscopy*. Washington, DC: American Chemical Society, **1992**.
11. A.T. Zander and G.M. Hieftje, *Applied Spectroscopy*, **1981**, *35*, 357.
12. K.J. Jankowski and E. Reszke, *Microwave induced plasma analytical spectrometry*. Cambridge: Royal Society of Chemistry, **2010**.
13. D. Beauchemin, J.C. Yves Le Blanc, G.R. Peters, and A.T. Persaud, *Analytical Chemistry*, **1994**, *66*, 462.
14. J.A.C. Broekaert and E. Hywel Evans, "Atomic Spectroscopy," in *Ullmann's Encyclopedia of Industrial Chemistry*, Wiley-VCH Verlag GmbH & Co. KGaA, Ed. Weinheim, Germany: Wiley-VCH Verlag GmbH & Co. KGaA, **2003**.

15. J.A.C. Broekaert, "Plasma optical emission and mass spectrometry," in *Determination of Trace Elements*, Z.B. Alfassi, Ed. Weinheim, Germany: Wiley-VCH Verlag GmbH, **1994**, pp. 191–251.
16. J.A.C. Broekaert, N. Bings, C. Prokisch, and M. Seelig, *Spectrochimica Acta Part B Atomic Spectroscopy*, **1998**, 53, 331.
17. C. Yang, Z. Zhuang, Y. Tu, P. Yang, and X. Wang, "*Spectrochimica Acta Part B Atomic Spectroscopy*, **1998**, 53, 1427.
18. U. Engel, A. M. Bilgiç, O. Haase, E. Voges, and J.A. Broekaert, *Analytical Chemistry*, **2000**, 72, 193.
19. N. Ozbek and S. Akman, *LWT - Food Science Technology*, **2015**, 61, 532.
20. N. Ozbek and S. Akman, *Food Chemistry*, **2016**, 192, 295.
21. N. Ozbek and S. Akman, *Food Chemistry*, **2016**, 200, 245.
22. Y. Zhao *et al.*, *Spectrochimica Acta Part B Atomic Spectroscopy*, **2015**, 112, 6.
23. Y. Lu, F. Zhu, J. Chen, H. Gan, and Y. Guo, *Environmental Monitoring and Assessment*, **2007**, 134, 429.
24. J.W. Doran and Soil Science Society of America, Eds., *Defining soil quality for a sustainable environment: proceedings of a symposium sponsored by Divisions S-3, S-6, and S-2 of the Soil Science Society of America, Division A-5 of the American Society of Agronomy, and the North Central Region Committee on Soil Organic Matter (NCR-59) in Minneapolis, MN, 4-5 November 1992*. Madison, Wis: SSSA : American Society of Agronomy, **1994**.
25. C. Trasar-Cepeda, C. Leirs, F. Gil-Sotres, and S. Seoane, *Biology and Fertility of Soils*, **1997**, 26, 100.
26. G. Várallyay, *Cereal Research Communication*, **2007**, 35, 1277.
27. G. Várallyay, *Agrokém. És Talajt.*, **2006**, 55, 9.
28. G.D. Bending, C. Putland, F. Rayns, *Biology and Fertility of Soils*, **2000**, 31, 78.
29. Z. Györi and J. Prokisch, *Journal of Agricultural and Food Chem.*, **1999**, 47, 2751.
30. M.A. Elbagermi, H.G.M. Edwards, and A.I. Alajtal, *International Journal of Analytical Chemistry*, **2013**, 1.
31. E. Simon *et al.*, *Ecological Indicators*, **2016**, 60, 258.
32. G. Tyler, *Forest Ecology and Management*, **2005**, 206, 167.
33. T.-B. Chen *et al.*, *Chemosphere*, **2005**, 60, 542.
34. R. Ballesta, P. Bueno, J. Rubi, R. Giménez, *Open Geosciences*, **2010**, 2, 441.
35. I. Massas, C. Ehaliotis, S. Gerontidis, and E. Sarris, *Environmental Monitoring and Assessment*, **2009**, 151, 105.
36. O. Morton-Bermea, E. Hernández-Álvarez, G. González-Hernández, F. Romero, R. Lozano, and L. E. Beramendi-Orosco, *Journal of Geochemical Exploration*, **2009**, 101, 218.
37. M. Imperato, P. Adamo, D. Naimo, M. Arienzo, D. Stanzione, and P. Violante, *Environmental Pollution*, **2003**, 124, 247.
38. Z.A. Begum, I.M.M. Rahman, Y. Tate, H. Sawai, T. Maki, and H. Hasegawa, *Chemosphere*, **2012**, 87, 1161.

COMPUTATIONAL INVESTIGATION OF SPECTROSCOPIC PARAMETERS IN PUTATIVE SECONDARY STRUCTURE ELEMENTS FOR POLYLACTIC ACID AND COMPARISON WITH EXPERIMENT

IZABELLA IRSAI^a, ALEXANDRU LUPAN^a, CORNELIA MAJDIK^a,
RADU SILAGHI-DUMITRESCU^{a*}

ABSTRACT. Putative elements of secondary, tertiary and quaternary structure were examined for polylactic acid chains, attempting a parallel with secondary structure elements known from protein biology and also attempting an estimate, based on accurate atomic-level calculations, of interaction energies between polylactic acid chains. Spectroscopic parameters were predicted for all types of structure examined, in an attempt to aid our on-going efforts in synthesis and characterization of polylactic acid variants.

Keywords: *polylactic acid, secondary structure, NMR, EPR, DFT, semiempirical*

INTRODUCTION

Poly(lactic acid) (PLA) as a biodegradable polymer has a tremendous potential in medical, pharmacological and environmental applications [1-4]. It degrades to nontoxic lactic acid which is naturally present in human body.

PLA homopolymer can crystallize in three polymorphs: α [5-9], β [8,10] and γ [7, 12]. The crystal structures have been studied by X-ray method, the experiments show the presence of 10_3 and 3_1 helical chains of molecules [6,11].

The equimolecular mixture of poly(L-lactic acid) (PLLA) and poly(D-lactic acid) (PDLA) enantiomers has another crystal modification known as the sc-form with 3_1 helices [13-19].

^a Babeş-Bolyai University, Faculty of Chemistry and Chemical Engineering, 11, Arany Janos Street, RO-4000228 Cluj-Napoca, Romania

* Corresponding author: rsilaghi@chem.ubbcluj.ro

The crystal structures were also analyzed by computational chemistry. The poly(lactic acid) polymorphs were studied by rotational isomeric state models [20, 21], molecular dynamics [9, 10], Monte Carlo models [21,22], molecular mechanics [9] and quantum chemical [23-25] simulations. It was found that neither a pre 10_3 nor 3_1 helix could fit the experimental data perfectly, suggesting a certain degree of disorder in the structure.

RESULTS AND DISCUSSION

Four secondary-types structure were optimized – helical structures (α , π , 10_3) and β -sheet – employing molecular mechanics, semiempirical, ab initio and density functional methods. The highest-level method (DFT/M062x) denotes that the α , π and 10_3 structures have very similar energies, with π slightly favored by values, this in a contrast with results obtained with less accurate semiempirical and empirical methods, which predict larger differences and other structures as favorites.

Figure 1 shows optimized geometries for models of polylactic acid (PLA) employed in the present study. Decameric structures of L-lactic acid (PLLA) as well as of alternating D,L monomers (PDLLA) were employed. Details of these structures and their relative energies are described elsewhere. The energy in the case of PLLA are generally smaller than in the case of PDLLA, suggesting that such structures are more stable.

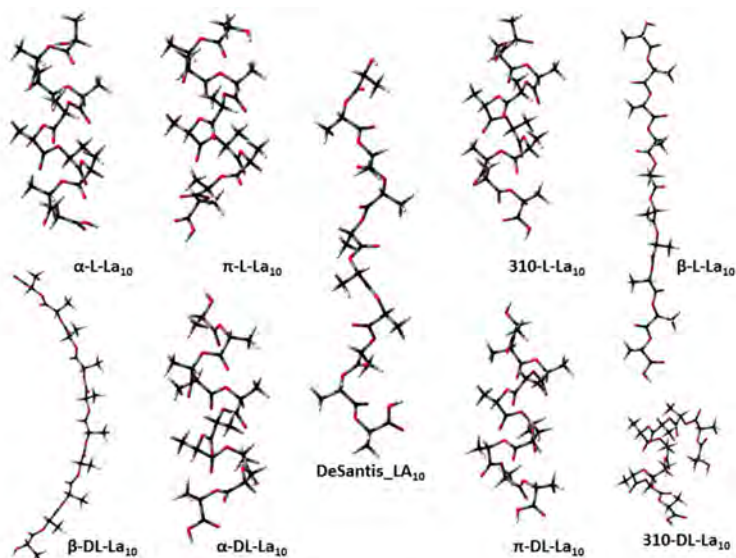


Figure 1. Graphical representation of poly(lactic acid) geometries optimized by DFT

The vibrational frequencies were computed for these optimized structures. In addition it was calculated the vibrational frequencies of the polylactic structure described by DeSantis.

The IR spectra shows characteristic bands mainly due to methylene and carboxylic C=O bonds. A repeat unit of PLA consists of three skeletal bonds: C-O, O-C $_{\alpha}$, C $_{\alpha}$ -C. For PLA the bands are assigned due to backbone bond stretching (C-O, O-C $_{\alpha}$, C-C $_{\alpha}$), backbone bond angle bending (O-C-C $_{\alpha}$, C-O-C $_{\alpha}$, O-C $_{\alpha}$ -C), for the side branches the bending (O-C $_{\alpha}$ -C $_{\beta}$, C-C $_{\alpha}$ -C $_{\beta}$, C $_{\alpha}$ -C=O) and stretching (C $_{\alpha}$ -C $_{\beta}$, C=O).

Figure 2 shows the IR spectrum of polylactic acid prepared as described in the Methods section. It can be seen the bands of C=O stretching (1751,20 cm $^{-1}$), C-OC stretching (1117,42 cm $^{-1}$) and CH bending and C-OC stretching (1064,37 cm $^{-1}$).

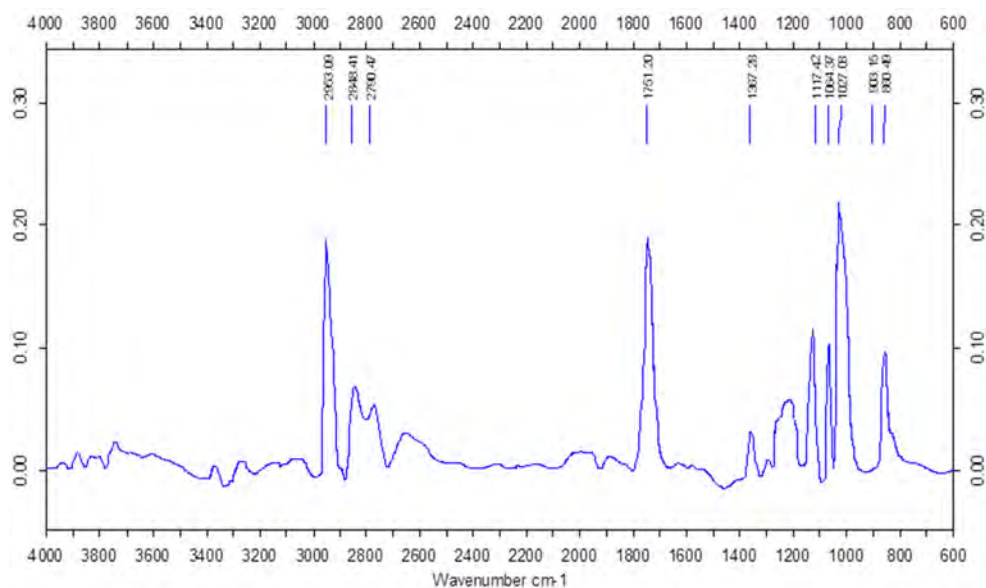


Figure 2. IR spectrum of poly(L-lactic acid) (cf. Materials and Methods)

Figure 3 shows computed IR spectra for the five secondary structure elements considered in the present work. The intensity of IR vibrations depend on the structure of the poly(lactic acid).

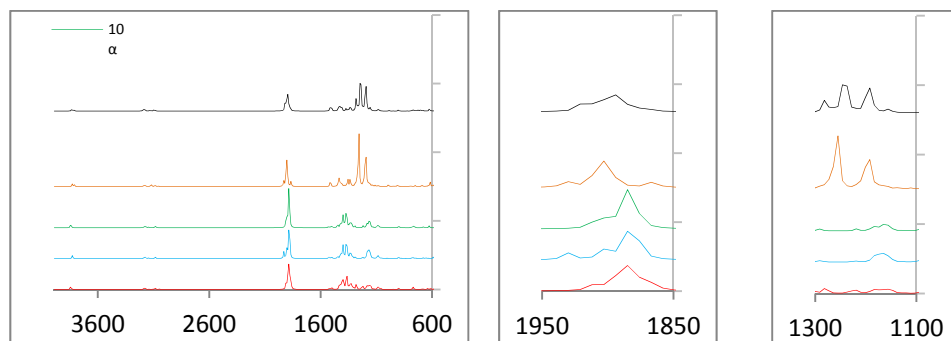


Figure 3. IR spectra of PLLA (M062x/6-31G**):(a) full spectrum; (b) carbonyl stretching region; (c) backbone stretching region

The IR spectra of the five structures show the same number of bands. The solvation does not involve any additional band.

The bands below 225 cm^{-1} are mainly due to the skeletal torsion. The $225\text{-}925\text{ cm}^{-1}$ region bands are assigned due to the bending of the side branches. There are no significant intensities.

The CH_3 is responsible for the appearance of the band in the $925\text{-}1110\text{ cm}^{-1}$ region due to the rocking vibrations. The solvation increases the intensities in the case of the three helical structures.

The C-CH_3 and C-OC stretching cause the presence of bands in the $1124\text{-}1213\text{ cm}^{-1}$ backbone stretching region. The intensities of the bands corresponding to C-CH_3 stretch are medium in the case of the helical structures, the water double these values. The β -sheet and the structure described by DeSantis provide weak bands. C-OC stretching bands are shown in $1151\text{-}1217\text{ cm}^{-1}$ region. Assignment of the β -sheet is the most intensive, six times higher than the others. The solvation increases the intensity further. The structure described by DeSantis has a strong band in this region.

In the $1215\text{-}1412\text{ cm}^{-1}$ region it can be seen bands assigned to CH , CH_3 bending and C-O-C stretching. The intensity of the CH bending and C-O-C stretching in the case of β -sheet and the structure described by DeSantis are very strong in contrast with the helical structure. These are the highest intensity bands in the entire spectrum. The water does not influence these intensities. The CH bending intensities are roughly the same with the exception of structure described by DeSantis. The solvation increases the

intensities in the case of the helical structures. A different medium band appear in this region due to the CH bending and CH₃ scissoring. It is worth noting the assignments in the 1407-1437 cm⁻¹ region. In this interval appear the bands due to CH₃ scissoring vibrations. In the case of the three helical structures are not significant intensities, but in the case of β -sheet the intensity is notable.

IR spectra of the PLLA in the range of 1865-1932 cm⁻¹ appear to be distinct for each of the five conformations. There is not much difference between the C=O stretching intensities calculated by DFT/M062x/6-31G** method. In turn the solvation increases the intensities in all five structures. The five conformers exhibit single absorption bands, spaced by about 9 and 18 cm⁻¹ from each other.

The CH stretching, the symmetric and asymmetric stretching of CH₃ result the appearance of weak bands in the 3050-3191 cm⁻¹ CH spectral region. It can be seen that the stretching frequencies are higher than the corresponding bending frequencies.

The calculated frequencies (cm⁻¹) and peak band assignment for the helical structures and β -sheet of PLLA are shown in tables 1-4.

In order to demonstrate that the chain conformation changes the interval of IR frequencies it was calculated the IR spectra of PDLLA and then compared to experimental data. Figure 4. shows the IR spectrum of PDLLA. The spectrum represent the bands of CH bending and C-OC stretching (1088 cm⁻¹), C-OC stretching (1188 cm⁻¹), C=O stretching (1752 cm⁻¹), CH₃ symmetric stretching (2945 cm⁻¹), CH₃ asymmetric stretching (2997 cm⁻¹) and OH stretching (3737 cm⁻¹).

In the IR spectra of PDLLA it can be seen the same bands as in the case of PLLA. The bands below 900 cm⁻¹ represent weak intensities. The CH₃ rocking and C-CH₃ stretching band intensities decrease slightly compared to PLLA. The C-OC stretching's bands appear at lower values (1146-1215 cm⁻¹) than in the case of PLLA. The intensities of the α helix and the β -sheet increase significantly. The calculated intensity of assignment of β -sheet is bigger in vacuum than in the solvated model.

The CH bending and C-OC stretching bands have equivalent values in the 1204-1325 cm⁻¹ interval, but bigger than the PLLA's one; the β -sheet and the structure described by DeSantis bands' intensities are 5-8 higher than in the case of the helices. It was observed that intensities of β -sheet in vacuum and solvation show outstanding values over the others, but these values are much smaller than in the case of PLLA.

Table 1. Peak band assignments for α -L-LA₁₀

α -L-LA ₁₀				
M062X 6-31G**		M062X 6-31G** water		Assignment
$\nu(\text{cm}^{-1})$	Intensity	$\nu(\text{cm}^{-1})$	Intensity	
18-224	0-6	13-216	0-9	skeletal torsion
233-296	0-6	224-266	0-12	CH ₃ rocking
302-399	0-48	299-394	0-73	CH ₃ wagging
402	147	399	216	OH (free) bending
407-411	32-59	401-405	32-88	CH ₃ wagging
413	63	406	88	OH (free) bending
416-558	1-18	409-592	0-148	CCO bending
627	91	631	116	OH (COOH) bending
663-789	1-34	663-787	1-38	C=O bending
848	7	841	11	C-CO (carboxyl) stretching
879-909	1-31	880-908	2-37	CH ₃ bending + COC bending
925-1105	1-107	924-1096	1-238	CH ₃ rocking
1127-1164	13-105	1120-1155	11-220	C-CH ₃ stretching
1167-1189	5-82	1158-1182	2-127	C-OC stretching
1218-1331	1-118	1217-1330	31-228	CH bending + C-OC stretching
1336-1373	1-328	1331-1366	13-1022	CH bending
1376-1406	10-287	1367-1402	17-303	CH bending + CH ₃ scissoring
1417-1427	2-53	1409-1421	3-65	CH ₃ scissoring
1447	19	1434	104	CH ₃ twisting (COOH end)
1448	159	1439	148	CH ₃ twisting (OH end)
1494-1532	1-19	1483-1516	3-22	CH ₃ twisting
1876-1909	30-947	1854-1885	72-1580	C=O stretching
3074-3094	7-10	3078-3089	9-18	CH ₃ sym stretching
3110-3153	1-9	3140-3152	2-15	CH stretching
3162-3196	1-16	3164-3196	1-25	CH ₃ asym stretching
3839	61	3817	155	OH (free) stretching
3846	94	3820	96	OH (COOH) stretching

The intensities of the bands appearing in the IR spectra due to CH bending are much smaller in all five structures than the corresponding bands of PLLA. The band caused by CH bending and CH₃ scissoring vibrations have the same intensity, with the exception the β -sheet.

The values of the CH₃ scissoring vibrations show tremendous growth relative to PLLA. In the C=O stretching region the bands are very strong, but they are slightly smaller than the corresponding values in PLLA. The

solvation increases importantly the intensities of CH bending and C-OC stretching and C=O stretching vibrations. In the 1815-1935 cm^{-1} region are the C=O stretching bands of PDLLA. The greatest intensity is shown by the β -sheet calculated in the solvated model.

Table 2. Peak band assignments for 3_{10} -L-LA₁₀

3_{10} -L-LA ₁₀				
M062X 6-31G**		M062X 6-31G** water		Assignment
$\nu(\text{cm}^{-1})$	Intensity	$\nu(\text{cm}^{-1})$	Intensity	
19-226	0-11	17-214	0-8	skeletal torsion
234-281	0-14	219-286	0-9	CH ₃ rocking
299-400	0-58	295-396	0-170	CH ₃ wagging
409	22	399	141	OH (free) bending
410-416	9-40	403-406	4-8	CH ₃ wagging
419	4	407	5	OH (free) bending
425-588	1-230	410-596	1-135	CCO bending
636	70	644	63	OH (COOH) bending
655-788	0-35	660-775	0-50	C=O bending
824	14	842	21	C-CO (carboxyl) stretching
878-910	1-45	891-909	1-37	CH ₃ bending + COC bending
925-1106	1-93	925-1099	0-217	CH ₃ rocking
1127-1164	15-106	1104-1161	41-232	C-CH ₃ stretching
1167-1189	5-146	1162-1185	3-213	C-OC stretching
1222-1331	3-89	1213-1329	8-369	CH bending + C-OC stretching
1332-1372	11-403	1331-1365	4-938	CH bending
1373-1403	6-182	1367-1402	11-311	CH bending + CH ₃ scissoring
1412-1426	3-88	1407-1421	12-80	CH ₃ scissoring
1445	28	1430	1430	CH ₃ twisting (COOH end)
1448	83	1445	120	CH ₃ twisting (OH end)
1495-1528	0-46	1486-1518	1-33	CH ₃ twisting
1875-1931	32-756	1852-1894	57-1074	C=O stretching
3078-3094	7-10	3071-3091	9-17	CH ₃ sym stretching
3115-3152	1-9	3120-3154	4-13	CH stretching
3171-3193	0-14	3159-3194	2-25	CH ₃ asym stretching
3826	62	3850	75	OH (free) stretching
3830	100	3807	159	OH (COOH) stretching

Table 3. Peak band assignments for π -L-LA₁₀

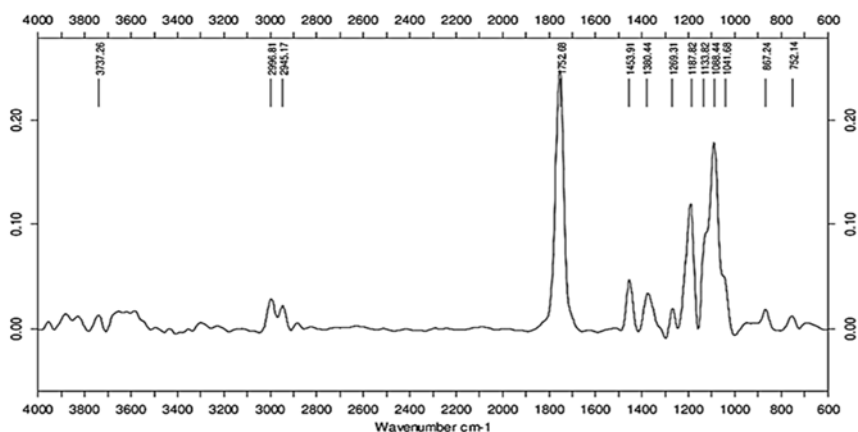
π -L-LA ₁₀				
M062X 6-31G**		M062X 6-31G** water		Assignment
$\nu(\text{cm}^{-1})$	Intensity	$\nu(\text{cm}^{-1})$	Intensity	
18-225	0-6	10-222	0-6	skeletal torsion
239-286	0-66	229-291	1-12	CH ₃ rocking
290-398	0-66	296-393	1-157	CH ₃ wagging
403	22	398	47	OH (free) bending
408-411	7-26	400-403	3-81	CH ₃ wagging
414	6	406	23	OH (free) bending
420-587	2-34	410-586	1-87	CCO bending
611	73	606	95	OH (COOH) bending
640-790	1-71	638-789	2-78	C=O bending
832	5	835	8	C-CO (carboxyl) stretching
894-915	0-47	890-911	12-70	CH ₃ bending + COC bending
928-1102	0-91	927-1097	2-240	CH ₃ rocking
1124-1165	8-85	1106-1157	45-233	C-CH ₃ stretching
1166-1217	9-150	1163-1186	8-127	C-OC stretching
1231-1330	11-192	1216-1334	22-320	CH bending + C-OC stretching
1334-1373	6-416	1335-1365	21-586	CH bending
1378-1411	6-222	1368-1407	6-291	CH bending + CH ₃ scissoring
1417-1433	6-104	1409-1426	9-104	CH ₃ scissoring
1436	53	1431	110	CH ₃ twisting (COOH end)
1451	3	1432	121	CH ₃ twisting (OH end)
1494-1530	2-20	1487-1513	0-29	CH ₃ twisting
1865-1910	34-999	1854-1878	56-1313	C=O stretching
3050-3090	6-32	3080-3098	9-21	CH ₃ sym stretching
3093-3154	0-11	3100-3151	2-15	CH stretching
3170-3191	1-12	3166-3201	1-24	CH ₃ asym stretching
3835	53	3854	72	OH (free) stretching
3846	98	3821	155	OH (COOH) stretching

CH₃ scissorings cause bands in 1409-1438 cm⁻¹ region. The intensities are medium, with the solvated β -sheet showing larger values.

The calculated frequencies (cm⁻¹) and peak band assignment for the helical structures and β -sheet of PDLLA are shown in tables 5-8.

Table 4. Peak band assignments for β -L-LA₁₀

β -L-LA ₁₀				
M062X 6-31G**		M062X 6-31G** water		Assignment
$\nu(\text{cm}^{-1})$	Intensity	$\nu(\text{cm}^{-1})$	Intensity	
5-202	0-31	5-203	0-36	skeletal torsion
220-313	0-18	208-301	0-145	CH ₃ rocking
317	65	314	8	OH (free) bending
327-402	0-18	329-397	1-26	CH ₃ wagging
421-579	0-38	416-578	0-62	CCO bending
587	79	593	102	OH (COOH) bending
602-801	0-40	601-799	2-134	C=O bending
844	13	844	14	C-CO (carboxyl) stretching
896-912	1-22	894-909	2-36	CH ₃ + COC bending
932-1110	0-54	928-1106	0-49	CH ₃ rocking
1130-1145	1-20	1124-1143	0-47	C-CH ₃ stretching
1157-1213	23-970	1151-1187	3-2171	C-OC stretching
1215-1290	4-3164	1213-1286	3-3093	CH bending + C-OC stretching
1318-1370	1-378	1316-1366	1-341	CH bending
1375-1412	1-83	1369-1407	2-54	CH bending + CH ₃ scissoring
1414-1437	4-332	1408-1433	8-455	CH ₃ scissoring
1447	76	1444	109	CH ₃ twisting (COOH end)
1468	5	1459	9	CH ₃ twisting (OH end)
1508-1518	5-55	1495-1509	2-75	CH ₃ twisting
1865-1932	9-563	1850-1898	4-1293	C=O stretching
3058-3095	5-23	3076-3104	8-22	CH ₃ sym stretching
3117-3130	5-22	3125-3134	8-16	CH stretching
3169-3196	3-14	3163-3196	7-25	CH ₃ asym stretching
3829	112	3819	103	OH (free) stretching
3810	81	3806	169	OH (COOH) stretching


Figure 4. IR spectrum of poly(DL-lactic acid).

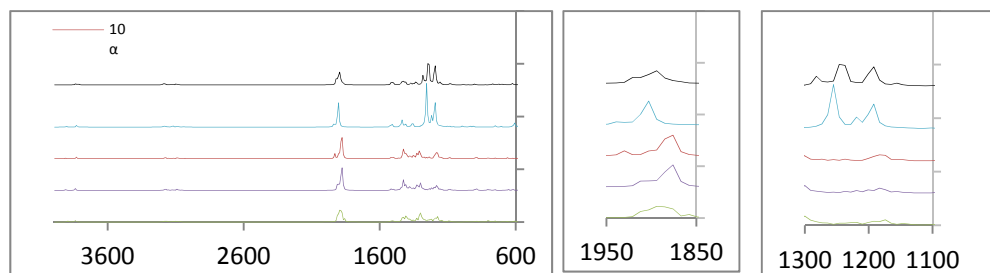


Figure 5. IR spectra of PDLLA (M062x/6-31G^{**}):(a) full spectrum; (b) carbonyl stretching region; (c) backbone stretching region

Table 5. Peak band assignments for α -DL-LA₁₀

α -DL-LA ₁₀				
M062X 6-31G ^{**}		M062X 6-31G ^{**} water		Assignment
$\nu(\text{cm}^{-1})$	Intensity	$\nu(\text{cm}^{-1})$	Intensity	
8-190	0-6	13-189	0-9	Skeletal torsion
199-241	0-44	201-237	0-5	CH ₃ rocking
242	56	238	1-5	OH (free) bending
246-290	1-7	241-294	0-18	CH ₃ rocking
302-408	0-26	298-422	1-156	CH ₃ wagging
428-580	1-47	427-567	2-96	CCO bending
585	41	576	63	OH (COOH) bending
593-807	0-57	603-802	1-87	C=O bending
819	22	821	37	C-CO (carboxyl) stretching
881-900	3-56	881-900	2-63	CH ₃ bending + COC bending
923-1092	1-35	923-1087	1-71	CH ₃ rocking
1139-1168	3-39	1130-1164	10-90	C-CH ₃ stretching
1175-1199	12-296	1167-1198	17-289	C-OC stretching
1232-1323	10-320	1225-1324	22-838	CH bending + C-OC stretching
1327-1380	7-163	1326-1374	17-258	CH bending
1383-1416	13-147	1378-1412	7-294	CH bending + CH ₃ scissoring
1419-1429	7-287	1414-1424	14-230	CH ₃ scissoring
1436	29	1437	62	CH ₃ twisting (COOH end)
1464	31	1451	40	CH ₃ twisting (OH end)
1492-1528	0-35	1481-1515	1-30	CH ₃ twisting
1871-1930	42-875	1854-1888	127-1047	C=O stretching
3039	28	3029	40	CH stretching
3073-3101	3-17	3082-3102	4-20	CH ₃ sym stretching
3111-3137	1-13	3115-3150	5-11	CH stretching
3153-3213	1-26	3167-3209	2-25	CH ₃ asym stretching
3907	48	3882	78	OH (free) stretching
3830	103	3809	160	OH (COOH) stretching

Table 6. Peak band assignments for 10₃-DL-LA₁₀

10 ₃ -DL-LA ₁₀				
M062X 6-31G**		M062X 6-31G** water		Assignment
v(cm ⁻¹)	Intensity	v(cm ⁻¹)	Intensity	
15-203	0-6	23-184	0-8	Skeletal torsion
211-248	0-73	191-227	0-3	CH ₃ rocking
249	0-6	23-184	0-8	OH (free) bending
252-292	1-5	236-291	1-10	CH ₃ rocking
295-420	0-17	298-420	2-192	CH ₃ wagging
428-572	2-39	431-560	3-105	CCO bending
581	10	564	28	OH (COOH) bending
604-808	0-76	601-798	0-141	C=O bending
826	10	814	21	C-CO (carboxyl) stretching
882-903	2-43	867-889	1-135	CH ₃ bending + COC bending
924-1093	1-28	911-1080	1-123	CH ₃ rocking
1138-1171	1-40	1111-1141	31-258	C-CH ₃ stretching
1174-1202	13-120	1146-1177	10-264	C-OC stretching
1218-1325	28-455	1204-1313	62-1119	CH bending + C-OC stretching
1330-1384	7-203	1316-1368	11-286	CH bending
1385-1419	11-139	1369-1407	4-310	CH bending + CH ₃ scissoring
1421-1429	7-248	1410-1418	13-40	CH ₃ scissoring
1443	115	1428	66	CH ₃ twisting (COOH end)
1464	37	1444	28	CH ₃ twisting (OH end)
1496-1533	0-26	1486-1513	6-20	CH ₃ twisting
1871-1910	62-672	1815-1840	31-1034	C=O stretching
3052	26	3045	34	CH stretching
3073-3096	3-21	3071-3097	8-15	CH ₃ sym stretching
3108-3141	2-8	3117-3155	2-22	CH stretching
3154-3215	0-25	3158-3196	1-22	CH ₃ asym stretching
3839	104	3764	159	OH (COOH) stretching
3907	50	3854	76	OH (free) stretching

Comparing the calculated data with the experimental data it can be seen that the calculated frequency values are bigger than the experimental values.

Table 7. Peak band assignments for π -DL-LA₁₀

π -DL-LA ₁₀				
M062X 6-31G**		M062X 6-31G** water		Assignment
$\nu(\text{cm}^{-1})$	Intensity	$\nu(\text{cm}^{-1})$	Intensity	
15-200	0-5	14-186	0-10	Skeletal torsion
202-247	0-3	192-236	0-7	CH ₃ rocking
249	3	240	4	OH (free) bending
253-290	1-53	242-296	0-21	CH ₃ rocking
304-405	1-26	298-409	1-97	CH ₃ wagging
437-565	3-36	410-568	2-59	CCO bending
585	11	572	15	OH (COOH) bending
588-805	1-72	596-803	1-141	C=O bending
832	9	825	48	C-CO stretching
879-903	2-25	857-902	0-43	CH ₃ bending + COC bending
923-1099	1-32	923-1087	1-96	CH ₃ rocking
1134-1169	4-59	1125-1163	11-144	C-CH ₃ stretching
1171-1199	31-144	1167-1196	36-185	C-OC stretching
1221-1323	20-433	1209-1323	24-1048	CH bending+ C-OC stretching
1329-1379	6-177	1331-1372	11-213	CH bending
1386-1417	14-209	1377-1412	12-178	CH bending + CH ₃ scissoring
1421-1438	1161-101	1413-1429	6-236	CH ₃ scissoring
1440	40	1437	106	CH ₃ twisting (COOH end)
1466	18	1454	33	CH ₃ twisting (OH end)
1488-1526	3-20	1482-1516	2-32	CH ₃ twisting
1856-1910	29-531	1854-1881	87-886	C=O stretching
3066	12	3031	40	CH stretching
3084-3102	3-15	3081-3101	4-19	CH ₃ sym stretching
3109-3154	2-9	3118-3153	5-14	CH stretching
3163-3210	1-29	3167-3208	2-22	CH ₃ asym stretching
3893	51	3882	79	OH (free) stretching
3836	102	3815	156	OH (COOH) stretching

Table 8. Peak band assignments for β -DL-LA₁₀

β -DL-LA ₁₀				
M062X 6-31G**		M062X 6-31G** water		Assignment
$\nu(\text{cm}^{-1})$	Intensity	$\nu(\text{cm}^{-1})$	Intensity	
4-197	0-47	5-194	0-41	Skeletal torsion
212-244	0-7	208-240	0-4	CH ₃ rocking
248	23	244	2	OH (free) bending
256-318	1-11	249-316	0-161	CH ₃ rocking
329-389	0-16	320-384	1-22	CH ₃ wagging
396-600	0-71	390-602	0-102	CCO bending
607	205	615	24	OH (COOH) bending
613-808	1-45	616-803	1-224	C=O bending
844	11	846	14	C-CO (carboxyl) stretching
896-912	2-43	891-908	1-29	CH ₃ bending + COC bending
931-1105	1-46	926-1104	1-93	CH ₃ rocking
1126-1146	1-24	1121-1140	2-32	C-CH ₃ stretching
1152-1215	9-1571	1147-1201	5-1311	C-OC stretching
1217-1286	1-2570	1211-1283	3-2270	CH bending + C-OC stretching
1295-1367	7-166	1301-1363	13-150	CH bending
1367-1411	1-102	1365-1406	0-80	CH bending + CH ₃ scissoring
1412-1435	1-254	1409-1435	1-403	CH ₃ scissoring
1445	88	1449	102	CH ₃ twisting (COOH end)
1454	37	1452	55	CH ₃ twisting (OH end)
1507-1523	3-37	1495-1516	6-57	CH ₃ twisting
1900-1935	24-888	1870-1901	5-2423	C=O stretching
3042	28	3065	34	CH stretching
3075-3092	5-15	3077-3094	8-321	CH ₃ sym stretching
3114-3125	9-13	3128-3137	5-27	CH stretching
3156-3198	0-20	3162-3199	7-23	CH ₃ asym stretching
3827	110	3797	170	OH (COOH) stretching
3903	39	3887	81	OH (free) stretching

NMR

Another important tool to characterize the structure of the polymer is the NMR spectroscopy. It was used ¹H NMR and ¹³C NMR spectroscopy. In the ¹H NMR spectra the determined chemical shifts correspond to CH and CH₃ resonance. CO, CH₃ and CH resonance are found in ¹³C NMR spectra. The ¹H NMR spectra of the PDLLA obtained by polycondensation of DL-lactic acid is shown in figure 6. The NMR analysis of poly(lactic acid) were found

considerably improved by recording spectra in DMSO-d₆ instead of CDCl₃ [27]. The most intensive signals were those located at 1.45 and 4.93 respectively 1.46 and 5.16 ppm which correspond to CH and CH₃ resonance in PLLA respectively PDLLA.

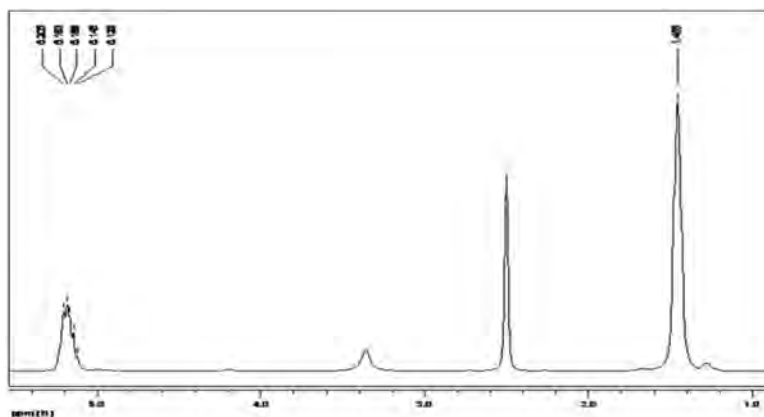


Figure 6. ¹H-NMR spectrum of PDLLA.

The simulated ¹H NMR spectrum of PLLA is shown in figure 7.

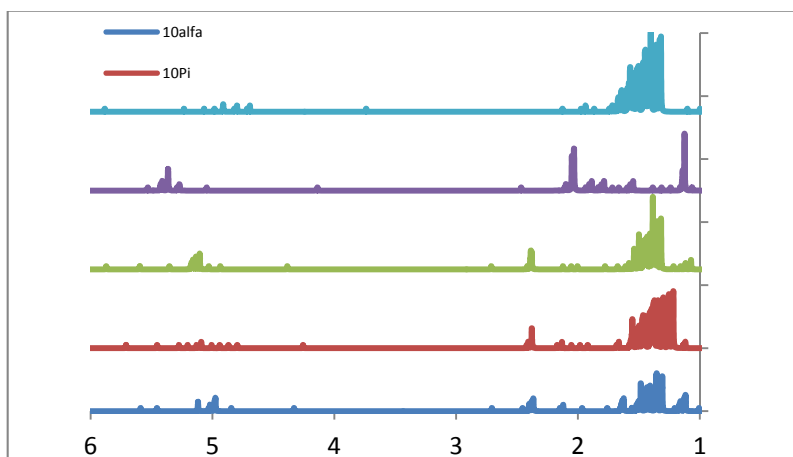


Figure 7. ¹H NMR spectra of PLLA (M062x/6-31G**).

The shifts of ^{13}C NMR spectrum of the four secondary-type structure of PLLA calculated by DFT/M062x/6-31G** method are larger than those calculated in solvated models (Table 9.). The ^1H NMR chemical shifts of PLLA are not always smaller in solution (Table 10.). Taking into account all five NMR signals covered by these two Tables, the β and π structures appear to generally yield the closest values to the experiment.

Table 9. Computed and experimental ^{13}C NMR Chemical shifts (δ , in ppm) of CO, CH and CH_3 of PLLA in vacuum (v) and water (w), respectively

PLLA	α		π		10_3		β		Exp.
	v	w	v	w	v	w	v	w	
δ (CO)	178	175	178	175	177	175	175	172	172
δ (CH)	72	68	72	68	72	68	72	67	66
δ (CH_3)	19	13	19	13	18	13	19	14	17

Table 10. Computed and experimental ^1H NMR Chemical shifts (δ , in ppm) of CH and CH_3 of PLLA in vacuum (v) and water (w), respectively

PLLA	α		π		10_3		β		Exp.
	v	w	v	w	v	w	v	w	
δ (CH)	5.2	5.1	5.1	5.1	5.2	5.1	5.3	5.5	4.9
δ (CH_3)	1.7	1.7	1.7	1.6	1.7	1.7	1.7	1.6	1.5

Figure 8 shows the calculated ^1H NMR spectrum of PDLLA.

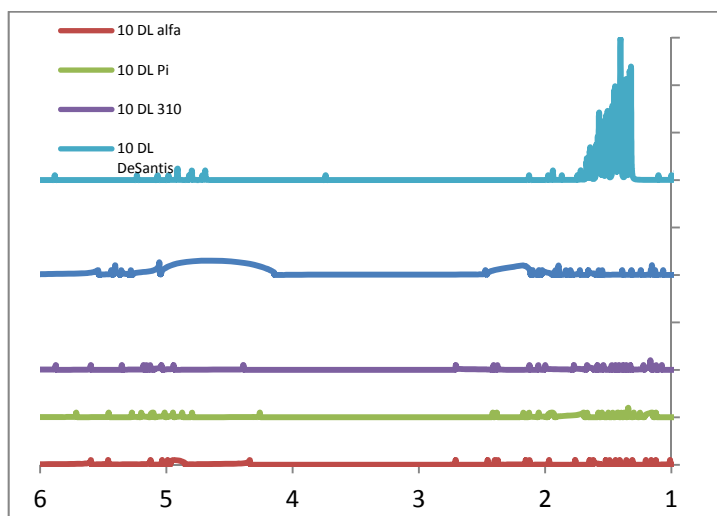


Figure 8. ^1H NMR spectra of PDLLA (M062x/6-31G**).

Same as in the case of PLLA the chemical shifts of ^{13}C NMR spectrum of PDDLA show smaller values in solvated model (Table 11.). The ^1H NMR shifts due to CH resonance are bigger in all four structures (Table 12.).

Table 11. ^{13}C NMR Chemical shifts (δ , in ppm) of CO, CH and CH_3 of PDDLA in vacuum (v) and water (w), respectively

PDDLA	α		π		10_3		β		Exp.
	v	w	v	w	v	w	v	w	
δ (CO)	177	174	177	174	178	176	175	172	169
δ (CH)	73	68	73	69	73	67	71	67	69
δ (CH_3)	18	13	18	13	18	13	19	14	16

Table 12. ^1H NMR Chemical shifts (δ , in ppm) of CH and CH_3 of PDDLA in vacuum (v) and water (w), respectively

PDDLA	α		π		10_3		β		Exp.
	v	w	v	w	v	w	v	w	
δ (CH)	5.0	5.1	5.1	5.1	5.1	5.1	5.4	5.5	5.2
δ (CH_3)	1.7	1.7	1.6	1.6	1.7	1.6	1.5	1.6	1.5

The NMR spectra of PLA can give information about the stereochemistry of the composition. The CO chemical shifts are larger in the α , π and β forms of PLLA, while the CH_3 shifts are larger in the case of the three helical structures of PLLA. The chemical shifts of ^1H NMR spectra of PLLA show larger values in all cases except the CH shifts of β -sheet.

CONCLUSIONS

Geometry optimization performed on polylactic acid at different levels of DFT methods suggest that the most stable of the four structures is the π helix and the least stable is the β sheet.

The calculated chemical shifts of both ^{13}C NMR and ^1H NMR are slightly larger than the experimental one. The solvation reduces the value of the NMR chemical shifts.

The secondary structure of poly(lactic acid) cannot be conclusively clarified from the calculated IR and NMR spectra, suggesting either a need for using more appropriate computational methods or the occurrence of previously unconsidered elements of secondary structure, or the total lack thereof.

EXPERIMENTAL SECTION

Materials. Aqueous solutions of L-(+)-lactic acid from Sigma-Aldrich (80%), DL-lactic acid from Fluka (90%) were used. PLLA and PDLLA were synthesized by direct dehydropolycondensation. Lactic acid, toluene and 0.1% tin(II) 2-ethylhexanoate catalyst were mixed into a reaction vessel equipped with a Dean-Stark-type condenser, and heated to the refluxing temperature of the solvent. The reaction time was 20 h. The final product was dissolved in chloroform and precipitated in diethyl ether for purification. The polymer was then filtered out from diethyl ether and dried under vacuum.

Measurements. NMR spectra were recorded with a Bruker Avance 300 spectrometer at the following frequencies: ^1H , 300.13 MHz; ^{13}C , 75.47 MHz (reference TMS) with DMSO- d_6 as the solvent. IR spectra were recorded with a Vector 22 Bruker spectrometer by direct introduction method and a Jasco FT/IR Specord 600 spectrometer in KBr pills. The molecular weights were determined by MALDI-TOF MS (Matrix Assisted Laser Desorption Ionization) analysis with a Bruker BIFLEX IIITM spectrometer.

Molecular simulation. A vibrational analysis and NMR simulation has been carried out to analyze the secondary structure of poly(lactic acid) resulted from esterification of ten lactic acid units, hereafter referred to as LA₁₀. These models were built in the Hyperchem [28] software package using built-in options of the Editor module for creating helical structures as well as sheet. Spectroscopic parameters were predicted for helical (α , π , 103) and β -sheet structures, in an attempt to aid our on-going efforts in the synthesis and characterization of poly(lactic acid) variants.

The methods tested here include density functional (M062X/6-31G*, M062X/6-31G**, solvated M062X/6-31G**) applied with standard convergence criteria as defined in Gaussian 09 [29]. Spectral parameters were invoked using the commands Freq and NMR. In terms of the importance of solvation, this is estimated by comparing values computed in water (as a limit of very polar medium) and vacuum (as a limit of completely non-polar medium). Further detail on geometry optimizations and on relative energies of the structures are given elsewhere [30].

ACKNOWLEDGMENTS

This work was supported by CNCSIS-UEFISCDI, projects PNII – ID 312/2008 (RSD and AL), project Parteneriate 72152/2008 (to CM) and by a PhD scholarship from Contract POSDRU/88/1.5/S/60185 – “Innovative doctoral studies in a knowledge based society” (to II).

REFERENCES

1. R.A. Jain, *Biomaterials*, **2000**, 21, 2475.
2. A. Dev, N.S. Binulal, A. Anitha, S.V. Nair, T. Furuike, H. Tamura, R. Jayakumar, *Carbohydrate Polymers*, **2010**, 80, 833.
3. M.A. Ibrahim, A. Ismail, M.I. Fetou, A. Gopferich, *Journal of Controlled Release*, **2005**, 106, 241.
4. S. Fredenberg, M. Wahlgren, M. Reslow, A. Axelsson, *International Journal of Pharmaceutics*, **2011**, 415, 34.
5. T. Miyata, T. Masuko, *Polymer*, **1997**, 38, 4003.
6. J. Kobayashi, T. Asahi, M. Ichiki, A. Okikawa, H. Suzuki, T. Watanabe, E. Fukada, Y. Shikinami, *Journal of Applied Physics*, **1995**, 77, 2957.
7. W. Hoogsteen, A.R. Postema, A.J. Pennings, G.G ten Brinke, P. Zugenmaier, *Macromolecules*, **1990**, 23, 634.
8. S. Sasaki, T. Asakura, *Macromolecules*, **2003**, 36, 8385.
9. D. Brizzolara, H.J. Cantow, K. Diederichs, E. Keller, A.J. Domb, *Macromolecules*, **1996**, 29, 191.
10. C. Aleman, B. Lotz, J. Puiggali, *Macromolecules*, **2001**, 34, 4795.
11. P. De Santis, J. Kovacs, *Biopolymers*, **1968**, 6, 299.
12. J. Puiggali, Y. Ikada, H. Tsuji, L. Cartier, T. Okihara, B. Lotz, *Polymer*, **2000**, 41, 8921.
13. T. Okihara, M. Tsuji, A. Kawagushi, K.I. Katayama, H. Tsuji, S.H. Hyon, Y. Ikada, *Journal of Macromolecular Science Physics B*, **1991**, 30, 119.
14. L. Cartier, T. Okihara, Y. Ikada, H. Tsuji, J. Puiggali, B. Lotz, *Polymer*, **2000**, 41, 8909.
15. Y. Ikada, K. Jamshidi, H. Tsuji, S.H. Hyon, *Macromolecules*, **1987**, 20, 904.
16. H. Tsuji, *Macromolecular Bioscience*, **2005**, 5, 569.
17. H. Tsuji; Y. Ikada, *Polymer*, **1999**, 40, 6699.
18. H. Tsuji, I. Fukui, *Polymer*, 2003, 44, 2891.
19. D. Sawai, Y. Tsugane, M. Tamada, T. Kanamoto, M. Sungil, S.H. Hyon, *Journal Polymer Science, Part B: Polymer Physics*, **2007**, 45, 2632.
20. N. Rahman, T. Kawai, G. Matsuba, K. Nishida, T. Kanaya, H. Watanabe, H. Okamoto, M. Kato, A. Usuki, M. Matsuda, K. Nakajima, N. Honma, *Macromolecules*, **2009**, 42, 4739.
21. S. Kang, S.L. Hsu, H.D. Stidham, B.P. Smith, A. Leugers, X. Yang, *Macromolecules*, **2001**, 34, 4542.
22. K. Aou, S.L. Hsu, *Macromolecules*, **2006**, 39, 3337.
23. J. Blomqvist, L.O. Pietila, B. Mannfors, *Polymer*, **2001**, 42, 109.
24. J. Blomqvist, *Polymer*, **2001**, 42, 3515.
25. T.T. Lin, X.Y. Liu, C. He, *J. Phys. Chem. B*, **2010**, 114, 3133.
26. X. Yang, S. Kang, Y. Yang, K. Aou, S.L. Hsu, *Polymer*, **2004**, 45, 4241.
27. J.L. Espartero, I. Rashkov, S.M. Li, N. Manolova, M. Vert, *Macromolecules*, **1996**, 29, 3535.

28. Hyperchem. HyperChem(TM) Molecular Modelling System, Release 4.5 SGI, Hypercube; Hyperchem(TM) Molecular Modelling System, Release 5.01 for Windows, Hypercube, Inc. (1998)
29. M.J Frisch, G.W. Trucks, H.B. Schlegel, G.E. Scuseria, M.A. Robb, J.R. Cheeseman, J. Montgomery, A.T. Vreven, K.N. Kudin, J.C. Burant, J.M. Millam, S.S. Iyengar, J. Tomasi, V. Barone, B. Mennucci, M. Cossi, G. Scalmani, N. Rega, G.A. Petersson, H. Nakatsuji, M. Hada, M. Ehara, K. Toyota, R. Fukuda, J. Hasegawa, M. Ishida, T. Nakajima, Y. Honda, O. Kitao, H. Nakai, M. Klene, X. Li, J.E. Knox, H.P. Hratchian, J.B. Cross, V. Bakken, C. Adamo, J. Jaramillo, R. Gomperts, R.E. Stratmann, O. Yazyev, A.J. Austin, R. Cammi, C. Pomelli, J.W. Ochterski, P.Y. Ayala, K. Morokuma, G.A. Voth, P. Salvador, J.J. Dannenberg, V.G. Zakrzewski, S. Dapprich, A.D. Daniels, M.C. Strain, O. Farkas, D.K. Malick, A.D. Rabuck, K. Raghavachari, J.B. Foresman, J.V. Ortiz, Q. Cui, A.G. Baboul, S. Clifford, J. Cioslowski, B.B. Stefanov, G. Liu, A. Liashenko, P. Piskorz, I. Komaromi, R.L. Martin, D.J. Fox, T. Keith, M.A. Al-Laham, C.Y. Peng, A. Nanayakkara, M. Challacombe, P.M.W. Gill, B. Johnson, W. Chen, M.W. Wong, C. Gonzalez, J.A. Pople, Gaussian 09, Gaussian, Inc., Wallingford CT, 2004. (2009)
30. I. Irsai, C. Majdik, A. Lupan, R. Silaghi-Dumitrescu. *Journal of Mathematical Chemistry*, **2011**, 50(4), 703.